The Role of Peridotite and Serpentinite in the Deep Carbon Cycle

Constraints from Ophiolites and Exhumed Metamorphic Terranes

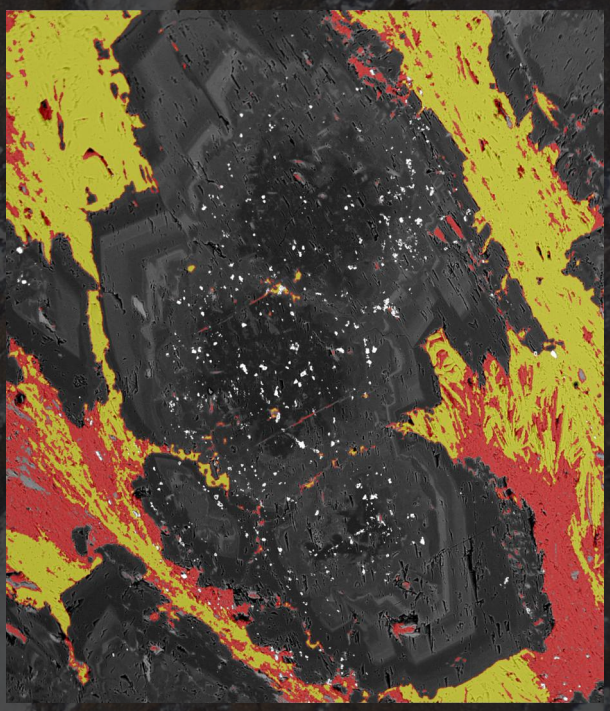

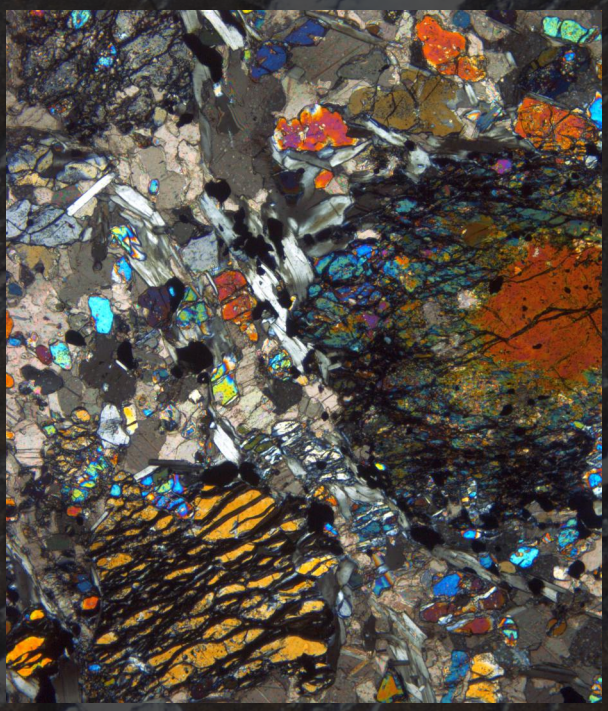

Manuel D. Menzel

CSIC
IACT INSTITUTO ANDALUZ DE CIENCIAS DE LA TIERRA
ugr Universidad de Granada
Programa Doctorado Ciencias de la Tierra

Tesis Doctoral, 2019

THE ROLE OF PERIDOTITE AND SERPENTINITE IN THE DEEP CARBON CYCLE

CONSTRAINTS FROM OPHIOLITES AND EXHUMED METAMORPHIC TERRANES

MANUEL D. MENZEL

Ph.D. Thesis – Tesis Doctoral

Memoria de Tesis Doctoral presentada por M.Sc. en Geología Manuel Menzel para optar al grado de Doctor por la Universidad de Granada

Esta Tesis Doctoral ha sido dirigida por el Dr. Carlos J. Garrido Marín, del Instituto Andaluz de Ciencias de la Tierra (CSIC-UGR), y el Dr. Vicente López Sánchez-Vizcaíno, del Departamento de Geología (Unidad asociada al CSIC), Universidad de Jaén.

En Granada, 28 de mayo de 2019

Editor: Universidad de Granada. Tesis Doctorales
Autor: Manuel Dominik Menzel
ISBN: 978-84-1306-275-4
URI: http://hdl.handle.net/10481/56594

Funding: Research presented in this Ph.D. thesis has been funded by the People Programme (Marie Curie Actions) of the European Union's Seventh Framework Programme FP7/2007-2013/ under REA grant agreement n°608001, in the frame of the Marie-Curie Initial Training Network ABYSS. I also acknowledge funding from the Spanish "Agencia Estatal de Investigación" (AEI) under grants no. CGL2016–75224–R, CGL2016–81085–R, and grant nº PCIN–2015–053. The "Junta de Andalucía" is also thanked for funding of research groups under grants nº RNM–131, RNM–374, and P12–RNM–3141. This research and the research infrastructure at the IACT have benefitted from (co)funding from the European Social Fund and the European Regional Development Fund.

Buy yourselves shoes,
Get away to the mountains,
Search the valleys, the deserts,
the shores of the sea,
and the deepest recesses of the earth,
watch and experiment without wearying.
In this way, and no other,
Will you arrive at a knowledge of things…
Peter Severinus, 1571

Abstract

Subduction of oceanic lithosphere is the only active flux of carbon from Earth's atmosphere-hydrosphere-crustal system reservoirs into the deep convecting mantle. Serpentinites in the mantle wedge of the forearc can sequester and store carbon derived from the subducting slab and exert an important control on the carbon mass balance in subduction zones. At subarc depths of subduction zones, devolatilization reactions and fluid-rock interaction mostly regulate the balance between the carbon returned by arc volcanism and that retained and transported by subducting slabs into the deep mantle. Dehydration of antigorite serpentinite at these depths releases a large amount of fluids that react with other slab lithologies, playing a decisive role in the modulation of the deep carbon fluxes.

The main aim of the present Ph.D. thesis is to improve our understanding of carbonation processes of serpentinized peridotite and the fate of serpentinite-hosted carbon during high-pressure metamorphism, in order to better constrain their role in the deep carbon cycle of subduction zones. To advance in this overall research goal, this Ph.D. thesis presents the results of two natural case studies of key processes of carbon transfer during fluid-rock interaction in subduction zones: (i) listvenites from the Baie Verte ophiolite (Newfoundland, Canada), a natural analogue for carbon storage in the forearc mantle of subduction zones by carbonation of peridotites; and (ii) meta-ophicarbonates from the Nevado-Filábride Complex (Spain), which provide unprecedented insights into the stability of carbonates during antigorite-serpentinite dehydration in a paleo-subduction terrane. The combination of field, (micro) structural, petrological and geochemical data with thermodynamic modelling sheds new light on the interaction of fluids with the hydrated mantle, which regulates the carbon mobility at forearc and subarc depths of subduction zones. By means of thermodynamic models of prograde and high-pressure infiltration-driven devolatilization reactions in serpentinite-hosted meta-carbonate rocks, this thesis further investigates the effects of electrolytic fluids and the role of open-system flux of serpentinite dehydration fluids on the fluid-mediated release of carbon in subduction zones.

The association of listvenite, soapstone, and carbonated antigorite-serpentinite in the Advocate Ophiolite Complex (Newfoundland) formed by a sequence of carbonation reactions of a partly serpentinized harzburgite precursor with CO_2-rich fluids. The field appearance, whole rock, and mineral compositions and microstructures are consistent with a continuous,

progressive carbonation reaction pathway at isothermal and isobaric conditions, and indicate that incipient carbonation occurred coeval with the prograde transformation of lizardite to antigorite at temperatures of about 280 – 420 °C. Variable incorporation of iron in magnesite growth rims reflects the consumption of magnetite, Fe-rich antigorite and Fe-poor talc, resulting in a concomitant rise in fluid oxygen fugacity during progressive carbonation. The structural position of the listvenites and their stable isotope composition indicate that they likely formed during obduction of supra-subduction zone oceanic crust onto the Laurentian passive margin, with CO_2-rich fluids emanating from metamorphism of partly subducted margin sediments into the overlying oceanic mantle lithosphere.

Meta-ophicarbonate lenses in the Milagrosa and Almirez ultramafic massifs of the Nevado-Filábride Complex (S-Spain) show a chemical composition and mineral assemblage in accordance with high-pressure subduction metamorphism of an oceanic, serpentinite-hosted ophicalcite protolith. Thermodynamic modelling and the occurrence of aragonite indicate that they reached the same peak metamorphic conditions as the host antigorite serpentinites and chlorite harzburgites, and experienced high fluid-fluxes produced by the breakdown of antigorite in serpentinite at Almirez. Despite the high capacity of antigorite dehydration fluids to mobilize carbon, the ophicarbonate retains high amounts of carbonate, suggesting limited fluid infiltration and that the fluid composition remained rock-buffered. Their preservation beyond the antigorite stability demonstrates that ophicarbonates can transfer carbon beyond sub-arc depths in any thermal subduction regime, with implications for the carbon balance between mantle, crust, and surface throughout Earth´s history.

Thermodynamic modelling shows that carbon loss during the prograde devolatilization of serpentinite-hosted meta-carbonate rocks to subarc depths of warm and cold subduction zones is negligible even accounting for electrolytic fluids. Models of infiltration-driven devolatilization of meta-ophicalcite and carbonate-talc rocks during serpentinite dehydration indicate that carbon release is accompanied by significant Ca loss, particularly at high pressures ($P > 3.5$ GPa). The carbon solubility in fluids equilibrated with meta-ophicalcite and carbonate–talc rocks is markedly higher than for pure aragonite due to open-system buffer reactions between carbonates, silicates, and electrolytic fluid. Mass balance calculations and parameterization of the P–T conditions of serpentinite dehydration in cold and warm subduction zones indicate that meta-ophicalcites can transport carbon into the deep mantle, while carbonate-talc rocks at the slab interface are most likely sources of carbon at subarc depths.

Extended abstract

Subduction of oceanic lithosphere is the only active flux of carbon from Earth's atmosphere-hydrosphere-crustal system reservoirs into the deep convecting mantle. Serpentinites in the mantle wedge of the forearc can sequester and store carbon derived from the subducting slab and exert an important control on the carbon mass balance in subduction zones. At subarc depths of subduction zones, devolatilization reactions and fluid-rock interaction mostly regulate the balance between the carbon returned by arc volcanism and that retained and transported by subducting slabs into the deep mantle. Dehydration of antigorite serpentinite at these depths releases a large amount of fluids that react with other slab lithologies, playing a decisive role in the modulation of the deep carbon fluxes.

The main aim of the present Ph.D. thesis is to improve our understanding of carbonation processes of serpentinized peridotite and the fate of serpentinite-hosted carbon during high-pressure metamorphism, in order to better constrain their role in the deep carbon cycle of subduction zones. To advance in this overall research goal, this Ph.D. thesis presents the results of two natural case studies of key processes of carbon transfer during fluid-rock interaction in subduction zones: (i) listvenites from the Baie Verte ophiolite (Newfoundland, Canada), a natural analogue for carbon storage in the forearc mantle of subduction zones by carbonation of peridotites; and (ii) meta-ophicarbonates from the Nevado-Filábride Complex (Spain), which provide unprecedented insights into the stability of carbonates during antigorite-serpentinite dehydration in a paleo-subduction terrane. The combination of field, (micro) structural, petrological and geochemical data with thermodynamic modelling sheds new light on the interaction of fluids with the hydrated mantle, which regulates the carbon mobility at forearc and subarc depths of subduction zones. By means of thermodynamic models of prograde and high-pressure infiltration-driven devolatilization reactions in serpentinite-hosted meta-carbonate rocks, this thesis further investigates the effects of electrolytic fluids and the role of open-system flux by serpentinite dehydration fluids on the fluid-mediated release of carbon in subduction zones.

In *a first chapter*, this thesis presents the microstructural and petrological record of carbonation of peridotite by CO_2-rich fluids in a forearc setting, as evidenced by the formation of listvenites in the Advocate ophiolite complex (Newfoundland, Canada). The mantle section of the Advocate ophiolite contains unique outcrops of listvenite (magnesite-

quartz), antigorite- and quartz-bearing talc-magnesite rock, and carbonated antigorite-serpentinite. This lithological sequence records the sequential carbonation of serpentinite by CO_2-rich hydrothermal fluids. High Cr and Ni contents and preservation of Cr-spinel with a composition similar to that of Atg-serpentinite (molar Mg/Mg+Fe = 0.50 – 0.65; Cr/Cr+Al = 0.50 – 0.70), show that the Advocate listvenite and talc-magnesite rocks formed by carbonation of variably serpentinized mantle harzburgite. Replacement of lizardite by magnesite coeval with the breakdown of lizardite to antigorite + brucite and the lack of prograde olivine and magnetite in antigorite serpentinite and talc-magnesite rocks constrain the temperature of carbonation between c. 280 °C and 420 °C. Thermodynamic modelling of carbonation of serpentinite at 300 ºC and 0.2 – 0.5 GPa accounts for the sequence of carbonated rocks in the Advocate complex. Phase relations and petrological observations indicate that the aqueous $a SiO_2$ and $a CO_2$ of the infiltrating CO_2-rich fluid were buffered at the Atg-Tlc-Mgs and Qtz-Tlc-Mgs pseudo-invariant points, forming dominantly three-phase rocks by variable extents of carbonation at these pseudo-invariant points. Listvenites formed at large fluid-rock ratio when quartz became saturated in the fluid and precipitated along magnesite grain boundaries and in variably sized tensional veins.

The whole rock Fe^{3+}/Fe_{total} ratio of the Advocate carbonate-bearing sequence decreases with increasing whole rock carbon content, from 0.65 – 0.80 in brucite-bearing antigorite serpentinite to 0.10 – 0.30 in talc-magnesite rocks and listvenite. The whole rock iron reduction is associated with an increase in the ferrous iron content of magnesite and the formation of hematite and goethite, indicating a concomitant increase of the fluid oxygen fugacity. The sequence of carbonation reactions is uniquely preserved in three main growth zones characteristic of listvenite magnesite: (i) an inner zone of magnetite-bearing, Fe-poor, Mn-bearing magnesite formed by carbonation of lizardite, brucite and olivine from Atg-serpentinite; (ii) an outer zone of Fe-rich magnesite formed by carbonation of antigorite and in equilibrium with Fe-poor talc; and (iii) an outermost rim of Fe-poor magnesite formed by carbonation of talc.

Carbonation of the Advocate serpentinized mantle harzburgite likely occurred in a supra-subduction upper plate ophiolite by fluxing of slab-derived, CO_2-rich fluids channelled along deep faults at the onset of accretion of the forearc basin (c. 300 ºC, < 0.5 GPa). The rather constant $\delta^{18}O$ (11.0 – 14.4 ‰ V-SMOW) and relatively low $\delta^{13}C$ (–8.9 to –5.0 ‰ V-PDB) of magnesite throughout the sequence of carbonated rocks in the Advocate complex is consistent with CO_2-rich fluids derived from decarbonation or dissolution of organic carbon-

and carbonate-bearing meta-sediments, such as those occurring in the underlying Birchy complex —the partially subducted continental margin of Laurentia. Carbonation of serpentinized oceanic or continental mantle lithosphere by reactive percolation of CO_2-rich fluids derived from the slab in forearc settings may represent a significant carbon reservoir for the deep carbon cycle.

In *a second chapter*, this thesis provides new insights into the petrology and phase relations of meta-ophicarbonates during subduction metamorphism. At subarc depths, the release of carbon from subducting slab lithologies is mostly controlled by fluid released by devolatilization reactions such as dehydration of antigorite (Atg-) serpentinite to prograde peridotite. This chapter investigates carbonate-silicate rocks hosted in Atg-serpentinite and prograde chlorite (Chl-) harzburgite in the Milagrosa and Almirez ultramafic massifs in the paleo-subducted Nevado-Filábride Complex (NFC, Betic Cordillera, S Spain). These massifs present a unique opportunity to study the stability of carbonate during subduction metamorphism at P–T conditions before and after the dehydration of Atg-serpentinite in a warm subduction setting.

In the Milagrosa massif, carbonate–silicate rocks occur as lenses of Ti-clinohumite-diopside-calcite marbles, diopside-dolomite marbles, and antigorite-diopside-dolomite rocks hosted in clinopyroxene-bearing Atg-serpentinite. In Almirez, carbonate-silicate rocks are hosted in Chl-harzburgite and show a high-grade assemblage composed of olivine, Ti-clinohumite, diopside, chlorite, dolomite, calcite, Cr-bearing magnetite, pentlandite, and rare aragonite inclusions. These NFC carbonate-silicate rocks have variable CaO and CO_2 contents at nearly constant Mg/Si ratio, and high Ni and Cr contents, indicating that their protoliths were variable mixtures of serpentine and Ca-carbonate (i.e. ophicarbonates). Thermodynamic modelling shows that the carbonate-silicate rocks attained peak metamorphic conditions similar to those of their host serpentinite (Milagrosa massif; 550 – 600 °C and 1.0 – 1.4 GPa) and Chl-harzburgite (Almirez massif; 1.7 – 1.9 GPa and 680 °C).

Microstructures, mineral chemistry, and phase relations indicate that the hybrid carbonate-silicate bulk rock compositions formed before prograde metamorphism, likely during seawater hydrothermal alteration, and subsequently underwent subduction metamorphism. In the $CaO–MgO–SiO_2$ ternary, these processes resulted in a compositional variability of NFC serpentinite-hosted carbonate-silicate rocks along the serpentinite–calcite mixing trend, similar to that observed in serpentinite-hosted carbonate-rocks in other paleo-subducted metamorphic terranes. Thermodynamic modelling using classical models of binary

H_2O–CO_2 fluids shows that the compositional variability along this binary determines the temperature of the main devolatilization reactions, the fluid composition, and the mineral assemblages of reaction products during prograde subduction metamorphism. Thermodynamic modelling considering electrolytic fluids reveals that H_2O and molecular CO_2 are the main fluid species and charged carbon-bearing species occur only in minor amounts in equilibrium with carbonate-silicate rocks in warm subduction settings. Consequently, accounting for electrolytic fluids at these conditions slightly increases the solubility of carbon in the fluids compared with predictions based on classical binary H_2O–CO_2 fluids, but does not affect the topology of phase relations in serpentinite-hosted carbonate-rocks.

Phase relations, mineral composition and assemblages of Milagrosa and Almirez (meta)-serpentinite-hosted carbonate-silicate rocks are consistent with local equilibrium between an infiltrating fluid and the bulk rock composition and indicate a limited role of infiltration-driven decarbonation. Our study shows natural evidence for the preservation of carbonates in serpentinite-hosted carbonate-silicate rocks beyond the Atg-serpentinite breakdown at subarc depths, demonstrating that carbon can be recycled into the deep mantle.

In *a third chapter*, this thesis investigates the effects of electrolytic fluid compositions and open-system flux of serpentinite dehydration fluids on fluid-mediated carbon release in subduction zones by means of thermodynamic models. Serpentinite-hosted carbonate rocks formed during the oceanic stage of subducting oceanic lithosphere (ophicalcite) and metasomatism at the subduction plate interface (hybrid carbonate–talc rocks) can be important sources of carbon at subarc depths. If hosted in the hydrated mantle lithosphere of the incoming slab, these carbonate-rocks may be preserved from the infiltration of fluids produced by prograde metamorphism of the overlying meta-sediments and the hydrated oceanic crust to subarc depths, where they are fluxed by fluids derived from dehydration of their host serpentinite. Because the dissolution of carbonate in aqueous fluids is enhanced at high P and T, fluid-mediated carbon release at subarc depth is critical to understand the global carbon balance and magnitude of carbon fluxes from the subducting plate into the deep mantle. This section of the thesis presents thermodynamic modelling — using the implementation of the DEW aqueous database in Perple_X — of prograde devolatilization reactions (*solids = fluid + solids*) and infiltration-driven devolatilization reactions (*external fluid + solids = fluid + solids*) of serpentinite-hosted carbonate rocks. In line with previous studies of prograde devolatilization of carbon-bearing oceanic crust, our models show that, in

warm and cold subductions zones, the solubility of carbon in fluids produced by subsolidus devolatilization reactions of meta-ophicalcite and carbonate-talc rocks is limited even considering metal ion complexes of electrolytic fluids. Therefore, serpentinite-hosted meta-carbonate rocks are likely to be preserved to subarc depths where they undergo infiltration-driven devolatilization by Atg-serpentinite dehydration fluids. At the P–T conditions of Atg-breakdown of cold to warm subduction zones, models of infiltration-driven devolatilization of meta-ophicalcite and carbonate-talc rocks indicate that carbon release is accompanied by significant Ca loss, particularly at high pressures (P > 3.5 GPa) due to the high activity of $CaHCO_3^+$ in the fluid. The carbon solubility in fluids equilibrated with meta-ophicalcite and carbonate–talc rocks is markedly higher than for pure aragonite due to open-system buffer reactions between carbonates, silicates, and fluid. Mass balance considerations combined with the parameterization of the P–T conditions of Atg-serpentinite dehydration as a function of the thermal parameter of subduction zones allow us to investigate the carbon loss caused by infiltration of serpentinite dehydration fluids. Unlike the dissolution of $CaCO_3$, the carbonate dissolution of serpentinite-hosted meta-carbonate rocks is highest at the slab surface of warm subduction zones and is lowest at Moho depths of cold subduction zones where Atg-serpentinite dehydration takes place at greater depths. The subduction of meta-ophicalcite —with thicknesses of up to 70 m observed in oceanic ophicalcite— will preserve carbonate beyond subarc depths, and will recycle carbonate-garnet-clinopyroxene-olivine rocks into the deep mantle even in hot subduction zones. On the other hand, infiltration-driven devolatilization of subducted carbonate-talc rocks is an efficient source of carbon at subarc depths where they readily transform to orthopyroxenite in most subduction zone regimes.

Keywords: deep carbon cycle, CO_2 sequestration, peridotite carbonation, listvenite, serpentinization, forearc, Advocate complex, ophicarbonate, subduction fluids, serpentinite dehydration, Nevado-Filábride Complex, electrolytic fluids, thermodynamic modelling, devolatilization reactions, fluid infiltration

Resumen extendido

La subducción de la litosfera oceánica es el único flujo activo de carbono desde los reservorios del sistema atmósfera–hidrosfera–corteza terrestre hacia el manto convectivo profundo. Las serpentinitas en la cuña del manto del antearco de las zonas de subducción secuestran y almacenan el carbono derivado de las reacciones de devolatilización más superficiales regulando así el flujo de carbono que transporta la placa subducida hacia las regiones más profundas de la zona de subducción. A las profundidades del arco volcánico, las reacciones de devolatilización y la interacción fluido-roca en la placa subducida regulan el balance del carbono que vuelve a la atmósfera y la corteza a través del volcanismo de arco y el que se retiene en la placa subducida, reciclándose hacia el manto terrestre profundo. La deshidratación de las serpentinitas con antigorita a estas profundidades desempeña un papel decisivo en la modulación de los flujos de carbono ya que esta reacción libera una gran cantidad de fluidos que reaccionan y disuelven el carbono en otras litologías de la placa subducida.

El principal objetivo de la presente tesis doctoral es el de mejorar nuestra comprensión de los procesos de carbonatación de peridotitas serpentinizadas y el destino del carbono alojado en las serpentinitas durante el metamorfismo de alta presión; la finalidad ultima de este estudio es contribuir a un mejor entendimiento del papel que juegan estos procesos en el ciclo profundo del carbono en las zonas de subducción. Para avanzar en este objetivo general de investigación, en esta tesis se presentan los resultados de estudios de afloramientos naturales fósiles en los que se registran dos procesos clave de transferencia de carbono durante la interacción fluido-roca en zonas de subducción: (i) las listvenitas de la ofiolita de Baie Verte (Terranova, Canadá), que constituye un análogo natural del almacenamiento de carbono por carbonatación de peridotitas del manto de antearco de una zona de subducción; y (ii) los meta-oficarbonatos del complejo Nevado-Filábride (Cordillera Bética, España), que proporcionan información unica sobre la estabilidad de los carbonatos durante la deshidratación de serpentinitas con antigorita en un terreno metamórfico de paleo-subducción. La combinación de datos de campo, (micro) estructurales, petrológicos y geoquímicos con modelos termodinámicos ha proporcionado una mejor comprensión de la interacción de los fluidos con el manto hidratado, que regula la movilidad del carbono en las profundidades del antearco y arco volcánico de las zonas de subducción. Mediante modelos termodinámicos de las reacciones de devolatilización en sistema cerrado y abierto, esta tesis

investiga los efectos de los fluidos electrolíticos y el papel de los fluidos de deshidratación de serpentinita en la liberación de carbono en rocas carbonatadas en serpentinitas de la placa que subduce de las zonas de subducción.

En un primer capítulo, esta tesis presenta el registro microestructural y petrológico de la carbonatación de peridotita por fluidos ricos en CO_2 en un entorno de antearco, tal y como se registra en la formación de listvenitas del complejo ofiolítico de Advocate (Terranova, Canadá). La sección mantélica de la ofiolita de Advocate contiene afloramientos únicos de listvenita (magnesita-cuarzo), roca de talco-magnesita que contiene cuarzo y antigorita, y serpentinita con antigorita carbonatada. Esta secuencia litológica registra la carbonatación secuencial de la serpentinita por fluidos hidrotermales ricos en CO_2. Los altos contenidos de Cr y Ni y la conservación de Cr-espinela con una composición similar a la de la serpentinita (Mg / Mg + Fe = 0,50 – 0,65; Cr / Cr + Al = 0,50 – 0.70) muestran que las listvenitas y las rocas de talco-magnesita en esta ofiolita se formaron por la carbonatación de un manto harzburgítico variablemente serpentinizado. La ausencia de olivino y magnetita prograd en las serpentinitas con antigorita y las rocas de talco-magnesita implican una temperatura de carbonatación entre c. 280 y 420 °C. El modelado termodinámico de la carbonatación de serpentinita a 300 ºC y 0,2 a 0,5 GPa explica la secuencia de rocas carbonatadas en el complejo ofiolítico de Advocate. Las relaciones de fase y las observaciones petrológicas muestran que la actividades de $a\mathrm{SiO}_{2,aq}$ y $a\mathrm{CO}_{2,aq}$ del fluido infiltrado rico en CO_2 están tamponados en los puntos pseudo-invariantes Atg-Tlc-Mgs y Qtz-Tlc-Mgs formando rocas predominantemente trifásicas con proporciones variables de carbonatos. Las listvenitas se forman a altas razones fluido-roca cuando el cuarzo está saturado en la fase fluida y precipita en los bordes de grano de la magnesita y en venas de tensión de tamaño variable.

La relación Fe^{3+}/Fe_{total} de la roca total en la secuencia de carbonatación de la ofiolita de Advocate disminuye al aumentar el contenido de carbono de la roca desde 0,65 a 0,80 en las serpentinitas con antigorita y brucita, y desde 0,10 a 0,30 en las rocas de talco-magnesita y las listvenitas. La reducción total del hierro en la roca se asocia a un aumento en el contenido de hierro ferroso de la magnesita y la formación de hematites y goethita, lo que indica un aumento concomitante de la fugacidad de oxígeno en el fluido. La secuencia de reacciones de carbonatación se registra de manera excepcional en la zonación de crecimiento característica de la magnesita de las listvenitas, que consta de: (i) una zona interior con magnesita rica en Mn y pobre en Fe que contiene magnetita y que se forma por la carbonatación de la lizardita, brucita y olivino de la serpentinita con antigorita; (ii) una zona

intermedia con magnesita rica en Fe formada por carbonatación de antigorita y en equilibrio con talco pobre en Fe; y (iii) un borde más externo de magnesita pobre en Fe formada por la carbonatación de talco.

La carbonatación del manto harzburgítico serpentinizado en la ofiolita de Advocate se produjo probablemente cuando formaba parte de la placa superior de un antearco en un contexto de suprasubducción debido a la circulación de fluidos ricos en CO_2 canalizados en fallas profundas al comienzo de la formación de la cuenca de antearco (c. 300 ºC, <0,5 GPa). Los valores constantes de $\delta^{18}O$ (11,0 – 14,4 ‰ V-SMOW) y relativamente bajos de $\delta^{13}C$ (–8,9 a –5,0 ‰ V-PDB) de la magnesita en la secuencia de rocas carbonatadas del complejo de Advocate son consistentes con fluidos ricos en CO_2 derivados de la descarbonatación o la disolución de meta-sedimentos con carbono y carbonatos de origen orgánico similares a los que aparecen en el complejo tectónico subyacente de Birchy, que constituía el margen continental parcialmente subducido de Laurencia. Este estudio demuestra que la carbonatación del manto litosférico oceánico o continental serpentinizado debida a la percolación reactiva de fluidos ricos en CO_2 derivados de la placa subducida en contextos de anterarco puede ser un reservorio importante de carbono del ciclo profundo del carbono.

En el segundo capítulo de la tesis se presenta el estudio de la petrología y las relaciones de fase en meta-oficarbonatos durante el metamorfismo de subducción. A las profundidades de la placa subducida donde se encuentra al arco volcánico, la liberación de carbono de las litologías de la placa subducida está controlada principalmente por la cantidad de fluido liberado en las reacciones metamórficas de devolatilización, tales como la de la deshidratación de serpentinita con antigorita a peridotita prograda. En este capítulo de la tesis se investigan rocas con carbonatos-silicatos que aparecen en las serpentinitas con antigorita y en harzburgita con clorita de los macizos ultramáficos de la Milagrosa y el Almirez en el Complejo Nevado-Filábride (CNF, Cordillera Bética, España). Estos macizos proporcionan una oportunidad única para investigar la estabilidad del carbonato durante el metamorfismo de subducción antes y después de la deshidratación de serpentinita con antigorita en un contexto de subducción caliente.

En el macizo de la Milagrosa, las rocas con carbonatos-silicatos aparecen como lentes de mármoles con Ti-clinohumita-diópsido-calcita, mármoles con diópsido-dolomita y rocas con antigorita-diópsido-dolomita que aparecen en el seno de serpentinitas con antigorita que contienen clinopiroxeno. En Almirez, las rocas con carbonatos-silicatos aparecen como lentes en las harzburgitas con clorita y poseen una asociación mineral de alto grado compuesta por

olivino, Ti-clinohumita, diópsido, clorita, dolomita, calcita, magnetita con Cr, pentlandita e inclusiones ocasionales de aragonito. Las rocas con carbonatos-silicatos del CNF tienen contenidos variables de CaO y CO_2 con una relación Mg / Si casi constante, y altos contenidos de Ni y Cr, lo que indica que sus protolitos eran mezclas de serpentina y carbonato cálcico (es decir, oficarbonatos). El modelado termodinámico muestra que las rocas con carbonatos-silicatos alcanzaron condiciones metamórficas pico similares a las de las serpentinitas (macizo de la Milagrosa; 550 – 600 °C y 1,0 – 1,4 GPa) y harzburgitas con clorita encajantes (macizo del Almirez; 1,7 – 1,9 GPa y 680 °C).

Las microestructuras, la química mineral y las relaciones de fase indican que las composiciones híbridas con carbonatos-silicatos se formaron antes del metamorfismo prograd, probablemente durante la alteración hidrotermal con agua de mar, y posteriormente sufrieron un metamorfismo de subducción. En el diagrama ternario de CaO-MgO-SiO_2 estos procesos generaron una variabilidad composicional de las rocas con carbonatos-silicatos encajadas en las serpentinita a lo largo de la línea de mezcla calcita-serpentinita, que es similar a la que se observa en rocas carbonatadas encajadas en serpentinita de otros terrenos metamórficos de subducción. El modelado termodinámico considerando modelos clásicos de fluidos moleculares binarios H_2O–CO_2 muestra que la variabilidad composicional a lo largo de este binario determina la temperatura de las principales reacciones de devolatilización, la composición del fluido y las asociaciones minerales de los productos de reacción durante el metamorfismo prograd de subducción. El modelado termodinámico considerando fluidos electrolíticos revela que el H_2O y el CO_2 moleculares son las principales especies en los fluidos y que las especies cargadas de carbono aparecen solo en pequeñas cantidades en los equilibrios de las rocas con carbonatos-silicatos de contextos de subducción caliente. En consecuencia, el uso de fluidos electrolíticos en los modelos termodinámicos a estas condiciones solo aumenta ligeramente la solubilidad del carbono en el fluido en comparación con las solubilidades obtenidas con los modelos que consideran fluidos binarios H_2O–CO_2, y no afecta a la topología de las relaciones de fase de las rocas carbonatadas en serpentinitas.

Las relaciones de fase, la composición mineral y las asociaciones minerales de las rocas carbonatadas en los macizos ultramáficos de la Milagrosa y Almirez son consistentes con una evolución metamórfica prograda en la que las reacciones de descarbonatación debidas a la infiltración de fluidos externos han tenido un papel muy limitado. Nuestro estudio muestra que los carbonatos de las rocas con carbonatos-silicatos en serpentinitas pueden preservarse más allá de la deshidratación de las serpentinitas con antigorita a las

profundidades de la placa que subduce situadas bajo los arcos volcánicos, lo que demuestra que este carbono puede ser reciclado hacia el manto terrestre profundo.

En un tercer capítulo de la tesis se investigan mediante modelos termodinámicos los efectos de los fluidos electrolíticos y el papel de la infiltración de fluidos derivados de la deshidratación de serpentinita a alta presión en la solubilidad de carbono en los fluidos de las zonas de subducción. Las rocas carbonatadas encajadas en serpentinita se forman bien durante la etapa oceánica de subducción de la litosfera oceánica (oficalcitas) o durante el metasomatismo en la interfaz de la placa de subducción (rocas híbridas con carbonato-talco). Estas rocas pueden ser importantes fuentes de carbono en las regiones fuente de los arcos volcánicos. Puesto que aparecen intercaladas en la sección mantélica hidratada de la placa subducente, las rocas carbonatadas encajadas en serpentinitas pueden preservarse hasta las profundidades del arco volcánico de la infiltración de los fluidos externos producidos por el metamorfismo progrado de meta-sedimentos y de la corteza oceánica hidratada en los niveles superiores de la placa que subduce. Una vez que son trasportadas a estas profundidades, las rocas carbonatadas incluidas en serpentinitas son infiltradas por los fluidos externos derivados de la deshidratación a alta presión de las serpentinitas encajantes. Debido a que la disolución del carbonato en fluidos acuosos es mayor a altas presiones y temperaturas, la liberación de carbono por la infiltración de fluidos en la placa que subduce a niveles del arco volcánico es fundamental para comprender el balance global de carbono y la magnitud de los flujos de carbono desde la placa hacia el manto profundo. En este capítulo de la tesis se presenta un modelo termodinámico —utilizando la implementación de la base de datos DEW (Deep Earth Water model) en el programa Perple_X— de las reacciones de devolatilización prograda (*sólidos = fluido + sólidos*) y de las reacciones de devolatilización promovidas por la infiltración de fluidos (*fluido externo + sólidos = fluido + sólidos*) derivados de la deshidratación de serpentinita y que afectan a los principales litologías de rocas carbonatadas que aparecen en serpentinitas. En línea con los estudios previos de la devolatilización progresiva de corteza oceánica hidratada, nuestros modelos muestran que, en las zonas de subducción calientes y frías, la solubilidad del carbono en los fluidos producidos por las reacciones de devolatilización subsolida de meta-oficalcitas y rocas con carbonato-talco es muy limitada, incluso si se considera la presencia de complejos de iones metálicos con modelos de fluidos electrolíticos. Por lo tanto, es probable que las rocas de metacarbonato alojadas en serpentinita se conserven en la placa que subduce hasta las profundidades del arco volcánico, donde sufren devolatilización promovida por la infiltración de los fluidos

derivados de la deshidratación de las serpentinitas con antigorita encajantes. En las condiciones de presión y temperatura de la deshidratación de la antigorita de zonas de subducción frías a cálidas, los modelos de devolatilización de meta-oficalcita y rocas de carbonato-talco promovida por infiltración de fluidos derivados de la deshidratación de serpentinita indican que la pérdida de carbono en estas rocas está acompañada de una pérdida significativa de calcio, particularmente a altas presiones (P> 3,5 GPa) debido a la alta actividad de $CaHCO_3^+$ en el fluido. La solubilidad del carbono en los fluidos equilibrados con meta-oficalcitas y rocas con carbonato-talco es más alta que la de fluidos en equilibrio con aragonito a las mismas condiciones debido a las reacciones tampón en sistema abierto entre carbonatos, silicatos y fluidos. Modelos que combinan balances de masas con la parametrización de las condiciones P y T de deshidratación de serpentinita con antigorita en función del parámetro térmico de las zonas de subducción nos permiten investigar la pérdida de carbono causada por la infiltración de los fluidos de deshidratación de serpentinita en función del estado térmico de la zona de subducción. A diferencia de la disolución de $CaCO_3$, la disolución de carbonatos en las rocas carbonatadas en serpentinitas es más alta en la superficie de la placa que subduce de las zonas de subducción calientes, y más baja a profudidades de la Moho de la placa que subduce en las zonas de subducción frías, donde la deshidratación de serpentinita con antigorita tiene lugar a mayores profundidades. Nuestros modelos muestran que la subducción de meta-oficalcitas —con espesores de hasta 70 m, como los observados en oficalcitas oceánicas—conserva los carbonatos más allá de las profundidades del arco volcánico incluso en zonas de subducción calientes, reciclándose éstas hacia el manto profundo como rocas con carbonatos-granate-clinopiroxeno-olivino. Por el contrario, las reacciones de devolatilización de las rocas con carbonato-talco promovidas por la infiltración de fluidos derivados de la deshidratación de serpentinitas disuelven grandes cantidades de carbonato, por lo que estas litologías son una fuente eficiente de carbono a profundidades del arco volcánico, donde se transforman en ortopiroxenita en la mayoría de los regímenes térmicos de las zonas de subducción.

Palabras clave: *ciclo profundo del carbono, secuestro de CO_2, carbonatación de peridotitas, listvenitas, serpentinización, cuenca de antearco, complejo ofiolítico de Advocate, oficarbonatos, fluidos de subducción, deshidratación de serpentinita, complejo Nevado-Filábride, modelado termodinámico, fluidos electrolíticos, reacciones de devolatilización, infiltración de fluidos.*

Zusammenfassung

Subduzierende ozeanische Lithosphäre stellt den einzigen Kohlenstofffluss von Oberflächennahen Speichern in den Erdmantel dar. Entwässerungsreaktionen und Wechselwirkungen zwischen Gesteinen und Fluiden in Subduktionszonen bestimmen maßgeblich wieviel Kohlenstoff in der subduzierenden Platte verbleibt und wieviel durch Suduktionszonenvulkanismus wieder an die Atmosphäre zurückgelangt. Serpentinisierte Peridotite sind von herausragender Bedeutung für den langfristigen Kohlenstoffkreislauf, da einerseits die Entwässerung von Antigorit-Serpentinite eine der wichtigsten Fluidquellen in mittleren Tiefen in Subduktionszonen ist. Andererseits kann gelöster Kohlenstoff in Serpentiniten der oberen Platte (*mantle wedge*) ausfällen und gespeichert werden, und somit die Kohlenstoffflüsse in Subduktionszonen beeinflussen. Die vorliegende Dissertation hat zum Ziel unser Verständnis von Karbonatisierungsprozessen und der Stabilität kohlenstoffhaltiger Serpentinite unter hohen Drücken zu verbessern, um die Bedeutung serpentinisierter Peridotite für die Freisetzung und Speicherung von Kohlenstoff in Subduktionzonen zu evaluieren. Hierfür habe ich im Zuge der Dissertation natürliche Gesteinsvorkommen untersucht, die Schlüsselprozesse im Kohlenstoffkreislauf in Subduktionszonen darstellen: (i) Listvenit-gesteine aus Neufundland (Kanada), als Analog für Karbonatisierung des Mantels oberhalb subduzierender Lithosphäre; und (ii) Metaophikarbonate des Nevado-Filábride Komplexes (Spanien), die einzigartige Einblicke zur Stabilität von Karbonaten unter Hochdruckmetamorphose und während der Entwässerung von Serpentinit ermöglichen. Die Kombination von Gelände- und Strukturuntersuchung mit petrologischen und geochemischen Daten sowie thermodynamischer Modellierung gewährt neue Erkenntnisse zu Fluid-Gesteins Wechselwirkungen bei hohen Drücken und zur Mobilität von Kohlenstoff in Subduktionzonen. Die vorliegende Dissertation untersucht zudem die Bedeutung der elekrolytischen Fluidzusammensetzungen von perkolierenden Fluiden, die durch Entwässerung von Serpentinit entstehen, für die Kohlenstofffüsse in Subduktionszonen, unter Anwendung thermodynamischer Modellierung von prograden und infiltrationsbedingten Entgasungsreaktionen bei hohen Drücken in Metakarbonat-führenden Serpentinitgesteinen.

Ein *erster Teil* der Dissertation behandelt die mikro-strukturellen und petrologischen Aspekte der Karbonatisierungsreaktionen von Peridotit mit CO_2-haltigen Fluiden, die zur Bildung von Listvenit im Advocate Komplex (Neufundland, Kanada) geführt haben. Die

Mantelgesteine des Advocate Ophiolits beinhalten spektakuläre Aufschlüsse von Listvenit (Magnesit-Quartz Gesteine), Antigorite- und Quartz-haltigen Talk-Magnesit Gesteinen und karbonatführenden Antigorit-serpentiniten. Diese Lithologieabfolge zeichnet the schrittweise Karbonatisierung von teilweise serpentinisiertem Peridotit durch CO_2-haltige Fluide nach. Hohe Gehalte an Cr und Ni im Gesamtgestein und reliktischer Cr-spinel mit einer Zusammensetzung ähnlich derer in Antigorit-Serpentinit (Mg/Mg+Fe = 0.50 – 0.65; Cr/Cr+Al = 0.50 – 0.70) deuten darauf hin dass Advocate Listvenit und Talk-Magnesit Gesteine durch Karbonatisierung von teilweise serpentinisiertem Harzburgit gebildet wurde. Zeitgleiche Verdrängung von Lizardit durch Magnesit und durch Antigorit + Brucit, sowie das Fehlen von prograde m Olivin und Magnetit in Antigorit-Serpentinit und Talk-Magnesit Gestein begrenzen die Temperaturebedingungen der Karbonatisierung auf ca. 280 – 420 °C. Thermodynamische Modellierung der Karbonatisierung von Serpentinit bei 300 °C und 0.2 – 0.5 GPa stimmt mit der verschieden karbonatisierten Lithologieabfolge im Advocate Komplex überein. Phasengleichgewichte und petrologische Beobachtungen lassen darauf schließen dass $a SiO_2$ und $a CO_2$ in wässriger Lösung der infiltrierenden Fluide an den Pseudo-invarianten Punkten Atg-Tlc-Mgs und Qtz-Tlc-Mgs gepuffert wurden, da hauptsächlich drei-phasige Paragenesen entsprechend dieser Pseudo-invarianten Punkte gebildet wurden. Die Listvenite deuten auf hohe Fluid-Gesteins-Verhältnisse hin, bei denen Quarz aus gesättigter Lösung entlang von Magnesit Korngrenzen und in variabel dimensionierten Tensions-Adern ausfiel.

Das Verhältnis von Fe^{3+}/Fe_{total} im Gesamtgestein der Karbonatgesteine des Advocate Mantelkomplexes nimmt mit zunehmendem Kohlenstoffgehalt des Gesamtgesteins ab, von 0.65 – 0.80 in Brucit-haltigem Antigorit-Serpentinit auf 0.10 – 0.30 in Talk-Magnesit-Gesteinen und Listvenit. Die Reduktion vom Fe^{3+} im Gesamtgestein ist mit einer Zunahme des Eisengehalts von Magnesit und der Bildung von Hämatit und Goethit verbunden, was auf eine gleichzeitige Zunahme der Sauerstoff-Fugazität in den Fluiden hinweist. Die Abfolge der Karbonatisierungsreaktionen ist in drei charakteristischen Hauptwachstumszonen in Listvenit-Magnesit einzigartig erhalten: (i) eine innere Zone aus Magnetit-haltigem, eisenarmem und Mn-haltigem Magnesit, die durch Karbonatisierung von Lizardit, Brucit und Olivin aus Atg-Serpentinit gebildet wurde; (ii) eine äußere Zone von eisenreichem Magnesit, gebildet durch Karbonatisierung von Antigorit und im Gleichgewicht mit eisenarmem Talk; und (iii) einen äußersten Rand aus eisenarmem Magnesit, der durch Karbonatisierung von Talk gebildet wurde.

Die Karbonatisierung des serpentinierten Advocate Mantels erfolgte warscheinlich im Ophiolith der oberen Platte einer Subduktionszone durch CO_2-haltige Fluide, die vom subduziertem Slab freigesetzt wurden und entlang tiefer Verwerfungen zu Beginn der Akkretion des forearc-beckens in den darüberliegenden Ophiolite aufstiegen (bei ca. 300 ºC, < 0.5 GPa). Relativ konstante $\delta^{18}O$ (11.0 – 14.4 ‰ V-SMOW) und niedrige $\delta^{13}C$ (–8.9 to –5.0 ‰ V-PDB) Isotopenverhältnisse von Magnesit in den karbonatisierten Mantelgesteinen im Advocate-Komplex sind mit CO_2-reichen Fluiden vereinbar, die aus der Dekarbonisierung oder Auflösung von graphit- und karbonathaltigen Metasedimenten stammen, wie sie im darunter liegenden Birchy-Komplex vorkommen — dem teilweise subduzierten Kontinentalrand von Laurentia. Die Karbonatisierung von serpentinisierter ozeanischer oder kontinentaler Mantellithosphäre durch reaktive Infiltration von CO_2-reichen Fluiden, die aus der subduzierten Platte unter forearc-Bedingungen hervorgehen, kann folglich ein bedeutendes Kohlenstoffreservoir für den tiefen Kohlenstoffkreislauf darstellen.

In *einem zweiten Kapitel* liefert diese Dissertation neue Einblicke in die Petrologie und die Phasenbeziehungen von Meta-Ophikarbonaten während hochdruck-Metamorphose in Subduktionszonen. In *subarc*-Tiefen von Subduktionszonen wird die Freisetzung von Kohlenstoff aus Lithologien der subduzierenden Platte hauptsächlich durch Fluide gesteuert, die durch Entwässerungsreaktionen wie der Dehydratisierung von Antigorit (Atg-) Serpentinit zu prograde Peridotit freigesetzt werden. In diesem Kapitel werden Karbonat-Silikat-Gesteine untersucht, die in Atg-Serpentinit und prograde Chlorit (Chl-) Harzburgit in den ultramafischen Milagrosa- und Almirez-Massiven des paläo-subduzierten Nevado-Filábride-Komplexes (NFC, Betic Cordillera, Spanien) vorkommen. Diese Ultramafite bieten die einzigartige Gelegenheit, die Stabilität von Karbonatmineralen während der Subduktionsmetamorphose unter Druck-Temperatur (P-T) Bedingungen vor und nach der Dehydratisierung von Atg-Serpentinit in warmen Subduktionszonen zu untersuchen.

Im Milagrosa-Massiv treten Karbonat-Silikat-Gesteine als Linsen von Ti-Clinohumit-Diopsid-Calcit-Marmor, Diopsid-Dolomit-Marmor und Antigorit-Diopsid-Dolomit-Gesteinen auf, die in Clinopyroxen-haltigem Atg-Serpentinit eingeschlossen sind. Im Almirez-Massiv kommen Karbonat-Silikat-Gesteine in Chl-Harzburgit vor und weisen eine metamorphe Paragenese von Olivin, Ti-Clinohumit, Diopsid, Chlorit, Dolomit, Calcit, Cr-haltigem Magnetit, Pentlandit und seltenen Aragonit-Einschlüssen auf. Diese NFC-Karbonat-Silikat-Gesteine haben variable CaO- und CO_2-Gehalte bei nahezu konstantem Mg/Si-Verhältnis und hohe Ni- und Cr- Gehalte, was darauf hinweist, dass ihre Protolithe variable Gemische aus

Serpentin und Ca-Karbonat (d. h. Ophikarbonaten) waren. Thermodynamische Phasengleichgewichte zeigen, dass die Karbonat-Silikat-Gesteine metamorphe Druck-Temperatur-Bedingungen erreichten, die denen ihres Wirts Serpentinit (Milagrosa-Massiv; 550 – 600 °C and 1.0 – 1.4 GPa) und Chl-Harzburgit (Almirez-Massiv; 1.7 – 1.9 GPa and 680 °C) entprechen.

Mikrostrukturen, Mineralchemie und Phasenverhältnisse deuten darauf hin, dass die Gesamtgesteinschemie der hybriden Karbonat-Silikat-Gesteine sich vor der prograden Metamorphose herausgebildet hat —wahrscheinlich bereits während einer hydrothermalen Ozeanbodenmetamorphose— und anschließend während der Subduktionsmetamorphose überprägt wurde. Im ternären System CaO-MgO-SiO_2 führten diese Prozesse zu einer Variabilität der Zusammensetzung der NFC-Karbonat-Silikat-Gesteine entlang des Serpentinit-Calcit Mischungstrends, ähnlich wie dies bei karbonat-führendem Serpentinit in anderen paläo-subduzierten metamorphen Komplexen zu beobachten ist. Die thermodynamische Modellierung mit klassischen Modellen binärer H_2O-CO_2-Fluide zeigt, dass die Variabilität der Zusammensetzung entlang dieses Mischungstrends die Temperatur der Hauptentwässerungsreaktionen, die Fluidzusammensetzung und die Mineralparagenese von Reaktionsprodukten während der prograden Subduktionsmetamorphose bestimmt. Thermodynamische Modelle unter Berücksichtigung elektrolytischer Fluide zeigen, dass H_2O und molekulares CO_2 die Hauptfluidkomponenten sind und geladene kohlenstoffhaltige Verbindungen in wässriger Lösung nur eine geringfügige Rolle spielen in Fluiden im Gleichgewicht mit Karbonat-Silikat-Gesteinen in warmen Subduktionszonen. Somit erhöht die Berücksichtigung elektrolytischer Fluide unter diesen Bedingungen die Löslichkeit von Kohlenstoff in wässriger Lösung geringfügig im Vergleich zu klassischen Modellen binärer H_2O-CO_2-Fluide, hat jedoch keinen Einfluss auf die Topologie der Phasenbeziehungen in Meta-Ophikarbonatgesteinen.

Phasenbeziehungen und Mineralzusammensetzung Karbonat-Silikat-Gesteinen in den Meta-Serpentiniten von Milagrosa- und Almirez stehen im Einklang mit einem lokalen Gleichgewicht zwischen Infiltrationsfluiden und der Gesteinszusammensetzung und weisen auf eine begrenzte Rolle von infiltrationsbedingter Dekarbonisierung hin. Diese Studie belegt, dass Karbonatminerale in von Serpentinit umgebenen Karbonat-Silikat-Gesteinen über die Entwässerung von Atg-Serpentinit in *subarc*-Tiefen von Subduktionszonen hinaus erhalten bleiben können. Dies zeigt, dass Kohlenstoff in den tiefen Mantel zurückgeführt werden kann.

In einem dritten Teil untersucht diese Dissertation mit Hilfe von thermodynamischen Modellen die Auswirkungen elekrolytischer Fluidzusammensetzungen und des Flusses von Serpentinit-Entwässerungsfluiden auf die Kohlenstofffreisetzung in Subduktionszonen. In Serpentinit eingeschlossene Karbonatgesteine, die während der Ozeanbodenmetamorphose von subduzierter Ozeanlithosphäre (Ophicalcit) oder durch Metasomatismus entlang der Subduktionsplattengrenze (hybride Karbonat-Talk-Gesteine) gebildet werden, können wichtige Kohlenstoffquellen in Subarc-Tiefen sein. Wenn diese Karbonatgesteine in der hydratisierten Mantellithosphäre der subduzierenden Platte enthalten sind, können sie vor der Infiltration von Fluiden bewahrt werden, die durch die prograde Metamorphose der darüber liegenden Metasedimente und der alterierten ozeanischen Kruste freigesetzt werden, und bis in subarc-Tiefen erhalten bleiben, wo sie von Serpentinit-Entwässerungsfluiden infiltriert werden. Da die Karbonatlöslichkeit in wässrigen Fluiden mit Druck und Temperatur zunimmt, ist die Freisetzung von Kohlenstoff in infiltrierenden Fluiden in diese Tiefen entscheident um die globale Kohlenstoffbilanz und die Größenordnung der Kohlenstoffflüsse von der Subduktionsplatte in den tiefen Mantel zu verstehen. Dieser Abschnitt der Dissertation befasst sich mit der thermodynamische Modellierung — unter Verwendung der DEW-Datenbank in Perple_X — von prograden Entgasungsreaktionen (Gestein = Fluid + Gestein) und infiltrationsbedingten Entgasungsreaktionen (externe Fluide + Gestein = Fluid + Gestein) in Karbonatgesteinen von Serpentiniten. Die Modellierung zeigt, dass die Lösung von Kohlenstoff aus Meta-Ophicalcit und Karbonat-Talk Gesteinen während prograder Entgasungsreaktionen niedrig ist, selbst wenn ionische Metall-führende Komplexe in wässriger Lösung elektrolytischer Fluide in Betracht gezogen werden. Dies steht im Einklang mit früheren Untersuchungen prograder Entgasungsreaktionen in kohlenstoffhaltiger Ozeankruste. In Serpentinit eingeschlossene Karbonatgesteine bleiben daher mit hoher Wahrscheinlichkeit bis in subarc-Tiefen erhalten, wo sie infiltrationsbedingten Entgasungsreaktionen während der Entwässerung von Antigorit unterliegen. Entsprechende Modelle von durch Fluidinfiltration ausgelöster Entgasungreaktionen in Meta-Ophicalcit und Karbonat-Talk Gesteinen unter den Druck-Temperatur Bedingungen der Entwässerung von Antigorite in kalten und warmen Subduktionszonen deuten darauf hin, dass die Freisetzung von Kohlenstoff mit einem signifikanten Verlust von Ca einhergeht. Dies ist insbesondere bei hohen Drücken (> 3.5 GPa) der Fall und ist auf eine hohe $CaHCO_3^+$ Konzentration im Fluid zurückzuführen. Die Löslichkeit von Kohlenstoff in Fluid im thermodynamischen Gleichgewicht mit Meta-Ophicalcit und Karbonat-Talk Gesteinen ist deutlich höher als in reinem Aragonit aufgrund von Pufferreaktionen zwischen Karbonaten, Silikaten und dem

Fluid. Massenbilanzberechnungen in Kombination mit der Parametrisierung der Druck-Temperatur Bedingungen der Entwässerung von Antigorit-serpentinit in Abhängigkeit der thermischen Struktur von Subduktionzonen ermöglichen es die Freisetzung von Kohlenstoff durch infiltrierende Serpentinit-Entwässerungsfluide zu quantifizieren. Im Gegensatz zu $CaCO_3$ ist die Lösung von Karbonat aus in Serpentinit eingeschlossenen Metakarbonatgesteinen an der Grenzfläche zischen subduzierender Platte und darüberliegendem Mantel in warmen Subduktionszonen am höchsten, wohingegen weniger Karbonat in Gesteinen nahe der Moho der subduzierenden Platte in kalten Subduktionszonen gelöst werden kann. Während der Subduktion von Meta-Ophicalciten, die bis zu 70 m mächtige ozeanische Abfolgen darstellen können, bleiben Karbonatminerale bis in über den subarc hinaus gehende Tiefen erhalten in Form von Karbonat-Granat-Klinopyroxen-Olivin Gesteinen, welche selbst in warmen Subduktionszonen bis in den tiefen Mantel recyclet werden. Infiltrationsbedingte Entgasungsreaktionen in Karbonat-Talk Gesteinen stellen hingegen eine Kohlenstoffquelle in subarc-Tiefe unter Vulkanbögen dar, wodurch diese Gesteine in den meisten Subduktionszonen in Orthopyroxenit umgewandelt werden.

Schlagworte: Tiefer Kohlenstoffkreislauf, CO_2 Sequestrierung, Peridotit Karbonatisierung, Listwanit, Forearc, Advocate Komplex, Ophikarbonat, Subduktionsfluide, Serpentinitdehydratation, Nevado-Filábride Komplex, elektrolytische Fluide, Thermodynamische Modellierung, Entgasungsreaktionen, Infiltrationsmetamorphose

Acknowledgements

It comes nearly as a surprise, the realization that the work is done, even though it took its time and many new questions opened up on the way. I would like to thank all those who contributed to making this PhD an exciting, challenging and successful journey:

First of all, my gratitude goes to my advisors **Carlos J. Garrido** and **Vicente López Sánchez-Vizcaíno**, for their enthusiastic commitment to the project and guidance. Thank you, **Carlos**, for providing a healthy supervision by letting me explore and follow interesting ideas but also keeping me from getting carried away too much. From your great capability of taking extremely detailed aspects and complex relationships, and framing them into a big-picture perspective without losing the scientific rigor, I learned a lot about how we can advance our understanding of fundamental processes in Earth. I appreciated very much the infinite time you invested on guidance during field work, shaping of manuscripts and many creative discussions, and thank you for all your advice and caring that go far beyond this Ph.D. thesis. An equally big thanks to you, **Vicente**! I am very happy to have had your kind, humorous and insightful support and guidance. Thanks for introducing me to the wonders (and pitfalls) of Perplex, and for your amazingly sharp eye and critical mind —be it in the field, when looking at the microscope or pseudosections, and while revising manuscripts.

I am grateful to **Claudio Marchesi**, who was committed to this Ph.D. project from the start as tutor. I appreciated very much your commitment and expertise, in particular your help with official paperwork, field and laboratory work, and during revision of manuscripts.

A special thanks goes to **Károly Hidas**, who took away my fear of hitting detectors while tilting the stage and made me an independent EBSD user. Thank you so much for all the help, shared expertise and exciting discussions; I am lucky to have you as my co-author!

I also want to acknowledge the efforts of **Monica Escayola** to facilitate a smooth field campaign in Newfoundland, and **Antonio Delgado Huertas** for his friendly collaboration during stable isotope analysis. I appreciate having both of them as co-authors.

I would like to express my gratitude to the members of the examination panel, **Dr. José Miguel Azañón Hernández** (UGR), **Dr. Antonio Jabaloy Sánchez** (UGR), **Dr. Wolfgang Bach** (Univ. Bremen), **Dr. Alberto Vitale Brovarone** (Univ. Torino), **Dr. Marguerite Godard** (CNRS Montpellier), and the substitute panel experts **Dr. Guillermo Booth Rea** (UGR) and **Dr. María Isabel Abad Martínez** (UJA), for their time and interest in this work.

I am grateful to **Benoit Ildefonse**, **Bjørn Jamtveit**, and **Wolfgang Bach** of the ABYSS network for giving me the opportunities to spend research secondments at Geosciences Montpellier, Bremen University and Universitetet i Oslo, and for their dedication to share very specialized knowledge about EBSD data processing, thermodynamic modeling and the structural and physical aspects of carbonation reactions. I would also like to thank all the other scientists involved in the ABYSS project: first of all **Marguerite Godard** for coordinating the network, and **Damon Teagle**, **Bénédicte Ménez**, **Patrizia Fumagalli**, **Elisabetta Rampone**, **Jürgen Koepke**, and **Suzanne McEnroe** for organizing priceless training activities and providing stimulating feedback and discussions during various meetings.

I also wish to acknowledge **Maria Teresa Gómez-Pugnaire**, **José Alberto Padrón Navarta**, **Kurt Bucher**, **Muriel Andreani** and **Peter Kelemen**, among others, for their interest in my research and inspiring scientific feedback; **Jamie Connolly** for his kind and rapid responsiveness to any kind of Perplex questions; and **Matthieu Galvez**, **Thomas Pettke** and three anonymous reviewers for their constructive criticism during peer-review of the published articles. The stimulating and critical feedback I received from all these experienced researchers had been very valuable to improve the research presented in this Ph.D. thesis.

This thesis wouldn't have been possible (or would have taken years longer) without the help of the technicians of the IACT: **Alpiste**, **Mayte**, **Chari**, **Inma** y **Arsenio**, muchísimas gracias por las miles de ayudas en cualquier cosa y por el apoyo y las sonrisas que siempre tenéis para un doctorando perdido! Hicisteis que cada día me sentí bien acogido en el IACT. También quiero agradecer a **Xavier** de la microsonda de Barcelona, porque era un placer hacer análisis allí.

Doing a field campaign in unknown terrain has its difficulties. I would like to acknowledge Dr. Jean Bédard and Tom Skulski from the Canada Geological Survey, and Dr. Martin Batterson, Director of the Newfoundland Geological Survey for their help in the arrangements for the fieldwork in Newfoundland, and Janet Sacrey, town clerk of Pacquet, for her help with housing and logistic, and her warm hospitality during our stay in Pacquet (Newfoundland). I am further grateful to the Sierra Nevada National Park (Spain) for providing permits for fieldwork and sampling at the Almirez massif.

To my dear ABYSS fellows **Justine**, **Val**, **Carlotta**, **Sofia**, **Adriana**, **Karin**, **Barbara**, **Kristina**, **Zeudia**, **Rachael**, **Manolis**, **Tom**, **Pavel** and **Aurélien**: Thanks for your great company and all the time we had discovering different places in Europe. Having such a team was invaluable during all this time. I hope to see all of you again soon on conferences and elsewhere!

A mis compañeros del IACT, siempre apoyando en momentos difíciles y compartiendo muchas risas, café, comidas, discusiones (no siempre) científicas, tapas, cervezas, y noches inolvidables: **Nicole**, **Manolis**, **Marievi**, **Erwin**, **Amel**, **Mari**, **Yassamina**, **Muhammad**, **Annika**, **Antonio**, **Marga**, **Bob**, **Álvaro**, **Claudia**, **Laura**, **Nieves**, **Ari**, **Dimitris**, **Adrian**, **Ruben**, **Sara**, **Jorge**, **Llane**, **Leonardo**, **Gan**, **Electra**, y todos los demás: muchas gracias, sois grandes!

Quiero agradecer también a mis amigos de Granada, por todos los actividades y momentos memorables que también ayudaban recargar las pilas para seguir trabajando con más energía: a mis compañeros de swing **Nicole**, **Julia**, **Aitana**, **Leo**, **Miguel**, **Fernanda**, **Lea**, **Rosa**, **José**, **Maile** y **Anabél** (olé a los tardes y noches épicas de baile); a mis compis de piso, sobre todo **Bob** (y **Raquel**, que casi cuentas), **Javi**, **Katha**, **Eloisa**, **Guillem**, **Rob** y **Henek** (gracias por cenas y fiestas legendarias, y por hacer que mi español se mejoraba tanto!); a los de hortigas (olé skalabayzineros y las verduras riquísimas); y a mis compañeros de viaje y montana por descubrir tantas partes preciosas de este país – muchísimas gracias por esas experiencias **Nicole**, **Julia**, **Ruben**, **Gan**, **Laura**, **Ari**, **Eva**, **Lea**, **Ángel**, **Lidia**, **Jon**, **Mada**, **Bob**, **Raquel**, y toda la cuadrilla de Euskal herria!

Of course I should also mention my other friends of old and new. Thanks for being so wonderful people, for hosting, visiting, or “accidently” meeting me in so different parts of the world! I won’t list you all, but you will know. Thanks! Danke! Merci! Takk!

Zum Schluss darf natürlich ein ganz großes Dankeschön an meine Familie nicht fehlen, an meine Brüder und vor allem meine Eltern, die mich meinen Weg selbst aussuchen ließen, um mich dann tatkräftig dabei zu unterstützten, selbst bei so einer irrationalen Entscheidung wie einem PhD in metamorpher Petrologie (und dann auch noch in Spanien). Danke dafür!

Contents

PART I – INTRODUCTION, AIMS, THESIS OUTLINE AND METHODOLOGY

Part I

INTRODUCTION, AIMS, THESIS OUTLINE AND METHODOLOGY

1 Introduction

The present PhD thesis explores the role hydrated peridotites play in the terrestrial cycling of carbon between surface, crust and mantle reservoirs. I present the results of detailed field and petrological case studies of carbonated peridotites from the Baie Verte ophiolites (Newfoundland) and of subduction metamorphism of meta-ophicarbonates from the Nevado-Filábride Complex (Betic Cordillera, Spain). These case studies and related thermodynamic models provide new insights into the mechanisms of two key processes related to deep carbon cycling: carbon storage in the forearc mantle of subduction zones by carbonation of peridotites, and the release vs. retention of carbon in subducting meta-ophicarbonates during high fluid fluxes caused by serpentinite dehydration at high pressure. This chapter provides the background and state of knowledge about hydrated and carbonated peridotites in relation to the long-term cycling of carbon, their mechanisms of formation, and their properties during subduction metamorphism. A short introduction to the settings of the investigated case studies is further given at the end of this chapter.

1.1 The deep carbon cycle

The presence of carbon in the oceans, atmosphere and biosphere critically determines Earth's climate and habitability throughout geological time (Berner and Kothavala, 2001; Hayes and Waldbauer, 2006; Zahnle et al., 2007). However, these surface-near reservoirs contain only a tiny fraction of Earth's carbon, while most of it resides in the core, mantle and crust (Fig. 1.1) (Dasgupta and Hirschmann, 2010; Hirschmann, 2018). Therefore, on long time scales (> 10^6 years), different rates of metamorphic or volcanic CO_2 emissions into the atmosphere ("outgassing") and the transfer of carbon into the mantle by subduction of oceanic lithosphere ("ingassing") can strongly modulate the surface-near carbon content, and, thus, climate (Berner, 1999; Dasgupta, 2013; Dasgupta and Hirschmann, 2010; Evans, 2011). This long-term and large-scale feedback of carbon has been termed the "deep carbon cycle", and is subject of an exhaustive global research effort within the Deep Carbon Observatory[1]. Deep carbon cycling is crucial to the Earth's system because it is —after water— the second-most important flux agent for magmatism, and, in consequence, for maintaining mantle convection and active plate tectonics on Earth (Dasgupta, 2013). Furthermore, redox reactions related to

[1] *https://deepcarbon.net.*

the formation of carbonates and organic carbon play a decisive role in determining the oxygen fugacity of the Earth's mantle and atmosphere through time (Duncan and Dasgupta, 2017; Hayes and Waldbauer, 2006; Stagno, 2019).

1.1.1 The carbon cycle through Earth's history

The present day carbon inventory of the different deep and surface-near reservoirs is a result of the inherited carbon distribution from early Earth differentiation in the Hadean Eon, and the feedback processes of plate tectonic cycling from the Archean to the present (Fig. 1.1). Most processes in the Hadean are highly speculative, but it is clear that the element fractionation related to core formation, magma ocean differentiation, and formation of an early proto-atmosphere determined the initial carbon distribution on Earth (Dasgupta, 2013). With the formation of a solid crust and the ensuing continent accretion, the mechanism of carbon exchange between mantle and atmospheric reservoirs changed from direct equilibration to geochemical fluxes controlled by plate tectonic processes. In the Archean and early Proterozoic, carbon outgassing by volcanic emissions likely exceeded the rate of carbon transported back into the mantle, because the hotter thermal state of the asthenospheric

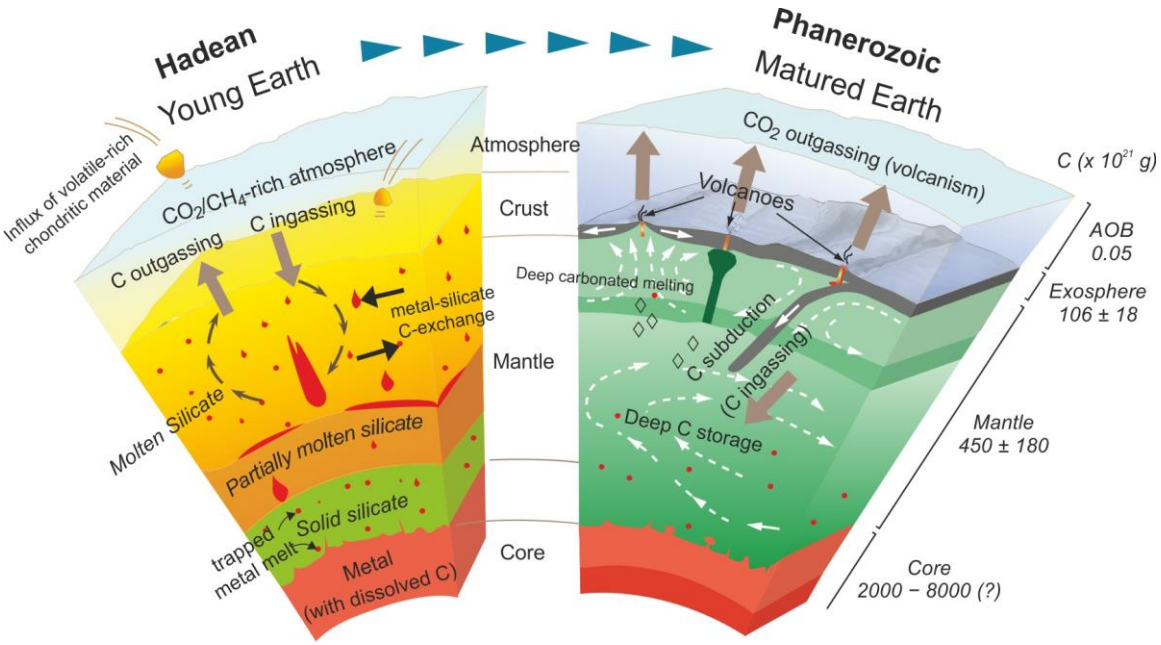

Figure 1.1. *Cartoon illustrating deep-Earth processes relevant for the long-term carbon cycle during the magma ocean stage in the Hadean in comparison to the Phanerozoic and present-day plate tectonic framework (from Dasgupta, 2013); and estimations of present-day carbon contents in the large-scale reservoirs (absolute C amounts in x 10^{21} g). AOB = atmosphere, oceans and biosphere reservoirs (after Berner, 1999); exosphere = surface-near volatile inventory in surficial deposits and the continental and oceanic crust (Hirschmann, 2018). Mantle C includes the subcontinental and convecting mantle (from Hirschmann, 2018); core C estimate is from Dasgupta and Hirschmann, 2010.*

mantle and subduction zones prevented carbon ingassing into the deep mantle (Dasgupta, 2013; Herzberg, 2016). This imbalance of the carbon fluxes between mantle and surface could have provided the necessary greenhouse conditions to maintain liquid water and prevent long-lasting snowball Earth conditions, counteracting a dim early Sun in the Archean (Dasgupta, 2013). Secular cooling of the mantle and colder subduction geotherms in the Proterozoic and Phanerozoic set the conditions for deep mantle recycling pathways of subducting carbonate and organic carbon (Fig. 1.1) (Dasgupta and Hirschmann, 2010), as evidenced for instance by geochemical and isotopic characteristics of deep diamonds (Burnham et al., 2015; Nestola et al., 2018; Timmerman et al., 2017). Variations in the long-term feedback of carbon in- and outgassing between mantle and surface-near reservoirs may have contributed to relatively stable and habitable climate conditions in the matured Earth system (Fig. 1.1). However, the different carbon fluxes and balances through time remain uncertain, and short-term perturbations in the deep carbon cycle may have had a critical influence on extreme climate conditions, for instance during the Cretaceous warm period or the recovery from Neoproterozoic ice-house conditions (Dasgupta and Hirschmann, 2010; Hoffman et al., 1998; Johnston et al., 2011; Kerrick, 2001).

1.1.2 Phanerozoic carbon fluxes

The Phanerozoic deep carbon cycle is principally characterized by the balance between the ingassing carbon flux via subduction of oceanic lithosphere, versus outgassing fluxes of CO_2 emitted from diffuse vents and mid-ocean ridge (MOR), intra-plate and arc volcanoes (Fig. 1.2). Due to their inaccessibility for direct observation, the long-term mass fluxes related to the deep carbon cycle and their controlling mechanisms in large parts remain insufficiently constrained, despite important recent advances (Hirschmann, 2018; Kelemen and Manning, 2015).

1.1.2.1 The oceanic lithosphere – a sink of carbon

The storage of carbon in marine sediments, altered crust and hydrated lithospheric mantle of oceanic plates and their subsequent subduction at convergent margins is responsible for the transfer of 40 – 66 x 10^{12} g C/year into subduction zones (Fig. 1.2) (Kelemen and Manning, 2015). Because this is substantially higher than the carbon fluxes released by degassing of CO_2 from magmas at mid-ocean ridges and intra-plate volcanoes (Marty and Tolstikhin, 1998), the oceanic lithosphere forms a net sink of carbon. Marine sediments (Plank and

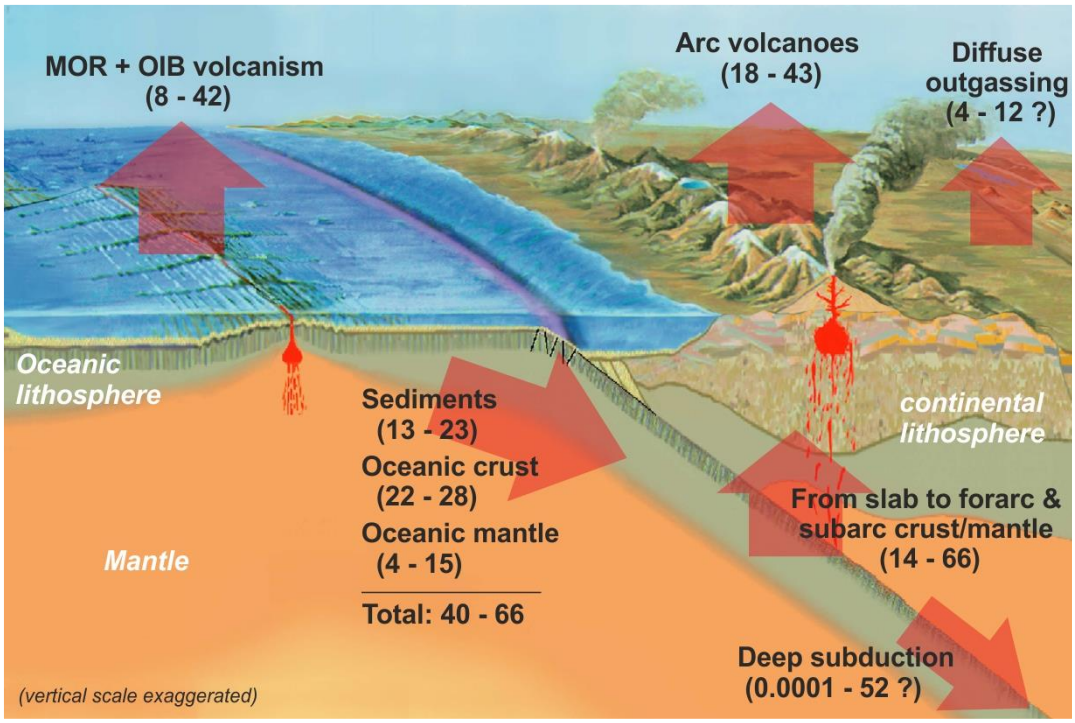

Figure 1.2. *Estimates of major, present-day carbon fluxes (x 10^{12} g C/year) between mantle and surface-near reservoirs (after Kelemen and Manning, 2015). MOR & OIB: mid-ocean ridge and intraplate ocean island basalt volcanism.*

Langmuir, 1998) and altered oceanic crust (Alt and Teagle, 1999) make up ~80 – 90 % of the carbon budget of current subducting oceanic lithosphere (35 – 51 x 10^{12} g C/year; Fig 1.2), while the hydrated lithospheric mantle represents a relatively minor sink of carbon (4 – 15 x 10^{12} g C/year) (Alt et al., 2013; Kelemen and Manning, 2015).

Oceanic lithosphere varies in style depending on spreading velocity, from 5 – 7 km thick crustal basalt and gabbro sections above peridotites at fast spreading mid-ocean ridges, to heterogeneous, thinned crust composed of gabbroic bodies and exhumed mantle peridotite formed at slow spreading ridges (Ildefonse et al., 2007). Tectonically controlled, non-volcanic spreading at slow spreading ridges makes the oceanic lithosphere more susceptible to hydration, for instance along deeply rooted detachment faults (Fig. 1.3) (Faccenda, 2014). Because the carbon content of altered crust and mantle is linked to the availability and depth of seawater percolation (Alt and Teagle, 1999; Kelemen and Manning, 2015), the contribution of lithospheric mantle to the carbon budget of oceanic plates is substantially larger when formed at slow spreading ridges than at "standard" fast spreading ridges. In the current plate tectonic situation, lithosphere formed at fast spreading ridges —with generally no seafloor exposures of mantle rocks— subducts at nearly all major active convergent plate margins (Fig 1.4). At present, oceanic lithosphere created at a slow spreading ridge, to large

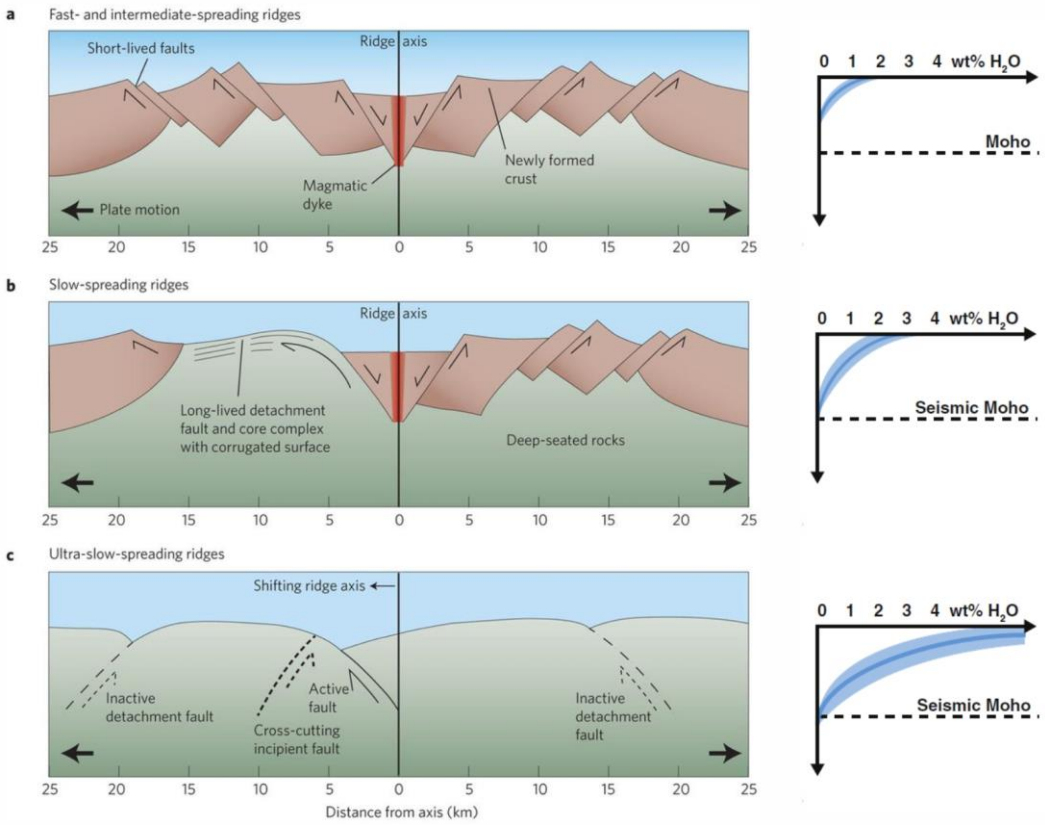

Figure 1.3. *Schematic sketches of different styles of fast, slow and ultra-slow spreading mid-ocean ridges (from Smith, 2013), and corresponding degree of hydration of the oceanic crust and mantle lithosphere (from Faccenda, 2014).*

parts consisting of altered mantle peridotite, is being subducted only at the Lesser Antilles active margin (Bouysse, 1984). However, over periods of Earth`s history, altered ultramafic mantle rocks have acted as a more relevant sink of carbon, when subduction of oceanic lithosphere formed at slow and ultra-slow spreading ridges was more common (Müller and Dutkiewicz, 2018). Further uncertainty of the carbon budget of oceanic mantle arises from a relatively low amount of available samples and the large spatial heterogeneity of carbon content, which is often concentrated in localized carbonate-bearing veins and zones of intense alteration (e.g. Bach et al., 2011; Schroeder et al., 2015) that are poorly recovered by ocean drilling.

1.1.2.2 Carbon fluxes in subduction zones and arc volcanism

Subduction of oceanic lithosphere is the only active flux of carbon from surface-near reservoirs into the convecting mantle during the Phanerozoic and at present. However, the amount of carbon retained in subducting slabs beyond sub-arc depths, and that returned to the atmosphere through arc-volcanoes and diffuse outgassing is poorly constrained (Fig. 1.2).

Resolving the uncertainties in the magnitude of carbon fluxes in subduction zones is therefore fundamental for understanding the Phanerozoic carbon cycle.

The mass-balance of incoming carbon fluxes (i.e. the carbon budget of the subducting oceanic lithosphere) versus the outgassing fluxes from arc volcanoes and diffuse vents can be assessed by geochemical/isotope proxies and extrapolation of direct measurements (e.g. Burton et al., 2013; Hirschmann, 2018; Kelemen and Manning, 2015). Such mass balance estimations suggest that arc volcanic carbon fluxes (18 – 43 Mt C/yr) and diffuse outgassing (4 – 12 Mt C/yr) together are of similar magnitude to that of the incoming carbon of subducting plates (Fig. 1.2) (Kelemen and Manning, 2015). However, carbon emitted in arc volcanoes is in parts derived from interaction of magma with crustal carbonate rocks (Carter and Dasgupta, 2016; Mason et al., 2017), and the cold parts of the mantle wedge above the subducting slab may act as a substantial, but highly uncertain, reservoir of carbon (Kelemen and Manning, 2015). Therefore, the fraction of carbon introduced deeper into the mantle by subduction zones is difficult to estimate from mass balance considerations alone.

Further constraints on the role of subducting slabs to transfer carbon into the deep mantle are based on thermodynamic predictions in conjunction with experiments and field

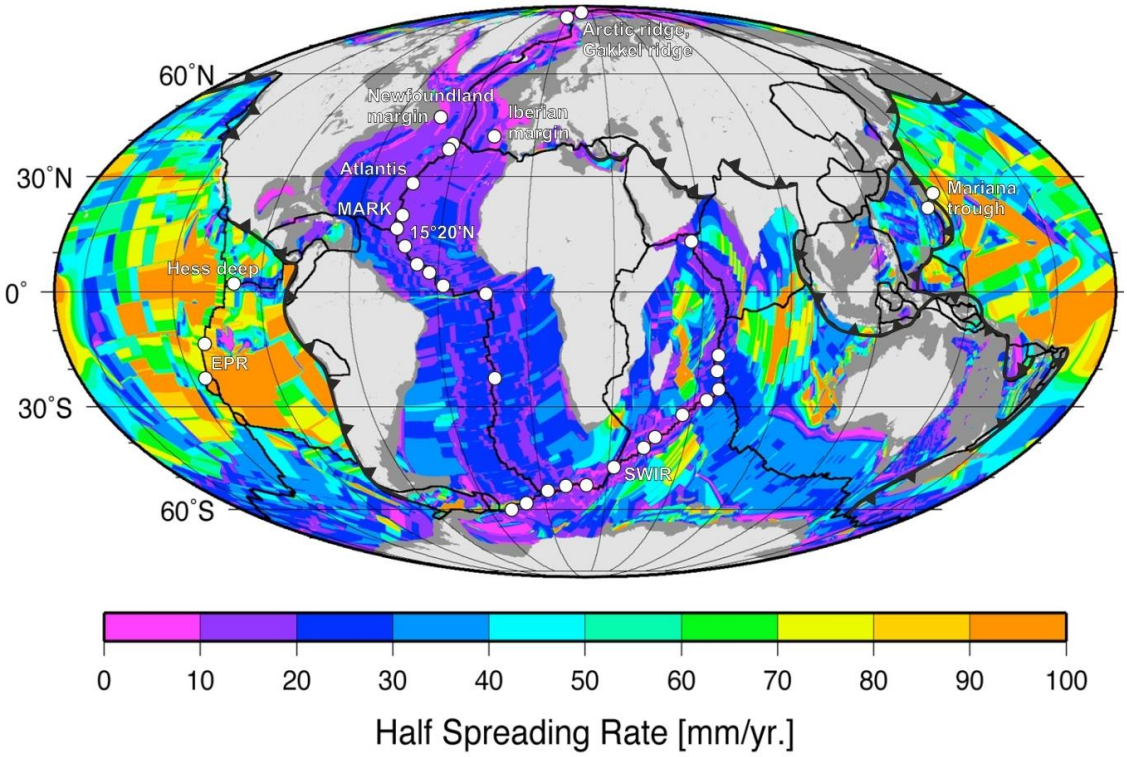

Figure 1.4. *Half spreading rates of ocean crust formation (Müller et al., 2008) and locations where serpentinized peridotites have been recovered from the seafloor (after Deschamps et al., 2013; Warren, 2016).*

observations from exhumed paleo-subducted terranes (e.g. Dasgupta and Hirschmann, 2010; Kerrick and Connolly, 2001a; Stewart and Ague, 2018). In particular, experiments and thermodynamic models are designed to predict the depth at which different slab lithologies release carbon into sub-solidus aqueous fluids (Manning et al., 2013; Molina and Poli, 2000; Schneider and Eggler, 1986), super-critical liquids (Poli, 2015) or melts (Dasgupta et al., 2004; Dvir and Kessel, 2017; Tumiati et al., 2013; Woodland et al., 2018), and to what extent carbon mobilizes or is retained in the slab during subduction metamorphism. Thermodynamic models suggest that slab sediments, altered oceanic crust and the hydrated mantle retain large fractions of their carbon contents during subduction metamorphism (Gorman et al., 2006; Johnston et al., 2011; Kerrick and Connolly, 1998, 2001a, b), indicating that metamorphic decarbonation reactions alone are not sufficient to explain arc volcanic carbon fluxes. Experiments to constrain the solidus temperatures for partial melting of different carbonate-bearing slab lithologies also show that carbon can be retained in the subducting slab, in particular if hosted in altered oceanic crust and mantle (Dasgupta, 2013; Dasgupta et al., 2004). Carbon flux estimates attained by experiments and thermodynamic models have difficulties to account for natural complexities such as heterogeneous carbon distribution in the slab, the effect of localized fluid pathways (Plümper et al., 2017; Tian and Ague, 2014), or physical transfer of solid carbon from the slab to the overlying mantle wedge in buoyancy-driven diapirs (Behn et al., 2011). Field studies of paleo-subducted metamorphic terranes and numerical models are therefore key to resolve the finer details of carbon fluxes in subduction zones. Because of the high solidus temperatures of carbonated peridotite relative to that of carbon-bearing crustal rocks and sediments (Dasgupta, 2013), the lithospheric mantle of the slab is particularly likely to transport carbon into the deep mantle. However, how much carbon dissolves from carbonate-bearing peridotites into sub-solidus fluids during subduction and how much is preserved in the slab is largely unknown.

This PhD thesis aims to provide new insights on the mechanisms that control the storage of carbon in the mantle wedge by studying the natural record of carbonation of peridotite in a forearc analogue setting. The presented work further aims to improve our understanding of the processes that determine the subarc release or retention of carbon contained in subducting oceanic mantle lithosphere, using the preserved natural record of paleo-subducted metamorphic terranes and thermodynamic modelling.

1.2 Hydration and carbonation of peridotite

Most mantle peridotites are harzburgites or lherzolites composed of more than 50 vol% olivine and variable amounts of ortho- and clinopyroxene (Bodinier and Godard, 2007). In abyssal peridotites, harzburgite compositions are most common (Warren, 2016), whereas relatively more lherzolites occur in orogenic peridotites sourced from the subcontinental mantle lithosphere (Bodinier and Godard, 2007). Olivine and pyroxenes in these rocks readily hydrate to form serpentine minerals when in contact with aqueous fluids, because they are far from equilibrium at weathering and low temperature metamorphic conditions. Depending on the relative proportions of olivine and orthopyroxene in the rock, fully hydrated harzburgites are either composed of brucite-serpentine or talc-serpentine assemblages (Fig. 1.5, assemblages 1 and 2, respectively). Serpentinization of lherzolite may additionally form diopside or tremolite (Klein et al., 2013). Lizardite and chrysotile are the predominant serpentine phases formed at low-temperature (< 250 °C), whereas antigorite is stable at temperatures between ~300 and 650 °C (Fig. 1.5) (Evans, 2004). Serpentinization is linked to oxidation of ferrous iron contained in primary olivine and orthopyroxene to ferric iron incorporated in serpentine and magnetite, a process that produces hydrogen and, in presence of carbon, methane and organic carbon compounds (Bach et al., 2004; Frost, 1985; Klein et al., 2014; McCollom and Bach, 2009; Ménez et al., 2018). Strong redox gradients and the abiotic production of hydrogen and higher carbon compounds make serpentinization environments possible candidates to host the emergence of life on Earth, and, possibly, other planets or moons (Ménez et al., 2012; Russell et al., 2010).

Serpentinization is widespread where oceanic mantle lithosphere is exposed to seawater alteration — for instance at magma-poor spreading ridges (Fig. 1.3) (Cannat et al., 2010; Rüpke and Hasenclever, 2017), along oceanic transform faults (Schlaphorst et al., 2016), or along deep bend faults at the outer rise prior to subduction (Faccenda, 2014; Ranero et al., 2003). Serpentine mud volcanoes and geophysical evidence further show that extensive amounts of serpentinites can form in the cold (T < 650 °C) leading edge of the mantle wedge in subduction zones when fluxed by fluids derived from pore waters or devolatilization of subducting slab lithologies (Fryer et al., 1999; Hyndman and Peacock, 2003).

In principle, peridotites can also be carbonated in all environments where serpentinization occurs, if in contact with fluids that bear dissolved inorganic carbon. These fluids can cause the precipitation or replacive growth of carbonate minerals in serpentinized

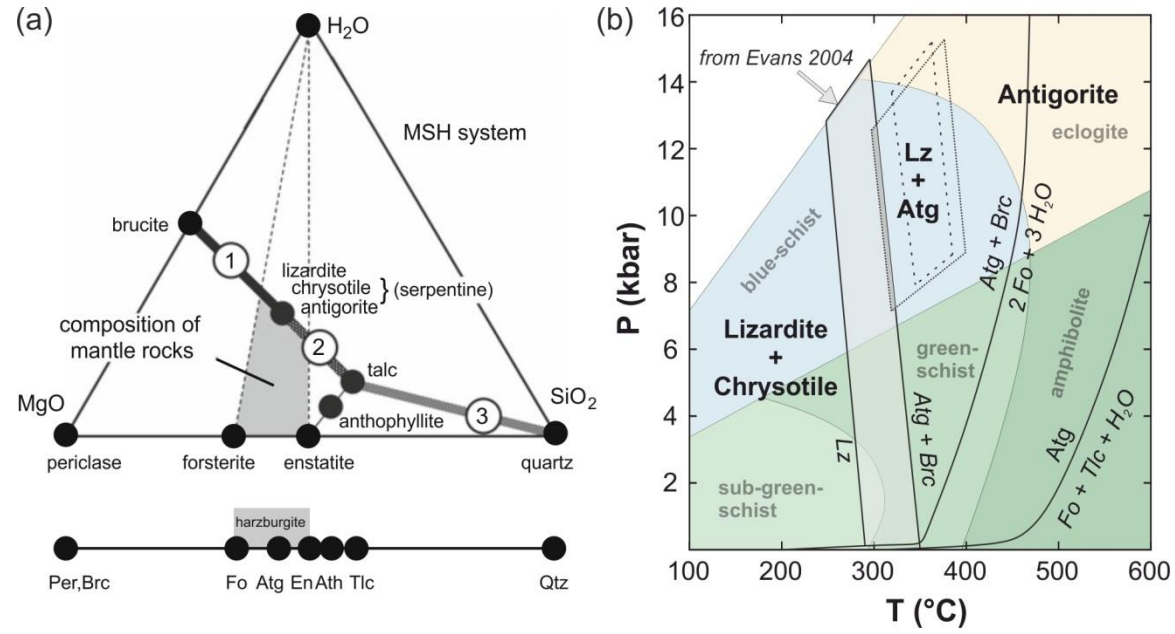

Figure 1.5. *Chemography and phase stability of hydrated peridotites.* ***(a)*** *Chemography of the ultramafic MSH system, showing maximum hydrated assemblages brucite-serpentine (1) and talc-serpentine (2), and the projection from H_2O onto the MgO-SiO_2 binary (after Bucher and Grapes, 2011).* ***(b)*** *P-T phase diagram of serpentinites superposed on the metamorphic facies fields of metabasalts (after Schwartz et al., 2013), and showing the transition from lizardite / chrysotile to antigorite at 250 - 350 °C (after Evans, 2004). If not stated otherwise, mineral abbreviations in this figure and the following figures are after Whitney and Evans (2010).*

peridotite, a process favoured by the fast kinetics of carbonation reactions and the high capacity of serpentinites to buffer CO_2-bearing fluids (Andreani et al., 2009; Grozeva et al., 2017; Hövelmann et al., 2011). The metasomatic change of the peridotite composition and the types of carbonate that form depend mainly on the fluid composition and temperature of carbonation. This variability is reflected in different main reaction trends of peridotite carbonation, namely forming ophicarbonates, talc-carbonate rocks / listvenites[2], magnesite-orthopyroxene rocks (sagvandites; Ohnmacht, 1974), serpentinite-hosted travertine, or cryptocrystalline magnesite. Travertine and cryptocrystalline magnesite deposits are mostly related to reaction of atmospheric CO_2 in meteoric fluids with peridotites in surface exposures of accreted ophiolites (Aharon, 1988; Kelemen and Matter, 2008; Kralik et al., 1989; Schwarzenbach et al., 2016), while sagvandites are likely mostly related to high temperature – low pressure regional metamorphism (Schreyer et al., 1972; Srikantappa et al., 1985). Because these are not that relevant for the deep recycling of carbon in oceanic subduction zones, this thesis focuses on ophicalcites and talc-carbonate rocks / listvenites.

[2] Different spelling variants of listvenite are in use, in particular in older literature (e.g. listwanite, listwaenite); here, I use the writing as recommended by Halls and Zhao, 1995.

1.2.1 Formation of ophicalcite by seawater alteration

Ophicalcites are serpentinized peridotites that contain variable amounts of serpentine and Ca-carbonate minerals of hydrothermal and/or sedimentary origin, reaching up to 100 m in thickness (Schwarzenbach et al., 2013; Treves and Harper, 1994). Fluids derived from serpentinized peridotites contain leached alkali earth metals and have a high pH, precipitating carbonate minerals when mixing with fluids that contain dissolved inorganic carbon (Bonatti et al., 1980; Eickmann et al., 2009; Ludwig et al., 2006). Ophicalcites from seafloor serpentinites show that aragonite, calcite, and, occasionally, dolomite precipitate in veins (Bach et al., 2011; Bonatti et al., 1980; Eickmann et al., 2009; Schroeder et al., 2015), cementing serpentinite breccias (Picazo et al., 2019), and in carbonate chimneys of active hydrothermal vents (Ludwig et al., 2006). Low temperatures (< 150 °C) and low Mg/Ca and C/Ca ratios of the hydrothermal fluids in these environments favour the precipitation of Ca-carbonates, whereas magnesite precipitation is kinetically inhibited (Grozeva et al., 2017).

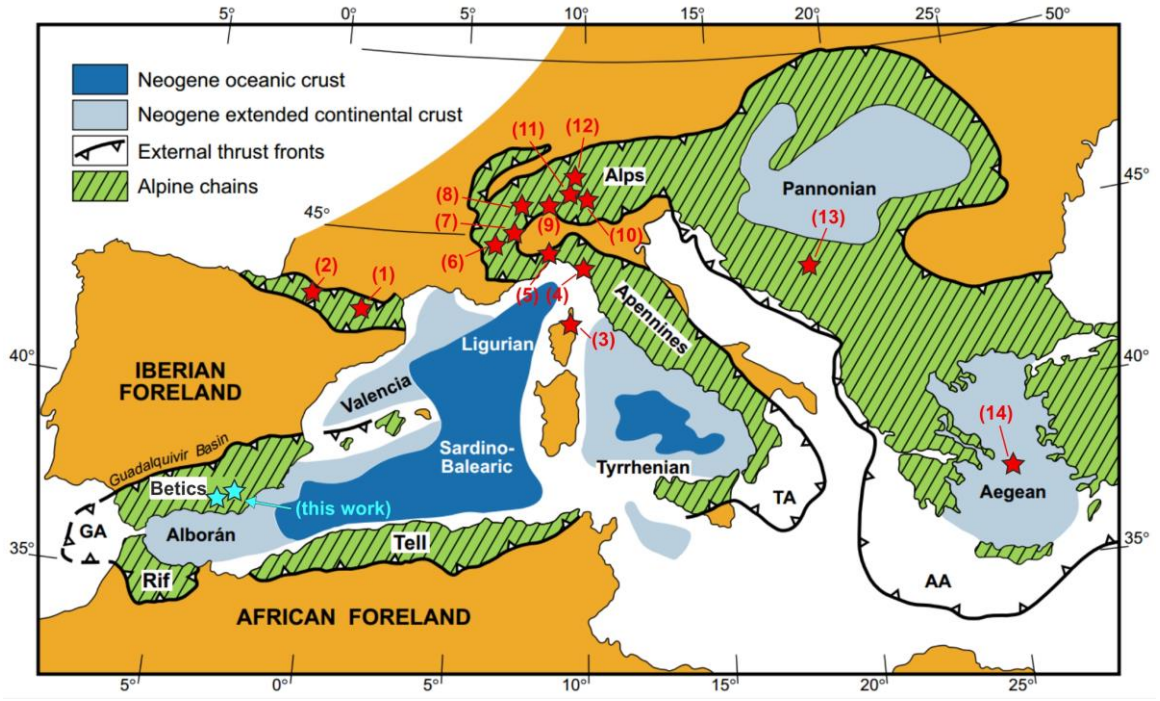

Figure 1.6. *Sketch of the tectonic setting in the Mediterranean (after Comas et al., 1999), and location of selected ophicarbonates described in the literature (red stars) and this PhD thesis (blue stars). (1) Lherz; (2) Urdach (both from (Clerc et al., 2014)); (3) Alpine Corsica (Vitale Brovarone et al., 2011); (4) Northern Apennines (Schwarzenbach et al., 2013); (5) Voltri (Scambelluri et al., 2016); (6) Chennaillet (Lafay et al., 2017); (7) Lanzo (Vitale Brovarone et al., 2017); (8) Zermatt-Saas (Collins et al., 2015); (9) Central Alps - Cima de Gagnone, Bellinzona-Dascia unit (Pfiffner and Trommsdorff, 1998; Stucki, 2001); (10) Malenco, Val Ventina (Ferry, 1995; Trommsdorff and Evans, 1977a); (11) Platta (Coltat et al., 2019); (12) Totalp (Mateeva et al., 2017); (13) Dinarides & Vadar (Faul et al., 2014); (14) Tinos (Hinsken et al., 2017).*

Exhumed ophicalcites are particularly widespread in ophiolites related to the closure of the Tethys during the alpine orogenic cycle (Fig. 1.6), but occur also in ophiolites obducted along sutures in older orogenies (Chi and Lavoie, 2000; Lavoie and Cousineau, 1995). Stable isotopes compositions of carbonates reveal an oceanic origin of most of the ophicalcites hosted in ophiolites and metamorphic terranes (e.g. Clerc et al., 2014; Collins et al., 2015; Chi and Lavoie, 2000; Schwarzenbach et al., 2013).

1.2.2 Carbonation of peridotite by CO_2-rich fluids

In presence of a CO_2-rich fluid, peridotites react to form magnesite-bearing rocks (Fig. 1.7) (Johannes, 1969). At temperatures of ~150 – 400 °C and if the carbonation reaction is isochemical with respect to non-volatile elements, zones with distinctive assemblages form, which correspond to different (generalized) reaction steps (Frost, 1985; Johannes, 1967; Klein and Garrido, 2011; Klein and McCollom, 2013):

$$olivine + pyroxene + H_2O + CO_2 = serpentine + magnesite \pm brucite \quad (1.1)$$

$$serpentine + CO_2 = magnesite + talc + H_2O \quad (1.2)$$

$$talc + CO_2 = magnesite + quartz + H_2O \quad (1.3)$$

Carbonated peridotites in ophiolites and metamorphic complexes occasionally record these arrested reaction steps in related occurrences of *ophimagnesite* (product of reaction step 1.1),

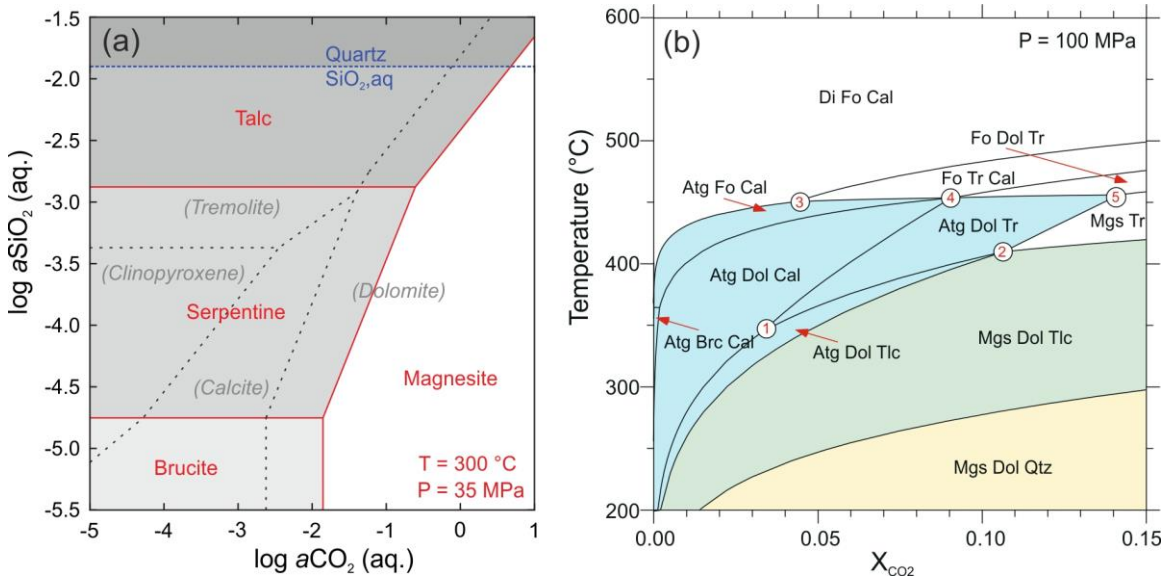

Figure 1.7. *Phase stabilities of carbonate-bearing ultramafic rocks in the system MgO–CaO–SiO_2–H_2O–CO_2.* ***(a)*** *Activity-activity plot in the MS-HC (red lines and minerals) and CMS–HC systems (dashed grey lines and minerals); after Grozeva et al. (2017), extended to higher $aSiO_2$ and with quartz saturation from Klein and Garrido (2011).* ***(b)*** *T–X_{CO2} phase diagram at 100 MPa showing ophicarbonate assemblages (blue; serpentine + carbonate), soapstone (green) and listvenite (yellow) (from Bucher and Grapes, 2011).*

soapstone (reaction step 1.2) and *listvenite* (reaction step 1.3), showing increasing carbon contents towards a zone of high degree of fluid-rock interaction (e.g. Beinlich et al., 2012; Hansen et al., 2005; Schandl and Naldrett, 1992). The fluid compositions corresponding to carbonation reactions (1.1) to (1.3) can be predicted by thermodynamic models such as isobaric-isothermal activity-activity diagrams (Fig. 1.7a), or T–X_{CO2} phase diagrams (Fig. 1.7b; with X_{CO2} being the molar fraction of CO_2/[CO_2+H_2O] in fluid). At low temperatures (< 150 °C), listvenite may also form directly by reaction of hydrated peridotite with CO_2-rich fluids without formation of intermediate talc-bearing assemblages, as documented for instance in the Samail ophiolite in Oman (Falk and Kelemen, 2015). At high temperatures (> 600 °C), carbonation of peridotite can proceed without previous or simultaneous hydration of peridotite to form *sagvandite* (Bucher-Nurminen, 1990; Koziol and Newton, 1998; Ohnmacht, 1974), according to the reaction:

$$olivine + CO_2 = enstatite + magnesite \quad (1.4)$$

If the protolith is a Ca-bearing ultramafic rock, or if the fluids apart from CO_2 also introduce dissolved non-volatile elements such as Ca or Si, calcite, dolomite, amphibole and/or diopside may become relevant product phases, depending on temperature and fluid composition (Fig. 1.7). Thermodynamic models show that in presence of Ca in the system, Ca-bearing carbonates such as calcite or dolomite are stable at lower $aCO_{2,aq}$ (grey dashed lines in Fig. 1.7a) and X_{CO2} (Fig. 1.7b) than magnesite.

Magnesite-bearing serpentinites and soapstones often occur in peridotites of ophiolites and metamorphic complexes worldwide, whereas listvenites (Fig. 1.8) and sagvandites (Bucher-Nurminen, 1991) are less common. Listvenites are particularly rare because they contain high carbon contents (> 30 wt% CO_2, stored in carbonates), which requires peridotites to be flushed by large amounts of fluids rich in CO_2 (Beinlich et al., 2012; Hansen et al., 2005).

Because listvenites are testament of effective solid storage of carbon by mineral carbonation, they are receiving increased attention as they are natural analogues for artificial carbon sequestration strategies (Beinlich et al., 2012; Kelemen et al., 2011; Matter and Kelemen, 2009). The finding of 10 – 200 m thick listvenite bodies at the base of the mantle section of the Samail ophiolite, Oman, formed by interaction of carbon-bearing fluids derived from underlying carbonate sediments of the metamorphic sole with serpentinized peridotite, further shows that listvenites may store significant amounts of carbon in forearc settings, with important implications for carbon fluxes in subduction zones (Falk and Kelemen, 2015;

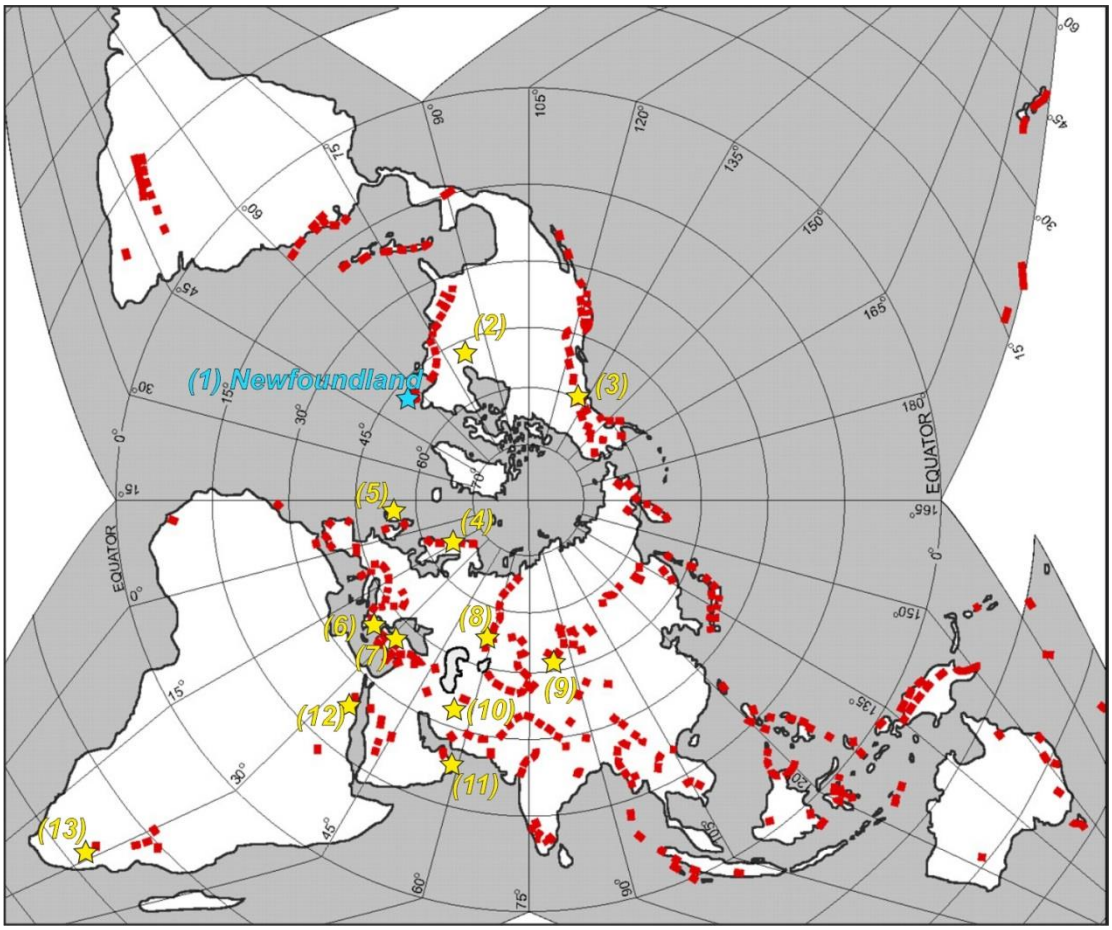

Figure 1.8. *Global distribution of ophiolite (red; from (Oze et al., 2007)) and listvenite occurrences reported in literature (blue and yellow stars). (1) Baie Verte, Newfoundland (this work; Escayola et al., 2009); (2) Abitibi Belt, Ontario (Schandl and Naldrett, 1992); (3) Atlin, British Columbia (Hansen et al., 2005); (4) Linnajavri, Norway (Beinlich et al., 2012); (5) Ireland (Halls and Zhao, 1995); (6) & (7) Anatolia, Turkey (Akbulut et al., 2006; Aydal, 1990); (8) South Ural (Belogub et al., 2017); (9) NW China (Qiu and Zhu, 2015; Robinson et al., 2005); (10) Iran (Aftabi and Zarrinkoub, 2013; Nosouhian et al., 2016); (11) Samail ophiolite, Oman (Falk and Kelemen, 2015); (12) Egypt (Emam and Zoheir, 2013); (13) Barberton Belt, South Africa (Grosch et al., 2012).*

Kelemen et al., 2017; Kelemen and Manning, 2015). Nevertheless, detailed documentation of the microstructures and phase relations that arise from progressive carbonation in natural rocks — as recorded in magnesite-bearing serpentinites, soapstones and listvenites— and their comparison to thermodynamic predictions (e.g. Klein and Garrido, 2011) are lacking.

1.3 Subduction metamorphism and volatile recycling

The depth at which carbon and other fluid-mobile components are mobilized from subducting sediments, altered oceanic crust and hydrated mantle is strongly coupled to the thermal stability of H_2O-bearing phases in these lithologies, because their devolatilization upon heating releases water-rich fluids that govern the geochemical transfer of geochemical

components (Hacker, 2008; Schmidt and Poli, 2014; van Keken et al., 2011). The stability of hydrous and carbon-bearing phases during subduction metamorphism in turn is intimately linked to the structural, seismic and thermal characteristics of subduction zones.

1.3.1 Subduction zone settings

Subduction zones are the sites where cooled oceanic crust and mantle lithosphere sink into the mantle at convergent plate margins. The slab pull of the descending plate is the main driving force of plate tectonic motion and represents the down-welling part of the asthenospheric thermal convection (Stern, 2002). Subduction zones further are Earth's largest recycling systems, carrying crustal rocks and volatiles back into the mantle, and are regions of high geohazard risk related to earthquakes and volcanoes. Subduction of the incoming oceanic plate below an overriding plate causes the development of a typical succession of structures and geomorphologies parallel to the convergent plate margin (Fig. 1.9). These are usually defined as (1) trench, (2) forearc, (3) magmatic arc, and (4) back-arc basin (Fig. 1.9).

(1) Deep-sea trenches are flanked by an outer high caused by the bending of the incoming plate, and an accretionary prism (Fig. 1.9). Tensional stresses during bending are responsible for reactivation and opening of normal faults in the oceanic plate, which can lead to substantial hydration of the oceanic crust and mantle prior to subduction (Faccenda, 2014; Ranero et al., 2003).

(2) The forearc is defined as the non-magmatic part of subduction zone where the slab is subducted to up to 40 – 60 km depth below the crust and lithospheric mantle of the overriding plate (Fig. 1.9). The slab and the overlying, leading edge of the mantle wedge in the forearc are too cold for partial melting. Forearc mass transfer occurs by subduction erosion of the overriding accretionary prism and crust and their incorporation into melange rocks at the plate interfaces, and by aqueous fluids released from the slab into the overlying lithospheric mantle, where they form serpentinites (Fryer et al., 1999; Hyndman and Peacock, 2003).

(3) The magmatic arc is located where the mantle wedge and/or the slab-mantle interface are hot enough to allow partial melting and melt migration (Fig. 1.9). In contrast to mid-ocean ridges, magmas are not produced by decompression melting but mostly by flux melting induced by H_2O and CO_2 bearing fluids that lower the solidus temperature (Dasgupta et al., 2004; Schmidt and Poli, 2014; Tumiati et al., 2013). Different scenarios of dry or wet melting of slab sediments or melange rocks at the

subduction interface (Grove et al., 2006; Schmidt and Poli, 2014; Spandler and Pirard, 2013; Walowski et al., 2015), and buoyancy-driven solid diapirism that produce melts higher up in the mantle wedge (Behn et al., 2011; Codillo et al., 2018; Mallik et al., 2016; Marschall and Schumacher, 2012) exist to explain arc magma genesis and the transfer of slab components through the mantle wedge. Common to these mechanisms is that the presence of hydrous minerals and H_2O-rich fluids in the slab or at the slab-mantle interface is required to produce sufficiently large quantities of magma at subarc depths.

(4) Backarc basins may form by rifting or spreading behind the magmatic front if the subduction zones comprises a steeply dipping oceanic plate (Stern, 2002). Backarc magmas can contain a significant recycled slab component (Stern, 2002), but they don't appear to be relevant recycling pathways of slab-derived carbon (Macpherson et al., 2010) — in contrast to volcanic arc and diffuse arc and forearc emissions (cf. Sec. 1.1.2.2).

The geometry and thermal structure of a subduction zone depends in first order on the age of the incoming plate, the convergence velocity, the dip angle, and the relative proportions of sediments, oceanic crust and hydrated mantle in the subducting slab (Stern, 2002; Syracuse et al., 2010). Further relevant factors are the amount of frictional heating produced by deformation (e.g. Kohn et al., 2018), and the depth at which the subducting slab and the

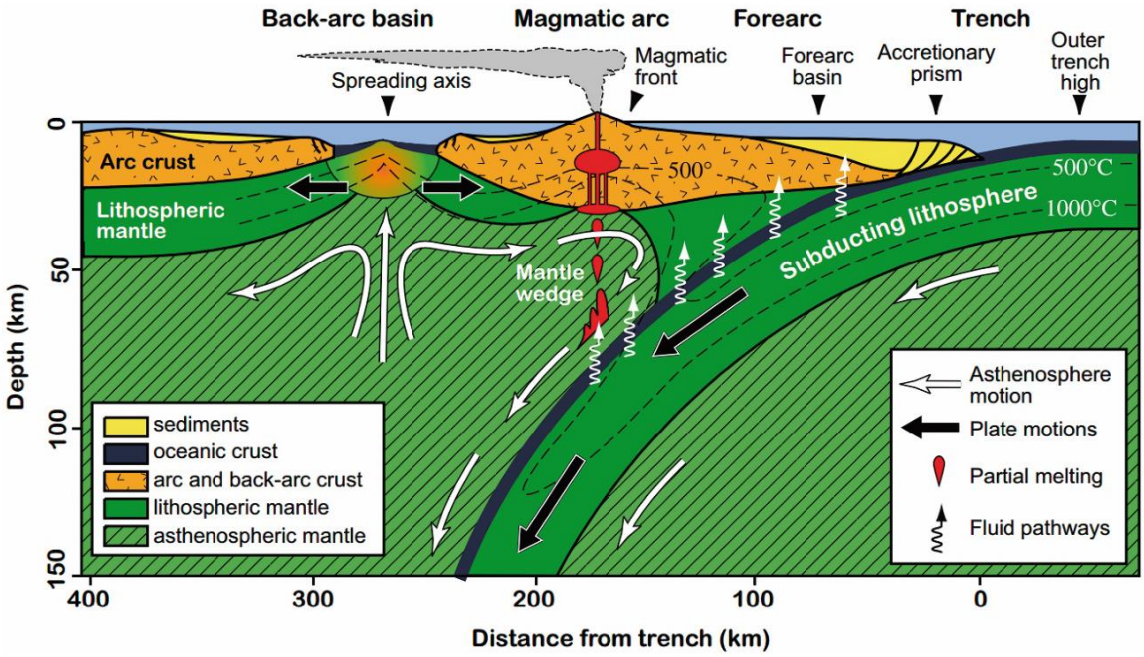

Figure 1.9. *Sketch of a subduction zone setting (modified by Padrón-Navarta (2010) from Stern (2002)).*

overlying mantle wedge become mechanically coupled and descent in parallel motion (Abers et al., 2006; Wada and Wang, 2009). All these parameters strongly influence the metamorphic pressure-temperature (P–T) path of the subducting slab, and, thus, the depth and extent to which different slab lithologies devolatilize (Syracuse et al., 2010; van Keken et al., 2011). Because the interdependence of the geometry of a subduction zone, its mechanical parameters and its thermal structure is not straightforward, numerical models are used to predict the thermal profile of a slab and its P–T path during subduction (Syracuse et al., 2010). Based on their thermal structure, warm, intermediate and cold subduction zones are commonly distinguished, where a given temperature and devolatilization condition at a certain position within the slab is met at lower pressures in warm subduction zones than in cold ones.

1.3.2 Dehydration reactions

The presence of water-rich fluids plays a fundamental role for partial melting, deformation, and seismicity in subduction zones (e.g. Hacker et al., 2003; Wassmann and Stöckhert, 2013). Water is present in subducting slabs as pore fluids, structurally bound H_2O or hydroxyl

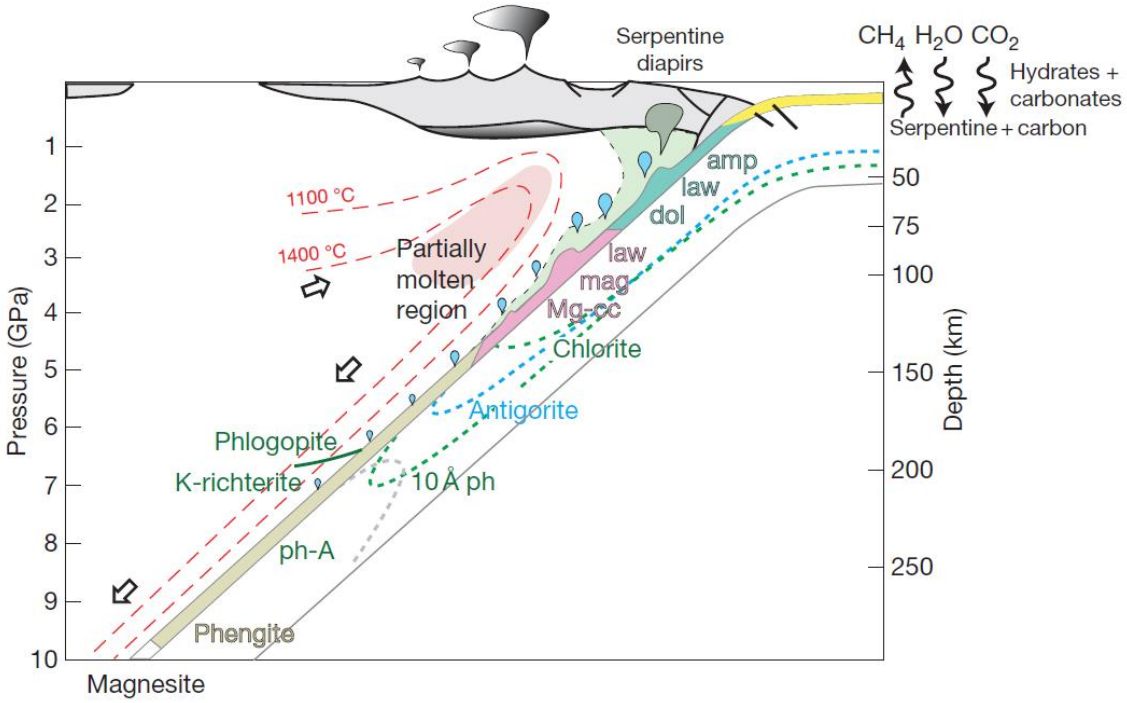

Figure 1.10. *Schematic representation of devolatilization processes in subduction zones, showing the stability of major volatile phases in the subducting oceanic crust (yellow, blue and pink colors) and the slab mantle lithosphere (green and blue dashed lines), and serpentinization of the mantle wedge (green field). amp: amphibole; law: lawsonite; dol: dolomite; mag: magnesite; Mg-cc: magnesian calcite;10 Å ph: 10 Å-phase; ph-A: phase A (from Schmidt and Poli, 2014).*

groups in hydrous minerals (Fig. 1.10), as fluid inclusions in minerals, and in nominally anhydrous minerals (Faccenda, 2014). Compaction of sediments and rocks of the upper ocean crust expels pore fluids from the slab at shallow depths (Hyndman and Peacock, 2003). The main fluid fluxes at forearc and subarc depths arise from devolatilization due to metamorphic breakdown reactions of hydrous minerals in sediments (e.g. clay minerals, biotite, phengite, chloritoid, zoisite), altered oceanic crust (e.g. chlorite, lawsonite, epidote, biotite, amphibole), and hydrated mantle (e.g. brucite, lizardite, antigorite, chlorite, talc, 10Å-phase, humite-group minerals, phase A) (Faccenda, 2014; Schmidt and Poli, 2014). Part of the water contained in the slab — in particular that stored in phengite in the ocean crust and phase A in meta-serpentinite (Fig. 1.10) — subducts deeply beyond subarc depths (Hacker, 2008).

Thermodynamic models indicate that devolatilization reactions in meta-sediments and oceanic crust of the subducting slab continuously produce fluids at different forearc depths, whereas in these lithologies relatively little devolatilization occurs at subarc depth (Fig. 1.10) (Gorman et al., 2006; Hyndman and Peacock, 2003; Schmidt and Poli, 2014). In contrast, serpentinized mantle can produce a distinct fluid pulse, releasing 40 – 60 % of their initial water content at subarc depth during the dehydration of antigorite (Hacker, 2008; Rüpke et al., 2004; Ulmer and Trommsdorff, 1995). Furthermore, volatiles released from the slab at forearc depths rise to the slab-mantle interface, where they are incorporated to large parts in mantle wedge serpentinite and minor, hybrid melange rocks that are rich in amphibole, talc and chlorite (Bebout, 1991; Spandler et al., 2008). These melange rocks and forearc mantle wedge serpentinites may be dragged down with the slab and thereby deliver volatiles to depths of arc magma genesis (Hyndman and Peacock, 2003; Spandler and Pirard, 2013). Hence, serpentinites are considered the potentially most important water source below the magmatic arc in subduction zones (Padrón-Navarta et al., 2010b; Ulmer and Trommsdorff, 1995).

1.3.2.1 Serpentinite dehydration

Fully hydrated peridotites composed of lizardite, chrysotile and brucite can contain up to 14 wt% H_2O. During subduction metamorphism, such serpentinites release up to 2 wt% H_2O during compaction and the reaction of lizardite/chrysotile to antigorite (at 250 – 350 °C; Fig. 1.5), 0 – 2.2 wt% H_2O by the dehydration of brucite to metamorphic olivine (at 400 – 500 °C), and 6 – 11 wt% H_2O during the dehydration of antigorite (Fig. 1.11) (Padrón-Navarta et al., 2013, and references therein). Depending on pressure and the Al content of the rock,

dehydration of antigorite occurs at 500 – 680 °C (Fig. 1.11) (Bromiley and Pawley, 2003; Padrón-Navarta et al., 2010a; Padrón-Navarta et al., 2013; Ulmer and Trommsdorff, 1995), according to the reactions:

$$antigorite = talc + olivine + H_2O \quad (1.5)$$

$$antigorite = olivine + orthopyroxene + chlorite + H_2O \quad (1.6)$$

$$antigorite = orthopyroxene + phase\ A + water \quad (1.7)$$

The phase assemblage produced by the low-pressure dehydration reaction (1.5) is common in contact-metamorphic serpentinites (e.g. Trommsdorff and Evans, 1972). Reaction (1.6) is the most relevant serpentinite dehydration reaction along warm and intermediate P-T paths in

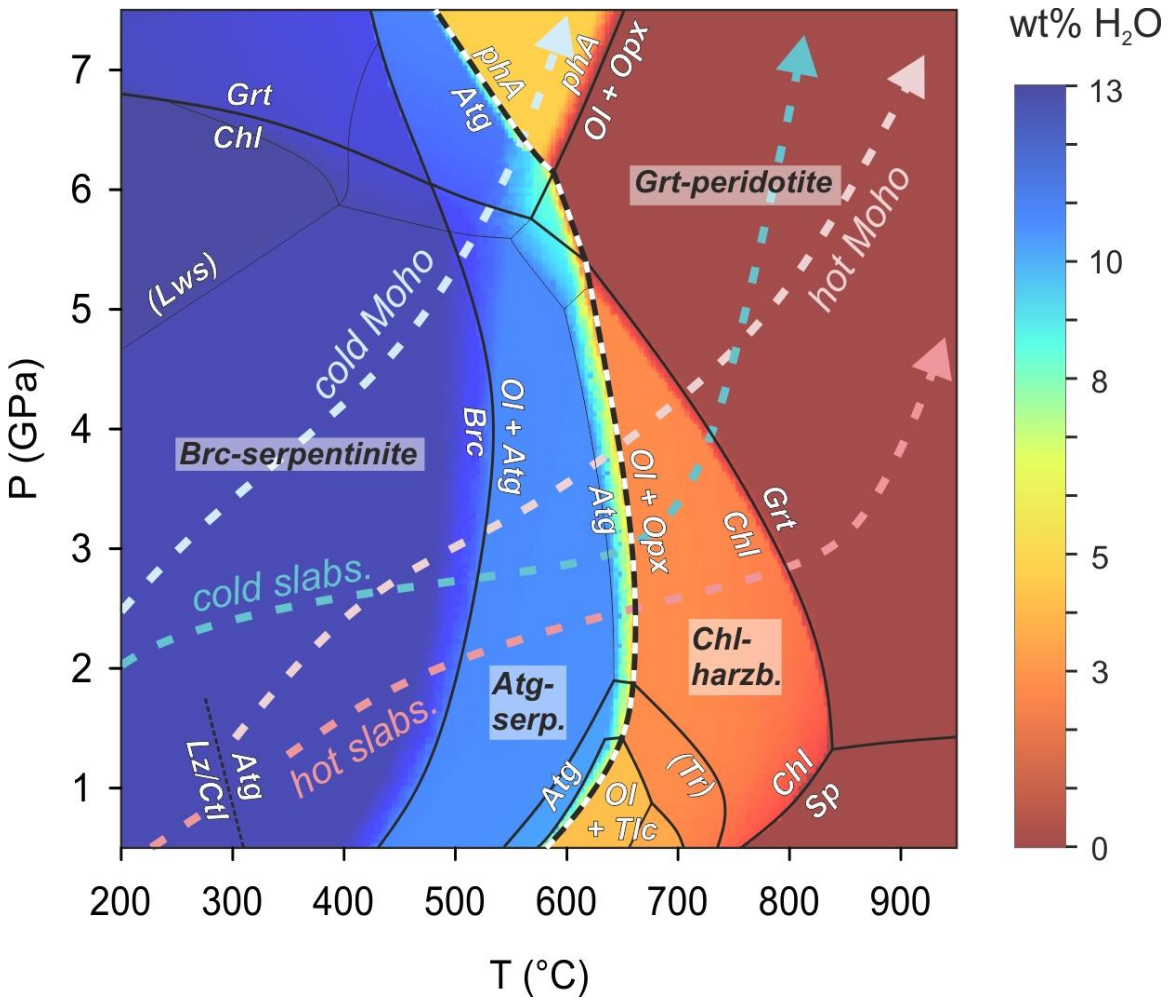

Figure 1.11. *P–T phase diagram of serpentinite showing the main (simplified) dehydration reactions for a Ca- and Al- bearing serpentinite in a fluid-saturated system, superposed on the H_2O content of the solid (in wt%, colorscale on the right; note that the colormap of the water content does not account for the Lz/Ctl to Atg transition). Also shown are P–T paths of the slab-surface and the slab Moho depth for hot and cold subduction zones (rose and blue dashed arrows, respectively; after Syracuse et al. (2010)). Calculated using the Perple_X software (cf. Ch. 3.4.2).*

subduction zones, producing prograde chlorite-harzburgite (Bromiley and Pawley, 2003; Trommsdorff et al., 1998). Chlorite produced by this reaction dehydrates at 50 – 100 °C higher temperature than antigorite (Fig. 1.11), forming prograde garnet peridotites (Bromiley and Pawley, 2003; Padrón-Navarta et al., 2013; Scambelluri et al., 2014). In cold subduction zones, water can be retained in phase A after the breakdown of antigorite (reaction 1.7) (Maurice et al., 2018; Rüpke et al., 2004) and in humite-group minerals (Garrido et al., 2005; Shen et al., 2014), contributing to water delivery into the deep mantle. Natural rocks and experiments indicate that the breakdown of antigorite-serpentinite to chlorite-harzburgite (reaction 1.6) is accompanied by the reduction of Fe^{3+} in magnetite to Fe^{2+} incorporated in olivine and orthopyroxene and a coupled formation of hematite and oxidation of Fe-Ni-sulphides to fluid-mobile sulphate (Alt et al., 2012; Debret et al., 2015; Merkulova et al., 2017). Hence, antigorite dehydration fluids can transfer oxidized volatiles and contribute to oxidation of the overlying mantle wedge.

The P–T conditions of antigorite breakdown (Fig. 1.11) are consistent with those encountered within the slab at subarc depths of subduction zones (typically 80 – 140 km depth), making fluids derived from this dehydration reaction the most important agent to leach fluid mobile elements (FME) from other slab lithologies and transfer them to the source region of arc magmas in the mantle wedge (Deschamps et al., 2013; Schmidt and Poli, 2014; Ulmer and Trommsdorff, 1995). The geochemical fingerprint of fluids produced by serpentinite dehydration — enriched in FME (Deschamps et al., 2013; Marchesi et al., 2013), isotopic enrichment of ^{18}O, D, ^{34}S (Alt et al., 2012) and $\delta^{11}B$ (Harvey et al., 2014), and depletion in high field strength elements (Garrido et al., 2005) — consistent with that of arc magmas (e.g. Scambelluri et al., 2019 and references therein) further points to an important role of serpentinite breakdown reactions in subduction zones.

1.3.3 Carbon mobility in subduction zone fluids

Carbon is distributed heterogeneously in different lithologies of subducting slabs, in the form of carbonate minerals, organic carbon compounds or graphite, and in fluid or multi-phase inclusions in silicate minerals. During subduction metamorphism at subsolidus conditions, multivariate equilibria between carbonate and hydrous silicates mainly control the composition of fluids. For most subduction P–T paths, thermodynamic models predict that the general sequence of stable carbonate phases with increasing metamorphic grade is *Mg-calcite – aragonite*/*dolomite – aragonite*/*magnesite* in meta-sediments (Kerrick and

Connolly, 2001a), and *Mg-calcite/aragonite – dolomite – magnesite* in altered oceanic crust (Fig. 1.10) (Kerrick and Connolly, 2001b) and carbonate-bearing, hydrated mantle (Kerrick and Connolly, 1998). These models indicate relatively little carbon release during subduction metamorphism, in particular for ophicarbonates and meta-sediments with elevated carbon contents (Kerrick and Connolly, 1998, 2001a). Meta-sediments with high carbonate contents — i.e., calcite marbles or siliceous dolomite marbles — can show similar phase relations as meta-ophicalcites during metamorphism, and are in equilibrium with H_2O-rich fluid compositions (low X_{CO2}) at high pressure (Ferrando et al., 2017; Kerrick and Connolly, 1998; Trommsdorff and Evans, 1977b). Because they typically also contain low Na and K contents in comparison to meta-pelites (Plank and Langmuir, 1998), these rocks are refractory during partial melting and thus particularly susceptible to transporting carbon into the deep mantle (Dasgupta, 2013), if the carbonates are not dissolved in open system fluids at subsolidus P–T conditions.

Classical thermodynamic approaches to model metamorphic devolatilization reactions of carbonate rocks consider fluids composed of H_2O and CO_2 (Connolly and Trommsdorff, 1991; Holland and Powell, 1991), such as the decarbonation of calcite and quartz to wollastonite:

$$calcite + quartz = wollastonite + CO_2 \quad (1.8a)$$

However, spectroscopic analysis of fluids in high-pressure experiments and of fluid inclusions from paleo-subducted lithologies have revealed that dissolved non-volatile aqueous complexes are highly relevant in subduction zones fluids (Facq et al., 2014; Frezzotti and Ferrando, 2015; Frezzotti et al., 2011; Sanchez-Valle, 2013). Hence, thermodynamic models of devolatilization reactions in the fluid-rich setting of subduction zones need to consider complex fluid compositions (Manning, 2004; Schneider and Eggler, 1986), and the example reaction (1.8a) would be more appropriately represented according to the reaction:

$$calcite + quartz + fluid = wollastonite + fluid \quad (1.8b)$$

In reaction (1.8b), fluid may consist of H_2O, $CO_{2,aq}$, HCO_3^-, $HCOO^-$, Ca^{2+}, $CaOH^+$, $SiO_{2,aq}$, $HSiO_3^-$, and other aqueous species in variable proportions, depending on their activity relations and the dissociation equilibria of the solid minerals at the respective P–T conditions. This has important implications for the mobility of carbon in subduction zones, suggesting that previous estimations of carbon fluxes by devolatilization of slab lithologies have been too low because they did not take into account charged aqueous carbon species (Ague and

Nicolescu, 2014; Frezzotti et al., 2011; Kelemen and Manning, 2015). Recent advances in the thermodynamic treatment of fluid–rock interactions at high pressure and the respective aqueous species databases (cf. Ch. 3.4) (Connolly and Galvez, 2018; Dolejš, 2013; Galvez et al., 2016; Galvez et al., 2015; Sverjensky et al., 2014a) call for a re-evaluation of the carbon fluxes related to prograde devolatilization reactions in carbonate-bearing rocks in subduction zones.

Metasomatized peridotites of the mantle wedge can contain carbonate minerals, elementary carbon (graphite/diamond) or carbon-bearing fluid inclusions, indicating that carbon in COH-fluids released from subducting slabs by devolatilization is partly trapped again once in contact with mantle rocks (Forster et al., 2017; Malaspina and Tumiati, 2012; Sapienza et al., 2009). Reducing fluids — e.g. H_2-bearing fluids derived from serpentinization of mantle wedge olivine and pyroxene — may cause the formation of graphite from carbonates that previously precipitated in the mantle wedge above the slab-mantle interface (Galvez et al., 2013; Vitale Brovarone et al., 2017). This process can produce abiotic methane and other organic carbon compounds in subduction zone fluids, which influences carbon mobility (Galvez et al., 2013; Sverjensky et al., 2014b; Tumiati et al., 2017) and the oxidation state of the slab-mantle interface and arc magmas (Arai et al., 2012; Tao et al., 2018). However, the relevance of reduced mobile carbon compounds in comparison to CO_2 and aqueous carbonate complexes in subduction fluids for large scale carbon fluxes and oxygen transfer is not well understood.

1.4 Geological setting of the case studies and previous work

The following sections provide short overviews of the geological settings of the investigated case studies and previous work; further details are given in Chapters 4 and 5, respectively.

1.4.1 Listvenites in the Baie Verte Ophiolites, Newfoundland

The Baie Verte Ophiolites of Newfoundland comprise dismembered sections of Early Ordovician oceanic crust and mantle lithosphere that have been obducted onto the Neoproterozoic continental margin of Laurentia. Metasomatic trace element patterns of otherwise depleted mantle harzburgite, and a boninitic affinity of cumulates, sheeted dykes and lavas in the Baie Verte Ophiolites point to the formation of oceanic crust by forearc seafloor spreading (Bédard and Escayola, 2010; Bédard et al., 1998), related to the partial

subduction of the continental margin (Castonguay et al., 2014). Early reconnaissance work and mapping show that carbonated peridotites such as talc-magnesite rocks and listvenites are ubiquitous in harzburgites and cumulate rocks of the different ophiolite exposures on the Baie Verte peninsula (Chao et al., 1986; Kidd, 1974; Kidd et al., 1978). Bédard and Escayola (2010) and Escayola et al. (2009) investigated possible links between listvenite formation, metasomatism of peridotites, and gold mobilization in the Advocate and Point Rousse complexes of the Baie Verte Ophiolites, respectively, but the conditions of serpentinization and carbonation of the ultramafic rocks, the formation mechanisms and related fluid sources all remain unconstrained. Considering the supra-subduction setting (Bédard et al., 1998; Castonguay et al., 2014) and that most listvenites occurrences in these complexes occur along regional thrust faults parallel to shear zones that separate the ophiolites from the underlying continental margin (Kidd, 1974), the carbonated peridotites of the Advocate complex —the ophiolite section proximal to the margin— represent a key target site to gain new insights on the transport and storage of carbon from subducted crust to overlying forearc mantle.

1.4.2 Meta-ophicalcites of the Nevado-Filábride Complex

The Nevado-Filábride Complex is a paleo-subducted terrane of the westernmost segment of the Alpine orogeny, exposed as a metamorphic core complex in the Betic Cordillera (South Spain) (e.g. Behr and Platt, 2012). Ultramafic massifs in the Nevado-Filábride Complex show a remarkable record of alpine Miocene subduction metamorphism with little to no retrograde overprint because of their fast exhumation (López Sánchez-Vizcaíno et al., 2001; Trommsdorff et al., 1998). The Almirez ultramafic massif reached the highest peak metamorphic conditions of the different parts of the Nevado-Filábride Complex, and preserves the prograde dehydration reaction of antigorite serpentinite to chlorite harzburgite in the field (Padrón-Navarta et al., 2011; Trommsdorff et al., 1998). This makes the Almirez a unique field laboratory to study in a warm subduction setting the effects of serpentinite dehydration on trace element and volatile recycling (Alt et al., 2012; Garrido et al., 2005; Harvey et al., 2014; Kendrick et al., 2018; Marchesi et al., 2013; Scambelluri et al., 2001), oxidation state of subduction fluids and the slab (Debret et al., 2015; Laborda-López et al., 2018), and the physical mechanisms that govern high-pressure fluid release and drainage (Dilissen et al., 2018; Padrón-Navarta et al., 2012; Padrón-Navarta et al., 2010b; Padrón-Navarta et al., 2015).

Rare studies of metamorphic phase relations in sedimentary carbonate rocks from the Nevado-Filábride Complex show that they in parts encountered similar metamorphic pressure-temperature (P-T) conditions as the ultramafic massifs (Gómez-Pugnaire et al., 1994; López Sánchez-Vizcaíno, 1994; López Sánchez-Vizcaíno et al., 1997). In contrast to their counterparts in the Alps, Apennines and Pyrenees (Fig. 1.6), ophicalcites in ultramafic massifs of the Nevado-Filábride Complex have never been studied in detail, apart from their use as ornamental stones (Navarro et al., 2013). Field mapping and reconnaissance work by Hürlimann (1999) and Schönbächler (1999) revealed lenses of carbonate rocks within the prograde chlorite-harzburgite at Almirez. The authors inferred that some of these carbonate rocks may be meta-ophicarbonates due to their stable C and O isotope signature and the high content of magnetite, pentlandite and pyrrhotite that is unusual for sedimentary marbles. However, the chemistry, microstructures and metamorphic phase relations of these rocks have never been investigated, despite their conspicuous presence inside chlorite-harzburgite, which bears important implications for the stability of carbonates during serpentinite dehydration in subduction zones.

2 Aims and Thesis Outline

2.1 Motivation

The present Ph.D. thesis is part of the European Commission FP–7 Marie Curie Initial Training Network (ITN) 'ABYSS' on reactive geological systems from the mantle to the abyssal sub-seafloor. The ITN ABYSS aimed at training Early Stage Researchers in geodynamics, mineralogy, hydrodynamics, thermodynamics and (bio)geochemistry of mid-ocean ridge processes and their environmental and economic impacts. The motivation behind the ITN ABYSS is to make significant advances in the understanding of the coupled tectonic, magmatic, hydrothermal and (bio-) geochemical mechanisms that control the structure and composition of the oceanic lithosphere. One of the main goals of the ABYSS project is to improve the understanding of the mechanisms and magnitude of chemical fluxes related to alteration of the oceanic lithosphere; in particular, the role of the lower crustal section and upper mantle as sinks for fluid-mobile elements.

Within the framework of the ABYSS project, the present thesis aims at providing new insights into the role of serpentinite carbonation in the global carbon cycle through the study of natural examples of carbonated serpentinites preserving different stages of carbonation of ultramafic rocks. Moreover, the present Ph.D. thesis project is part of the Deep Carbon Observatory (DCO) initiative, a global community of more than 1000 scientists on a ten-year quest to understand the quantities, movements, forms, and origins of carbon inside Earth. One of the DCO's decadal goals is to "determine the seafloor carbon budget and global rates of carbon input into subduction zones"[1]. As outlined in Ch. 1, the DCO research initiative has led to significant improvement of the estimates of carbon fluxes in subduction zones, but also revealed several key uncertainties, in particular regarding (i) the extent of carbon storage in the forearc mantle wedge, and (ii) the amount of carbon subducted beyond subarc depths.

[1] CARBON IN EARTH Quantities, Movements, Forms, and Origins; Midterm Scientific Report of the Deep Carbon Observatory, December 2014 (https://deepcarbon.net).

2.2 Aims

The main goal of this Ph.D. thesis is to improve our understanding of carbonation processes of hydrated peridotites and the fate of serpentinite-hosted carbon during high-pressure metamorphism, in order to better constrain their role for storage and release of carbon in subduction zones. Because they provide the unique opportunity of investigation at a variety of scales (10^{-6} to 10^{3} m), the study of key exposures of peridotites in exhumed ophiolites and paleo-subducted metamorphic terranes combined with state-of-the-art thermodynamic modelling will contribute to filling gaps in the current state of knowledge on deep fluxes, sinks and sources of carbon in subduction zones. To advance in this overall research goal, the Ph.D. thesis is aiming to:

i. decipher the microstructural and petrological record of carbonation of peridotite by CO_2-rich fluids in forearc settings.

ii. constrain the petrology and phase relations of meta-ophicarbonates that underwent subduction metamorphism to conditions before and after the breakdown and dehydration of antigorite.

iii. investigate the effects of electrolytic fluids and open system fluid flux on the stability of serpentinite-hosted carbonate rocks during antigorite dehydration in subduction zones, and their implications for deep carbon fluxes.

To address the first aim (i), I have carried out a detailed field, petrographic, microstructural and petrological study of a sequence of carbonated peridotites, soapstones and listvenites from the Advocate Complex of the Baie Verte ophiolites, Newfoundland, Canada. This study aims to give a comprehensive view of the natural record of a complete sequence of carbonation reactions from partially serpentinized peridotites to fully carbonated listvenites, by integrating at multiple scales the chemical and (micro-)structural changes with reaction progress and corresponding model predictions. I further used stable isotope geochemistry of carbonates to assess fluid provenance and thermodynamic phase relations to estimate the P–T conditions of carbonation of the Advocate ophiolite peridotites.

To tackle the second aim (ii), I have investigated (meta-) serpentinite-hosted carbonate rocks from the Milagrosa and Almirez ultramafic massifs of the Nevado-Filábride Complex (NFC) (Betic Cordillera, SE Spain). I studied their microstructures, and whole rock and mineral chemistry to constrain the timing of their protolith formation in the geodynamic context and the respective imprints of subduction metamorphism and exhumation. Because

the Almirez massif is a natural laboratory that provides unique insights into the mechanisms of serpentinite dehydration during subduction, particular attention was paid to textures and metamorphic phase relations to decipher the effect of open system flux of serpentinite dehydration fluids on the meta-ophicarbonates.

Finally, in order to constrain the effect of serpentinite dehydration on carbon fluxes in different subduction zones put forth in the third goal (iii) of my Ph.D. thesis, I have used recent advances in thermodynamic modelling to make predictions about the solubility of carbonate rocks during open-system flux of electrolytic, high-pressure fluids. I modelled fluid–rock interactions of meta-ophicarbonates and talc-carbonate rocks with fluids derived from antigorite breakdown to attain insights into the reaction mechanisms, fluid compositions and speciation, and the time-integrated fluid flux required for complete carbonate dissolution. By exploring variable P–T conditions corresponding to different settings within the subducting slab and at the slab-wedge interface, the models provide improved mass-balance estimates of carbon fluxes from these lithologies during serpentinite dehydration in different thermal regimes of subduction zones.

2.3 Structure of the Thesis

The thesis comprises four main parts. **Part I** contains an introduction to the background and state-of-knowledge of the subject (**Chapter 1**), the research motivation, aims and overview of the structure of the thesis (**Chapter 2**), and a description of the applied methodology (**Chapter 3**). For clarity and consistency, part of the introduction and methodology that are specific of the research addressed in the result sections are provided in their respective chapters in Part II.

Part II shows the main findings and results of my thesis. **Chapter 4** addresses the first aim of the thesis, presenting a detailed field, petrological and thermodynamic assessment of peridotite carbonation by CO_2-rich fluids in the Advocate Complex of the Baie Verte ophiolite, Newfoundland. The results of this study have been published in the JCR journal *Lithos*[2]. **Chapter 5** contains the results of the field and petrological investigation of (meta-) serpentinite-hosted carbonate rocks from the Milagrosa and Almirez ultramafic massifs of the Nevado-Filábride Complex (NFC), Spain. Based on the petrographic and chemographic

[2] Menzel, M.D., Garrido, C.J., López Sánchez-Vizcaíno, V., Marchesi, C., Hidas, K., Escayola, M.P., Delgado Huertas, A., 2018. Carbonation of mantle peridotite by CO_2-rich fluids: the formation of listvenites in the Advocate ophiolite complex (Newfoundland, Canada). *Lithos* 323, 238-261. DOI: 10.1016/j.lithos.2018.06.001.

relationships in these rocks and corresponding thermodynamic modelling, this chapter discusses the metamorphic evolution of meta-ophicarbonates during subduction. These results have been published with open access in the JCR journal *Journal of Metamorphic Geology*[3]. **Chapter 6** is a draft of a manuscript that addresses the third aim of this thesis, investigating the stability of meta-ophicarbonates and talc-carbonate rocks during open-system fluid flux in different subduction settings, using thermodynamic modelling of high-pressure fluid–rock interactions and mass-balance calculations.

Part III presents the main conclusions of the three studies and open questions for future investigations (**Chapter 7**), followed by a list of the references cited throughout the thesis (**Part IV**).

In addition to the publications cited above, the results of this thesis have been disseminated at different international conferences and meetings, including several European Geoscience Union General Assemblies (2016–2018; Vienna, Austria), a Deep Carbon Observatory Thematic Institute (Berkely, USA, 2015), the conference on Subduction Interface Processes (Barcelona, Spain, 2017), the 12th International Eclogite Conference (Åre, Sweden, 2017), the 3 minute thesis (3MT) presentation at the ABYSS Meeting (Granada, Spain, 2017), a talk at the 5th Granada–Münster Discussion Meeting (Granada, Spain, 2017), and a talk at the EGU Galileo conference "Exploring new frontiers in fluids processes in subduction zones" (Leibnitz, Austria, 2018). The research of this thesis has further been conveyed to the wider public in two outreach articles in the ABYSS *SeaRocksBlog*[4] and a feature article published in the newsletter and on the homepage of the Deep Carbon Observatory[5].

[3] Menzel, M.D., Garrido, C.J., López Sánchez-Vizcaíno, V., Hidas, K., Marchesi, C., 2019. Subduction metamorphism of serpentinite-hosted carbonates beyond antigorite serpentinite dehydration (Nevado-Filábride Complex, Spain). *Journal of Metamorphic Geology*. DOI: 10.1111/jmg.12481.

[4] https://searocksblog.wordpress.com/2015/11/25/the-story-of-the-oceanic-crust-and-the-deep-carbon-cycle/; https://searocksblog.wordpress.com/2016/08/24/continued-the-story-of-the-deep-carbon-cycle/

[5] https://deepcarbon.net/studies-exhumed-seafloor-show-fate-subducting-carbon

3 Methodology

3.1 Field methods and sampling

Carbonated peridotites of the Baie Verte ophiolites (Newfoundland) were sampled during a field campaign in July 2015. The field work in the Advocate complex focused on an area of 1.0 x 0.5 km at the North-Western corner of Flatwater Pond close to the Baie Verte road (49°47'59.88"N / 56°19'15.61"W; cf. Fig. 4.1), because road-cuts and the lake shoreline provided good outcrop exposures of the studied listvenite ridges. Macroscopic characterization of these outcrops allowed a petrological and structural assessment and mapping of differently carbonated domains. Particular attention was given to structures related to transitions between different domains and to documenting the spatial distribution, orientation and thickness of quartz veins in listvenite. Several sections were sampled through the transitions between magnesite-bearing serpentinized peridotite, soapstone, and listvenite, in addition to serpentinized peridotite on both sides of the listvenite ridges. A total of 43 samples were taken in the Advocate carbonated peridotites, of which 42 were selected for detailed investigation (see Table A-4.1 of the Appendix to Ch. 4). All samples except for one (Adv-38) were geographically oriented during sampling, and thin sections billets were cut in the geographic reference frame after correcting a magnetic declination of 19.5° W.

Field work and sampling of serpentinites, chlorite-harburgites and carbonate-bearing rocks from the Milagrosa and Almirez ultramafic massifs of the Nevado-Filábride Complex (Spain) were made in spring and early summer of 2015 and 2016. The investigated outcrops are located in the Eastern Sierra de los Filabres (Milagrosa) and the Eastern part of Sierra Nevada (Almirez) (cf. Fig. 5.2). Fieldwork in the Milagrosa massif focused on an abandoned serpentinite quarry located 0.7 km west of El Marchal village, close to Lubrín (37°12'55.2" N / 002°01'57.5" W). A total of 57 samples of serpentinite-hosted carbonate rock lenses and veins, serpentinites, and adjacent meta-basic and meta-sedimentary rock units were collected in the Milagrosa massif, or which 37 were selected for thin-section investigation and 22 for bulk rock analysis (see Table A-5.1 of the Appendix to Ch. 5). Of these, a detailed sampling section through a series of marble lenses and carbonate-bearing lithologies within the serpentinites received special attention. In the Almirez, fieldwork and sampling were done mainly in two parts of the ultramafic massif: tremolite-carbonate veins and contact relations

between chlorite-harzburgite and marbles were studied at the eastern flank of Cerro del Almirez (2400 – 2450 m altitude); carbonate rock lenses inside and in contact to chlorite harzburgite were examined at Prado Mocho Bajo (1900 – 2050 m altitude). In total, 44 samples were taken in the Almirez massif, of which 32 were selected for more detailed investigations (see Table A-5.2 of the Appendix to Ch. 5). In both Milagrosa and Almirez massifs, a number of samples were geographically oriented in the field to permit correlation of structures and microfabrics in oriented thin sections (samples marked with * in Tables A-5.1 and A-5.2).

3.2 Bulk rock analytical methods

3.2.1 X-ray fluorescence, ferrous iron and C, S analysis

Rock chips were cut from homogeneous and non-weathered parts of the rock samples, cleaned in distilled water ultrasonic bath, crushed in a jaw crusher, and powdered (< 50 µm mesh) in an agate vibratory ring mill at the Instituto Andaluz de Ciencias de la Tierra (IACT, Granada, Spain). Analyses were carried out at the GeoLabs of the Ontario Geological Service (Canada). Major elements (ISO-accredited) and Co, Cu, Cr, Ni, V and Zn were analysed by XRF on fused glass beads. Ferrous iron was determined by potentiometric titration, and total carbon and sulphur by furnace infrared absorption. In calcite-bearing samples, the absolute carbonate amounts and the relative fractions of Ca-carbonate vs. dolomite/Mg-carbonate were analysed using a Chittick apparatus (Dreimanis, 1962). Duplicate analyses of sample aliquots show reproducibility better than 3% for most elements. The accuracy of major elements analyses are better than 5% for most elements as deduced from analyses of the reference materials dolomite JDo-1 (Geological Society of Japan) and calcareous sandstone Ou-8 (International Association of Geoanalysts) (Table 3.1).

3.2.2 Stable C and O isotopes of carbonates

Homogenized and dried whole rock powders and hand-drilled powders (5 – 10 mg) from veins and specific regions of interest from carbonated peridotites of the Advocate Complex were ground to <200 mesh to be reacted with 100% phosphoric acid at 50ºC (Al-Aasm et al., 1990; Sharma et al., 2002) at the IACT. In the case of samples containing dolomite and magnesite, we eliminated CO_2 evolved from dolomite by reaction with phosphoric acid at 50 °C during 24 h. This CO_2 was analysed, but the results are not shown because they

represent mixtures of dolomite and about 20% reaction yield from magnesite (Al-Aasm et al., 1990; Sharma et al., 2002). In a second step, the samples were subjected to vacuum for 60 minutes in order to remove remaining CO_2 from dolomite, and flushed with helium. Finally, CO_2 aliquots from magnesite were taken after an additional 108 h reaction at 50 °C. C-O stable isotopes were measured in CO_2 isolated by chromatographic column by means of a GasBench connected to a mass spectrometer (Delta XP, Thermo-Finnigan) at the IACT. All samples were compared to simultaneously analysed reference CO_2 obtained from in-house standards of calcites (Carrara and EEZ-1) and two varieties of magnesite, which have been previously calibrated with NBS-18 and NBS-19. The oxygen isotope ratios were calculated using the fractionation factor for acid decomposition at 50 ºC for magnesite and calcite (Sharma et al., 2002). Results are reported in the standard δ notation relative to VPDB ($^{13}C/^{12}C$) and VSMOW ($^{18}O/^{16}O$) (cf. Table 4.3). Three replicates were measured for each sample, with an analytical uncertainty less than ± 0.15 ‰.

3.3 Micro-analytical methods

3.3.1 Raman spectroscopy

Raman spectroscopy allows for easy and rapid distinction between antigorite, lizardite and chrysotile, due to the characteristic stretching vibrations of their OH groups, and the diagnostic vibrational band of antigorite at 1045 cm^{-1} (Petriglieri et al., 2015; Schwartz et al., 2013). Non-polarized micro-Raman spectra of serpentine with different microstructures (mesh, bastite, interlocked, coarse pleochroic, veins) have been acquired at the IACT on thin-sections both in the low- and high-wavenumber regions, using a LabRAM-HR spectrometer attached to a microscope (Jobin-Yvon, Horiba) with long-working distance 50× objective. A 523 nm wavelength of a diode laser has been used as excitation line, and a Peltier cooled charge-couple device detector (1064 × 256 pixels). The system was calibrated before each session using the 520.6 cm^{-1} Raman peak of a silicon wafer. Two repeated acquisitions for 15 s each with a 600 mm^{-1} diffraction grid were recorded for each spectrum, with a spectral resolution of c. 3 cm^{-1} and a spatial resolution of about 2 µm.

3.3.2 Scanning Electron Microscopy (SEM, EDS, EBSD)

We obtained EDS and EBSD maps using a Zeiss EVO® MA 15 SEM equipped with an Oxford Instruments 80 mm^2 X-Max^N EDS silicon drift detector and Nordlys Nano EBSD at

the IACT. The Oxford Instruments AZtec software platform was used for data acquisition and processing. Simultaneous EBSD–EDS maps were carried out in geographically oriented thin sections, using a standard setup (70° tilt, 24 mm working distance) in non-coated thin sections with a final colloidal silica polishing. EDS and EBSD maps were acquired at ~10^{-5} mbar for most samples, and at 10 Pa in carbonate-rich and serpentinite thin sections to avoid charging. For large area EBSD maps, and depending on the grain size of the sample, we used step sizes of 4 – 15 µm. For high-resolution mapping of carbonate inclusions and fine-grained antigorite, we used step sizes of 0.8 – 1.5 µm. Mean angular deviations (MAD) were in the range of 0.3 – 0.6° for carbonates, diopside and olivine, and 0.7 – 0.9° for chlorite and antigorite. Misindexation of Ti-clinohumite and Ti-chondrodite as olivine was common.

Removal of wild spikes and successive filling of non-indexed pixels based on 8, 7 and 6 neighbouring pixel orientations, were performed during data treatment using the Oxford Channel 5 software. Misindexation of calcite and dolomite analyses induced by their close crystal symmetries were discriminated using the simultaneously acquired EDS spectra. Systematic misindexation of olivine (60° [100]), dolomite (180° [100]), calcite (60° [001]) and antigorite (60° and 120° [001]), was removed using the Channel 5 software rotation algorithm. The Matlab toolbox MTEX (version 4.5.2) (Bachmann et al., 2010) was used for grain boundary rendering (15° segmentation angle) and small grains removal (5 and 8 pixel threshold in high resolution and large area maps, respectively).

3.3.3 Electron microprobe analysis (EMPA)

A Cameca SX100 (Centro de Instrumentación Científica, Universidad de Granada, Spain) and a JEOL JXA-8230 electron microprobe (Scientific and Technological Centers of the Universitat de Barcelona, Spain) were used to analyse the mineral chemistry of silicates, carbonates and oxides in carbon-coated thin-sections. The respective choice of natural and synthetic standard materials for calibration of wavelength-dispersive spectrometric analyses and detailed analytical settings are given in Table 3.2. Typical analytical conditions of 20 kV acceleration voltage and a beam current of 15 – 20 nA were adopted for silicates and oxides; for analysis of carbonates, a reduced beam current (6 – 10 nA) and a widened beam (10 µm) were used. Major elements and volatile elements were analysed first and for short times to prevent possible volatilization or drift due to beam damage on carbonates and sheet silicates.

3.4 Thermodynamic phase modelling and aqueous speciation

Thermodynamic modelling is invaluable to constrain P–T conditions for carbonated peridotites, because only one geothermometer — the calcite-dolomite miscibility gap— and no geobarometer exist for these chemical systems (Bucher and Grapes, 2011). Thermodynamic models further allow making predictions of the fluid composition at metamorphic conditions, which is critical to constrain the mobility of carbon in subduction zones. To attain the metamorphic P–T conditions and the aqueous geochemistry of corresponding fluids for the two case studies (Ch. 4 and 5) and to explore the stability of carbonates in open system fluid flux (Ch. 6), I used the recently developed Deep Earth Water model (Sverjensky et al., 2014), and classical and novel approaches of Gibbs free energy minimization of the Perple_X software (Connolly, 2005; Connolly and Galvez, 2018).

3.4.1 Deep Earth Water model

Modelling of water – rock interactions at low pressure metamorphic conditions has been possible since the 1970's based on the theoretical framework developed by Helgeson and co-workers (e.g. Helgeson et al., 1978; Helgeson and Kirkham, 1976), which includes the Helgeson–Kirkham–Flowers (HKF) equations of state for prediction of the properties of aqueous species (Helgeson et al., 1981). The revised HKF equations allowed estimation of the equation of state coefficients of the different aqueous species, and, in conjunction with the respective standard partial molal properties relative to 25 °C and 1.0 bar, the prediction of aqueous fluid–rock equilibria to conditions up to 1000 °C and 0.5 GPa, as part of the SUPCRT92 database and software (Fig. 3.1a) (Johnson et al., 1992; Shock and Helgeson, 1988). However, the lack of knowledge of the relative permittivity of water at high pressures (> 0.5 GPa) hampered the application of the revised HKF model for fluids produced at high pressure conditions in subduction zones (Sverjensky, 2019). The relative permittivity (or dielectric constant) is the factor by which a material — in this case water — decreases the electric field between two charges relative to vacuum. Hence, this parameter plays a fundamental role in the Born equation of solvation, which is part of the HKF approach to compute the standard partial molal properties of aqueous species as a function of pressure and temperature (Helgeson et al., 1981; Sverjensky et al., 2014). Using experimental data and *ab-initio* molecular models of the properties of water at high pressure as calibration, Sverjensky et al. (2014) recently developed an empirical extrapolation of the relative permittivity of H_2O

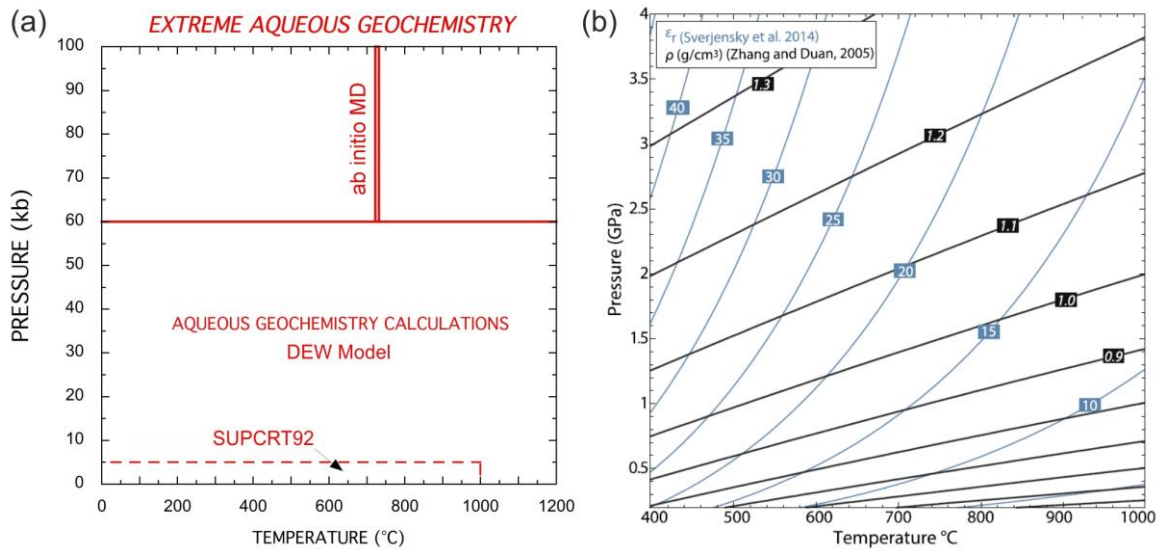

Figure 3.1. (a) *P–T limits of quantitative geochemical modelling of aqueous fluids based on the applicable extrapolation of the relative permittivity of water in SUPCRT92 (Johnson et al., 1992) and the DEW model (Sverjensky et al., 2014). MD = molecular dynamics models* ***(b)*** *Variability of the relative permittivity (ε_r; blue contours) and density (black contours) of H_2O with pressure and temperature (from Galvez et al., 2015). Relative permittivity is after the equations of state by Sverjensky et al. (2014); density values from Zhang and Duan (2005).*

(Fig. 3.1 a & b) that overcomes the restriction to low pressures and extends the applicability of the revised HKF equations of state to up to 6.0 GPa. The equation of state coefficients for aqueous species of the SUPCRT database were re-estimated according to the revised correlations between water density and dielectric constant at high pressures (Sverjensky et al., 2014), which form the core of the Deep Earth Water (DEW) model and enables prediction of equilibrium constants of mineral hydrolysis and aqueous speciation at high pressure (Sverjensky, 2019).

3.4.2 Gibbs free energy minimization (Perple_X)

Gibbs free energy minimization is a classical approach to compute thermodynamic phase stabilities in petrology (Fig. 3.2). In this thesis, I used the linear gridded Gibbs Free energy minimization algorithms contained in the software package Perple_X (Connolly, 2005, 2009) to obtain metamorphic phase relations and fluid compositions in the different chemical systems of interest (soapstones/listvenites: $CaO–MgO–FeO–Fe_2O_3–SiO_2–H_2O–CO_2$; meta-ophicarbonates: $FeO–CaO–MgO–Al_2O_3–SiO_2–H_2O–CO_2$; aqueous geochemistry and open system modelling: Fe–Ca–Mg–Al–Si–C–H–O), following a global equilibrium approach and using adequate solid solution models for the different mineral phases. Parameters and appropriate solution models vary slightly for the chemical systems and conditions of the

different case studies, therefore, these details are provided in the respective chapters of part II of this Ph.D. thesis (cf. Ch. 4, section *4.5.2*; Ch. 5, section *5.4.1*; and Ch. 6, section *6.3*).

Because of the complexity of activity relations of aqueous species and their poorly constrained thermodynamic data at high pressures, classical Gibbs free energy minimization models usually considered fluids composed of H_2O, CO_2, CH_4, and H_2 solvent species (COH-fluid) in graphite-bearing systems (e.g. Connolly and Cesare, 1993), or binary H_2O–CO_2 fluids for carbonate-dominated systems such as those of impure marbles and meta-ophicarbonate rocks (e.g. Connolly and Trommsdorff, 1991; Trommsdorff and Evans, 1977). However, charged aqueous complexes become relevant in high-pressure fluids, due to the higher relative permittivity of water at higher pressure (Fig. 3.1b). The "lagged speciation" algorithm of Perple_X (Connolly and Galvez, 2018) overcomes this restriction as it accounts for electrolytic fluid chemistry using the extension of the revised HKF model (Helgeson et al., 1981) to high pressures by the DEW model (Sverjensky et al., 2014), while considering overall equilibrium between rock, solvent and solute species (Connolly and Galvez, 2018; Galvez et al., 2015). In contrast to the DEW model, non-ideal molecular solution models are used to treat neutral carbonic volatiles as solvent species (COH-fluid), because predictions of their concentration as solute species in a pure H_2O solvent become unreliable at high concentrations (Galvez et al., 2016; Galvez et al., 2015). In the computation, the fluid speciation, ionic strength and pH are derived from the chemical potentials defined by the phase stabilities, concentrations and partial molar Gibbs free energies of solvent and solids,

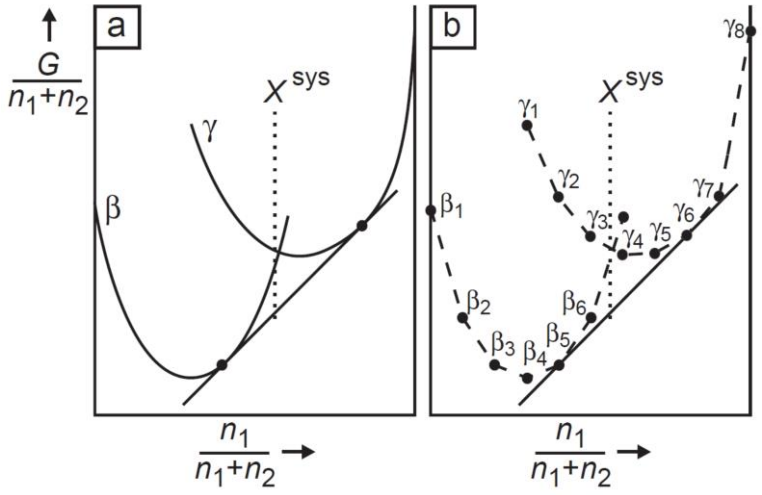

Figure 3.2. *Schematic isobaric–isothermal free energy-composition diagram for a binary system with two possible phases β and γ, illustrating the non-linear solution of Gibbs free energy minimization (a) and the linear approximation by pseudo-compounds as used by Perple_X (Connolly, 2005).*

using charge-balance and the Davies extension of the Debye-Hueckel equation to compute activity coefficients for electrolytes (Galvez et al., 2016; Galvez et al., 2015). The solution consistent with the solute-free initial condition is iteratively refined until chemical potentials converge to conform to mass-balance between solid, solvent and solute (Connolly and Galvez, 2018). Accounting for electrolytic fluids in Gibbs free energy minimization provides a more realistic view on the rock-buffered composition of subduction zone fluids (Galvez et al., 2016). The global equilibrium approach to model the complex phase relations between solid solutions (minerals), solvent and solutes of Perple_X further enables new avenues of modelling open system fluid flux and metasomatism in subduction zones, which have rarely been explored from a thermodynamic point of view (Connolly and Galvez, 2018).

Table 3.1: *Quality control of XRF measurements - results of certified reference materials (CRM)*

			CRM JDo-1 (Dolomite)		**CRM Ou-8 (calcareous sandstone)**			**CRM and in-house standards by Canada Lab**		
	Units	*D. L.*	JDo-1	*JDo-1 Ref*	Ou-8	Ou-8 DUP	*OU-8 Ref*	LK-NIP-1	GSP-2	*GSP-2 Ref*
SiO_2	wt%	*0.04*	0.17	*0.21*	54.46	54.44	*54.12*	49.59	67.08	*66.60*
TiO_2	wt%	*0.01*	<0.01	*0.01*	0.24	0.24	*0.24*	1.14	0.67	*0.66*
Al_2O_3	wt%	*0.02*	<0.02	*0.01*	6.57	6.55	*6.55*	15.5	15.04	*14.90*
Cr_2O_3	wt%	*0.002*	<0.002	*0.00*	<0.002	<0.002	*0.00*	0.02	0	*0.00*
Fe_2O_3	wt%	*0.01*	0.01	*0.02*	1.3	1.31	*1.30*	13.67	4.91	*4.90*
MnO	wt%	*0.002*	0.005	*0.01*	0.141	0.144	*0.14*	0.193	0.036	*0.04*
MgO	wt%	*0.01*	18.27	*17.82*	1.89	1.89	*1.88*	7.36	0.99	*0.96*
CaO	wt%	*0.006*	33.475	*30.42*	16.245	16.258	*16.71*	10.102	2.038	*2.10*
BaO	wt%	*0.004*	<0.004	*0.00*	0.06	0.05	*0.06*	0.01	0.15	*0.15*
Na_2O	wt%	*0.02*	<0.02	*0.01*	0.67	0.66	*0.68*	2.42	2.82	*2.78*
K_2O	wt%	*0.01*	<0.01	*0.01*	2.99	2.99	*2.97*	0.46	5.42	*5.38*
P_2O_5	wt%	*0.002*	0.032	*0.04*	0.02	0.02		0.109	0.292	*0.29*
LOI	wt%	*0.05*	47.15	*46.58*	15.45	15.48	*15.30*	0.08	0.78	*0.80*
Total	wt%		99.11	*95.14*	100.04	100.03	*99.95*	100.65	100.22	*99.56*
Co	ppm	*12*	<12	*0.17*	<12	<12		66	8	*7.3*
Ni	ppm	*9*	<9	*2.90*	<9	13		150	20	*17*
V	ppm	*8*	<8	*3.14*	32	36	*29.80*	282	49	*52*
Zn	ppm	*5*	37	*35.00*	17	17	*7 - 16*	107	121	*120*
Cu	ppm	*14*	<14	*1.40*	21	16	*8.36*	167	44	*43*

D.L. = detection limit; certified reference values (Ref) in italics; DUP = duplicate measurement

Table 3.2 (a) *Analytical settings of electron microprobe measurements; Cameca SX100; Centro de Instrumentación Científica, Universidad de Granada, Spain*

Silicates *Voltage: 20 kV; I: 20 nA*; Beam size: 5 µm.*

Element / line	spectr.	crystal	peak position	peak time (s)	BG (–)	BG (+)	slope (BG)	BG time (s)	Calibration	Intensity (cps/nA)
Na Ka	Sp4	LTAP	46362	20	-1900	1900		10	Albite_Na_20kV	189.8
Mg Ka	Sp4	LTAP	38504	50	-1600	1600		25	Periclase_Mg_20kV	3375.6
Si Ka	Sp5	LTAP	27736	30	-2450	2000		15	SiO_2_Si_20kV	4682.8
Al Ka	Sp5	LTAP	32456	70	-2160	1860		35	Al_2O_3_Al_20kV	4535.8
K Ka	Sp1	LPET	42765	20	-2000	2000		10	Sanidine_K_20kV	231.5
Fe Ka	Sp3	LLIF	48086	30	-1500	1500		15	Fe_2O_3_Fe_20kV	716
Ca Ka	Sp1	LPET	38385	20	-1800	2100		10	Diopside_Ca_20kV	516.3
Mn Ka	Sp1	LPET	23984	30	-1250	1250		15	$MnTiO_3$_Mn_20kV	1039.2
Ti Ka	Sp1	LPET	31406	30	-1380	1740		15	TiO_2_Ti_20kV	2021
F Ka	Sp2	LPC0	41161	30		5500	1.06	15	CaF_2_F_20kV	250.1
Cr Ka	Sp3	LLIF	56866	30	-1700	1700		15	Cr_2O_3_Cr_20kV	561
Ni Ka	Sp3	LLIF	41175	40	-1700	1700		20	NiO_Ni_20Kv	858.5

Carbonates *Voltage: 20 kV; I: 10 nA; Beam size: 10 µm.*

Element / line	spectr.	crystal	peak position	peak time (s)	BG (–)	BG (+)	slope (BG)	BG time (s)	Calibration	Intensity (cps/nA)
Mg Ka	Sp4	LTAP	38499	20	-1900	1900		10	Dolomite_Ca_Mg	538.2
Ca Ka	Sp1	LPET	38387	20	-1700	1350		10	Dolomite_Ca_Mg	618.6
Fe Ka	Sp3	LLIF	48086	20	-1500	1500		10	Fe_2O_3_Fe_20kV	716
Mn Ka	Sp3	LLIF	52203	20	-1250	1250		10	$MnTiO_3$_Mn_20kV	320.1
Sr La	Sp1	LPET	78415	40		1000	1	20	Celestine_Sr	199
Si Ka	Sp5	LTAP	27736	60	-2450	2000		30	SiO_2_Si_20kV	4682.8
Ni Ka	Sp3	LLIF	41175	20	-1700	1700		10	NiO_Ni_20Kv	858.5

Oxides *Voltage: 20 kV; I: 20 nA; Beam size: 5 µm.*

Element / line	spectr.	crystal	peak position	peak time (s)	BG (–)	BG (+)	slope (BG)	BG time (s)	Calibration	Intensity (cps/nA)
Mg Ka	Sp4	LTAP	38504	50	-1700	1700		25	Periclase_Mg_20kV	3375.6
Al Ka	Sp5	LTAP	32456	50	-1900	1900		25	Al_2O_3_Al_20kV	4535.8
Si Ka	Sp5	LTAP	27736	40	-2700	2600		20	SiO_2_Si_20kV	4682.8
Fe Ka	Sp3	LLIF	48086	20	-1500	1500		10	Fe_2O_3_Fe_20kV	716
Cr Ka	Sp1	LPET	26142	30	-1200	1200		15	Cr_2O_3_Cr_20kV	2310.7
Mn Ka	Sp1	LPET	23984	40	-1250	1250		20	$MnTiO_3$_Mn_20kV	1039.2
Ti Ka	Sp1	LPET	31406	40	-900	900		20	TiO_2_Ti_20kV	2021
V Ka	Sp3	LLIF	62186	30	-1000	1000		15	Vanadinite_Cl_V_20kV	70.5
Ni Ka	Sp3	LLIF	41175	20	-1600	1300		10	NiO_Ni_20Kv	858.5
Zn Ka	Sp3	LLIF	35642	20	-800	800		10	ZnS_Zn_20kV	591.2
Co Ka	Sp3	LLIF	44428	20	-2000	2000		10	Co_Co	1135.7

**for Brucite: 5 nA, 10 µm beamsize*

Table 3.2 (b) *Analytical settings of electron microprobe measurements; JEOL JXA-8230; Scientific and Technological Centers of the Universitat de Barcelona, Spain*

Silicates *Voltage: 20 kV; I: 15 nA; Beam size: 5 µm.*

Element / line	spectr.	crystal	peak position	peak time (s)	BG (–)	BG (+)	BG time (s)	Calibration	Intensity (cps)	S.D. (%)
Si Ka	1	TAP	77.25	10	7	5	5.0 (s)	Wollastonite	11958.4	0.13
Al Ka	1	TAP	90.566	10	5	3.5	5.0 (s)	Corundum	21968.3	0.1
Ti Ka	2	PETJ	87.735	10	2.1	3	5.0 (s)	Rutile	8622.6	0.15
Ca Ka	2	PETJ	107.341	10	2.5	2.3	5.0 (s)	Wollastonite	5263.1	0.2
K Ka	2	PETJ	119.617	10	4	6	5.0 (s)	Orthoclase	1472.5	0.37
F Ka	3	TAPH	199.736	10	5	3.4	5.0 (s)	Fluorite	724.6	0.54
Na Ka	3	TAPH	129.625	10	4	2.5	5.0 (s)	Albite	392.7	0.73
Mg Ka	3	TAPH	107.49	10	5	3	5.0 (s)	Periclase	14138	0.12
Ni Ka	5	LIFL	115.239	20	3.5	4.8	10.0 (s)	Ni	26891.9	0.09
Fe Ka	5	LIFL	134.592	10	4.5	3	5.0 (s)	Fe_2O_3	13442.2	0.12
Mn Ka	5	LIFL	146.151	10	5	4.7	5.0 (s)	Rhodonite	4930.3	0.2
Cr Ka	5	LIFL	159.22	20	6	3.6	10.0 (s)	Cr_2O_3	8972	0.15

Carbonates *Voltage: 20 kV; I: 6 nA; Beam size: 8-10 µm.*

Element / line	spectr.	crystal	peak position	peak time (s)	BG (–)	BG (+)	BG time (s)	Calibration	Intensity (cps)	S.D. (%)
Mg Ka	1	TAP	107.539	10	5	3	5.0 (s)	Periclase	16920.3	0.11
Si Ka	1	TAP	77.266	10	7	5	5.0 (s)	Wollastonite	12192.7	0.13
Sr La	1	TAP	74.416	30	4.2	6.5	15.0 (s)	Celestine	8689.5	0.16
Ca Ka	2	PETJ	107.341	10	2.5	2.3	5.0 (s)	$CaCO_3$	2962.3	0.26
Mg Ka	3	TAPH	107.49	10	5	3	5.0 (s)	Periclase	14138	0.12
Fe Ka	5	LIFL	134.592	10	4.5	3	5.0 (s)	Fe_2O_3	13442.2	0.12
Mn Ka	5	LIFL	146.151	20	5	4.7	10.0 (s)	Rhodonite	4930.3	0.2
Ni Ka	5	LIFL	115.239	20	3.5	4.8	10.0 (s)	Ni	26891.9	0.09

Oxides *Voltage: 20 kV; I: 20 nA; Beam size: 5 µm.*

Element / line	spectr.	crystal	peak position	peak time (s)	BG (–)	BG (+)	BG time (s)	Calibration	Intensity (cps)	S.D. (%)
Si Ka	1	TAP	77.25	10	7	5	5.0 (s)	Wollastonite	11958.4	0.13
Al Ka	1	TAP	90.566	10	5	3.5	5.0 (s)	Corundum	21968.3	0.1
Cr Ka	2	PETJ	72.95	20	3.6	3.2	10.0 (s)	Cr_2O_3	8798.7	0.15
Ti Ka	2	PETJ	87.735	20	2.1	3	10.0 (s)	Rutile	8622.6	0.15
Ca Ka	2	PETJ	107.341	10	2.5	2.3	5.0 (s)	Wollastonite	5263.1	0.2
K Ka	2	PETJ	119.617	10	4	6	5.0 (s)	Orthoclase	1472.5	0.37
Na Ka	3	TAPH	129.625	10	4	2.5	5.0 (s)	Albite	392.7	0.73
Mg Ka	3	TAPH	107.49	10	5	3	5.0 (s)	Periclase	14138	0.12
Ni Ka	5	LIFL	115.239	20	3.5	4.8	10.0 (s)	Ni	26891.9	0.09
Fe Ka	5	LIFL	134.592	10	4.5	3	5.0 (s)	Fe_2O_3	13442.2	0.12
Mn Ka	5	LIFL	146.151	10	5	4.7	5.0 (s)	Rhodonite	4930.3	0.2
Zn Ka	5	LIFL	99.715	20	2.7	2.3	10.0 (s)	Sphalerite	15149.1	0.12
V Ka	5	LIFL	174.101	20	3	3	10.0 (s)	V	11818	0.13
Co Ka	5	LIFL	124.373	20	3.4	4.8	10.0 (s)	Co	24920	0.09

Part II

RESULTS

4 Carbonation of mantle peridotite by CO_2-rich fluids: the formation of listvenites in the Advocate ophiolite complex (Newfoundland, Canada)[1]

4.1 Introduction

Because mantle peridotites are far from equilibrium under weathering and low temperature metamorphic conditions, they tend to hydrate and carbonate when in contact with aqueous fluids. Oceanic ophicarbonates (e.g. Schwarzenbach et al., 2013) and carbonate travertine in peridotite-hosted alkaline springs (e.g. Kelemen and Matter, 2008) show that serpentinized peridotites have a high capacity to bind dissolved CO_2 derived from seawater and the atmosphere. When in contact with CO_2-rich hydrothermal fluids, serpentinized peridotite is often pervasively replaced by talc-magnesite and quartz-magnesite rocks (e.g. Beinlich et al., 2012; Falk and Kelemen, 2015; Hansen et al., 2005). Due to the fast kinetics of carbonation reactions in serpentinized peridotites, they are a target for carbon sequestration strategies by mineral carbonation to reduce atmospheric carbon contents (e.g. Andreani et al., 2009; Hövelmann et al., 2011; Kelemen et al., 2011; van Noort et al., 2013). These characteristics make differently carbonated peridotites sensitive markers of carbon fluxes in mantle rocks, providing clues on the transfer of carbon between shallow and deep reservoirs. Understanding the processes involved in carbon transfer and the knowledge of total long-term fluxes between such carbon reservoirs are important for past climate reconstructions. In particular, carbonated peridotite in the cold, leading edge of the mantle wedge above subduction zones may represent a significant, but largely unrecognized carbon reservoir in the deep carbon cycle (Kelemen and Manning, 2015). Thick listvenite occurrences at the basal thrust of the Oman ophiolites (Falk and Kelemen, 2015; Kelemen et al., 2017) and along thrust faults in ophiolites elsewhere (e.g. Qiu and Zhu, 2015; Sofiya et al., 2017; Zhang et al., 2015) demonstrate that carbonation of peridotite can be widespread in similar tectonic settings as those found in the tip of the mantle wedge in cold subduction zones.

[1] *This chapter has been published in Menzel, M.D., Garrido, C.J., López Sánchez-Vizcaíno, V., Marchesi, C., Hidas, K., Escayola, M.P., Delgado Huertas, A., 2018. Carbonation of mantle peridotite by CO_2-rich fluids: the formation of listvenites in the Advocate ophiolite complex (Newfoundland, Canada). Lithos 323, 238-261.*

Listvenites are fuchsite (Cr-rich mica)- and Cr-spinel bearing quartz-magnesite rocks that form by reaction of aqueous, CO_2-rich fluids with ultramafic rocks (Halls and Zhao, 1995). Besides CO_2, potassium, sulphur and gold are often added during fluid infiltration, leading to the formation of fuchsite and Au-bearing sulphides that can be of economic interest (Emam and Zoheir, 2013; Qiu and Zhu, 2015). Listvenites can form at temperature as low as 80 – 100 °C (Falk and Kelemen, 2015) and up to of 200 – 350 °C (Beinlich et al., 2012; Hansen et al., 2005; Schandl and Naldrett, 1992). In high-temperature listvenites, several zones with distinctive assemblages are predicted to record a stepwise (simplified) carbonation reaction of peridotite: olivine + H_2O ± CO_2 = serpentine ± magnesite; serpentine + CO_2 = magnesite + talc; talc + CO_2 = magnesite + quartz (Johannes, 1969; Klein and Garrido, 2011). Because the carbonation reaction progress is mainly limited by the availability and transport of CO_2-bearing aqueous fluid, natural listvenites often record, to some extent, these arrested reaction steps (e.g. Beinlich et al., 2012; Hansen et al., 2005). Therefore, they are ideal natural laboratories to study the controlling factors and timescales of carbon-bearing fluid flux and carbonation reaction progress at large scale.

Here we report extensively carbonated mantle rocks from the Central Advocate complex, Newfoundland (Canada), that preserve a complete set of arrested progressive carbonation reactions from un-reacted, serpentinized harzburgite protolith to talc-magnesite rocks and listvenites. By means of a detailed petrographic and petrological study, thermodynamic modelling and stable isotope geochemistry, we document the reaction sequence of carbonation of serpentinite by CO_2-rich hydrothermal fluids likely derived from metamorphic devolatilization in a forearc setting.

4.2 Geological Setting

The Baie Verte Peninsula, Newfoundland, comprises the boundary between the Neoproterozoic continental margin of Laurentia and a set of Early Ordovician ophiolites (the Baie Verte Ophiolites; Fig. 4.1a) and their Early to Middle- Ordovician supra-crustal, sedimentary cover rocks (Bédard and Escayola, 2010; Skulski et al., 2010). The ophiolite cover sequences consist of rather thick volcanic rocks with boninite to tholeiitic and calc-alkaline affinities, alternating with clastic to pelagic sediments derived from the continental margin, island arc material and the ophiolite crust itself, and deposited onto the oceanic crust (e.g. Kidd et al., 1978; Skulski et al., 2010). The Baie Verte ophiolites (490 – 480 Ma) are thought to have formed by forearc spreading due to incipient east-ward subduction of the

Taconic seaway below several micro-continent slices (Castonguay et al., 2014). Closure of the Taconic seaway led to obduction of the Baie-Verte forearc ophiolite and its cover sequences onto the continental basement of the Laurentian margin along the Baie Verte line, a polyphase brittle-ductile shear zone that is part of the Baie Verte – Brompton line (Fig.

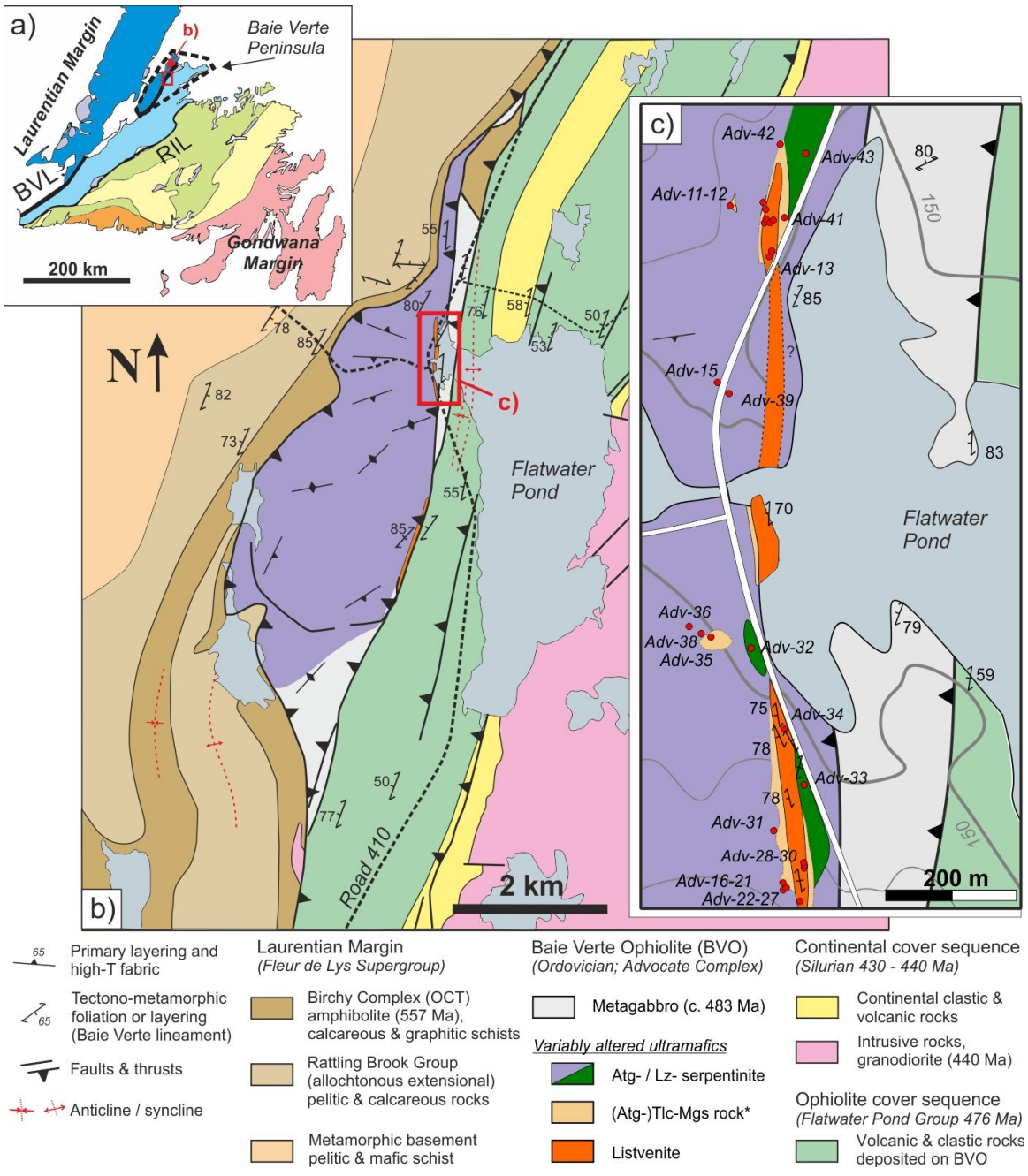

Figure 4.1. ***(a)*** *Tectonic overview of Newfoundland (after Castonguay et al., 2014). BVL = Baie Verte Line; RIL = Red Indian Line.* ***(b)*** *Simplified geology of the central Advocate complex at Flatwater Pond, with location of studied listvenites (map modified after Bédard and Escayola, 2010; Kidd, 1974; Skulski et al., 2010); representative ages of units after Castonguay et al. (2014); Skulski et al. (2010).* ***(c)*** *Detailed geological map of listvenite occurrences (inset in b) with sample locations; *Atg-Tlc-Mgs and Qtz-Tlc-Mgs rocks are not distinguished in the map.*

4.1a) (Castonguay et al., 2014; Skulski et al., 2010; Waldron and van Staal, 2001). In the Laurentian continental margin, meta-gabbro and graphitic metapelite of the Birchy complex, in tectonic contact with the ophiolites (Fig. 4.1b), record eclogite-facies peak conditions (1.0 – 1.2 GPa, 450 – 500 °C) with amphibolite-facies overprint (0.70 – 0.85 GPa, c. 550 °C) (Jamieson, 1990; van Staal et al., 2013). These units have ocean-continent transition (OCT) characteristics, indicating that parts of the hyper-extended Laurentian margin subducted beneath the Baie Verte oceanic crust and were exhumed synchronous with the ophiolite obduction as part of a subduction channel (Castonguay et al., 2014; van Staal et al., 2013). In contrast to the continental margin, rocks associated with the Baie Verte ophiolites only show a weak greenschist facies metamorphic imprint. Both the continental basement and the ophiolitic sequences are intruded by post-collisional, Early Silurian granitoid plutons (Whalen et al., 2006).

Listvenites and talc-magnesite rocks are part of the ultramafic units throughout the Baie Verte ophiolite sequence; major occurrences are in the Point Rousse complex (Escayola et al., 2009), and in the Advocate complex (Bédard and Escayola, 2010; Kidd, 1974; Skulski et al., 2009). At Point Rousse, listvenitization of ultramafic cumulates occurred by hydrothermal alteration at around 200 °C, probably associated with tectonic deformation along the Baie Verte – Brompton Line (Escayola et al., 2009).

4.2.1 The Advocate complex

The Advocate complex (Fig. 4.1b) is a highly discontinuous and tectonically dismembered ophiolite sequence that forms the westernmost leading edge of the Baie Verte ophiolites, obducted onto the partially subducted Laurentian continental margin (Bédard and Escayola, 2010; Castonguay et al., 2014). It consists of fault-bounded slivers of serpentinized harzburgite, gabbro, sheeted dykes and rare volcanic mafic rocks (Skulski et al., 2010), which crop out along the Baie Verte line. In large segments along-strike of the Baie Verte line, the crustal sequence of the Advocate complex is absent and only thin tectonically dissected remnants of serpentinized mantle rocks — in parts completely carbonated to listvenite — remain (Kidd, 1974). The primary texture of larger harzburgite slivers and enclosed pyroxenite and dunite layers are oriented oblique to the main regional cleavage that correlates with thrusting along the Baie Verte line (Fig. 4.1b & c; and Kidd, 1974).

4.3 Field relations and sampling

Listvenites, Qtz-Tlc-Mgs rocks[2], Atg-Tlc-Mgs rocks, and carbonated serpentinites crop out in the central Advocate complex along a N-S oriented, 40 – 80 m thick zone of about 1 km length close to the Baie-Verte Road, at the NW corner of Flatwater Pond (Fig. 4.1b & c, and Table 4.1). They are situated in the eastern part of the central Advocate mantle rocks surrounded by Atg-serpentinite and, locally, strongly deformed Lz-serpentinite (Fig. 4.1c). The extent of carbonation systematically increases from slightly carbonated Atg-serpentinites to the central listvenite domain (Table 4.1), with sharp contacts, anastomosing between carbonated Atg-serpentinite and Atg-Tlc-Mgs rocks, and gradual decimetre-scale transitions between Qtz-Tlc-Mgs rocks and listvenite. Direct contacts between listvenites and serpentinites are not exposed. Table A-4.1 of the Appendix[3] provides a list of all studied samples with their GPS coordinates.

Table 4.1: *Main characteristics of the carbonate-bearing lithologies associated with the Advocate serpentinites.*

Lithology	**CO_2 (TC, wt%)**	**main mineralogy**	**minor & trace phases**	**comments**
(carbonated) Atg-serpentinite	0 – 10	Atg > Lz, Ol	Brc, Mgs, Cr-Sp, Mag, Dol, Pn	Interlocked Atg with Lz-bastite; Ol partially preserved. Where Brc is present it forms veins with Mag.
(carbonated) Lz-serpentinite	0 – 13	Lz > Atg	Mgs/Dol ,Cr-Sp, Mag, Pn	Lz mesh and bastite textures; Atg and Ctl predominantly in veins
Atg-Tlc-Mgs rock	10 – 18	Tlc > Mgs > Atg	Cr-Sp, Fe-Chr, Chl, Gt, Pn, ± Mag	Massive, coarse grained, with Atg-serpentinite relics
Qtz-Tlc-Mgs rock	22 – 33	Mgs > Tlc, Qtz	Chl, Cr-Sp, Fe-Chr, Py, Hem/Gt	Pronounced layering; Qtz content & veining increase towards listvenites
Listvenite (sensu stricto*)	34 – 40	Mgs > Qtz	Fuchs, Chl, Cr-Sp, Fe-Chr, Py, Hem/Gt	Abundant Qtz veins, weak layering; Rare Tlc in inclusions
Si-depleted listvenite	> 40	Mgs	Fuchs, Qtz, Cr-Sp, Fe-Chr, Rv	Nearly pure Mgs-rock
Magnesite-veins	> 39	Mgs	Cr-Sp, Atg, Tlc, Py	Decimetre-scale veins (2 samples) of predominantly fine-grained Mgs

**Listvenite as defined by Halls and Zhao (1995). Bulk rock carbon is total measured carbon (TC) given as CO_2. Minor & trace phases are listed with decreasing abundance. Atg = antigorite; Lz = lizardite; Ctl = chrysotile; Ol = olivine; Brc = brucite; Tlc = talc; Fuchs = Cr-mica (fuchsite); Qtz = quartz; Mgs = magnesite; Dol = dolomite; Cr-Sp = Cr-spinel; Fe-Chr = ferrit-chromite; Mag = magnetite; Hem = hematite; Gt = goethite; Pn = pentlandite; Py = pyrite; Rv = reevesite.*

[2] Mineral abbreviations used throughout Ch. 4: see Table 4.1
[3] Appendices of this study are provided at the end of Ch. 4.

4.3.1 Serpentinized ultramafics

The mantle rocks in the central Advocate complex crop out in an area of approximately 9 km² west of Flatwater Pond (Fig. 4.1b). They consist of variably serpentinized harzburgites, subordinate dunite dykes and pyroxenite layers, and rare chromitite (Bédard and Escayola, 2010; Escayola et al., 2011). Serpentinization is generally moderate to strong (> 60 – 80 wt% serpentine minerals), with common olivine relicts and very rare primary pyroxene preserved in the least serpentinized parts of the complex (Kidd, 1974). Antigorite is the dominant serpentine mineral in most of the studied serpentinite samples that are hereafter referred to as Atg-serpentinite (Table 4.1). They have mostly a massive appearance, and in places Cr-spinel and oriented bastite after orthopyroxene mark a weak primary layering that is oblique to the contacts between the different carbonate-bearing lithologies of the sequence and the Baie Verte line (Fig. 4.1b & c). Locally, abundant serpentine, talc, brucite and carbonate veins crosscut the Atg-serpentinites (Fig. 4.2a). The easternmost part of the Advocate mantle rocks, close to the tectonic contact with metagabbro, is characterized by the presence of foliated serpentinites that crop out in several road cuts (Fig. 4.1c). These are fully serpentinized peridotites that mostly consist of lizardite with rare antigorite veins, while brucite and olivine are absent, and we refer to them as lizardite (Lz-)-serpentinites (Table 4.1). They show an anastomosing network of serpentine veins —mostly fibrous chrysotile— wrapping around more competent, lenticular serpentinite domains (Fig. 4.2b). Different generations of lizardite, chrysotile and antigorite veins, and rare magnetite and magnesite veins crosscut the Lz-serpentinites.

4.3.2 Atg-Tlc-Mgs & Qtz-Tlc-Mgs rocks

Relatively dark, massive Atg-Tlc-Mgs rocks occur as variably sized veins and thick anastomosing zones with sharp contacts to the host Atg-serpentinite, occasionally preserving isolated relict serpentinite lenses (Fig. 4.2c & d; Table 4.1). They consist of coarse (0.5 – 3 mm) intergrowths of magnesite and antigorite flakes and Tlc-rich aggregates (domain III in Fig. 4.2e & f), bending around finer-grained (< 0.5 mm), rounded domains poorer in Tlc (domain II; Fig. 4.2e & f).

Towards the contact with listvenite, Qtz-Tlc-Mgs rocks with a well-developed foliation defined by oriented talc aggregates prevail (Fig. 4.2g). Alternating magnesite- and talc-rich layers give the appearance of a gneissic texture striking N-S with vertical dip (Fig. 4.2g). The contacts between Atg-Tlc-Mgs and Qtz-Tlc-Mgs rocks are not well exposed. The gradual

transition from Qtz-Tlc-Mgs rocks to listvenite is always marked by a sudden onset of abundant quartz and quartz-magnesite veins in the listvenites (Fig. 4.2h).

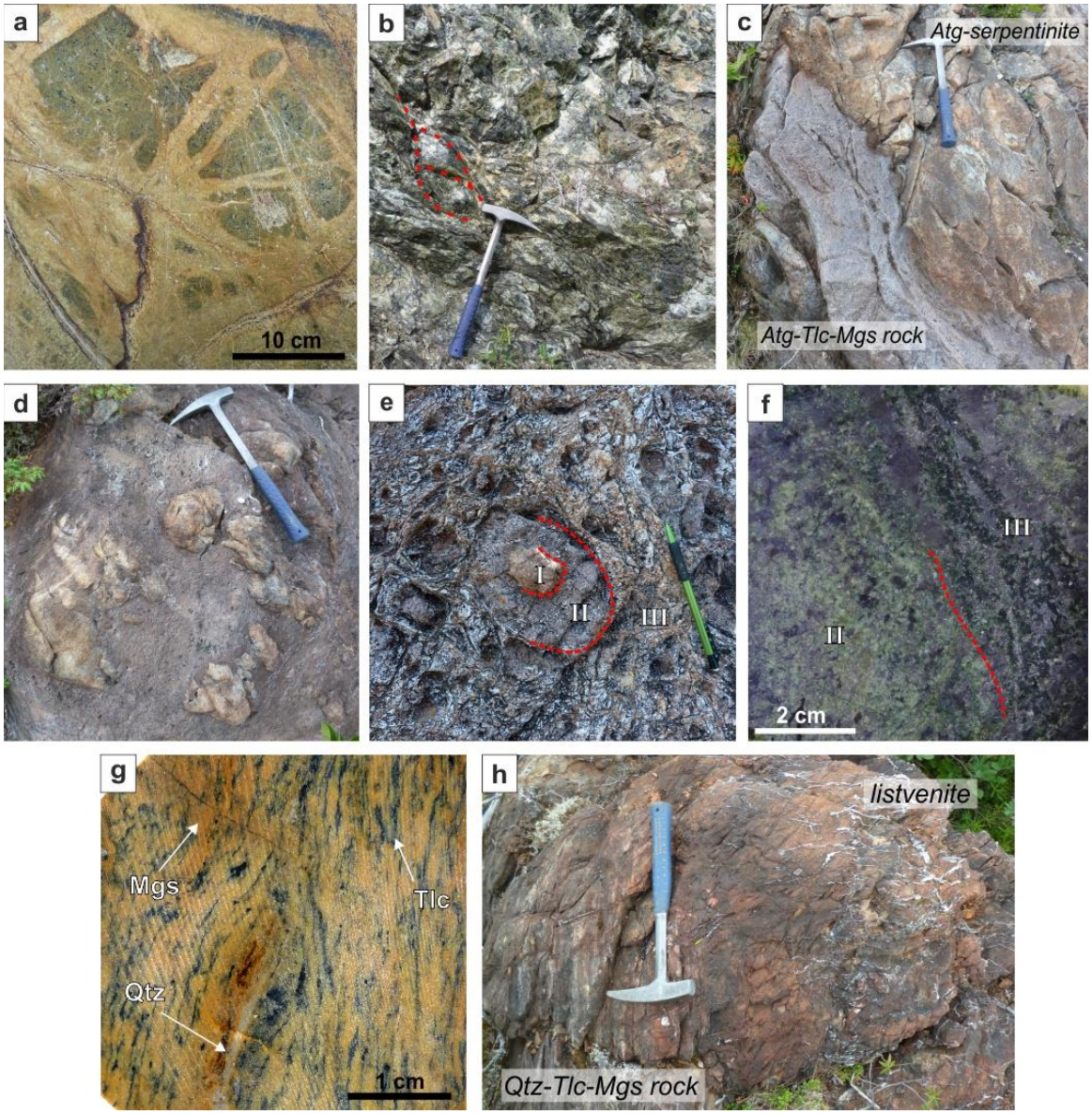

Figure 4.2. *Field images of the Advocate serpentinites and carbonate-bearing lithologies (hammer for scale is 40 cm).* ***(a)*** *Serpentinized harzburgite with bastite and mesh structure crosscut by abundant antigorite veins.* ***(b)*** *Lz-serpentinite with chrysotile-rich shear planes around lenticular serpentinite blocks (highlighted by red dashed lines).* ***(c)*** *Contact of Atg-serpentinite and Atg-Tlc-Mgs rock.* ***(d)*** *Serpentinite relicts floating in Atg-Tlc-Mgs rock.* ***(e)*** *Kernel pattern in Atg-Tlc-Mgs rock, with serpentinite relicts (domain I) and increasing talc content from domain II to III (pen for scale is 15 cm).* ***(f)*** *Rock slab of massive Atg-Tlc-Mgs rock with domains as in e), showing coarse green antigorite flakes and talc rich parts (dark grey); sample Adv-35.* ***(g)*** *Rock slab of Qtz-Tlc-Mgs rock with well-developed layering of talc (blue-grey) and magnesite-rich layers (orange) (sample Adv-23).* ***(h)*** *Contact between mylonitic Qtz-Tlc-Mgs rock and listvenite, with sudden onset of veining in listvenite.*

4.3.3 Listvenites

The listvenite outcrops form pronounced, 20 – 30 m thick ridges (Fig. 4.3a). They have red-brown weathering rims (Fig. 4.3b) and are either light green or yellowish coloured on fresh surfaces, depending on whether fuchsite is present or not (Fig. 4.3c – e). Most listvenites show a layering parallel to the elongation of the outcrop ridges (Fig. 4.3b & d), but minor coarse-grained (up to 0.5 cm) and massive listvenites also occur (Fig. 4.3e). They are crosscut by abundant syntaxial quartz, quartz-magnesite and magnesite veins (Fig. 4.3 a–e). The layering strikes N-S and has a nearly vertical dip in the southern exposure of the listvenites, coplanar with the Baie Verte line orientation and the related regional foliation (Fig. 4.1b & c). Thick quartz veins (> 1 cm) are mostly oriented normal to the layering (striking N-070 to N-110 and dipping > 80° towards N or S), or form curved and blocky aggregates (e.g. Fig. 4.3b). Shallower dipping, thinner veins are often curved and form rare conjugate and en-echelon sets (Fig. 4.3a, b & d). A set of thin continuous veins (< 1 mm) is oriented parallel to the layering. In the northern listvenite outcrops, the layering and veins record wide open folds with the fold axis dipping 60 – 70° to W. Locally, thin, crenulated fuchsite veins (< 0.5 cm) occur, often oriented sub-parallel to the layering and crosscut by both quartz and magnesite

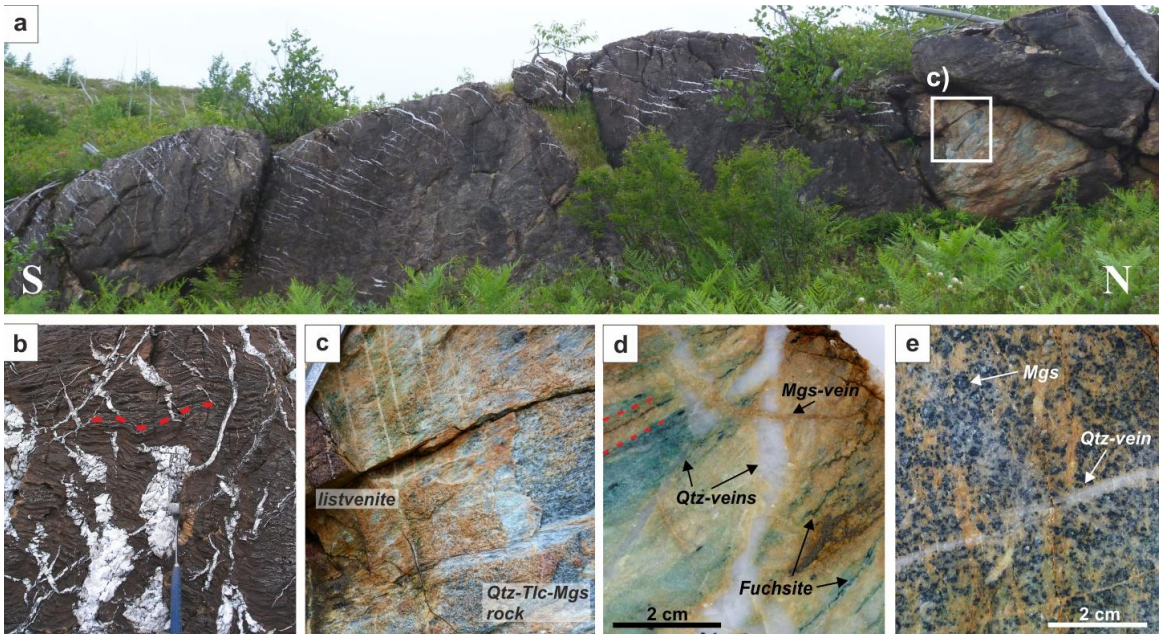

Figure 4.3. *Field images of the Advocate listvenites.* ***(a)*** *Listvenite ridge in the Central Advocate complex with transition of non-veined Qtz-Tlc-Mgs rock (right hand-side) to veined listvenite (left hand-side).* ***(b)*** *Quartz-veins crosscutting layering (red dashed line) in listvenite.* ***(c)*** *Transition from non-veined bluish Qtz-Tlc-Mgs rock to green fuchsite-bearing, veined listvenite (detail from a).* ***(d)*** *Hand specimen of layered listvenite with crosscutting quartz-, magnesite- and fuchsite-veins; layering highlighted by red dashed lines (sample Adv-13).* ***(e)*** *Hand specimen of non-layered listvenite domain with coarse euhedral magnesite (dark; sample Adv-30).*

veins (Fig. 4.3d). In the central part of the listvenites, nearly pure, layered, magnesite rocks with minor fuchsite, dolomite and relict Cr-spinel occur (termed Si-depleted listvenite in Table 4.1). These rocks are crosscut by thin magnesite and fuchsite veins (mostly < 2 mm), and minor quartz veins. They are locally referred to as *virginites* and used as craftstones, due to their green colour derived from fuchsite (Chao et al., 1986).

4.4 Petrography

4.4.1 Atg-serpentinite

Atg-serpentinites in the central Advocate complex consist of antigorite with interlocked texture, lizardite bastite (orthopyroxene pseudomorphs; 10 – 25 vol%; Fig. 4.4a), minor lizardite in mesh centre domains, olivine, magnetite, Cr-spinel, brucite, carbonate (dolomite and magnesite), and rare Fe-Ni-sulphides (pentlandite, pyrite-pyrrhotite, heazlewoodite). Raman spectroscopy reveals that mesh-centre and bastite serpentine occasionally consist of fine intergrowths of lizardite and antigorite (cf. Ch. 3, section *3.3.1*; Appendix Fig. A-4.1). In some samples, the variable abundances of bastite and magnetite, and grain size variations of serpentine (< 30 µm – 200 µm) mark a layering at the thin section scale. In brucite-bearing Atg-serpentinites, primary olivine can be preserved (Fig. 4.4a), whereas primary pyroxene is absent. Olivine is crosscut by lizardite-magnetite and antigorite-brucite-magnetite veins (Fig. 4.4a & b). In these Atg-serpentinites, brucite occurs as thin vermicular veinlets (20 – 50 µm), thicker (0.2 – 4.0 mm) straight veins associated with antigorite and magnetite, and small (< 30 µm) dispersed flakes in the antigorite matrix (Fig. 4.4a & d). Dolomite and magnesite are locally common in brucite veins. Magnesite aggregates occur in similar textural positions as mesh-centre lizardite and olivine, and locally within or at rims of lizardite bastite (Fig. 4.4c & d; Appendix Fig. A-4.2g). Cr-spinel has subhedral to holly-leaf shapes, is rimmed by Fe-chromite and Cr-bearing magnetite and can contain inclusions of amphibole, olivine and Al-rich serpentine (Fig. 4.5a). The extent of Cr-spinel alteration to chlorite is generally minor; instead, magnetite and magnesite rims occur locally (Fig. 4.5a and Appendix Fig. A-4.2h). Fine-grained magnetite (< 30 µm) outlines a mesh texture (Fig. 4.4c) and is preferentially concentrated in and around bastite, marking the former cleavage of pyroxene (Fig. 4.4e).

In carbonate-bearing, brucite-free Atg-serpentinites, magnetite is less abundant, and rare pyrite and talc can be present. In these rocks, magnesite preferentially occurs as vermicular veinlets (similar to brucite in Atg-serpentinites with low carbonate content), and as

intergrowths with coarse antigorite and dispersed magnetite, with textures resembling those of bastite (Fig. 4.4f). In places, serpentine-magnesite veins crosscut the Atg-serpentinites (Fig. 4.4g). They are composed of euhedral, coarse-grained magnesite (up to 5 mm) growing from the vein walls into the lizardite vein centre, and are surrounded by dolomite- and

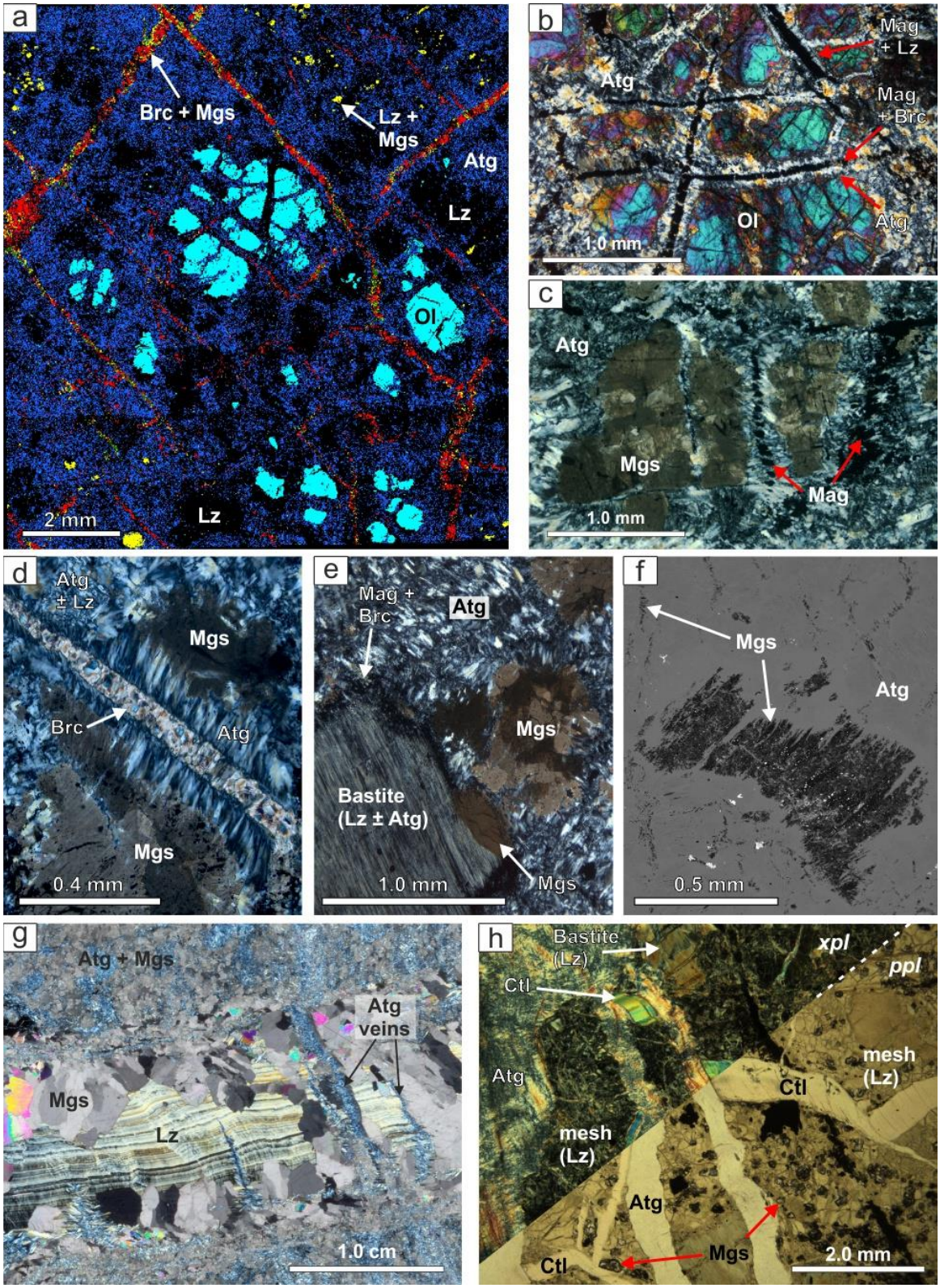

magnesite- rich halos (2 – 3 cm) in the adjacent Atg-serpentinite. Thin veins of coarse antigorite flakes (0.2 – 1 mm) crosscut these lizardite-magnesite veins (Fig. 4.4g).

4.4.2 Lizardite-serpentinite

Lizardite-serpentinite consists dominantly of lizardite with mesh-texture and minor bastite domains (Fig. 4.4h). The lizardite mesh is crosscut by abundant chrysotile veins, and younger, fine-grained antigorite veins that locally offset the chrysotile veins (Fig. 4.4h). Cr-spinel, carbonate, and magnetite are minor phases (Table 4.1), the latter tracing mesh and bastite domains and occurring in veins with lizardite. Magnesite occurs mostly as euhedral, zoned grains overgrowing the lizardite mesh microstructure (Fig. 4.4h), while rare dolomite is concentrated in carbonate veins.

4.4.3 Atg-Tlc-Mgs rocks

Besides magnesite, antigorite, and talc, Atg-Tlc-Mgs rocks contain minor Cr-spinel rimmed by Fe-chromite and Cr-bearing magnetite, and rare chlorite and Fe-Ni-sulphides (such as pentlandite, Fig. 4.5b). Magnetite is generally much less abundant than in serpentinites or absent, and goethite with magnesite inclusions occurs locally. Antigorite is present as coarse (up to 2 mm), yellow-green pleochroic flakes that are closely intergrown with magnesite (Atg^{II}, Fig. 4.6a). Coarse subhedral magnesite (0.5 – 1.5 mm) may preserve Fe-poor cores with abundant magnetite inclusions, whereas inclusion-free rims and smaller matrix grains (30 – 200 µm) are Fe-richer (Mgs^{I} and Mgs^{II} in Fig. 4.6b). The magnetite inclusions form hollow euhedral shapes with aggregates of Fe-rich magnesite, antigorite and talc inside (Fig. 4.6c). Residual magnetite tracing the former euhedral grains is rich in Cr (Fig. 4.5c).

◄ ***Figure 4.4.*** *Microstructures of incipient carbonation in brucite-bearing Atg-serpentinite (a – e; sample Adv-39), carbonate-rich Atg-serpentinite (f & g; samples Adv-36 and Adv-38) and Lz-serpentinite (h; sample Adv-32).* ***(a)*** *EBSD raw phase map (16 µm stepsize) showing distribution of olivine (cyan), brucite (red), magnesite (yellow), dolomite (green, in veins with brucite and magnesite), antigorite (dark blue) and lizardite (dominant non-indexed phase, black).* ***(b)*** *Serpentinization textures of primary olivine.* ***(c)*** *Magnesite in mesh centres replacing olivine or lizardite formed by serpentinization of olivine.* ***(d)*** *Brucite vein associated with antigorite and magnesite after lizardite.* ***(e)*** *Lizardite bastite with brucite-bearing, magnetite-rich rim in interlocked antigorite matrix, and incipient growth of magnesite.* ***(f)*** *Magnesite (dark) in thin vermicular veins, and together with antigorite and magnetite (bright) tracing former bastite in carbonated Atg-serpentinite (BSE image).* ***(g)*** *Magnesite-lizardite vein with carbonation halo in Atg-serpentinite, crosscut by flaky antigorite veinlets.* ***(h)*** *Carbonated Lz-serpentinite with magnesite in the lizardite mesh, and crosscutting antigorite and chrysotile veins; straight (ppl) and crossed (xpl) polarizers. Crossed polarized images if not indicated otherwise; mineral abbreviations are given in Table 4.1.*

Pentlandite locally has rims of Si- and Mg-bearing Fe-Ni hydroxides and Fe-Ni-rich silicate aggregates (Fig. 4.5b & c; Appendix Fig. A-4.3) similar to those reported by Malvoisin et al. (2017) in high-P serpentinites.

4.4.4 Qtz-Tlc-Mgs rocks

With increasing carbon content and disappearing antigorite, the modal proportions of talc and quartz increase (see Table 4.1); in addition, minor Cr-spinel and rare chlorite occur, and pyrite and goethite are abundant in places. Flattened talc aggregates mark a well-defined

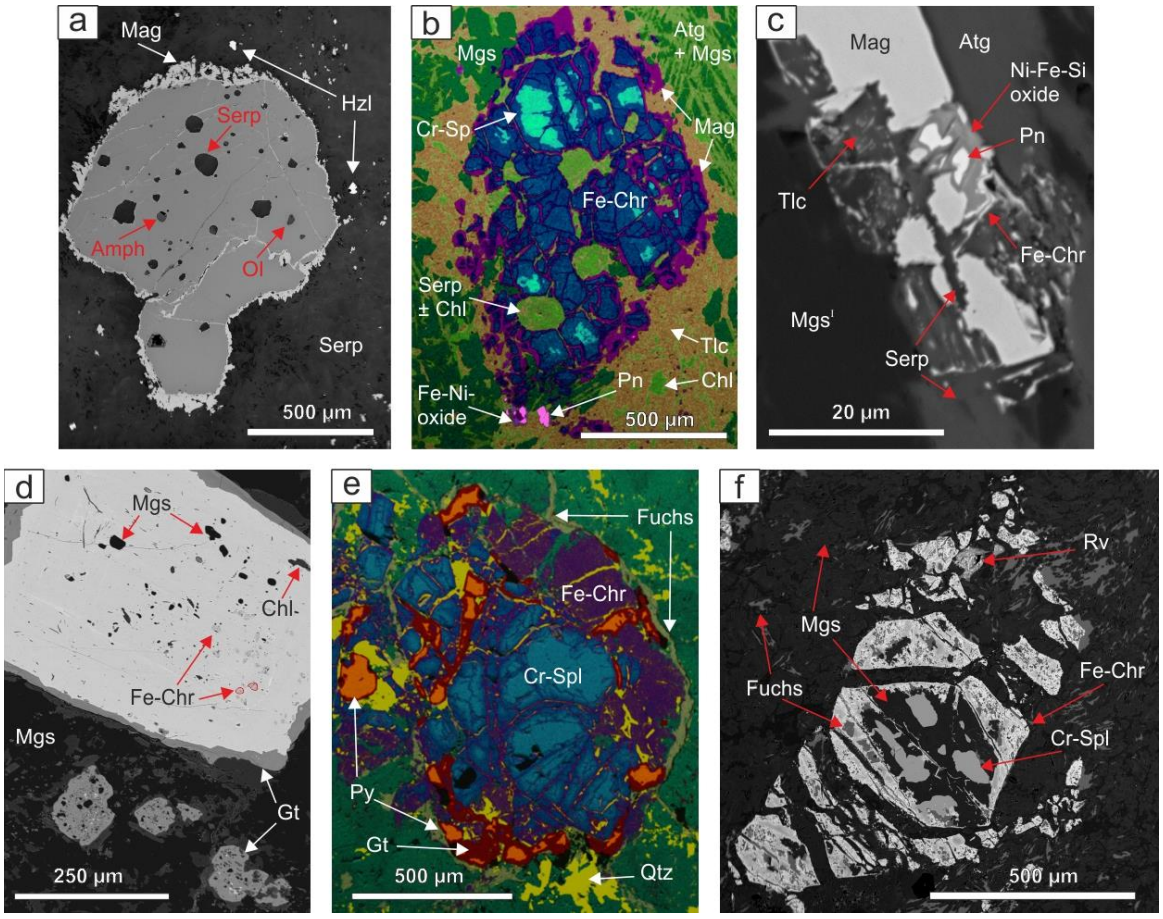

Figure 4.5. ***(a)*** *Cr-spinel with inclusions of amphibole (Amph), olivine, and serpentine (Serp), rimmed by magnetite; heazlewoodite (Hzl) occurs in the serpentine matrix (BSE; sample Adv-15).* ***(b)*** *Cr-spinel altered to ferrit-chromite with a magnetite rim in a talc-rich domain of a Atg-Tlc-Mgs rock (EDS-SEM false color phase map; sample Adv-11).* ***(c)*** *Magnetite in a Atg-Tlc-Mgs rock (BSE; sample Adv-42) decomposing to serpentine, talc, Fe-rich magnesite and residual Cr-rich magnetite or Fe-Chr tracing the former euhedral crystal shape; pentlandite has a Ni-Fe-Si-oxide rim (detail of Fig. 4.6d).* ***(d)*** *Euhedral pyrite in a Qtz-bearing Tlc-Mgs rock (BSE; sample Adv-22) with inclusions of magnesite, chlorite and ferrit-chromite, and rimmed by goethite.* ***(e)*** *Relict Cr-spinel in listvenite (EDS-SEM false color phase map; sample Adv-30), with a Si-bearing ferrit-chromite rim (violet) and alteration to pyrite/goethite and Cr-mica fuchsite (beige) in magnesite-quartz matrix (green and yellow, respectively).* ***(f)*** *Relict Cr-spinel in a Si-depleted listvenite (BSE; sample Adv-09) with alteration to magnesite; fuchsite replaces Fe-Chr rims; reevesite occurs. If otherwise not indicated, mineral abbreviations are in Table 4.1*

foliation anastomosing around coarser magnesite grains (0.5 – 5 mm; Fig. 4.6d & f). Euhedral magnesite grains show a weak shape preferred orientation parallel to the orientation of talc aggregates. As in Atg-Tlc-Mgs rocks, coarse magnesite displays an oscillatory euhedral growth zonation with Fe-poor cores and an Fe-rich rim generation, but with again Fe-poorer compositions towards the outermost rims (e.g. Fig. 4.6e & f). Some magnesite cores are rich in small magnetite and talc inclusions (Fig. 4.6f), and fragments of partially overgrown magnesite veins are preserved (Fig. 4.6e). Cores and Fe-rich rims of an early magnesite generation have slightly rounded boundaries, whereas the outer Fe-poorer rims are euhedral with straight faces. The length scale of the magnesite zonation is highly variable, showing extended growth in contact with talc and inhibited growth in contact with quartz (red arrows in Fig. 4.6e). The magnesite zonation is less pronounced in samples with finer grain sizes of talc (< 50 µm) and magnesite (< 200 µm). Quartz in Qtz-Tlc-Mgs rocks occurs in micro- to millimetre- scale syntaxial veins, in interstitial, fine grained (< 50 µm) aggregates between magnesite grains, and as isolated aggregates in talc-rich domains. Euhedral pyrite is rimmed by goethite and often contains inclusions of magnesite, chlorite, Cr-bearing magnetite and pentlandite (Fig. 4.5d).

4.4.5 Listvenite

The listvenites consist of magnesite and quartz, minor fuchsite or chlorite – depending on the abundance of potassium –, pyrite, relict Cr-spinel, and rare dolomite. Different generations of quartz and magnesite veins are common in both fine-grained layered and coarse-grained, massive listvenites (Fig. 4.6g & h). The layering is defined by anastomosing fuchsite and chlorite aggregates (Fig. 4.6g), a weak preferred orientation of coarse magnesite, and alternating planar domains of quartz and magnesite of different grain size (magnesite grain sizes are < 0.2 mm in very fine-grained layers, and 0.25 – 1.0 mm in coarse-grained layers). Magnesite is similar to that in Qtz-Tlc-Mgs rocks, with common magnetite inclusions in cores and talc inclusions in rims of coarse magnesite grains. In comparison with Qtz-Tlc-Mgs rocks, the youngest rock-forming magnesite generation consists of anhedral Fe-poor magnesite rims and interstitial grains between quartz. In Si-depleted listvenites (Table 4.1), the latest magnesite generation constitutes a fine-grained, subhedral matrix interstitial between coarser, Fe-richer magnesite. Relict Cr-spinel in listvenites shows abundant replacement by ferrit-chromite and fuchsite, and is partly overgrown by pyrite rimmed with goethite (Fig. 4.5e & f). Pseudomorphic replacement of Cr-spinel by fuchsite is rare; rather,

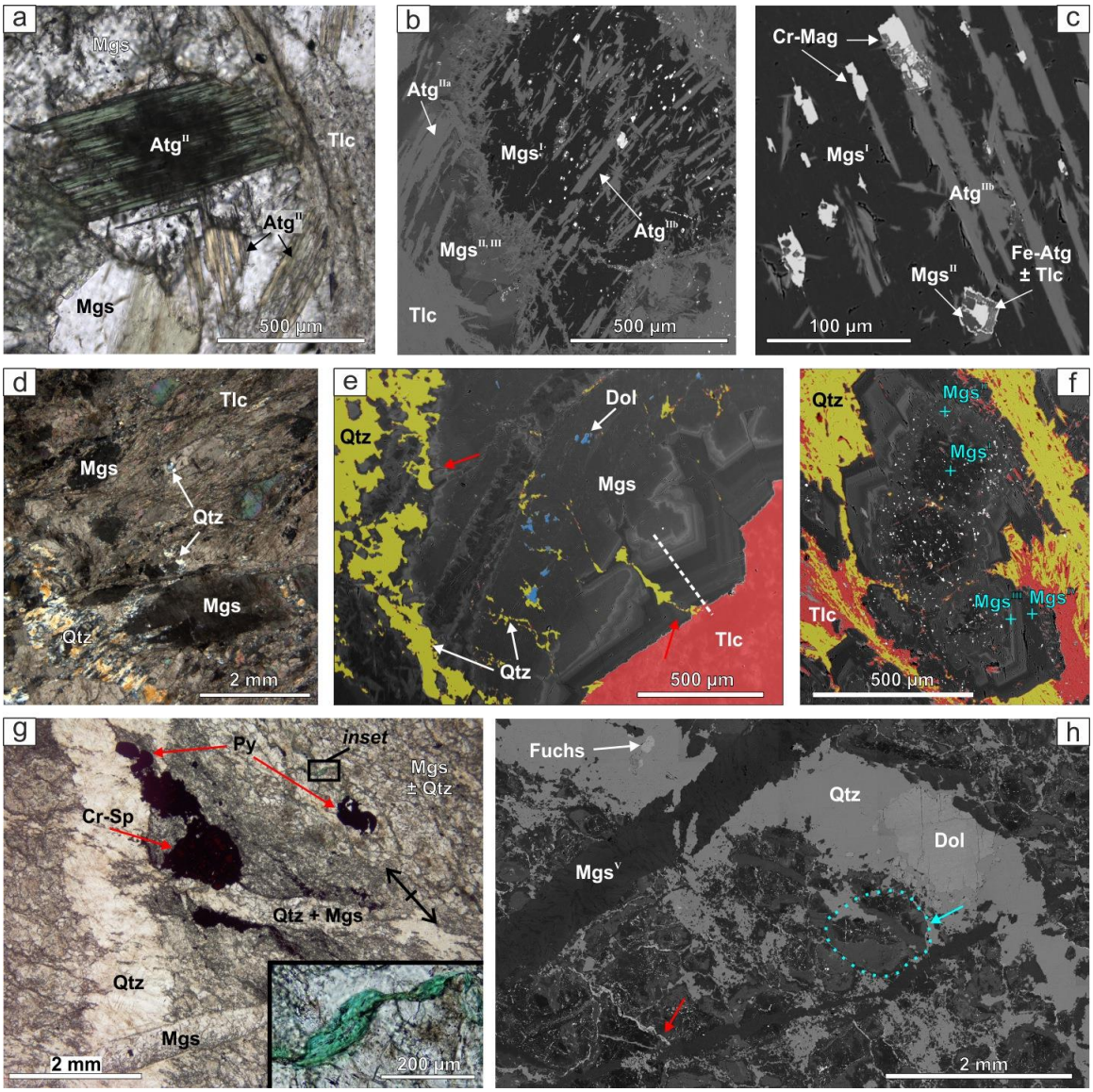

Figure 4.6. *Microstructures of Atg-Tlc-Mgs rock (a - c), Qtz-Tlc-Mgs rock (d - f) and listvenite (g, h).* ***(a)*** *Pleochroic antigorite flakes (green and yellow) intergrown with magnesite (plain polarized light, sample Adv-35).* ***(b)*** *Coarse, Fe-poor magnesite with pentlandite and magnetite inclusions, and Fe-richer rims (dark and medium grey levels) intergrown with antigorite in a Atg-Tlc-Mgs rock (BSE image, sample Adv-42).* ***(c)*** *Decomposing magnetite in a magnesite core from an Atg-Tlc-Mgs rock (BSE image).* ***(d)*** *Anastomosing talc bands around coarse magnesite, and incipient quartz formation in the matrix and as veins in a Qtz-Tlc-Mgs rock (sample Adv-29).* ***(e)*** *BSE image with partially superposed phase map (EDS-SEM) in a Qtz-Tlc-Mgs rock, showing zoned Fe-content in a magnesite aggregate (BSE-image) with dolomite inclusions (blue), and thin quartz micro-veins (yellow) formed during carbonation of talc (light red). The white dashed line marks the location of the chemical profile in Fig. 9.* ***(f)*** *Superposed BSE image and phase map of a zoned magnesite single crystal with inclusion-rich core, in a quartz-talc matrix.* ***(g)*** *Quartz and magnesite veins crosscutting a small-grained listvenite matrix showing a weak layering (black arrow); inset: detail of fuchsite (ppl; sample Adv-27).* ***(h)*** *Microstructures in coarse non-layered listvenite (tiled BSE-image; sample Adv-30) with interstitial quartz (medium bright) between fragmented coarse magnesite with inclusion-rich cores (e.g. grain highlighted by blue arrow; all dark grey levels are magnesite); and bright fuchsite veinlets (red arrow).*

fuchsite and Cr-chlorite form thin, anastomosing veinlets and dispersed small grains interstitial between magnesite (Fig. 4.5f).

Quartz-, quartz-magnesite- and minor, late magnesite veins in listvenites (Fig. 4.6g & h) are predominantly syntaxial and show coarsening towards the vein centres. Dolomite may preferentially occur in centres of quartz veins (e.g., Fig. 4.6h) and magnesite veins. Magnesite-bearing, coarse-grained (> 1 mm) quartz stretching veins occasionally show small fluid-inclusion bands marking crack-seal events. Rare antitaxial quartz veins in Si-depleted listvenites consist of fibrous quartz and have thin talc seams at the vein rims.

4.5 Methods

4.5.1 Mass balance computation of mineral mode

The mode (mol%) of major phases were calculated by mass balance from the bulk chemistry, assuming all Ca to be present in dolomite and that organic carbon is absent (i.e., that the measured C is present only as CO_2 in carbonates). Mean Mg- and Fe-contents of magnesite measured by electron microprobe (Appendix Table A-4.3) were used to determine the residual bulk amount of MgO available to form talc and serpentine. Assuming that serpentine is present dominantly as antigorite with polysome m = 17 [$M_{2.879}Si_{2.052}O_7(OH)_{3.741}$] (Mellini et al., 1987), we estimated the proportions of coexisting talc and serpentine by balancing SiO_2 and MgO as:

$$\text{Tlc (mol\%)} = 0.533\,[SiO_2]_{bulk\ mol} - 0.378\,[MgO]_{bulk\ mol\ -\ MgO(Mgs)}$$

$$\text{Atg (mol\%)} = -0.5516\,[SiO_2]_{bulk\ mol} + 0.736\,[MgO]_{bulk\ mol\ -\ MgO(Mgs)}$$

Because the effect of Fe and Al substitutions in antigorite was neglected in the mass-balance, the proportions of antigorite are slightly underestimated. Talc was considered to be absent in samples containing brucite, in accordance with observations by optical microscopy. In samples where the MgO-content in excess after magnesite calculation could be balanced entirely by talc, serpentine was assumed to be absent and remaining Si was balanced by quartz. The accurateness of the resulting mineral modes within the limits of measurement errors and the described assumptions was confirmed by optical microscopy and chemical SEM-EDS maps of selected samples.

4.5.2 Thermodynamic modelling

We calculated fluid-saturated, isobaric T-X_{CO2} phase diagram sections in the CaO-MgO-FeO-Fe_2O_3-SiO_2-H_2O-CO_2 system using Perple_X (version 6.7.6; Connolly, 2005; Connolly, 2009), where X_{CO2} is the molar CO_2 fraction in a binary H_2O-CO_2 fluid in equilibrium with the respective mineral assemblage. The CORK equation of state (Holland and Powell, 1991) was used to calculate the behaviour of H_2O-CO_2 fluids. Al and Cr were not considered in the calculations, because minor Cr-spinel, ferrit-chromite, chlorite, and fuchsite are accessory phases that do not have a major impact on other phase stabilities. Solid solution models for olivine, magnesite-siderite and dolomite-ankerite, and the internally consistent thermodynamic database by Holland and Powell (1998) (revised version of 2002) were used for computations. The solution model of antigorite by Padrón-Navarta et al. (2013) was adopted; ideal solution models were used for tremolite, talc, brucite and magnetite-magnesioferrite. Quartz and hematite were considered as pure phases.

4.6 Results

4.6.1 Whole rock chemistry

The Advocate serpentinites and related carbonated rocks have highly variable CO_2 contents and plot close to the serpentine-CO_2 tie line in the MgO-FeO-SiO_2-CO_2 composition space (Fig. 4.7a). On a volatile-free basis, all analysed samples have compositions with 44 – 47 wt% SiO_2 and 44 – 48 wt% MgO (Fig. 4.7b), low Al_2O_3 and CaO (0.4 – 1.2, and 0.1 – 1.3 wt%, respectively; Table 4.2), high Cr- and Ni contents (Fig. 4.7c), and molar MgO/(MgO+FeO_{total}) ratio of 0.90 – 0.93. Listvenites and some Qtz-Tlc-Mgs rocks have higher Mg/Si ratios (Fig. 4.7a), which may be attributed to silica precipitation in thick quartz veins that were not included in the whole rock analysis. The proportions of main minerals calculated by mass-balance (cf. section *4.5.1*) from the whole rock MgO, SiO_2, and CO_2 contents are in good agreement with those observed by microscopic methods (e.g., Table 4.1), showing increasing modal amounts of talc with decreasing serpentine and the presence of quartz in rocks with CO_2 > c. 22 wt% (Fig. 4.7a & d). Whole rock CO_2 is primarily contained in magnesite and minor or rare dolomite; no other carbonate phase was observed (Fig. 4.7d). The whole rock Fe^{3+}/Fe_{total} ratio decreases abruptly from brucite-bearing Atg-serpentinite and Lz-serpentinite to increasingly carbonated Atg-serpentinites and Atg-Tlc-Mgs rocks (from 0.75 – 0.79 to 0.2 – 0.4; Fig. 4.7e and Table 4.2), and further decreases with

increasing quartz content and high carbon contents from Qtz-Tlc-Mgs rocks towards listvenite (from 0.18 – 0.26 to 0.07 – 0.15 in listvenite). One sample of Qtz-Tlc-Mgs rock (Adv-41) and one carbonated Lz-serpentinite (Adv-32) have higher Fe^{3+}/Fe_{total} ratios not in accordance with the general trend (Fig. 4.7e and Table 4.2). In contrast to the Fe^{3+}/Fe_{total}

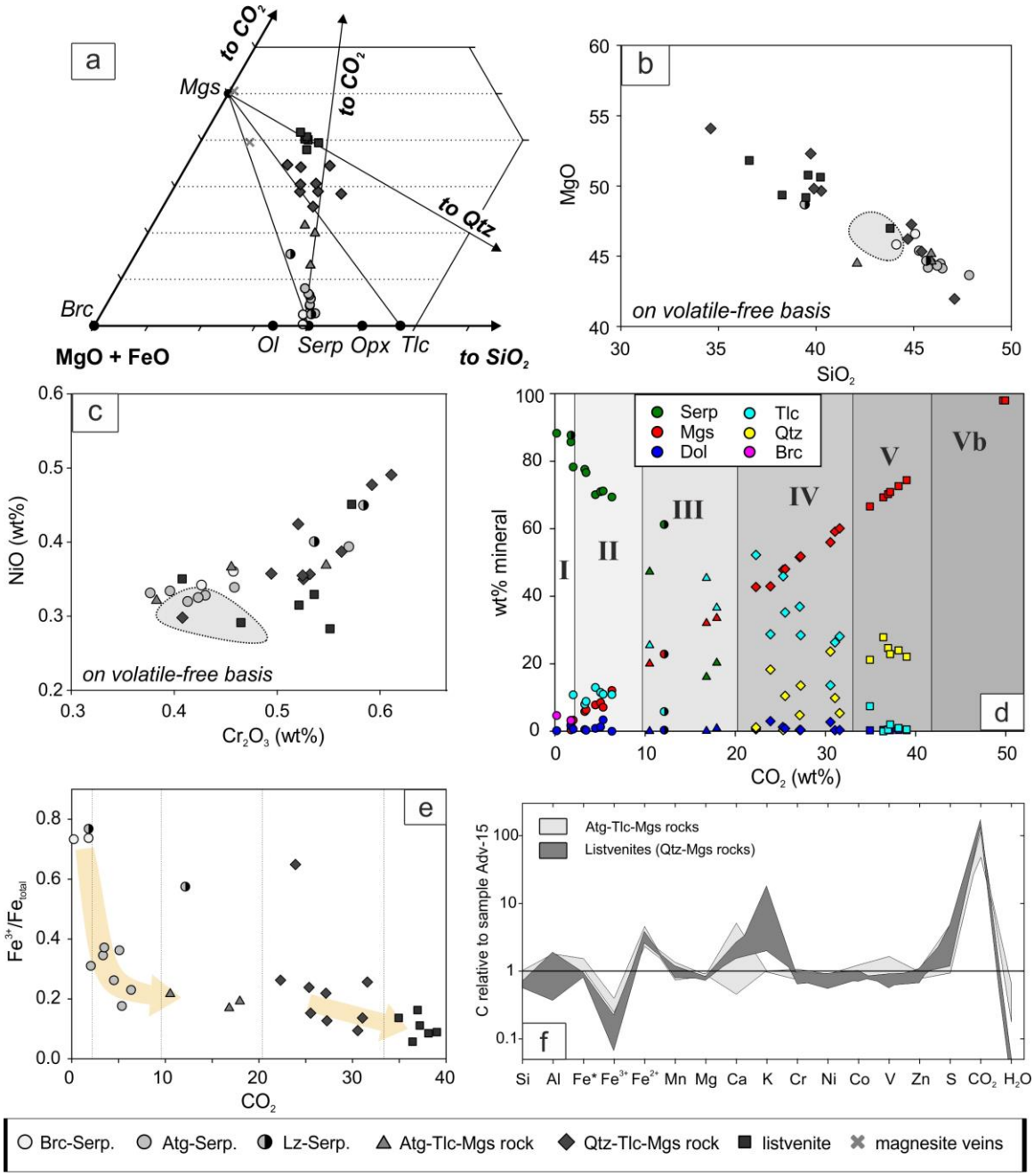

Figure 4.7. *Bulk chemical variations of the Advocate carbonate-bearing lithologies (Brc-Serp. = Brc-bearing Atg-serpentinite).* ***(a)*** *Molar proportions of MgO+FeO, SiO_2 and CO_2 in a ternary plot; all samples plot close to the tie-line between serpentine and CO_2.* ***(b)*** *MgO vs. SiO_2 contents on volatile-free basis; grey field: serpentinized harzburgite in Advocate complex from Bédard and Escayola (2010).* ***(c)*** *Cr_2O_3 vs NiO (wt%) bulk chemical variability; grey field as in b).* ***(d)*** *Modal proportions of main minerals calculated by mass-balance vs. CO_2 bulk rock content.* ***(e)*** *Whole rock molar Fe^{3+}/Fe_{total} ratio against CO_2 content.* ***(f)*** *Element gains and losses in Atg-Tlc-Mgs rocks and listvenites relative to the least carbonated Atg-serpentinite sample (Adv-15).*

ratios, the total Fe content does not differ systematically between the least carbonated samples and carbonate-richer lithologies but remains roughly constant throughout the studied samples (Fe* in Fig. 4.7f). In listvenites, there is a clear gain in K_2O and loss of H_2O with increasing CO_2 (Table 4.2; and Fig. 4.7f).

Table 4.2a *Whole rock compositions of serpentinite, carbonated serpentinites, Atg-Tlc-Mgs rocks, Qtz-Tlc-Mgs rocks and listvenites in the Advocate complex. TiO_2, Na_2O and P_2O_5 are below detection limits in all samples.*

Lithology	**Atg-srp***	**Atg-srp***	**Atg-srp**	**Atg-srp**	**Atg-srp**	**Atg-srp**	**Atg-srp**	**Atg-srp**	**Atg-srp**	**Lz-srp**
Sample	**Adv 15**	**Adv 39**	**Adv 19**	**Adv 38**	**Adv 12**	**Adv 31**	**Adv 16**	**Adv 36**	**Adv 10**	**Adv 33**
SiO_2 (wt%)	39.42	38.27	41.81	39.74	39.83	39.53	38.99	38.75	37.89	39.17
Al_2O_3	0.38	0.46	0.49	0.63	0.39	0.59	0.45	0.49	0.39	0.65
$Fe_2O_{3\,(calc)}$	4.54	5.29	2.00	2.38	2.64	1.80	2.54	1.21	1.66	4.56
FeO[a]	1.49	1.70	4.01	4.06	4.02	4.56	4.03	5.10	5.01	1.24
MnO	0.092	0.116	0.071	0.071	0.084	0.074	0.081	0.084	0.101	0.05
MgO	40.73	39.75	38.14	38.11	38.19	37.53	37.85	37.43	37.98	38.33
CaO	0.07	0.49	0.20	0.17	0.10	0.27	0.41	1.03	0.01	1.00
K_2O	0.01	0.01	0.01	0.01	0.01	0.02	0.01	0.01	0.01	0.01
S	0.02	0.04	0.12	0.02	0.02	0.12	0.27	0.02	0.01	0.05
CO_2 (TC)[b]	0.22	1.79	2.05	3.34	3.48	4.51	5.09	5.36	6.34	1.80
LOI	12.68	13.37	13.10	14.32	14.18	14.79	14.96	15.80	16.35	13.73
Cr (ppm)	2737	2532	2532	3353	2326	2668	2189	2395	2463	3147
Co (ppm)	96	105	100	110	114	108	110	100	99	136
Cu (ppm)	b.d.	b.d.	b.d.	b.d.	b.d.	b.d.	b.d.	b.d.	b.d.	b.d.
Ni (ppm)	2477	2331	2232	2660	2253	2265	2212	2129	2157	2700
V (ppm)	34	33	34	35	24	36	35	32	33	37
Zn (ppm)	40	42	47	56	50	46	36	41	43	60
Total (LOI)	100.07	100.08	100.45	100.27	100.02	99.81	99.88	100.49	99.99	99.49
$Mg/(Mg+Fe^{2+})$[c]	0.98	0.98	0.94	0.94	0.94	0.94	0.94	0.93	0.93	0.98
Fe^{3+}/Fe_{total}[c]	0.73	0.74	0.31	0.35	0.37	0.26	0.36	0.18	0.23	0.77

*Lithology abbreviations: Atg-srp = antigorite-dominated serpentinite (*brucite-bearing); Lz-srp = lizardite-dominated serpentinite; atm = Atg-Tlc-Mgs rock; qtm = Qtz-Tlc-Mgs rock; list = listvenite (sensu stricto); mv = magnesite-veins (cf. Table 4.1).*

LOI = loss on ignition (corrected for oxidation gain); b.d. = below detection limit (see Table 3.1); n.m. = not measured (nearly pure magnesite rock).

[a] *Determined separately by Mn-permanganate titration.*

[b] *Total carbon given as CO_2 determined by IR-spectroscopy.*

[c] *Calculated molar ratios.*

Table 4.2b *Whole rock compositions of serpentinite, carbonated serpentinites, Atg-Tlc-Mgs rocks, Qtz-Tlc-Mgs rocks and listvenites in the Advocate complex. TiO_2, Na_2O and P_2O_5 are below detection limits in all samples.*

Lithology	**Lz-srp**	**atm**	**atm**	**atm**	**qtm**	**qtm**	**qtm**	**qtm**	**qtm**	**qtm**	**qtm**
Sample	**Adv 32**	**Adv 42**	**Adv 11**	**Adv 35**	**Adv 20**	**Adv 21**	**Adv 41**	**Adv 22**	**Adv 03**	**Adv 23**	**Adv 29**
SiO_2 (wt%)	31.05	37.28	35.98	32.28	33.75	29.10	36.58	32.88	28.29	31.65	32.32
Al_2O_3	0.38	0.36	0.67	0.65	0.31	0.21	0.52	0.22	0.46	0.23	0.70
$Fe_2O_{3\,(calc)}$	4.73	1.43	1.12	1.79	1.34	1.54	4.32	0.91	1.38	0.75	0.56
FeO[a]	3.15	4.66	4.94	6.79	3.45	4.46	2.10	4.56	4.42	4.61	4.84
MnO	0.168	0.096	0.068	0.068	0.096	0.12	0.07	0.10	0.13	0.08	0.06
MgO	38.35	36.69	34.98	34.11	35.49	35.87	29.38	32.82	35.33	32.73	28.80
CaO	0.12	0.03	0.05	0.28	0.09	0.34	0.93	0.27	0.14	0.14	0.85
K_2O	0.01	0.01	0.01	0.01	0.01	0.01	0.01	0.01	0.01	0.01	0.01
S	0.05	0.08	0.02	0.05	0.04	0.04	b.d.	0.06	b.d.	0.01	0.02
CO_2 (TC)[b]	12.14	10.52	16.82	17.96	22.30	25.33	23.90	25.54	27.17	27.27	30.57
LOI	21.26	18.66	21.63	23.03	24.72	27.59	25.35	27.16	28.88	28.65	31.00
Cr (ppm)	3147	2532	2053	2874	2737	2600	2874	2600	2874	2395	1916
Co (ppm)	139	104	82	120	100	105	104	98	97	89	69
Cu (ppm)	b.d.	b.d.	b.d.	b.d.	b.d.	b.d.	b.d.	28	b.d.	24	b.d.
Ni (ppm)	2783	2337	1977	2222	2096	1981	2271	2019	2660	1989	1607
V (ppm)	27	28	26	56	20	20	39	27	27	25	28
Zn (ppm)	49	44	31	39	44	45	26	41	45	35	30
Total (LOI)	99.98	99.84	99.96	99.67	99.88	99.83	99.96	99.53	99.75	99.42	99.60
$Mg/(Mg+Fe^{2+})$[c]	0.96	0.93	0.93	0.90	0.95	0.93	0.96	0.93	0.93	0.93	0.91
Fe^{3+}/Fe_{total}[c]	0.57	0.22	0.17	0.19	0.26	0.24	0.65	0.15	0.22	0.13	0.09

*Lithology abbreviations: Atg-srp = antigorite-dominated serpentinite (*brucite-bearing); Lz-srp = lizardite-dominated serpentinite; atm = Atg-Tlc-Mgs rock; qtm = Qtz-Tlc-Mgs rock; list = listvenite (sensu stricto); mv = magnesite-veins (cf. Table 4.1).*
LOI = loss on ignition (corrected for oxidation gain); b.d. = below detection limit (see Table 3.1); n.m. = not measured (nearly pure magnesite rock).

[a] *Determined separately by Mn-permanganate titration.*

[b] *Total carbon given as CO_2 determined by IR-spectroscopy.*

[c] *Calculated molar ratios.*

Table 4.2c *Whole rock compositions of serpentinite, carbonated serpentinites, Atg-Tlc-Mgs rocks, Qtz-Tlc-Mgs rocks and listvenites in the Advocate complex. TiO_2, Na_2O and P_2O_5 are below detection limits in all samples.*

Lithology	**qtm**	**qtm**	**qtm**	**list**	**list**	**list**	**list**	**list**	**mv**	**mv**
Sample	**Adv 01**	**Adv 14**	**Adv 02**	**Adv 34**	**Adv 30**	**Adv 28**	**Adv 25**	**Adv 27**	**Adv 43**	**Adv 17**
SiO_2 (wt%)	26.65	23.27	25.99	27.93	25.04	24.22	24.70	22.55	11.60	1.09
Al_2O_3	0.43	0.46	0.43	0.24	0.52	0.72	0.14	0.48	0.44	0.08
$Fe_2O_{3\ (calc)}$	0.58	1.72	0.69	0.31	1.03	0.77	0.48	0.57	1.33	1.86
FeO[a]	3.31	4.49	3.90	4.53	4.76	5.55	4.65	5.22	6.31	6.27
MnO	0.17	0.15	0.11	0.08	0.10	0.09	0.10	0.08	0.24	0.28
MgO	35.09	36.38	32.72	29.96	31.20	31.25	31.68	31.95	39.57	39.94
CaO	0.12	0.13	0.11	0.15	0.18	0.11	0.13	0.12	0.27	1.45
K_2O	0.01	0.01	0.02	0.09	0.06	0.06	0.04	0.18	0.01	b.d.
S	b.d.	b.d.	b.d.	0.08	0.06	0.02	0.03	0.05	0.08	0.23
CO_2 (TC)[b]	31.07	31.59	34.94	36.43	36.96	37.19	38.12	39.02	36.33	49.33
LOI	32.36	32.75	35.21	35.76	36.54	36.82	37.55	38.21	39.25	47.87
Cr (ppm)	2805	2395	2532	1779	2326	2258	1984	2326	3147	2053
Co (ppm)	88	97	98	86	70	79	74	70	129	112
Cu (ppm)	b.d.	b.d.	48	b.d.	b.d.	b.d.	b.d.	b.d.	b.d.	b.d.
Ni (ppm)	2587	2242	2290	1756	1642	1567	1428	1371	2549	1726
V (ppm)	17	21	20	21	29	31	23	30	26	13
Zn (ppm)	34	40	39	27	41	38	31	30	41	35
Total (LOI)	99.40	99.96	99.79	99.50	99.95	100.10	99.91	99.84	99.76	99.33
$Mg/(Mg+Fe^{2+})$[c]	0.95	0.94	0.94	0.92	0.92	0.91	0.92	0.92	0.92	0.92
Fe^{3+}/Fe_{total}[c]	0.14	0.26	0.14	0.06	0.16	0.11	0.09	0.09	0.16	0.21

*Lithology abbreviations: Atg-srp = antigorite-dominated serpentinite (*brucite-bearing); Lz-srp = lizardite-dominated serpentinite; atm = Atg-Tlc-Mgs rock; qtm = Qtz-Tlc-Mgs rock; list = listvenite (sensu stricto); mv = magnesite-veins (cf. Table 4.1).*
LOI = loss on ignition (corrected for oxidation gain); b.d. = below detection limit (see Table 3.1); n.m. = not measured (nearly pure magnesite rock).

[a] *Determined separately by Mn-permanganate titration.*

[b] *Total carbon given as CO_2 determined by IR-spectroscopy.*

[c] *Calculated molar ratios.*

4.6.2 Stable C and O isotopes

Oxygen and carbon isotope compositions of magnesite in the variably carbonate-bearing lithologies in the Advocate mantle complex range from $\delta^{13}C$ = –8.9 to –5.0 ‰ (V-PDB) and $\delta^{18}O$ = 11.0 – 14.4 ‰ (V-SMOW; Table 4.3). Magnesite in one brucite-bearing Atg-serpentinite sample (Adv-39) is characterized by lighter carbon ($\delta^{13}C$ = –11.25 ‰). No systematic differences are evident between the oxygen isotope compositions of magnesite in Atg-serpentinites, Lz-serpentinites, Atg-Tlc-Mgs rocks, Qtz-Tlc-Mgs rocks and listvenites, but $\delta^{13}C$ of magnesite in carbonate-rich lithologies is slightly higher in comparison to brucite-bearing Atg-serpentinites (Table 4.3). Magnesite in veins hosted in Atg-serpentinites, Qtz-Tlc-Mgs rocks, and listvenites shows a range of carbon and oxygen isotope composition that is similar to that of magnesite in the host rock (Table 4.3).

Table 4.3. *Carbon and oxygen isotope composition of magnesite*

Sample	Lithology[a]	Sample type	$\delta^{18}O$ ‰ (V-SMOW)	$\delta^{13}C$ ‰ (PDB)	CO_2 (wt%)[b]
Adv-39	Atg-serp*	w.r.	13.42	-11.25	1.79
Adv-36	Atg-serp	w.r.	12.29	-8.59	5.36
Adv-38	Atg-serp	w.r.	11.50	-8.93	3.34
Adv-38	Atg-serp	Mgs-Lz-vein	12.37	-7.02	
Adv-33	Lz-serp	w.r.	14.43	-5.13	1.80
Adv-32	Lz-serp	w.r.	12.02	-8.29	12.14
Adv-11	atm	w.r.	11.03	-7.78	16.82
Adv-35	atm	w.r.	12.84	-6.75	17.96
Adv-20	qtm	w.r.	12.92	-5.35	22.30
Adv-41	qtm	w.r.	12.95	-5.89	23.90
Adv-41	qtm	Mgs-vein	11.46	-7.94	
Adv-40	qtm	drill powder	12.29	-5.01	
Adv-23	qtm	w.r.	12.06	-6.37	27.27
Adv-34a	list	w.r.	13.79	-5.16	36.43
Adv-28	list	drill powder[c]	12.76	-6.45	37.19
Adv-28	list	Qtz-Mgs-vein	11.26	-6.85	
Adv-27	list	w.r.	12.67	-6.66	39.02
Adv-13	list	Mgs-vein	13.29	-5.40	
Adv-09	mr	w.r.	12.89	-6.12	49.95
Adv-07	mr	Mgs-vein	12.32	-6.84	49.70
Adv-43	mv	w.r.	11.95	-6.33	36.33
Adv-17	mv	w.r.	10.67	-7.42	49.33

w.r. = whole rock powder; [a] lithology abbreviations as in Table 4.2; [b] whole rock carbon content from IR-spectroscopy; [c] in coarse, non-foliated part of sample.

4.6.3 Mineral Chemistry

Relict olivine in Brc-bearing Atg-serpentinite has $Fo_{90.5}$ – $Fo_{92.5}$, with NiO c. 0.4 wt% and MnO c. 0.1 – 0.2 wt% (Appendix Table A-4.2), resembling olivine in the least serpentinized part of the ultramafic complex (Bédard and Escayola, 2010). Brucite in Atg-serpentinites is poor in iron (X_{Mg} ~ 0.98; Appendix Table A-4.2) and contains minor amounts of NiO and MnO. Serpentine in brucite-bearing serpentinites is similarly Fe-poor ($Mg/(Mg+Fe_{total})$ = 0.97 – 0.99). Similar to serpentinites elsewhere (e.g. Lafay et al., 2017; Rouméjon et al., 2015), bastite-texture lizardite has elevated Al_2O_3 and Cr_2O_3 contents (up to 2.5 and 1.0 wt%, respectively) in comparison to interlocked antigorite in Atg-serpentinites. Mesh lizardite in Lz-serpentinite is occasionally also rich in Al. Lizardite in both Atg- and Lz-serpentinites often has a non-ideal stoichiometry with elevated Si-contents, suggesting the presence of fine-grained mixtures with antigorite (Fig 4.8; Appendix Table A-4.2). Antigorite has generally Si-rich compositions $[(Mg,Fe)_{2.85–2.81}Si_{2.05–2.09}O_{5.13–5.17}(OH)_{3.66–3.74}]$, with only minor tschermak substitution by Al and Cr (mostly < 0.1 atoms per formula unit). Relatively Si-poor antigorite and lizardite compositions are rare or absent in carbonate-rich serpentinites and Atg-Tlc-Mgs-rocks. The iron content in antigorite increases significantly in serpentinites with higher carbonate content, reaching up to 9.2 wt% FeO_{total} (X_{Mg} = 0.87; Appendix Table A-4.2) in coarse, green pleochroic antigorite flakes in Atg-Tlc-Mgs rocks (Fig. 4.6a; see discussion and Fig. 4.8 for considerations on the Fe^{3+}/Fe^{2+} ratio of antigorite). Minor NiO

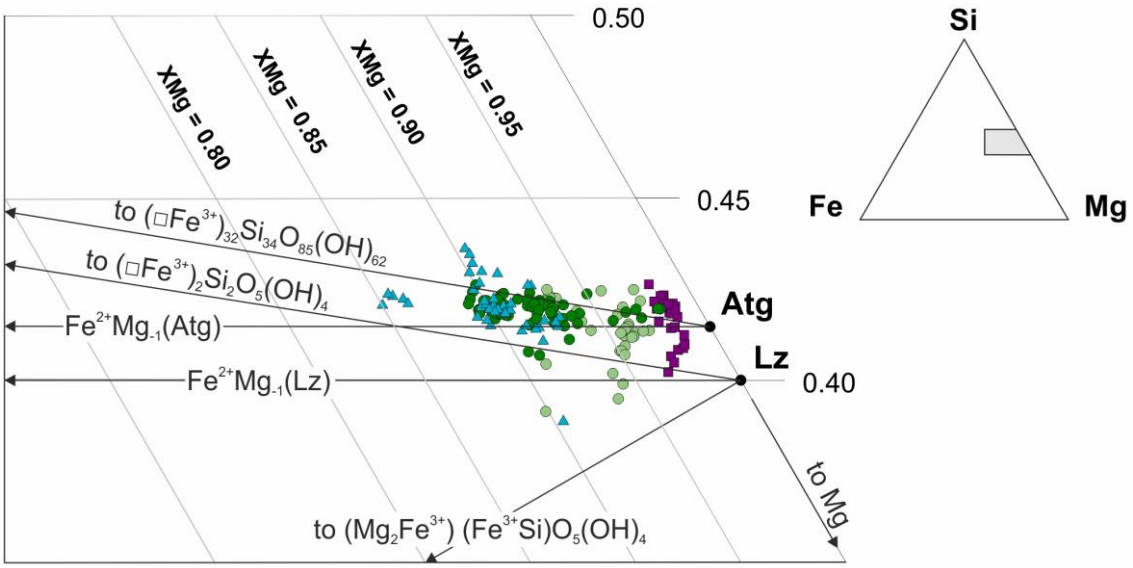

Figure 4.8. *Detail of ternary plot of Mg, Fe and Si (a.p.f.u per 7 oxygens) in serpentine minerals in Brc-bearing Atg-serpentinite (purple), Lz-serpentinite (light green), carbonated serpentinite (dark green) and Atg-Tlc-Mgs rocks (blue triangles), and vectors of possible Fe substitutions.*

(0.10 – 0.25 wt%) is present in serpentine of Atg- and Lz-serpentinites and Atg-Tlc-Mgs rocks.

Talc contains minor FeO and NiO (1.5 – 2.6 wt%, and 0.2 – 1.6 wt%, respectively; Appendix Table A-4.2). In Qtz-Tlc-Mgs rocks, the Ni-content of talc in the matrix is significantly higher than in talc inclusions in magnesite and in talc of Atg-Tlc-Mgs rocks (Appendix Table A-4.2). Rare chlorite is characterized by moderate FeO (Mg# = 0.89 – 0.93) and high Cr_2O_3 and NiO contents, in particular in listvenites (1.0 – 5.3 and 0.2 – 2.4 wt%, respectively; Appendix Table A-4.2). Cr-rich mica (fuchsite) in potassium-bearing listvenites shows a highly variable substitution of Al by Cr (Cr# = Cr/(Cr+Al) = 0.13 – 0.40) and minor contents of MgO, FeO and NiO (Appendix Table A-4.2).

Magnesite in brucite-bearing Atg-serpentinites has low FeO and elevated MnO contents (Mgs^{I}; X_{FeCO3} = c. 0.005 and X_{MnCO3} = 0.015), in addition to Si-impurities from fine-grained antigorite intergrowths. Rare dolomite associated with brucite and magnesite is also slightly enriched in MnO, and has very low X_{FeCO3} (Appendix Table A-4.3). In carbonate-richer Atg-serpentinites, magnesite with high X_{FeCO3} and minor X_{MnCO3} (0.086 – 0.135 and 0.005 – 0.012, respectively; Mgs^{II} in Appendix Table A-4.3) occurs in aggregates resembling the

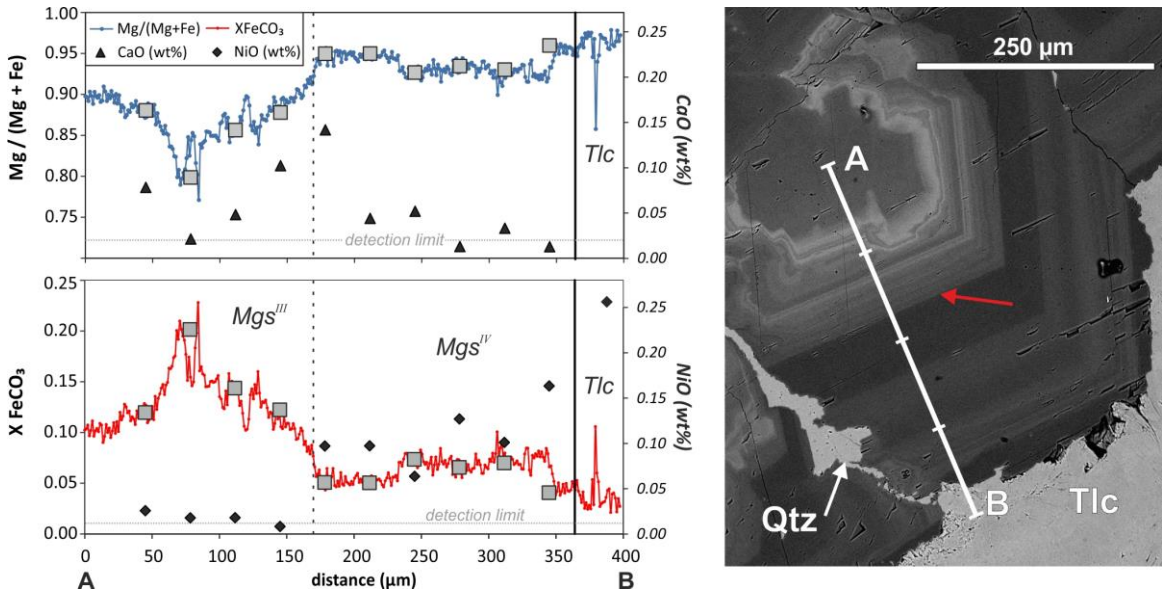

Figure 4.9. *Chemical variation perpendicular to the zonation of magnesite in Qtz-Tlc-Mgs rock (along profile line A-B as given in the BSE-image on the right; detail of Fig. 4.6f) measured by semi-quantitative SEM-EDS line scans (lines) and discrete electron microprobe (EMPA) measurements (grey squares, the size of the symbols corresponds to the beam size of 10 µm), shown as molar Mg/(Mg+Fe) and X_{FeCO3} ratios, and minor CaO and NiO contents (black symbols; with detection limit of EMPA indicated). The dashed vertical line marks the onset of Ni incorporation into magnesite, which coincides with a decreasing Fe content (white arrow in the BSE image).*

textural positions of olivine and bastite in less carbonated serpentinites (Fig. 4.4c & f); on the other hand, Mgs^{I} magnesite is preserved in cores of such aggregates and relict veins. Two compositionally equivalent magnesite generations occur in carbonated Lz-serpentinite (Fig. 4.4h), where Fe-rich magnesite rims overgrow Fe-poor cores with elevated Mn-contents (Appendix Table A-4.3). Magnesite in textural equilibrium with talc and antigorite in Atg-Tlc-Mgs rocks (Mgs^{III} in Fig. 4.6b and Appendix Table A-4.3) has high X_{FeCO3} (0.1 – 0.16) and relatively low X_{MnCO3} (< 0.005), and overgrows relict Mgs^{I} and Mgs^{II} grains that are rich in magnetite inclusions (Fig. 4.6b). The outermost magnesite rims (Mgs^{IIIb} in Appendix Table A-4.3) are Fe-poor in rocks with higher bulk carbon content and lower antigorite abundance. In Qtz-Tlc-Mgs rocks, Ni-bearing (0.10 – 0.45 wt% NiO), relatively Fe-poor (X_{FeCO3} = 0.04 – 0.08) magnesite (Mgs^{IV} in Fig. 4.6f, Fig. 4.9, and Appendix Table A-4.3) overgrows the previous Mgs generations. In listvenites, the outermost magnesite rims and smaller grains interstitial between quartz have relatively Fe-poor compositions (X_{FeCO3} = 0.03 – 0.07), similar to the composition of magnesite veins (Mgs^{V} in Fig. 4.6h and Appendix Table A-4.3).

Relict Cr-spinel in all studied carbonate-bearing lithologies shows compositions similar to those in olivine- and brucite-bearing serpentinite, with Cr# and Mg# ranging from 0.50 – 0.70 and 0.45 – 0.70, respectively (Appendix Table A-4.4). Ferrit-chromite rims around Cr-Spinel in the carbonate-bearing lithologies contain variable amounts of Cr and Fe (Cr# = 0.85 – 1.0; Fe^{3+}/Fe_{total} = 0.44 – 0.63), and are poor in Al and Mg (usually < 2 and < 0.8 wt%, respectively; Appendix Table A-4.4). In Atg-serpentinites, magnetite at Cr-spinel rims has relatively high Cr-contents (c. 0.8 – 3.1 wt% Cr_2O_3), whereas it is Cr-poor where associated with brucite veins (Appendix Table A-4.4). Goethite contains minor amounts of SiO_2 (2.3 – 2.9 wt%) and MgO (0.5 – 0.9 wt%) and can have rather high NiO contents (up to 2.4 wt%; Appendix Table A-4.4).

4.7 Discussion

4.7.1 Nature of the protolith of the Advocate listvenites

Whole rock major element and textural evidence indicate that the protolith of the Advocate listvenites and related carbonated rocks was serpentinized mantle harzburgite similar to that outcropping elsewhere in the Advocate ophiolite (Bédard and Escayola, 2010). The similarity of the whole rock major element compositions on an anhydrous basis of all lithologies with variable CO_2 (Fig. 4.7b & c) demonstrates that carbonation of serpentinized harzburgite

occurred by addition of CO_2 and minor removal of SiO_2 (Fig. 4.7b). Atg-serpentinites with evidence of incipient carbonation generally have slightly lower Mg/Si ratios than the least serpentinized harzburgites from the present and previous studies (Fig. 4.7b). This relatively low Mg/Si ratio can be a primary feature of harzburgite due to variable ratios of orthopyroxene/olivine arising from igneous processes (Kelemen et al., 1998; Varas-Reus et al., 2016). Alternatively, low temperature seawater alteration may have led to dissolution of brucite, leading to low Mg/Si in serpentinite (Snow and Dick, 1995), or serpentinization was associated with a minor gain in Si (Malvoisin, 2015). A serpentinized harzburgite protolith is evidenced by the presence of relict Cr-spinel in the carbonate-bearing lithologies with composition (Appendix Table A-4.4) similar to those in the least serpentinized Advocate harzburgites (Bédard and Escayola, 2010). Relict Cr-spinel with compositions equivalent to those of their protolith host rocks is common in listvenites elsewhere (e.g. Halls and Zhao, 1995; Robinson et al., 2005; Sofiya et al., 2017; Streit et al., 2012).

4.7.2 Origin of serpentinite in the Advocate complex

4.7.2.1 Formation of lizardite/chrysotile serpentinite

The presence of lizardite in mesh textures around olivine and bastite replacing orthopyroxene overprinted by carbonate shows that the Advocate harzburgite was variably serpentinized prior to carbonation. Serpentinization of olivine and orthopyroxene locally produces brucite and talc, respectively, in addition to serpentine and magnetite (e.g. Bach et al., 2004; Frost and Beard, 2007; Klein et al., 2014; McCollom and Bach, 2009). A widespread feature of the Advocate serpentinite is the pervasive transformation of orthopyroxene to bastite, while relict olivine is still preserved (Fig. 4.4a & e; see also Kidd (1974)). Based on an initial olivine proportion of c. 85 mol.%, the observation that all orthopyroxene is transformed into lizardite bastite and the assumption that c. 70% of olivine was transformed to serpentine, serpentinization of the Advocate harzburgite can be balanced according to the overall reaction:

$$4\ Mg_{1.8}Fe_{0.2}SiO_4 + Mg_{1.8}Fe_{0.2}Si_2O_6 + 6.33\ H_2O$$
Olivine (Fo_{90}) Orthopyroxene (En_{90})

$$= 2.2\ Mg_3Si_2O_5(OH)_4 + 0.4\ Mg_3Si_4O_{10}(OH)_2 + 1.2\ Mg(OH)_2 + 0.33\ Fe_3O_4 + 0.33\ H_2 \quad (4.1)$$
Lizardite/Chrysotile Talc Brucite Magnetite

The lack of talc and the transformation of orthopyroxene to lizardite bastite indicate that talc or $SiO_{2,aq}$ reacted with brucite to form serpentine (Bach et al., 2006):

$$0.4\ Mg_3Si_4O_{10}(OH)_2 + 1.2\ Mg(OH)_2 = 0.8\ Mg_3Si_2O_5(OH)_4 \quad (4.2)$$

Talc *Brucite* *Lizardite/Chrysotile*

Because the reaction rate of the hydrolysis of olivine is generally slower than that of orthopyroxene at T > 250 °C (Allen and Seyfried, 2003), the preferential serpentinization of orthopyroxene can be indicative of high-T serpentinization (e.g. Bach et al., 2004). Alternatively, at T > 315 °C, and depending on the local composition, serpentinization reaction path modelling predicts that olivine can be in equilibrium with an aqueous fluid, limiting the extent of serpentinization (McCollom and Bach, 2009).

The onset of serpentinization may have occurred at lower temperatures, where reaction (4.1) produces Fe-brucite and Fe-rich serpentine rather than magnetite (McCollom and Bach, 2009; McCollom et al., 2016). Fe-brucite and Fe-rich lizardite are not present in Advocate serpentinite, suggesting that either low-T serpentinization did not occur, or that these phases recrystallized to lizardite and magnetite during high-T serpentinization.

4.7.2.2 Breakdown of lizardite/chrysotile to antigorite

The microstructure of antigorite and brucite in Advocate serpentinite shows that their formation post-dates that of lizardite and chrysotile (Fig. 4.4a – h). Similar textures and high contents of brucite are also found in carbonate-free Atg-serpentinites (e.g. sample Adv-15; Table 4.2). The textural occurrence of brucite in veins in Advocate Atg-serpentinite is different from that commonly observed in abyssal serpentinites, where it occurs in the centres of mesh textures (e.g. Bach et al., 2004). In Advocate serpentinite, the ubiquitous spatial association of brucite and antigorite (Fig. 4.4a & d) points toward brucite being the reaction product of the prograde recrystallization of lizardite or chrysotile to antigorite according to the reaction (Evans, 2004; Schwartz et al., 2013):

$$17\ (Mg,Fe)_3Si_2O_5(OH)_4 = Mg_{48}Si_{34}O_{85}(OH)_{62} + 3\ Mg(OH)_2\ (\pm\ Fe_3O_4) \quad (4.3)$$

Lizardite/Chrysotile *Antigorite* *Brucite* *Magnetite*

The Fe-poor composition of brucite (Appendix Table A-4.2) in Advocate serpentinite indicates that iron partitioned into magnetite in reaction (4.3).

Because the Mg/Si ratio (atoms per formula unit) of the antigorite polysomatic series is lower than that of lizardite and chrysotile (Mellini et al., 1987; Padrón-Navarta et al., 2008),

antigorite is stable at higher aqueous silica activities (Evans, 2004). The presence of antigorite veins without brucite in Lz-serpentinite (Fig. 4.4h) therefore most likely testifies for the formation of antigorite according to the reaction:

$$16\ (Mg,Fe)_3Si_2O_5(OH)_4 + 2\ SiO_{2,aq} = (Mg,Fe)_{48}Si_{34}O_{85}(OH)_{62} + H_2O \quad (4.4)$$

Lizardite/Chrysotile *Antigorite*

Thermodynamic modelling predicts that the transformation of lizardite to antigorite (reaction 4.3) occurs between 280 – 350 °C during greenschist facies metamorphism (Evans, 2004). At blueschist facies metamorphic conditions, the prograde formation of antigorite in natural serpentinites occurs between 320 – 390 °C (Schwartz et al., 2013). As discussed below, microstructures and phase relations indicate that incipient carbonation was coeval with the breakdown of lizardite to antigorite at T > c. 300 °C.

4.7.3 Unravelling the sequence of carbonation reactions of serpentinized peridotite

4.7.3.1 Preliminary thermodynamic considerations

As long as the infiltrating fluid has a high enough $CO_{2,aq}$ activity, carbonation of serpentinite can form listvenites without the need of Si or Mg metasomatism (Falk and Kelemen, 2015; Hansen et al., 2005; Klein and Garrido, 2011). At low pressure (< 0.05 GPa), carbonation of serpentinite is favoured at low to intermediate temperature (c. 200 ºC), but requires rather high $aCO_{2,aq}$ in the fluids (Klein and Garrido, 2011). Due to limitations in available thermodynamic modelling, previous studies have not yet explored the effect of carbonation at pressure above 0.3 GPa. The recently developed Deep Earth Water (DEW) model (Sverjensky et al., 2014) extends the Helgeson-Kirkham-Flowers equations of state for aqueous species through extrapolation of the dielectric constant and density of water, and allows computation at substantially higher pressures. Figure 4.10 shows the $a SiO_{2,aq}$–$a CO_{2,aq}$ activity diagram for progressive carbonation at 300 °C and different pressures calculated using the DEW model (Sverjensky et al., 2014; see caption of Fig. 4.10 for details on the calculation). As predicted by thermodynamic considerations (Evans, 2004), at 300 °C chrysotile/lizardite is metastable with respect to brucite and antigorite (grey dashed lines in Fig. 4.10). Upon infiltration of a CO_2-rich fluid into serpentinite, antigorite and brucite buffer the fluid $a SiO_{2,aq}$ and $a CO_{2,aq}$ at pseudo-invariant point i1 (Fig. 4.10) until all chrysotile/lizardite and brucite is transformed to magnesite and antigorite. Continued fluid

infiltration of CO_2-rich fluids (black dashed arrow between pseudo-invariant points i1 and i2; Fig. 4.10), leads to a two-order of magnitude increase of the $aSiO_{2,aq}$ until talc forms at the pseudo-invariant point i2 (Fig. 4.10) and buffers the fluid composition. If the $aCO_{2,aq}$ of the infiltrating fluid is sufficiently high (black dashed arrow between pseudo-invariant point i2 and Q-sat; Fig. 4.10), talc is consumed and quartz precipitates because it is saturated in the fluid phase (solid blue line in Fig. 4.10). At 300 °C, quartz precipitation requires a minimum log $aCO_{2,aq}$ of –0.33 at 0.5 GPa, while at 1.5 GPa it requires a substantially lower log $aCO_{2,aq}$

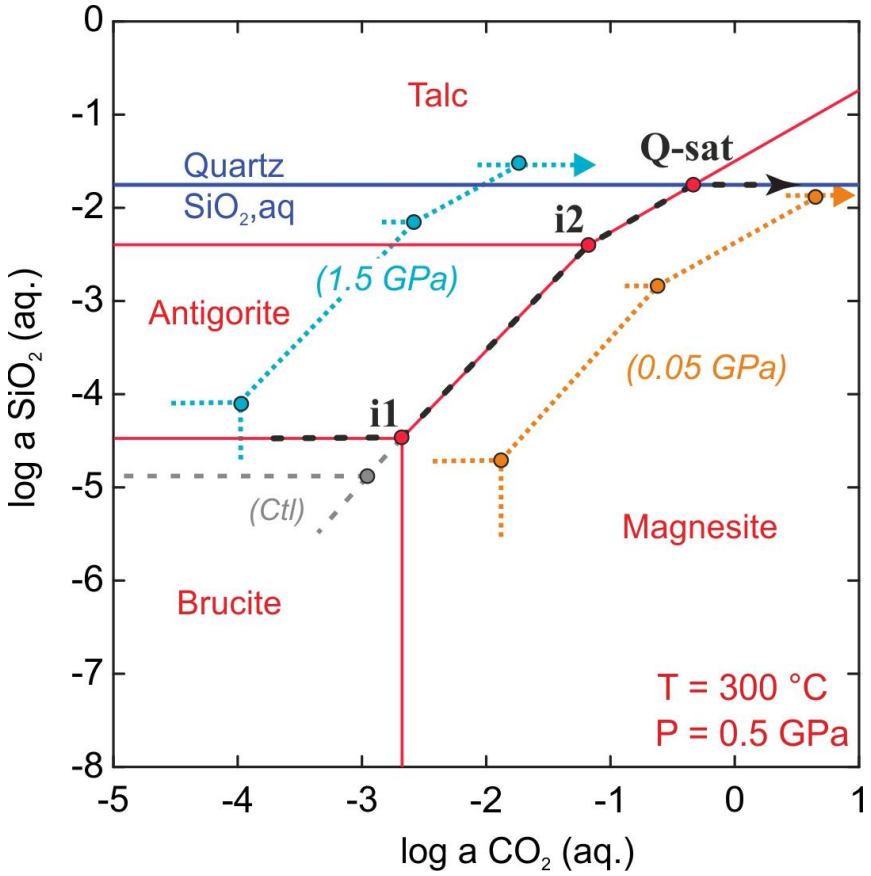

Figure 4.10. *Activity-activity diagram showing an isothermal carbonation reaction path of serpentinite for 0.5 GPa (red lines and black dashed arrow). Lines are conditions of equal activity of the solid phases; metastable chrysotile (Ctl) is marked by grey dashed lines. Position of reaction path and pseudo-invariant points for 1.5 GPa (blue dotted) and 0.05 GPa (orange dotted; after Klein and Garrido (2011)) are shown for comparison. The activities at 0.5 and 1.5 GPa were calculated assuming a water activity close to one and using the DEW-model with water density after Zhang and Duan (2005), Helgeson et al. (1978) for water Gibbs Free Energy extrapolation and the thermodynamic mineral database by Berman (1988). Calculation of dielectric constant and quartz saturation (blue line) are after Sverjensky et al. (2014). Chrysotile is shown instead of lizardite because the latter is not available in common databases; but phase stabilities are likely similar. Because rare dolomite was the only observed Ca-bearing phase throughout all studied samples and whole-rock Ca-contents are generally small, reactions involving Ca were not considered.*

of –1.76 (Fig. 4.10). At low pressure, quartz saturation at T > c. 250 °C would require orders of magnitude higher $aCO_{2,aq}$ in the fluid (Fig. 4.10, orange dotted boundaries for 0.05 GPa and 200 °C from Klein and Garrido, 2011). These results highlight the important role of pressure in enhancing carbonation of serpentinite and formation of listvenite in natural systems. As we will discuss later, this preliminary consideration points to fluxing of forearc serpentinite by CO_2-rich fluids in a subduction setting as a probable setting favouring listvenite formation. The important role of pressure in carbonation of ultramafic rocks is exemplified by the formation of metasomatic marbles (Piccoli et al., 2018; Piccoli et al., 2016) and HP-ophicarbonates (Scambelluri et al., 2016) in subduction-related metamorphic terranes.

4.7.3.2 Sequence of carbonation reactions in the Advocate complex

In the Advocate complex, the lithological sequence of carbonated serpentinite, Atg-Tlc-Mgs and Qtz-Tlc-Mgs rocks, and listvenite is consistent with their formation by reactive infiltration of CO_2-rich fluids into serpentinite (Fig. 4.10). The presence of dominantly three-phase (Atg-Tlc-Mgs and Qtz-Tlc-Mgs; Fig. 4.7a) rocks points to the fluid composition being locally buffered at the pseudo-invariant points i2 and Q-sat (Fig. 4.10). The wide range of whole rock carbon content in three-phase rocks (Fig. 4.7d) records different extents of reaction buffered at these pseudo-invariant points. The sharp contacts between carbonate-bearing lithologies (e.g. Fig. 4.2c & h) further indicate local rock-buffered equilibrium. Only a few of the studied samples are predominantly two-phase (Tlc-Mgs and Atg-Mgs) rocks (Fig. 4.7a) that likely formed by fluid-controlled $aSiO_{2,aq}$ and $aCO_{2,aq}$ along the reaction path boundaries between i1 – i2 (Atg+Mgs) and i2 – Q-sat (Tlc+Mgs) (Fig. 4.10). Below we discuss the textural and mineral composition evidences that constrain the sequence of carbonation reactions that resulted in the formation of listvenite after infiltration of serpentinized harzburgite by reactive CO_2–rich fluids. The temperature and, to a lesser extent, pressure conditions of carbonation and the nature and provenance of the CO_2-rich fluids will be discussed in more detail later on.

4.7.3.3 Incipient carbonation of serpentinite

Textural observations show that magnesite in Advocate serpentinite preferentially occurs replacing serpentine group minerals, relict olivine, and brucite (Fig. 4.4a – h). This is particularly apparent in carbonated Atg-serpentinite where magnesite fully replaces the lizardite-bearing mesh centres, lizardite bastite, and vermicular veins after brucite (Fig. 4.4c –

f). These ubiquitous textural relations in carbonated serpentine indicate that magnesite was not formed by direct precipitation from a Mg- and CO_2-rich fluid phase, but by fluid-mediated, coupled dissolution-precipitation reactions that dissolved serpentine minerals and brucite and precipitated magnesite.

During infiltration of CO_2-rich fluid into serpentinite, brucite and lizardite/chrysotile reacted with $CO_{2,aq}$ to form magnesite, H_2O, and $SiO_{2,aq}$, according to the reactions:

$$Mg(OH)_2 + CO_{2,aq} = MgCO_3 + H_2O \quad (4.5)$$

Brucite *Magnesite*

and

$$Mg_3Si_2O_5(OH)_4 + 3\ CO_{2,aq} = 3\ MgCO_3 + 2\ SiO_{2,aq} + 2\ H_2O \quad (4.6)$$

Lizardite/chrysotile *Magnesite*

Any relict olivine —i.e., preserved after serpentinization— also reacted with $CO_{2,aq}$ to form magnesite and release $SiO_{2,aq}$ (Johannes, 1969). Atg-serpentinite shows textural evidence of incipient replacement of brucite by magnesite in antigorite-brucite-magnetite veins (Fig. 4.4a). In the same sample, magnesite replaces bastite lizardite (Fig. 4.4e) and occurs in centres of serpentine mesh textures (Fig. 4.4a, c & d), suggesting that lizardite (reaction 4.6) or olivine reacted with $CO_{2,aq}$ to form magnesite. Similar textures of carbonate in serpentine mesh centres (Fig. 4.4c) are also common in ophicalcites, where relict olivine is replaced by calcite or dolomite (Andreani et al., 2009; Grozeva et al., 2017; Lafay et al., 2017). The composition of incipient magnesite (Mgs^{I} in Appendix Table A-4.3) with X_{Mg} similar to that of coexisting lizardite, antigorite and brucite (Fig. 4.11a; and Appendix Table A-4.2), points to its formation by carbonation of primarily lizardite and brucite, but Fe-rich magnesite in pseudomorphs after olivine (Mgs^{II} in Appendix Table A-4.3) also occurs in places. The observation that brucite veins in the Advocate Atg-serpentinites show minor replacement by magnesite and dolomite, while replacement of adjacent lizardite by magnesite is common (Fig. 4.4a, c & d), most likely indicates that carbonation of lizardite (reaction 4.6) was thermodynamically favoured over carbonation of brucite (reaction 4.5).

Aqueous silica ($SiO_{2,aq}$) produced by reaction (4.6) promotes the formation of antigorite from chrysotile and lizardite (reaction 4.4), buffering the $a SiO_{2,aq}$ at pseudo-invariant point i1 (Fig. 4.10). The well-crystallized, interpenetrating microstructure of antigorite coexisting with magnesite (Fig. 4.4d & e) suggests that $SiO_{2,aq}$ released by carbonation of lizardite/chrysotile may have enhanced the growth of antigorite, pointing to chemical

feedbacks between reactions (4.6) and (4.4). Chemical feedbacks between these reactions may account for the growth of euhedral antigorite veinlets spatially related to magnesite and replacing lizardite veins in Atg-serpentinite (Fig. 4.4g), and the crystallization of antigorite in veins in carbonated Lz-serpentinite (Fig. 4.4h). These observations support that incipient carbonation was coeval with the transformation of lizardite to antigorite, and postdate the serpentinization reactions that formed Lz-serpentinite.

At the P-T conditions of the breakdown of lizardite/chrysotile to antigorite and brucite (reaction 4.3), lizardite/chrysotile is metastable with respect to brucite + magnesite because the $a\mathrm{CO}_{2,aq}$ of the fluid in equilibrium with chrysotile + magnesite is lower than that of the fluid in equilibrium with brucite + magnesite (grey dashed and red boundaries, respectively, in Fig. 4.10). In Advocate Atg-serpentinite, microstructures (Fig. 4.4a – f) and the presence of antigorite-brucite-magnesite assemblages with metastable lizardite/chrysotile, therefore, indicates that the fluid $a\mathrm{SiO}_{2,aq}$ and $a\mathrm{CO}_{2,aq}$ were buffered by reactions (4.3) through (4.6) close to pseudo-invariant point i1 at T > c. 280 °C (Fig. 4.10). At lower temperatures, brucite is metastable with respect to lizardite/chrysotile + magnesite, and it is unlikely that any metastable brucite can be preserved during infiltration of a CO_2-bearing fluid due to the fast kinetics of brucite carbonation reactions (Hövelmann et al., 2012).

4.7.3.4 Formation of Atg-Tlc-Mgs rock and breakdown of magnetite

With further infiltration of CO_2-rich fluid and the consumption of lizardite and brucite, $\mathrm{CO}_{2,aq}$ reacts with antigorite to form magnesite and talc, buffering the $a\mathrm{SiO}_{2,aq}$ and $a\mathrm{CO}_{2,aq}$ of the fluid at point i2 (Fig. 4.10) according to the reactions:

$$\mathrm{Mg_{48}Si_{34}O_{85}(OH)_{62}} + 48\ \mathrm{CO_{2,aq}} = 48\ \mathrm{MgCO_3} + 34\ \mathrm{SiO_{2,aq}} + 31\ \mathrm{H_2O} \quad (4.7a)$$

Antigorite *Magnesite*

and

$$\mathrm{Mg_{48}Si_{34}O_{85}(OH)_{62}} + 30\ \mathrm{SiO_{2,aq}} = 16\ \mathrm{Mg_3Si_4O_{10}(OH)_2} + 15\ \mathrm{H_2O} \quad (4.7b)$$

Antigorite *Talc*

In most of the Advocate Atg-Tlc-Mgs rocks, whole rock silica content is conservative, and their talc modal proportion (Fig. 4.7a & d) is in good agreement with the formation of antigorite and talc by reactions (4.7a) and (4.7b). The Ni-contents of talc in Qtz-Tlc-Mgs rocks are significantly higher than in Atg-Tlc-Mgs rocks (Appendix Table A-4.2), indicating that Ni released during antigorite carbonation and pentlandite oxidation (Fig. 4.5c) preferentially partitioned into talc (Fig. 4.11b).

Apart from one carbonated Lz-serpentinite and one Atg-Tlc-Mgs rock sample with anomalously high bulk Fe^{3+}/Fe_{total} (Adv-32 and Adv-41; Table 4.2 and Fig. 4.7) and compared with brucite-bearing Atg-serpentinite, Advocate carbonated Atg-serpentinite and Atg-Tlc-Mgs rocks show a sharp decrease of their whole rock Fe^{3+}/Fe_{total} ratio (Fig. 4.7e). Textures (Fig. 4.5c; Fig. 4.6c) and a substantial decrease in magnetite abundance show that the change to low whole rock Fe^{3+}/Fe_{total} is due to the breakdown of magnetite, in contrast to some soapstones elsewhere where new magnetite formed during an equivalent carbonation stage (Tominaga et al., 2017). The breakdown of magnetite and related whole rock trends can be accounted for by the following carbonation and redox-reactions:

$$Fe_3O_4 + 3\ CO_{2,aq} = 3\ FeCO_3 + 0.5\ O_{2,aq} \quad (4.8)$$

Magnetite *Siderite*

and

$$16\ Fe_3O_4 + 34\ SiO_{2,aq} + 31\ H_2O = Fe_{48}Si_{34}O_{85}(OH)_{62} + 8\ O_{2,aq} \quad (4.9)$$

Magnetite *Fe-antigorite*

In these reactions, the magnetite ferric iron is reduced to ferrous iron that is incorporated into the siderite and ferrous serpentine components of magnesite and antigorite, respectively, while releasing oxygen into the fluid. Accordingly, antigorite and magnesite (Mgs^{III} in Appendix Table A-4.3) in carbonated Atg-serpentinite and Atg-Tlc-Mgs rocks have significantly higher Fe contents (lower X_{Mg} in Fig. 4.11a) than antigorite and magnesite in textural equilibrium with brucite and magnetite. Thermodynamic reaction path modelling also predicts a decrease in X_{Mg} of serpentine and carbonate during carbonation (cf. 200 °C and 300 °C models by Klein and Garrido, 2011). [4]

The increasing incorporation of total iron into antigorite (Fig. 4.8, Appendix Table A-4.2) due to magnetite breakdown and the limited partitioning of iron into talc (Fig. 4.11a) may account for the recrystallization and growth of coarse, green pleochroic, Fe-rich antigorite in Advocate Atg-Tlc-Mgs rocks (Fig. 4.6a & b, and Appendix Table A-4.2). The unusual habit and pleochroism of this antigorite may be due to ferric iron, as serpentine

[4] *Note added by the authors after publication:* Because the solubility of oxygen in fluids is very low, reactions (4.8) and (4.9) can only proceed if coupled oxidation reactions take place. The breakdown of Ni-Fe sulfides to pyrite and the formation of minor hematite and goethite (Fig. 4.5 b – d) can accommodate part of this oxidation potential, but the amount of sulfides is likely not sufficient to explain the sharp decrease of the whole rock Fe^{3+}/Fe_{total} ratio from brucite-bearing Atg-serpentinite to magnesite-bearing assemblages (Fig. 4.7e). On the other hand, H_2, CH_4 and, potentially, graphite produced by serpentinization of relic olivine in the partially serpentinized protolith (cf. e.g. Vitale-Brovarone et al., 2017) during the incipient carbonation reaction step, or reduced aqueous components in the externally derived fluids may have acted as a redox couple and facilitated the reduction of Fe^{3+} of magnetite to Fe^{2+} in magnesite (reaction 4.8).

minerals can incorporate significant amounts of Fe^{3+} (Debret et al., 2015; Klein et al., 2017; Streit et al., 2012). The high Si-content of antigorite in Advocate serpentinite and Atg-Tlc-Mgs rocks (close to 2.07 a.p.f.u. Si+(Al,Cr)/2, corresponding to an apparent polysome m = 13; see Fig. 4.8 and Appendix Table A-4.2) indicates that ferric iron was not accommodated as an Fe^{3+}-tschermak component, but most likely by a vacancy-coupled substitution of $(Mg^{2+})_3$ by $\square(Fe^{3+})_2$ in the antigorite octahedral sites (Evans, 2008; Streit et al., 2012). The incorporation of ferric iron into antigorite would lead to more gradual iron reduction and fluid oxygen fugacity (fO_2) changes than those produced by the single operation of reaction (4.9). Magnesite overgrowths with a very high siderite component (Mgs^{III} in Fig. 4.6b & f and Appendix Table A-4.3) — as recorded also in zoned magnesite in Qtz-Tlc-Mgs rock and listvenite (Fig. 4.9) — demarcate the eventual carbonation of recrystallized Fe-rich antigorite and breakdown of remaining magnetite by reactions (4.7a & b) and (4.8).

As predicted by phase relations, magnetite breakdown at the onset of talc formation by reactions (4.8) and (4.9) increases the local fluid fO_2 to near the hematite-magnetite (HM) redox buffer (Frost, 1985; Klein and Garrido, 2011). In Advocate Atg-Tlc-Mgs and Qtz-Tlc-Mgs rocks, the elevated fluid fO_2 is recorded in Fe-Ni-O-S phase assemblages and accounts for the replacement of pentlandite by Ni-oxide or hydroxide (Fig. 4.5b & c), and the growth of goethite and pyrite with magnesite inclusions (Table 4.1 & 4.A4; Fig. 4.5d).

4.7.3.5 Formation of listvenite

The segregation of quartz into veins at different scales and the precipitation of magnesite at rims over pre-existing grains (Fig. 4.6d & e) suggest that the replacement of talc by magnesite and quartz in the Advocate listvenite occurred by dissolution-precipitation in a fluid-rich environment. Once antigorite is consumed by reactions (4.7a & b), and upon further fluxing of CO_2-rich fluids, talc reacts with $CO_{2,aq}$ to produce magnesite (Mgs^{IV}), H_2O and $SiO_{2,aq}$ following the reaction:

$$Mg_3Si_4O_{10}(OH)_2 + 3\ CO_{2,aq} = 3\ MgCO_3 + 4\ SiO_{2,aq} + H_2O \qquad (4.10)$$

Talc *Magnesite*

This reaction increases the $aSiO_{2,aq}$ of the fluids and quartz becomes oversaturated and precipitates (Q-sat in Fig. 4.10). In Advocate Qtz-Tlc-Mgs rocks, the growth of magnesite rims in textural equilibrium with talc and quartz (Fig. 4.6f) records the onset of talc carbonation by reaction (4.10). This new generation of magnesite has distinctly higher Ni and lower Fe-contents than previously formed magnesite generations (Fig. 4.9; Fig. 4.10a). The

breakdown of Ni-bearing talc (reaction 4.10) causes the incorporation of Ni into magnesite and the formation of minor reevesite ($Ni_6Fe^{3+}_2(OH)_{16}(CO_3) \cdot 4H_2O$) (Fig. 4.5f; Appendix Table A-4.4). Apart from relict magnetite inclusions in cores of coarse magnesite grains —corresponding to relict Mgs^I— and relict Cr-spinel cores, no phases from Lz- and Atg-serpentinites are preserved in Advocate listvenites. The composition of the different growth zones of magnesite and inclusions within them — such as magnetite and talc (e.g. Fig. 4.6e, f & h) — record the progressive carbonation of Atg-Tlc-Mgs and Qtz-Tlc-Mgs rocks according to reactions (4.5) through (4.10). In the Advocate complex, there is no textural and compositional evidence of listvenite being produced directly from serpentinite by dissolution of antigorite and olivine and precipitation of magnesite and quartz. This indicates that infiltrating fluids followed a progressive reaction path as that predicted by modelling, where listvenite formed after fluid buffering at pseudo-invariant point i2 and further fluid infiltration up to quartz saturation (Fig. 4.10). The formation of Si-depleted listvenite (Table 4.1, Fig. 4.5f) —that is almost devoid of quartz but otherwise bears all the characteristics of listvenites— records continued fluid infiltration and quartz dissolution at

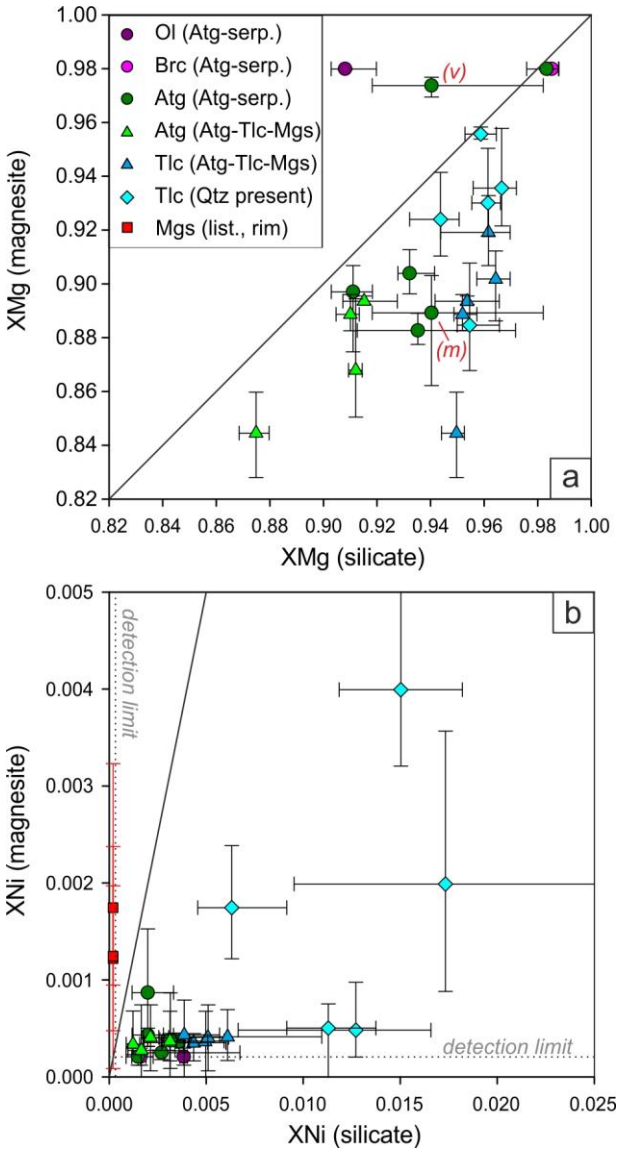

Figure 4.11. ***(a)*** *Mg and* ***(b)*** *Ni partitioning between olivine, brucite, antigorite, talc, and the coexisting magnesite generation in the different rock types (X_{Mg} and X_{Ni} are molar Mg/(Mg+Fe+Ni+Mn) and Ni/(Mg+Fe+Ni+Mn) ratios). Average values of grains in textural equilibrium are plotted, with the measured natural variability shown by the error bars; solid lines mark 1:1 partitioning. Red labels in a) denote compositions of mesh-centre pseudomorphic magnesite (m) and vein-like magnesite (v) and the composition of coexisting antigorite in the same Atg-serpentinite sample. Rim compositions of magnesite in listvenite in b) plotted for comparison only.*

elevated temperatures (T ≥ 200 °C), as predicted by Klein and Garrido (2011). Mobilized aqueous silica from these rocks gave rise to the formation of pervasive quartz and quartz-magnesite veins in listvenite (e.g. Fig. 4.2h; Fig. 4.3a – d).

Anastomosing fuchsite veinlets and dispersed grains associated with quartz and altered relict Cr-spinel (Fig. 4.5e & f; Fig. 4.6g & h) show that the fluid involved in reaction (4.10) was K-rich. However, little is known about the stability of fuchsite. Therefore, it is not clear whether the infiltrating fluids were K-rich throughout most of the carbonation reaction path — but formed fuchsite only where alteration of Cr-spinel locally released sufficient Cr and Al into fluids —, or exclusively during late stages of infiltration.

As in Atg-Tlc-Mgs rocks, a high fluid fO_2 is evident in Qtz-Tlc-Mgs rocks and listvenites. Magnetite rims around Cr-spinel are replaced by porous ferrit-chromite — with high Fe^{3+}/Fe^{2+} ratios (Fig. 4.5d, e & f; Appendix Table A-4.4) —, and goethite rims on pyrite are abundant (Fig. 4.5d & e). The latter indicate either dissolution of pyrite and re-deposition of iron into goethite due to decreasing total sulphur activities in the fluid (lower log ∑S in Fig. 9 of Frost (1985)), or oxidation of pyrite to sulphate in the fluids at fO_2 > HM.

4.7.4 Pressure-temperature conditions of carbonation

In order to constrain the P-T conditions of the discussed phase assemblages and compositions without neglecting the effect of iron in solid solutions, we calculated T-X_{CO2} pseudosections for an Atg-serpentinite whole rock composition (Fig. 4.12 a & b; see section *4.5.2* for calculation details). Because of the drastic change in bulk rock Fe^{3+}/Fe_{total} ratios from brucite-bearing Atg-serpentinites to more carbonated lithologies, two T-X_{CO2} diagrams with different Fe_2O_3 and FeO contents are shown (Fig. 4.12a & b), as otherwise phase relations and compositions are not well represented. As discussed previously, the replacement of lizardite by magnesite in brucite-bearing Atg-serpentinite occurred simultaneously with the prograde transformation of lizardite/chrysotile to antigorite-brucite (reaction 4.3), placing a minimum temperature of c. 300 °C for serpentinite carbonation in the Advocate complex (green fields in Fig. 4.12a & b).

The rare occurrence (Bédard and Escayola, 2010; Kidd, 1974) or absence of metamorphic olivine in Advocate serpentinite, along with the prevalence of goethite/hematite and lack of Tlc-Mgs-Do-Mag assemblages, further places an upper bound of 420 °C (at 0.3 GPa; Fig. 4.12a & b) to the temperature of carbonation. Based on chlorite thermometry, Escayola et al. (2009) estimated that listvenite and birbirite —Mg-depleted, qtz-rich

listvenite— in the Point Rousse complex formed at temperatures of c. 200 °C. Preferential dissolution of magnesite is favoured at this temperature (Klein and Garrido, 2011), what would explain the formation of birbirite in the Point Rousse complex. The absence of birbirite in the Advocate complex is, on the other hand, in agreement with a relatively higher temperature of carbonation and the preferential dissolution of quartz (Klein and Garrido, 2011), producing Si-depleted listvenite (Table 4.1). The widespread occurrence of brucite veins in Atg-serpentinite equally precludes pervasive infiltration of CO_2-rich fluids at low temperature in the Advocate complex.

The mineral assemblages —and their compositions— produced by carbonation of serpentinite are not greatly pressure dependent (Johannes, 1969). Therefore, the pressure of carbonation of Advocate serpentinite is unconstrained. For greenschist facies, regional metamorphism with a geothermal gradient of 30 – 40 °C / km, temperatures of c. 300 °C would be attained at a lithostatic pressure of 0.2 – 0.3 GPa, corresponding to depths of 8 – 10

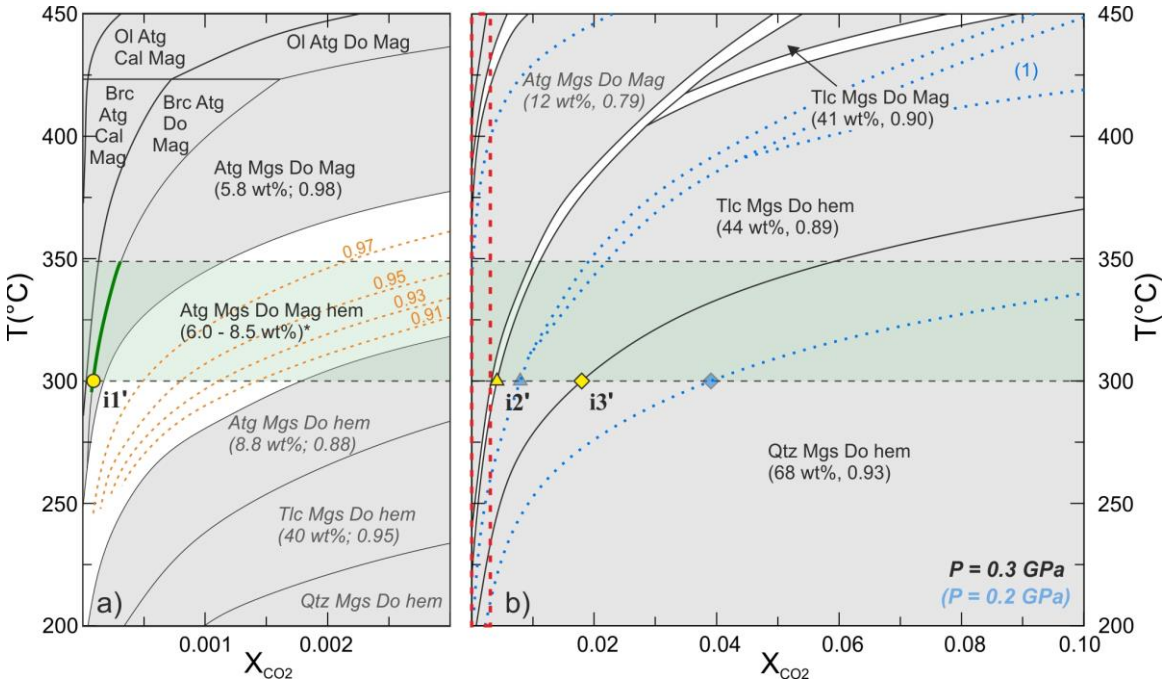

Figure 4.12. *Isobaric, fluid saturated T-X_{CO2} pseudosections in the CFMSHO-C system for an Atg-serpentinite whole rock composition (sample Adv-39; Table 4.2), with predicted average mode and X_{Mg} composition of magnesite for selected fields shown in brackets.* ***(a)*** *Detail at low molar X_{CO2} fractions in the fluid, calculated with the measured $Fe^{3+}/(Fe_{total})$ = 0.71 in Atg-serpentinite (red dashed inset in b), and* ***(b)*** *for a wider X_{CO2} range, calculated with $Fe^{3+}/(Fe_{total})$ = 0.23 of carbonated serpentinite (see Table 4.2). The blue dotted lines are phase boundaries at 0.2 GPa (field (1) has the assemblage Tlc-Mgs-Do-Mag). The temperature range of lizardite to antigorite transformation at 0.3 GPa (after Evans, 2004) is marked by the green field in a) and b). For fields with italic labels of the mineral paragenesis (and *), calculations in the other diagram (a or b, respectively), with a different bulk rock Fe oxidation state, are more appropriate.*

km. At these P-T conditions, Advocate listvenite may have formed by fluxing of serpentinite with fluids with an initial X_{CO2} greater than 0.02 – 0.04 (Fig. 4.12b). Although magnesite rims produced by different carbonation steps (reactions 4.7 and 4.10) could have formed at different temperatures, the similar $\delta^{18}O$ of magnesite in all studied carbonate-bearing lithologies, and carbonate veins (Fig. 4.13) points to quasi-isothermal and isobaric carbonation. Depending on the effective fluid-rock ratio in the differently infiltrated domains, the local fluid X_{CO2} at 300 °C and 0.3 GPa would be buffered by the mineral assemblages to 0.0001 (brucite present, point i1' in Fig. 4.12a), 0.004 (antigorite-talc, point i2' in Fig. 4.12b) and 0.02 (talc-quartz, point i3' in Fig. 4.12b).

The mineral proportions and X_{Mg} of magnesite calculated in the thermodynamic model (Fig. 4.12a & b) are in rather good agreement with the measured mode and composition of magnesite in the variably carbonated rocks (Fig. 4.7d and Fig. 4.11), even though the model cannot account for magnesite zonation and Fe^{3+} in antigorite. In particular, a substantial decrease of magnesite X_{Mg} in parallel with magnetite breakdown to hematite is predicted for the divariant field Atg-Mgs-Dol-Mag-hem (cf. orange isopleths in Fig. 4.12a). This is in accordance with textural observations (Fig. 4.6c), the decrease in the abundance of magnetite, and the formation of Fe-rich magnesite rims (Mgs^{II} and Mgs^{III} in Fig. 4.6b & f and Appendix Table A-4.3) in carbonated serpentinite containing > 3 wt% CO_2 (Fig. 4.7d). Hence, the reduction of ferric iron in magnetite to ferrous iron in magnesite (reaction 4.8) does not require a specific initial fO_2 for the infiltrating fluid, but is inherent to the carbonation of serpentinite. Because the abundance of hematite/goethite (mostly < 2 wt%) is significantly lower than that predicted by the calculation (4.7 wt% in the field Atg-Mgs-Dol-hem in Fig. 4.12a), likely a significant amount of oxygen was released during this carbonation stage, as also indicated by the decrease in bulk rock Fe^{3+}/Fe_{total} (Fig. 4.7e). This process would produce fluids with high fO_2, favouring the oxidation of sulphides and organic carbon.

As shown previously, the preservation of olivine in Advocate serpentinite may indicate serpentinization at relatively high temperatures, similar to those of carbonation. However, the redox conditions during serpentinization (fO_2 ~ FMQ–4) and carbonation (fO_2 > HM) are radically different (Frost, 1985), making synchronous serpentinization and carbonation rather unlikely (Klein and McCollom, 2013). Moreover, microstructures clearly show that carbonation and the breakdown of lizardite to brucite-antigorite postdate the serpentinization of olivine and pyroxene to lizardite/chrysotile, implying that carbonation occurred during a metamorphic overprint as opposed to retrograde alteration.

4.7.5 Stable isotope constraints on the provenance of CO_2-rich fluids and carbonation conditions

Carbon and oxygen stable isotopes in carbonates provide important constraints on the temperature and the nature and source of the fluid involved in the carbonation of peridotite (García del Real et al., 2016; Hoefs, 2009; Schwarzenbach et al., 2016). Besides being controlled by the fluid isotope composition, there is a strong temperature dependence of oxygen isotope fractionation between fluids and carbonates, in contrast to a minor to negligible temperature dependence of carbon isotope fractionation between dissolved carbon and solid carbonate. (Aharon, 1988; Alt et al., 2007; García del Real et al., 2016; Hoefs, 2009). Potential sources of fluids for carbonation of serpentinite are seawater, primary magmatic fluids, meteoric water, and diagenetic or metamorphic fluids from devolatilization of carbonate or organic carbon-rich rocks, or a combination of these sources. Below we discuss possible fluid sources, comparing the Advocate magnesite stable carbon and oxygen isotope composition with that of carbonated serpentinites elsewhere.

Ordovician ophicalcite in Appalachians ophiolites in Quebec —that, like the Advocate ophiolite, are now exposed along the Baie-Verte-Brompton line— has a seawater $\delta^{13}C$ signature, demonstrating that some mantle rocks of these ophiolites were exposed to seafloor alteration and carbonate precipitation from seawater (Fig. 4.13; Chi and Lavoie, 2000). The negative $\delta^{13}C$ of Advocate magnesite (Fig. 4.13), however, excludes carbonation of serpentinite from seawater. Mantle-derived carbon represents a potential source of ^{13}C-depleted dissolved carbon (Deines, 2002; Hoefs, 2009), as proposed for magnesite in Tlc-carbonate rocks of the Caledonian Leka ophiolite (Bjerga et al., 2015) and for serpentinite-hosted magnesite veins in the Arabian-Nubian shield (Boskabadi et al., 2017), which have stable isotope compositions similar to those of magnesite in the Advocate complex (Fig. 4.13). Such CO_2-bearing fluids may derive from juvenile fluids of magmatic intrusions or fluid inclusions in mantle olivine. Furthermore, oceanic serpentinites can contain up to 0.8 wt% total organic carbon (TOC) with $\delta^{13}C_{TOC}$ of –28 to –10 ‰ (Alt et al., 2013; Alt et al., 2007; Delacour et al., 2008; Schwarzenbach et al., 2013). Considering the high fluid fO_2 attained during carbonation, oxidation of organic carbon may have contributed to the low $\delta^{13}C$ of magnesite. However, the large mass of carbon involved in the formation of the Advocate listvenites (up to 13 wt.% C) with a pervasive ^{13}C-depleted composition of magnesite makes it very unlikely that carbon derived from fluid inclusions or organic carbon

in serpentinite alone may have controlled the isotopic signature of CO_2-rich fluids that formed magnesite.

Carbon-bearing meteoric waters are commonly depleted in ^{13}C and ^{18}O (Hoefs, 2009). For meteoric waters with a fluid $\delta^{18}O$ of ≤ -5 ‰, the $\delta^{18}O$ of Adovcate magnesite (Table 4.3) could only be attained if carbonate precipitation had occurred at temperatures below 100 °C (calculated using the oxygen isotope exchange coefficients for water-magnesite after Aharon (1988)), in disagreement with the temperature constrained from textural, compositional and

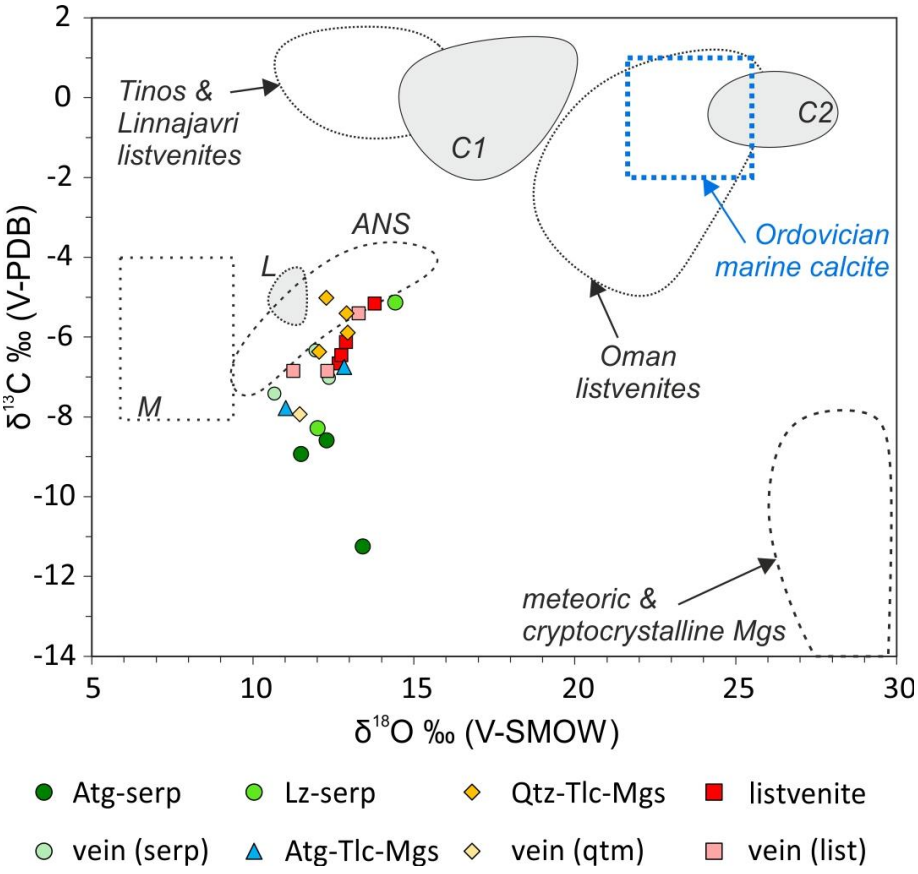

Figure 4.13. *Stable isotope composition of matrix and vein magnesite in carbonate-bearing lithologies in the Advocate complex (cf. Table 4.3), in comparison to other carbonated ultramafic rocks (fields). C1 and C2 are seawater-derived ophicalcites formed at high (100 - 150 °C) and low T in ophiolites along the Baie-Verte-Brompton Line, Quebec Appalachians (Chi and Lavoie, 2000). Fields for selected carbonated peridotites: Tinos listvenites, Greece (Hinsken et al., 2017); Linnajavri listvenites, Norwegian Caledonides (Beinlich et al., 2012); Oman listvenites, Samail ophiolite (Falk and Kelemen, 2015); L = Tlc-Mgs rocks from Leka, Norwegian Caledonides (Bjerga et al., 2015); ANS = carbonate veins in serpentinite of the Arabian-Nubian Shield (Boskabadi et al., 2017). The field for meteoric & cryptocrystalline magnesite is from Quesnel et al. (2016) and compilation by García del Real et al. (2016). M = mantle carbonatites (Deines, 2002); Ordovician marine calcite from Qing and Veizer (1994).*

phase relations. Furthermore, cryptocrystalline and meteoric magnesite commonly has much higher $\delta^{18}O$ and substantially lower $\delta^{13}C$ values (García del Real et al., 2016; Quesnel et al., 2016; Schwarzenbach et al., 2016) (Fig. 4.13). However, because of the large variability of $\delta^{18}O$ in meteoric waters, we cannot exclude a contribution from dissolved carbon with ^{13}C-depleted composition in groundwater mixed with high temperature hydrothermal fluids.

Because the negative $\delta^{13}C$ of magnesite in the Advocate carbonate-bearing rocks does not point to a specific fluid source, the $\delta^{18}O$ of the external CO_2-rich fluids ($\delta^{18}O_{fluid}$) is unknown and the temperature of carbonation cannot be estimated from the $\delta^{18}O$ of magnesite ($\delta^{18}O_{Mgs}$). On the other hand, at 300 °C —as deduced from phase relations— the calculated $\delta^{18}O_{fluid}$ in equilibrium with magnesite is +3.8 to +7.0 ‰ (V-SMOW; for $\delta^{18}O_{Mgs}$ of Advocate magnesite in the range 11.0 – 14.4 ‰; Table 4.3 and Fig. 4.13; oxygen isotope exchange coefficients for water-magnesite after Aharon (1988)). This $\delta^{18}O_{fluid}$ is within the range of diagenetic (connate) pore fluids and fluids produced by metamorphic devolatilization reactions (Hoefs, 2009). The negative $\delta^{13}C$ values of magnesite in Advocate carbonate-bearing rocks may therefore have derived from a mixture of fluids generated by devolatilization or compaction of sediments containing organic and inorganic carbon. Equilibration of fluids with graphite can produce ^{13}C-depleted dissolved carbon (e.g. $\delta^{13}C_{fluid}$ ~ –10 to –20 ‰ in equilibrium with graphite $\delta^{13}C$ ~ –18 to –28 ‰ at 500 °C; Irwin et al. (1977); equilibrium fractionation factors after Scheele and Hoefs (1992)). Mixing of 40 – 80 % of such fluids with 20 – 60 % of fluids produced by dissolution or decarbonation of sedimentary marine carbonate ($\delta^{13}C_{fluid}$ ~ +3 to +5 ‰ for marine calcite $\delta^{13}C$ ~ –1 to +2 ‰ at 500 °C; Qing and Veizer (1994); equilibrium fractionation factors after Scheele and Hoefs (1992)) may account for the negative $\delta^{13}C$ composition of Advocate magnesite.

4.7.6 Geodynamic setting of listvenite formation in the Advocate complex

The highly refractory nature of the Advocate complex harzburgite (Bédard and Escayola, 2010) and the presence of boninites in correlative ophiolites (e.g., Betts Cove ophiolite; Bédard (2000)) suggest their formation in a hot supra-subduction setting during forearc spreading (Bédard et al., 1998; Castonguay et al., 2014). Serpentinization of the Advocate complex harzburgite may have occurred during oceanic spreading due to seawater hydrothermal alteration (e.g. Bach et al., 2004; Cannat et al., 2010; Klein et al., 2017), or in a forearc setting due to infiltration by slab dehydration fluids (Fig. 4.14) (e.g. Kahl et al., 2015; Mottl et al., 2004). Most serpentinization likely occurred by high temperature hydrothermal

circulation during oceanic spreading, as pervasive or complete serpentinization in the mantle wedge of hot subduction settings is unlikely (e.g. Hyndman and Peacock, 2003).

Further geochronological, structural and geochemical studies would be necessary to clarify the timing of peridotite carbonation in the Advocate complex, and whether the listvenites are cogenetic with regional gold mineralization (Escayola et al., 2009; Ramezani et al., 2000). Below, we speculate about potential geodynamic settings for carbonation of Advocate serpentinite that are in accordance with the petrological and geochemical characteristics of the Advocate carbonate-bearing lithologies from the present work.

Mixed, CO_2-rich fluids derived from metasediment devolatilization are consistent with the stable isotope composition of Advocate magnesite, and with whole rock gains in potassium and, likely, sulphur in the listvenite (Fig. 4.7f). Such hydrothermal fluids may have derived from post-peak metamorphic, Silurian granitoid intrusions (Whalen et al., 2006) by mixing of juvenile fluids with fluids produced by contact-metamorphic decarbonation of the ophiolite cover sequence. Mesothermal gold deposits associated with calcite-chlorite alteration of crustal segments of the Baie Verte ophiolites show some evidence for this origin (Ramezani et al., 2000). However, the occurrences of carbonated peridotites throughout the

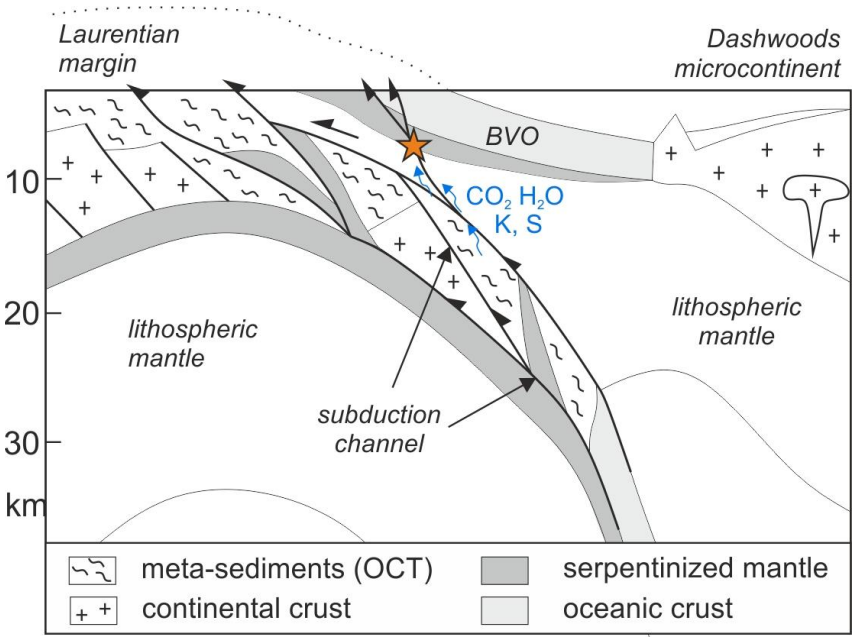

Figure 4.14. *Schematic sketch of a possible geodynamic setting for listvenite formation in the Advocate complex (star) during obduction of the Baie Verte Ophiolite, with fluids deriving from structurally lower sedimentary units of higher metamorphic grade. BVO: Baie Verte Ophiolite supra-subduction zone, forearc spreading oceanic crust. OCT: ocean-continent transition sequences of Laurentian margin. Sketch modified after Castonguay et al. (2014).*

different parts of the Baie Verte ophiolites have no spatial relation with the intrusions, and large-scale contact metamorphism that could produce large quantities of CO_2-rich fluids is not documented.

Alternatively, gains in potassium may imply input from continental crust-derived metasediments with fluids derived by meta-sediment devolatilization during regional metamorphism. Graphitic metapelites and calcareous schists recording eclogite- and amphibolite-facies metamorphism occur in the Birchy complex (Fig. 4.1b), an ocean-continent transition that partly subducted below the mantle rocks of the Advocate complex (Castonguay et al., 2014). This complex contains rare slices of ultramafic rocks altered to talc-carbonate-tremolite schists, fuchsite-actinolite schists and listvenites (van Staal et al., 2013), showing that carbonation of ultramafic rocks by CO_2-rich fluids also occurred in the footwall of the Advocate complex, likely at higher P-T conditions (as indicated by the stability of tremolite/actinolite). The internal structure of the Central Advocate complex shows that the infiltration of CO_2-rich fluids was to some extent controlled by thrust faults and regional metamorphism. The alignment of the Advocate listvenite outcrops, their internal layering, and the weak preferred orientation of magnesite are all parallel to the main regional foliation, which is related to obduction along the Baie Verte line ophiolite (Fig. 4.1b & c).

The above evidence supports that carbonation of serpentinized harzburgite in the Advocate complex occurred by CO_2-rich fluids derived from the dehydration and decarbonation of subducting metasediments now exposed in the Birchy complex (Fig. 4.14). Slab-derived, CO_2-rich fluids may have been channelized along thrust faults and reacted with peridotites of the Baie Verte ophiolite during back thrusting and accretion of these forearc ophiolites onto the Laurentian continental margin (Fig. 4.14). Strain partitioning into overpressured fluid and talc-rich domains of carbonated serpentinites might have facilitated thrust movement and obduction. This could explain the predominant planar fabric of Qtz-Tlc-Mgs rocks (Fig. 4.2g and 3b) and listvenites while preserving the euhedral, progressive growth zonation of magnesite without major recrystallization of carbonate. Listvenites in the nearby Point Rousse complex also occur along a thrust fault, and show deformation structures, folding and brittle veins (Escayola et al., 2009; Kidd et al., 1978), suggesting that carbonation of ultramafic rocks in much of the Baie Verte ophiolites was contemporaneous with long-lasting thrust faults associated with the Early to Middle Ordovician (481 – 456 Ma; Castonguay et al., 2014) collision between Laurentia and the Notre Dame arc and Dashwoods microcontinent during closure of the Taconic seaway.

Forearcs appear to be a very favourable setting for carbonation of the upper plate serpentinized mantle lithosphere, making them a significant carbon reservoir within the deep carbon cycle (Kelemen and Manning, 2015). A correlation between listvenite formation and thrust faults such as in the Baie Verte ophiolites is also evident in listvenites of the Atlin ophiolite complex (Canada) (Ash and Arksey, 1989; Hansen et al., 2005), and in ubiquitous listvenites along the basal thrust of the Samail ophiolite mantle (Oman) (Falk and Kelemen, 2015; Kelemen et al., 2017; Streit et al., 2012). Carbonation in the latter case occurred at several stages during obduction of the leading mantle wedge — temperatures range from 80 – 130 °C for most listvenites, to 300 °C in Talc-Mgs-rocks at Wadi Abyad (Falk and Kelemen, 2015) —, indicating that extensive carbonation may be common during thrust faulting.

4.8 Appendices

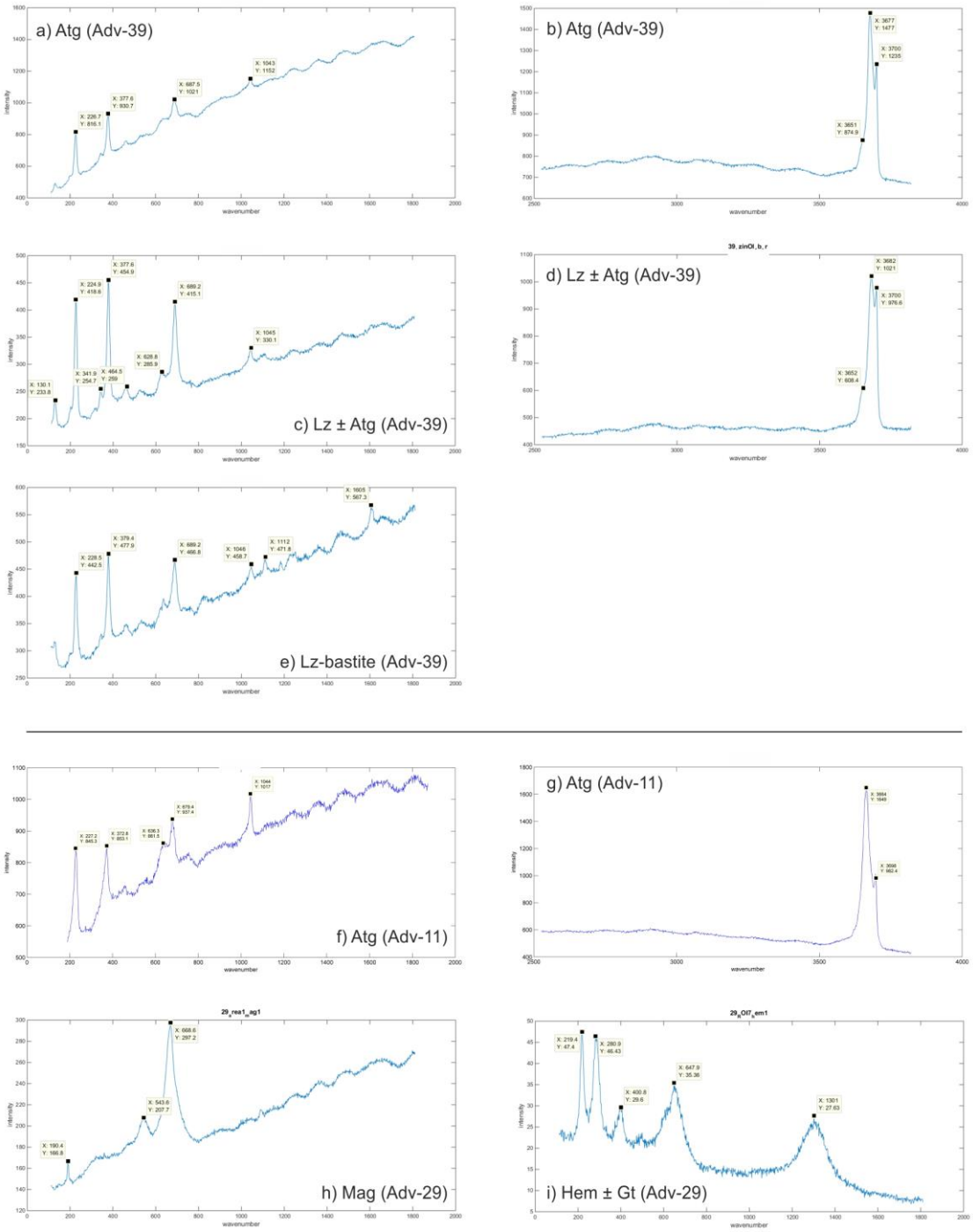

Figure A-4.1. *Selected Raman spectra of serpentine minerals in Atg-serpentinite* ***(a – e)*** *and Atg-Tlc-Mgs rocks* ***(f – g)****, and of magnetite and hematite in Qtz-Tlc-Mgs rock* ***(h – i)*** *to support phase identification in addition to petrographic, chemical and/or EBSD methods. The spectra are not processed, i.e. no background subtraction or smoothing was applied.*

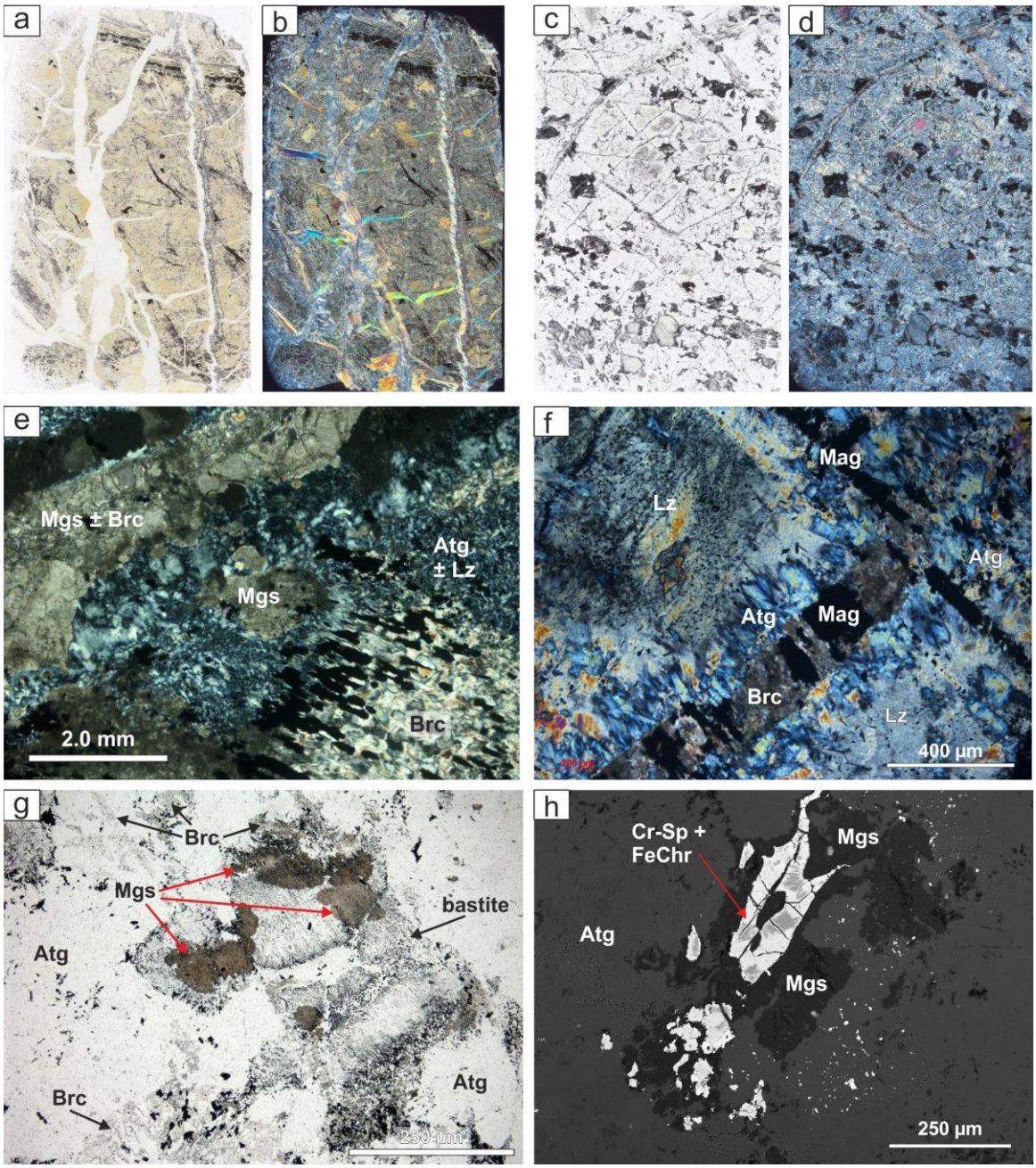

Figure A-4.2. *Thin section scans of Lz-serpentinite (**a & b**; Adv-32) and brucite-bearing Atg-serpentinite (**c & d**; Adv-39) and additional petrography and textures of Advocate serpentinites.* ***(a)*** *Plain polarized (ppl) thin section scan of Lz-serpentinite with Atg- and Ctl veins;* ***(b)*** *Crossed polarized (xpl) image of a);* ***(c)*** *Plain polarized thin section scan of Ol- and Brc- bearing Atg-serpentinite with bastite-rich layer in lower part;* ***(d)*** *Crossed polarized image of c);* ***(e)*** *Magnesite replacing brucite vein in Atg-serpentinite (xpl; Adv-39);* ***(f)*** *Brucite-magnetite vein with antigorite seam crosscutting a lizardite domain (xpl; Adv-39);* ***(g)*** *Lizardite bastite with fine magnetite tracing former cleavage, being replaced by magnesite while brucite veins and dispersed brucite in the antigorite matrix are not carbonated (ppl; Adv-39);* ***(h)*** *Magnesite occurring preferentially at rims of Cr-spinel (BSE image; Adv-10).*

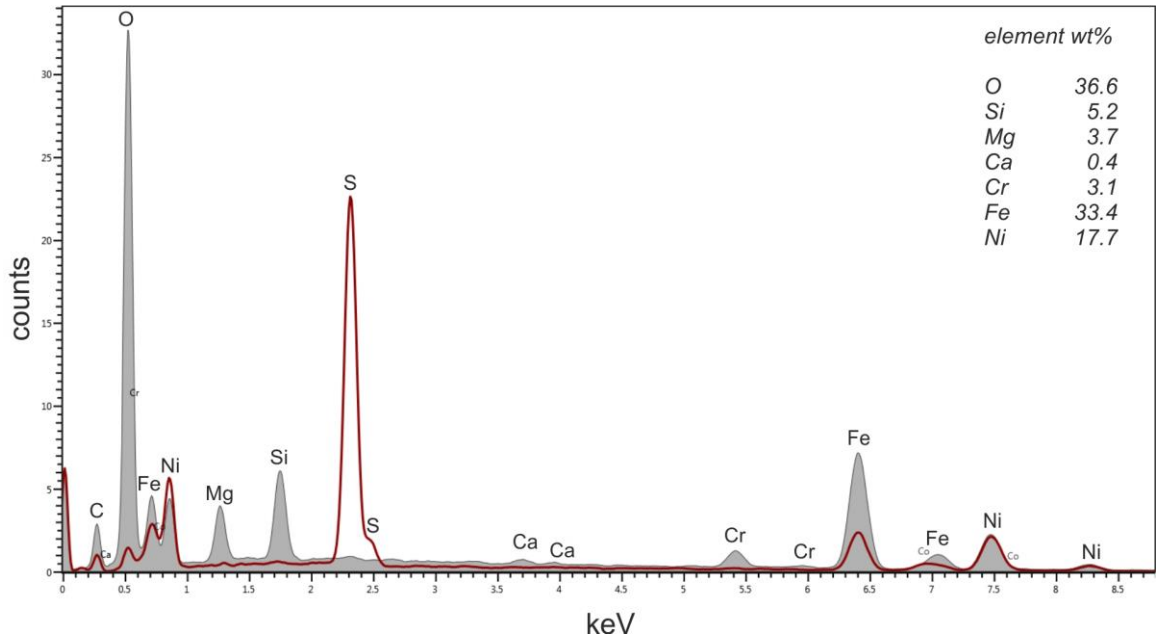

Figure A-4.3. *EDS spectra of pentlandite (red line) and Fe-Ni-Si oxide or FNS-aggregate rim (grey spectrum) replacing pentlandite in Atg-Tlc-Mgs rock (cf. Fig. 4.5c; sample Adv-42). Semi-quantitative element weight-proportions of the FNS phase are shown (normalized to 100%).*

Table A-4.1 *List of rock samples of carbonated peridotites in the Central Advocate Complex, Baie Verte Ophiolite (Newfoundland)*

Sample	Field-based lithology	Latitude (N)*	Longitude (W)	Elevation (m)	TS	Bulk	EMPA	EBSD
Adv 01	transition talc-carbonate to listvenite	49.804734	-56.319084	162	x	x	x	
Adv 02	listvenite, unspecified	49.804734	-56.319084	162	x	x	x	x
Adv 03	talc-carbonate gneiss	49.804742	-56.319085	162	x	x		
Adv 04	transition talc-carbonate to listvenite	49.804742	-56.319085	162	x			
Adv 05	transition talc-carbonate to listvenite	49.804742	-56.319085	162	x		x	
Adv 06	listvenite, unspecified	49.804742	-56.319085	162	x			
Adv 07	listvenite, fuchsite-rich	49.804709	-56.319150	164	x	x		x
Adv 08	listvenite, fuchsite-absent	49.804709	-56.319264	163	x			x
Adv 09	listvenite, fuchsite-rich	49.804756	-56.319215	164	x	x	x	
Adv 10	harzburgite tectonite	49.804996	-56.319267	167	x	x	x	
Adv 11	transition ultramafic to talc-carbonate	49.804968	-56.319959	176	x	x	x	
Adv 12	harzburgite tectonite	49.804968	-56.319959	176	x	x		
Adv 13	listvenite, fuchsite-rich	49.804241	-56.319195	157	x			x
Adv 14	transition talc-carbonate to listvenite	49.804319	-56.319133	156	x	x		
Adv 15	serpentinite schist	49.802518	-56.320323	157	x	x	x	
Adv 16	harzburgite tectonite	49.795536	-56.319448	194	x	x		
Adv 17	carbonate vein	49.795536	-56.319448	194	x	x	x	

Table A-4.1 *List of rock samples of carbonated peridotites in the Central Advocate Complex, Baie Verte Ophiolite (Newfoundland)*

Adv 18	carbonate vein	49.795516	-56.319490	194	x			x
Adv 19	harzburgite tectonite	49.795610	-56.319493	194	x	x	x	
Adv 20	transition ultramafic to talc-carbonate	49.795610	-56.319493	194	x	x	x	
Adv 21	talc-carbonate gneiss	49.795610	-56.319493	194	x	x	x	
Adv 22	transition talc-carbonate to listvenite	49.795351	-56.319192	194	x	x	x	
Adv 23	transition talc-carbonate to listvenite	49.795351	-56.319192	194	x	x		x
Adv 24	transition talc-carbonate to listvenite	49.795351	-56.319192	194	x			
Adv 25	listvenite, unspecified	49.795351	-56.319192	194	x	x		x
Adv 26	listvenite, fuchsite-rich	49.795351	-56.319192	194	x			
Adv 27	listvenite, fuchsite-rich	49.795351	-56.319192	194	x	x	x	x
Adv 28	transition talc-carbonate to listvenite	49.795852	-56.318996	183	x	x	x	x
Adv 29	transition talc-carbonate to listvenite	49.795809	-56.319033	183	x	x	x	x
Adv 30	listvenite, unspecified	49.795811	-56.319044	189	x	x	x	
Adv 31	harzburgite tectonite	49.796329	-56.319619	186	x	x		
Adv 32	serpentinite schist	49.798870	-56.319931	152	x	x	x	
Adv 33	massive serpentinite	49.796945	-56.318961	160	x	x	x	
Adv 34	listvenite, fuchsite-rich	49.797727	-56.319314	159	x	x		
Adv 35	talc-carbonate gneiss	49.799043	-56.320766	150	x	x	x	x
Adv 36	harzburgite tectonite	49.799199	-56.321201	158	x	x	x	
Adv 37	carbonated serpentinite	49.799056	-56.320969	150				
Adv 38	carbonated serpentinite	49.799056	-56.320969	150	x	x	x	
Adv 39	massive serpentinite	49.802382	-56.320152	155	x	x	x	x
Adv 40	transition talc-carbonate to listvenite	49.804897	-56.319232	165	x		x	x
Adv 41	talc-carbonate rock	49.804774	-56.318839	158	x	x	x	
Adv 42	carbonated serpentinite	49.805784	-56.318862	170	x	x	x	
Adv 43	carbonated serpentinite	49.805649	-56.318348	158	x	x	x	

** Latitude/Longitude in WGS84 Datum; TS = thin section.*

Table A-4.2a *Representative electron microprobe analysis of silicate minerals in Advocate serpentinites and carbonate-bearing lithologies. Analytical settings: see Ch.3.3 and Table 3.2.*

Lithology	Atg-srp*	Atg-srp*	Atg-srp*	Atg-srp*	Atg-srp*	Atg-srp	Atg-srp	Lz-srp	Lz-srp	Lz-srp	atm	atm
Sample	*Adv-39*	*Adv-15*	*Adv-15*	*Adv-39*	*Adv-39*	*Adv-19*	*Adv-36*	*Adv-33*	*Adv-33*	*Adv-33*	*Adv-11*	*Adv-35*
Mineral	Ol	Amph	Brc	Lz	Atg	Atg	Atg	Lz	Lz	Atg	Atg	Atg
Comment		*in Cr-Sp*	*Vein*	*Bastite*	*Matrix*	*Matrix*		*Bastite*	*Mesh*	*Vein*	*Coarse*	*Coarse*
SiO_2	40.68	50.94	0.17	41.70	44.63	44.55	43.45	40.93	41.78	44.78	43.02	43.10
TiO_2	b.d.	0.07	b.d.	b.d.	b.d.	b.d.	b.d.	b.d.	b.d.	b.d.	b.d.	b.d.
Al_2O_3	b.d.	5.91	b.d.	1.96	0.41	0.23	0.39	2.90	0.50	0.54	1.02	0.79
Cr_2O_3	b.d.	3.62	b.d.	0.76	0.22	0.04	0.17	0.95	0.80	0.24	0.60	0.06
FeO	8.49	2.35	2.05	1.65	1.47	4.38	6.10	3.59	3.57	1.65	6.14	9.17
NiO	0.40	0.12	0.20	0.09	0.10	0.16	0.20	0.14	0.17	0.11	0.23	0.19
MnO	0.13	0.07	0.26	0.03	0.04	0.03	0.04	0.02	0.03	0.04	b.d.	b.d.
MgO	50.35	21.35	67.70	40.18	41.18	38.54	37.08	38.85	40.22	40.27	36.51	34.68
CaO	0.02	10.38	b.d.	b.d.	b.d.	b.d.	0.02	b.d.	b.d.	0.01	b.d.	b.d.
Na_2O	b.d.	3.26	b.d.	b.d.	b.d.	b.d.	b.d.	b.d.	b.d.	b.d.	b.d.	b.d.
K_2O	b.d.	0.12	b.d.	0.02	b.d.	0.02	0.02	0.01	b.d.	0.01	0.02	b.d.
F	0.09	b.d.	b.d.	b.d.	b.d.	b.d.	b.d.	b.d.	b.d.	b.d.	b.d.	b.d.
Total	100.19	98.27	70.43	86.41	88.07	87.96	87.47	87.43	87.08	87.69	87.59	88.05
H_2O calc.		2.15	30.94	12.78	12.26	12.08	11.89	12.78	12.72	12.21	11.88	11.79
Total calc.	100.19	100.42	101.37	99.19	100.32	100.04	99.35	100.21	99.80	99.89	99.47	99.84
# Ions per O	*4*	*23*	*(*)*	*7*	*116*	*116*	*116*	*7*	*7*	*116*	*116*	*116*
Si	0.992	7.098	0.002	1.957	33.843	34.262	33.965	1.920	1.969	34.097	33.642	33.964
Ti	b.d.	0.007	b.d.	b.d.	b.d.	b.d.	b.d.	b.d.	b.d.	b.d.	b.d.	b.d.
Al	b.d.	0.971	b.d.	0.109	0.367	0.210	0.358	0.161	0.028	0.481	0.941	0.731
Cr	b.d.	0.399	b.d.	0.028	0.129	0.023	0.104	0.035	0.030	0.144	0.371	0.039
Fe^{2+}	0.173	0.274	0.017	0.065	0.931	2.816	3.988	0.141	0.141	1.054	4.018	6.046
Ni	0.008	0.014	0.002	0.003	0.064	0.097	0.125	0.005	0.006	0.069	0.145	0.120
Mn	0.003	0.009	0.002	0.001	0.024	0.018	0.024	0.001	0.001	0.023	b.d.	b.d.
Mg	1.831	4.436	0.978	2.811	46.548	44.188	43.209	2.717	2.826	45.706	42.558	40.743
Ca	0.001	1.549	b.d.	b.d.	b.d.	b.d.	0.020	b.d.	b.d.	0.010	b.d.	b.d.
Na	b.d.	0.882	b.d.	b.d.	b.d.	b.d.	b.d.	b.d.	b.d.	b.d.	b.d.	b.d.
K	b.d.	0.022	b.d.	0.001	b.d.	0.017	0.020	0.001	b.d.	0.012	0.019	b.d.
F	0.007	b.d.	b.d.	b.d.	b.d.	b.d.	b.d.	b.d.	b.d.	b.d.	b.d.	b.d.
OH (ideal)		2.00	2.00	4.00	62.00	62.00	62.00	4.00	4.00	62.00	62.00	62.00
∑ cations	3.01	15.66	1.00	4.98	81.91	81.63	81.81	4.98	5.00	81.60	81.70	81.65
Mg#	0.914	0.942	0.983	0.977	0.980	0.940	0.916	0.951	0.953	0.977	0.914	0.871
Cr#				0.207	0.260	0.098	0.225	0.180	0.518	0.231	0.283	0.050
X_{Mg} [a]	0.909	0.937	0.980	0.976	0.979	0.938	0.913	0.949	0.950	0.976	0.911	0.869
X_{Fe} [a]	0.086	0.058	0.017	0.022	0.020	0.060	0.084	0.049	0.047	0.022	0.086	0.129
X_{Ni} [a]	0.004	0.003	0.002	0.001	0.001	0.002	0.003	0.002	0.002	0.001	0.003	0.003
X_{Mn} [a]	0.001	0.002	0.002	0.000	0.000	0.000	0.001	0.000	0.000	0.000		
Si+(Cr,Al)/2 [b]				2.025	2.057	2.075	2.064	2.018	1.998	2.076	2.070	2.073

Lithology abbreviations: Atg-srp = antigorite-dominated serpentinite (*brucite-bearing; brucite normalized to 1 cation); Lz-srp = lizardite-dominated serpentinite; atm = Atg-Tlc-Mgs rock; qtm = Qtz-Tlc-Mgs rock; list = listvenite.

b.d. = below detection limit; Mg# = Mg/(Mg + Fe); Cr# = Cr/(Cr + Al).

[a] Molar divalent metal fractions calculated as $XM^{2+} = M^{2+}/(Mg + Fe + Ni + Mn)$; all Fe is assumed to be ferrous.

[b] Si (apfu) in serpentine normalized to 7 O and including tschermak components Al and Cr on tetrahedral sites, ideal values are: lizardite: 2.0, antigorite with polysome m = 13: 2.07, antigorite with polysome m = 21: 2.04.

Table A-4.2b *Representative electron microprobe analysis of silicate minerals in Advocate serpentinites and carbonate-bearing lithologies. Analytical settings: see Ch.3.3 and Table 3.2.*

Lithology	Atg-serp	atm	qtm	qtm	qtm	atm	qtm	list	list	list	list
Sample	Adv-10	Adv-35	Adv-22	Adv-29	Adv-29	Adv-35	Adv-29	Adv-28	Adv-30	Adv-27	Adv-27
Mineral	Tlc	Tlc	Tlc	Tlc	Tlc	Chl	Chl	Chl	mica	Fuchs	Fuchs
Comment				*Matrix*	*in Mgs*		*Veinlet*				
SiO_2	62.12	62.42	63.36	62.38	62.49	34.32	31.11	29.76	48.89	49.42	47.55
TiO_2	b.d.	b.d.	0.03	b.d.	b.d.	b.d.	b.d.	0.05	b.d.	0.07	0.08
Al_2O_3	0.03	b.d.	0.05	0.07	0.10	11.73	14.77	15.65	31.16	25.89	19.44
Cr_2O_3	b.d.	b.d.	0.07	0.09	b.d.	2.78	5.23	4.51	b.d.	7.54	13.90
FeO	1.97	2.36	1.93	1.59	3.47	5.52	5.98	4.08	0.38	0.44	0.86
NiO	0.31	0.28	0.85	1.45	0.11	0.18	1.53	2.75	0.04	0.04	0.22
MnO	b.d.	b.d.	0.02	b.d.	b.d.	0.02	b.d.	0.02	b.d.	b.d.	0.03
MgO	30.15	29.73	29.78	29.73	29.97	32.74	28.96	28.03	2.28	2.66	3.75
CaO	b.d.	b.d.	0.02	0.01	b.d.	b.d.	0.06	0.03	b.d.	b.d.	b.d.
Na_2O	b.d.	b.d.	b.d.	b.d.	0.03	b.d.	0.03	0.03	0.10	0.14	0.07
K_2O	0.02	0.02	0.02	b.d.	0.03	0.01	b.d.	0.02	10.51	8.87	8.40
F	b.d.	b.d.	b.d.	b.d.	b.d.	b.d.	b.d.	0.17	0.18	b.d.	b.d.
Total	94.66	94.87	96.11	95.34	96.22	87.32	87.67	85.10	93.58	95.13	94.33
H_2O calc.	4.66	4.67	4.73	4.68	4.71	12.53	12.34	11.92	4.37	4.44	4.29
Total calc.	99.33	99.54	100.84	100.03	100.93	99.85	100.00	96.84	97.77	99.51	98.60
# Ions per O	22	22	22	22	22	28	28	28	22	22	22
Si	7.985	8.013	8.027	7.986	7.951	6.569	6.048	5.948	6.580	6.637	6.620
Ti	b.d.	b.d.	0.002	b.d.	b.d.	b.d.	b.d.	0.007	b.d.	0.007	0.008
Al	0.004	b.d.	0.007	0.010	0.015	2.646	3.384	3.686	4.943	4.098	3.190
Cr	b.d.	b.d.	0.007	0.010	b.d.	0.421	0.804	0.713	b.d.	0.801	1.530
Fe^{2+}	0.212	0.254	0.204	0.170	0.369	0.884	0.972	0.682	0.043	0.049	0.100
Ni	0.032	0.029	0.086	0.149	0.011	0.027	0.239	0.442	0.005	0.005	0.025
Mn	b.d.	b.d.	0.002	b.d.	b.d.	0.003	b.d.	0.003	b.d.	b.d.	0.004
Mg	5.777	5.690	5.624	5.674	5.685	9.342	8.393	8.349	0.458	0.533	0.778
Ca	b.d.	b.d.	0.002	0.002	b.d.	b.d.	0.011	0.006	b.d.	b.d.	b.d.
Na	b.d.	b.d.	b.d.	b.d.	0.008	b.d.	0.012	0.011	0.026	0.035	0.020
K	0.003	0.003	0.003	b.d.	0.005	0.003	b.d.	0.005	1.804	1.520	1.492
F	b.d.	b.d.	b.d.	b.d.	b.d.	b.d.	b.d.	0.110	0.076	b.d.	b.d.
OH (ideal)	4.00	4.00	4.00	4.00	4.00	16.00	16.00	15.89	3.92	3.97	3.99
∑ cations	14.01	13.99	13.96	14.01	14.05	19.90	19.86	19.85	13.86	13.68	13.77
Mg#	0.965	0.957	0.965	0.971	0.939	0.914	0.896	0.924	0.914	0.915	0.886
Cr#						0.137	0.192	0.162	0.000	0.163	0.324
X_{Mg} [a]	0.959	0.953	0.951	0.947	0.937	0.911	0.874	0.881	0.906	0.907	0.858
X_{Fe} [a]	0.035	0.042	0.035	0.028	0.061	0.086	0.101	0.072	0.085	0.084	0.110
X_{Ni} [a]	0.005	0.005	0.015	0.025	0.002	0.003	0.025	0.047	0.009	0.008	0.027
X_{Mn} [a]			0.000			0.000		0.000			0.004

Lithology abbreviations: Atg-srp = antigorite-dominated serpentinite (*brucite-bearing; brucite normalized to 1 cation); Lz-srp = lizardite-dominated serpentinite; atm = Atg-Tlc-Mgs rock; qtm = Qtz-Tlc-Mgs rock; list = listvenite.

b.d. = below detection limit; Mg# = Mg/(Mg + Fe); Cr# = Cr/(Cr + Al).

[a] Molar divalent metal fractions calculated as $XM^{2+} = M^{2+}/(Mg + Fe + Ni + Mn)$; all Fe is assumed to be ferrous.

[b] Si (apfu) in serpentine normalized to 7 O and including tschermak components Al and Cr on tetrahedral sites, ideal values are: lizardite: 2.0, antigorite with polysome m = 13: 2.07, antigorite with polysome m = 21: 2.04.

Table A-4.3a *Representative electron microprobe analysis of carbonates in Advocate serpentinites and carbonate-bearing lithologies. Analytical settings: see Ch.3.3 and Table 3.2.*

Lithology	Atg-serp*	Atg-serp*	Atg-serp	Atg-serp	Atg-serp	Atg-serp	Lz-serp	Lz-serp	Lz-serp
Sample	Adv-39	Adv-39	Adv-19	Adv-19	Adv-36	Adv-38	Adv-33	Adv-32	Adv-32
Mineral	Mgs^{I}	Dol	Mgs^{I}	Mgs^{II}	Mgs^{II}	Mgs^{II}	Dol	Mgs^{I}	Mgs^{II}
Comment	*after Lz*	*Brc-vein*	*vein relic*	*after Ol?*	*Cr-Sp rim*	*Lz-vein*		*core*	*rim*
SiO_2	0.34	0.03	b.d.	b.d.	b.d.	0.02	0.07	0.23	0.03
FeO	0.37	0.31	1.32	7.02	7.21	7.23	0.22	2.24	6.03
NiO	b.d.	b.d.	0.04	0.04	b.d.	0.03	0.01	0.07	b.d.
MnO	1.28	0.44	0.70	0.77	0.62	0.52	0.63	0.47	0.66
MgO	44.81	21.61	45.52	41.16	41.23	42.03	21.05	46.11	42.53
CaO	0.12	29.83	0.10	0.08	0.06	0.11	30.32	0.19	0.09
SrO	0.02	0.03	b.d.	b.d.	b.d.	b.d.	0.02	b.d.	b.d.
CO_2	50.54	47.53	51.07	49.81	49.87	50.75	47.42	52.19	50.61
Total	97.48	99.78	98.77	98.88	98.99	100.70	99.75	101.50	99.96
X_{CaCO3}	0.002	0.493	0.002	0.001	0.001	0.002	0.503	0.003	0.001
X_{MgCO3}	0.978	0.497	0.974	0.902	0.903	0.904	0.486	0.965	0.917
X_{FeCO3}	0.004	0.004	0.016	0.086	0.089	0.087	0.003	0.026	0.073
X_{MnCO3}	0.016	0.006	0.009	0.010	0.008	0.006	0.008	0.006	0.008
X_{NiCO3}			0.001	0.001		0.000	0.000	0.001	

Table A-4.3b *Representative electron microprobe analysis of carbonates in Advocate serpentinites and carbonate-bearing lithologies. Analytical settings see Ch.3.3 and Table 3.2.*

Lithology	atm	atm	atm	atm	tm	tm	tm	qtm	qtm
Sample	Adv-42	Adv-42	Adv-11	Adv-35	Adv-21	Adv-21	Adv-21	Adv-22	Adv-22
Mineral	Mgs^{I}	Mgs^{III}	Mgs^{III}	Mgs^{III}	Mgs^{II}	Mgs^{III}	Mgs^{IIIb}	Dol	Dol
Comment	*core*	*rim*			*core*	*rim 1*	*rim 2*		
SiO_2	0.03	b.d.	0.03	0.02	b.d.	b.d.	0.03	0.08	0.08
FeO	2.00	10.06	8.91	12.00	5.55	9.98	7.01	0.49	2.53
NiO	0.02	0.03	0.02	0.06	0.05	0.01	0.03	b.d.	b.d.
MnO	0.85	0.15	0.27	0.29	1.15	0.29	0.38	0.21	0.09
MgO	45.11	39.30	40.54	38.83	42.34	40.09	41.96	20.75	19.55
CaO	0.09	0.17	0.13	0.11	0.31	0.14	0.06	30.90	30.07
SrO	0.03	b.d.	b.d.	0.03	b.d.	b.d.	b.d.	0.04	b.d.
CO_2	51.14	49.32	50.00	50.06	50.62	50.18	50.46	47.47	46.66
Total	99.27	99.03	99.92	101.39	100.03	100.70	99.93	99.94	98.98
X_{CaCO3}	0.001	0.003	0.002	0.002	0.005	0.002	0.001	0.512	0.507
X_{MgCO3}	0.964	0.870	0.885	0.847	0.913	0.872	0.909	0.479	0.459
X_{FeCO3}	0.024	0.125	0.109	0.147	0.067	0.122	0.085	0.006	0.033
X_{MnCO3}	0.010	0.002	0.003	0.004	0.014	0.004	0.005	0.003	0.001
X_{NiCO3}	0.000	0.000	0.000	0.001	0.001	0.000	0.000		

Table A-4.3c *Representative electron microprobe analysis of carbonates in Advocate serpentinites and carbonate-bearing lithologies Analytical settings: see Ch.3.3 and Table 3.2.*

Lithology	qtm	qtm	list	list	list	list	list	list
Sample	Adv-02a	Adv-29	Adv-28	Adv-28	Adv-28	Adv-28	Adv-28	Adv-30b
Mineral	Mgs^{IV}	Mgs^{IV}	Mgs^{I}	Mgs^{II}	Mgs^{III}	Mgs^{IV}	Mgs^{V}	Mgs^{V}
Comment	*outer rim*	*outer rim*	*core 1*	*core 2*	*rim 1*	*rim2*	*outer rim*	*vein*
SiO_2	0.03	0.03	0.03	b.d.	0.03	0.04	0.02	0.02
FeO	3.48	6.22	1.08	4.63	9.88	17.98	5.00	5.38
NiO	0.31	0.18	0.01	0.04	0.01	0.13	0.17	0.09
MnO	0.02	b.d.	0.76	0.39	0.14	0.13	b.d.	0.11
MgO	45.07	42.50	45.91	43.66	39.33	33.45	43.28	43.18
CaO	0.02	0.04	0.21	0.18	0.10	0.02	b.d.	0.40
SrO	b.d.	b.d.	b.d.	b.d.	b.d.	b.d.	b.d.	b.d.
CO_2	51.56	50.40	51.48	50.91	49.21	47.77	50.45	50.88
Total	100.49	99.37	99.49	99.81	98.70	99.53	98.94	100.07
X_{CaCO3}	0.000	0.001	0.003	0.003	0.002	0.000		0.006
X_{MgCO3}	0.955	0.922	0.975	0.936	0.873	0.766	0.937	0.927
X_{FeCO3}	0.041	0.076	0.013	0.056	0.123	0.231	0.061	0.065
X_{MnCO3}	0.000		0.009	0.005	0.002	0.002		0.001
X_{NiCO3}	0.004	0.002	0.000	0.000	0.000	0.002	0.002	0.001

*Magnesite generations are labeled MgsI through MgsV based on their composition and texture (see text for details); CO2 by stoichiometry after ZAF correction; b.d. = below detection. Lithology abbreviations: Atg-serp = antigorite-dominated serpentinite (*brucite-bearing); Lz-serp = lizardite-dominated serpentinite; atm = Atg-Tlc-Mgs rock; tm = in qtz-absent domain of Qtz-Tlc-Mgs rock sample Adv-21; qtm = Qtz-Tlc-Mgs rock; list = listvenite.*

Table A-4.4a *Composition of oxide phases from electron microprobe analysis. Analytical settings: see Ch.3.3 and Table 3.2.*

Lithology	Atg-srp*	Atg-srp*	Atg-srp*	Atg-srp*	Lz-srp	Lz-srp	Lz-srp	atm	atm	atm	atm
Sample	Adv-15	Adv-15	Adv-39	Adv-39	Adv-33	Adv-32	Adv-32	Adv-42	Adv-11	Adv-11	Adv-11
Mineral	Cr-Sp	Mag	Cr-Sp	Mag	Cr-Sp	Cr-Sp	Fe-Chr	goe	Cr-Sp	Fe-Chr	Mag
Comment	*core*	*rim*		*(Brc vein)*		*core*	*rim*		*core*	*rim1*	*rim2*
SiO_2 (wt%)	0.05	0.06	0.27	0.06	0.35	0.05	0.10	2.70	0.05	0.06	0.07
TiO_2	0.02	b.d.	0.01	b.d.	0.02	0.06	b.d.	b.d.	0.02	0.11	0.02
Al_2O_3	15.15	b.d.	21.55	b.d.	24.24	26.68	1.63	b.d.	27.09	0.50	b.d.
Cr_2O_3	52.36	3.01	45.75	b.d.	41.11	41.41	32.17	b.d.	40.51	33.97	0.60
V_2O_3	0.31	0.03	0.24	0.02	0.20	0.17	0.05	b.d.	0.19	0.14	0.04
FeO	20.62	88.10	19.09	91.65	19.10	14.56	58.76	77.56	17.97	59.65	93.11
NiO	0.06	1.20	0.02	1.08	0.12	0.11	0.16	1.18	0.11	0.19	0.30
MnO	0.48	0.44	1.06	0.18	0.48	0.34	0.76	b.d.	0.34	0.37	b.d.
MgO	10.51	0.95	11.27	1.12	13.48	15.22	0.32	1.79	12.99	0.26	0.03
ZnO	0.17	0.03	0.52	0.06	0.29	0.13	0.74	b.d.	0.21	0.62	0.03
CoO	0.05	0.25	0.14	0.21	0.05	0.08	0.13	0.04	0.08	0.10	0.15
Total	*99.77*	*94.07*	*99.94*	*94.38*	*99.42*	*98.82*	*94.82*	*83.48*	*99.56*	*95.95*	*94.35*
Fe_2O_3	3.21	66.72	2.42	70.35	4.87	2.70	32.91	86.19	2.48	32.97	68.99
FeO	17.73	28.06	16.91	28.35	14.72	12.12	29.14		15.74	29.98	31.03
Sum	*100.09*	*100.74*	*100.18*	*101.42*	*99.91*	*99.09*	*98.11*	*91.91*	*99.81*	*99.25*	*101.26*
Cations p.f.u.	*3*	*3*	*3*	*3*	*3*	*3*	*3*		*3*	*3*	*3*
Si	0.002	0.002	0.009	0.002	0.011	0.001	0.004		0.001	0.002	0.003
Ti	0.001	b.d.	0.000	b.d.	0.000	0.001	b.d.		0.000	0.003	0.000
Al	0.575	b.d.	0.792	b.d.	0.871	0.945	0.073		0.966	0.022	b.d.
Cr	1.334	0.090	1.128	b.d.	0.991	0.984	0.972		0.969	1.020	0.018
V	0.008	0.001	0.006	0.001	0.005	0.004	0.001		0.005	0.004	0.001
Fe^{3+}	0.078	1.904	0.057	1.995	0.112	0.061	0.946		0.057	0.943	1.974
Fe^{2+}	0.478	0.890	0.441	0.893	0.375	0.305	0.931		0.398	0.953	0.987
Ni	0.001	0.036	0.001	0.033	0.003	0.003	0.005		0.003	0.006	0.009
Mn	0.013	0.014	0.028	0.006	0.012	0.009	0.025		0.009	0.012	b.d.
Mg	0.505	0.054	0.524	0.063	0.613	0.682	0.018		0.586	0.015	0.002
Zn	0.004	0.001	0.012	0.002	0.007	0.003	0.021		0.005	0.017	0.001
Co	0.001	0.008	0.003	0.006	0.001	0.002	0.004		0.002	0.003	0.005
∑ trivalent	2.00	2.00	1.99	2.00	1.99	2.00	2.00		2.00	1.99	2.00
∑ divalent	1.00	1.00	1.01	1.00	1.01	1.00	1.00		1.00	1.01	1.00
Mg#	0.51	0.06	0.54	0.07	0.62	0.69	0.02		0.60	0.02	0.00
Cr#	0.70		0.59		0.53	0.51	0.93		0.50	0.98	
Fe^{3+}#	0.04	0.95	0.03	1.00	0.06	0.03	0.48		0.03	0.47	0.99

Lithology abbreviations: cf. Table A-4.2. b.d. = below detection limit.
Mg# = Mg / (Mg + Fe); Cr# = Cr / (Cr + Al); Fe^{3+}# = Fe^{3+} / (Cr + Al + Fe^{3+})

Table A-4.4b *Composition of oxide phases from electron microprobe analysis. Analytical settings: see Ch.3.3 and Table 3.2.*

Lithology	atm	qtm	qtm	qtm	qtm	qtm	qtm	qtm	list	list
Sample	Adv-35	Adv-02	Adv-02	Adv-05	Adv-22	Adv-29	Adv-29	Adv-29	Adv-09	Adv-09
Mineral	Cr-Sp	Fe-Chr	Hem	Cr-Sp	goe	Cr-Sp	Fe-Chr	goe	Cr-Sp	reevesite
Comment								*rim (Py)*		
SiO_2 (wt%)	0.09	0.91	0.07	0.06	2.71	0.16	0.38	2.31	0.05	0.26
TiO_2	b.d.	b.d.	b.d.	b.d.	0.04	b.d.	0.08	b.d.	b.d.	b.d.
Al_2O_3	22.57	0.59	b.d.	20.64	0.10	16.76	1.08	0.02	21.69	b.d.
Cr_2O_3	47.06	37.34	0.20	45.35	0.22	46.57	40.82	0.13	47.55	0.09
V_2O_3	0.23	0.14	0.10	0.20	b.d.	0.22	0.24	b.d.	0.23	b.d.
FeO	15.04	54.29	90.41	15.05	79.03	32.50	51.77	75.00	15.34	10.60
NiO	0.09	1.31	0.02	0.11	0.60	0.09	0.29	2.36	0.07	48.21
MnO	0.36	0.22	b.d.	0.36	b.d.	0.21	0.09	b.d.	0.43	b.d.
MgO	14.04	0.13	b.d.	13.02	1.73	2.75	0.41	0.85	13.69	0.10
ZnO	0.13	0.74	b.d.	0.15	b.d.	1.04	1.27	b.d.	0.15	0.04
CoO	0.08	0.22	0.14	0.05	b.d.	0.09	0.06	0.15	0.08	0.85
Total	*99.69*	*95.91*	*90.97*	*95.01*	*84.78*	*100.49*	*96.63*	*81.08*	*99.28*	*60.15*
Fe_2O_3	1.66	27.09	100.48	1.99	87.83	3.25	24.31	83.35	1.82	
FeO	13.55	29.92		13.26		29.58	29.89		13.70	
Sum	*99.85*	*98.61*	*101.01*	*95.20*	*93.22*	*100.72*	*98.92*	*89.18*	*99.46*	
Cations p.f.u.	*3*	*3*	*2*	*3*		*3*	*3*		*3*	
Si	0.003	0.035	0.002	0.002		0.005	0.014		0.002	
Ti	b.d.	b.d.	b.d.	b.d.		b.d.	0.002		b.d.	
Al	0.813	0.027	b.d.	0.785		0.664	0.048		0.789	
Cr	1.138	1.124	0.004	1.157		1.237	1.220		1.160	
V	0.006	0.004	0.002	0.005		0.006	0.007		0.006	
Fe^{3+}	0.038	0.776	1.990	0.048		0.082	0.692		0.042	
Fe^{2+}	0.346	0.953	0.000	0.358		0.831	0.945		0.354	
Ni	0.002	0.040	0.000	0.003		0.002	0.009		0.002	
Mn	0.009	0.007	b.d.	0.010		0.006	0.003		0.011	
Mg	0.640	0.007	b.d.	0.626		0.138	0.023		0.630	
Zn	0.003	0.021	b.d.	0.004		0.026	0.035		0.003	
Co	0.002	0.007	0.003	0.001		0.003	0.002		0.002	
∑ trivalent	2.00	1.97	2.00	2.00		1.99	1.98		2.00	
∑ divalent	1.00	1.03	0.00	1.00		1.01	1.02		1.00	
Mg#	0.65	0.01	0.00	0.64		0.14	0.02		0.64	
Cr#	0.58	0.98		0.60		0.65	0.96		0.60	
Fe^{3+}#	0.02	0.40	1.00	0.02		0.04	0.35		0.02	

Lithology abbreviations: cf. Table A-4.2. b.d. = below detection limit.
Mg# = Mg / (Mg + Fe); Cr# = Cr / (Cr + Al); Fe^{3+}# = Fe^{3+} / (Cr + Al + Fe^{3+})

5 Subduction metamorphism of serpentinite-hosted carbonates beyond antigorite-serpentinite dehydration (Nevado-Filábride Complex, Spain) [1]

5.1 Introduction

Subduction zones transfer carbon from the Earth´s surface to its deep interior and control the long-term deep carbon cycle. Sediments, altered oceanic crust, and the hydrated lithospheric mantle in the subducting slab contain carbon in the form of carbonate minerals and organic carbon. During subduction of the slab, metamorphic devolatilization reactions of hydrous minerals release fluids that enhance decarbonation reactions (Connolly, 2005; Gorman et al., 2006) and induce partial melting of the overlying mantle wedge (Dasgupta et al., 2004; Poli, 2015; Tumiati et al., 2013). Metamorphic devolatilization reactions thus play a vital role in the deep-carbon cycle by ultimately modulating the amount of the subducted carbon returned to the Earth surface via arc volcanism (Dasgupta, 2013; Kerrick and Connolly, 2001). Different estimates of the carbon fluxes at sub-arc depths mainly arise from uncertainties about the efficiency of rock-buffered devolatilization reactions, the role of congruent carbonate dissolution in fluid-dominated conditions, and the pathways of fluids (Connolly and Galvez, 2018; Galvez et al., 2016; Kelemen and Manning, 2015).

Because it releases high amounts of H_2O-rich fluids — 9 wt% H_2O at c. 660 °C — dehydration of Atg-serpentinite is potentially the most relevant devolatilization reaction to mobilize carbon at sub-arc depths into fluids from slab and mantle wedge lithologies (Bromiley and Pawley, 2003; Padrón-Navarta et al., 2010a; Rüpke et al., 2004; Ulmer and Trommsdorff, 1995). There is mounting evidence that fluids generated during high-P deserpentinization are oxidizing —close to the hematite-magnetite oxygen buffer— and are mildly alkaline (Alt et al., 2012; Debret et al., 2015; Debret and Sverjensky, 2017; Evans et al., 2017; Galvez et al., 2016). If so, deserpentinization fluids could mobilize both reduced and inorganic carbon as $CO_{2(aq)}$ and HCO_3^- (Facq et al., 2014). Antigorite dehydration fluids

[1] *This chapter has been published in Menzel, M.D., Garrido, C.J., López Sánchez-Vizcaíno, V., Hidas, K., Marchesi, C., 2019. Subduction metamorphism of serpentinite-hosted carbonates beyond antigorite-serpentinite dehydration (Nevado-Filábride Complex, Spain). Journal of Metamorphic Geology (in press).*

are rich in non-volatile components (Scambelluri et al., 2004), which may form aqueous complexes such as $NaHCO_3$ and $CaHCO_3^+$ and increase carbon solubility (Facq et al., 2016; Galvez et al., 2016). Therefore, deserpentinization fluids might constitute very effective agents for the recycling of carbon back to arc volcanism in the subduction factory.

Exhumed metamorphic terranes provide essential insights into the mechanisms of deep carbon recycling and mobilization in subduction zones (Bebout and Penniston-Dorland, 2016; Ferrando et al., 2017; Piccoli et al., 2016; Scambelluri et al., 2016). Thermodynamic calculations and studies of eclogite-facies marbles and carbonated eclogites and serpentinites in paleo-subducted metamorphic terranes show that carbonate minerals undergo variable extents of decarbonation and can be stable at high pressure (Collins et al., 2015; Connolly, 2005; Cook-Kollars et al., 2014; Ferrando et al., 2017; Proyer et al., 2008). Studies of natural examples of high-pressure metamorphism of carbonate-bearing rocks during Atg-serpentinite dehydration are scarce and limited to assess the mass balance of carbon during dehydration (Alt et al., 2012). Most of the available estimates of carbon release in deserpentinization fluids heavily rely on numerical and thermodynamic modelling (Gorman et al., 2006; Kelemen and Manning, 2015). The study of serpentinite-hosted carbonates (e.g., ophicarbonates) can provide a direct record of the impact of antigorite dehydration fluids on carbon release mechanisms in subduction zones.

Exhumed paleo-subducted metamorphic terranes offer a unique opportunity to investigate the metamorphism of serpentinite-hosted ophicarbonate. Examples of meta-ophicarbonate associated to prograde metamorphism of serpentinite are numerous in the geological record (Fig. 5.1). Many examples are preserved in brucite- or olivine-bearing Atg-serpentinites that underwent metamorphism in intermediate to warm subduction settings (*cf.* orange and pink dotted paths in Fig. 5.1) (Collins et al., 2015; Scambelluri et al., 2016; Vitale Brovarone et al., 2017). Examples of serpentinite-hosted meta-ophicarbonate recording metamorphic grade approaching or exceeding the P-T conditions of antigorite breakdown are very rare (e.g. in the Bellinzona-Dascio unit and at the Bergell aureole, Central Alps; fields labelled BD and BA in Fig. 5.1), and mostly associated to shallow contact metamorphism (Stucki, 2001; Trommsdorff and Connolly, 1996).

In this contribution, we present a petrological study of two occurrences of carbonate lenses hosted in high-pressure Atg-serpentinite (Milagrosa ultramafic massif) and prograde Chl-harzburgite (Almirez ultramafic massif), recording, respectively, subduction metamorphism prior to and after the conditions of antigorite breakdown in a hot subduction

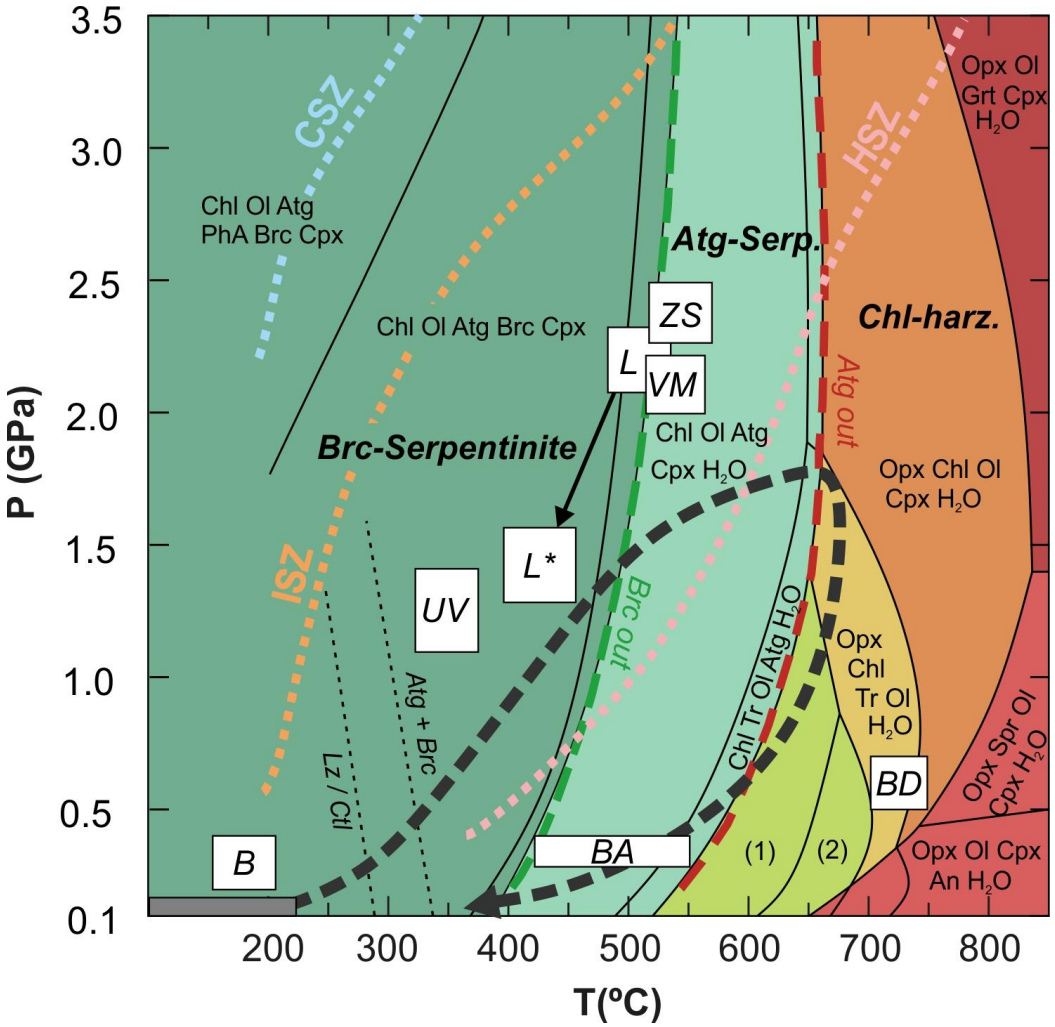

Figure 5.1. *Compilation of peak P–T conditions of meta-ophicarbonates (white fields) superposed on the pseudosection of a Ca-bearing serpentinite from the Almirez massif. VM: Voltri massif (Scambelluri et al., 2016); ZS: Zermatt-Saas; B: Bracco Unit, Internal Ligurides; UV: Ubaye Valley, Western Alps (all from Collins et al., 2015). L, L*: Lanzo massif peak conditions and P–T of graphite-formation in ophicarbonate, respectively (Vitale Brovarone et al., 2017); BA: contact-metamorphic ophicarbonates, Bergell aureole (Pozzorini and Früh-Green, 1996; Trommsdorff and Connolly, 1996); BD: Bellinzona-Dascio unit, Central Alps (Stucki, 2001). Dark grey field: maximum P–T conditions for hydrothermal ophicarbonate formation in seafloor serpentinites (Schwarzenbach et al., 2013). The P–T path of the Almirez massif (after Laborda-López et al., 2018) hosting meta-ophicarbonates beyond the antigorite stability (this study) is shown by the black dashed arrow. P–T paths at the Moho depth of the slab for hot, intermediate and cold subduction zones (HSZ, ISZ and CSZ, respectively) after van Keken et al. (2011). Numbered fields: (1) Chl, Tlc, Tr, Ol, H2O; (2) Chl, Ath, Tr, Ol, H2O. P–T conditions of lizardite-antigorite transition after Evans (2004). PhA = phase A; see Table 5.1 for other mineral names abbreviations.*

setting. In the Almirez massif, the dehydration reaction of serpentinite to Chl-harzburgite is preserved in the field, which makes it a unique case study to investigate the mobility of carbon during the breakdown of antigorite in subduction zones (Alt et al., 2012; Garrido et al., 2005; Padrón-Navarta et al., 2011). Comparison of these two natural examples of prograde metamorphism of serpentinite-hosted ophicarbonate sheds new light on the processes that control carbon fluxes in subduction zones.

5.2 The Nevado-Filábride Complex

The Nevado-Filábride Complex (NFC) is part of the internal zone of the Betic Cordilleras (S. Spain; Fig. 5.2a & b), and records Alpine subduction-related high-pressure (HP) metamorphism during early to middle Miocene (18-14 Ma; Gómez-Pugnaire et al., 2012; Kirchner et al., 2016; López Sánchez-Vizcaíno et al., 2001; Platt et al., 2006). Estimates of the peak pressure-temperature (P–T) conditions for different units of this complex range from ~1.0 – 2.2 GPa and 550 – 700 °C (Booth-Rea et al., 2015; Gómez-Pugnaire et al., 1994; Jabaloy-Sánchez et al., 2015; Li and Massonne, 2018; López Sánchez-Vizcaíno et al., 1997; Platt et al., 2013). The NFC constituted a Jurassic extended continental margin (Gómez-Pugnaire et al., 2012) or narrow oceanic basin (Puga et al., 2011) that separated Iberia from the allochthonous Alborán domain units, which were part of the AlKaPeCa terranes in the central Mediterranean (Hinsbergen et al., 2014). In the middle Miocene, the margin was subducted below the Alborán domain, and metamorphic rocks of the NFC rapidly exhumed in a two-stage process, first along the subduction interface and finally exhumed along E-W extensional domes now exposed in the Sierra Nevada, Sierra de los Filabres, and Sierra Alhamilla ranges (Fig. 5.2c) (Booth-Rea et al., 2015; Platt et al., 2013).

The NFC is subdivided into the lower Veleta unit, made up of graphite-bearing mica schists and metapsammites, and the upper Mulhacén unit, composed of Paleozoic dark schists (Montenegro formation), light schists (Tahal formation) and an upper heterogeneous sequence of alternating marbles, calc-schists, mica schists and gneisses (Fig. 5.2b; Gómez-Pugnaire et al. (2012)). Intercalated in this sequence occur several ultramafic bodies of variable size (up to 2.3 km²), mainly composed of Atg-serpentinite and Chl-harzburgite (Gómez-Pugnaire et al., 2012; Jabaloy-Sánchez et al., 2015; Padrón-Navarta et al., 2011). The Milagrosa and Almirez ultramafic massifs crop out in the uppermost part of the NFC, and are located in the eastern Sierra de los Filabres and eastern Sierra Nevada, respectively (Fig. 5.2b).

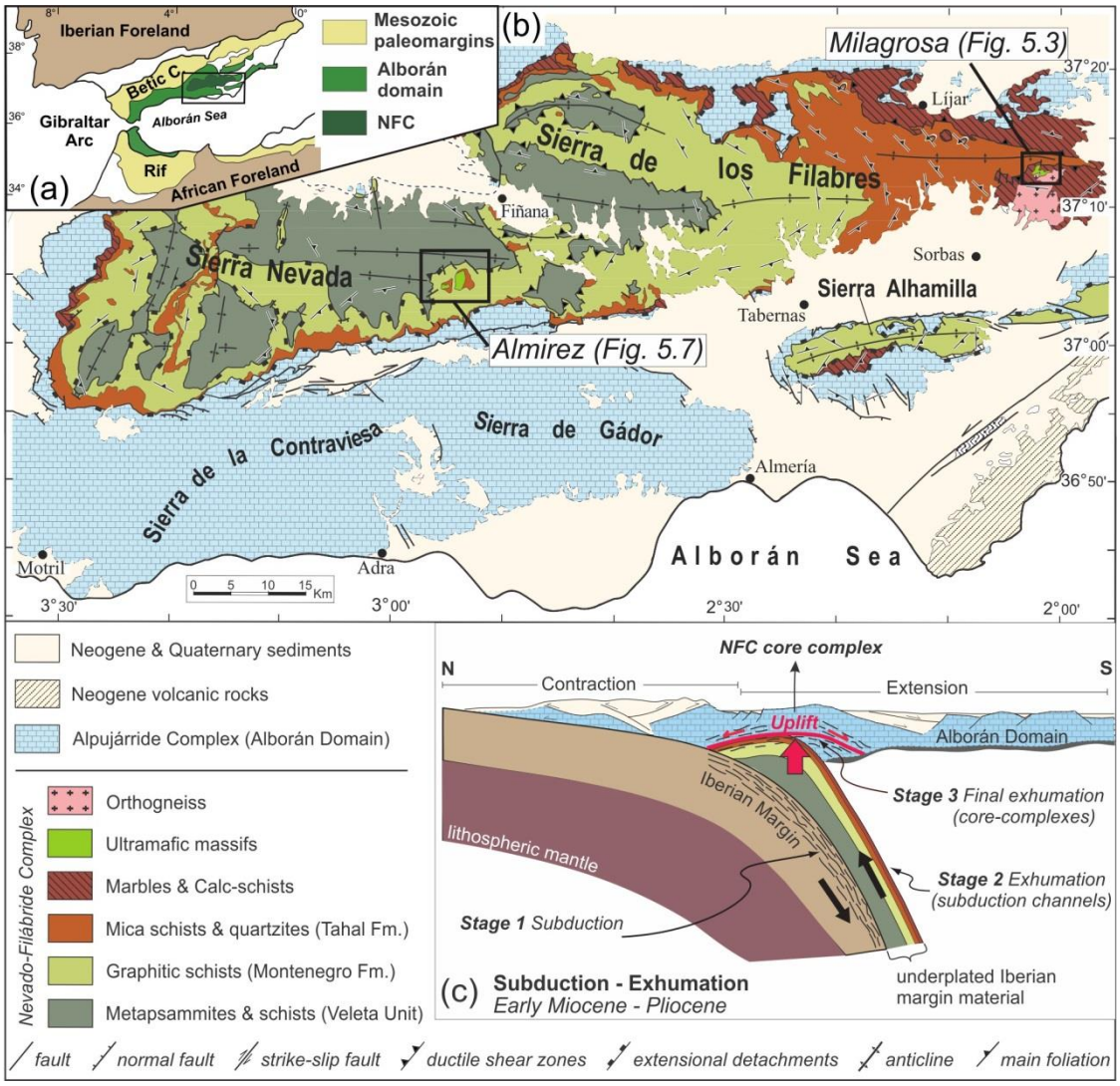

Figure 5.2. (a) *Location of the Nevado-Filábride Complex (NFC) in the Betic-Rif belt (modified from Jabaloy-Sánchez et al., 2015).* ***(b)*** *Geological map of the NFC in the central part of the Betic Cordillera (South Spain), with location of the two studied ultramafic massifs Almirez and Milagrosa; modified from Martínez-Martínez et al. (2010).* ***(c)*** *Conceptual sketch of subduction and exhumation of the NFC (after (Dilissen et al., 2018) modified from (Behr and Platt, 2012)).*

5.3 Meta-ophicarbonates in the NFC ultramafic massifs

5.3.1 The Milagrosa ultramafic massif

5.3.1.1 Field relations and sampling

The Milagrosa ultramafic massif consists of massive to schistose Atg-serpentinite, hosting variably sized marble lenses. The massif is tectonically bounded by metasediments (garnet-mica schists and phlogopite-quartz marbles) and metabasites (garnet-amphibolites with

Table 5.1. *Overview of the lithologies discussed in this study and their mineral assemblages.*

Lithology	Mineral assemblage	Retrograde phases	Key features / trace phases
Milagrosa			
TiCl-Cal marble*	Cal + Chl + Di + TiCl + Dol ± TiChn	± Qtz	Carbonate dominated; banded / ± Ap, Po, Py, Mag, Ilm, Prv
Di-Dol marble*	Dol + Di + Chl + Cal ± Tr ± TiCl ± TiChn ± Mag	Tr + Cal (?); Tlc, Qtz	Carbonate/silicate modal ratio 1:1; greenish in hand sample / ± Atg, Ilm, Ap
Atg-Di-Dol rock*	Atg + Dol + Di + Chl ± Cal ± TiCl ± Mag	± Qtz, Cal-veins, Ni-sepiolite	Atg-Di-Dol-Chl in equilibrium in matrix, but also Atg/Chl pods and fragments occur
Cpx-serpentinite*	Atg + Di + Mag ± Chl ± TiCl ± Ol ± Dol ± Tr ± Cal	± Tlc, Cal-veins, Qtz	anastomosing schistosity, high TiCl+Chl content when wrapping marble lenses. Dusty Di + Mag after Cpx; / ± Ilm, Pn
Atg-serpentinite	Atg + Mag ± TiCl ± Cal	Cal	Massive with no visible schistosity; Atg shape preferred orientation / ± Ilm, Pn
Dol-Atg-schist	Atg + Dol + Mag ± Mgs		very schistose with stretched flat domains of Dol-Atg intergrowth; Dol has oscillatory zoning
Carbonate-Tr-Chl veins (zones rim to center)	(host): Atg + Cal-Dol-Mgs + Mag (I): Chl + Cal + Tlc + Atg + Dol + Mag ± Hem ± Ilm ± Mgs (II): Chl + Tlc + Dol ± Tr ± Mag ± Hem (III): Tr + Chl + Dol ± Cal ± Hem	Fe-hydroxides	Calcite porphyroblasts in serpentinite close to veins contain Mgs-inclusions and Dol intergrowth; Grain sizes of Tr, Chl, Dol increase towards vein center
Almirez			
Meta-ophicarbonate° (granofelsic)	Di + Dol + Cal + Ol + Chl + TiCl + Mag ± TiChn ± Pn ± Arg	Cal, Srp (Lz)	Granofelsic, with coarse Ol-porphyroblasts with Arg, Dol, Chl and Mag inclusions
Meta-ophicarbonate° (gneissic)	Di + Dol + Chl + TiCl + Mag ± TiChn	± Srp, Tr, Qtz-Cal veins	Gneissic banding, with coarse TiCl-porphyroblasts /± Pn as inclusions in TiCl
Tr-Di-Dol rock° *(SN-143)*	Tr + Dol + Di + Chl ± Mgs ± Ilm/Chr	Cal; Tr-Dol (?)	Raft within carbonate breccia lens; Di as inclusions in Tr
Tlc-Mgs rock	Mgs + Tlc + Chl + Dol + Cal ± Ilm	Cal; Tlc-Chl ?	Penetrative foliation of Tlc-Chl aggregates parallel to gneissic meta-ophicarbonate; late replacement of Mgs by Cal. / ± Rt, Ap
Mgs-Tr rocks / veins	Mgs + Tr + Chl + Mag ± TiCl ± Dol, Cal	± Cal	Very coarse-grained, euhedral Mgs and Tr
Dol-marble	Dol + Phl + Qtz ± Cal ± Phg ± Tlc ± Drv ± Plag ± Tr ± Zoi ± Als		Different Dol-marble assemblages constitute the majority of clasts in breccia / ± Rt, Ttn, Ap
Carbonate breccia (matrix assemblage)	Cal + Tr + Dol + Chl + Chl + Phl ± Tlc ± Drv ± Qtz	(?)	Mineral fragments in Cal-matrix
Carbonate breccia (rock fragments, clasts)	Dol-marble; Tr-Di-Dol rock; Chl-Tr-rock; chloritite; Tr-Ol-Atg-Chl rock; Chl-harzburgite; coarse dolomite		angular to rounded, meter-sized rafts to millimeter-scale clasts; matrix-supported

** = lithologies directly associated with marble lenses within serpentinite (Milagrosa); ° = meta-ophicarbonate lenses (Almirez). Minerals are listed in order of decreasing abundance. Mineral abbreviations throughout Ch. 5 are given following the recommendations by the IUGS Subcommission on the Systematics of Metamorphic Rocks (Siivola and Schmid, 2007), with the exception of titano-clinohumite (TiCl) and titano-chondrodite (TiChn).*

intercalations of garnet-bearing quartz-calcite schists) from the uppermost Mulhacén unit (Fig. 5.3a). The internal structure of this massif is well exposed in the Milagrosa quarry (Fig. 5.3b). In the NW of the quarry, the contact with garnet-mica schists and marbles is a fault composed of polymictic breccia grading into up to 10 m thick carbonated serpentinite breccia (Fig. 5.3b). In the SE part of the quarry, a fine-grained brittle fault gauge zone separates the Atg-serpentinites from metabasites. The foliation of Atg-serpentinite — mostly N-020, dipping 70° – 85° to NNE — is oblique to the contacts with the country rocks (Fig. 5.3b).

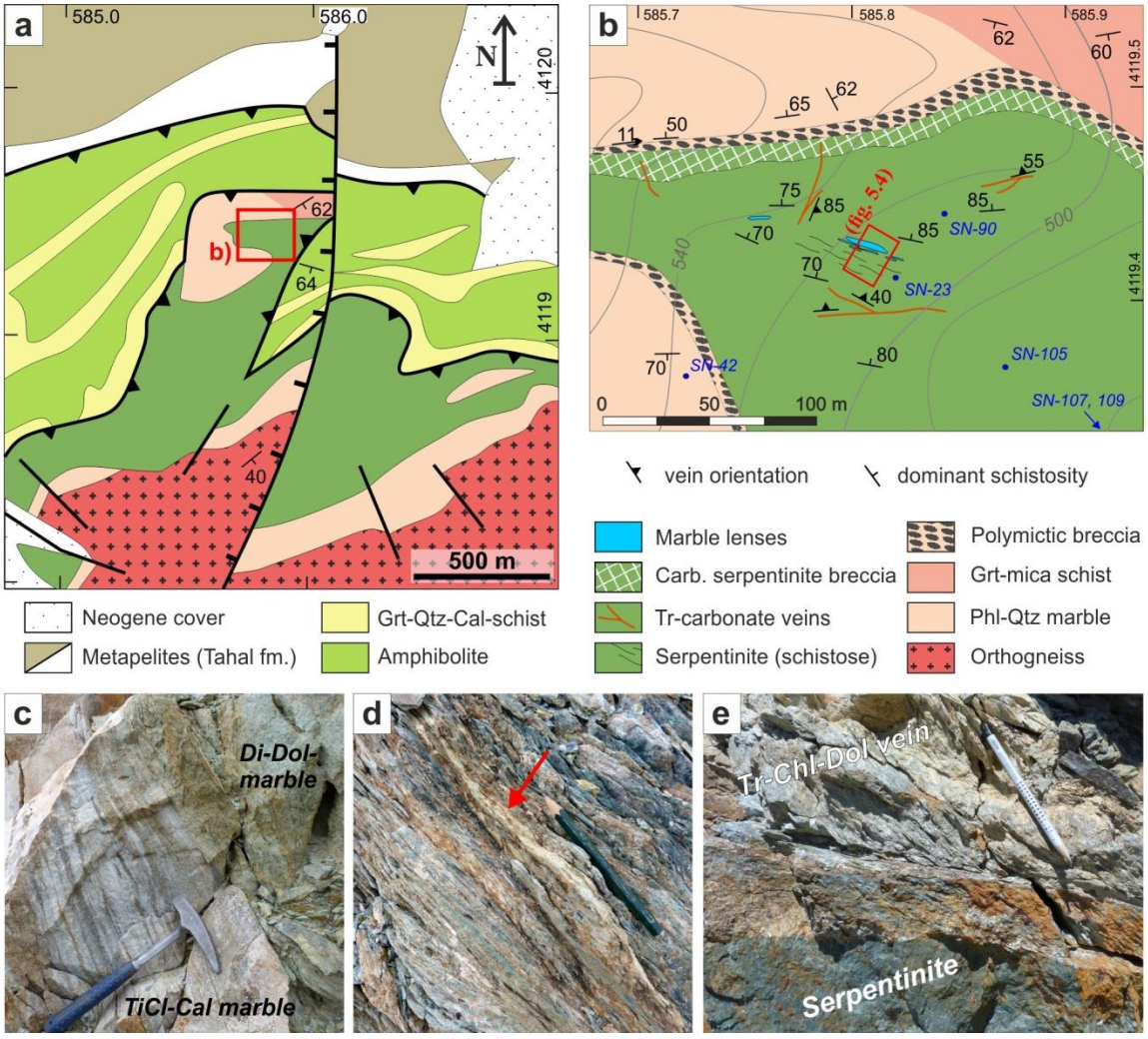

Figure 5.3. *Field relations in the Milagrosa serpentinite massif.* ***(a)*** *Geological map of the Milagrosa serpentinite massif (after Kampschuur and García Monzón, 1975).* ***(b)*** *Detailed geological map from inset in a) of the Milagrosa serpentinite quarry with location of sampled marble lenses (red field; Fig. 5.4) and Tr-carbonate veins.* ***(c)*** *Banded TiCl-Cal marble and Di-Dol marble lenses within serpentinite.* ***(d)*** *Cpx-serpentinite with brown weathering TiCl-porphyroblasts and carbonate vein (arrow).* ***(e)*** *Massive serpentinite crosscut by a zoned Tr-Chl-carbonate vein. Mineral abbreviations: see Table 5.1.*

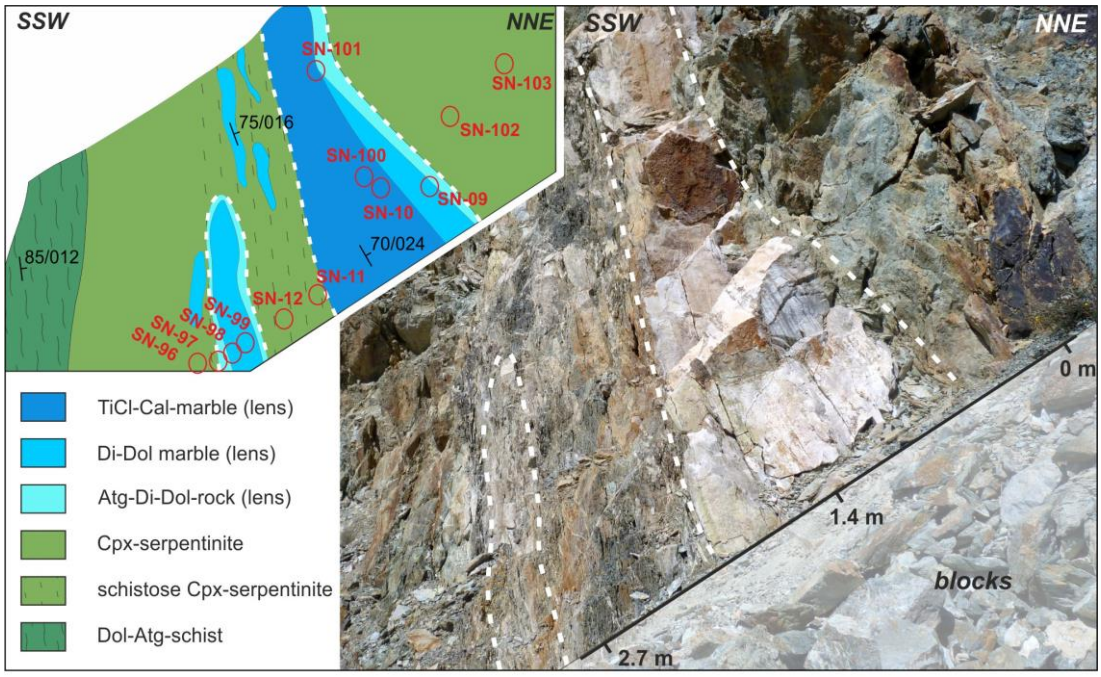

Figure 5.4. *Milagrosa marble lenses within foliated Cpx-serpentinite, and corresponding sketch with sampling sites and small-scale lithological changes throughout the illustrated sequence (scale represents true thickness perpendicular to the schistosity).*

For the present study, we sampled a sequence of marble lenses and host serpentinites in the central part of the Milagrosa quarry (Fig. 5.4). Table 5.1 provides a description of the lithologies and their mineral assemblages; a list of all sample locations is shown in Table A-5.1 of the Appendix[2]. The marble lenses occur as boudins — 20 – 130 cm thick and up to 20 m long — oriented sub-parallel to the mylonitic to schistose foliation of the enclosing Atg-serpentinite (Fig. 5.3b), and show a compositional banding due to variations in the silicate mineral content (dark patches; Fig. 5.3c) and relative proportion of calcite to dolomite (white and brown bands, respectively; Fig. 5.3c). We distinguish two types of marbles: TiCl-Cal marbles and impure Di-Dol marbles (Fig. 5.4; see Table 5.1 caption for mineral abbreviations). Atg-Di-Dol rocks (5 – 20 cm thick) —composed of variable proportions of carbonate, light green diopside, chlorite-antigorite pods, and minor magnetite and Ti-clinohumite (Table 5.1)— occur at the contact between marble and serpentinite (Fig. 5.4). The serpentinites are massive to foliated, fine-grained Atg-serpentinite and Cpx-serpentinite (Table 5.1). Atg-serpentinite contains scarce Ti-clinohumite porphyroblasts and veins, and lacks olivine. In the vicinity of the marble lenses, dark Cpx-serpentinites with coarse grained, white patchy diopside-rich domains prevail (Fig. 5.4). Towards the contact with the marble

[2] Appendices to this study are provided at the end of Ch. 5.

lenses, Cpx-serpentinite displays an increasingly penetrative schistose to mylonitic foliation defined by fine-grained antigorite around Ti-clinohumite porphyroblasts, whitish coarse-grained diopside-rich domains (Fig. 5.4) and, at the lens contact, almond-shaped diopside porphyroblasts. Well-foliated Dol-Atg schists with elongated dolomite-rich patches occur in a 7 – 10 m wide zone close to the marble lenses (Fig. 5.4).

Carbonate-tremolite-chlorite veins (Table 5.1), up to 1.5 m thick, are cross-cutting at variable angles the Atg-serpentinite foliation (Fig. 5.3e), and are in turn cross-cut by calcite veins (0.2 – 1 cm thick; Fig. 5.3d). Because they overprint the prograde Atg-serpentinite foliation, veins are not considered in the present study.

5.3.1.2 Petrography

TiCl-Cal marbles (Table 5.1; Fig. 5.5a) are composed of calcite, minor diopside, chlorite, Ti-clinohumite and dolomite. Accessory phases are apatite, Fe-oxides, pyrrhotite and occasional pyrite, pentlandite, and ilmenite. Ilmenite occasionally contains rare Ca-perovskite cores and zirconolite and uraninite inclusions (Fig. 5.6a). The marbles show a weak foliation defined by oriented chlorite and a porphyroblastic texture made up of inclusion-rich Ti-clinohumite porphyroblasts with occasional Ti-chondrodite (TiChn) cores in a medium to fine-grained matrix of calcite, diopside, and chlorite. Dolomite occurs as small, spotty to vermicular exsolutions in calcite (Fig. 5.5a), and as large resorbed, inclusion-rich aggregates. Quartz occurs as fine-grained retrograde aggregates around Ti-clinohumite or diopside.

Di-Dol marbles are composed of diopside, dolomite and chlorite, minor euhedral tremolite, calcite, magnetite-ilmenite intergrowths, apatite, talc, and rare antigorite. Yellow, pleochroic Ti-clinohumite porphyroblasts occur in domains where tremolite is absent, embedded in a granoblastic matrix.

Atg-Di-Dol rocks (Table 5.1; Fig. 5.5 b–d) have a very heterogeneous modal composition at the hand specimen scale. Diopside, dolomite and antigorite-chlorite aggregates display a weak shape preferred orientation forming an anastomosing foliation with occasional Ti-clinohumite porphyroblasts with abundant inclusions of dolomite, chlorite, apatite and magnetite-ilmenite intergrowths (Fig. 5.5c). Diopside has inclusions of calcite, dolomite, and rare antigorite. Cr-bearing magnetite occurs as porphyroblasts or elongated aggregates of smaller grains. Magnetite porphyroblast cores commonly have abundant chlorite inclusions, while their rims and smaller grains are free of inclusions and occasionally

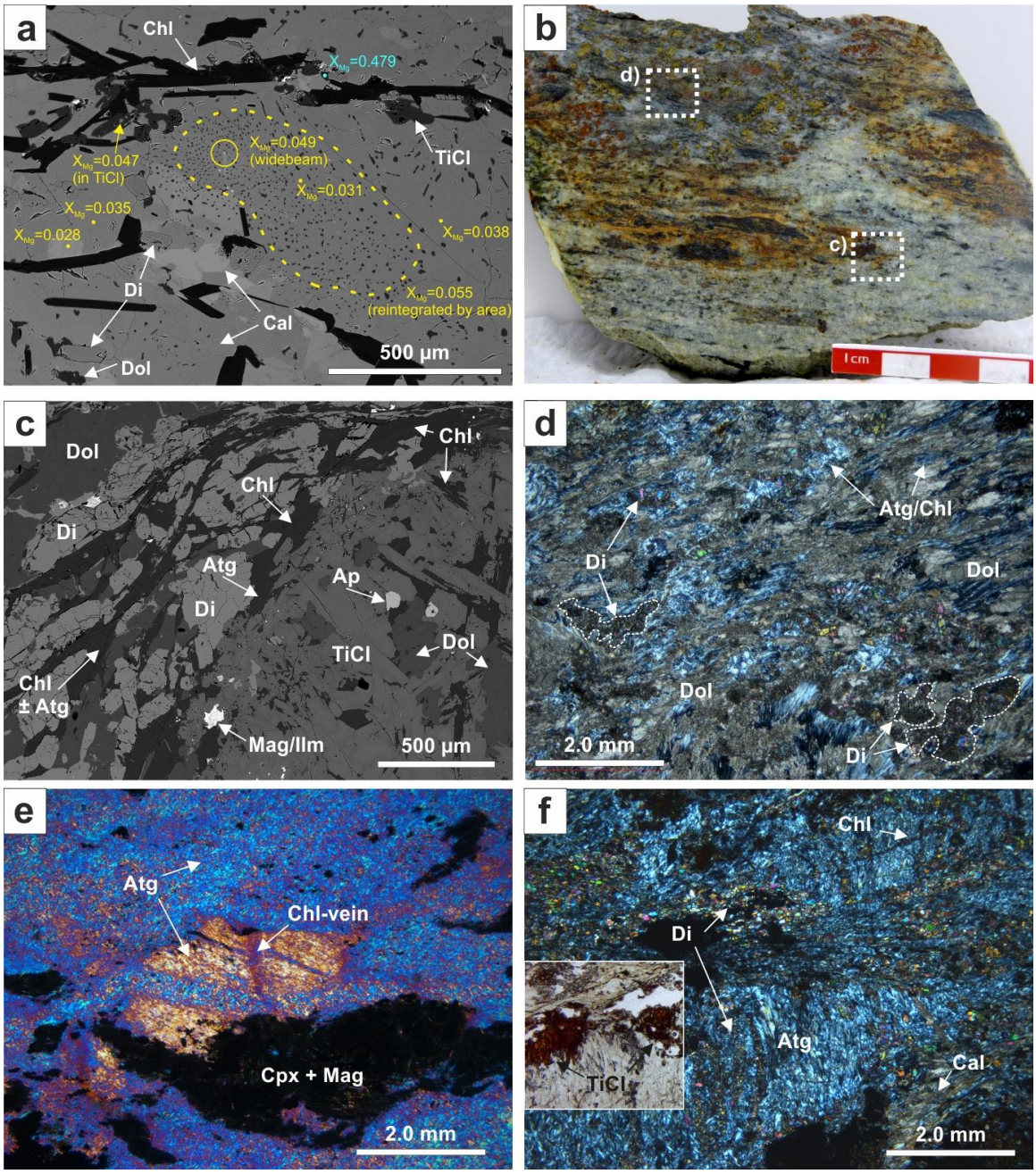

Figure 5.5. *Hand specimen, micrographs and back-scattered electron (BSE) images of host serpentinites, marble lenses and Atg-Di-Dol rocks from Milagrosa.* ***(a)*** *BSE image of TiCl-calcite marble lens displaying the measured $XMgCO_3$ of carbonates; dolomite forms fine grained exsolutions from calcite.* ***(b)*** *Polished slab of Atg-Di-Dol rock with darker Atg-Chl domains and red-brown Ti-clinohumite in a Di-Dol-matrix; the approximate positions of micrographs in c) and d) are also shown.* ***(c)*** *BSE-image of an inclusion-rich Ti-clinohumite-porphyroblast wrapped by diopside, dolomite, chlorite and minor antigorite.* ***(d)*** *Atg-Di-Dol-rock with aligned Atg-Chl aggregates and diopside-rich domains (white dotted lines) (crossed polarizers).* ***(e)*** *Cpx-serpentinite, showing dusty resorbed clinopyroxene-magnetite porphyroblasts, and antigorite domains with differing preferred orientation crosscut by chlorite veins, likely after bastite (crossed polarizers with inserted compensator).* ***(f)*** *Cpx-serpentinite rich in chlorite and red-brown Ti-clinohumite (plane polarized inset, at the same position) and diopside neoblasts aligned with antigorite in almond-shaped domains, and diopside and chlorite aligned with antigorite in narrow anastomosing bands (crossed polarizers).*

replaced by hematite (Fig. 5.6b). Magnetite in the host serpentinites shows similar textures. Antigorite and chlorite form fine intergrowths with an interlocked texture.

Atg-serpentinites show a weak foliation marked by the shape-preferred orientation of antigorite crystals, and a lineation defined by elongated aggregates of anhedral magnetite (3 – 5 vol%). Locally, domains of antigorite with an interlocked texture show a distinct shape and crystallographic preferred orientation (Fig. 5.5e). Rare ilmenite-magnetite intergrowths, Ni-Fe-sulphides, and Ti-clinohumite — as fragmented grains or in veins — are present (Table 5.1).

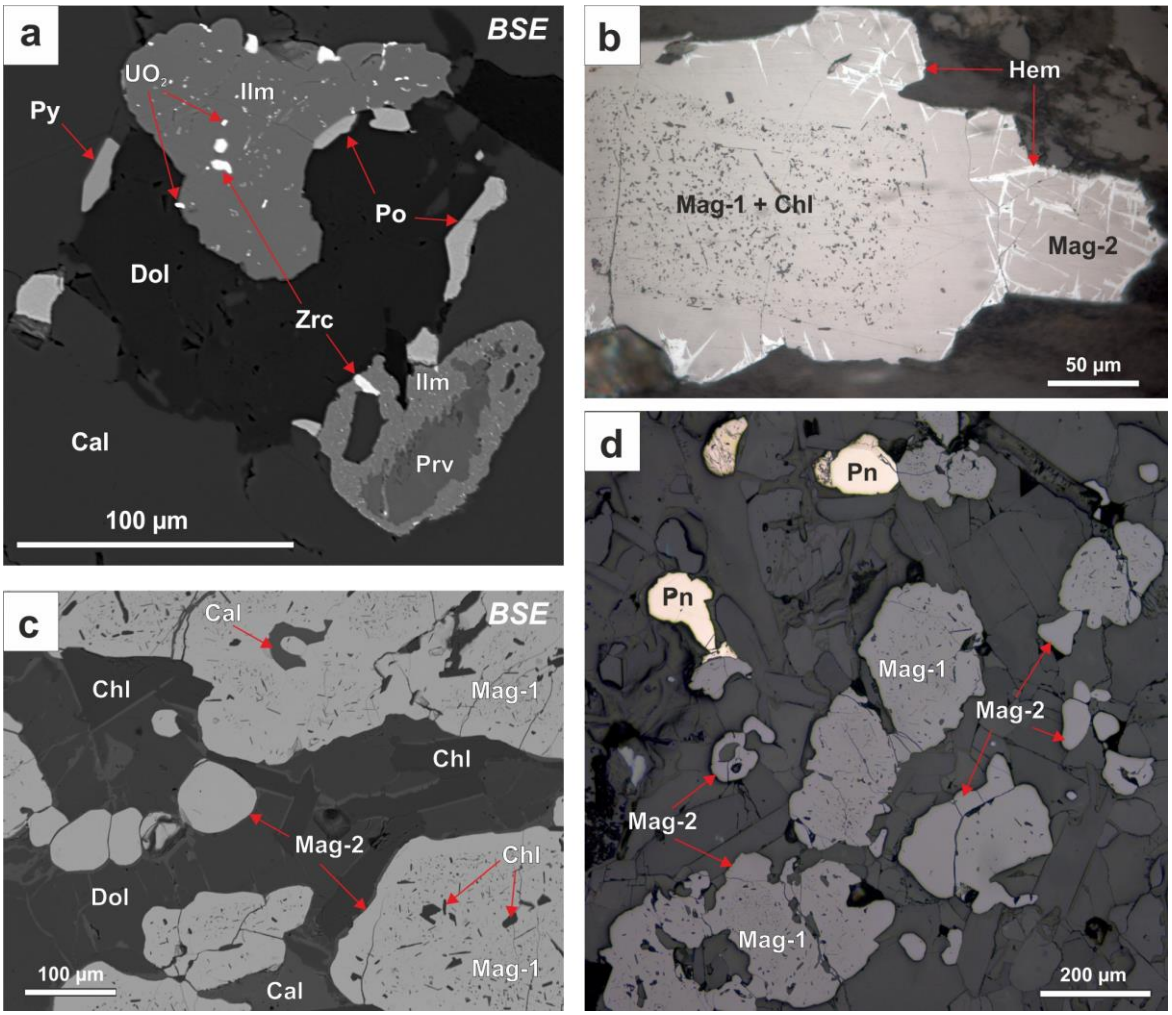

Figure 5.6. *BSE and reflected light images of oxides in Milagrosa and Almirez rocks.* ***(a)*** *Association of Ca-Ti-perovskite (Prv) rimmed by ilmenite (Ilm) with inclusions of uraninite (UO_2) and zirconolite (Zrc), pyrite (Py), and pyrrhotite (Po) in Milagrosa TiCl-Cal marble (SN-100; BSE image).* ***(b)*** *Cr-bearing magnetite in Milagrosa Atg-Di-Dol rock (SN-98), with the core rich in chlorite inclusions (likely tracing magnetite after Cr-spinel) and inclusion-free rims (Mag-2). Rims are locally replaced by hematite (reflected light image).* ***(c)*** *BSE image of magnetite in Almirez meta-ophicarbonate (SN-138), showing cores with abundant chlorite inclusions and inclusion-free rims and neoblasts.* ***(d)*** *Reflected light image of the same sample as in c), showing similar magnetite textures, and relatively abundant pentlandite (Pn).*

Cpx-serpentinites have a planar texture marked by elongated clinopyroxene aggregates, flattened magnetite, and a weak shape-preferred orientation of antigorite. They contain abundant porphyroblasts of dusty and clear clinopyroxene (5 – 10 vol%) —often associated with magnetite—, minor chlorite (1 – 3 vol%), and rare calcite and tremolite. Near the marble lenses, the modal amounts of diopside (up to 30 vol%), chlorite (10-20 vol%), Ti-clinohumite (5-8 vol%) and minor carbonates increase. Narrow to anastomosing bands of strongly oriented antigorite intersect and wrap around coarse diopside-magnetite aggregates, euhedral Ti-clinohumite porphyroblasts, and almond-shaped domains of antigorite with a different orientation (Fig. 5.5f). Elongated aggregates of diopside neoblasts and chlorite are parallel to the antigorite orientation in bands and almond-shaped domains (Fig. 5.5f). Ti-clinohumite porphyroblasts contain inclusions of chlorite, dolomite, and clinopyroxene, and are occasionally rimmed by fine-grained olivine. Rare, red-brown Ni-bearing Fe-Si-aggregates occur in the antigorite matrix, occasionally rimming sulphides and magnetite. Similar Fe-Ni-Si-aggregates are common in HP-serpentinites elsewhere (Malvoisin et al., 2017).

Dol-Atg schists (Table 5.1) consist of strongly orientated antigorite and flattened domains of magnetite, dolomite and coarse-grained, interlocked antigorite. Magnesite, pentlandite and cronstedtite are accessory phases.

5.3.2 The Almirez Massif

5.3.2.1 Field relations and sampling

The Almirez ultramafic massif is a dismembered section of subducted serpentinite, comprising Atg-serpentinites and their prograde dehydration products, Chl-harzburgites (Fig. 5.7a) (Padrón-Navarta et al., 2011; Trommsdorff et al., 1998). Minor meta-rodingites, clinopyroxenites, and carbonate lenses are also present. A sharp isograd — oblique to the prograde high-pressure antigorite-serpentinite foliation — records the high-pressure dehydration of Atg-serpentinite to Chl-harzburgite (1.8 – 1.9 GPa, ~660 °C) (López Sánchez-Vizcaíno et al., 2009; Padrón-Navarta et al., 2010a).

Carbonate-bearing lithologies occur in the western part of the Almirez Chl-harzburgite section, as lenses of yellow, banded dolomite marble, polymictic carbonate breccia, and meta-ophicarbonate (Table 5.1; Fig. 5.7a & b; Appendix Table A-5.2). The dolomite marbles contain rather simple mineral assemblages (tremolite, quartz; see Table 5.1) and make up the majority of rock fragments in the carbonate breccias (Table 5.1). Here, we focus on two

lenses of meta-ophicarbonate (5 – 10 m thick; yellow lenses in Fig. 5.7b & c). The meta-ophicarbonates show a coarse-grained, granofelsic texture with Ti-clinohumite and olivine porphyroblasts (up to 1 cm) and a weak modal layering sub-parallel to the lens elongation (Fig. 5.7b; Fig. 5.8a). The granofelsic meta-ophicarbonate contains grey banded levels (30 – 50 cm thick) with a gneissic texture (Fig. 5.7d; Fig. 5.8b). Locally, Tlc-Mgs rocks (3 – 5 m thick) with abundant euhedral magnesite crystals (up to 5 cm) occur in the meta-ophicarbonates (Fig. 5.7b & e; Table 5.1). Talc-chlorite aggregates in these rocks show a penetrative foliation sub-parallel to the gneissic foliation and the modal layering of the meta-ophicarbonates.

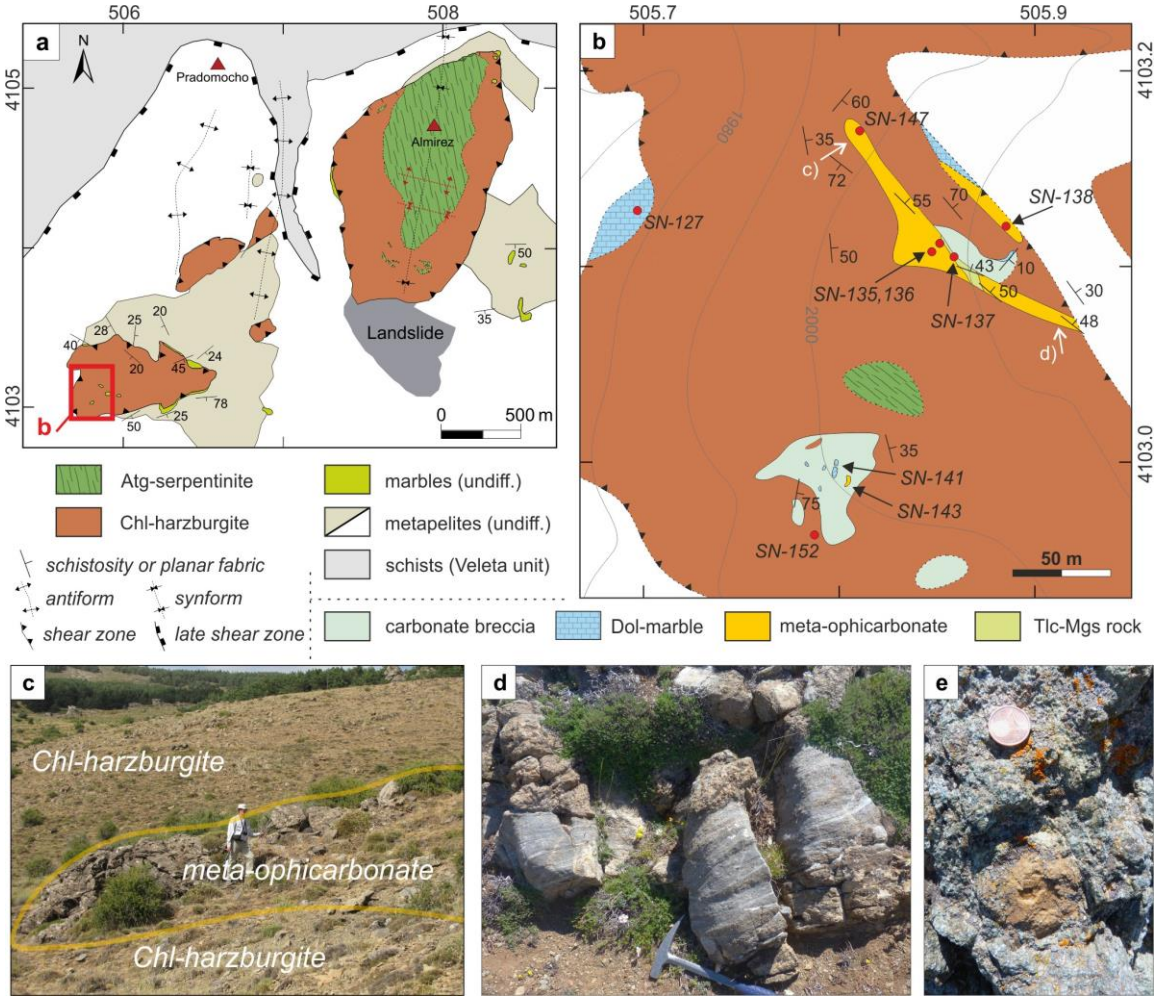

Figure 5.7. *Meta-ophicarbonate lenses within Chl-harzburgite at Almirez.* ***(a)*** *Geological map of the Almirez ultramafic massif (after Jabaloy-Sánchez et al., 2015).* ***(b)*** *Detailed geological map of carbonate lenses in Chl-harzburgite and key sample locations (inset in a); the locations of field pictures c) and d) are marked by white arrows.* ***(c)*** *Field picture of the Almirez meta-ophicarbonate lens hosted in Chl-harzburgite.* ***(d)*** *Coarse-grained, granofelsic meta-ophicarbonate rich in olivine and Ti-clinohumite (yellowish-brown in colour), crosscut by gneissic dolomite-dominated meta-ophicarbonate (grey colour).* ***(e)*** *Tlc-Mgs rock with coarse brown magnesite blasts (coin for scale is 2 cm).*

The contact of Chl-harzburgite with meta-ophicarbonate is not well exposed. Chl-harzburgite surrounding the meta-ophicarbonate lenses has — like in other parts of the Almirez massif (Padrón-Navarta et al., 2011) — spinifex and granofels textures, and is commonly recrystallized (Fig. 5.7b) (Padrón-Navarta et al., 2012; Padrón-Navarta et al., 2010b). Magnesite- and dolomite-bearing Tr-Chl-TiCl-Ol-rocks (e.g. sample SN-152 in Fig. 5.7b) and Ti-clinohumite bearing magnesite-tremolite-chlorite veins occur locally in Chl-harzburgite.

5.3.2.2 Petrography

The Almirez meta-ophicarbonates consist of carbonate (c. 25 – 45 vol%; dolomite, calcite, and rare aragonite), diopside, olivine, Ti-clinohumite / -chondrodite, chlorite and minor Cr-magnetite, pentlandite, pyrrhotite, and apatite (Table 5.1). The meta-ophicarbonates show a planar texture marked by chlorite and weakly oriented diopside and dolomite (Fig. 5.8c & d) around olivine and Ti-clinohumite porphyroblasts. Grain boundaries are mostly polygonal between all phases. Domains richer in diopside, olivine or carbonate, respectively, constitute a modal layering parallel to this planar texture (Fig. 5.8d). Calcite is rare in some coarse-grained dolomite-rich domains (Fig. 5.8e) and gneissic intercalations (Fig. 5.8b; Table 5.1). The latter further contain rare olivine and sulphides. Ti-clinohumite, olivine, and diopside have abundant inclusions of chlorite, calcite, dolomite, and, locally, magnetite, sulphides and apatite (Fig. 5.8 c–g). Furthermore, Electron Backscatter Diffraction (EBSD) and Energy-Dispersive Spectrometry (EDS) analyses have revealed the presence of aragonite inclusions (5 – 30 µm in size) in olivine and diopside (Fig. 5.8 f–h). Yellow pleochroic Ti-clinohumite porphyroblasts occasionally have Ti-chondrodite cores and olivine rims (Fig. 5.8c). Cr-bearing magnetite occurs as coarse, elongated aggregates with abundant chlorite inclusions, and as inclusion-free rims and subhedral grains in the granoblastic matrix (Fig. 5.6c & d). Lizardite locally replaces Ti-clinohumite and olivine porphyroblasts along veins and grey-black pleochroic rims (Fig. 5.8 c & h). Calcite, quartz, and tremolite occur locally in veins (0.5 – 2.0 mm thick) crosscutting the layering.

Meta-ophicarbonate clasts in carbonate breccia (sample SN-143; Table 5.1) are composed of dolomite, tremolite, chlorite, minor diopside, and rare magnesite, Fe-oxide, chromite-ilmenite intergrowths and apatite. They have a well-developed gneissic texture marked by chlorite orientation and tremolite- and dolomite-rich bands.

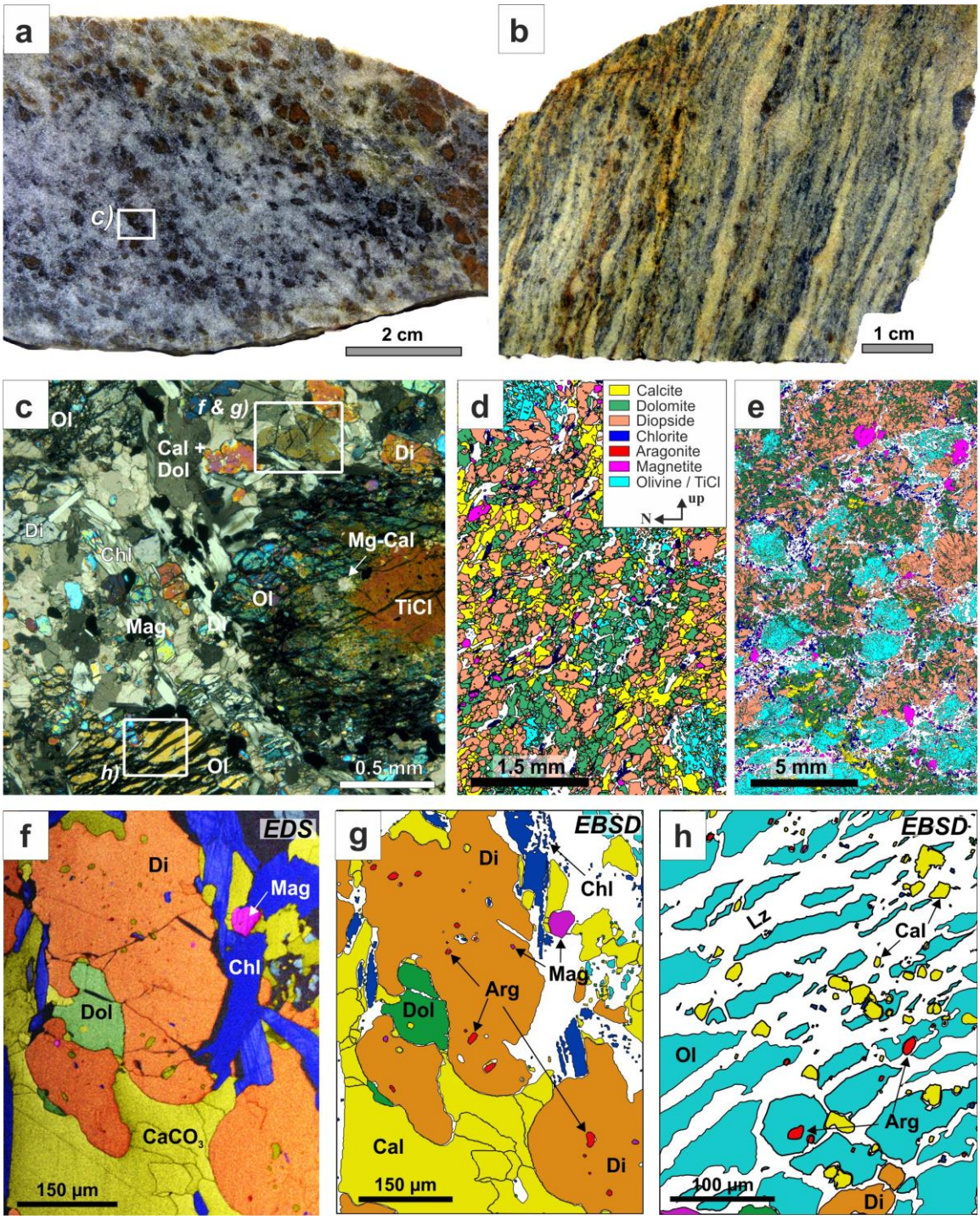

Figure 5.8. *Petrography of Almirez meta-ophicarbonates.* ***(a)*** *Polished slab of massive meta-ophicarbonate with large red-brown Ti-clinohumite and olivine in a carbonate-diopside-chlorite matrix (sample SN-135).* ***(b)*** *Polished slab of a banded, olivine-poor sample with gneissic appearance (sample SN-136).* ***(c)*** *Micrograph of meta-ophicarbonate in a); the insets correspond to the positions of the chemical and phase maps in f), g) and h).* ***(d)*** *EBSD phase map showing representative mineral distribution in meta-ophicarbonate (sample SN-135).* ***(e)*** *EBSD phase map of coarse, calcite-poor meta-ophicarbonate (sample SN-147; colour legend as in d).* ***(f) & (g)*** *Chemical false-color map (EDS) superposed on band-contrast, and corresponding EBSD phase map of diopside with aragonite inclusions.* ***(h)*** *EBSD phase map of inset in d), showing preserved aragonite (red) and re-equilibrated calcite inclusions within olivine crosscut by lizardite veins. White areas in all EBSD phase maps (non-indexed) are mainly chlorite and lizardite.*

The Tlc-Mgs level (Table 5.1) is made up of coarse magnesite (up to 5 cm; Fig. 5.7e) rimmed by calcite and dolomite, and minor chlorite-talc aggregates. Ilmenite, rutile, and apatite are accessory phases; Cr-bearing phases (Cr-magnetite or chromite) are absent. Almond-shaped chlorite-talc aggregates define a penetrative foliation.

The host Chl-harzburgites have similar textures and mineral assemblages as elsewhere in the massif (Padrón-Navarta et al., 2011), and are occasionally overprinted by chrysotile/lizardite serpentinization. Tr-Chl-TiCl-Ol-rocks consist of olivine, Ti-clinohumite, chlorite, and tremolite, and minor magnetite, magnesite and dolomite (~5 vol% carbonates). Magnesite occurs as coarse interstitial grains rimmed by dolomite, and tremolite has inclusions of diopside, indicating that the peak assemblage was TiCl-Ol-Chl-Di-Mgs and tremolite and dolomite formed after diopside and magnesite in the retrograde path.

5.4 Methods

5.4.1 Thermodynamic modelling methods

To investigate the P–T conditions of equilibration, phase relationships, and equilibrium fluid composition, we calculated P–T, T–X_{CO2} and T–X pseudosections in the FeO–CaO–MgO–Al_2O_3–SiO_2–H_2O–CO_2 (FCMASHC) system using Perple_X 6.7.3 (Connolly, 2009). For these calculations, we used the internally consistent thermodynamic database of Holland and Powell (1998) (version 2002) and the compensated Redlich-Kwong (CORK) equation of state (Holland and Powell, 1991) for H_2O–CO_2 fluids, because they allow the consistent application of solid solution models, such as the antigorite model by Padrón-Navarta et al. (2013) that accounts for Al Tschermak's and Fe-Mg exchanges. All applied solid solution models are provided in Appendix Table A-5.3.

Because the available antigorite solid solution model does not consider Fe^{3+} in antigorite, which may have Fe^{3+}/Fe_{total} up to 0.7 (Debret et al., 2014), this solution model overestimates Al Tschermak's -exchange and may result in an erroneous prediction of brucite and olivine in detriment of chlorite. Due to this limitation, we estimated the amounts of Fe_2O_3 in antigorite and of magnetite in the bulk samples by mass balance and from the modal abundance in serpentinites, using Fe^{3+}/Fe_{total} = 0.6 as an intermediate estimate for ferric iron in antigorite (Debret et al., 2015). The equivalent quantities of FeO and Fe_2O_3 were then subtracted from the bulk compositions, to obtain model FeO contents for bulk compositions in the FCMASH system (FeO_{model} in Table 5.2). This subtraction improves the calculation of phase relations

between olivine, clinopyroxene, and tremolite in serpentinites with high bulk Fe^{3+}/Fe_{total} at 500–650 °C, and reproduces the observed assemblage Cpx–Tr–Atg. However, because in this way the bulk rock Mg/(Mg+Fe) is fixed and magnetite assumed to be non-reactive, the model underestimates the Fe content of olivine at high temperature and modelled temperatures of dehydration reactions may be slightly overestimated (Bretscher et al., 2018). Ti-clinohumite was not included because an F-rich endmember is not available, leading to an overestimation of the amount of olivine in the calculations.

To explore the effect of electrolytic fluids on carbon solubility, we further calculated the speciation of carbon-bearing solutes in equilibrium with meta-ophicarbonate rocks using the "lagged speciation" algorithm of Perple_X 6.8.5 (Connolly and Galvez, 2018). To be consistent with the classical models with binary X_{CO2} fluids, we used the implementation of aqueous species thermochemical data of the DEW model (Sverjensky et al., 2014) (May 2017 version) in the thermodynamic database of Holland and Powell (1998) (version 2002), the same mineral solid solution models as described previously (Appendix Table A-5.3), and the CORK equation of state for H_2O and CO_2. For CH_4, we employed the modified Redlich-Kwong (MRK) equation of state, even though calculations showed that reduced carbon species are negligible in fluids in equilibrium with carbonate-rich rocks. The use of different hybrid solvent equations of state results in only slight differences in speciation and solubility for the conditions of interest of this study. Minor differences between carbon solubilities predicted by binary X_{CO2} models and those from electrolytic fluids are further due to different fluid mixing models. Redox conditions in the speciation calculation were fixed by using a bulk oxygen content corresponding to the respective metal oxides, all carbon as CO_2 and Fe^{3+}/Fe_{total} fixed to 0.57, providing a redox budget similar to that of natural serpentinites (Debret et al., 2015) and meta-ophicarbonates (Table 5.2). Because no Na- or K- bearing solid phases occur in the Milagrosa serpentinites, Atg-Di-Dol rocks and marble lenses or in the Almirez meta-ophicarbonates (Table 5.1) and concentrations of both elements are on the threshold of detection limits (Table 5.2), we restricted the calculations to the Fe-Ca-Mg-Al-Si-C-H-O system. Highly fluid mobile elements such as Cl were also neglected because antigorite breakdown fluids have a relatively low salinity (Scambelluri et al., 2004) and accounting for them would require externally constrained chemical potentials (Galvez et al., 2016). As a result, our calculations slightly underestimate carbon solubility, because the models do not consider potentially C-bearing complexes — such as $NaHCO_3$ (Facq et al., 2016) — that form in presence of Na, K, or Cl (Facq et al., 2016; Galvez et al., 2016).

5.5 Results

5.5.1 Bulk rock chemistry

The major bulk rock composition of the Milagrosa marbles, Atg-Di-Dol rocks and serpentinites, and the Almirez meta-ophicarbonates and host Chl-harzburgites are given in Table 5.2. In the CaO-MgO-SiO_2 ternary, the bulk compositions of Milagrosa and Almirez carbonate lenses plot along the calcite–antigorite join, mostly due to highly variable CaO and CO_2 contents at nearly constant Mg/Si ratio (Fig. 5.9a). In this ternary, the Milagrosa serpentinites and the Almirez Chl-harzburgite hosting the carbonate lenses have similar or lower Mg/Si ratios and have variable Ca/Si ratios plotting away from antigorite towards enstatite, tremolite, and diopside (Fig. 5.9b). Milagrosa serpentinite has bulk compositions similar to Almirez serpentinite (Garrido et al., 2005; Marchesi et al., 2013), and to abyssal peridotite, but are slightly richer in CaO, Al_2O_3 and SiO_2 (Fig. 5.9b, Table 5.2).

Milagrosa TiCl-Cal marbles have the lowest SiO_2 and MgO and the highest CaO contents among the investigated samples (Fig. 5.9a). Associated Di-Dol marbles have higher SiO_2 contents and lower CaO/MgO ratios, plotting close to the intersection of the antigorite-calcite and dolomite-diopside joins (Fig. 5.9a). The Milagrosa Atg-Di-Dol rocks are richer in SiO_2 and MgO while poorer in CaO and CO_2, remarkably similar to the Almirez meta-ophicarbonates (Fig. 5.9a).

Major variations in CaO, MgO and SiO_2 contents of the carbonate-bearing lithologies in both localities correlate with variable bulk rock CO_2 content, as illustrated by the inverse linear correlation between CO_2 and SiO_2 (Fig. 5.9c). The Al_2O_3 and total Fe_2O_3 contents decrease with increasing CaO and CO_2, and range from the relatively high Al_2O_3 (2.8 – 3.5 wt%) and Fe_2O_3 (7.5 – 9.1 wt%) in the host serpentinites and Chl-harzburgite to very low Al_2O_3 (0.5 – 0.7 wt%) and Fe_2O_3 (0.6 – 1.1 wt%) of the Milagrosa TiCl-Cal marble lenses

► ***Figure 5.9.*** *Bulk rock compositional variations of carbonate lenses and host peridotites from Milagrosa and Almirez.* ***(a)*** *CaO-MgO-SiO_2 (CMS) ternary compositional diagram with molar whole rock proportions, and projected mineral endmembers for comparison. Typical meta-sedimentary carbonate rocks fall within the field to the left of the dolomite-diopside join. Fields for compositions of other meta-ophicarbonates shown as a reference (Voltri Massif from Scambelluri et al. (2016); Central Alps: Stucki (2001); Fig. 5.1). See text for further discussion.* ***(b)*** *Detail from the Ca-poor part of the CMS-diagram in a). Data of Almirez Atg-serpentinites (hollow symbols) are from Garrido et al. (2005), Alt et al. (2012) and Marchesi et al. (2013).* ***(c)*** *Total carbon given as CO_2 vs. whole rock SiO_2.* ***(d)*** *Ni and Cr whole rock contents.* ***(e)*** *Calcite-dolomite weight ratio (as obtained from analysis by Chittick-apparatus) of carbonate rich lithologies plotted against CO_2-content.* ***(f)*** *Molar ferric / total iron ratio against CO_2 content; field of Almirez Chl-harzburgites after Marchesi et al. (2013).*

(Table 5.2). Milagrosa Atg-Di-Dol rocks and Almirez meta-ophicarbonates have intermediate Al_2O_3 (1.9 – 2.3 wt%) and Fe_2O_3 (4.0 – 6.2 wt%) contents.

The Na_2O and K_2O contents of carbonate lenses are close to or below the detection limits of XRF analyses, as in the host serpentinites and Chl-harzburgites (Table 5.2). The Almirez meta-ophicarbonate lenses are highly enriched in Ni and Cr (> 2000 ppm), approaching

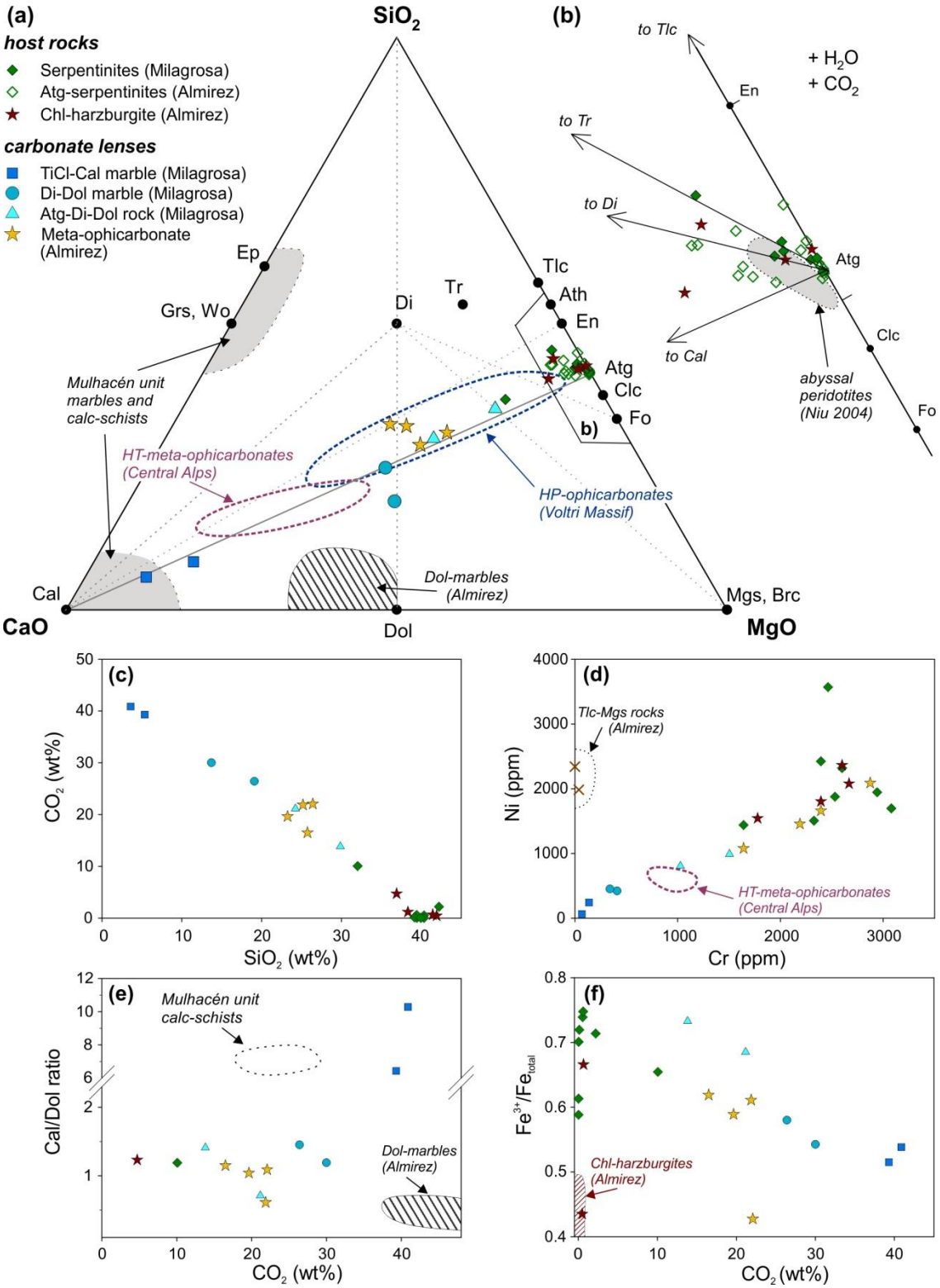

Table 5.2. *Whole-rock major element compositions of the serpentinites, marbles and meta-ophicarbonates from Milagrosa and Almirez; analysed by XRF (major and minor elements), IR-spectroscopy (C, S), potentiometric titration (FeO (titr)) and Chittick apparatus (calcite & dolomite fractions). Oxides and S are given in wt%; Cr, Co, Cu, Ni, V, and Zn in ppm*

Locality	**Milagrosa**													
Lithology	Dol-Atg-schist	Atg-serpentinite		Cpx-serpentinite					Atg-Di-Dol rock		Di-Dol marble		TiCl-Cal marble	
Sample	SN-23	SN-107	SN-109	SN-90	SN-96	SN-105	SN-102	SN-11	SN-97	SN-98	SN-99	SN-09	SN-101	SN-10
SiO_2 (wt%)	40.35	39.15	39.95	39.46	39.44	40.34	42.22	32.03	29.87	24.23	19.10	13.72	5.36	3.59
TiO_2	0.01	0.09	0.11	0.11	0.13	0.10	0.05	0.21	0.10	0.08	0.09	0.09	0.01	0.01
Al_2O_3	0.84	2.94	3.07	3.44	3.39	3.36	2.79	3.08	2.52	2.11	2.25	2.03	0.65	0.53
Fe_2O_3 [a]	5.73	5.87	4.74	6.33	6.26	5.08	5.37	3.79	3.75	2.78	1.64	1.38	0.57	0.35
$FeO_{(titr)}$	1.82	2.06	2.69	2.43	1.90	3.20	1.94	1.80	1.23	1.15	1.07	1.05	0.48	0.27
MnO	0.10	0.09	0.11	0.12	0.11	0.12	0.07	0.08	0.10	0.11	0.08	0.12	0.11	0.11
MgO	37.02	37.00	36.73	34.98	34.92	35.11	31.69	28.11	27.00	22.05	18.52	19.52	6.44	3.88
CaO	0.32	0.11	0.03	1.64	1.17	1.04	3.33	12.32	13.89	22.23	28.21	27.59	45.55	49.72
BaO	b.d.	b.d.	b.d.	b.d.	b.d.	b.d.	b.d.	b.d.	b.d.	b.d.	b.d.	b.d.	b.d.	b.d.
Na_2O	b.d.	b.d.	0.06	b.d.	0.09	0.03	b.d.	b.d.	b.d.	b.d.	0.02	b.d.	b.d.	b.d.
K_2O	0.01	0.01	0.01	0.01	0.02	0.01	0.01	0.01	0.01	0.01	0.01	b.d.	b.d.	b.d.
P_2O_5	0.002	0.003	0.009	0.004	0.002	0.005	b.d.	0.019	0.008	0.009	0.015	0.015	0.007	0.004
LOI	12.80	11.90	11.98	10.97	11.94	11.37	12.22	17.88	21.16	24.83	28.87	33.92	40.43	41.09
S	0.004	0.005	b.d.	b.d.	0.013	0.015	b.d.	0.028	b.d.	0.008	b.d.	b.d.	b.d.	0.028
CO_2 (TC)	0.55	0.12	0.03	0.04	0.61	0.03	2.19	10.08	13.82	21.16	26.40	30.01	39.31	40.88
Cr (ppm)	2600	2532	2326	2942	2395	2463	3079	1642	1505	1026	411	342	137	68
Co	109	94	88	87	80	93	51	67	42	34	18	23	b.d.	b.d.
Cu	b.d.	b.d.	27	15	26	b.d.	24	b.d.	21	b.d.	b.d.	b.d.	b.d.	b.d.
Ni	2320	1877	1506	1946	2423	3570	1696	1438	989	805	419	450	243	64
V	34	67	63	78	78	74	69	55	49	39	35	31	15	13
Zn	45	36	51	51	51	51	55	45	31	26	18	19	9	7
Total	99.63	99.81	100.00	100.14	99.98	100.51	100.32	99.73	99.97	99.83	99.98	99.54	99.66	99.58
Fe^{3+}/Fe_{total}	0.74	0.72	0.61	0.70	0.75	0.59	0.71	0.65	0.73	0.69	0.58	0.54	0.52	0.54
FeO_{model} [b]			1.47	1.24				1.49	0.92			0.90		0.12
X_{Serp} [c]	0.99	1.00	1.00	0.99	0.98	0.99	0.95	0.80	0.74	0.58	0.47	0.45	0.16	0.09
Cal (wt%)								12.67	17.71	24.20	35.29	35.83	73.08	84.13
Dol (wt%)								10.67	12.59	34.09	24.32	30.05	11.36	8.18
Cal/Dol ratio								1.19	1.41	0.71	1.45	1.19	6.43	10.28
Carb. fraction								0.23	0.30	0.58	0.60	0.66	0.84	0.92

b.d.: below detection limit (cf. Table 3.1); n.a.: not analysed; LOI: loss on ignition (corrected for oxidation gain).

[a] *Fe_2O_3 by difference from total Fe_2O_3 (XRF) and FeO (determined separately).*

[b] *Estimated effective FeO used in pseudosection models after subtracting magnetite and Fe^{3+} in antigorite (estimated by mass-balance and image analysis; cf. Sec. 5.4.1).*

[c] *X_{Serp} = projected position on the compositional mixing vector serpentinite-calcite used in Fig. 5.16 [calculated as ∑ (Mg, Si, Al, Fe, H_2O) / ∑ (Mg, Si, Al, Fe, H_2O, Ca, CO_2)]*

Table 5.2. continued. *Whole-rock major element compositions of the serpentinites, marbles and meta-ophicarbonates from Milagrosa and Almirez; analysed by XRF (major and minor elements), IR-spectroscopy (C, S), potentiometric titration (FeO (titr)) and Chittick apparatus (calcite & dolomite fractions). Oxides and S are given in wt%; Cr, Co, Cu, Ni, V, and Zn in ppm*

		Almirez													
Calc-schist		Meta-ophicarbonate				Tlc-Mgs rock	Tr-Mgs rock	Dol-marble				(Carb-bearing) Chl-harzburgite			
SN-30	SN-42	SN-143	SN-136	SN-135	SN-138	SN-137b	SN-131	SN-124	SN-127a	SN-141	SN-130	SN-128	SN-134	SN-139	SN-146
41.57	34.70	26.42	25.18	23.26	25.74	8.52	14.44	2.92	2.27	2.73	6.35	41.93	36.92	38.34	41.45
0.19	0.05	0.07	0.03	0.03	0.06	0.12	0.17	0.01	0.02	0.02	0.12	0.05	0.03	0.05	0.08
4.21	1.14	2.19	1.86	1.94	2.29	2.30	5.12	0.41	0.46	0.46	2.64	2.59	2.09	1.68	2.82
1.13	0.29	1.14	3.65	3.33	4.06	2.38	1.89	0.04	0.00	0.42	1.28	3.63	3.73	6.07	5.91
0.91	0.22	1.37	2.09	2.09	2.25	1.77	2.88	0.30	0.23	0.15	1.89	4.24	2.72	2.15	2.67
0.31	0.01	0.06	0.12	0.13	0.13	0.26	0.11	0.04	0.04	0.03	0.09	0.09	0.07	0.10	0.10
0.66	1.80	17.92	18.61	21.17	23.47	25.65	28.47	20.26	20.30	14.74	14.79	37.84	32.38	34.50	32.81
26.90	32.69	26.44	23.73	24.10	20.87	19.64	12.98	29.26	29.75	35.94	32.50	0.04	5.82	1.27	3.83
0.01	b.d.	b.d.	b.d.	b.d.	b.d.	0.02	0.01	b.d.	b.d.	b.d.	b.d.	b.d.	b.d.	b.d.	b.d.
0.64	0.07	0.28	0.02	b.d.	b.d.	b.d.	0.05	b.d.	b.d.	0.03	0.17	b.d.	b.d.	b.d.	0.07
0.50	0.35	0.06	0.01	0.01	0.01	0.01	0.01	0.15	0.12	0.09	0.03	0.01	0.01	0.01	0.02
0.063	0.060	0.028	0.019	0.014	0.006	0.010	0.067	0.009	0.011	0.011	0.037	0.012	0.010	0.011	0.004
22.53	28.00	23.82	24.13	23.01	19.71	39.44	33.01	45.73	46.06	44.76	39.61	9.20	15.69	14.21	9.28
b.d.	0.022	b.d.	b.d.	0.120	0.182	0.007	0.013	b.d.	b.d.	b.d.	b.d.	0.025	0.010	0.008	0.103
21.87	28.40	22.07	21.88	19.63	16.50	38.26	28.97	46.15	44.72	45.85	39.24	0.48	4.72	1.20	0.65
b.d.	b.d.	1642	2189	2395	2874	b.d.	684	b.d.	b.d.	b.d.	b.d.	2668	1779	2600	2395
12	b.d.	38	83	146	120	93	124	b.d.	b.d.	b.d.	22	96	69	103	94
62	b.d.	43	74	36	15	46	404	b.d.	b.d.	b.d.	b.d.	b.d.	b.d.	b.d.	b.d.
27	b.d.	1077	1456	1659	2087	2002	4198	b.d.	b.d.	15	102	2078	1543	2362	1803
35	18	62	48	52	62	22	37	13	11	11	27	57	40	55	68
42	34	22	43	64	53	22	45	10	10	9	27	64	60	74	47
99.64	99.39	100.16	99.94	99.63	99.25	100.34	99.79	99.13	99.26	99.38	99.52	100.25	99.91	99.03	99.59
0.53	0.54	0.43	0.61	0.59	0.62	0.55	0.37	0.10	0.00	0.72	0.38	0.43	0.55	0.72	0.67
					1.25										
		0.51	0.54	0.57	0.63							0.99	0.91	0.98	0.96
	59.75	24.72	18.48	25.60	20.19			27.51	36.51	30.88	29.34		7.82		
	8.03	22.77	30.05	24.59	17.53			69.90	62.11	57.63	50.92		6.38		
	7.44	1.09	0.61	1.04	1.15			0.39	0.59	0.54	0.58		1.23		
	0.68	0.47	0.49	0.50	0.38			0.97	0.99	0.89	0.80		0.14		

b.d.: below detection limit (cf. Table 3.1); n.a.: not analysed; LOI: loss on ignition (corrected for oxidation gain).

[a] *Fe_2O_3 by difference from total Fe_2O_3 (XRF) and FeO (determined separately).*

[b] *Estimated effective FeO used in pseudosection models after subtracting magnetite and Fe^{3+} in antigorite (estimated by mass-balance and image analysis; cf. Sec. 5.4.1).*

[c] *X_{Serp} = projected position on the compositional mixing vector serpentinite-calcite used in Fig. 5.16 [calculated as $\sum$ (Mg, Si, Al, Fe, H_2O) / $\sum$ (Mg, Si, Al, Fe, H_2O, Ca, CO_2)]*

contents typical of mantle peridotites and similar to those of the host Chl-harzburgite (Fig. 5.9d). The Milagrosa Atg-Di-Dol rocks and Di-Dol marbles show a lesser, but significant, enrichment in Ni and Cr, which decreases with increasing carbonate content (Fig. 5.9 c & d). These bulk chemical characteristics distinguish the Milagrosa and Almirez serpentinite-hosted carbonate rocks (marble lenses, Atg-Di-Dol rocks and meta-ophicarbonates) from other widespread carbonate rocks of the NFC Mulhacén unit. These carbonate rocks that are not hosted in serpentinites or Chl-harzburgite have markedly different bulk MgO/SiO_2 ratios (grey and dashed fields in Fig. 5.9a), and Ni and Cr contents below detection limit of XRF analysis (Table 5.2). Likewise, the calcite to dolomite ratio in the carbonate fraction of the Almirez and Milagrosa carbonate lenses mostly ranges between 0.6 – 1.4 (except for TiCl-Cal marbles), independently of the bulk rock CO_2-content and metamorphic grade (Fig. 5.9e). In contrast, the carbonate fraction in NFC Dol-marbles and calc-schists is either dominated by dolomite or calcite (Fig. 5.9e; Table 5.2).

The bulk rock Fe^{3+}/Fe_{total} ratio decreases with increasing CO_2-contents, from 0.59 – 0.75 in Milagrosa serpentinites to 0.52 – 0.54 in the TiCl-Cal marble lenses (Fig. 5.9f, Table 5.2). Milagrosa Atg-Di-Dol rocks have bulk rock Fe^{3+}/Fe_{total} ratios similar to some of their host serpentinites (Fig. 5.9f), and higher than the Almirez meta-ophicarbonate of equivalent major element composition. These differences may be due to the incorporation of Fe^{3+} in antigorite in the lower metamorphic grade Milagrosa serpentinites and Atg-Di-Dol rocks, while in the Almirez antigorite-absent meta-ophicarbonate ferric iron is mostly partitioned into magnetite. The lower bulk Fe^{3+}/Fe_{total} of meta-ophicarbonate lenses within prograde Almirez Chl-harzburgites relative to the serpentinite-hosted Milagrosa Atg-Di-Dol rocks (Fig. 5.9f) is in accordance with the decrease in bulk Fe^{3+}/Fe_{total} from Atg-serpentinite to Chl-harzburgite described elsewhere in Almirez (Debret et al., 2015; their Figure 4). However, the Almirez meta-ophicarbonates have generally higher bulk Fe^{3+}/Fe_{total} (~0.6) than the host Chl-harzburgite (0.4 – 0.5; Fig. 5.9f).

5.5.2 Mineral Chemistry

Representative compositions and structural formulae of all minerals are listed in Tables A-5.4 – A-5.8 of the Appendix to Ch. 5 (section *5.7*).

5.5.2.1 Carbonates

In the Milagrosa marble lenses, calcite in the matrix shows a large variation in X_{MgCO3} [X_{MgCO3} = Mg / (Mg + Ca + Fe)] from nearly pure $CaCO_3$ to Mg-calcite with X_{MgCO3} = 0.047 (Fig. 5.5a; Appendix Fig. A-5.1). Tr-bearing Di-Dol marbles contain calcite with generally lower X_{MgCO3} values (0.005 – 0.038) than the TiCl-Cal-marbles, but in both cases there is a relatively large variability of Mg-contents within single samples; often with sharp compositional contrasts between neighbouring calcite grains (Fig. 5.5a). The highest Mg-contents in Mg-calcite are present in inclusions within Ti-clinohumite and diopside (X_{MgCO3} = 0.024 – 0.072). Such Mg-calcite inclusions can be used to estimate minimum peak temperatures for the formation of the host mineral phases (Ferry, 2001; Mizuochi et al., 2010). Using the Fe-free formulation of the calcite-dolomite solvus thermometer by Anovitz and Essene (1987), calcite inclusions with the highest Mg-contents within Ti-clinohumite and diopside from the Milagrosa marble lenses (5 measurements) yield temperatures of 515 – 600 °C (Appendix Table A-5.4). In matrix calcite, reintegration of vermicular dolomite exsolutions (using microprobe analysis with a widened beam and image analysis to estimate the fraction of exsolved dolomite, Fig. 5.5a) gives X_{MgCO3} values of 0.049 – 0.055, corresponding to 520 – 550 °C. Calcite in all Milagrosa lithologies mostly has very low Fe contents (X_{FeCO3} < 0.005). Dolomite has similar low Fe contents in TiCl-Cal-marbles, and is significantly Fe-richer in Di-Dol-marbles and Atg-Di-Dol rocks (X_{FeCO3} = 0.009 – 0.150).

Calcite in Almirez meta-ophicarbonates shows similarly variable X_{MgCO3} values (Appendix Fig. A-5.1). The highest measured Mg content (X_{MgCO3} = 0.096) in a Mg-calcite inclusion within a Ti-clinohumite porphyroblast yields a minimum peak temperature of about 660 °C. Matrix calcite in equilibrium with dolomite has substantially lower X_{MgCO3} (0.017 – 0.052; corresponding to 310 – 580 °C) than Mg-calcite inclusions. Aragonite-inclusions in olivine, diopside and Ti-clinohumite have X_{MgCO3} -values close to or below the detection limit and negligible Fe-contents (Appendix Table A-5.4). Unlike Mg-calcite, dolomite has relatively homogeneous compositions (X_{CaCO3} = 0.503 – 0.513). Dolomite in the Almirez meta-ophicarbonates is not zoned, unlike dolomite in HP/UHP carbonate rocks elsewhere (e.g. Ferrando et al., 2017; Li et al., 2014). In the Mgs-Tlc level, dolomite has a very restricted compositional range (X_{CaCO3} = 0.496 – 0.501), and magnesite is rich in iron (3.5 – 4.0 wt%). Scarce dolomite and magnesite in Chl-harzburgites close to the carbonate lenses have compositions very similar to those in the Mgs-Tlc level. Dolomite in meta-

ophicarbonate clasts enclosed in carbonate breccia (Tr-Di-Dol rocks) is enriched in Fe and has lower X_{CaCO3} (0.498 – 0.508) than in the meta-ophicarbonate lens.

5.5.2.2 Olivine

Olivine in Almirez meta-ophicarbonate has a forsterite content of X_{Mg} = 0.93 – 0.95 [X_{Mg} = Mg/(Mg-Fe)] (Fig. 5.10a), significantly higher than olivine in the host Chl-harzburgites and in Cpx-serpentinites at Almirez (X_{Mg} = 0.89 – 0.91 and 0.91 – 0.93, respectively (Padrón-Navarta et al., 2011)), and is not zoned. Notably, olivine in the meta-ophicarbonate has high NiO (0.12 – 0.24 wt%) and relatively high MnO contents (0.25 – 0.36 wt%; Appendix Table A-5.5), which is comparable to olivine compositions in Atg-serpentinite and Cpx-serpentinite at Almirez (Padrón-Navarta et al., 2011). In contrast, olivine in high grade or contact-metamorphic marbles has typically very low NiO (normally below detection limit) and contains less iron (e.g. Mazzoli et al., 2013; Mizuochi et al., 2010). Rare olivine in Cpx-serpentinites at Milagrosa has compositions similar to those of Cpx-serpentinites at Almirez (about Fo_{92}, with relatively low NiO contents; Fig. 5.10a).

5.5.2.3 Ti-clinohumite and Ti-chondrodite

Divalent cation contents (Mg, Fe, Mn, Ni) in Ti-clinohumite in Almirez meta-ophicarbonate are very similar to those of coexisting olivine (X_{Mg} = 0.93 – 0.96, and slightly lower NiO values, Fig. 5.10b and Appendix Table A-5.5). This agrees with the nearly equal partitioning of divalent cations between olivine and Ti-clinohumite reported by López Sánchez-Vizcaíno et al. (2005) for Atg-serpentinites and Chl-harzburgites at Almirez. Ti-clinohumite and olivine in the meta-ophicarbonate lenses contain less Fe than those in the host Chl-harzburgites (Fig. 5.11a & b), in accordance with the lower Fe contents of the bulk rock. This is also the case at Milagrosa: while Ti-clinohumite contains only little Fe and no NiO in TiCl-Cal-marbles, the content of these two elements in Ti-clinohumite increases to X_{Mg} = 0.92 – 0.94 and up to 0.07 wt% NiO in Atg-Di-Dol rock, and to X_{Mg}=0.91 – 0.93 and up to 0.20 wt% NiO in host serpentinites (Fig. 5.10b).

TiCl-Cal marbles lenses at Milagrosa contain Ti-clinohumite with X_{Ti} = 0.17 – 0.24 (X_{Ti} = Ti atoms per 13 cations) and X_F = 0.18 – 0.21 (X_F = F/2; Fig. 5.10c). In contrast, Ti-clinohumite is fluorine-free and nearly saturated in Ti in Atg-serpentinites (5.1 – 5.5 wt% TiO_2, X_{Ti} = 0.42 – 0.47), similar to that in the Almirez Atg-serpentinites (López Sánchez-Vizcaíno et al., 2005). Ti-clinohumite in Milagrosa Cpx-serpentinite and Atg-Di-Dol rock has

intermediate compositions between the two extremes, with X_{Ti} = 0.28 – 0.39 and X_F = 0.07 – 0.10 in cores, and rim compositions of X_{Ti} = 0.2 and X_F = 0.18 (Fig. 5.10c). These values are somewhat similar to Ti-clinohumite compositions in Chl-harzburgites at Almirez (López Sánchez-Vizcaíno et al., 2005), but with a more pronounced variability along the $TiO_2Mg_{-1}F_{-2}$ exchange vector. Ti-clinohumite in the Almirez meta-ophicarbonate lenses is clearly distinct from Ti-clinohumite reported by López Sánchez-Vizcaíno et al. (2005) and Padrón-Navarta et al. (2011) for the host Chl-harzburgites, showing high fluorine contents (Fig. 5.10c). High-T metamorphic Ti-clinohumite in sedimentary marbles (as for example from the western Betic Cordillera, Spain (Mazzoli et al., 2013) or from the Bergell contact aureole (Gieré, 1987)) tend to have even higher fluorine contents, which often exceed the 1:1 $TiO_2Mg_{-1}F_{-2}$ exchange that is limited by the maximum Ti-content in TiCl of X_{Ti} = 0.5 (Fig. 5.10c).

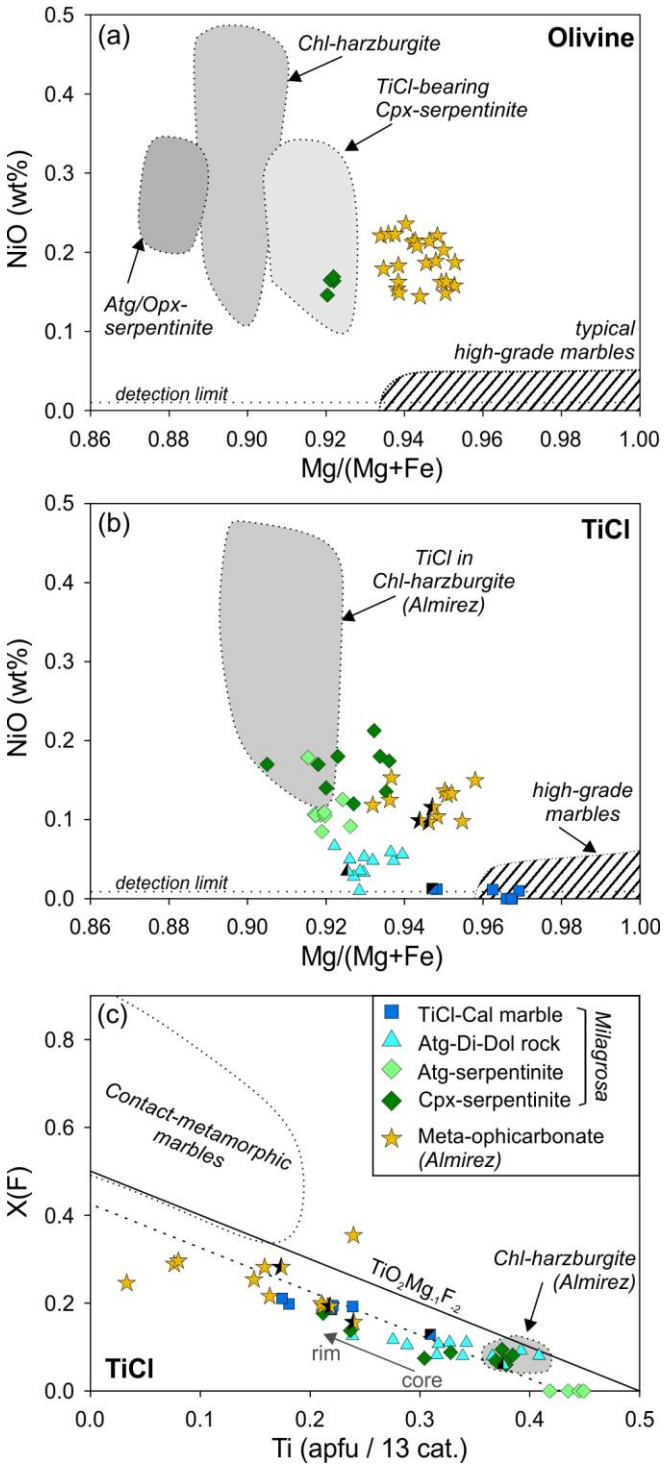

► ***Figure 5.10.*** *Composition of olivine* ***(a)*** *and Ti-clinohumite* ***(b & c)*** *in carbonate lenses and host peridotites at Milagrosa and Almirez (common legend in Fig. 5.10c); in comparison with olivine and Ti-clinohumite from Almirez Chl-harzburgites and serpentinites (grey fields; López Sánchez-Vizcaíno et al., 2005; Padrón-Navarta et al., 2011) and contact metamorphic high-grade marbles of the western Betics (Mazzoli et al., 2013). X(F) = F (atoms per 13 cations) / 2. Half-black symbols in b & c show co-existing Ti-chondrodite compositions (normalized to 7 cations).*

Ti-chondrodite (TiChn) is preserved occasionally in the cores of Ti-clinohumite porphyroblasts in Milagrosa carbonate lenses and Almirez meta-ophicarbonate. Compared to Ti-clinohumite, Ti-chondrodite is generally richer in TiO_2 (about 3 – 4 wt% higher than coexisting Ti-clinohumite) and has lower X_F, with similar NiO contents and X_{Mg} values (half-black symbols in Fig. 5.10b & c; Appendix Table A-5.5).

5.5.2.4 Clinopyroxene

Clinopyroxene in the carbonate rock lenses from Milgrosa and Almirez is almost pure diopside (X_{Mg} = 0.97 – 0.99). Al_2O_3-contents of diopside are low in both cases, but they are slightly higher in the Almirez meta-ophicarbonates (about 0.05 – 0.09 wt%) than in the marble lenses and Atg-Di-Dol rocks at Milagrosa (< 0.03 wt%). In the Milagrosa Cpx-serpentinites, relict primary clinopyroxene is partially preserved, with 0.8 – 1.4 wt% Al_2O_3, ca. 0.4 wt% Cr_2O_3, 0.25 – 0.48 wt% Na_2O and 0.2 – 0.5 wt% TiO_2, but most clinopyroxene is also relatively pure diopside (with X_{Mg} =0.96 – 0.98) (Appendix Table A-5.6).

5.5.2.5 Antigorite

Antigorite in the Milagrosa serpentinites is generally rich in Al_2O_3 (up to 4 wt%), rather poor in Fe [$Mg/(Mg + FeO_{total})$ = 0.95 - 0.97], Cr_2O_3 (up to 0.4 wt%) and NiO (< 0.35 wt%; Appendix Table A-5.7), and diverges from the ideal Tschermak's exchange vector towards lower Al and Si values (Fig. 5.11). No major compositional differences exist between antigorite in Cpx-serpentinite and Atg-serpentinite. In a plot of Si vs. y_{Atg} = Al/8 (Padrón-Navarta et al., 2013) (Fig. 5.11), most of the analyses cluster close to the maximum solubility of Al in antigorite. In contrast to the very high Al-contents of Atg in the Milagrosa serpentinites, Atg-Di-Dol rocks contain antigorite with y_{Atg} = 0.1 – 0.4.

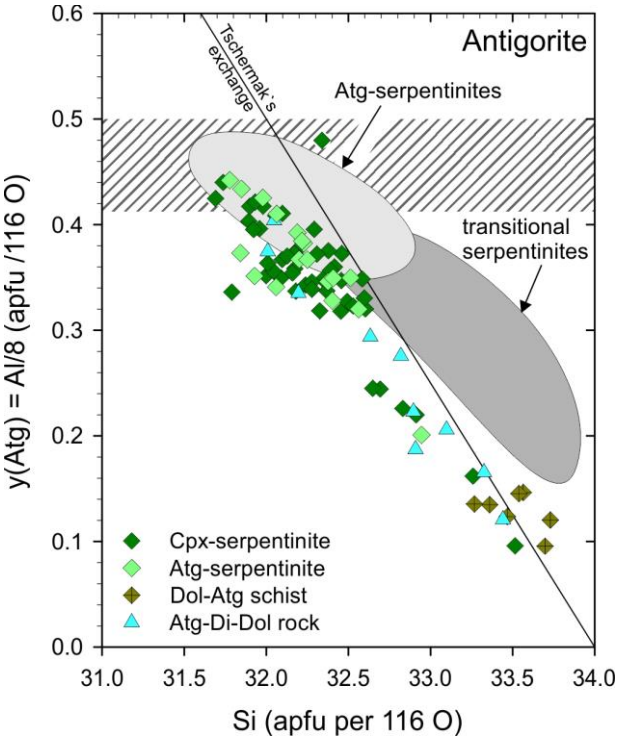

Figure 5.11. *Antigorite compositions in Milagrosa serpentinites and Atg-Di-Dol-rocks in comparison to Almirez serpentinites and transitional rocks (grey fields; after Padrón-Navarta et al., 2011) in a y(Atg) = total Al / 8 vs. Si plot (calculated on the basis of 116 O, assuming a polysome m = 17). The line represents an ideal Tschermak`s exchange, with the maximum solubility of Al in Atg indicated by the horizontal band (Padrón-Navarta et al., 2013).*

The lower y_{Atg} values correspond to mineral assemblages dominated by Di-Dol-Chl with only minor antigorite, while the higher y_{Atg} values characterize rocks in which antigorite is more abundant than chlorite. Antigorite in Dol-Atg-schists situated about 6 m apart from the Milagrosa marble lenses has distinctly lower y_{Atg} (~0.13).

5.5.2.6 Chlorite

Chlorite in host peridotites and carbonate rock lenses at both Milagrosa and Almirez is dominantly penninite with high X_{Mg} (0.94 – 0.98). Al_2O_3-contents are relatively low (12 – 16 wt%; 2.8 – 3.8 Al atoms per formula unit per 28 O; Appendix Table A-5.7). Chlorite in Cpx-serpentinites from Milagrosa shows minor deviation from an ideal Tschermak's exchange due to the substitution of up to 0.14 apfu Cr for Al (Fig. 5.12). The same trend of chlorite compositions along the $CrAl_{-1}$ exchange is typical for peridotites and has been reported for Chl-serpentinites and transitional lithologies at Almirez (Padrón-Navarta et al., 2011). The Cr content in chlorite from Milagrosa TiCl-Cal-marble and Di-Dol-marble lenses is below or close to the detection limit, whereas Atg-Di-Dol rocks contain chlorite with Cr-contents resembling those of the host serpentinites. Chlorite in the Almirez meta-ophicarbonate lenses has elevated contents of Al (3.0 – 3.9 apfu) and Cr (up to 0.35 apfu). The trend towards higher Al contents in these rocks is comparable to that of chlorite formed during Atg-breakdown in spinifex-harzburgites at Almirez (grey fields in Fig. 5.12), but with a higher Tschermak's exchange.

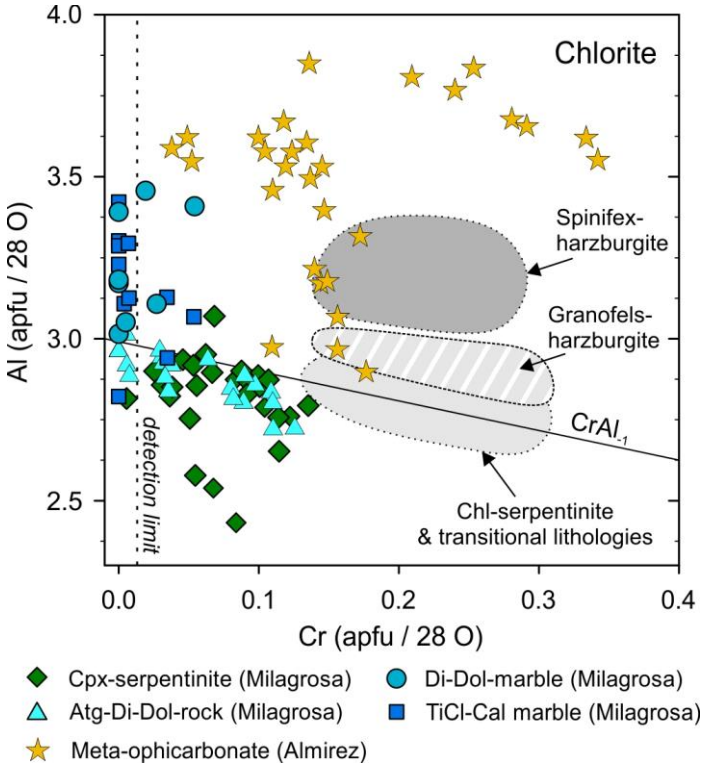

► ***Figure 5.12.*** *Al vs. Cr compositions of chlorite in Milagrosa carbonate lenses and host serpentinites, and in Almirez meta-ophicarbonate. The grey fields show the range of chlorite compositions in the Almirez serpentinites and Chl-harzburgite (from Padrón-Navarta et al., 2011); the line represents the CrAl-1 exchange vector.*

5.5.2.7 Other phases

Scarce tremolite in Milagrosa Cpx-serpentinites and retrograde tremolite in carbonate lenses are very close to the pure endmember, with X_{Mg} = 0.97 – 0.99, Na and Al < 0.15 wt% (Appendix Table A-5.6). Notably, magnetite in the Almirez meta-ophicarbonates is enriched in Cr_2O_3 (3 – 6 wt%), MgO (1.5 – 2.5 wt%), MnO and NiO (both about 0.3 – 0.6 wt%) (Appendix Table A-5.8). Magnetite in Milagrosa Atg-Di-Dol rocks and Di-Dol marble shows a similar, but less pronounced enrichment in Cr, Mg, Mn and Ni. Associated ilmenite has high MgO and MnO contents (up to 9.1 and 4.5 wt%, respectively).

5.5.3 P-T-t constraints

5.5.3.1 Milagrosa serpentinite and marble lenses

Calcite–dolomite thermometry in Milagrosa serpentinite-hosted marble lenses yields peak metamorphic temperatures in the range of ~550–600 °C (*cf.* section *5.5.2.1*). Although metamorphic olivine is abundant in typical serpentinite at this temperature range (Bucher and Grapes, 2011), olivine is mostly absent in Milagrosa serpentinites due to their relatively low Mg/Si and high Fe^{3+}/Fe_{tot} bulk rock ratios (Fig. 5.9). In the P–T pseudosection of Cpx-serpentinite —obtained after subtracting the bulk rock ferric iron in magnetite (cf. section *5.4.1*)— the observed assemblage Chl-Atg-Tr-Cpx in Milagrosa Cpx-serpentinite is stable in a large divariant field (Fig. 5.13a). The absence of serpentinite with Chl-Ol-Atg-Tr and Chl-Atg-Cpx-Opx assemblages constrains the equilibrium temperature to <550–650 °C, depending on the equilibration pressure (Fig. 5.13a). At ~600 °C —as obtained from carbonate thermometry in the marble lenses— olivine would form at <0.9 GPa, providing a minimum pressure estimate for the assemblage Chl-Atg-Tr-Cpx (Fig. 5.13a). The equilibration of Milagrosa serpentinite at >0.8 GPa and <650 °C is further supported by the lack of petrographic evidence of breakdown of F-free, Ti-saturated Ti-clinohumite to olivine + ilmenite (brown dashed line in Fig. 5.13a), which is observed in higher-T Atg-serpentinite from the Almirez massif (López Sánchez-Vizcaíno et al., 2009; López Sánchez-Vizcaíno et al., 2005).

The minimum temperatures of 550–600 ° C estimated by calcite–dolomite thermometry of Mg-calcite inclusions in Ti-clinohumite from the marble lenses (*cf.* section *5.5.2.1*; Fig. 5.5a) are consistent with pseudosection constraints of marble lenses and Atg-Di-Dol rocks (Fig. 5.13b). In the fluid-saturated isobaric T–X_{CO2} pseudosection of the TiCl-Cal marble

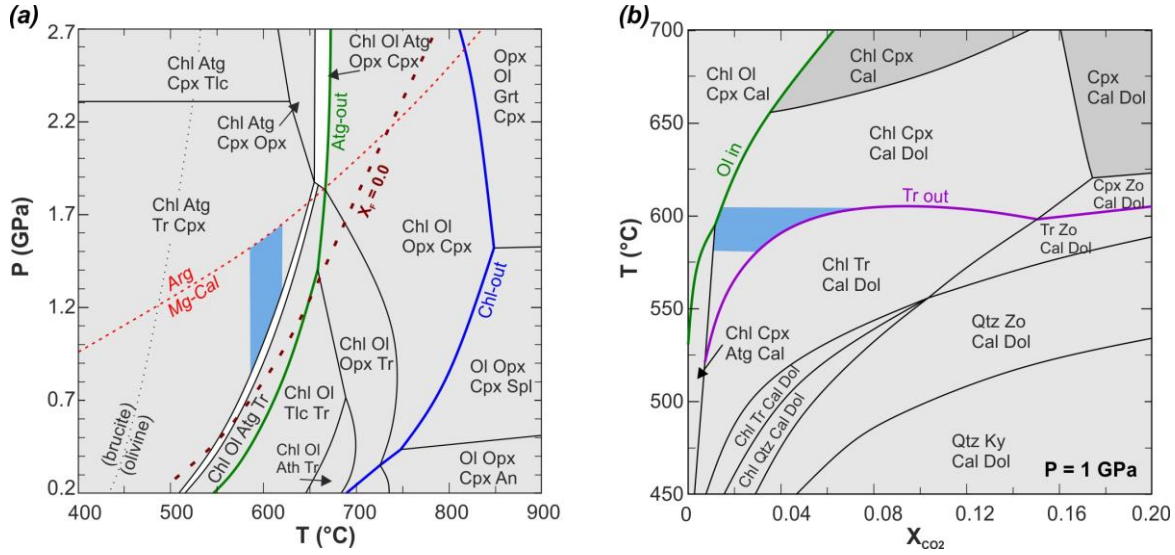

Figure 5.13. *P–T constraints for Milagrosa Cpx-serpentinite (a) and TiCl-Cal marble (b).* ***(a)*** *P–T section computed from bulk composition SN-90 using a reduced model FeO content (Table 5.2; Sec. 4.4). The blue box area represents the estimated field of peak metamorphism when assuming that no aragonite was present. The TiCl-breakdown curve (brown dashed line) at XF=0.0 for F-free, Ti-saturated Ti-clinohumite in serpentinite is taken from experiments by Weiss (1997). All fields contain a H_2O-fluid phase.* ***(b)*** *Fluid-saturated, isobaric T–X_{CO2} pseudosection of Milagrosa TiCl-Cal-marble (SN-10). The range of T and X_{CO2} conditions estimated for peak metamorphism is shown in blue.*

(Fig. 5.13b), the absence of tremolite or antigorite at 1 GPa in the peak assemblage Chl-Cpx-Cal-Dol constrains equilibration temperature >525 °C at 0.01 > X_{CO2} > 0.08. Although F and Ti stabilize Ti-clinohumite and Ti-chondrodite at high-T (Engi and Lindsley, 1980; Evans and Trommsdorff, 1983; Grützner et al., 2017; López Sánchez-Vizcaíno et al., 2005), no suitable solid solution models exist to model phase relations of Ti-clinohumite and Ti-chondrodite in fluorine- and titanium-bearing carbonate system (Weiss, 1997). In the computed pseudosection of Fig. 5.13b (F- and Ti-free system) these phases are metastable but their topologies are likely similar to that of olivine (Franz and Ackermand, 1980; Rice, 1980).

Figure 5.14a shows the P–T pseudosection for Almirez meta-ophicarbonates. This pseudosection is also appropriate to illustrate the phase relations of Milagrosa Atg-Di-Dol rocks due to their similar bulk composition (cf. section *5.5.1*; Fig. 5.9; Table 5.2). The isobaric prograde evolution for this bulk composition as a function of X_{CO2} is illustrated in T–X_{CO2} pseudosections at 1.0 and 1.7 GPa (Fig. 5.14b & c). In Milagrosa Atg-Di-Dol rocks, the common assemblage Atg-Chl-Cpx-Dol (± Cal, without Tr) provides a minimum P–T range of stability of >0.6 GPa at 550 °C (Tr-out line in Fig. 5.14a) and 1.0 GPa at 580 °C (Fig. 5.14b) (Connolly and Trommsdorff, 1991; their Figures 9b, 10b). These minimum P–T estimates are consistent with those derived from Milagrosa serpentinite and marble lenses (Fig. 5.13). The absence of olivine in Milagrosa Atg-Di-Dol rocks constrains their maximum equilibration

temperature to <615 °C (at 1.0 GPa) (Fig. 5.14b). At higher temperature, antigorite reacts out to form olivine, regardless of the fluid X_{CO2} (Fig. 5.14b). For this bulk composition, upper conditions for the stability of antigorite are 615 °C and $X_{CO2} < 0.025$ at 1.0 GPa (point i2' in Fig. 5.14b) or 625 °C and $X_{CO2} < 0.006$ at 1.7 GPa (point i2 in Fig. 5.14c). In the range of equilibration temperature (550 – 600 °C) of Milagrosa serpentinites and marble lenses, the absence of aragonite bounds their equilibration pressure to <1.4 – 1.5 GPa (aragonite-in reaction in Fig. 5.14a). Due to the fast kinetics of the aragonite–calcite phase transition, we cannot exclude, however, that aragonite was present at peak pressure but broke down to Mg-calcite during exhumation. The P–T conditions (1.0 – 1.4 GPa; 550 – 600°C) estimated for the Milagrosa carbonate-silicate rocks are within the range of peak metamorphic conditions inferred for marbles, calcschists, and amphibolite and garnet mica schists of the eastern part of the NFC, but are lower than the peak conditions recorded in eclogites and metaevaporites (Booth-Rea et al., 2015; Gómez-Pugnaire et al., 1994; Gómez-Pugnaire et al., in press; López Sánchez-Vizcaíno et al., 1997).

5.5.3.2 Almirez meta-ophicarbonate lenses

Experimental work, phase modelling and petrological constraints indicate that dehydration of Atg-serpentinite to Chl-harzburgite in Almirez occurred at ~660 °C and 1.8–1.9 GPa (Fig. 5.14a; yellow star on the P-T-t path) (López Sánchez-Vizcaíno et al., 2009; Padrón-Navarta et al., 2010a). Thermodynamic phase modelling reveals that the Almirez meta-ophicarbonates reached similar P-T peak conditions as their host Chl-harzburgite (Fig. 5.14a & c). The assemblage Chl-Ol-Cpx-Dol-Arg of Almirez meta-ophicarbonate requires equilibration at T > 580°C and P > 1.6 GPa (Fig. 5.14c). These minimum equilibration conditions are consistent with the absence of antigorite (Fig. 5.14a & c; T beyond the Atg-out condition) and the coexistence of aragonite in equilibrium with diopside and olivine (Fig. 5.8g & h and Fig. 5.14a, solid red and stippled orange lines). The composition of calcite inclusions (X_{CaCO3} = 0.897) in olivine and Ti-clinohumite is similar to that of Mg-calcite formed after aragonite breakdown as experimentally determined at 650 – 670°C and 1.8 – 2 GPa (Hermann et al., 2016). The phase proportions predicted by thermodynamic modelling at these P-T conditions are in good agreement with the observed modal proportions (yellow star in Fig. 5.14a). These data indicate that Almirez meta-ophicarbonate was stable in the Chl-harzburgite facies beyond the conditions of antigorite dehydration (Fig. 5.14a). For peak temperatures in the range of 670 – 680 °C (Fig. 5.14a; P-T-t path after Laborda-López et al., 2018), the assemblage Chl-Ol-Cpx-Dol-Cal limits the composition of the fluid to $0.004 < X_{CO2} < 0.007$

(yellow star in Fig. 5.14a & c). Calcite–dolomite thermometry of matrix carbonate yields T <550 °C, which records retrograde re-equilibration conditions (Appendix Table A-5.4), a common feature of high-grade carbonate rocks (Ferry, 2001; Mizuochi et al., 2010).

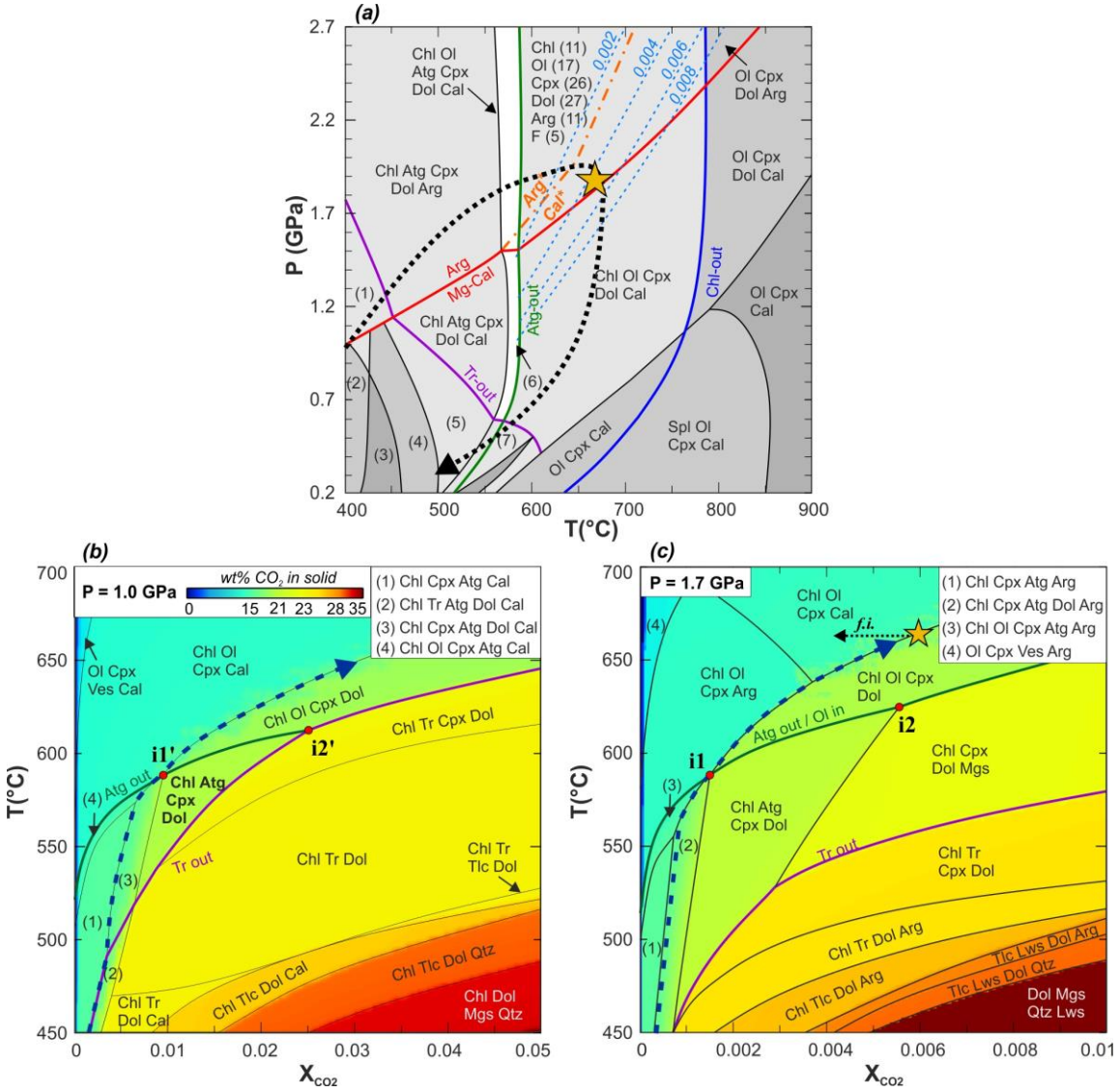

Figure 5.14. *P–T–X_{CO2} constraints of meta-ophicarbonate.* ***(a)*** *P–T pseudosection of Almirez meta-ophicarbonate (SN-138). Calculated mineral modes (wt%; including fluid F) are given in brackets at the peak conditions (yellow star) according to the Almirez P–T path (black dotted arrow, after Laborda-López et al., 2018). All fields contain fluid with X_{CO2} in equilibrium with the ophicarbonate (blue dashed lines). The aragonite-calcite transition is shown as predicted by the model (red solid line) and as determined experimentally by Hermann et al. (2016) in a carbonate-pure system (orange stippled line). Assemblages in numbered fields: (1) Chl Atg Tr Dol arag, (2) Atg Tr Dol Cal, (3) Atg Tr Cal, (4) Chl Atg Tr Cal, (5) Chl Atg Tr Cpx Cal, (6) Chl Ol Atg Cpx Dol Cal, (7) Chl Ol Tr Dol Cal.* ***(b and c)*** *Isobaric fluid-saturated T-XCO2 pseudosections at 1.0 and 1.7 GPa for the same rock composition as in (a), superposed on the solid rock CO_2 content (common colour scale in b). Coexisting aragonite/calcite and dolomite indicate a rock-buffered fluid evolution path as shown by the blue dashed arrows. Black dotted arrow (f.i.): expected evolution if pervasive fluid-infiltration decarbonation during host serpentinite dehydration occurs.*

5.6 Discussion

5.6.1 Origin of the protoliths of NFC serpentinite-hosted carbonate-silicate rocks

Meta-serpentinites from the NFC record a history of Jurassic seafloor alteration (Alt et al., 2012; Laborda-López et al., 2018; Puga et al., 2011) possibly in an ocean-continent transition setting (the S–SE Iberian paleo-margin) and narrow oceanic basin, similarly to that proposed for the origin of their Alps and Apennines counterparts (Lagabrielle et al., 2015). In the middle Miocene, subduction of the Iberian margin beneath the extended Alborán continental domain caused HP metamorphism of the NFC (cf. section *5.2*; Fig. 5.2c). In the investigated NFC ultramafic massifs, carbonates occur in the Milagrosa TiCl-Cal and Di-Dol marbles, and Atg-Di-Dol rocks, all of them hosted in serpentinite (Fig. 5.9a), while in the Almirez massif they occur as meta-ophicarbonate lenses hosted in Chl-harzburgite; hereafter, we will refer to all these lithologies as (meta-) serpentinite-hosted carbonate-silicate rocks. These NFC lithologies may have formed —and modified— during the Jurassic oceanic stage of development of the passive margin, and the ensuing Miocene subduction of this basin and its continental margin (Fig. 5.15).

Ophicarbonates and related carbonate-silicate rocks with variable bulk major element compositions —notably SiO_2, CaO, and MgO— may form in oceanic and subduction settings (Fig. 5.15), by leaching of alkali earth elements from silicate minerals and precipitation of carbonate upon mixing with dissolved inorganic carbon. In slow spreading mid-ocean ridges (Fig. 5.15a), serpentinite-hosted carbonate-silicate rocks occur in the stockwork of submarine low-T hydrothermal fields (Lafay et al., 2017; Ludwig et al., 2006; Schwarzenbach et al., 2013), in detachment faults of oceanic core complexes (Bach et al., 2011; Picazo et al., 2013; Schroeder et al., 2015), and in transform faults (Alt et al., 2018; Bonatti et al., 1980). In these settings, carbonates are heterogeneously distributed at different scales in veins, replacing serpentine mesh textures, and as matrix cement of tectonic or sedimentary serpentinite breccias (Fig. 5.15a) (Bonatti et al., 1980; Grozeva et al., 2017; Klein et al., 2015; Lafay et al., 2017; Picazo et al., 2013; Schroeder et al., 2015). Infiltration of seawater into deeply rooted faults in intermediate- to fast spreading oceanic crust and faults formed during bending of the slab in the outer rise of subduction zones (Ranero et al., 2003) might also result in serpentinization and carbonation of sub-crustal peridotite (Fig. 5.15b). Serpentinite-hosted ophicalcites are symptomatic of seawater carbonation because the relatively low

$aCO_{2,aq}$ and Mg/Ca ratio of seawater and serpentinization fluids —in comparison to metamorphic fluids— promote crystallization of calcite and aragonite instead of Mg-carbonates (Bonatti et al., 1980; Eickmann et al., 2009b; Grozeva et al., 2017; Schroeder et al., 2015; Schwarzenbach et al., 2013).

In subduction zones, serpentinite-hosted carbonate-silicate rocks may also form in the subducting slab, the slab interface, and in the overlying mantle wedge (Fig. 5.15c). Metamorphic devolatilization reactions of altered oceanic crust and sediments in the slab generate C- and Mg/Ca-rich fluids (Caciagli and Manning, 2003; Facq et al., 2014; Tiraboschi et al., 2017). At different arc depths, reaction of these fluids with slab and mantle wedge serpentinites may produce ophimagnesite (magnesite–antigorite rocks), talc–magnesite rocks and listvenites (Falk and Kelemen, 2015; Menzel et al., 2018; Sieber et al., 2018), HP-ophicarbonate (e.g. Scambelluri et al., 2016), and carbonate–enstatite rocks (Tumiati et al., 2013). Tectonic mixing and prograde metamorphism of serpentinite and carbonate-bearing sediments in the slab interface may also generate hybrid rocks with a bulk composition similar to that of ophicarbonates (Scambelluri et al., 2016).

In the SiO_2–MgO–CaO ternary, the bulk compositions of the Milagrosa and Almirez (meta-)serpentinite-hosted carbonate-silicate rocks plot along the calcite–antigorite join (Fig. 5.9 a–c) indicating that their bulk compositions can be accounted for mixtures of ophicalcite (calcite ± aragonite) and serpentinite-group minerals (Fig. 5.15). High-temperature (700 – 750 °C, 0.6 GPa; Fig. 5.1) meta-ophicarbonates from the central Alps (Stucki, 2001), and Voltri Massif (Ligurian Alps) serpentinite-hosted HP ophicarbonates (>500 °C, 2.0 – 2.5 GPa; Fig. 5.1) composed of garnet-dolomite marbles and hybrid rocks (Scambelluri et al., 2016), also plot along this join (Fig. 5.9a). Most ophicalcites in ophiolites from the Alps, Apennines and Pyrenees are thought to have formed during their oceanic evolution due to seawater interaction with serpentinite (Fig. 5.15a) (Clerc et al., 2014; Collins et al., 2015; Lafay et al., 2017; Pozzorini and Früh-Green, 1996; Schwarzenbach et al., 2013).

Subduction metamorphism and deformation have obliterated the primary textures of Milagrosa and Almirez serpentinite-hosted carbonate-bearing rocks, preventing any inference from their primary structure. However, variable mixtures of serpentinite and ophicalcite account well for the bulk compositional trend of Milagrosa and Almirez carbonate rocks along the $CaCO_3$–Serpentine-group mineral join (Fig. 5.15; trend I), suggesting that their protoliths formed during the Jurassic oceanic stage. The elevated Ni and Cr bulk rock contents (Fig. 5.9d), enrichment of Ni in Ti-clinohumite (Fig. 5.10b) and Cr in chlorite (Fig.

5.12), and the trace occurrence of pyrrhotite, pentlandite, ilmenite/perovskite and Cr-bearing magnetite (Table 5.1; Fig. 5.6a), are in agreement with the formation of Milagrosa TiCl-Cal-marbles and Di-Dol-marbles by prograde metamorphism of a carbonated serpentinite protolith. Milagrosa TiCl-Cal-marbles (Fig. 5.4) might then have formed after ophicarbonates precipitated in high-permeability zones, and Atg-Di-Dol rocks (Fig. 5.4) in domains of lower fluid flux or after carbonate-bearing veins and breccias in adjacent serpentinites. Alternatively, the protoliths of the Milagrosa marble lenses may have originated from mixtures of marine carbonates and serpentinite detritus (Fig. 5.15a). Tectonic mixing, dissolution of marble carbonates, and coeval Ca-metasomatism of host serpentinites during HP metamorphism may account for the current tectonic fabric and mineral assemblages of Milagrosa Atg-Di-Dol rocks and Di-Dol-marbles.

Like in the Milagrosa serpentinite-hosted carbonate rocks, the high bulk rock Cr and Ni contents (Fig. 5.9e), and Ti-clinohumite and olivine composition (Fig. 5.10) of Almirez meta-ophicarbonate demonstrate that diopside, olivine, and Ti-clinohumite derived from prograde metamorphism of a carbonate–serpentinite protolith. In the SiO_2-CaO-MgO ternary, Almirez meta-ophicarbonate lenses plot at relatively high MgO/CaO ratio along the calcite–antigorite join (Fig. 5.9a), implying higher contents of serpentinite-group mineral in their bulk composition than in the Milagrosa TiCl-Cal marble lenses. Precipitation or replacement of serpentine minerals by calcite and aragonite in an ellipsoid-shaped vein network or ophicarbonate breccia zone in oceanic fault zones might account well for the Almirez protolith.

The calcite–antigorite trend of NFC serpentinite-hosted carbonate-silicate rocks indicates the limited role of open-system precipitation or mechanical mixing of dolomite and magnesite in the genesis of their protoliths. Binary mixtures of these carbonate minerals with serpentinite plot along the dolomite–antigorite (Fig. 5.15; Trend II) and magnesite–antigorite joins (Fig. 5.15; Trend III). Serpentinite-hosted dolomite —ophidolomite— and magnesite —i.e., ophimagnesite, talc-magnesite rocks and listvenite— assemblages require higher $a\mathrm{CO}_{2,aq}$ and Mg/Ca ratios than those of seawater hydrothermal systems (cf. Fig. 1.7a, and Figure 6b of Grozeva et al., 2017) and, consequently, are uncommon in seafloor serpentinites (Eickmann et al., 2009a; Grozeva et al., 2017) and ophiolite related ophicarbonates (Lafay et al., 2017). Interaction of Mg and C-bearing fluids equilibrated with serpentine-bearing sediments may favor the precipitation of dolomite (Fig. 5.15b; Trend II), which might occur, for instance, during reactivation of normal faults in the outer rise of the incoming oceanic

slab (Fig. 5.15b). Open system formation of dolomite and magnesite is also preponderant in the forearc — associated to listvenites (Ch. 4; Menzel et al., 2018) — and during HP precipitation of magnesite veins (ophimagnesite) (Tumiati et al., 2013) (Fig. 5.15c; Trend III). Milagrosa and Almirez late carbonate-tremolite veins and Tlc-Mgs rocks (Table 5.1; Fig. 5.3b; Fig. 5.7e) may record such open-system HP precipitation of dolomite and magnesite, but their conditions of formation are beyond the scope of the present study.

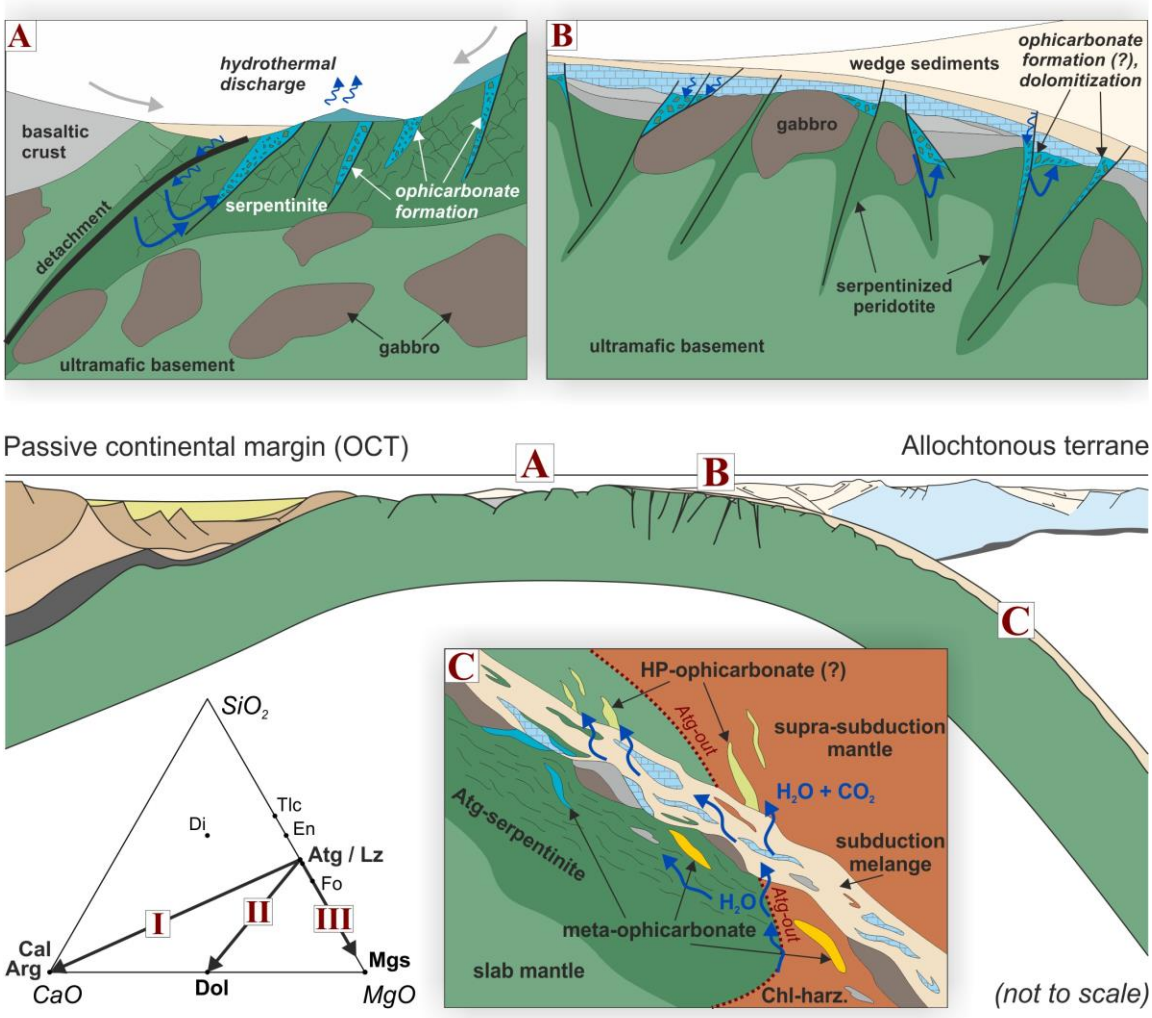

Figure 5.15. *Conceptual sketch of settings in which ophicarbonates may form. A: Oceanic stage, subseafloor serpentinite-hosted hydrothermal systems in slow spreading crust (modified after Lafay et al., 2017). B: By fluid interaction between marine sediments and serpentinite along bend faults in the outer rise of subduction. C: During subduction by interaction of fluids derived from devolatilization reactions (e.g. Atg-out) with serpentinite or Chl-harzburgite in the slab, along the plate interface or in the supra- subduction mantle (light green lenses). Blue and yellow lenses illustrate Atg-bearing and partially dehydrated slab meta-ophicarbonates, respectively. The CaO-MgO-SiO_2 ternary shows bulk chemical trends corresponding to the formation of ophicalcite (I), ophidolomite (II) and ophimagnesite (III).*

5.6.2 Metamorphic evolution

5.6.2.1 Phase relationships and devolatilization reactions

To illustrate the phase relations during subduction metamorphism of hybrid compositions with variable serpentinite and meta-ophicarbonate fractions, such as those encountered in Milagrosa and Almirez (Section *5.6.1*; Fig. 5.9a), we calculated a T– X_{Serp} pseudosection covering the compositional variation between pure $CaCO_3$ and natural serpentinite (Fig. 5.16a), where X_{Serp} corresponds to the weight fraction of serpentinite in the binary mixing with $CaCO_3$. The T–X pseudosection is computed for eclogite facies (1.7 GPa; Fig. 5.16a) relevant for the metamorphic conditions at Almirez, but is applicable to lower pressures because phase assemblages in meta-ophicarbonates do not change much with pressure (Fig. 5.14a). Also shown are the changes in modal mineral abundances with temperature for different bulk compositions (Fig. 5.16 b–d), which illustrate the different prograde reactions provided in Table 5.3.

At blueschist-facies conditions (450 – 550 °C), an assemblage composed of antigorite and aragonite, with minor clinopyroxene, dolomite and chlorite, is predicted for most compositions (Fig. 5.16a). The formation of olivine after brucite (T > 500 °C and X_{Serp} < 0.05 in Fig. 5.16a) depends on the bulk rock $(Mg+Fe^{2+})/Si$; this reaction would also occur for compositions near the serpentinite endmember (grey dotted line in Fig. 5.16a) for bulk Fe^{3+}/Fe^{2+} lower than those considered in our calculation (see section *5.4.1*).

The first major prograde devolatilization event occurs at 570 – 590 °C with the reaction of antigorite with $CaCO_3$ to diopside, chlorite and olivine (Reaction 5.1 in Table 5.3). The CO_2 released in this reaction may be buffered by reaction 5.2 (Table 5.3) decreasing the X_{CO2} of the fluid (~0.0014 at 1.7 GPa) by forming additional dolomite (Table 5.3; this reaction step corresponds to pseudo-invariant point i1 in Fig. 5.14b & c). For bulk compositions with X_{Serp} < 0.72 (> 28 wt% $CaCO_3$ in the precursor ophicarbonate) at T > 590 °C, antigorite is consumed by reactions 5.1+5.2 (Table 5.3) resulting in a partially dehydrated Chl-Ol-Cpx-Dol-$CaCO_3$ assemblage similar to that of Almirez meta-ophicarbonate (Fig. 5.16a & b).

For bulk compositions with X_{Serp} > 0.72 (Fig. 5.16a), antigorite is still present after reaction with $CaCO_3$ (Fig. 5.16c & d; see also additional T-X_{CO2} pseudosections in Appendix Fig. A-5.2). At 625 °C, this antigorite reacts with dolomite (mostly produced by reaction 5.2) to form diopside, olivine and chlorite (Reaction 5.3 in Table 5.3; Fig. 5.16c). The formation of magnesite according to reaction 5.4 (Table 5.3) buffers the fluid X_{CO2} to 0.005 (at 1.7 GPa;

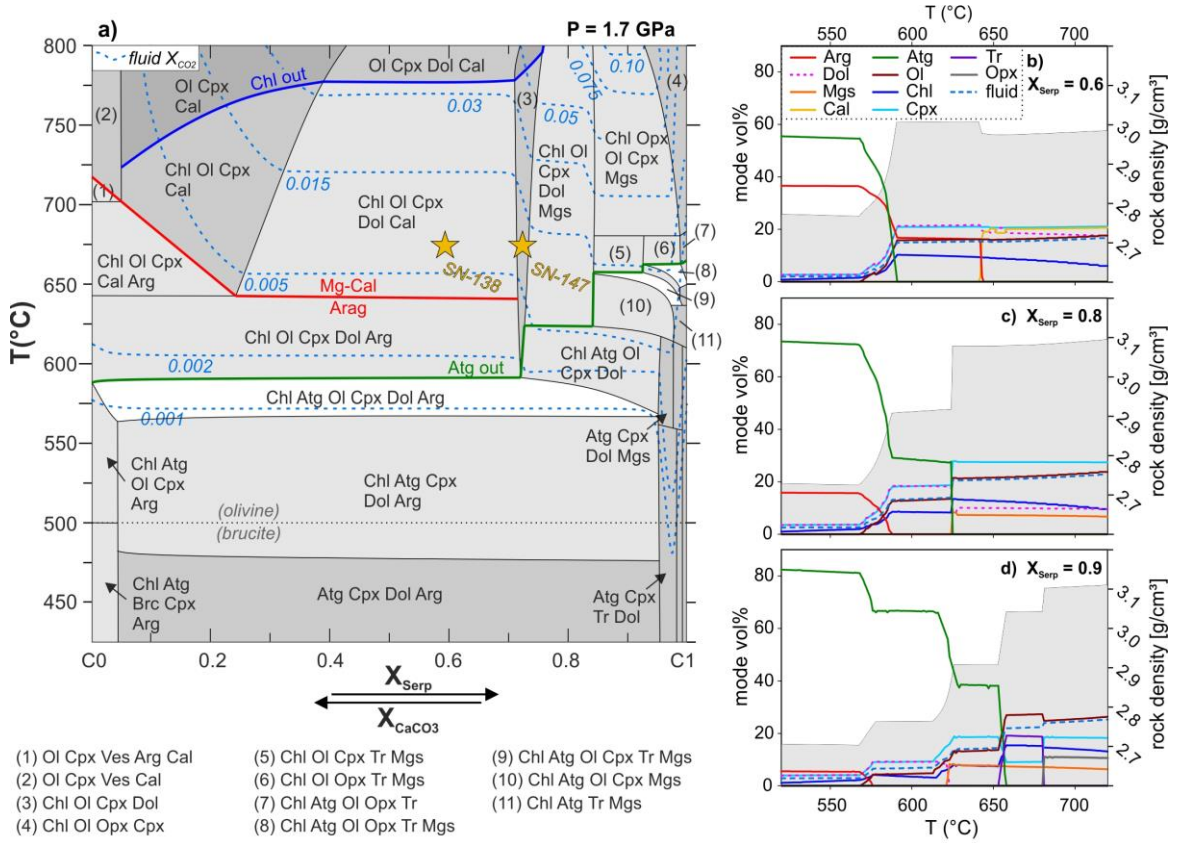

Figure 5.16. *(a) Isobaric T-X pseudosection for the compositional variation between pure $CaCO_3$ (C0) and serpentinite (C1); and (b–d) evolution of the modal phase abundance (including fluid) and solid rock density (grey shaded background and axis on the right) with temperature at three representative X_{Serp} showing different devolatilization behaviour at 1.7 GPa (X_{Serp} = fraction of serpentinite composition C1; see text for discussion). For the model serpentinite composition C1, the Fe-content of the bulk chemical composition of serpentinite sample SN-109 (Table 5.2) was modified by subtracting 2.0 wt% Fe_2O_3 to account for Fe^{3+} in antigorite and 4.1 wt% magnetite, resulting in a model C1 FeO content of 1.47 wt% (cf. Sec 4.4). If less Fe_2O_3 is subtracted, the brucite/olivine stability fields at T < 570 °C expand to compositions with higher X_{Serp} at the expense of dolomite (grey dotted line). The blue dashed lines in a) show fluid X_{CO2} in equilibrium with the mineral assemblage. Yellow stars: compositions and peak metamorphic conditions of Almirez meta-ophicarbonates.*

blue dotted lines in Fig. 5.16a). The overall reaction (Reactions 5.3+5.4 in Table 5.3; Fig. 5.16c) of antigorite with dolomite to diopside, olivine, chlorite and magnesite — corresponding to pseudo-invariant points i2 in Figure 5.14c and Appendix Figure A-5.2— produces the high-grade assemblage Chl-Ol-Cpx-Dol-Mgs (Fig. 5.16a). At lower pressure (e.g. 1 GPa), the reaction product is tremolite instead of diopside (e.g. Trommsdorff and Evans, 1977), and the fluid is buffered to higher X_{CO2} (pseudo-invariant points i2' in Fig. 5.14b and Appendix Fig. A-5.2).

For $X_{Serp} > 0.84$ (Fig. 5.16a), three dehydration reaction steps involving antigorite occur, consuming $CaCO_3$ by reactions 5.1 & 5.2 at 570 – 590 °C, and dolomite by reactions 5.3 &

5.4 at 615 – 625 °C (Fig. 5.16d). Excess antigorite breaks down at 650 – 660 °C to olivine, orthopyroxene and chlorite, producing the assemblage Chl-Opx-Ol-Cpx-Mgs (Fig. 5.16a & d). At P < 1.8 GPa, tremolite may form at the expense of diopside in an intermediate reaction step (fields 5 & 6 in Fig. 5.16a; Fig. 5.16d). With continued heating (T > 620 °C), reactions of diopside with dolomite (for $X_{Serp} < 0.75$) or magnesite (for $0.72 < X_{Serp} < 0.84$; Fig. 5.16a) to olivine + carbonate release CO_2, increasing the fluid X_{CO2} (reactions 5.5 & 5.6 in Table 5.3; blue dotted arrow in Fig. 5.14c). Chlorite eventually breaks down to Al-bearing clinopyroxene and olivine (Fig. 5.14a; Fig. 5.16a), producing lower fluid amounts compared to the breakdown of antigorite. Like antigorite, chlorite breakdown occurs at lower temperatures in $CaCO_3$ richer compositions (~780 °C for $X_{Serp} < 0.75$; Fig. 5.16a) than in pure serpentinite (> 820 °C; Fig. 5.13a).

5.6.2.2 Role of infiltration-driven devolatilization

As long as the fluid composition is rock-buffered (Ferrando et al., 2017; Kerrick and Connolly, 1998), the prograde devolatilization reactions in meta-ophicarbonate do not lead to substantial decarbonation during subduction because the X_{CO2} isopleths are essentially parallel to subduction P–T paths (Fig. 5.1; Fig. 5.14a). However, fluids derived from devolatilization and dissolution reactions of different subducting lithologies (Bebout and Penniston-Dorland, 2016) (Fig. 5.15c) can lead to open-system carbonation or removal of carbon. Subduction metamorphic terranes show evidence of infiltration-driven devolatilization and carbon release caused by channelized fluid flushing (Ague and Nicolescu, 2014; Angiboust et al., 2014; Vitale Brovarone et al., 2018). Carbonate re-deposited in veins in lower grade subduction lithologies further provides indirect evidence of high carbon mobility in subduction fluids (e.g. Piccoli et al., 2018). In serpentinite-hosted carbonate-silicate rocks, infiltration of H_2O-rich fluids at isobaric and isothermal conditions (e.g. Fig. 5.14c, black dotted arrow labelled f.i.) induces decarbonation through reactions 5.5 or 5.6 (Table 5.3). On the other hand, infiltration of CO_2-rich fluids stabilizes dolomite and magnesite over Ca-carbonate (fields with Chl-Atg-Cpx-Dol, Chl-Ol-Cpx-Dol and Chl-Cpx-Dol-Mgs assemblages in Fig. 5.14c). During prograde subduction metamorphism of serpentinite, fluids are released by the breakdown of brucite and antigorite. Infiltration of H_2O-rich fluids —causing isothermal, infiltration-driven devolatilization reactions— was probable in the serpentinite-hosted carbonate-silicate rocks at Milagrosa and Almirez, because their peak metamorphic temperatures exceed the stability conditions of brucite and antigorite, respectively (Sections *5.5.3.1* and *5.5.3.2*).

Table 5.3. *Key prograde reactions in meta-ophicarbonates in the CaO-MgO-Al_2O_3-SiO_2-H_2O-CO_2 system, using simplified compositions of Atg [$Mg_{47}Al_2Si_{33}O_{85}(OH)_{62}$], Chl [$Mg_{10}Al_4Si_6O_{20}(OH)_{16}$] and Dol [$CaMg(CO_3)_2$]. Depending on P-T, $CaCO_3$ may be calcite or aragonite.*

#	**Metamorphic reaction**
(5.1)	Atg + 6 $CaCO_3$ = 6 Di + 18 Fo + 0.5 Chl + 6 CO_2 + 27 H_2O
(5.2)	Atg + 42 $CaCO_3$ + 12 CO_2 = 15 Di + 27 Dol + 0.5 Chl + 27 H_2O
(5.1+5.2) [a)]	Atg + 17.92 $CaCO_3$ = 8.98 Di + 12.04 Fo + 8.94 Dol + 0.5 Chl + 27 H_2O + 0.04 CO_2
(5.3)	Atg + 4.5 Dol = 4.5 Di + 21 Fo + 0.5 Chl + 9 CO_2 + 27 H_2O
(5.4)	Atg + 15 Dol + 27 CO_2 = 15 Di + 42 Mgs + 0.5 Chl + 27 H_2O
(5.3+5.4) [b)]	Atg + 8.93 Dol = 8.93 Di + 12.14 Fo + 0.5 Chl + 17.72 Mgs + 27 H_2O + 0.14 CO_2
(5.5)	Di + 3 Dol = 2 Fo + 4 $CaCO_3$ + 2 CO_2
(5.6)	Di + 4 Mgs = 2 Fo + Dol + 2 CO_2

[a)] Balanced overall reaction, for X_{CO2} = 0.0015 at 580 °C, 1.7 GPa (point i1 in Figure 5.13c);

[b)] Balanced overall reaction, for X_{CO2} = 0.0052 at 620 °C, 1.7 GPa.

The mineral assemblages and compositions of Milagrosa Atg-Di-Dol rocks and marble lenses are consistent with their formation by incipient reaction of antigorite with carbonate (reactions 5.1 & 5.2 in Table 5.3). The absence of antigorite in TiCl-Cal marble, along with the predominance of dolomite and lack of olivine in Atg-Di-Dol rock (Table 5.1), indicates that the X_{CO2} of fluid at peak metamorphic conditions (Fig. 5.13b; and Chl-Atg-Cpx-Dol field in Fig. 5.14b) was higher than that predicted for an internally buffered fluid evolution path of a calcite-antigorite protolith (blue dashed arrow in Fig. 5.14b). This could be explained by dolomitization of the antigorite–calcite protolith prior to peak metamorphism or by infiltration of CO_2-bearing fluids during subduction metamorphism. Thus, the observed phase-relations of the Milagrosa carbonate-silicate rocks do not show a clear record of H_2O-rich fluid infiltration.

In the Almirez meta-ophicarbonates several observations indicate that during prograde dehydration and decarbonation reactions the fluid composition was buffered by the rock, following a fluid evolution similar to that shown in Figure 5.14c (blue dashed arrow). The abundance of aragonite, dolomite, and chlorite inclusions in olivine and diopside (Fig. 5.8 g–h) indicates that these two minerals formed by reactions 5.1 and 5.2 (Table 5.3). This implies that the fluid evolved along a path that passed through the pseudo-invariant point i1 in Figure 5.14c. The composition of chlorite, olivine and Ti-clinohumite shows that they formed by

reaction of Ni- and Cr-bearing antigorite with carbonate. Dolomite and $CaCO_3$ (mainly calcite) —with well-equilibrated polygonal grain boundaries— are abundant in most samples (Fig. 5.8c & d; Table 5.2), showing that the fluid X_{CO2} evolved along the pseudo-univariant line defined by the Chl-Ol-Cpx-Dol-Arg assemblage (Fig. 5.14c). If the fluid composition was controlled externally and the time-integrated fluid flux large, $CaCO_3$ (external fluid with $X_{CO2} > 0.005$) or dolomite (if $X_{CO2} < 0.005$ at 650°C) would have become unstable (reaction 5.5 in Table 5.3). Dolomite is the main carbonate phase in gneissic-textured meta-ophicarbonate (Fig. 5.7d; Fig. 5.8b; sample SN-136) and in one granofelsic sample (Fig. 5.8e; sample SN-147), which may point to infiltration-driven open-system reactions (reaction 5.5 or 5.6, Table 5.3). The observed assemblage chlorite-diopside-dolomite-Ti-clinohumite (with minor or rare olivine and Ca-carbonate) in the gneissic meta-ophicarbonate intercalations may point to infiltration of CO_2-bearing fluids and a related depletion in sulfur in these domains (Sample SN-136 in Table 5.2), but the timing of this event in relation to the metamorphic evolution is unclear. In the case of the granofelsic, dolomite-rich meta-ophicarbonate (Fig. 5.8e; sample SN-147), aragonite inclusions are abundant while magnesite is absent, suggesting that the dolomite-rich assemblage was controlled by the protolith composition (close to X_{Serp} = 0.73; field 3 in Fig. 5.16a) and not by H_2O-rich fluid infiltration. Zonation in carbonates indicative of dissolution and re-precipitation by fluids observed in subduction-related carbonate rocks elsewhere (Ferrando et al., 2017) are not present in the Almirez meta-ophicarbonates. All these observations point to a limited role of open system fluid-driven decarbonation in Milagrosa and Almirez serpentinite-hosted meta-ophicarbonates.

5.6.2.3 Equilibrium fluid composition and speciation: implications for carbon mobility

During prograde subduction, metamorphism of serpentinite-hosted meta-ophicarbonates of variable composition (Fig. 5.16 b–d) may produce differing X_{CO2} fluid composition (blue dashed isopleths in Fig. 5.16a). At the same temperature, the X_{CO2} of fluid in equilibrium with bulk compositions with low $CaCO_3$ content is higher than for $CaCO_3$-rich compositions (Fig. 5.16a). For instance, at 660 °C and 1.7 GPa, X_{CO2} of fluids is ~0.006 for $X_{Serp} < 0.72$, 0.011 for X_{Serp} 0.72 – 0.84, and ~0.015 for X_{Serp} 0.84–0.98 (see also Appendix Fig. A-5.2). During prograde subduction metamorphism and devolatilization, the variable fluid X_{CO2} in serpentinite-hosted ophicarbonates with variable effective bulk compositions may lead to dissolution and/or precipitation at different length scales (Fig. 5.4; Fig. 5.8 a–e). Therefore,

serpentinite-hosted ophicarbonates with low bulk $CaCO_3$ content (X_{Serp} > 0.72) —e.g. marginal veined ophicalcite zones— would release more carbon into dehydration fluids than carbonate-rich domains (X_{Serp} < 0.72; Fig. 5.16a). At 720 °C, for a bulk composition with X_{Serp} of 0.98 (~0.88 wt% CO_2) all carbon is dissolved in the fluid phase (field 4 in Fig. 5.16a), while for a bulk rock composition similar to that of the Almirez meta-ophicarbonate lenses fluids would only contain ~0.2 wt% CO_2. On the other hand, devolatilization fluids produced by dolomite-consuming reactions 5.3 and 5.4 (Table 5.2) in bulk rocks with X_{Serp} > 0.72 may precipitate carbonate if they infiltrate into meta-ophicarbonate with X_{Serp} < 0.72 because the fluid would be buffered to lower X_{CO2} (Fig. 5.16a; Appendix Fig. A-5.2).

Previous studies have shown that accounting for electrolytic fluids in thermodynamic models increases the solubility of carbon in subduction fluids by a factor of ~2 relative to models that use pure molecular H_2O–CO_2 fluids (Connolly and Galvez, 2018; Kelemen and Manning, 2015). The effect of variable bulk composition, pressure and temperature in the speciation of carbon-bearing solutes in equilibrium with meta-ophicarbonate rocks are shown in Figures 5.17 and 5.18 (see section *5.4.1* for details on the computation). At the P–T conditions of antigorite breakdown, molecular CO_2 is the dominant C-bearing species in fluid in equilibrium with serpentinite-hosted carbonate-silicate rocks with variable bulk composition (Fig. 5.17). While the calculations likely slightly underestimate carbon solubility due to neglecting solute species involving Na, K, and Cl (cf. section *5.4.1*), charged carbon-bearing species, such as $CaHCO_3^+$, $CaCO_{3,aq}$, and HCO_3^-, are generally minor and result in a small increase in the solubility of total carbon in the fluid (e.g. by ~0.2 mol C per kg fluid at 660°C, 1.7 GPa; Fig. 5.17). Congruent dissolution of $CaCO_3$ to $CaHCO_3^+{}_{aq}$ and $HCO_3^-{}_{aq}$ is more important at < 550 – 575 °C and higher pressure (Fig. 5.17; Fig. 5.18). On the other hand, the contribution of charged carbon-bearing species to total carbon solubility becomes insignificant at T > 650 °C and P < 1 GPa (Fig. 5.18). These results suggest that — at the conditions of interest and considering the general uncertainties in thermodynamic data — molecular models underestimate only slightly the fluid carbon solubility relative to models accounting for electrolyte fluids, and, therefore, are appropriate to model phase relations and devolatilization reactions in carbonate-silicate rocks such as those at Milagrosa and Almirez (Table 5.3; Fig. 5.14; Fig. 5.16; see also: Trommsdorff and Evans (1977); Will et al. (1990)).

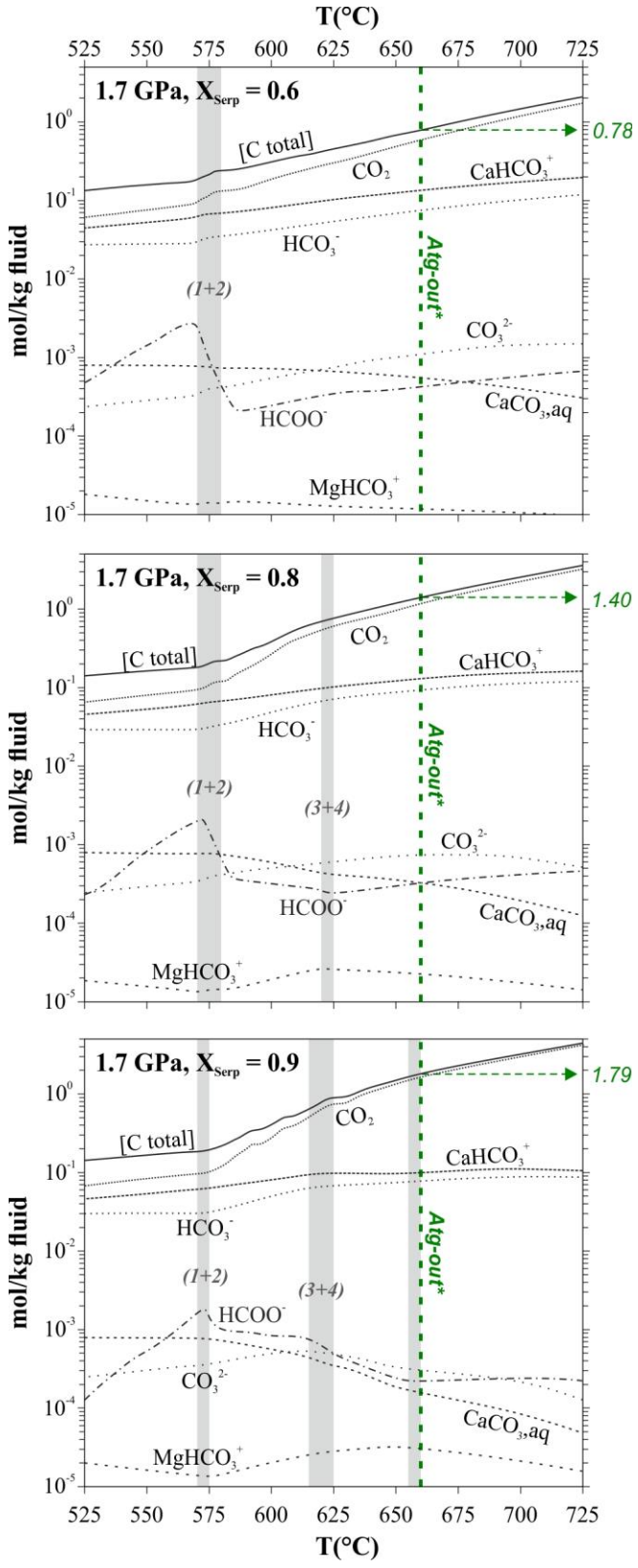

◄ ***Figure 5.17.*** *Predicted carbon speciation and solubility (C total) in fluid in equilibrium with different meta-ophicarbonate compositions (XSerp = 0.6, 0.8, and 0.9) at 1.7 GPa. Grey fields show temperature ranges of prograde devolatilization reactions (see Table 5.3, Fig. 5.16). The green dashed line illustrates conditions of Atg-breakdown in host serpentinite, and total carbon solubility (mol/kg fluid) at this temperature. Calculated using lagged speciation mode for electrolytic fluids in Perple_X 6.8.5 (see section 5.4.1).*

The dissolution of carbonate by external fluids depends on the local fluid/rock ratio, and the relative permeability of meta-ophicarbonates and their host serpentinites. If local equilibrium between rock, solvent and solute is attained, the predominance of molecular CO_2 in the fluids (Fig. 5.17; Fig. 5.18) implies that infiltration-driven devolatilization of meta-ophicarbonates would be mainly controlled by reactions involving carbonates and silicates (Section *5.6.2.2*; e.g. reactions 5.5 & 5.6 in Table 5.3). This condition may be attained at low fluid-rock ratios and fast reaction kinetics, resulting in olivine and Ca-carbonate-rich assemblages when infiltrated by H_2O-fluids (see section *5.6.2.2*). High fluid/rock ratios and slower kinetics of silicate mineral dissolution may lead to a preferential congruent dissolution of carbonate relative to that of

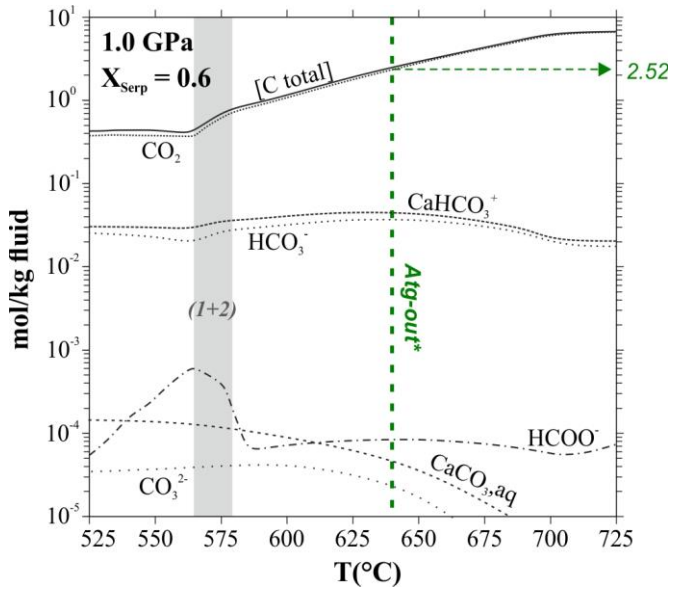

◄ ***Figure 5.18.*** *Predicted carbon speciation and solubility (C total) in fluid in equilibrium with meta-ophicarbonate (XSerp = 0.6) at 1.0 GPa. Grey fields show temperature ranges of prograde devolatilization reactions, and the green dashed line conditions and total C solubility (mol/kg fluid) at serpentinite dehydration, as in Figure 5.17. Calculated using lagged speciation mode for electrolytic fluids in Perple_X 6.8.5 (computation details see section 5.4.1).*

silicates. This process may produce diopside-olivine-chlorite rocks after carbonate-silicate rock, and precipitation of secondary carbonate upstream along the fluid path.

The Almirez meta-ophicarbonates show no evidence of such disequilibrium processes indicating that fluid infiltration was limited, as also shown by the phase relations (Section *5.6.2.2*). Relative to the dehydration of antigorite in the host serpentinite, the lower temperature of the main devolatilization reactions in carbonate-silicate rocks may favour their preservation beyond the conditions of antigorite breakdown. The presence of Ca-carbonate in the protolith changes the nature of the overall antigorite dehydration from a single discontinuous reaction for carbonate-free serpentinite at 660 °C to a stepwise reaction series at lower temperatures in meta-ophicarbonates (Fig. 5.16 a–d). If fluids produced by devolatilization reactions 5.1 – 5.4 (Table 5.3) are efficiently drained, stepwise dehydration increases the density of the solid rock (grey filled curves in Fig. 5.16 b–d). Meta-ophicarbonate lenses may then attain very low permeability domains relative to the host dehydrating serpentinite, favouring anisotropic fluid channelling around such lenses. Furthermore, at the conditions of antigorite breakdown in host serpentinite at 1.7 GPa, differences in bulk rock composition imply a 1 molal higher carbon solubility of fluids in equilibrium with Chl-Ol-Cpx-Tr-Mgs rocks (field 5 in Fig. 5.16a; X_{Serp} = 0.9 in Fig. 5.17) than with Chl-Ol-Cpx-Dol-Cal rocks (X_{Serp} = 0.6 in Fig. 5.17). Hence, carbonate-rich assemblages such as those in the Almirez meta-ophicarbonate lenses are more likely to be preserved during antigorite breakdown than domains that contained low carbonate amounts in the protolith.

5.7 Appendices

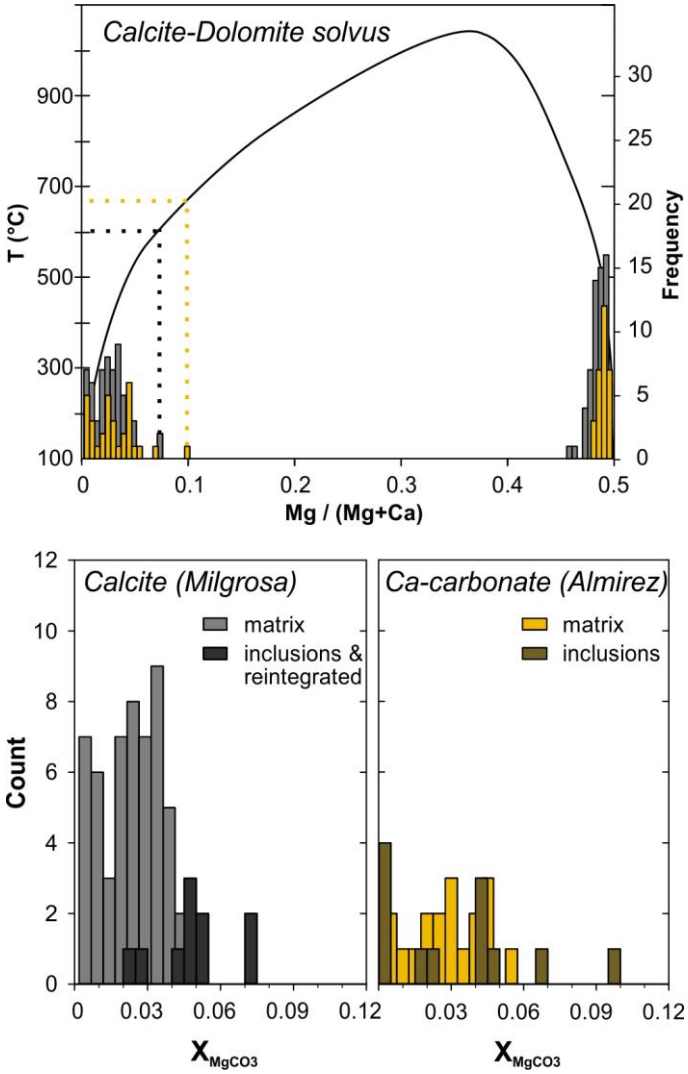

Figure A-5.1. *Histograms of frequency of measured* X_{MgCO3} *in calcite and dolomite analysed by electron microprobe from Milagrosa marble lenses (grey histogram) and Almirez meta-ophicarbonate (yellow histogram), and calcite-dolomite miscibility gap after Anovitz and Essene (1987).*

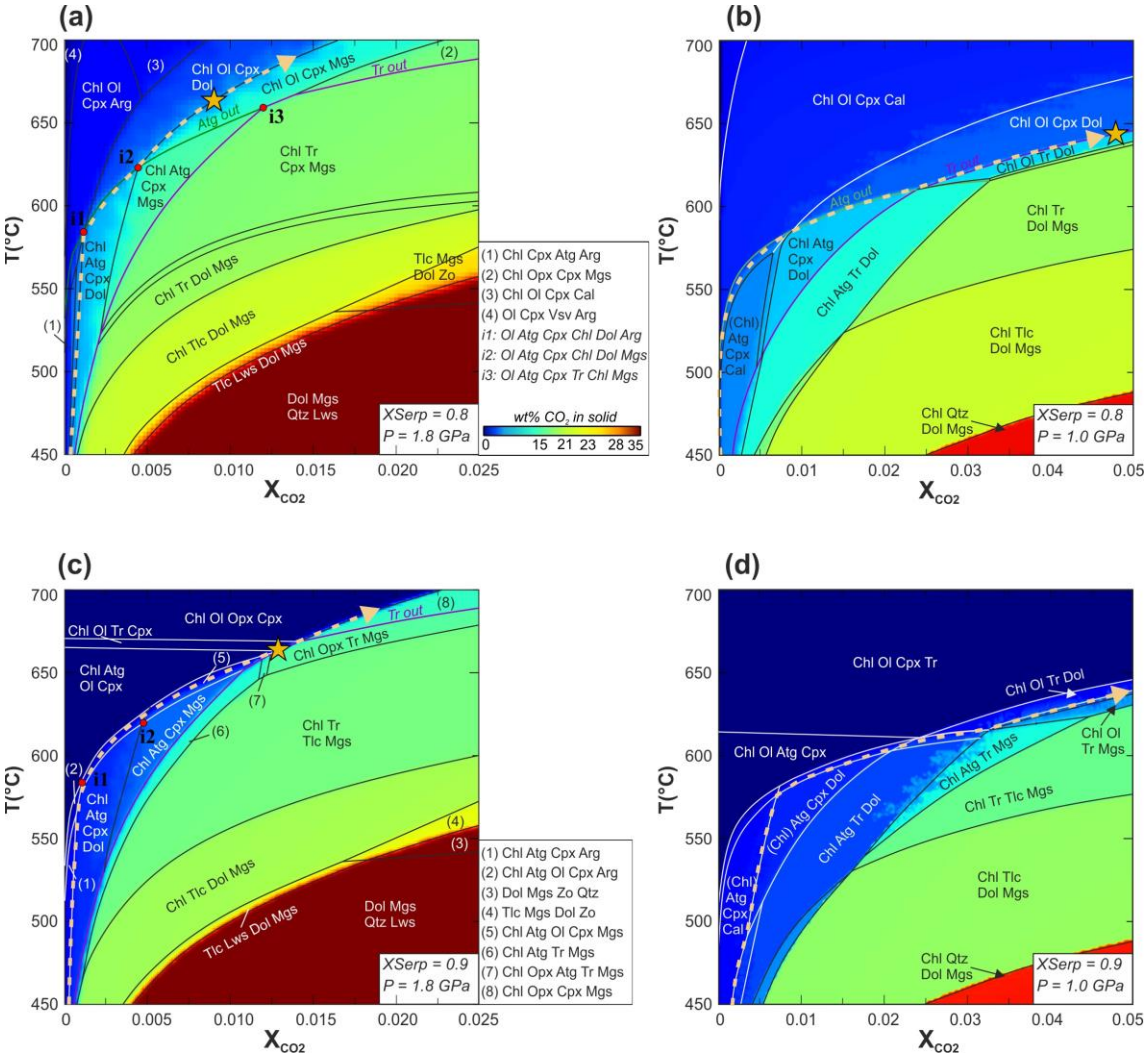

Figure A-5.2. *T-X_{CO2} pseudosections of meta-ophicarbonate compositions with X_{Serp} = 0.8* ***(a, b)*** *and 0.9* ***(c, d)*** *at 1.8 GPa and 1.0 GPa, respectively, superposed on the CO_2 content in the solid (common colorbar in a; the color scale is the same as in Fig. 5.14b & c). Yellow dashed arrows show rock-buffered fluid evolution paths for serpentine-calcite protoliths, with the yellow star indicating fluid X_{CO2} at conditions of antigorite breakdown in the host serpentinite.*

Table A-5.1 *List of rock samples of serpentinites and carbonate rocks in the Milagrosa ultramafic massif, and related country rocks (Nevado-Filábride Complex, Spain)*

Sample	Field-based lithology	Latitude (N)[a]	Longitude (W)	Elevation (m)	TS	Bulk	EMPA	EBSD
SN-01	Atg-serpentinite	37.215328	-2.032631	482	x			
SN-02	carbonated Atg-serpentinite	37.215137	-2.033233	487	x	x	x	x
SN-03	Cal-Chl-Tlc-vein in serpentinite (zone I)	37.215137	-2.033233	487	x	x	x	
SN-04a	Chl-Serp vein in serpentinite (zone II)	37.215137	-2.033233	487	x	x	x	
SN-04b	Tr-Tlc-Dol vein in serpentinite (zone III)	37.215137	-2.033233	487	x	x	x	
SN-05	Tr-Chl vein in serpentinite (zone IV)	37.215561	-2.034139	516	x	x	x	
SN-06	carbonate vein	37.215561	-2.034139	511				
SN-07	Atg-serpentinite	37.215682	-2.033735	511	x			
SN-08	carbonate vein	37.215682	-2.033735	511	x			
SN-09	Di-Dol marble lens	37.215713	-2.033784	513	x	x	x	
SN-10	TiCl-Cal marble lens	37.215713	-2.033784	513	x	x	x	
SN-11	Transition Cpx-serpentinite to Atg-Di-Dol rock	37.215713	-2.033784	513	x	x	x	
SN-12	TiCl-Chl rich Cpx-serpentinite	37.215713	-2.033784	513	x		x	
SN-13	Di-Dol marble lens	37.215713	-2.033784	513	x			
SN-14	serpentinite	37.215713	-2.033784	513	x			
SN-15	carbonate vein	37.215489	-2.032448	472				
SN-16	carbonate vein	37.215489	-2.032448	472				
SN-17	ophicalcite breccia	37.215953	-2.032177	484				
SN-18	carbonate vein	37.216168	-2.032654	523				
SN-19	carbonate vein	37.216168	-2.032654	523				
SN-20	carbonate vein	37.216168	-2.032654	523	x			
SN-21	serpentinite	37.215911	-2.033235	447				
SN-22	marble lens	37.215850	-2.034067	513				
SN-23	Dol-Atg schist	37.215647	-2.033777	504	x	x	x	x
SN-24	carbonated Atg-serpentinite	37.215894	-2.034301	540				
SN-25	Tr-carbonate vein in serpentinite	37.215894	-2.034301	540				
SN-26	coarse Dol vein in serpentinite	37.215894	-2.034301	540	x	x		
SN-27	Tr-carbonate vein in serpentinite	37.215930	-2.034248	535	x			
SN-28	ophicalcite breccia	37.216255	-2.033462	534	x			
SN-29	ophicalcite breccia	37.216255	-2.033462	534	x	x		
SN-30	Grt-calc-schist	37.213198	-2.032933	447	x	x	x	
SN-42*	Qtz-calc-schist	37.215211	-2.034933	540	x		x	
SN-43*	Grt-amphibolite	37.213863	-2.032388	437	x		x	
SN-44	calc-schist	37.216155	-2.035425	593				
SN-45	calc-schist	37.216155	-2.035425	593				

Table A-5.1 *List of rock samples of serpentinites and carbonate rocks in the Milagrosa ultramafic massif, and related country rocks (Nevado-Filábride Complex, Spain)*

SN-46*	Grt-mica-schist	37.216054	-2.031848	468	x			
SN-90*	Cpx-serpentinite	37.215911	-2.033514	500	x	x	x	x
SN-91*	carbonated serpentinite	37.215990	-2.033369	512	x		x	
SN-92*	carbonated serpentinite	37.216053	-2.033184	505				
SN-93*	carbonated serpentinite	37.216053	-2.033184	505				
SN-94*	carbonated serpentinite	37.216053	-2.033184	505				
SN-95*	serpentinite	37.216053	-2.033184	505				
SN-96*	Cpx-serpentinite	37.215713	-2.033784	513	x	x	x	
SN-97*	Atg-Di-Dol rock	37.215713	-2.033784	513	x	x	x	x
SN-98*	Atg-Di-Dol rock	37.215713	-2.033784	513	x	x	x	
SN-99*	Di-Dol marble lens	37.215713	-2.033784	513	x	x		x
SN-100*	TiCl-Cal marble lens	37.215713	-2.033784	513	x		x	x
SN-101*	contact marble - serpentinite	37.215713	-2.033784	513	x	x	x	x
SN-102*	Cpx-serpentinite	37.215713	-2.033784	513	x	x		
SN-103*	Cpx-serpentinite	37.215713	-2.033784	513	x		x	x
SN-104	serpentinite	37.215541	-2.034136	506				
SN-105*	Cpx-serpentinite	37.215271	-2.033201	477	x	x	x	x
SN-106	serpentinite (lose block)							
SN-107	Atg-serpentinite (lose block)				x	x	x	
SN-108	serpentinite (lose block)							
SN-109	Atg-serpentinite (lose block)				x	x		

[a] *– Latitude/Longitude in WGS84 Datum. Samples marked with (*) are geographically oriented.*

Table A-5.2 *List of rock samples of Chl-harzburgites and carbonate rocks from the Almirez ultramafic massif (Nevado-Filábride Complex, Spain)*

Sample	**Field-based lithology**	**Latitude (N)[a]**	**Longitude (W)**	**Elevation (m)**	**TS**	**Bulk**	**EMPA**	**EBSD**
SN-110	marble breccia	37.089663	-2.907571	2413				
SN-111	marble breccia	37.091155	-2.907235	2410				
SN-112	Tr-Chl-Qtz lens in marble breccia	37.091155	-2.907235	2410				
SN-113	marble	37.091089	-2.907245	2413				
SN-114	Qtz-mica schist	37.091089	-2.907245	2413				
SN-115	Tlc-vein in Chl-harzburgite	37.090970	-2.907303	2417				
SN-116a*	Dol-marble	37.090951	-2.907305	2421	x	x		
SN-116b*	Chl-harzburgite	37.090951	-2.907305	2421	x	x	x	x
SN-117*	Chl-harzburgite	37.090951	-2.907305	2421				
SN-118*	Dol-marble	37.091017	-2.907377	2420	x			
SN-119*	Chl-harzburgite	37.091017	-2.907377	2420				

Table A-5.2 *List of rock samples of Chl-harzburgites and carbonate rocks from the Almirez ultramafic massif (Nevado-Filábride Complex, Spain)*

SN-120*	Chl-harzburgite	37.091017	-2.907377	2420	x			
SN-121	Tr-Mgs vein in Chl-harzburgite	37.091253	-2.908500	2404	x			
SN-122	Tr-Mgs vein in Chl-harzburgite	37.091253	-2.908500	2404	x		x	
SN-123	Chl-harzburgite	37.088078	-2.909135	2452				
SN-124*	Dol-marble	37.083072	-2.918453	2252	x	x		
SN-125	Dol-marble	37.082901	-2.918560	2231				
SN-126	Dol-marble	37.072574	-2.937072	1954				
SN-127*	Dol-marble	37.072574	-2.937072	1954	x	x	x	
SN-128*	Tlc-rich Chl-harzburgite	37.072574	-2.937072	1954	x	x	x	
SN-129*	marble breccia	37.072293	-2.934957	2026	x		x	
SN-130*	Tr-Chl-marble	37.072293	-2.934957	2026	x	x	x	
SN-131*	Tr-Chl-Mgs rock	37.072293	-2.934957	2026	x	x		
SN-132*	Tr-Chl-Mgs rock	37.072293	-2.934957	2026	x		x	
SN-133*	Tr-Chl-Mgs rock	37.072293	-2.934957	2026	x			
SN-134*	carbonated Chl-harzburgite, Tr-Mgs rock	37.072293	-2.934957	2026	x	x	x	
SN-135*	meta-ophicarbonate	37.072415	-2.935349	2016	x	x	x	x
SN-136*	meta-ophicarbonate	37.072415	-2.935349	2016	x	x	x	x
SN-137*	Tlc-Mgs rock	37.072415	-2.935349	2016	x	x	x	
SN-138*	meta-ophicarbonate	37.072491	-2.934976	2024	x	x	x	x
SN-139*	serp. Chl-harzburgite	37.072516	-2.935163	2021	x	x		
SN-140*	carbonate breccia	37.071526	-2.935720	2004	x		x	
SN-141*	Dol-marble (raft in breccia)	37.071370	-2.935947	1999	x	x	x	
SN-142*	carbonate breccia	37.071370	-2.935947	1999	x			
SN-143*	Di-Tr-Chl-Dol rock (raft in breccia)	37.071324	-2.935870	1999	x	x	x	
SN-144	carbonate breccia	37.071324	-2.935870	1999				
SN-145*	Tlc-Tr rock (at contact breccia Chl-harzburgite)	37.071247	-2.936107	1993	x			
SN-146*	Tr-Ol-Chl-Atg rock	37.071482	-2.936075	1998	x	x	x	x
SN-147*	meta-ophicarbonate	37.072935	-2.935802	1995	x			x
SN-148*	Chl-harzburgite	37.072961	-2.936063	1984	x			
SN-149*	Chl-harzburgite	37.071587	-2.935802	2004	x			
SN-150	Tr-Mgs vein in Chl-harzburgite				x			
SN-151	Tr-Mgs vein in Chl-harzburgite	37.091253	-2.908500	2404	x			
SN-152	TiCl-Ol-Tr-Chl-Mgs rock	37.071071	-2.936061	1991	x			

[a] *– Latitude/Longitude in WGS84 Datum. Samples marked with (*) are geographically oriented.*

Table A-5.3. *Phases and solution models used for thermodynamic modelling.*

Phase	**Abbr.**	**Formula**	**Type/comment**	**Reference**
olivine	Ol(HP)	$Mg_{2x}Fe_{2(1-x)}SiO_4$		(Holland and Powell, 1998)
orthopyroxene	Opx(HP)	$[Mg_xFe_{1-x}]_{2-y}Al_{2y}Si_{2-y}O_6$	speciation model	(Holland and Powell, 1996)
clinopyroxene	Cpx(HP)	$Na_{1-y}Ca_yMg_{xy}Fe_{(1-x)y}Al_ySi_2O_6$	disordered	(Holland and Powell, 1996)
garnet	Gt(HP)	$Fe_{3x}Ca_{3y}Mg_{3z}Mn_{3(1-x-y-z)}Al_2Si_3O_{12}$, $x+y+z\leq1$		(Holland and Powell, 1998)
chlorite	Chl(HP)	$[Mg_xFe_wMn_{1-x-w}]_{5-y+z}Al_{2(1+y-z)}Si_{3-y+z}O_{10}(OH)_8$, $x+w\leq1$	speciation model	(Holland et al., 1998)
antigorite	Atg(PN)	$Mg_{x(48-y)}Fe_{(48-y)(1-x)}Al_{8y}Si_{34-y}O_{85}(OH)_{62}$	ideal, tschermak	(Padrón-Navarta et al., 2013)
carbonates	oCcM(EF)	$[Ca,Mg,Fe]_{0.5}[Ca,Mg,Fe]_{0.25}[Ca,Mg,Fe]_{0.25}CO_3$	van Laar type order-disorder	(Franzolin et al., 2011)
spinel	Sp(HP)	$Mg_xFe_{1-x}Al_2O_3$		(Holland and Powell, 1998)
talc	T	$[Mg_xFe_{1-x}]_{3-y}Al_{2y}Si_{4-y}O_{10}(OH)_2$	ideal	
brucite	B	$Mg_xFe_{1-x}(OH)_2$	ideal	
tremolite	Tr	$Ca_2Mg_{5x}Fe_{5(1-x)}Si_8O_{22}(OH)_2$	ideal	
anthophyllite	Anth	$Mg_{7x}Fe_{7(1-x)}Si_8O_{22}(OH)_2$	ideal	
Phase A	A-phase	$Mg_{7x}Fe_{7(1-x)}Si_2O_8(OH)_6$	ideal	
magnetite*	MF	$Mg_xFe_{3-x}O_4$	ideal	
fluid	F	$(H_2O)_x(CO_2)_{1-x}$		(Connolly and Trommsdorff, 1991)
fluid*	COH-Fluid+	$[H_2O\text{-}CO_2\text{-}CH_4]$-solvent	non-linear subdivision	(Connolly and Galvez, 2018)

Quartz, aragonite, zoisite, vesuvianite, lawsonite and hematite were considered pure phases. Solution models for phases marked with an asterix (*) were only used in speciation calculations when using Perple_X 6.8.5 (Fig. 5.17; Fig. 5.18).

Table A-5.4 (a) *Representative microprobe analyses (EMPA) of carbonates at Milagrosa. EMPA settings see Ch. 3, section 3.3.3, and Table 3.2.*

Lithology	TiCl-Cal marble							
Sample	SN-10	SN-10	SN-100	SN-100	SN-100	SN-10	SN-10	SN-100
Mineral	*Cal (matrix)*	*Cal (in TiCl)*	*Cal (matrix)*	*Cal (widebeam)*	*Cal (in TiCl)*	*Dol (coarse)*	*Dol (exsol.)*	*Dol (exsol)*
SiO_2	b.d.	b.d.	b.d.	b.d.	0.14	b.d.	0.07	b.d.
FeO	0.02	0.25	0.07	0.07	0.14	0.42	0.48	0.43
MnO	0.08	0.09	0.10	0.12	0.11	0.02	0.15	0.21
MgO	0.94	2.91	1.30	1.95	1.88	21.34	20.55	20.38
CaO	55.34	51.81	54.36	52.78	53.34	30.89	30.97	31.43
SrO	b.d.	b.d.	b.d.	b.d.	b.d.	b.d.	b.d.	b.d.
BaO	b.d.	b.d.	b.d.	b.d.	b.d.	b.d.	b.d.	b.d.
CO_2 (calc)	44.52	44.07	44.19	43.69	44.27	47.83	47.23	47.31
Total	100.90	99.13	100.02	98.61	99.88	100.51	99.45	99.76
Ions per 6 O								
Si	b.d.	b.d.	b.d.	b.d.	0.013	b.d.	0.007	b.d.
Fe	0.002	0.021	0.006	0.006	0.012	0.032	0.037	0.033
Mn	0.007	0.007	0.008	0.010	0.009	0.002	0.012	0.017
Mg	0.138	0.433	0.193	0.293	0.278	2.924	2.851	2.822
Ca	5.853	5.538	5.793	5.691	5.674	3.042	3.087	3.128
Sr	b.d.	b.d.	b.d.	b.d.	b.d.	b.d.	b.d.	b.d.
Ba	b.d.	b.d.	b.d.	b.d.	b.d.	b.d.	b.d.	b.d.
$\sum$ cations	6.000	6.000	6.000	6.000	5.987	6.000	5.993	6.000
X_{MgCO3}	0.023	0.072	0.032	0.049	0.047	0.488	0.477	0.472
X_{FeCO3}	0.000	0.004	0.001	0.001	0.002	0.005	0.006	0.006
X_{CaCO3}	0.977	0.924	0.967	0.950	0.951	0.507	0.517	0.523
T (°C) *	*379*	*603*	*443*	*523*	*514*			

Table A-5.4 (a) continued.

Lithology	Atg-Di-Dol rock					Cpx-serpentinite		Dol-Atg-schist		
Sample	SN-101	SN-101	SN-98	SN-98	SN-98	SN-12	SN-12	SN-23	SN-23	SN-23
Mineral	*Cal*	*Dol*	*Cal (in Di)*	*Dol*	*Dol (in Di)*	*Cal*	*Dol*	*Dol (zoned)*	*Dol (zoned)*	*Mgs*
SiO_2	b.d.	b.d.	0.07	b.d.	b.d.	0.11	b.d.	0.09	0.14	0.16
FeO	0.13	1.11	0.22	0.66	0.92	0.85	0.81	0.45	0.34	0.35
MnO	0.18	0.17	0.12	0.13	0.16	b.d.	0.13	0.01	b.d.	b.d.
MgO	1.48	20.93	2.16	20.96	20.00	1.30	20.79	20.38	21.42	48.47
CaO	54.30	29.84	52.38	30.41	30.07	53.87	29.78	31.40	30.82	0.19
SrO	b.d.	b.d.	b.d.	b.d.	b.d.	b.d.	b.d.	0.05	0.13	b.d.
BaO	b.d.	0.04	b.d.	b.d.	b.d.	b.d.	b.d.	b.d.	b.d.	b.d.
CO_2 (calc)	44.43	47.09	43.78	47.23	46.12	44.39	46.65	47.33	48.04	53.28
Total	100.52	99.18	98.73	99.39	97.27	100.53	98.15	99.71	100.88	102.45
Ions per 6 O										
Si	b.d.	b.d.	0.007	b.d.	b.d.	0.011	b.d.	0.008	0.012	0.013
Fe	0.011	0.086	0.018	0.052	0.074	0.070	0.064	0.035	0.026	0.024
Mn	0.015	0.013	0.010	0.010	0.013	b.d.	0.010	0.001	b.d.	b.d.
Mg	0.218	2.914	0.323	2.907	2.843	0.192	2.920	2.821	2.922	5.933
Ca	5.756	2.985	5.634	3.031	3.071	5.715	3.006	3.123	3.021	0.017
Sr	b.d.	b.d.	b.d.	b.d.	b.d.	b.d.	b.d.	0.003	0.007	b.d.
Ba	b.d.	0.002	b.d.	b.d.	b.d.	b.d.	b.d.	b.d.	b.d.	b.d.
∑ cations	6.000	6.000	5.993	6.000	6.000	5.989	6.000	5.992	5.988	5.987
X_{MgCO3}	0.036	0.487	0.054	0.485	0.475	0.032	0.488	0.472	0.490	0.993
X_{FeCO3}	0.002	0.014	0.003	0.009	0.012	0.012	0.011	0.006	0.004	0.004
X_{CaCO3}	0.962	0.499	0.943	0.506	0.513	0.956	0.502	0.522	0.506	0.003
T (°C) *	*466*		*543*			*443*				

*Cal = calcite; Arag = aragonite; Dol = dolomite; Mgs = magnesite; TiCl = Ti-clinohumite; TiChn = Ti-chondrodite; Ol = olivine; Di = diopside; b.d. = below detection limit; CO_2 calculated for ideal stoichiometry. *T from calcite-dolomite thermometry using the ternary carbonate model after Anovitz & Essene (1987).*

Table A-5.4 (b) *Representative microprobe analyses (EMPA) of carbonates at Almirez. EMPA settings see Ch. 3, section 3.3.3, and Table 3.2.*

Lithology	granofelsic meta-ophicarbonate							
Sample	SN-135	SN-138	SN-138	SN-135	SN-135	SN-138	SN-135	SN-138
Mineral	*Arag (in TiCl)*	*Arag (in Ol)*	*Cal (matrix)*	*Cal (in Ol)*	*Cal (in TiCl)*	*Cal (in TiCl)*	*Dol*	*Dol (in TiCl)*
SiO_2	0.07	0.10	b.d.	0.03	b.d.	0.04	b.d.	b.d.
FeO	0.18	0.26	0.09	0.19	0.19	0.48	0.56	0.86
MnO	0.02	0.03	0.11	0.02	0.14	0.14	0.14	0.16
MgO	0.06	0.04	1.46	0.81	1.78	3.93	20.83	20.72
CaO	56.51	56.23	54.38	55.51	53.87	51.15	30.55	30.36
SrO	b.d.	b.d.	b.d.	b.d.	b.d.	b.d.	b.d.	b.d.
BaO	b.d.	b.d.	b.d.	0.03	b.d.	b.d.	b.d.	b.d.
CO_2 (calc)	44.63	44.50	44.43	44.63	44.43	44.89	47.14	47.07
Total	101.46	101.16	100.48	101.21	100.41	100.64	99.23	99.17
Ions per 6 O								
Si	0.007	0.010	b.d.	0.003	b.d.	0.004	b.d.	b.d.
Fe	0.015	0.021	0.008	0.016	0.015	0.040	0.043	0.067
Mn	0.001	0.002	0.010	0.002	0.012	0.012	0.011	0.012
Mg	0.009	0.006	0.216	0.119	0.263	0.574	2.894	2.884
Ca	5.962	5.951	5.767	5.858	5.710	5.366	3.051	3.036
Sr	b.d.	b.d.	b.d.	b.d.	b.d.	b.d.	b.d.	b.d.
Ba	b.d.	b.d.	b.d.	0.001	b.d.	b.d.	b.d.	b.d.
∑ cations	5.993	5.990	6.000	5.997	6.000	5.996	6.000	6.000
X_{MgCO3}	0.001	0.001	0.036	0.020	0.044	0.096	0.483	0.482
X_{FeCO3}	0.002	0.004	0.001	0.003	0.003	0.007	0.007	0.011
X_{CaCO3}	0.996	0.995	0.963	0.978	0.954	0.897	0.509	0.507
T (°C) *			*464*	*348*	*502*	*665*		

Table A-5.4 (b) continued.

Lithology	gneissic meta-ophicarbonate					Tr-Di-Dol rock		
Sample	SN-136	SN-136	SN-136	SN-136	SN-136	SN-143	SN-143	SN-143
Mineral	Cal (vein)	Dol (matrix)	Dol (in TiCl)	Dol (in Di)	Dol (in Tr)	Cal (in Tr)	Dol	Mgs (in Dol)
SiO_2	0.18	b.d.	b.d.	0.06	0.06	0.05	0.09	b.d.
FeO	0.13	0.95	0.72	0.96	0.69	0.21	1.38	5.93
MnO	0.16	0.16	0.16	0.57	0.12	0.04	0.07	0.20
MgO	0.16	20.70	20.59	19.81	20.98	1.35	20.61	42.39
CaO	55.56	30.45	30.62	30.30	30.17	54.31	30.28	0.55
SrO	b.d.	b.d.	b.d.	b.d.	b.d.	b.d.	b.d.	b.d.
BaO	b.d.	b.d.	b.d.	b.d.	b.d.	b.d.	b.d.	0.04
CO_2 (calc)	44.21	47.17	47.04	46.44	47.17	44.34	47.29	50.49
Total	100.39	99.43	99.12	98.15	99.19	100.31	99.73	99.60
Ions per 6 O								
Si	0.017	b.d.	b.d.	0.006	0.005	0.005	0.009	b.d.
Fe	0.011	0.074	0.056	0.076	0.054	0.018	0.107	0.432
Mn	0.014	0.013	0.012	0.046	0.010	0.003	0.006	0.014
Mg	0.024	2.874	2.867	2.794	2.914	0.200	2.855	5.501
Ca	5.917	3.039	3.064	3.071	3.012	5.769	3.014	0.052
Sr	b.d.	b.d.	b.d.	b.d.	b.d.	b.d.	b.d.	b.d.
Ba	b.d.	b.d.	b.d.	b.d.	b.d.	b.d.	b.d.	0.001
∑ cations	5.983	6.000	6.000	5.994	5.995	5.995	5.991	6.000
X_{MgCO3}	0.004	0.480	0.479	0.470	0.487	0.033	0.478	0.919
X_{FeCO3}	0.002	0.012	0.009	0.013	0.009	0.003	0.018	0.072
X_{CaCO3}	0.994	0.508	0.512	0.517	0.504	0.964	0.504	0.009
T (°C) *						*450*		

Table A-5.4 (b) continued.

Lithology	Tlc-Mgs rock				Tr-Ol-Chl-Atg rock
Sample	SN-137	SN-137	SN-137	SN-137	SN-146
Mineral	Cal	Cal	Dol	Mgs	Dol
SiO_2	0.03	0.03	0.03	0.02	0.06
FeO	0.29	1.68	0.59	3.81	0.78
MnO	b.d.	0.31	0.15	0.40	0.20
MgO	1.55	0.26	21.30	44.02	21.31
CaO	54.59	53.87	30.15	0.75	30.12
SrO	b.d.	b.d.	b.d.	b.d.	0.07
BaO	b.d.	b.d.	0.08	b.d.	0.03
CO_2 (calc)	44.75	43.82	47.43	51.27	47.63
Total	101.21	99.97	99.73	100.28	100.20
Ions per 6 O					
Si	0.003	0.003	0.003	0.002	0.006
Fe	0.024	0.141	0.046	0.273	0.060
Mn	b.d.	0.026	0.012	0.029	0.016
Mg	0.226	0.039	2.942	5.625	2.931
Ca	5.743	5.788	2.992	0.069	2.977
Sr	b.d.	b.d.	b.d.	b.d.	0.004
Ba	b.d.	b.d.	0.003	b.d.	0.001
∑ cations	5.997	5.997	5.997	5.998	5.994
X_{MgCO3}	0.038	0.007	0.492	0.943	0.491
X_{FeCO3}	0.004	0.024	0.008	0.046	0.010
X_{CaCO3}	0.958	0.970	0.500	0.012	0.499
T (°C) *	*473*				

Cal = calcite; Arag = aragonite; Dol = dolomite; Mgs = magnesite; TiCl = Ti-clinohumite; TiChn = Ti-chondrodite; Ol = olivine; Di = diopside; b.d. = below detection limit; CO_2 calculated for ideal stoichiometry.
**T from calcite-dolomite thermometry using the ternary carbonate model after Anovitz & Essene (1987).*

Table A-5.5 (a) *Representative microprobe analyses of TiCl, TiChn and Ol in Milagrosa marbles and serpentinites. EMPA settings see Ch. 3, section 3.3.3, and Table 3.2.*

Lithology	TiCl-Cal marble*			Atg-Di-Dol rock	Cpx-serpentinite				Atg-serp.
Sample	SN-10	SN-10	SN-100	SN-98a	SN-11	SN-12	SN-12	SN-12	SN-107
Mineral	Ti-Chn	TiCl	TiCl	TiCl	TiCl	TiCl (rim)	TiCl (core)	Ol	TiCl
SiO_2	33.90	37.19	37.21	36.86	36.36	36.53	36.00	39.71	36.92
TiO_2	7.02	2.73	2.21	3.41	4.57	2.62	4.67	b.d.	5.19
Al_2O_3	b.d.	0.02	0.02	b.d.	b.d.	b.d.	b.d.	0.01	b.d.
Cr_2O_3	b.d.	b.d.	b.d.	b.d.	b.d.	b.d.	b.d.	b.d.	b.d.
FeO	5.06	5.09	3.12	6.85	7.89	7.25	8.00	7.99	6.19
NiO	0.01	0.01	0.01	0.03	0.11	0.09	0.11	0.15	0.14
MnO	0.25	0.19	0.31	0.24	0.22	0.25	0.23	0.23	0.48
MgO	50.78	52.32	55.00	50.76	49.91	51.05	49.83	51.79	50.22
CaO	0.13	0.05	0.16	0.02	0.01	0.06	0.01	b.d.	b.d.
Na_2O	b.d.	b.d.	b.d.	b.d.	0.02	b.d.	b.d.	b.d.	b.d.
K_2O	0.01	b.d.	b.d.	b.d.	b.d.	b.d.	b.d.	b.d.	b.d.
F	1.39	1.10	1.27	0.69	0.41	1.04	0.35	b.d.	b.d.
Cl	b.d.	b.d.	b.d.	b.d.	b.d.	b.d.	b.d.	b.d.	b.d.
Total	98.55	98.70	99.32	98.87	99.50	98.90	99.21	99.88	99.15
H_2O (calc)	2.87	1.67	1.76	1.70	1.57	1.71	1.57		1.63
O=F,Cl	0.59	0.46	0.53	0.29	0.17	0.44	0.15		0.00
Hydr. total	100.84	99.91	100.54	100.27	100.89	100.16	100.61		100.76
Ions per..	*7 cat.*	*13 cat.*	*13 cat.*	*13 cat.*	*13 cat.*	*13 cat.*	*13 cat.*	*4 O*	*13 cat.*
Si	1.986	3.971	3.903	3.958	3.903	3.924	3.875	0.971	3.954
Ti	0.309	0.219	0.174	0.275	0.369	0.212	0.378	b.d.	0.418
Al	b.d.	0.002	0.003	b.d.	b.d.	b.d.	b.d.	0.000	b.d.
Cr	b.d.	b.d.	b.d.	b.d.	b.d.	b.d.	b.d.	b.d.	b.d.
Fe	0.248	0.455	0.274	0.615	0.708	0.651	0.720	0.163	0.554
Ni	0.001	0.001	0.001	0.003	0.009	0.008	0.009	0.003	0.012
Mn	0.012	0.017	0.027	0.022	0.020	0.023	0.021	0.005	0.043
Mg	4.435	8.329	8.600	8.125	7.986	8.175	7.996	1.887	8.018
Ca	0.008	0.006	0.018	0.002	0.001	0.006	0.001	b.d.	b.d.
Na	b.d.	b.d.	b.d.	b.d.	0.004	b.d.	b.d.	b.d.	b.d.
K	0.001	b.d.	b.d.	b.d.	b.d.	b.d.	b.d.	b.d.	b.d.
F	0.258	0.372	0.421	0.233	0.138	0.353	0.120	b.d.	b.d.
Cl	b.d.	b.d.	b.d.	b.d.	b.d.	b.d.	b.d.	b.d.	b.d.
OH (calc)	1.124	1.190	1.230	1.216	1.124	1.223	1.124		1.164
∑ cations	7.000	13.000	13.000	13.000	13.000	13.000	13.000	3.029	13.000
Mg/(Mg+Fe)	0.95	0.95	0.97	0.93	0.92	0.93	0.92	0.92	0.94
∑M	4.70	8.80	8.90	8.76	8.72	8.86	8.75	2.06	8.63
X(F)=F/2	0.13	0.19	0.21	0.12	0.07	0.18	0.06		0.00

**see Table 5.1 for an overview of the lithologies.*

TiCl = Ti-clinohumite; TiChn = Ti-chondrodite; Ol = olivine; Dol = dolomite; b.d. = below detection limit; OH calculated for TiCl and TiChn as $[OH, F]_{(2-2x)}$ *with x = Ti in ideal structural formular.* ∑M = Fe+Mn+Ni+Mg.

Table A-5.5 (b) *Representative microprobe analyses of TiCl, TiChn and Ol in Almirez meta-ophicarbonates and Chl-harzburgite. EMPA settings see Ch. 3, section 3.3.3, and Table 3.2.*

Lithology	granofelsic meta-ophicarbonate					gneissic meta-ophicarbonate		host Chl-harzburgite			
Sample	SN-135	SN-138	SN-135	SN-138	SN-138	SN-136	SN-136	SN-128	SN-134	SN-146	SN-146
Mineral	Ol	Ol	TiCl	TiChn (core)	TiCl (rim)	TiChn	TiCl	Ol	Ol	Ol	Ol (in Dol)
SiO_2	40.93	40.27	36.92	33.69	37.59	35.03	37.13	39.94	41.87	39.73	41.93
TiO_2	b.d.	b.d.	2.63	5.43	1.02	3.93	2.02	b.d.	b.d.	0.02	b.d.
Al_2O_3	b.d.	b.d.	b.d.	b.d.	b.d.	b.d.	b.d.	b.d.	0.01	b.d.	b.d.
Cr_2O_3	b.d.	b.d.	b.d.	0.03	b.d.	0.03	b.d.	b.d.	b.d.	b.d.	b.d.
FeO	5.50	5.84	4.88	5.45	4.29	5.11	6.26	10.15	9.57	9.56	7.01
NiO	0.19	0.21	0.14	0.10	0.15	0.12	0.12	0.40	0.47	0.45	0.21
MnO	0.37	0.31	0.31	0.25	0.33	0.28	0.24	0.18	0.13	0.18	0.30
MgO	53.56	53.94	52.37	51.46	54.93	51.39	51.59	49.36	48.25	50.17	50.38
CaO	0.02	0.03	0.02	0.02	b.d.	0.02	0.02	0.02	0.07	b.d.	0.14
Na_2O	b.d.	0.02	b.d.	0.03	b.d.	b.d.	b.d.	0.03	b.d.	b.d.	b.d.
K_2O	b.d.	b.d.	b.d.	0.01	0.01	b.d.	b.d.	b.d.	b.d.	b.d.	b.d.
F	b.d.	b.d.	1.14	1.69	1.79	3.04	1.27	b.d.	b.d.	b.d.	b.d.
Cl	b.d.	b.d.	b.d.	b.d.	b.d.	b.d.	0.011	b.d.	b.d.	b.d.	0.009
Total	100.56	100.62	98.41	98.16	100.11	98.95	98.67	100.08	100.37	100.11	99.98
H_2O (calc)			1.67	3.09	1.79	2.78	1.73				
O=F,Cl			0.48	0.71	0.75	1.28	0.54				
Hydr. total			99.60	100.53	101.14	100.46	99.86				
Ions per..	*4 O*	*4 O*	*13 cat.*	*7 cat.*	*13 cat.*	*7 cat.*	*13 cat.*	*4 O*	*4 O*	*4 O*	*4 O*
Si	0.982	0.968	3.952	1.974	3.933	2.056	3.986	0.983	1.020	0.976	1.014
Ti	b.d.	b.d.	0.212	0.239	0.080	0.174	0.163	b.d.	b.d.	0.000	b.d.
Al	b.d.	b.d.	b.d.	b.d.	b.d.	b.d.	b.d.	b.d.	0.000	b.d.	b.d.
Cr	b.d.	b.d.	b.d.	0.001	b.d.	0.001	b.d.	b.d.	b.d.	b.d.	b.d.
Fe	0.110	0.117	0.437	0.267	0.375	0.251	0.562	0.209	0.195	0.196	0.142
Ni	0.004	0.004	0.012	0.005	0.013	0.005	0.011	0.008	0.009	0.009	0.004
Mn	0.007	0.006	0.028	0.012	0.030	0.014	0.022	0.004	0.003	0.004	0.006
Mg	1.915	1.934	8.357	4.496	8.568	4.497	8.255	1.811	1.751	1.838	1.816
Ca	0.000	0.001	0.003	0.001	b.d.	0.001	0.002	0.001	0.002	b.d.	0.004
Na	b.d.	0.001	b.d.	0.003	b.d.	b.d.	b.d.	0.002	b.d.	b.d.	b.d.
K	b.d.	b.d.	b.d.	0.001	0.001	b.d.	b.d.	b.d.	b.d.	b.d.	b.d.
F	b.d.	b.d.	0.386	0.313	0.592	0.564	0.431	b.d.	b.d.	b.d.	b.d.
Cl	b.d.	b.d.	b.d.	b.d.	b.d.	b.d.	0.002	b.d.	b.d.	b.d.	0.000
OH (calc)			1.190	1.208	1.248	1.089	1.240				
∑ cations	3.018	3.032	13.000	7.000	13.000	7.000	13.000	3.018	2.980	3.023	2.986
Mg/(Mg+Fe)	0.95	0.94	0.95	0.94	0.96	0.95	0.94	0.90	0.90	0.90	0.93
∑M	2.04	2.06	8.83	4.78	8.99	4.77	8.85	2.03	1.96	2.05	1.97
X(F)=F/2			0.19	0.16	0.30	0.28	0.22				

TiCl = Ti-clinohumite; TiChn = Ti-chondrodite; Ol = olivine; Dol = dolomite; b.d. = below detection limit; OH calculated for TiCl and TiChn as $[OH, F]_{(2-2x)}$ with x = Ti in ideal structural formular. ∑M = Fe+Mn+Ni+Mg.

Table A-5.6 (a) *Representative microprobe analyses of Cpx, Di ,Tr and Tlc in Milagrosa marbles and serpentinites. EMPA settings see Ch. 3, section 3.3.3, and Table 3.2.*

Lithology	TiCl-Cal marble		Di-Dol marble		Atg-Di-Dol rock	
Sample	SN-10	SN-100	SN-09	SN-09	SN-98	SN-101
Mineral	Cpx	Di	Di	Tr	Di	Di
SiO_2	55.44	54.99	55.20	58.53	54.78	54.74
TiO_2	0.02	0.02	b.d.	0.02	0.03	0.03
Al_2O_3	0.03	0.03	0.02	0.02	0.03	0.01
Cr_2O_3	b.d.	b.d.	b.d.	b.d.	b.d.	b.d.
FeO	0.90	0.38	1.20	0.81	0.74	1.01
NiO	0.01	b.d.	b.d.	0.02	b.d.	b.d.
MnO	0.05	0.05	0.06	0.05	0.07	0.05
MgO	18.24	18.49	17.59	24.36	18.60	18.14
CaO	25.26	26.13	25.71	13.70	25.99	26.05
Na_2O	0.03	0.04	0.04	0.05	b.d.	0.03
K_2O	b.d.	b.d.	b.d.	0.01	b.d.	b.d.
F				0.10		
Cl				b.d.		
Total	99.99	100.13	99.82	97.69	100.24	100.06
H_2O (calc)				2.15		
O=F,Cl				0.04		
Hydr. Total				99.80		
Ions per..	*6 oxygens*	*6 oxygens*	*6 oxygens*	*23 oxygens*	*6 oxygens*	*6 oxygens*
Si	2.003	1.987	2.008	7.970	1.981	1.986
Ti	0.000	0.001	b.d.	0.002	0.001	0.001
Al	0.001	0.001	0.001	0.003	0.001	0.001
Cr	b.d.	b.d.	b.d.	b.d.	b.d.	b.d.
Fe	0.027	0.012	0.036	0.092	0.022	0.031
Ni	0.000	b.d.	b.d.	0.003	b.d.	b.d.
Mn	0.002	0.001	0.002	0.006	0.002	0.001
Mg	0.983	0.996	0.954	4.944	1.003	0.981
Ca	0.978	1.012	1.002	1.998	1.007	1.012
Na	0.002	0.003	0.003	0.013	b.d.	0.002
K	b.d.	b.d.	b.d.	0.002	b.d.	b.d.
F				0.044		
Cl				b.d.		
OH (calc)				1.956		
$\sum$ cations	3.997	4.013	4.006	15.034	4.017	4.014
Mg/(Mg+Fe)	0.97	0.99	0.96	0.98	0.98	0.97

Di = diopside; Cpx = clinopyroxene; Tr = tremolite; Tlc = talc; TiCl = Ti-clinohumite; TiChn = Ti-chondrodite; Ol = olivine; Dol = dolomite; b.d. = below detection limit; all Fe reported as ferrous iron.

Table A-5.6 (a) continued. *Representative microprobe analyses of Cpx, Di ,Tr and Tlc in Milagrosa marbles and serpentinites. EMPA settings see Ch. 3, section 3.3.3, and Table 3.2.*

Lithology	Cpx-serpentinite						
Sample	SN-11	SN-12	SN-90	SN-91	SN-105	SN-105	SN-105
Mineral	Di	Di	Di	Di	Di	Cpx	Tr
SiO_2	55.83	54.61	54.72	55.03	55.77	54.87	58.13
TiO_2	0.05	0.02	b.d.	b.d.	0.02	0.18	0.02
Al_2O_3	b.d.	0.02	0.03	b.d.	0.01	0.86	0.12
Cr_2O_3	0.06	0.06	0.07	0.03	b.d.	0.43	b.d.
FeO	0.76	1.32	1.52	1.07	1.12	1.88	1.36
NiO	0.02	b.d.	0.05	0.03	0.05	0.14	0.08
MnO	0.05	0.07	0.18	0.10	0.13	0.17	0.11
MgO	17.83	18.21	18.06	18.43	17.53	16.73	24.44
CaO	25.81	25.69	25.62	25.76	25.43	24.87	13.76
Na_2O	b.d.	0.02	b.d.	0.04	0.05	0.30	0.14
K_2O	b.d.	b.d.	b.d.	b.d.	b.d.	b.d.	0.02
F							b.d.
Cl							0.008
Total	100.40	100.03	100.25	100.48	100.11	100.43	98.20
H_2O (calc)							2.20
O=F,Cl							0.00
Hydr. Total							100.39
Ions per..	*6 oxygens*	*6 oxygens*	*6 oxygens*	*6 oxygens*	*6 oxygens*	*6 oxygens*	*23 oxygens*
Si	2.009	1.983	1.985	1.987	2.015	1.986	7.906
Ti	0.001	0.001	b.d.	b.d.	0.001	0.005	0.002
Al	b.d.	0.001	0.001	b.d.	0.000	0.037	0.020
Cr	0.002	0.002	0.002	0.001	b.d.	0.012	b.d.
Fe	0.023	0.040	0.046	0.032	0.034	0.057	0.155
Ni	0.001	b.d.	0.001	0.001	0.001	0.004	0.009
Mn	0.001	0.002	0.006	0.003	0.004	0.005	0.013
Mg	0.957	0.986	0.977	0.992	0.944	0.903	4.955
Ca	0.995	0.999	0.996	0.996	0.984	0.964	2.005
Na	b.d.	0.002	b.d.	0.003	0.003	0.021	0.036
K	b.d.	b.d.	b.d.	b.d.	b.d.	b.d.	0.003
F							b.d.
Cl							0.002
OH (calc)							1.998
$\sum$ cations	3.989	4.016	4.013	4.014	3.986	3.995	15.102
Mg/(Mg+Fe)	0.98	0.96	0.95	0.97	0.97	0.94	0.97

Di = diopside; Cpx = clinopyroxene; Tr = tremolite; Tlc = talc; TiCl = Ti-clinohumite; TiChn = Ti-chondrodite; Ol = olivine; Dol = dolomite; b.d. = below detection limit; all Fe reported as ferrous iron.

Table A-5.6 (b) *Representative microprobe analyses of Cpx, Di ,Tr and Tlc in Almirez carbonate-silicate rocks. EMPA settings see Ch. 3, section 3.3.3, and Table 3.2.*

Lithology	granofelsic meta-ophicarbonate			gneissic meta-ophicarbonate		Tlc-Mgs rock
Sample	SN-135	SN-135	SN-138	SN-136	SN-136	SN-137
Mineral	Di (core)	Di (rim)	Di	Di	Tr	Tlc
SiO_2	56.01	56.04	55.08	54.89	58.59	63.33
TiO_2	b.d.	b.d.	b.d.	b.d.	b.d.	0.03
Al_2O_3	0.09	0.08	0.03	0.05	0.22	0.15
Cr_2O_3	0.15	0.04	b.d.	b.d.	b.d.	b.d.
FeO	1.04	0.72	0.60	0.78	0.75	0.65
NiO	0.01	b.d.	0.02	0.02	0.02	0.06
MnO	0.09	0.03	0.05	0.05	0.04	b.d.
MgO	17.70	17.85	18.46	17.84	24.16	31.55
CaO	25.39	25.92	26.05	25.99	13.79	0.07
Na_2O	0.12	b.d.	0.03	b.d.	0.14	0.10
K_2O	b.d.	b.d.	b.d.	b.d.	0.02	b.d.
F					0.09	b.d.
Cl					b.d.	0.012
Total	100.61	100.69	100.32	99.62	97.82	96.04
H_2O (calc)					2.16	4.76
O=F,Cl					0.04	0.00
Hydr. Total					99.94	100.70
Ions per..	*6 oxygens*	*6 oxygens*	*6 oxygens*	*6 oxygens*	*23 oxygens*	*22 oxygens*
Si	2.012	2.010	1.988	1.998	7.965	7.973
Ti	b.d.	b.d.	b.d.	b.d.	b.d.	0.003
Al	0.004	0.004	0.001	0.002	0.035	0.022
Cr	0.004	0.001	b.d.	b.d.	b.d.	b.d.
Fe	0.031	0.022	0.018	0.024	0.086	0.069
Ni	0.000	b.d.	0.001	0.001	0.002	0.006
Mn	0.003	0.001	0.002	0.002	0.004	b.d.
Mg	0.948	0.955	0.993	0.968	4.896	5.921
Ca	0.977	0.996	1.007	1.013	2.008	0.009
Na	0.009	b.d.	0.002	b.d.	0.037	0.024
K	b.d.	b.d.	b.d.	b.d.	0.004	b.d.
F					0.038	b.d.
Cl					b.d.	0.002
OH (calc)					1.962	3.998
$\sum$ cations	3.988	3.988	4.012	4.007	15.037	14.027
Mg/(Mg+Fe)	0.97	0.98	0.98	0.98	0.98	0.99

Di = diopside; Cpx = clinopyroxene; Tr = tremolite; Tlc = talc; TiCl = Ti-clinohumite; TiChn = Ti-chondrodite; Ol = olivine; Dol = dolomite; b.d. = below detection limit; all Fe reported as ferrous iron.

Table A-5.6 (b) continued. *Representative microprobe analyses of Cpx, Di ,Tr and Tlc in Almirez carbonate-silicate rocks. EMPA settings see Ch. 3, section 3.3.3, and Table 3.2.*

Lithology	Tr-Di-Dol rock				Tr-Ol-Chl-Atg rock	
Sample	SN-143	SN-143	SN-143	SN-143	SN-146	SN-146
Mineral	Di	Tr	Tr	Edenite	Di	Tr
SiO_2	54.94	56.00	57.56	47.26	55.24	58.26
TiO_2	b.d.	0.06	0.03	0.20	b.d.	0.02
Al_2O_3	0.07	1.36	0.43	8.49	0.05	0.32
Cr_2O_3	0.12	0.29	0.03	0.66	b.d.	0.03
FeO	1.56	2.49	1.03	4.95	1.41	1.57
NiO	0.03	0.16	0.01	0.08	0.02	0.07
MnO	0.04	0.02	0.02	b.d.	0.13	0.08
MgO	17.64	22.76	24.31	19.38	18.12	24.51
CaO	25.44	12.79	13.86	12.35	25.36	12.74
Na_2O	0.14	0.80	0.22	2.58	0.24	0.37
K_2O	b.d.	0.16	0.03	0.70	b.d.	0.10
F		0.11	0.16	0.19		b.d.
Cl		0.011	b.d.	0.243		0.015
Total	99.97	97.01	97.69	97.09	100.57	98.09
H_2O (calc)		2.10	2.11	1.93		2.20
O=F,Cl		0.05	0.07	0.14		0.00
Hydr. Total		99.06	99.73	98.87		100.29
Ions per..	*6 oxygens*	*23 oxygens*	*23 oxygens*	*23 oxygens*	*6 oxygens*	*23 oxygens*
Si	1.996	7.779	7.873	6.799	1.993	7.920
Ti	b.d.	0.006	0.003	0.021	b.d.	0.002
Al	0.003	0.222	0.069	1.440	0.002	0.051
Cr	0.004	0.032	0.003	0.075	b.d.	0.004
Fe	0.047	0.289	0.118	0.596	0.043	0.178
Ni	0.001	0.018	0.001	0.009	0.001	0.008
Mn	0.001	0.002	0.003	b.d.	0.004	0.009
Mg	0.955	4.713	4.957	4.156	0.975	4.967
Ca	0.990	1.903	2.031	1.903	0.980	1.855
Na	0.010	0.215	0.058	0.720	0.017	0.098
K	b.d.	0.029	0.004	0.128	b.d.	0.018
F		0.049	0.070	0.088		b.d.
Cl		0.003	b.d.	0.059		0.003
OH (calc)		1.948	1.930	1.853		1.997
$\sum$ cations	4.006	15.209	15.119	15.846	4.014	15.109
Mg/(Mg+Fe)	0.95	0.94	0.98	0.87	0.96	0.97

Di = diopside; Cpx = clinopyroxene; Tr = tremolite; Tlc = talc; TiCl = Ti-clinohumite; TiChn = Ti-chondrodite; Ol = olivine; Dol = dolomite; b.d. = below detection limit; all Fe reported as ferrous iron.

Table A-5.7 (a) *Representative microprobe analyses of serpentine and chlorite in Milagrosa carbonate rocks and serpentinites. EMPA settings see Ch. 3, section 3.3.3, and Table 3.2.*

Lithology	Atg-serpentinite		Cpx-serpentinite							
Sample	Sn-02	SN-107	SN-90	SN-91	SN-96	SN-105	SN-105	SN-12	SN-12	SN-11
Mineral	Atg	Atg	Atg	Atg	Atg	Atg	Chl	Atg	Chl	Chl
SiO_2	41.35	41.43	42.21	42.80	42.06	41.12	33.88	42.29	34.15	34.00
TiO_2	0.04	0.04	0.02	0.03	b.d.	b.d.	b.d.	b.d.	b.d.	b.d.
Al_2O_3	3.20	2.99	3.51	2.18	3.31	3.57	12.91	2.85	12.77	12.98
Cr_2O_3	0.24	0.43	0.33	0.12	0.33	0.40	0.66	0.30	0.37	0.58
FeO	5.23	2.77	3.02	2.54	3.49	4.77	4.39	3.22	3.69	4.00
NiO	0.13	0.22	0.22	0.07	0.40	0.32	0.09	0.06	0.05	0.08
MnO	0.13	0.06	0.10	0.04	0.04	0.11	0.08	0.02	0.05	0.04
MgO	37.34	39.34	38.72	40.39	38.23	37.04	35.07	38.95	35.60	35.24
CaO	0.01	b.d.	0.03	b.d.	0.04	b.d.	b.d.	0.02	0.03	0.04
Na_2O	b.d.	b.d.	0.03	b.d.	0.02	0.02	b.d.	b.d.	b.d.	0.02
K_2O	b.d.	b.d.	b.d.	b.d.	b.d.	b.d.	b.d.	b.d.	b.d.	b.d.
F	0.09	b.d.	0.17	b.d.	b.d.	b.d.	b.d.	0.10	0.09	b.d.
Cl	0.01	b.d.	b.d.	0.01	0.02	b.d.	b.d.	0.03	0.01	b.d.
Total	87.77	87.29	88.38	88.19	87.95	87.38	87.18	87.84	86.82	86.99
H_2O (calc)	11.89	12.01	12.07	12.18	12.07	11.91	12.63	12.03	12.60	12.65
O=F,Cl	0.04	0.00	0.07	0.00	0.00	0.00	0.00	0.05	0.04	0.00
Total	99.62	99.29	100.37	100.36	100.00	99.26	99.72	99.81	99.38	99.63
Ions per..	*116 oxygens*	*116 oxygens*	*116 oxygens*	*116 oxygens*	*116 oxygens*	*116 oxygens*	*28 oxygens*	*116 oxygens*	*28 oxygens*	*28 oxygens*
Si	32.20	32.06	32.29	32.65	32.38	32.10	6.43	32.53	6.48	6.45
Ti	0.02	0.03	0.01	0.02	b.d.	b.d.	b.d.	b.d.	b.d.	b.d.
Al^{IV}	1.80	1.94	1.71	1.35	1.62	1.90	1.57	1.47	1.52	1.55
Al^{VI}	1.14	0.79	1.46	0.61	1.38	1.38	1.32	1.11	1.33	1.35
Cr	0.15	0.26	0.20	0.07	0.20	0.25	0.10	0.18	0.06	0.09
Fe^{2+}	3.41	1.79	1.93	1.62	2.25	3.11	0.70	2.07	0.59	0.63
Ni	0.08	0.14	0.13	0.04	0.25	0.20	0.01	0.04	0.01	0.01
Mn	0.09	0.04	0.07	0.03	0.03	0.08	0.01	0.02	0.01	0.01
Mg	43.35	45.38	44.16	45.93	43.87	43.10	9.93	44.66	10.07	9.96
Ca	0.01	b.d.	0.03	b.d.	0.03	b.d.	b.d.	0.01	0.01	0.01
Na	b.d.	b.d.	0.05	b.d.	0.03	0.03	b.d.	b.d.	b.d.	0.01
K	b.d.	b.d.	b.d.	b.d.	b.d.	b.d.	b.d.	b.d.	b.d.	b.d.
F	0.21	b.d.	0.42	b.d.	b.d.	b.d.	b.d.	0.25	0.06	b.d.
Cl	0.02	b.d.	b.d.	0.01	0.02	b.d.	b.d.	0.03	0.00	b.d.
OH	61.77	62.00	61.58	61.99	61.98	62.00	16.00	61.72	15.94	16.00
∑ cations	82.24	82.42	82.04	82.32	82.03	82.15	20.07	82.09	20.07	20.06
Mg/(Mg+Fe)	0.93	0.96	0.96	0.97	0.95	0.93	0.93	0.96	0.95	0.94
y(Atg)=Al/8	0.37	0.34	0.40	0.25	0.38	0.41		0.32		

Atg = antigorite; Chl = chlorite; Serp = chrysotile/lizardite; b.d. = below detection limit. Atg normalized to 116 oxygen assuming a polysome m = 17 and an ideal polysomatic formular $M_{3m-3}T_{2m}O_{5m}(OH)_{4m-6}$. OH in chlorite calculated for ideal stoichiometry. All Fe given here as FeO, however Fe^{3+}/Fe_{total} in Atg ranges probably between 0.5 - 0.7 (see text).

Table A-5.7 (a) continued. *Representative microprobe analyses of serpentine and chlorite in Milagrosa carbonate rocks and serpentinites. EMPA settings see Ch. 3, section 3.3.3, and Table 3.2.*

Lithology	Dol-Atg-schist	Atg-Di-Dol rock				Di-Dol marble	TiCl-Cal marble
Sample	SN-23	SN-101	SN-98	SN-101	SN-98	SN-09	SN-100
Mineral	Atg	Atg	Atg	Chl	Chl	Chl	Chl
SiO_2	43.46	41.47	43.13	34.00	34.20	33.69	33.91
TiO_2	0.01	b.d.	0.04	b.d.	0.02	b.d.	0.01
Al_2O_3	1.20	2.93	1.82	12.53	12.14	13.59	14.58
Cr_2O_3	0.34	0.11	b.d.	0.59	0.73	0.03	b.d.
FeO	2.60	3.18	2.91	3.59	3.38	4.32	1.93
NiO	0.09	0.04	0.02	0.13	0.04	0.09	b.d.
MnO	0.06	0.07	0.06	0.04	b.d.	0.05	0.02
MgO	40.09	39.00	39.61	35.80	35.97	34.57	35.97
CaO	0.01	0.23	0.02	0.19	0.02	0.32	0.14
Na_2O	b.d.	0.02	0.06	b.d.	0.02	b.d.	b.d.
K_2O	b.d.	b.d.	b.d.	b.d.	b.d.	b.d.	b.d.
F	b.d.	b.d.	b.d.	b.d.	b.d.	b.d.	b.d.
Cl	0.02	0.02	0.01	0.01	0.01	0.02	0.02
Total	87.89	87.11	87.69	86.96	86.54	86.71	86.60
H_2O (calc)	12.14	11.97	12.11	12.64	12.61	12.59	12.76
O=F,Cl	0.00	0.00	0.00	0.00	0.00	0.00	0.00
Total	100.02	99.04	99.78	99.52	99.15	99.26	99.34
Ions per..	*116 oxygens*	*116 oxygens*	*116 oxygens*	*28 oxygens*	*28 oxygens*	*28 oxygens*	*28 oxygens*
Si	33.27	32.20	33.10	6.45	6.50	6.42	6.37
Ti	0.01	b.d.	0.02	b.d.	0.00	b.d.	0.00
Al^{IV}	0.73	1.80	0.90	1.55	1.50	1.58	1.63
Al^{VI}	0.35	0.88	0.75	1.25	1.22	1.47	1.60
Cr	0.20	0.07	b.d.	0.09	0.11	0.01	b.d.
Fe^{2+}	1.66	2.06	1.87	0.57	0.54	0.69	0.30
Ni	0.06	0.03	0.02	0.02	0.01	0.01	b.d.
Mn	0.04	0.05	0.04	0.01	b.d.	0.01	0.00
Mg	45.75	45.14	45.31	10.13	10.19	9.81	10.07
Ca	0.01	0.20	0.02	0.04	0.00	0.06	0.03
Na	b.d.	0.03	0.08	b.d.	0.01	b.d.	b.d.
K	b.d.	b.d.	b.d.	b.d.	b.d.	b.d.	b.d.
F	b.d.	b.d.	b.d.	b.d.	b.d.	b.d.	b.d.
Cl	0.02	0.03	0.02	0.00	0.00	0.01	0.00
OH	61.98	61.97	61.98	16.00	16.00	15.99	16.00
$\sum$ cations	82.08	82.44	82.10	20.10	20.08	20.06	20.01
Mg/(Mg+Fe)	0.96	0.96	0.96	0.95	0.95	0.93	0.97
y(Atg)=Al/8	0.14	0.34	0.21				

Atg = antigorite; Chl = chlorite; Serp = chrysotile/lizardite; b.d. = below detection limit. Atg normalized to 116 oxygen assuming a polysome m = 17 and an ideal polysomatic formular $M_{3m-3}T_{2m}O_{5m}(OH)_{4m-6}$. OH in chlorite calculated for ideal stoichiometry. All Fe given here as FeO, however Fe^{3+}/Fe_{total} in Atg ranges probably between 0.5 - 0.7 (see text).

Table A-5.7 (b) *Representative microprobe analyses of serpentine and chlorite in Almirez carbonate-silicate rocks. EMPA settings see Ch. 3, section 3.3.3, and Table 3.2.*

Lithology	granofelsic meta-ophicarbonate				gneissic meta-ophicarbonate		Tlc-Mgs rock
Sample	SN-138	SN-138	SN-138	SN-138	SN-136	SN-143	SN-137
Mineral	Serp	Serp	Chl	Chl	Chl	Chl	Chl
SiO_2	40.17	41.98	32.94	34.06	32.29	31.67	33.10
TiO_2	b.d.	b.d.	b.d.	b.d.	0.04	b.d.	0.06
Al_2O_3	b.d.	b.d.	15.26	13.11	15.73	15.67	15.59
Cr_2O_3	b.d.	0.02	0.98	1.19	0.79	2.25	b.d.
FeO	5.89	1.70	2.35	2.92	3.08	4.31	3.39
NiO	0.21	b.d.	0.07	0.13	0.12	0.31	0.08
MnO	0.23	0.12	0.02	0.04	0.05	0.03	0.03
MgO	38.16	40.92	35.02	36.09	34.12	32.20	34.41
CaO	0.06	0.35	0.02	0.22	0.03	0.02	0.08
Na_2O	b.d.	b.d.	b.d.	b.d.	b.d.	b.d.	b.d.
K_2O	b.d.	b.d.	b.d.	0.01	b.d.	b.d.	b.d.
F	b.d.	b.d.	b.d.	b.d.	b.d.	0.15	0.12
Cl	0.03	0.02	0.02	0.01	0.01	0.05	0.03
Total	84.81	85.11	86.68	87.82	86.31	86.69	86.90
H_2O (calc)	12.21	12.58	12.70	12.79	12.59	12.39	12.63
O=F,Cl	0.01	0.00	0.00	0.00	0.00	0.08	0.06
Total	96.94	97.68	99.37	100.57	98.85	98.97	99.46
Ions per..	*7 oxygens*	*7 oxygens*	*28 oxygens*	*28 oxygens*	*28 oxygens*	*28 oxygens*	*28 oxygens*
Si	1.972	2.001	6.22	6.39	6.15	6.09	6.26
Ti	b.d.	b.d.	b.d.	b.d.	0.01	b.d.	0.01
Al^{IV}	b.d.	b.d.	1.78	1.61	1.85	1.91	1.74
Al^{VI}	b.d.	b.d.	1.62	1.28	1.68	1.64	1.73
Cr	b.d.	0.001	0.15	0.18	0.12	0.34	b.d.
Fe^{2+}	0.242	0.068	0.37	0.46	0.49	0.69	0.54
Ni	0.008	b.d.	0.01	0.02	0.02	0.05	0.01
Mn	0.009	0.005	0.00	0.01	0.01	0.00	0.01
Mg	2.793	2.907	9.86	10.09	9.69	9.23	9.69
Ca	0.003	0.018	0.00	0.04	0.01	0.00	0.02
Na	b.d.	b.d.	b.d.	b.d.	b.d.	b.d.	b.d.
K	b.d.	b.d.	b.d.	0.00	b.d.	b.d.	b.d.
F	b.d.	b.d.	b.d.	b.d.	b.d.	0.09	0.07
Cl	0.002	0.001	0.00	0.00	0.00	0.02	0.01
OH	3.998	3.999	16.00	16.00	16.00	15.89	15.92
$\sum$ cations	5.028	4.999	20.01	20.08	20.02	19.96	20.00
Mg/(Mg+Fe)	0.92	0.98	0.96	0.96	0.95	0.93	0.95
y(Atg)=Al/8	0.00	0.00					

Chl = chlorite; Serp = chrysotile/lizardite; b.d. = below detection limit. OH in chlorite calculated for ideal stoichiometry. All Fe given here as FeO.

Table A-5.8 (a) *Representative microprobe analyses of oxides in Milagrosa carbonate rocks and serpentinites. EMPA settings see Ch. 3, section 3.3.3, and Table 3.2.*

Lithology	TiCl-Cal-marble		Di-Dol-marble		Atg-Di-Dol rock		
Sample	SN-100	SN-100	SN-09	SN-09	SN-98	SN-98	SN-98
Mineral	Prv	Ilm	Ilm	Mag	Ilm	Mag	Mag
SiO_2	0.03	b.d.	b.d.	b.d.	0.02	0.05	b.d.
TiO_2	57.35	53.03	51.36	0.12	53.40	1.22	0.21
Al_2O_3	0.04	b.d.	b.d.	b.d.	0.01	b.d.	b.d.
Cr_2O_3	b.d.	b.d.	0.06	1.78	b.d.	0.46	2.98
Fe_2O_3		3.89	4.67	67.66	4.95	67.33	66.57
FeO	0.80	35.13	34.37	30.62	29.44	31.65	29.43
NiO	b.d.	b.d.	0.03	0.13	b.d.	0.06	0.11
MnO	0.03	2.55	4.59	0.09	2.37	0.06	0.49
MgO	0.03	5.06	3.91	0.34	9.08	0.55	0.96
CaO	38.94	0.76	0.15	0.05	0.03	0.06	b.d.
ZnO	n.m.	n.m.	n.m.	n.m.	n.m.	n.m.	n.m.
V_2O_3	n.m.	n.m.	n.m.	n.m.	n.m.	n.m.	n.m.
Total	97.22	100.42	99.13	100.79	99.30	101.45	100.75
Ions per..	*3 oxygens*	*2 cations*	*2 cations*	*3 cations*	*2 cations*	*3 cations*	*3 cations*
Si	0.001	b.d.	b.d.	b.d.	0.000	0.002	b.d.
Ti	1.004	0.965	0.956	0.004	0.955	0.035	0.006
Al	0.001	b.d.	b.d.	b.d.	0.000	b.d.	b.d.
Cr	b.d.	b.d.	0.001	0.054	b.d.	0.014	0.089
Fe^{3+}		0.071	0.087	1.939	0.089	1.913	1.899
Fe^{2+}	0.016	0.710	0.711	0.975	0.585	0.999	0.933
Ni	b.d.	b.d.	0.001	0.004	b.d.	0.002	0.003
Mn	0.001	0.052	0.096	0.003	0.048	0.002	0.016
Mg	0.001	0.182	0.144	0.019	0.322	0.031	0.054
Ca	0.971	0.020	0.004	0.002	0.001	0.002	b.d.
Zn	n.m.	n.m.	n.m.	n.m.	n.m.	n.m.	n.m.
V	n.m.	n.m.	n.m.	n.m.	n.m.	n.m.	n.m.
$\sum$ cations	1.994	2.000	2.000	3.000	2.000	3.000	3.000

Prv = perovskite; Ilm = ilmenite; Mag = magnetite; Fe-Chr = Fe-chromite; Rt = rutile; n.m. = not measured; b.d. = below detection limit; ferric/ferrous iron calculated assuming charge balance.

Table A-5.8 (a) continued. *Representative microprobe analyses of oxides in Milagrosa carbonate rocks and serpentinites. EMPA settings see Ch. 3, section 3.3.3, and Table 3.2.*

Lithology	Atg-serpentinite		Cpx-serpentinite			
Sample	SN-107	SN-107	SN-105	SN-105	SN-96	SN-96
Mineral	Ilm	Mag	Ilm	Mag	Ilm	Mag
SiO_2	b.d.	b.d.	b.d.	0.03	0.02	b.d.
TiO_2	57.22	0.38	51.76	0.17	52.79	0.05
Al_2O_3	0.01	0.02	b.d.	b.d.	b.d.	b.d.
Cr_2O_3	0.03	b.d.	0.06	4.53	b.d.	1.66
Fe_2O_3	2.70	69.15	2.72	63.73	1.00	67.96
FeO	20.36	29.04	37.50	30.14	36.64	30.77
NiO	0.03	0.23	0.01	0.13	0.02	0.08
MnO	6.32	0.23	5.87	0.32	7.56	0.17
MgO	13.85	1.30	1.72	0.33	1.79	0.26
CaO	b.d.	0.01	0.01	0.03	0.01	0.01
ZnO	b.d.	b.d.	0.04	b.d.	b.d.	b.d.
V_2O_3	0.36	0.05	0.33	0.07	0.02	0.07
Total	100.87	100.40	100.01	99.48	99.85	101.03
Ions per..	*2 cations*	*3 cations*	2 cations	*3 cations*	*2 cations*	*3 cations*
Si	b.d.	b.d.	b.d.	0.001	0.001	b.d.
Ti	0.973	0.011	0.971	0.005	0.990	0.001
Al	0.000	0.001	b.d.	b.d.	b.d.	b.d.
Cr	0.000	b.d.	0.001	0.138	b.d.	0.050
Fe^{3+}	0.046	1.976	0.051	1.848	0.019	1.945
Fe^{2+}	0.385	0.922	0.782	0.971	0.764	0.979
Ni	0.001	0.007	0.000	0.004	0.000	0.002
Mn	0.121	0.007	0.124	0.011	0.160	0.005
Mg	0.467	0.074	0.064	0.019	0.067	0.015
Ca	b.d.	0.000	0.000	0.001	0.000	0.000
Zn	b.d.	b.d.	0.00	b.d.	b.d.	b.d.
V	0.006	0.001	0.007	0.002	0.000	0.002
$\sum$ cations	2.000	3.000	2.000	3.000	2.000	3.000

Prv = perovskite; Ilm = ilmenite; Mag = magnetite; Fe-Chr = Fe-chromite; Rt = rutile; n.m. = not measured; b.d. = below detection limit; ferric/ferrous iron calculated assuming charge balance.

Table A-5.8 (b) *Representative microprobe analyses of oxides in Almirez carbonate-silicate rocks and surrounding Chl-harzburgites. EMPA settings see Ch. 3, section 3.3.3, and Table 3.2.*

Lithology	meta-ophicarbonate		Tr-Di-Dol rock		Tlc-Mgs rock		Tr-Ol-Chl-Atg rock		
Sample	SN-138	SN-138	SN-143	SN-143	SN-137	SN-137	SN-146	SN-146	SN-146
Mineral	Mag	Mag	Ilm	Fe-Chr	Rt	Ilm	Mag	Mag	Ilm
SiO_2	b.d.	0.05	0.02	0.04	0.05	0.02	0.04	0.03	0.02
TiO_2	0.31	0.11	55.15	1.26	99.60	50.32	0.17	2.42	53.71
Al_2O_3	0.12	0.05	b.d.	1.96	0.01	0.01	0.02	b.d.	0.01
Cr_2O_3	3.33	5.46	0.15	40.48	0.04	b.d.	4.65	1.94	0.09
Fe_2O_3	66.60	64.35	2.23	23.87		7.20	63.96	63.67	6.05
FeO	26.78	28.12	31.97	26.60	0.99	38.85	29.18	32.80	28.20
NiO	0.42	0.26	0.01	0.11	b.d.	0.05	0.25	0.26	0.04
MnO	0.50	0.44	1.54	1.27	b.d.	1.50	0.28	0.15	3.62
MgO	2.51	1.57	9.02	3.31	0.02	2.73	0.96	0.46	9.21
CaO	0.03	0.25	0.02	b.d.	0.01	0.01	b.d.	b.d.	0.01
ZnO	0.07	0.03	b.d.	b.d.	b.d.	b.d.	b.d.	b.d.	b.d.
V_2O_3	0.17	0.15	0.02	0.55	0.04	0.03	0.08	0.08	b.d.
Total	100.83	100.87	100.13	99.46	100.77	100.73	99.60	101.81	100.96
Ions per..	*3 cations*	*3 cations*	*2 cations*	*3 cations*	*2 oxygens*	*2 cations*	*3 cations*	*3 cations*	*2 cations*
Si	b.d.	0.002	0.001	0.002	0.001	0.001	0.001	0.001	0.000
Ti	0.009	0.003	0.978	0.035	0.993	0.932	0.005	0.068	0.945
Al	0.005	0.002	b.d.	0.084	0.000	0.000	0.001	b.d.	0.000
Cr	0.098	0.162	0.003	1.170	0.000	b.d.	0.141	0.058	0.002
Fe^{3+}	1.874	1.820	0.040	0.657		0.133	1.843	1.801	0.107
Fe^{2+}	0.837	0.884	0.630	0.813	0.011	0.800	0.935	1.031	0.552
Ni	0.013	0.008	0.000	0.003	b.d.	0.001	0.008	0.008	0.001
Mn	0.016	0.014	0.031	0.039	b.d.	0.031	0.009	0.005	0.072
Mg	0.140	0.088	0.317	0.180	0.000	0.100	0.055	0.026	0.321
Ca	0.001	0.010	0.001	b.d.	0.000	0.000	b.d.	b.d.	0.000
Zn	0.002	0.001	b.d.	b.d.	b.d.	b.d.	b.d.	b.d.	b.d.
V	0.005	0.005	0.000	0.016	0.000	0.001	0.003	0.002	b.d.
$\sum$ cations	3.000	3.000	2.000	3.000	1.006	2.000	3.000	3.000	2.000

Ilm = ilmenite; Mag = magnetite; Fe-Chr = Fe-chromite; Rt = rutile; n.m. = not measured; b.d. = below detection limit; ferric/ferrous iron calculated assuming charge balance.

6 Fluid-mediated carbon release from serpentinite-hosted carbonates during dehydration of antigorite-serpentinite in subduction zones

6.1 Introduction

Subsolidus fluids composed of H_2O, CO_2, dissolved carbonate, silicate and salt components largely mediate forearc and subarc mass transport from the slab to the plate interface and mantle wedge of subduction zones (Ague and Nicolescu, 2014; Bebout and Penniston-Dorland, 2016; Frezzotti et al., 2011; Schneider and Eggler, 1986). Compared to molecular sub-solidus phase equilibrium models, the carbon concentration of high-P subduction fluids can be up to twice as high when solute species like HCO_3^-, $NaHCO_3$ or $CaHCO_3^+$ are considered (Connolly and Galvez, 2018; Kelemen and Manning, 2015). This enhanced carbon solubility through congruent mineral dissolution only accounts for part of the misbalance between carbon fluxes in arc volcanoes and those predicted by thermodynamic modelling of prograde devolatilization reactions (i.e., solid = solid + fluid) (Ague and Nicolescu, 2014; Kelemen and Manning, 2015). This carbon imbalance could, however, be reconciled if infiltration-driven devolatilization reactions (i.e., infiltrated fluid + solid = solid + fluid) are taken into account (Connolly and Galvez, 2018; Gorman et al., 2006). Because it produces large amounts of H_2O-rich fluids (~4.5 – 5.5 mol H_2O / kg serpentinite) at intermediate-depths of subductions zones (600 – 660 °C; Fig. 6.1) (Ulmer and Trommsdorff, 1995), the high-pressure dehydration of antigorite-serpentinite (Atg-serpentinite) of hydrated subducting slab lithosphere is a key reaction to promote infiltration-driven carbon release at subarc depths. Exhumed subduction melanges confirm the role of pervasive fluid flux and fluid-mediated carbon mobility along the plate interface (Ague and Nicolescu, 2014; Bebout and Penniston-Dorland, 2016).

Previous studies have investigated the carbon solubility of pure $CaCO_3$ in a fluid-dominated system, where at T > 500 °C the congruent solubility of carbonate increases with P and T (Fig. 6.1; see also Kelemen and Manning, 2015). Natural serpentinite-hosted carbonates typically are ophicalcite —formed during seawater-peridotite interaction in the oceanic lithosphere— and carbonate-talc rocks and carbonated melange serpentinite –formed

during prograde subduction— where carbonate solubility likely differs from that of pure $CaCO_3$ (Galvez et al., 2015; Menzel et al., 2019). In this contribution, we present the results of thermodynamic modelling —using the implementation of the DEW aqueous database in Perple_X (Connolly and Galvez, 2018; Galvez et al., 2015)— of the solubility, fluid speciation, and phase equilibria during prograde devolatilization and infiltration-driven devolatilization reactions of serpentinite-hosted carbonate rocks during dehydration of Atg-serpentinite in subduction zones with different thermal regimes. We calculate the prograde metamorphic evolution and devolatilization of serpentinite-hosted carbonates along warm (PD-15; Fig. 6.1) and cold (cold subd.; Fig. 6.1) subduction P–T paths that account for the range of thermal conditions predicted by numerical models for the slab-mantle interface of warm, intermediate and cold subduction zones (red, green and blue fields in Fig. 6.1) (Syracuse et al., 2010). The conditions of Atg-serpentinite dehydration to chlorite-harzburgite (Chl-harzburgite) are reached at different pressure for different paths (Fig. 6.1) leading to variable carbonate solubility in serpentinite dehydration fluids. At selected P–T conditions of Atg-serpentinite dehydration covering a large range of subduction thermal regimes (Points I – IV; Fig. 6.1), we present infiltration-driven devolatilization models of serpentinite-hosted carbonates to investigate the fluid-mediated carbon release from these lithologies during deserpentinization at subarc depths of subduction zones.

6.2 Subduction of serpentinite-hosted carbonates

6.2.1 Oceanic ophicalcite

While the carbon content of serpentinite is low compared to that of sediments and altered oceanic crust (Alt et al., 2013), the contribution of ophicalcite to the deep carbon budget could have been significant during subduction of slow-spreading mid-ocean ridges and oceanic passive margins (Schwarzenbach et al., 2013), as attested by exhumed metamorphic terranes in the Alps (Collins et al., 2015). Oceanic ophicalcites are commonly associated to serpentinites and form by the precipitation of Ca-carbonates during the interaction of high-pH, Ca-rich serpentinization-derived fluids with dissolved inorganic carbon in seawater (Fig. 6.2a) (Ludwig et al., 2006). The low Mg/Ca and C/Ca ratios of these fluids favour precipitation of aragonite and calcite instead of Mg-bearing carbonates (Grozeva et al., 2017). As a result, in the $CaO–MgO–SiO_2$ (mol.%) ternary, the bulk rock compositions of natural ophicalcite plot along the serpentine–calcite trend at constant Mg/Si (Fig. 6.2c, trend A) (Menzel et al., 2019). Ophicalcite is commonly associated to serpentinite in oceanic mantle

core complexes, and oceanic detachment and transform faults (Alt et al., 2018; Bonatti et al., 1980; Schwarzenbach et al., 2013). During subduction, ophicalcites would be present close to the slab surface (Fig. 6.2a) or deeper within the slab (Fig. 6.2b) and will be fluxed at subarc depths by fluids produced by dehydration of host or nearby Atg-serpentinite to Chl-harzburgite (Fig. 6.2b).

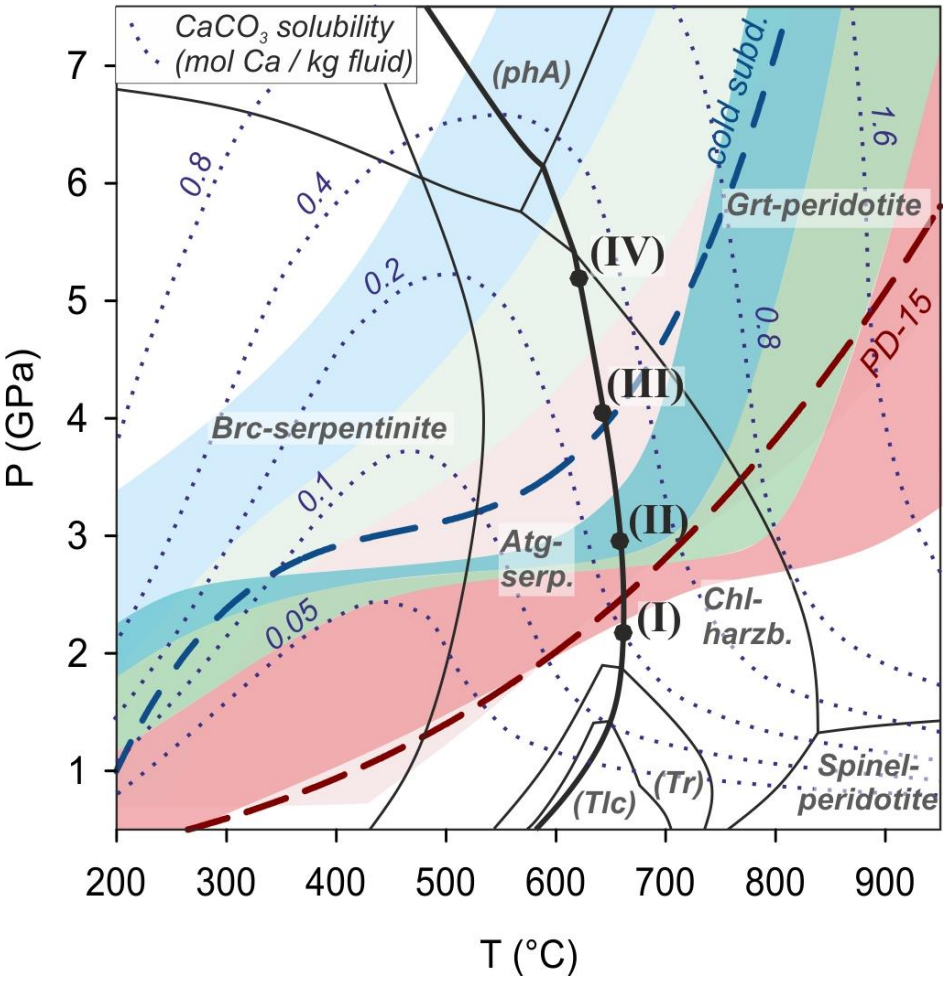

Figure 6.1. *P–T phase stabilities in meta-serpentinite, contours of carbon solubility of pure $CaCO_3$ (blue dotted lines, after Kelemen and Manning, 2015), and range of thermal conditions of cold, intermediate and warm subduction zones at the slab interface (dark blue, green, and red fields, respectively) and the crust-mantle transition of the slab (brighter fields) (after Syracuse et al., 2010). Boundaries of brucite (Brc-) serpentinite, antigorite (Atg-) serpentinite, chlorite (Chl-) harzburgite, and garnet (Grt-) peridotite are for a Ca-bearing serpentinite (Table 6.1). The average subduction geotherm recorded in metamorphic rocks is shown by the dashed red line ("PD-15"; from Penniston-Dorland et al., 2015); the blue dashed line ("cold subd.", as in Connolly and Galvez, 2018) shows a path exemplary for a very cold slab surface or the crust-mantle transition of a warm slab. Points I to IV: P–T conditions of the antigorite-out reaction (thick line) used in fluid-infiltration models of our study. phA: phase A; Tr = tremolite; Tlc = talc.*

Meta-ophicalcite rocks occur in ultramafic massifs of exhumed metamorphic terranes that underwent subduction (Alt et al., 2013; Menzel et al., 2019; Vitale Brovarone et al., 2017). As oceanic ophicalcite, the bulk rock compositions of natural meta-ophicalcite in subducted terranes plot along the serpentine–calcite trend at constant Mg/Si (Fig. 6.2c, trend A) (Menzel et al., 2019). Most (meta-)ophicalcites in paleo-subducted terranes formed in an oceanic setting, but hybrid rocks with similar bulk composition to ophicalcite may also form by mixing of serpentinite and sedimentary carbonate in subduction zones (Scambelluri et al., 2016).

6.2.2 Carbonation of mantle wedge and subduction of melange serpentinite

Serpentinite-hosted carbonate rocks may also form by carbonation of mantle wedge and melange serpentinite in subduction zones. C-bearing meta-sediments and altered oceanic crust release at forearc depths significant amounts of fluids (Gorman et al., 2006) that flux and serpentinize peridotite along the subduction interface and overlying mantle wedge ($T <$ ~650 °C; Fig. 6.2). There, carbonates may precipitate where the dissolved inorganic carbon content of these fluids exceeds that of fluids in equilibrium with Atg-serpentinite and antigorite-chlorite melange rocks (Fig. 6.2b) (Sieber et al., 2018). Fluids released by the devolatilization of altered oceanic crust have high Si contents and elevated C/Ca (Galvez et al., 2016), what favours the formation of dolomite or magnesite and talc during carbonation and Si-metasomatism of serpentinite (trend β in Fig. 6.2d). Devolatilization of carbonate-rich marls or marbles also produces fluids that may lead to the carbonation of serpentinite at constant Mg/Si (trend α in Fig. 6.2d), thus forming talc-magnesite and quartz-magnesite rocks, respectively, at increasing fluid $aCO_{2(aq)}$ (Menzel et al., 2018; Sieber et al., 2018). Alternatively, such fluids may leach Si from serpentinite and form carbonate-rich metasomatic veins (trend γ in Fig. 6.2d). In addition to fluid-rock reactions, mechanical mixing of serpentinite with mafic and sedimentary rocks (trends B & C in Fig. 6.2c) generates hybrid lithologies in subduction melanges that are potential carbon sources at subarc depths.

Examples of magnesite- and dolomite-bearing rocks produced by carbonation of serpentinite or antigorite-chlorite schist at slab interfaces occur in the exhumed subduction melanges in Syros (Schwarzenbach et al., 2018), New Caledonia (Spandler et al., 2008), and the Alps (Angiboust et al., 2014). These dolomite-antigorite-talc or magnesite-clinopyroxene-talc rocks evidence carbonate precipitation and silica addition to serpentinite (Angiboust et

al., 2014; Spandler et al., 2008). If incorporated into melange rocks at the subduction interface (yellow rims in Fig. 6.2b), hybrid carbonate-talc rocks and carbonated wedge serpentinite may release carbon at subarc depths where fluxed by Atg-serpentinite dehydration fluids ("Atg-out" and blue arrows in Fig. 6.2b) (Spandler et al., 2008).

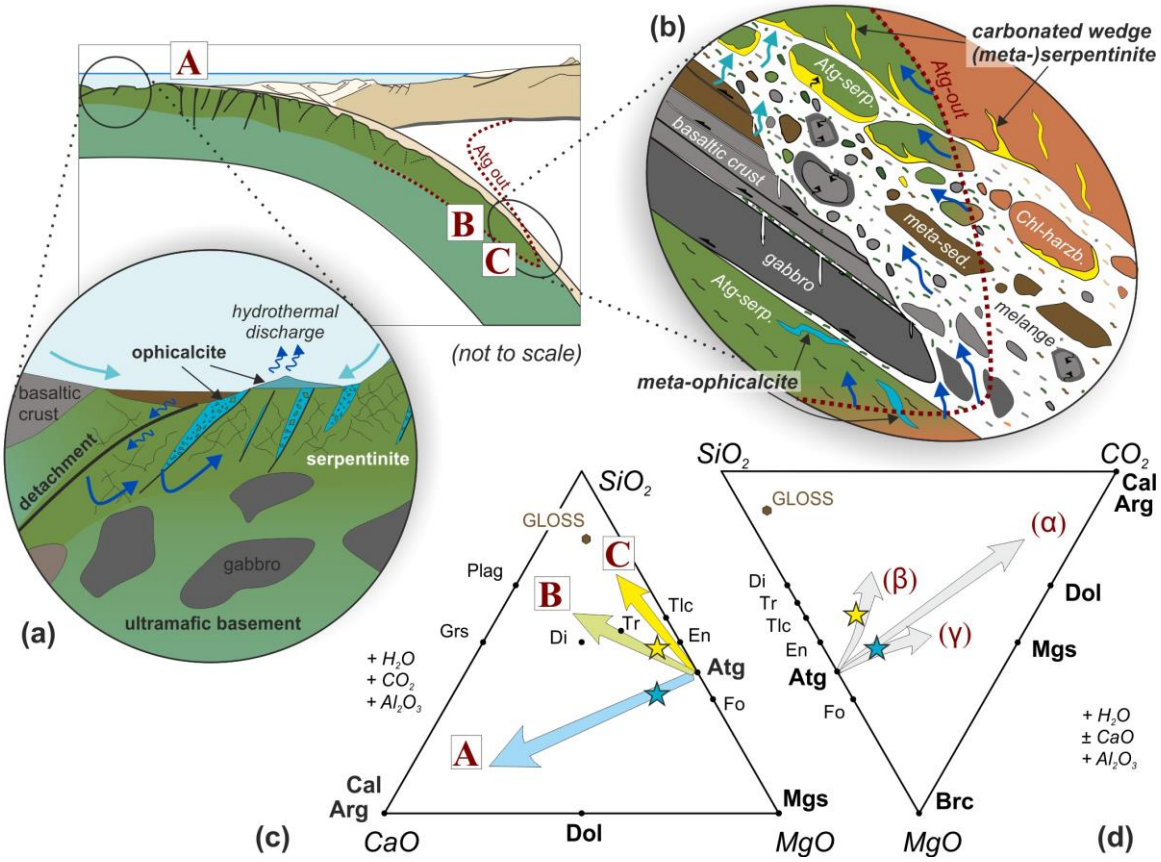

Figure 6.2. *Bulk chemical variations of ophicalcite and hybrid carbonate-talc rocks in subduction zones. Conceptual cartoon of* ***(a)*** *ophicalcite formation by oceanic alteration of exhumed peridotite (modified after Lafay et al., 2017), and* ***(b)*** *the subduction interface at conditions of antigorite-serpentinite (Atg-serp.) breakdown to Chl-harzburgite (Chl-harzb.) (modified after Bebout and Penniston-Dorland, 2016). In slabs derived from slow-spreading oceanic crust, ophicalcites (blue lenses) are common in a serpentinized section with interspersed gabbro + basaltic crust. Devolatilization of meta-sediments at forearc depths (light blue arrows) can cause carbonation and Si-metasomatism of wedge serpentinite (yellow rims) that later are fluxed by antigorite breakdown fluids at subarc depths (Atg-out; dark blue arrows).* ***(c)*** *SiO_2–CaO–MgO (mol.%) ternary showing compositional trends for ophicalcite (A) and Si-metasomatism and mixing of melange serpentinite (B & C).* ***(d)*** *MgO–SiO_2–CO_2 ternary showing compositional trends related to carbonation of serpentinite in these settings; α: ophicalcite, listvenite at constant Mg/Si; β: carbonation + Si-metasomatism; γ: carbonation related to Si-leaching. The blue and yellow stars in c) and d) are the ophicalcite and carbonate-talc rock bulk compositions used in the our study. Mineral abbreviations in this figure and throughout the chapter are from Whitney and Evans (2010).*

6.3 Thermodynamic modelling methods

6.3.1 Model rock compositions

To model the P–T conditions of antigorite dehydration (Fig. 6.1), we use the composition of a natural Ca- and Al-bearing Atg-serpentinite (Table 6.1) of the Almirez paleo-subduction ultramafic massif (Padrón-Navarta et al., 2011; Trommsdorff et al., 1998). The H_2O content of this sample (Alt et al., 2012) corresponds to a fully hydrated assemblage at 400 °C. We use a fixed redox budget defined by a bulk rock Fe^{3+}/Fe_{total} typical of Atg-serpentinite in subduction zones (Table 6.1) (Debret et al., 2015). The fluids produced at different P–T conditions (points I-IV; Fig. 6.1) by dehydration of this Atg-serpentinite are used as the fluids to model infiltration-driven devolatilization reactions of serpentinite-hosted carbonate rocks.

To investigate the carbonate stability during subduction of oceanic ophicalcite, we use an ophicalcite bulk composition corresponding to a 20 : 80 (wt.%) mixture of $CaCO_3$ and serpentinite (Table 6.1; blue stars in Fig. 6.2c & d). Natural meta-ophicarbonate may have significantly higher $CaCO_3$ contents (Menzel et al., 2019; Schwarzenbach et al., 2013), and hence our choice of bulk composition results in a conservative estimate of carbonate stability during subduction of ophicalcite.

The composition of a carbonate-talc rock from the New Caledonia paleo-subduction terrane (Table 6.1; yellow stars in Fig. 6.2c & d) is used to model the prograde devolatilization and fluid-mediated release of carbon from carbonated serpentinite-mafic hybrids from the slab-mantle interface during subduction and serpentinite breakdown. This sample is composed of a dolomite-antigorite-talc assemblage with minor magnetite and apatite, and has formed by fluid-rock interaction at 500 – 560 °C and 1.6 – 1.9 GPa in a subduction melange (Spandler et al., 2008).

6.3.2 Phase modelling and aqueous speciation

We computed P–T pseudosections of the selected bulk-rock compositions in the Ca-Fe-Mg-Al-Si-C-O-H system using Perple_X 6.8.5 (Connolly and Galvez, 2018; Galvez et al., 2015). Because it allows the consistent use of established solid solution models, we applied the thermodynamic database of solid phases of Holland and Powell (1998) (2002 version; ds5 Thermocalc version), complemented by the aqueous speciation database of the Deep Earth Water model (Sverjensky et al., 2014) (May 2017 revision). The solid solution models are given in Appendix Table A-6.1. We used the "lagged speciation" algorithm of Perple_X,

Table 6.1. *Bulk rock compositions used in thermodynamic models*

	Serpentinite [a)]	Aragonite+graphite[b)]	Ophicalcite [c)]	Carbonate-talc-schist [d)]
oxides (wt%)	AL98-4b	Ca-COH system	(synthetic)	Spandler-2814
SiO_2	39.33		31.46	45.5
Al_2O_3	3.29		2.63	0.9
Fe_2O_3 (total)	8.34		6.67	4.78
MgO	37.58		30.06	28.5
CaO	0.28		11.44	5.88
CO_2			8.89	9.67
H_2O	11.60		8.99	4.89
elements (mol/kg)				
Si	6.5185		5.2287	7.5637
Al	0.6426		0.5155	0.1763
Fe	1.0402		0.8344	0.5980
Mg	9.2851		7.4479	7.0628
Ca	0.0497	1.00000	2.0368	1.0473
C		1.01001	2.0176	2.1946
H_2	6.4121	0.20000	4.9820	2.7112
O_2	15.5423	1.60001	15.4023	15.6450
Fe^{3+}/Fe_{total} [e)]	*0.57*		*0.57*	*0.3 [f)]*

a) Almirez serpentinite after Garrido et al. (2005), with H_2O content from Alt et al. (2012), and Fe^{3+}/Fe_{total} of typical Atg-serpentinite in subduction zones (Debret et al., 2015).

b) Modelling composition used to calculate solubility in the Ca-COH system (Fig. 6.1), based on 1 mol aragonite + 0.01 mol C + 0.2 mol H_2O; a very small excess amount of CO_2 is added to avoid computational instabilities.

c) Ophicalcite composition obtained by mixing of 80 wt% serpentinite AL98-4b with 20 wt% $CaCO_3$.

d) Dolomite-antigorite-talc schist from New Caledonia subduction melange (from Spandler et al., 2008).

e) The initial redox budget of the rock compositions is fixed by calculating O_2 using a fixed Fe^{3+}/Fe_{total} bulk rock ratio and all C as CO_2.

f) Because the Fe^{3+}/Fe_{total} of this sample is unknown, we use a value of 0.3, similar to carbonate-bearing melange rocks from Syros (Schwarzenbach et al., 2018).

which calculates equilibria between solids and a solvent in a first step, and models the corresponding equilibrium fluid speciation using the chemical potentials and charge balance to derive activity coefficients (Connolly and Galvez, 2018). An iterative solution is subsequently obtained from the mass-balance of the equilibrium of solids, solvent, and solutes. The solvent in carbon-free serpentinite models is pure H_2O, while for carbonate rocks we use a mixed volatile CO_2–H_2O solvent (COH-Fluid) (Galvez et al., 2015) that provides more robust solutions in carbonate-rich systems. We applied the compensated Redlich-Kwong (CORK) EoS (Holland and Powell, 1991) for the CO_2–H_2O solvent since most modelled P–T conditions are well above sub-critical and ambient conditions and for consistency with solid solution models. The choice of other EoS for the solvent would cause

minor differences in the fluid composition and aqueous speciation because the extrapolation of the dielectric constant to high-P and T depends on water density. All calculations were done for relatively carbonate-rich compositions and a fixed redox budget corresponding to Fe^{3+}/Fe_{total} typical for serpentinites and melange rocks and carbon as C^{4+} (Table 6.1). Therefore, reduced molecular volatiles such as methane are minor and were not considered as solvent phases, except for the reference calculation of aragonite solubility in the Ca-COH system (Fig. 6.1).

Figure 6.1 shows the computed solubility of aragonite in the Ca-COH system (Ca-carbonate + graphite/diamond + fluid) from our thermodynamic modelling (Table 6.1; Fig. 6.1) that can be used for benchmarking our model with independent computations of the aragonite solubility elsewhere (Kelemen and Manning, 2015). The total Ca concentration in fluid computed by our model is only slightly higher than the $CaCO_3$ solubility predicted by previous calculations (Kelemen and Manning, 2015) and the shape and trends of solubility isopleths are similar.

6.3.3 Prograde devolatilization and infiltration-driven devolatilization models

The prograde devolatilization reactions in the selected bulk compositions were modelled using pseudosections of their equilibrium phase assemblages and electrolytic fluid composition; hence, carbon solubility in the fluids also considers dissolved species other than molecular $CO_{2(aq)}$. Following the prograde metamorphic evolution along the selected P–T paths (“PD-15” and “cold subd.”; Fig. 6.1), fluid released by prograde devolatilization reactions is fractionated from the initial rock compositions (cf. Table 6.1) at 1 °C intervals to simulate fluid removal during prograde subduction metamorphism (Raleigh fractionation).

As illustrated in Figure 6.3, we modelled infiltration-driven devolatilization by Atg-serpentinite dehydration fluids (meta-serpentinite; Table 6.1) at the selected isobaric and isothermal conditions (Fig. 6.1). Incremental fluid infiltration and fractionation is modelled by adding 1 mol of fluid in equilibrium with Atg-serpentinite to 1 kg of carbonate-rock and computing the equilibrium mineral assemblage and the fluid composition and speciation. The equilibrium fluid is then fractionated (outflow fluid), what changes the bulk composition and the total mass (Fig. 6.3). In subsequent increments, the sequential residual bulk composition is infiltrated by Atg-serpentinite fluids, equilibrated, and the fluid is again fractionated. The amount of infiltrating fluid at each step is 1 mol / kg of the initial rock mass (~4 vol%). The

infiltrated fluid is produced by dehydration of Atg-serpentinite (Table 6.1) at the modelled P–T conditions. In contrast, the composition of the outflow fluid and the phase assemblage of the residual rock evolve with increasing time-integrated fluid/rock ratio (given as wt/wt mass ratio in this study). The isobaric and isothermal P–T conditions for the modelling of infiltration-driven reactions correspond to the intersection of the Atg-serpentinite dehydration reaction with the geotherms at the slab-mantle interface of warm and cold subduction zones (conditions I and II, respectively; Fig. 6.1), and the Moho of warm and intermediate subduction zones (conditions III and IV; Fig. 6.1) (Syracuse et al., 2010).

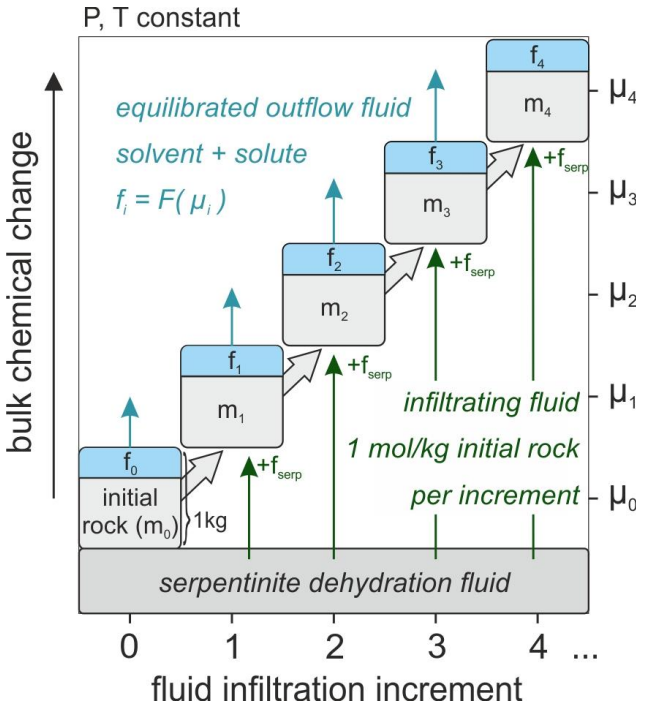

Figure 6.3. *Schematic representation of the 0-dimensional model of fluid infiltration and fractionation at isobaric and isothermal conditions from our study. The equilibrated fluid composition (f_i) and phase assemblage in the rock are defined by the chemical potentials of the system components at each increment (μ_i). The solid rock composition (m_i) evolves with the incremental infiltration of Atg-serpentinite dehydration fluid (f_{serp}) and the instant fractionation of the outflow fluid (f_i) in each step.*

6.3.4 Model simplifications and limitations

The modelled fluid composition depends on the equilibrium phase assemblage for the bulk composition and neglects potential kinetic effects due to different dissolution rates of minerals that may result in partial equilibrium. However, at the high-T and fluid-saturated conditions of our models, it is likely that equilibrium is readily attained due to fluid-enhanced diffusion and dynamic recrystallization.

Another limitation of the model is that it does not consider Na, K, and halogens components. When these components are considered, the speciation algorithm fails to converge in the infiltration models because the chemical potentials of their aqueous species are not sufficiently constrained in the fluid as they fully partition into the solute phase. Dissolved salts in subduction fluids increase the carbonate solubility in the fluid phase due to reactions such as:

magnesite + 2 $NaCl_{,aq}$ + H_2O = $NaHCO_{3,aq}$ + $MgCl_{2,aq}$ + Na^+ + OH^- (6.1)

Ophicarbonates and carbonate-talc rocks have very low Na and K contents (Menzel et al., 2019; Spandler et al., 2008) and, therefore, the impact of these elements in increasing the carbon solubility in the fluid phase —in aqueous complexes such as $NaHCO_{3,aq}$ and $KHCO_{3,aq}$— during prograde devolatilization reaction of these lithologies is likely small. The impact of these elements in increasing the carbon solubility in infiltration-driven devolatilization reactions depends on their content in the infiltrated fluid. For instance, in highly saline fluids (e.g. $NaCl_{,aq}$ > 1 molal) derived from Na-rich lithologies, the $NaHCO_{3,aq}$ complex significantly increases the solubility of carbon in the fluid phase (Facq et al., 2016; Newton and Manning, 2002). Fluids derived from dehydration of Atg-serpentinite, however, typically have a low salinity, and the transformation of Atg-serpentinite to Chl-harzburgite at subarc depths releases < 200 ppm Cl (Kendrick et al., 2018; Scambelluri et al., 2004). For 1 kg of Atg-serpentinite producing 9 wt% of H_2O, this Cl release results in fluids with $NaCl_{,aq}$ < 0.06 mol/kg. The relative increase of the carbon solubility in the fluid due to partitioning of this amount of dissolved $NaCl_{,aq}$ into different aqueous complexes —$NaCl_{,aq}$, Na^+, $NaHCO_{3,aq}$, $NaCO_3^-$, $NaOH_{,aq}$, and $NaHSiO_{3,aq}$— is only < c. 0.02 mol/kg. Hence, for the investigated lithologies, disregarding Na- and Cl- bearing species in devolatilization reactions driven by the infiltration of fluids derived from Atg-serpentinite dehydration likely has a minimal impact on the predicted solubility of carbon in our study.

6.4 Results and Discussion

6.4.1 Prograde devolatilization reactions

6.4.1.1 Fluids in equilibrium with meta-ophicalcite

While the composition of fluid in equilibrium with pure carbonates is determined by congruent mineral dissolution, carbonate-silicate buffer reactions determine the fluid composition during prograde metamorphism of carbonate–silicate mixtures (e.g. Trommsdorff and Evans, 1977). Therefore, the carbon solubility during prograde devolatilization of ophicalcite (Fig. 6.4a) differs significantly from that of fluids in equilibrium with pure Ca-carbonate (cf. Fig. 6.1; Kelemen and Manning, 2015). The relative difference in the solubility of carbon in the fluid is particularly large at high T and low P. When combining the effects of congruent mineral dissolution and carbonate-silicate buffer reactions, the carbon solubility in meta-ophicalcite fluids at T > 550 °C increases with

temperature and decreases with pressure, whereas it increases with pressure at T < 550 °C (Fig. 6.4a).

For the investigated ophicalcite bulk composition, dolomite and magnesite are the carbonate phases along the Atg-out reaction (Fig. 6.4c); for other meta-ophicalcite bulk compositions along the antigorite–calcite trend (Fig. 6.2), the type of carbonate would vary as a function of P and T (Appendix Fig. A-6.1) (Menzel et al., 2019). At the P–T conditions of Atg-serpentinite breakdown (Fig. 6.4a), meta-ophicalcites are composed of olivine-clinopyroxene-chlorite-carbonate (P < 3.6 GPa) or olivine-clinopyroxene-garnet-carbonate assemblages (Fig. 6.4c; Appendix Fig. A-6.1). Fluids in equilibrium at these conditions are alkaline (ΔpH = 1.6 – 2.5; Fig. 6.4b; where ΔpH is the deviation from neutral pH) and have carbon solubilities ranging from 0.1 to 1.0 mol C / kg fluid (Fig. 6.4a & 6.4b). Because the equilibria between silicates, dolomite, and magnesite buffer the fluids to a relatively high $aCO_{2,aq}$ (Fig. 6.4c), the carbon solubility at P < 3.4 GPa is significantly higher than that of fluids in pure Ca-carbonate (Fig. 6.1). The fluid C/(Ca+Mg) ratio decreases with pressure along the Atg-out isograd (Fig. 6.4b), indicating the increasing role of congruent dissolution

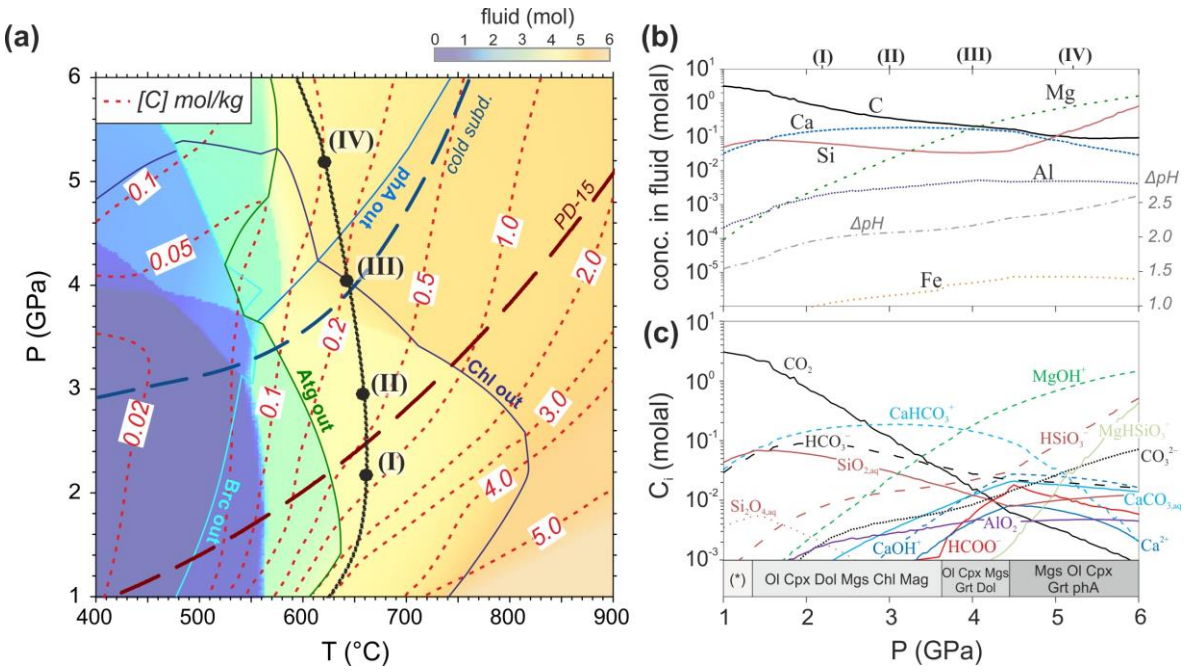

Figure 6.4. *Fluid composition in equilibrium with meta-ophicalcite.* ***(a)*** *Total carbon solubility (red dashed, contour lines) and upper stability of the main hydrous phases (coloured lines, e.g. Chl out) superposed on the colour map of the amount of fluid (mol/kg rock). The pseudosection with detailed phase relations is provided in Appendix Figure A-6.1. Also shown are the Atg-out reaction in pure serpentinite (thick black line), with selected P–T conditions I to IV; and warm and cold subduction paths used to calculate prograde devolatilization (cf. Fig. 6.1).* ***(b)*** *Major element solubility (left axis; mol/kg fluid) and ΔpH (stippled grey line; scale on the right axis), and* ***(c)*** *aqueous speciation in fluid and mineral assemblages with variable pressure along the Atg-out reaction;(*) Ol-Cpx-Dol-Chl-Tr-Mag.*

with pressure. At P > 4.5 GPa, the main C-bearing aqueous species in meta-ophicalcite are CO_3^{2-}, $CaHCO_3^+$, HCO_3^- and $CaCO_{3,aq}$ (Fig. 6.4c), but the total carbon solubility is lower than in pure aragonite (cf. Fig. 6.1 and Fig. 6.4a) because the equilibria between magnesite and Ca-bearing silicates buffer the concentration of these species in the fluid.

6.4.1.2 Fluids in equilibrium with carbonate-talc rocks

Fluids in equilibrium with carbonate-talc rocks show trends of carbon solubility with prograde devolatilization (Fig. 6.5a) similar to those observed for meta-ophicalcite. The fluid carbon contents at T > 620 °C are substantially higher than in the pure Ca-carbonate system (Fig. 6.1). Despite their similar bulk carbon content to meta-ophicalcite (Table 6.1), the carbon solubility in carbonate-talc rock fluids is significantly higher (0.15 – 2.0 mol C / kg fluid along the Atg-out reaction; Fig. 6.5a & b). This relatively higher solubility is due to the high $aCO_{2,aq}$ and lower pH (ΔpH = 1.2 – 1.9 along the Atg-out isograd; Fig. 6.5b) of fluids equilibrated with talc-tremolite-magnesite, talc-clinopyroxene-magnesite and talc-garnet-magnesite assemblages (Fig. 6.5c; Appendix Fig. A-6.2). Compared to meta-ophicalcite (Fig.

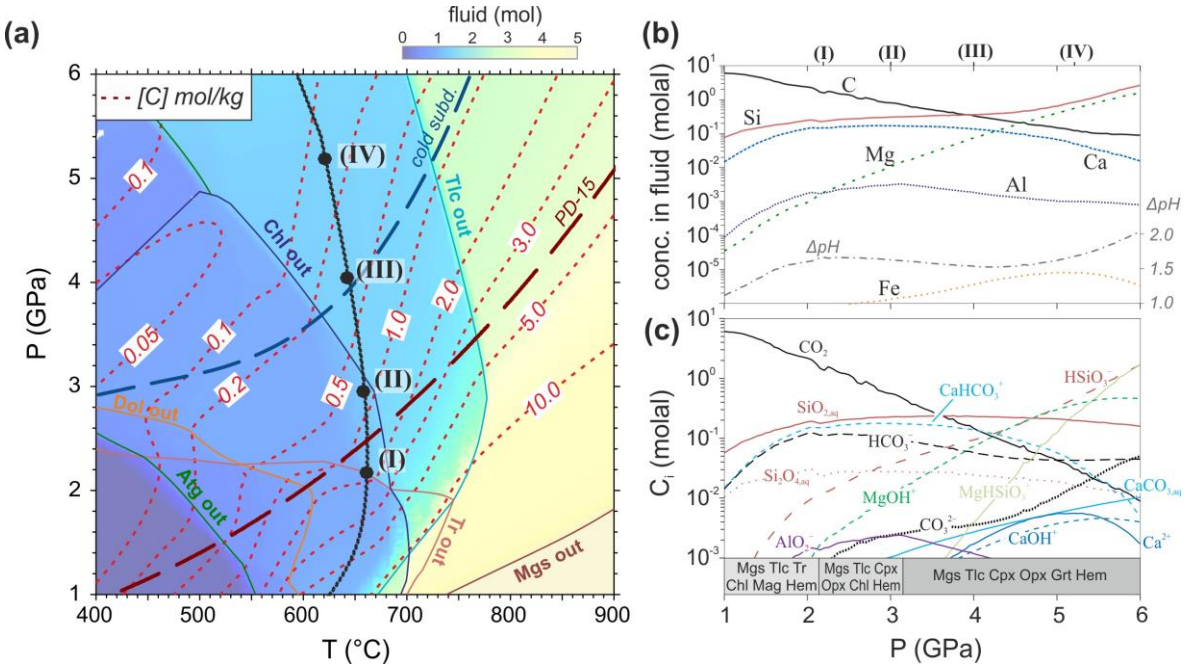

Figure 6.5. *Fluid composition in equilibrium with carbonate-talc rock.* ***(a)*** *Total carbon solubility (red dashed contour lines) and upper stability of key phases (coloured lines, e.g. Tlc out) superposed on the colour map of the amount of fluid (mol fluid / kg rock). The pseudosection with detailed phase relations is provided in Appendix Figure A-6.2. Also shown are the Atg-out reaction in pure serpentinite (thick black line), with selected P–T conditions I to IV; and warm and cold subduction paths used to calculate prograde devolatilization (cf. Fig. 6.1).* ***(b)*** *Major element solubility (mol/kg fluid; left axis) and ΔpH (right axis), and* ***(c)*** *aqueous speciation in the fluid and phase assemblages along the Atg-out reaction.*

6.4b & c), carbonate-talc rock fluids are enriched in silica (Fig. 6.5b & c). The high fluid C/(Ca+Mg) ratio at P < 4.5 GPa along the Atg-out isograd (Fig. 6.5b) indicates that silicate-carbonate buffer reactions are also prevalent at high P in carbonate-talc rocks.

6.4.1.3 Carbon loss during subsolidus prograde devolatilization

Figure 6.6 shows the prograde devolatilization of meta-ophicalcite and carbonate-talc rocks via Rayleigh fractionation —where the fluid phase is continuously removed from the system through fractional distillation— in warm and cold subduction zones (Fig. 6.6a & b, respectively). Despite the high amounts of H_2O released during prograde devolatilization of meta-ophicalcite and carbonate-talc rocks (solid blue and orange lines in Fig. 6.6a & b), the bulk carbon loss is negligible (dashed lines in Fig. 6.6a & b) even though considering the increased carbon solubility of electrolyte fluids relative to molecular H_2O–CO_2 fluids (Kerrick and Connolly, 1998). Just the high-T breakdown of talc in the carbonate-talc rock causes a minor C loss ("Tlc out" in Fig. 6.6a). We can then conclude that regardless of the thermal regime of the subduction zone (Fig. 6.6a & b), subsolidus devolatilization of meta-ophicalcite and carbonate-talc rocks releases minor amounts of C that are insufficient to balance the carbon flux from subducting slabs to the source regions of arc magmas. Previous works have reached a similar conclusion from similar modelling of prograde subsolidus devolatilization of C-bearing meta-pelite and altered oceanic crust (Connolly and Galvez, 2018; Gorman et al., 2006; Kerrick and Connolly, 2001a, b).

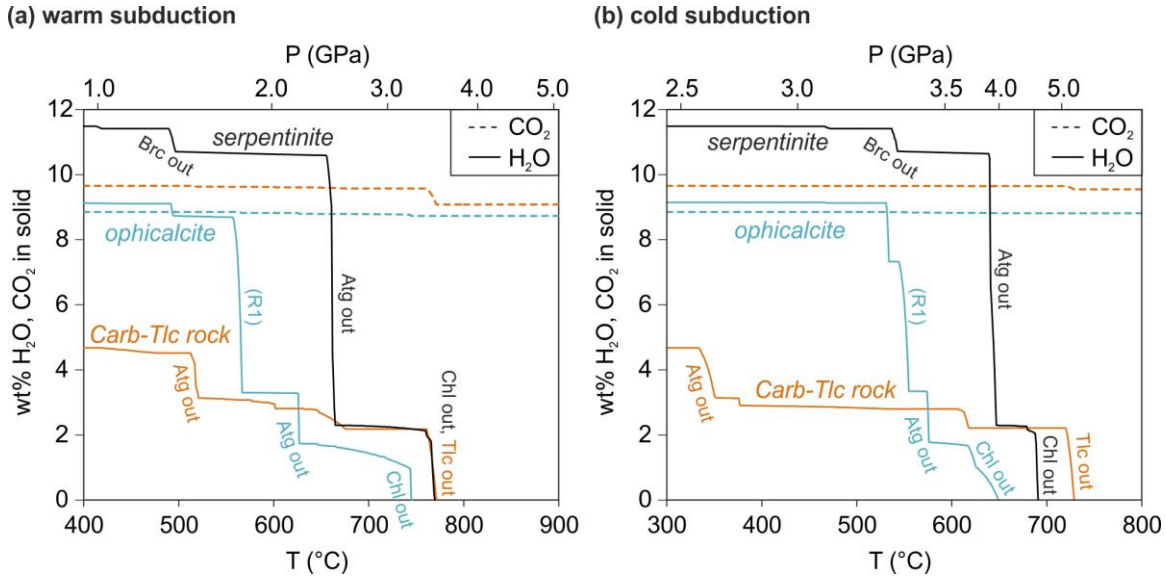

Figure 6.6. *Release of H_2O and CO_2 from serpentinite, ophicalcite and carbonate-talc rock during prograde devolatilization (Rayleigh fractionation of fluid; no external fluid infiltration) along* ***(a)*** *warm and* ***(b)*** *cold subduction paths ("PD-15" and "cold subd" paths in Figs. 6.1, 6.4a, 6.5a). R1: Atg + Arg = Ol + Cpx + Dol.*

6.4.2 Infiltration-driven devolatilization of ophicalcite and carbonate-talc rocks

Infiltration of external fluids produced by devolatilization reactions of hydrated slab lithologies into carbonate-bearing rocks is a more realistic scenario for modelling of carbon solubility in subduction zones (Ague and Nicolescu, 2014; Connolly and Galvez, 2018; Gorman et al., 2006). Serpentinite-hosted meta-ophicalcites and talc-carbonate rocks likely remain isolated from external fluids released by devolatilization of the overlying slab crustal lithologies to subarc depths where they undergo devolatilization driven by infiltration of dehydration fluids of their serpentinite hosts (Atg-out in Fig. 6.6a & b).

To investigate the role of carbon release during devolatilization reactions driven by Atg-serpentinite fluids, we will first address the composition and speciation of Atg-serpentinite dehydration fluids (Fig. 6.7). Pervasive infiltration of serpentinite-derived fluid into meta-ophicalcite and carbonate-talc rock will then be illustrated by isobaric and isothermal phase diagrams (Fig. 6.8; Fig. 6.9) at selected P–T conditions of Atg-serpentinite dehydration in hot, warm and cold subduction zones (points I – IV in Fig. 6.1 and Fig. 6.7). These isobaric and isothermal fluid-infiltration models show the evolution of mineral assemblages, aqueous speciation in the infiltrated and outflow fluids, and the maximum estimates for C and Ca losses from these lithologies with increasing time-integrated fluid/rock (f/r) ratio (cf. Sec. 6.3.3; Fig. 6.3). Although these models provide no direct information on chemical reactions, we derive them from the relative changes in modal mineral abundances and fluid composition with increasing time-integrated f/r ratio (cf. Fig. 6.8 and Fig. 6.9). For the sake of clarity, the derived reactions are simplified neglecting[1] Fe and Al, and — because of the generally alkaline characteristics of high-P fluids (Galvez et al., 2016)— charge balance is attained using OH^-.

6.4.2.1 Composition of fluids derived from Atg-serpentinite dehydration

The composition of Atg-serpentinite dehydration fluids depends on the thermal structure of the subduction zone and the position of serpentinite in the slab (Fig. 6.7). In accordance with the increasing dielectric constant of water with pressure (Sverjensky et al., 2014), the solubility of major elements in serpentinite-derived fluids increases with the depth of dehydration (Fig. 6.7). At P < 3.2 GPa, $SiO_{2,aq}$ is the main aqueous species in antigorite

[1] Accordingly, abbreviations for the solid solutions of e.g. clinopyroxene and olivine are given in phase diagrams (Appendix Fig. A-6.2, Fig. A-6.2; Figs. 6.4 & 6.5) and infiltration models (Fig. 6.8; Fig. 6.9), but the endmembers diopside and forsterite are used in the simplified derived reactions.

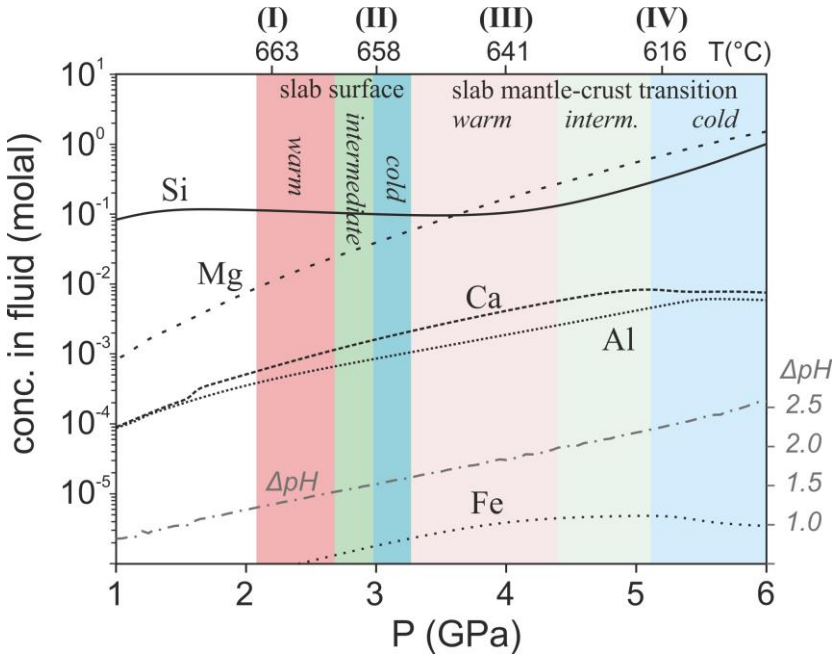

Figure 6.7. *Major element composition and deviation from neutral pH (ΔpH; grey stippled line) of fluid in equilibrium with meta-serpentinite at different pressures of the Atg-serpentinite dehydration. The predicted principal aqueous species are $SiO_{2,aq}$, $HSiO_3^-$, $MgOH^+$, $MgHSiO_3^+$, Ca^{2+}, $CaOH^+$, AlO_2^-, and $FeOH^+$ (not shown for clarity). Coloured fields and numbers I–IV indicate the P–T ranges of antigorite breakdown in subduction zones with different thermal regimes (cf. Fig. 6.1).*

dehydration fluids, whereas at P > 3.2 GPa $MgOH^+$, $HSiO_3^-$ and $MgHSiO_3^+$ become significant. The higher activity of positively charged aqueous complexes at high P makes the fluid pH alkaline, which results in an increase of ΔpH along the Atg-out reaction from c. +1.2 at 2 GPa to +2.2 at 5 GPa (Fig. 6.7; see also Galvez et al., 2016). Apart from higher $MgOH^+$ and lower ΔpH, the concentrations of $SiO_{2,aq}$, Al- and Ca-bearing species at 2 GPa are similar to those calculated for Atg-serpentinite dehydration fluids in previous studies (Debret and Sverjensky, 2017).

6.4.2.2 Infiltration-driven devolatilization of meta-ophicalcite

At the P–T conditions of Atg-serpentinite dehydration in the slab-mantle interface of warm subduction zones (point I in Fig. 6.1), infiltration of serpentinite-derived fluid into meta-ophicalcite induces bulk C loss due to the sequential consumption of magnesite, dolomite, and aragonite (Fig. 6.8a). Besides C, significant Ca is released into the outflow fluids, with the effect that their pH becomes more alkaline due to the increasing importance of charged solutes at higher f/r ratios (dashed black line and grey stippled line in Fig. 6.8a, respectively).

Based on the difference in the aqueous speciation of the infiltrating and outflow fluids (Fig. 6.8e), and the relative changes in pH and mineral abundance with increasing f/r at 2.2 GPa, the initial consumption of magnesite and clinopyroxene and formation of dolomite and olivine (f/r < 0.8 in Fig. 6.8a & e) can be balanced by the reaction:

19 *magnesite* + 5 *diopside* + $SiO_{2,aq}$ + 3 H_2O

= 2 *dolomite* + 11 *forsterite* + 10 $CO_{2,aq}$ + 3 $CaHCO_3^+$ + 2 HCO_3^- + OH^- (6.2)

The formation of positively charged Ca-bearing aqueous complexes is the primary reason for the higher pH of fluids equilibrated with meta-ophicalcite relative to that of Atg-serpentinite dehydration fluids (grey stippled line and star in Fig. 6.8a, respectively). Once magnesite is exhausted, aragonite is formed (0.8 > f/r > 4.5, Fig. 6.8a) by the reaction of dolomite with $SiO_{2,aq}$ from the infiltrated fluid, according to the reaction:

4 *dolomite* + 2 $SiO_{2,aq}$ + 3 H_2O

= *aragonite* + 2 *forsterite* + 3 $CO_{2,aq}$ + 3 $CaHCO_3^+$ + HCO_3^- + 2 OH^- (6.3)

This reaction is due to the higher $SiO_{2,aq}$ content of Atg-serpentinite dehydration fluids relative to that of fluids equilibrated with meta-ophicalcite (Fig. 6.8e), and accounts for the constant clinopyroxene content between 0.8 > f/r > 4.5 (Fig. 6.8a). In the 0.8 < f/r < 4.5 range (Fig. 6.8a), aragonite and dolomite in the assemblage buffer the fluid composition, which increases the amount of charged carbonate complexes relative to the preponderance of $CO_{2,aq}$ at lower f/r (reaction 6.2). Accordingly, the pH increases once magnesite is consumed and reaction 6.3 buffers the fluid composition (accounted for by OH^- in reaction 6.3; grey and orange lines in Fig. 6.8a & e, respectively). The total C solubility and loss decrease with increasing f/r due to the lower $aCO_{2,aq}$ (Fig. 6.8e). At f/r ≈ 4.5, dolomite reacts out and aragonite is the only remaining carbonate (Fig. 6.8a). This change is accompanied by a pH increase and a drop of $aCO_{2,aq}$ (Fig. 6.8e), indicating that the congruent dissolution of aragonite becomes prominent relative to carbonate-silicate buffer reactions. After infiltration of 280 mol fluid per 1 kg initial rock mass (f/r ≈ 6.2), all carbon is dissolved from meta-ophicalcite at 2.2 GPa, and the pH drops to values similar to that of the Atg-serpentinite dehydration fluid (Fig. 6.8a).

At the P–T conditions of Atg-serpentinite dehydration at the slab surface of cold subduction zones (point II in Fig. 6.1), the higher $CaHCO_3^+$ concentration in fluids in equilibrium with meta-ophicalcite — relative to lower P (Fig. 6.4c) — causes a greater Ca loss with increasing f/r (slope of black dashed line in Fig. 6.8b) and a greater consumption of

dolomite relative to magnesite. As a consequence, aragonite does not form by reaction 6.3 as at it occurs at lower P. The carbon loss with increasing f/r (dotted black line, Fig. 6.8b) is however lower than at 2.2 GPa and higher f/r are required to dissolve all C (310 mol; cf. Fig.

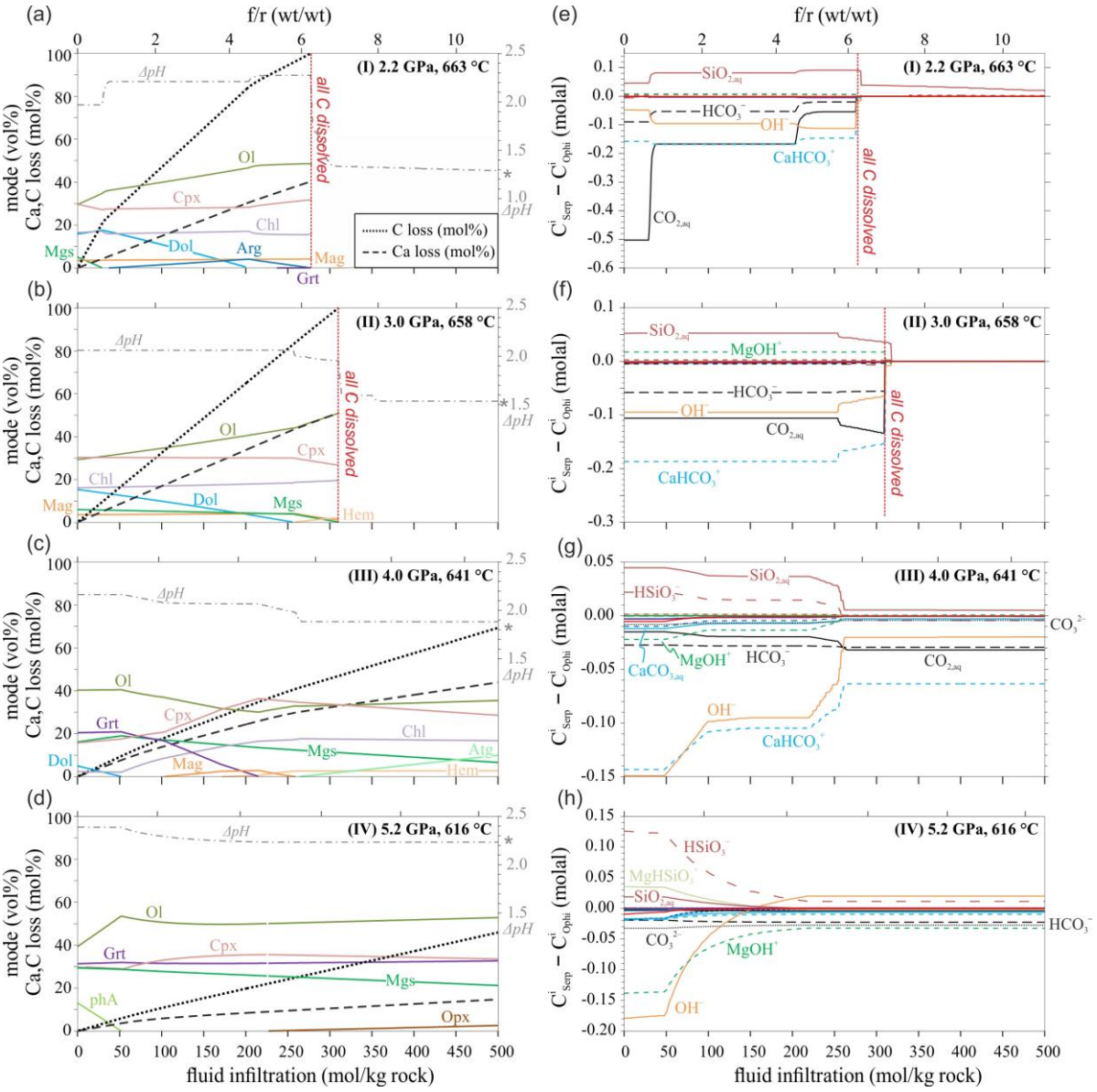

Figure 6.8. *Devolatilization driven by infiltration of serpentinite dehydration fluid into meta-ophicalcite at different P–T conditions of the antigorite-out reaction (corresponding to P–T conditions I to IV in Figs. 6.1, 6.4, and 6.7).* ***(a–d)*** *Changes in phase assemblages, ΔpH (grey stippled curves), and C and Ca losses (dotted and dashed curves, respectively) as a function of the amount of fluid infiltration. The x-axis shows the amount of infiltrated fluid in mol fluid / 1 kg initial rock mass, and the corresponding time-integrated fluid/rock ratio (f/r; in wt/wt). C and Ca losses are shown as mol% relative to the initial rock contents. The ΔpH of the infiltrating serpentinite dehydration fluid is marked by the grey star on the right axes.* ***(e–h)*** *Difference of aqueous speciation between the infiltrated (C^i_{Serp}) and the outflow fluid (C^i_{Ophi}) with f/r. Positive values indicate higher species concentration in the infiltrated fluid compared to the outflow fluid; negative values indicate (absolute) enrichment of species in the outflow fluid. Intervals of constant aqueous concentrations are due to buffer reactions.*

6.8b and Fig. 6.8a) because of the lower $aCO_{2,aq}$ of the equilibrated fluid (cf. Fig. 6.8f and Fig. 6.8e).

Meta-ophicalcites in deeper sections —and hence greater P— of cold subducting slabs are composed of olivine-clinopyroxene-garnet-carbonate at the P–T conditions of antigorite breakdown (conditions III & IV in Fig. 6.1 and Fig. 6.4a & c). Due to the higher concentration of charged aqueous complexes relative to neutral species (such as $CO_{2,aq}$) at high P, the phase assemblages of meta-ophicalcite evolve differently (Fig. 6.4c) during infiltration-driven devolatilization at Moho depths than at the slab interface. At 4 GPa, the magnesite abundance increases in detriment of dolomite at f/r < 1 (Fig. 6.8c; Fig. 6.8g) following the reaction:

12 *dolomite* + 3 *forsterite* + 2 $SiO_{2,aq}$ + $HSiO_3^-$ + 12 H_2O

= 12 *magnesite* + 3 *diopside* + 9 $CaHCO_3^+$ + 3 $MgOH^+$ + 2 HCO_3^- + $CO_{2,aq}$ + 11 OH^- (6.4)

In contrast to lower pressure at the slab interface (reaction 6.2 at 2.2 GPa) where magnesite and clinopyroxene react to form dolomite, olivine, and mainly $CO_{2,aq}$ (cf. Fig. 6.8c & g, and Fig. 6.8a & e), the reaction 6.4 at higher pressure produces magnesite, clinopyroxene, and a highly alkaline, C-bearing fluid. With increasing f/r, the high $CaHCO_3^+$ concentration in the fluid causes the loss of Ca and C, resulting in higher Mg and Si contents in the residual bulk compositions. Once dolomite is consumed (f/r > 1 in Fig. 6.8c), garnet reacts out to chlorite and clinopyroxene, and the pH and $CaHCO_3^+{}_{,aq}$ of the fluid decrease (Fig. 6.8c & g). Despite the total carbon decrease in the solid, the $CO_{2,aq}$ concentration of the outflow fluid increases (Fig. 6.8g).

At 5.2 GPa, the carbon loss from meta-ophicalcite during the infiltration of Atg-serpentinite dehydration fluids is mainly caused by the congruent dissolution of magnesite to $MgOH^+$, HCO_3^- and CO_3^{2-} (Fig. 6.4c; Fig. 6.8d & h). After the initial transformation of phase-A to olivine, minor olivine and orthopyroxene are formed at increasing f/r from the reaction of infiltrating fluid $HSiO_3^-$ with $MgOH^+$ produced by magnesite dissolution (Fig. 6.8d & h). The garnet stability at 5.2 GPa and the absence of Ca-carbonates reduce the effect of Ca-bearing aqueous complexes on the fluid composition and speciation, and, at low f/r, the pH of the outflow fluid is similar to that of the Atg-dehydration fluid (grey stippled line and star, Fig. 6.8d). Overall, for a similar f/r, the C loss at slab depths is higher (dotted line in Fig. 6.8d) than at Moho depths, where the complete dissolution of magnesite requires the infiltration of > 1500 mol fluid / kg initial rock (f/r ≈ 35; not shown in the figure).

At very high f/r, meta-ophicalcite becomes chlorite-clinopyroxene-olivine (carbonate-bearing and partially rehydrated) or orthopyroxene-garnet-clinopyroxene-olivine rocks (Fig. 6.8a–c and Fig. 6.8d, respectively), leading to carbonate-bearing, garnet-clinopyroxene-olivine rocks when subducted to greater depths (cf. Fig. 6.8; Appendix Fig. A-6.2). Such silicate rocks may account for some Ca-enriched meta-peridotites in deeply subducted serpentinite (e.g. clinopyroxene-rich garnet-peridotites in Cima de Gagnone; Scambelluri et al., 2014) or the protoliths for diamond-bearing meta-pyroxenite or peridotite (Brenker et al., 2005; Smith et al., 2018). Considering that antigorite breakdown releases up to 9 wt% fluid (Fig. 6.6) — c. 5 mol fluid / kg serpentinite— the total loss of carbon in the modelled meta-ophicalcite (with 2 mol C / kg; Table 6.1) in warm subduction zones requires the infiltration of fluids derived from a serpentinite mass 60 times greater than that of the initial meta-ophicalcite (Fig. 6.8a & b). In colder subduction geotherms (e.g., at the Moho within the slab; Fig. 6.8c & d), larger amounts of serpentinite-derived fluids would be required to transform meta-ophicalcite to a silicate rock.

6.4.2.3 Infiltration-driven devolatilization of carbonate–talc rocks

Carbonate–talc rocks in subduction melanges or carbonated and serpentinized mantle wedge (Fig. 6.2c) likely experience fluxing by Atg-serpentinite dehydration fluids near the slab surface at pressures of 2.2 to 3.0 GPa in warm and moderately cold subduction zones, respectively (conditions I & II in Fig. 6.1 & Fig. 6.5). The bulk compositional and mineralogical changes of carbonate-talc rocks due to infiltration-driven devolatilization are broadly similar at 2.2 and 3.0 GPa (Fig. 6.9 a & b, respectively), but, due to variations of carbon solubility (cf. Fig. 6.9 a & b, and Fig. 6.5a & b), differ in their relative carbon loss with increasing f/r. Talc reacts with magnesite to orthopyroxene for f/r < 1 and < 2 at 2.2 and 3.0 GPa, respectively (Fig. 6.9 a & b). At 2.2 GPa (Fig. 6.9a), this reaction releases mostly H_2O–CO_2 fluids with minor solutes (Fig. 6.9c). At 3.0 GPa, significant Ca loss indicates the reaction of clinopyroxene (Fig. 6.9b & d) via the reaction:

25 *magnesite* + 23 *talc* + 6 *diopside*

$$= 50\ \textit{enstatite} + 16\ CO_{2,aq} + 6\ CaHCO_3^+ + 3\ HCO_3^- + 4\ SiO_{2,aq} + 3\ OH^- + 17\ H_2O \qquad (6.6)$$

When talc is exhausted, olivine forms at the expense of magnesite and clinopyroxene for f/r > 1 and > 2 at 2.2 and 3.0 GPa, respectively (Fig.9 a & b). At 3 GPa, at f/r > 2 (Fig. 6.9b & d) the phase changes can be accounted for by the reaction:

6 *magnesite* + 2 *diopside* + 2 H_2O

= 4 *forsterite* + 3 $CO_{2,aq}$ + 2 $CaHCO_3^+$ + HCO_3^- + OH^- (6.7)

Reactions (6.6) and (6.7) increase OH^- in the fluid — and hence pH — relative to that of the serpentinite-derived infiltration fluid (grey stippled lines in Fig. 6.9 a & b). The fluid $CO_{2,aq}$ concentration decreases at high f/r when olivine forms (cf. reactions 6.6 & 6.7; Fig. 6.9b & d). This evolution accounts for the increasing pH at high f/r (Fig. 6.9b), and the higher aCO_2 of fluids in equilibrium with talc-magnesite relative to those in equilibrium with olivine. This result is consistent with experiments and solute-free thermodynamic modelling predictions (Sieber et al., 2018). The capacity of carbonate-talc assemblages to buffer infiltrated serpentinite dehydration fluids to higher pH (stippled grey lines in Fig. 6.9a & b) may have important implications for the speciation of sulphur and nitrogen (Mikhail et al., 2017) and the fluid solubility of trace elements that are mobilized by pH-dependent aqueous metal-ion

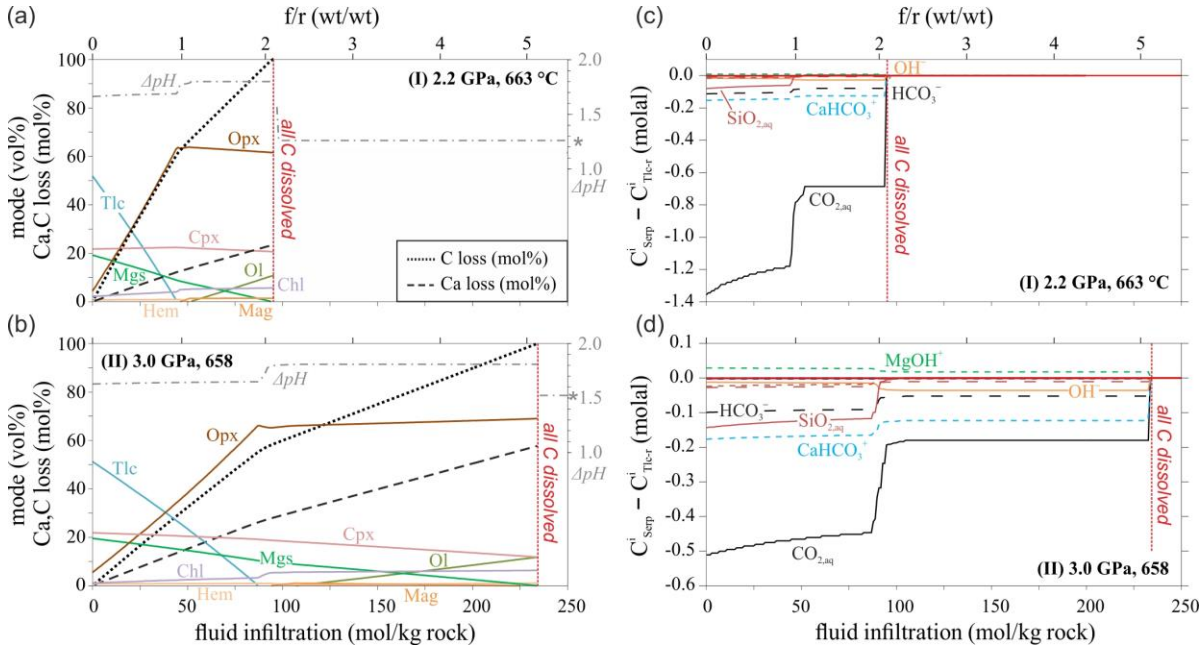

Figure 6.9. *Devolatilization driven by infiltration of serpentinite dehydration fluid into talc-carbonate rock at the P–T conditions of the antigorite-out reaction at the slab surface of* ***(a)*** *warm and* ***(b)*** *cold subduction zones (corresponding to P–T conditions I and II in Figs. 6.1, 6.5, and 6.7).* ***(a, b)*** *Changes in phase assemblages, ΔpH (grey stippled curves), and C and Ca losses (dotted and dashed curves, respectively) as a function of the amount of fluid infiltration. The x-axis shows the amount of infiltrated fluid in mol fluid / 1 kg initial rock mass, and the corresponding time-integrated fluid/rock ratio (f/r). C and Ca losses are shown as mol% relative to the initial rock contents. The ΔpH of the infiltrating serpentinite dehydration fluid is marked by a grey star on the right axes.* ***(c, d)*** *Difference of aqueous speciation between the infiltrated (C^i_{Serp}) and the outflow fluids ($C^i_{Tlc\text{-}r}$) with f/r. Positive values indicate higher species concentration in the infiltrating fluid compared to the outflow fluid, negative values indicate (absolute) enrichment of species in the outflow fluid. Intervals with constant aqueous concentrations are due to buffer reactions (see Sec. 6.3 for calculation methods).*

complexes (Kokh et al., 2017; Williams-Jones et al., 2012). Hence, Ca-bearing, serpentinite-hosted carbonate rocks at the slab-mantle interface may act as a sink for pH-sensitive trace elements and volatiles, modulating the geochemical signature of aqueous fluids released from the slab to the mantle wedge at subarc depths.

At high f/r, carbonate–talc rocks form chlorite-, olivine-, and clinopyroxene- bearing orthopyroxenite (Fig. 6.9a & b). For the studied carbonate–talc bulk rock composition, the transformation of carbonate–talc to orthopyroxene-rich assemblages requires fluids derived from 20 kg of Atg-serpentinite per kg of carbonate-talc rock transformed (~ 50 and 100 mol fluid infiltration, Fig. 6.9a & b, respectively). Magnesite-bearing olivine orthopyroxenite from the high-P Cabo Ortegal ultramafic complex (NW Spain) (Gil Ibarguchi et al., 1999) shows bulk compositions and phase proportions similar to those predicted by the infiltration models of carbonate-talc rock (Fig. 6.9a & b). Fluid-assisted, fast growth of orthopyroxene at the expense of talc and magnesite likely favours the entrapment of the solid reactant phases and fluid inclusions in growing porphyroblasts. This mechanism may account for some enigmatic carbonate-bearing (multi-phase) inclusions found in orthopyroxenite of exhumed high-pressure metamorphic complexes (Gil Ibarguchi et al., 1999; Malaspina and Tumiati, 2012).

6.4.3 Carbon solubility as a function of the thermal regime of subduction zones

For a given bulk composition, the mass of C dissolved by devolatilization reactions driven by infiltration of Atg-serpentinite dehydration depends on the P–T conditions of dehydration (Fig. 6.1), which, in turn, are established by where they occur in the slab (i.e., slab interface or Moho depths) and the thermal state of the subduction zone. The thermal state of subduction zones can be characterized by the thermal parameter, Φ, which depends on the dip angle, converging velocity, and age of the subducting slab (Syracuse et al., 2010; van Keken et al., 2011). To investigate the carbon release as a function of the thermal parameter of subduction zones, we have parametrized the P–T conditions of Atg-serpentinite dehydration at the surface and Moho depth of the slab as a function of Φ of the present-day subduction zones (Appendix Table A-6.2; see also Supplementary methods and Fig. A-6.7 of the Appendix). Although this parametrization applies to our Atg-serpentinite bulk composition of reference (Table 6.1), it can be generalized, within the fitting error, to other serpentinite compositions.

At a given P and T, the release of carbon during the infiltration of Atg-serpentinite fluids into serpentinite-hosted carbonate rocks is governed by the time-integrated fluid/rock ratio (f/r) and hence by the time-integrated amount of external fluids that react with a volume of carbonate-rocks. The amount of infiltrated fluids available for carbonate dissolution depends on the degree of serpentinization and the volume of serpentinite that dehydrates. This mass balance can be portrayed in terms of the length, L, of a serpentinite column —a square prism of square unit base—that upon dehydration produces the necessary amount of fluid to fully dissolve C from a given thickness of carbonate-rock in the column. This scenario would be equivalent to vertical fluxing of fluids derived from the dehydration of the serpentine column through a carbonate layer on the top of the column. This case would be the optimal scenario for C dissolution because all the fluid produced by dehydration of the serpentinite column passes through and reacts with the carbonate-rock layer. Figure 6.10 shows contour plots of the maximum thickness of pure $CaCO_3$, meta-ophicalcite and carbonate-talc rock that can be dissolved by the fluids produced by dehydration of a serpentinite column of length L as a function of the thermal parameter, Φ, of subduction zones. We note that for Atg-dehydration at P > 6 GPa —such as at the Moho of cold subduction zones— the same volume of serpentinite produces an up to 16% greater mass of fluid than at lower P due to the higher compressibility of antigorite at these depths (see Supplementary Methods and Figs. A-6.3 – A-6.6 of the Appendix for more details).

The solubility of carbon in fluids equilibrated with carbonate–silicate rocks (Fig. 6.4; Fig. 6.5) is higher than in fluids equilibrated with $CaCO_3$ (Fig. 6.1). Although $CaCO_3$ is an unrealistic bulk composition in subducted slabs, infiltration-driven dissolution of $CaCO_3$ provides a lower-bound estimate for —kinetically controlled— disequilibrium dissolution of $CaCO_3$ disregarding carbonate–silicate buffer reactions. Dissolution of a ~4 m thick layer of aragonite at the slab surface (solid contours in Fig. 6.10a) requires fluids derived from the dehydration of a 2200 – 1800 m serpentinite column in warm and cold subduction zones, respectively (~$4.2 – 5.1 \times 10^5$ kg fluid/m²). Due to the increasing solubility of aragonite with pressure (Fig. 6.1; Kelemen and Manning, 2015), the fluids generated from the dehydration of the same column length of serpentinite may dissolve an ~8 m thick aragonite layer at the Moho depth of cold subduction zones (dashed contours and $\Phi > 4000$ in Fig. 6.10a). As Atg-serpentinite dehydration takes places at increasing pressure from hot to cold subduction zones (Fig. 6.1), dissolution of aragonite driven by infiltration of Atg-serpentinite fluids is much higher in cold than in warm subduction zones (Fig. 6.10a).

An opposite trend is observed for the carbonate–silicate systems. Meta-ophicalcites are more likely to be preserved beyond the breakdown of antigorite in cold subduction zones, particularly if at the slab Moho depths (Fig. 6.10b). In the Iberian margin, up to 70 m thick ophicalcite bodies occur below a ~600 m sediment cover and are underlain by ~2000 m of partly serpentinized (c. 80%) peridotite (Chian et al., 1999; Schwarzenbach et al., 2013). If such ophicalcites subducted in a hot subduction zone such as Cascadia (Φ < 200) —the optimal setting for carbonate dissolution from meta-ophicalcite— less than 60 vol% of carbonate from the ophicalcite would be dissolved (40 m contour at Φ < 200 in Fig. 6.10b). This estimate considers a low bulk rock carbon content (Table 6.1) and a 1600 m thick column of serpentinite that is equivalent to 2000 m of partly serpentinized (80%) peridotite. If subducted in an intermediate warm subduction zone such as the Lesser Antilles (Φ ≈ 1050), only 30 m of ophicalcite would be dissolved at the

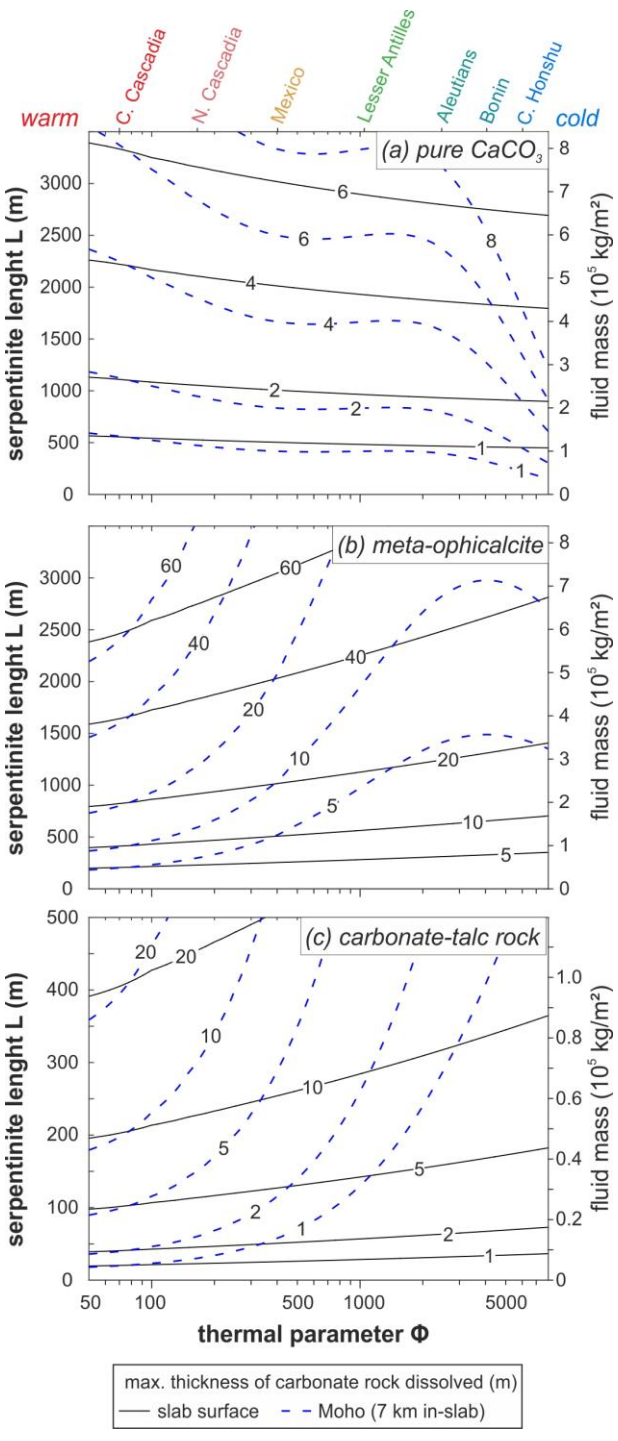

◄ ***Figure 6.10.*** *Contour plots of the maximum thickness (m) of carbonate rock dissolved by Atg-serpentinite dehydration fluids produced by a serpentinite column of length L as function of the thermal parameter (Φ) of the subduction zone. Contours show the dissolution for* ***(a)*** *pure $CaCO_3$,* ***(b)*** *meta-ophicalcite, and* ***(c)*** *carbonate-talc rock (see Table 6.1 for composition) located at the slab surface (solid black curves) and the Moho (7 km below the slab surface; dashed blue curves). The calculation uses a constant initial carbon solubility, which yields a maximum estimate of dissolution because the rock-buffered carbonate solubility decreases with f/r (cf. Fig. 6.8; Fig. 6.9). The right axis indicates the mass of water released for the corresponding length of the dehydrated serpentinite column for the case of slab surface. The top axis shows examples of subduction zones with different Φ (after Syracuse et al., 2010).*

slab surface and < 10 m at Moho depths (Fig. 6.10b). These are maximum estimates of the carbon release because Iberian margin ophicalcites have significantly higher carbon contents — up to 26 wt% CO_2, mostly in aragonite and calcite (Schwarzenbach et al., 2013) — than our reference carbonate-rocks (Table 6.1). These computations indicate that, in spite of infiltration-driven devolatilization by Atg-serpentinite dehydration fluids at subarc depths, substantial amounts of carbon in meta-ophicalcite may be recycled back into the deep mantle.

Recycling of carbon in meta-ophicalcite might have been important during the subduction of passive margins such as during the subduction of the Tethys Ocean in the Alpine orogeny (Johnston et al., 2011). In the Almirez massif (Betic Cordillera), the occurrence of ~7.5 m thick meta-ophicalcites lenses hosted in Chl-harzburgite formed by prograde Atg-serpentinite dehydration (cf. Ch. 5; Menzel et al., 2019) shows that meta-ophicarbonate lenses were preserved in a hot subducted slab —an optimal case for carbonate dissolution— even though dissolution of all carbonate would have only required fluids derived from the dehydration of a serpentinite column of < 400 m thickness (Fig. 6.10b). Preservation of the Almirez meta-ophicalcite likely indicates that in nature permeability contrasts between meta-ophicalcite and dehydrating Atg-serpentinite result in focused fluid flow and low effective time-integrated fluid/rock ratios.

Serpentinite-hosted carbonate-talc rocks in paleo-subduction zones such as the New Caledonia subduction melange are commonly < 3 m thick (Spandler et al., 2008). The infiltration-driven dissolution of all the carbonate in a 2 m thick carbonate-talc layer at the slab-surface of warm subduction zones (2 m contour and $\Phi < 500$; Fig. 6.10c) requires fluids derived from a 40 m serpentinite column (~0.1 x 10^5 kg fluid /m²). At the slab surface of cold subduction zones ($\Phi > 4000$), fluids from a 70 m column of serpentinite (~0.18 x 10^5 kg fluid /m²) are required (Fig. 6.10c). The capacity of antigorite breakdown fluids to dissolve carbonate-talc rocks at Moho depths of the slab (c. 7 km) strongly depends on Φ (dashed contours in Fig. 6.10c). Due to their limited thickness and the high solubility of carbonate–talc rock in Atg-serpentinite dehydration fluids, carbonate-talc rocks may be a significant source of carbon in subsolidus fluids at subarc depths and are most likely recycled into the deep mantle as pyroxenites (Fig. 6.9).

6.5 Appendices

6.5.1 Supplementary methods – parameters of mass-balance calculations

For modelling of the carbon solubility at the P–T conditions of Atg-serpentinite dehydration, we derived the P–T conditions along the Atg-out reaction from the pseudosection of the modelled bulk composition (cf. Table 6.1). Using the Perple_X werami module, we then obtained the fluid compositions for the investigated carbonate rocks along the Atg-out reaction (e.g. Fig. 6.4 b–c, Fig. 6.5 b–c) from their corresponding pseudosections (Appendix Figs. A-6.1 & A-6.2). Appendix figures A-6.3, A-6.4, and A-6.5 show the carbon solubilities and solid rock densities of aragonite, meta-ophicalcite, and carbonate-talc rock, respectively, and the polynomial functions used to account for these properties as P-dependent functions in the mass-balance calculations. The pressure dependence of fluid release and density of antigorite-serpentinite are shown in Appendix Figure A-6.6.

The P conditions along the Atg-out reaction were approximated as a function of T (°C) by a 3rd order polynomial function (eq. A-6.1):

$$P_{Atg-out}(GPa) = -7.332 \times 10^{-7} \times T^3 + 0.00108 \times T^2 - 0.542 \times T + 98.776 \quad \text{(A-6.1)}$$

From the intersection of this function with the fitted P–T geothermal gradients at the slab surface and the mantle-crust transition (Moho at 7 km below the slab surface) (Syracuse et al., 2010; thermal model D80), we obtained for the reference Atg-serpentinite the P–T conditions of antigorite breakdown in present-day subduction zones (Appendix Table A-6.2). The regression errors are smaller than the thermodynamic uncertainties of the temperature of antigorite dehydration (about ± 15 °C) that arise from variable bulk Al contents in serpentinite and the lack of solution models accounting for Fe^{3+} in antigorite (Bretscher et al., 2018; Padrón-Navarta et al., 2013).

The P of antigorite breakdown as a function of the subduction zone thermal parameter, Φ —where Φ is given by the product of plate age, convergence velocity, and the sine of the slab dip angle (Syracuse et al., 2010; van Keken et al., 2011)— at the slab surface (eq. A-6.2) and Moho depths (eq. A-6.3) can be expressed, respectively, as the logarithmic functions (Appendix Fig. A-6.7):

$$P_{surface}(GPa) = 0.125 \cdot ln(\Phi) + 1.908 \quad \text{(A-6.2)}$$

$$P_{Moho}(GPa) = 1.478 \cdot ln(\Phi + 221.34) - 5.969 \quad \text{(A-6.3)}$$

Although Φ is not a precise description of the thermal structure of a slab and single subduction zones diverge from the trend lines given by equations A-6.2 and A-6.3 (Fig. A-6.7), these calculations provide general insights into the influence of the thermal regime and geometry of subduction zones on the carbonate dissolution at the Atg-serpentinite dehydration (Fig. 6.10). Using interpolations of the P dependence of the carbonate solubility ($[C, molal]_{fluid}$) and rock densities ($\rho_{(serp)}$ and $\rho_{(layer)}$, in kg/m³; Figs. A-6.3 – A-6.6), the carbon dissolution expressed as the thickness of a layer *d* (m) of aragonite, meta-ophicalcite, or carbonate-talc rock dissolved in fluids derived from a serpentinite column of length, L (m), is:

$$d_{layer\,(m)} = \frac{\rho_{(serp)} \times L \times x(H2O)_{serp}}{100 \times \rho_{(layer)} \times m(CO2)_{layer}} \times 44.01 \times [C, molal]_{fluid} \quad \text{(A-6.4)}$$

where $x(H_2O)_{serp}$ is the amount of fluid (wt%) released by antigorite breakdown, and $m(CO_2)_{layer}$ the carbon content of the layer (in mol C / kg rock; cf. Table 6.1). Apart from L and $m(CO_2)_{layer}$, all other variables in equation A-6.4 are P dependent (cf. polynomial fits in Figs. A-6.3 – A-6.6). The substitution of equations A-6.2 and A-6.3 into the P-dependent terms of A-6.4 yields the expressions used to calculate and plot the thickness of aragonite, meta-ophicalcite and carbonate-talc rock dissolved in fluids derived from a serpentinite column of length, L (m), as a function of thermal parameter, Φ, of the subduction zone (Fig. 6.10).

6.5.2 Appendix Tables & Figures

Table A-6.1. *Phases and solution models used for thermodynamic modelling.*

Phase	**Perplex Abbr.**	**formula**	**type/comment**	**Reference**
olivine	Ol(HP)	$Mg_{2x}Fe_{2(1-x)}SiO_4$		(Holland and Powell, 1998)
orthopyroxene	Opx(HP)	$[Mg_xFe_{1-x}]_{2-y}Al_{2y}Si_{2-y}O_6$	speciation model	(Holland and Powell, 1996)
clinopyroxene	Cpx(HP)	$Na_{1-y}Ca_yMg_{xy}Fe_{(1-x)y}Al_ySi_2O_6$	disordered	(Holland and Powell, 1996)
garnet	Gt(WPH)	$Fe_{3x}Ca_{3y}Mg_{3z}Mn_{3(1-x-y-z)}Al_2Si_3O_{12}$, $x+y+z\leq 1$		(Holland and Powell, 1998)
chlorite	Chl(HP)	$[Mg_xFe_wMn_{1-x-w}]_{5-y+z}Al_{2(1+y-z)}Si_{3-y+z}O_{10}(OH)_8$, $x+w\leq 1$	speciation model	(Holland et al., 1998)
antigorite	Atg(PN)	$Mg_{x(48-y)}Fe_{(48-y)(1-x)}Al_{8y}Si_{34-y}O_{85}(OH)_{62}$	ideal, tschermak	(Padrón-Navarta et al., 2013)
dolomite	Do(HP)	$CaMg_xFe_{1-x}(CO_3)_2$		(Holland and Powell, 1998)
magnesite	M(HP)	$Mg_xFe_{1-x}CO_3$		(Holland and Powell, 1998)
spinel	Sp(HP)	$Mg_xFe_{1-x}Al_2O_3$		(Holland and Powell, 1998)
epidote	Ep(HP)	$Ca_2Al_{3-2x}Fe_{2x}Si_3O_{12}OH$		(Holland and Powell, 1998)
talc	T	$[Mg_xFe_{1-x}]_{3-y}Al_{2y}Si_{4-y}O_{10}(OH)_2$	ideal	
brucite	B	$Mg_xFe_{1-x}(OH)_2$	ideal	
tremolite	Tr	$Ca_2Mg_{5x}Fe_{5(1-x)}Si_8O_{22}(OH)_2$	ideal	
anthophyllite	Anth	$Mg_{7x}Fe_{7(1-x)}Si_8O_{22}(OH)_2$	ideal	
Phase A	A-phase	$Mg_{7x}Fe_{7(1-x)}Si_2O_8(OH)_6$	ideal	
magnetite	MF	$Mg_xFe_{3-x}O_4$	ideal	
fluid	COH-Fluid+	H_2O-CO_2	non-linear subdivision	(Connolly and Galvez, 2018)

Quartz (Qtz), coesite (Coe), aragonite (Arg), lawsonite (Lws), hematite (hem), and diamond (diam) were considered pure phases.

Table A-6.2 (a) *P–T conditions of Atg-breakdown at the slab surface predicted by the D80 thermal subduction model (Syracuse et al., 2010), and the corresponding carbonate solubility of aragonite, meta-ophicalcite, and carbonate-talc rock in present-day subduction zones.*

D80 - slab surface					Conditions & solubility of carbonate rocks at Atg dehydration [d]				
	Geometrical and thermal parameters				*P–T of Atg breakdown* [c]		*aragonite-graphite*	*meta-ophicalcite*	*carbonate-talc rock*
Subduction zone	**Dip** [a] **(°)**	**Vc** [a] **(km/Ma)**	**Age** [a] **(Ma)**	**φ** [b] **(km)**	**T (°C)**	**P (GPa)**	**log[Ca] (molal)**	**log[C] (molal)**	**log[C] (molal)**
Central Cascadia	19.8	30	6.9	70	665	2.44	-0.65	-0.19	0.14
North Cascadia	22.4	40	10.6	162	666	2.41	-0.66	-0.17	0.16
Northern Peru Gap	10.2	69.5	29	357	661	2.72	-0.60	-0.30	0.02
Mexico	59.5	47	10	405	666	2.38	-0.66	-0.16	0.17
Colombia/Ecuador	28	60	15	423	662	2.69	-0.61	-0.29	0.03
South Chile	34.2	74.9	10.3	434	661	2.72	-0.60	-0.30	0.02
Nankai	31.4	43	20	448	662	2.68	-0.61	-0.28	0.04
Central Peru Gap	13.2	66.7	33.9	516	662	2.71	-0.60	-0.30	0.03
Central Chile Gap	13.7	73.8	37.7	659	660	2.85	-0.58	-0.35	-0.03
South-Central Chile	29.5	74.7	23.5	864	658	2.94	-0.57	-0.39	-0.07
Guatemala/El Salvador	56.9	66.9	17.4	975	661	2.73	-0.60	-0.30	0.02
Costa Rica	58.9	75.4	15.8	1020	659	2.86	-0.58	-0.35	-0.04
South Lesser Antilles	42.4	17.9	86.6	1045	657	3.01	-0.57	-0.41	-0.10
Central Chile	27.5	71.6	32.4	1071	656	3.07	-0.56	-0.43	-0.13
Nicaragua	62.2	71.1	17.5	1101	660	2.79	-0.59	-0.33	-0.01
North Lesser Antilles	49.8	17.6	83	1116	657	3.04	-0.56	-0.42	-0.11
Peru	28.7	65.1	42.1	1316	663	2.63	-0.62	-0.26	0.06
North-Central Chile	23.6	77.4	42.8	1326	661	2.76	-0.60	-0.31	0.01
North Sumatra	49.1	41.5	48.3	1515	659	2.90	-0.58	-0.37	-0.05
Aegean	30.5	15	200	1523	658	2.97	-0.57	-0.40	-0.08
Alaska	42	49	47.1	1544	661	2.76	-0.60	-0.32	0.01
Kyushu	53.8	72	27	1569	661	2.71	-0.60	-0.30	0.03
Central Sumatra	46.4	40	54.8	1587	660	2.83	-0.59	-0.34	-0.02
North Vanuatu	71.3	39.6	44	1650	662	2.64	-0.61	-0.27	0.06
North Chile	29.3	79	46.2	1786	662	2.69	-0.61	-0.29	0.04
East Banda Sea	48	25.3	100	1880	661	2.77	-0.59	-0.32	0.00
North Marianas	61.5	15.3	147.8	1987	658	2.95	-0.57	-0.39	-0.08
Ryukyu	43.5	69.5	43	2057	662	2.69	-0.61	-0.29	0.04
Alaska Peninsula	45	59	52.2	2178	660	2.84	-0.59	-0.35	-0.03
New Britain	68.2	100.4	25	2330	657	2.99	-0.57	-0.40	-0.09
West Aleut	55.9	50.2	56.1	2332	658	2.93	-0.57	-0.38	-0.07
North Philippines	57.4	87.7	32.4	2394	659	2.92	-0.58	-0.38	-0.06

Table A-6.2 (a) continued.

D80 - slab surface					Conditions & solubility of carbonate rocks at Atg dehydration [d]				
	Geometrical and thermal parameters				*P–T of Atg breakdown* [c]		*aragonite-graphite*	*meta-ophicalcite*	*carbonate-talc rock*
Subduction zone	**Dip** [a] **(°)**	**Vc** [a] **(km/Ma)**	**Age** [a] **(Ma)**	**φ** [b] **(km)**	**T (°C)**	**P (GPa)**	**log[Ca] (molal)**	**log[C] (molal)**	**log[C] (molal)**
New Zealand	52	30.4	100	2396	660	2.84	-0.59	-0.35	-0.03
East Aleutians	45.6	64.2	55.3	2537	660	2.82	-0.59	-0.34	-0.02
South Sumatra	50.2	48.7	68.9	2578	661	2.75	-0.60	-0.31	0.01
Solomon	70.4	93.6	31	2733	658	2.98	-0.57	-0.40	-0.09
Central Aleutians	53.7	63.4	55.9	2856	659	2.87	-0.58	-0.36	-0.04
Scotia	64.6	60.8	59.1	3246	661	2.76	-0.60	-0.32	0.01
South Philippines	64.3	69	59.8	3718	659	2.90	-0.58	-0.37	-0.05
Sunda Strait	49.3	61	85.5	3954	657	3.04	-0.56	-0.42	-0.11
Bonin	62.8	31.6	145.3	4084	658	2.97	-0.57	-0.40	-0.08
Izu	46.1	45.6	135.4	4449	659	2.89	-0.58	-0.37	-0.05
North Honshu	28.7	81.6	129.3	5067	658	2.95	-0.57	-0.39	-0.08
South Vanuatu	66.8	112.7	50	5179	661	2.72	-0.60	-0.30	0.02
Kamchatka	50.7	75.1	92.9	5399	656	3.06	-0.56	-0.43	-0.12
Java	45.8	67.8	111.2	5405	657	3.04	-0.56	-0.42	-0.11
Kermadec	56.1	64.6	105.6	5662	657	3.03	-0.56	-0.42	-0.11
Hokkaido	41.9	74.7	115.2	5747	656	3.09	-0.56	-0.44	-0.13
Calabria	43	45	190	5831	657	3.04	-0.56	-0.42	-0.11
West Banda Sea	54.4	73.6	100	5984	659	2.91	-0.58	-0.37	-0.06
Central Honshu	33.9	82.7	130.5	6019	658	2.97	-0.57	-0.40	-0.08
South Kurile	46.4	77.4	108.5	6082	657	3.01	-0.57	-0.41	-0.10
South Marianas	56.9	50	151.6	6350	660	2.79	-0.59	-0.33	-0.01
North Kurile	50.4	78.3	105.6	6371	656	3.09	-0.56	-0.44	-0.13
Bali/Lombok	45.9	69.8	134.9	6762	657	3.02	-0.57	-0.42	-0.11
Tonga	52.4	165.8	109	14318	652	3.35	-0.54	-0.53	-0.24

a) Dip, convergence velocity and plate age from Syracuse et al. (2010)

b) Calculated as φ = plate age * convergence velocity Vc * sin (slab dip angle)

c) P–T conditions obtained from intersection of multiple polynomial regressions of the P–T paths of the D80 thermal subduction model between 500 - 700 °C (Syracuse et al., 2010) with the Atg-out reaction in Al-bearing serpentinite (black line in Fig. 6.1; composition cf. Table 6.1). Uncertainties in temperatures are about ± 15 °C given the effect of Al and Fe^{3+} tschermak's exchange on the thermal stability of antigorite (Padrón-Navarta et al., 2013).

d) Estimated solubilities in different carbonate lithologies (cf. Table 6.1) at the P–T conditions of antigorite-breakdown at the slab surface; obtained by polynomial interpolation of the P–T-dependent elemental solubility as from thermodynamic modelling (cf. Fig. 6.4b, 6.5b).

Table A-6.2 (b) *P–T conditions of Atg-breakdown at Moho depths predicted by the D80 thermal subduction model (Syracuse et al., 2010), and the corresponding carbonate solubility of aragonite, meta-ophicalcite, and carbonate-talc rock in present-day subduction zones.*

D80 – Moho depth					Conditions & solubility of carbonate rocks at Atg dehydration [d]				
	Geometrical and thermal parameters				*P–T of Atg breakdown* [c]		*aragonite-graphite*	*meta-ophicalcite*	*carbonate-talc rock*
Subduction zone	**Dip** [a] **(°)**	**Vc** [a] **(km/Ma)**	**Age** [a] **(Ma)**	**φ** [b] **(km)**	**T (°C)**	**P (GPa)**	**log[Ca] (molal)**	**log[C] (molal)**	**log[C] (molal)**
Central Cascadia	19.8	30	6.9	70	662	2.69	-0.61	-0.29	0.03
North Cascadia	22.4	40	10.6	162	663	2.64	-0.62	-0.27	0.06
Northern Peru Gap	10.2	69.5	29	357	652	3.36	-0.54	-0.53	-0.24
Mexico	59.5	47	10	405	661	2.78	-0.59	-0.32	0.00
Colombia/Ecuador	28	60	15	423	648	3.60	-0.53	-0.61	-0.34
South Chile	34.2	74.9	10.3	434	645	3.76	-0.53	-0.66	-0.40
Nankai	31.4	43	20	448	650	3.47	-0.54	-0.57	-0.29
Central Peru Gap	13.2	66.7	33.9	516	645	3.79	-0.53	-0.67	-0.41
Central Chile Gap	13.7	73.8	37.7	659	640	4.07	-0.53	-0.75	-0.51
South-Central Chile	29.5	74.7	23.5	864	626	4.75	-0.54	-0.90	-0.74
Guatemala/El Salvador	56.9	66.9	17.4	975	627	4.68	-0.54	-0.88	-0.72
Costa Rica	58.9	75.4	15.8	1020	604	5.63	-0.53	-1.03	-1.00
South Lesser Antilles	42.4	17.9	86.6	1045	631	4.49	-0.54	-0.84	-0.66
Central Chile	27.5	71.6	32.4	1071	621	4.97	-0.55	-0.94	-0.81
Nicaragua	62.2	71.1	17.5	1101	612	5.36	-0.54	-0.99	-0.92
North Lesser Antilles	49.8	17.6	83	1116	627	4.70	-0.54	-0.89	-0.73
Peru	28.7	65.1	42.1	1316	632	4.46	-0.54	-0.84	-0.64
North-Central Chile	23.6	77.4	42.8	1326	627	4.68	-0.54	-0.88	-0.72
North Sumatra	49.1	41.5	48.3	1515	624	4.83	-0.55	-0.91	-0.77
Aegean	30.5	15	200	1523	638	4.16	-0.53	-0.77	-0.54
Alaska	42	49	47.1	1544	631	4.50	-0.54	-0.85	-0.66
Kyushu	53.8	72	27	1569	588	6.11	-0.49	-1.06	-1.12
Central Sumatra	46.4	40	54.8	1587	628	4.66	-0.54	-0.88	-0.71
North Vanuatu	71.3	39.6	44	1650	608	5.48	-0.54	-1.01	-0.96
North Chile	29.3	79	46.2	1786	620	5.02	-0.55	-0.95	-0.83
East Banda Sea	48	25.3	100	1880	624	4.86	-0.55	-0.92	-0.77
North Marianas	61.5	15.3	147.8	1987	629	4.61	-0.54	-0.87	-0.69
Ryukyu	43.5	69.5	43	2057	605	5.58	-0.53	-1.02	-0.99
Alaska Peninsula	45	59	52.2	2178	608	5.48	-0.54	-1.01	-0.96
New Britain	68.2	100.4	25	2330	590	6.06	-0.49	-1.06	-1.11
West Aleut	55.9	50.2	56.1	2332	608	5.47	-0.54	-1.01	-0.96
North Philippines	57.4	87.7	32.4	2394	593	5.98	-0.50	-1.05	-1.09

Table A-6.2 (b) continued.

D80 - Moho depth					Conditions & solubility of carbonate rocks at Atg dehydration [d]				
	Geometrical and thermal parameters				*P–T of Atg breakdown* [c]		*aragonite-graphite*	*meta-ophicalcite*	*carbonate-talc rock*
Subduction zone	**Dip** [a] **(°)**	**Vc** [a] **(km/Ma)**	**Age** [a] **(Ma)**	**φ** [b] **(km)**	**T (°C)**	**P (GPa)**	**log[Ca] (molal)**	**log[C] (molal)**	**log[C] (molal)**
New Zealand	52	30.4	100	2396	608	5.51	-0.54	-1.01	-0.97
East Aleutians	45.6	64.2	55.3	2537	599	5.79	-0.52	-1.04	-1.04
South Sumatra	50.2	48.7	68.9	2578	590	6.07	-0.49	-1.06	-1.11
Solomon	70.4	93.6	31	2733	569	6.57	-0.40	-1.07	-1.23
Central Aleutians	53.7	63.4	55.9	2856	594	5.94	-0.51	-1.05	-1.08
Scotia	64.6	60.8	59.1	3246	601	5.72	-0.52	-1.03	-1.03
South Philippines	64.3	69	59.8	3718	576	6.41	-0.44	-1.07	-1.19
Sunda Strait	49.3	61	85.5	3954	560	6.73	-0.36	-1.07	-1.26
Bonin	62.8	31.6	145.3	4084	600	5.78	-0.52	-1.04	-1.04
Izu	46.1	45.6	135.4	4449	582	6.27	-0.46	-1.07	-1.16
North Honshu	28.7	81.6	129.3	5067	561	6.72	-0.36	-1.07	-1.26
South Vanuatu	66.8	112.7	50	5179	538	7.05	-0.26	-1.06	-1.33
Kamchatka	50.7	75.1	92.9	5399	525	7.17	-0.21	-1.06	-1.35
Java	45.8	67.8	111.2	5405	543	6.99	-0.28	-1.07	-1.32
Kermadec	56.1	64.6	105.6	5662	533	7.10	-0.24	-1.06	-1.34
Hokkaido	41.9	74.7	115.2	5747	538	7.04	-0.26	-1.06	-1.33
Calabria	43	45	190	5831	593	5.98	-0.50	-1.05	-1.09
West Banda Sea	54.4	73.6	100	5984	536	7.07	-0.25	-1.06	-1.33
Central Honshu	33.9	82.7	130.5	6019	540	7.02	-0.27	-1.06	-1.32
South Kurile	46.4	77.4	108.5	6082	526	7.17	-0.21	-1.06	-1.35
South Marianas	56.9	50	151.6	6350	571	6.53	-0.41	-1.07	-1.22
North Kurile	50.4	78.3	105.6	6371	528	7.15	-0.22	-1.06	-1.35
Bali/Lombok	45.9	69.8	134.9	6762	538	7.05	-0.26	-1.06	-1.33
Tonga	52.4	165.8	109	14318					

a) Dip, convergence velocity and plate age from Syracuse et al. (2010)

b) Calculated as φ = plate age * convergence velocity Vc * sin (slab dip angle)

c) P–T conditions obtained from intersection of multiple polynomial regressions of the P–T paths of the D80 thermal subduction model between 500 - 700 °C (Syracuse et al., 2010) with the Atg-out reaction in Al-bearing serpentinite (black line in Fig. 6.1; composition cf. Table 6.1). Uncertainties in temperatures are about ± 15 °C given the effect of Al and Fe^{3+} tschermak's exchange on the thermal stability of antigorite (Padrón-Navarta et al., 2013).

d) Estimated solubilities in different carbonate lithologies (cf. Table 6.1) at the P–T conditions of antigorite-breakdown at the slab surface; obtained by polynomial interpolation of the P–T-dependent elemental solubility as from thermodynamic modelling (cf. Fig. 6.4b, 6.5b).

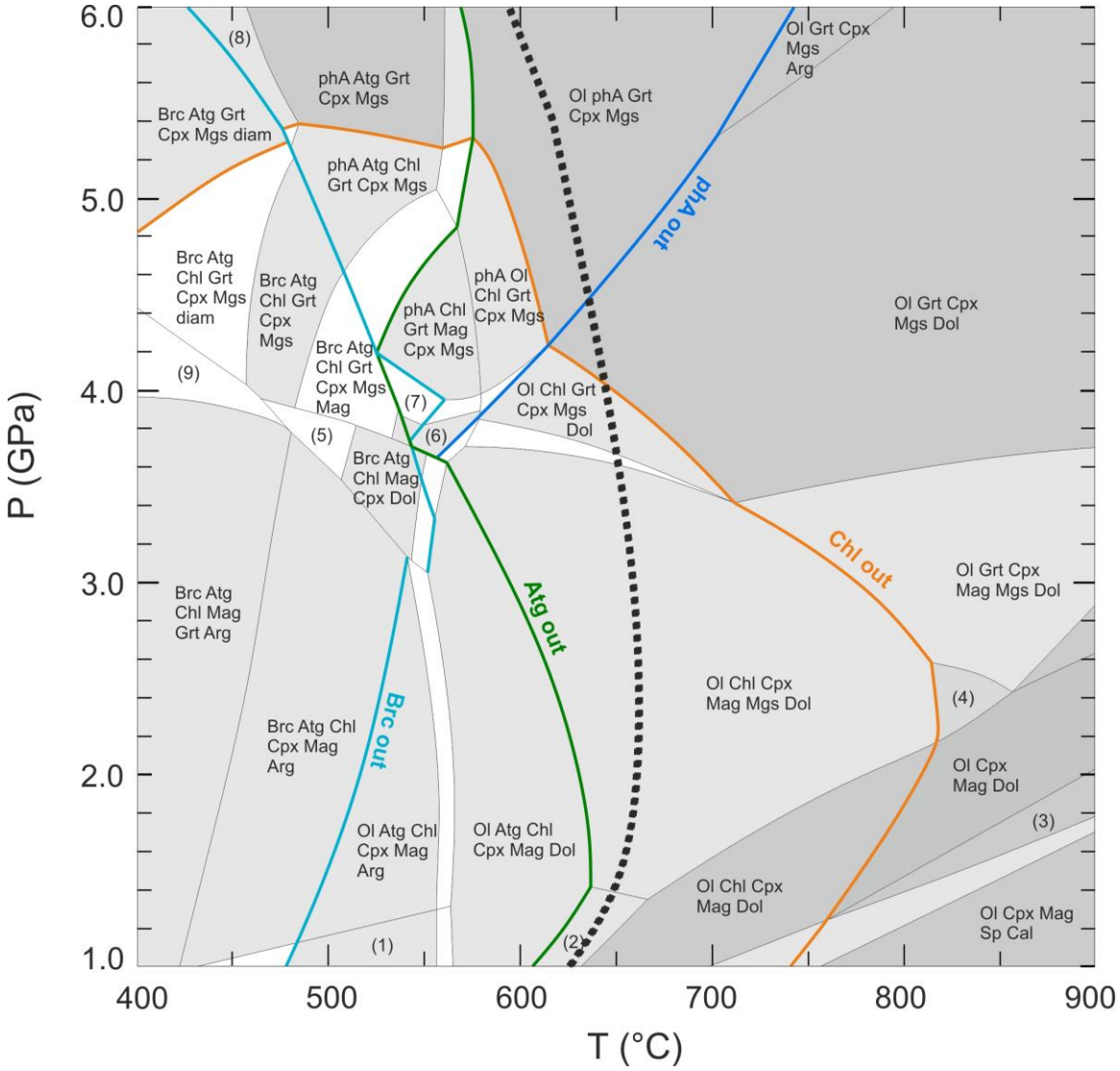

Figure A-6.1. *P–T pseudosection of meta-ophicalcite (Table 6.1). Main devolatilization reactions highlighted in colour; COH-fluid is stable in all fields. The black dotted line marks the antigorite breakdown in pure serpentinite. Numbered fields: (1) Ol Atg Chl Cpx Mag Cal; (2) Ol Tr Chl Cpx Mag Dol; (3) Ol Cpx Mag Dol Cal; (4) Ol Cpx Mag Dol Mgs; (5) Brc Atg Grt Chl Mag Cpx Dol; (6) phA Chl Cpx Mag Dol Mgs; (7) Brc phA Grt Chl Mag Cpx Mgs; (8) phA Atg Grt Cpx Mgs diam; (9) Brc Atg Chl Grt Mgs Arg diam. The phase assemblages in non-labelled fields can be deduced from neighbouring fields with lower variance (darker grey shading).*

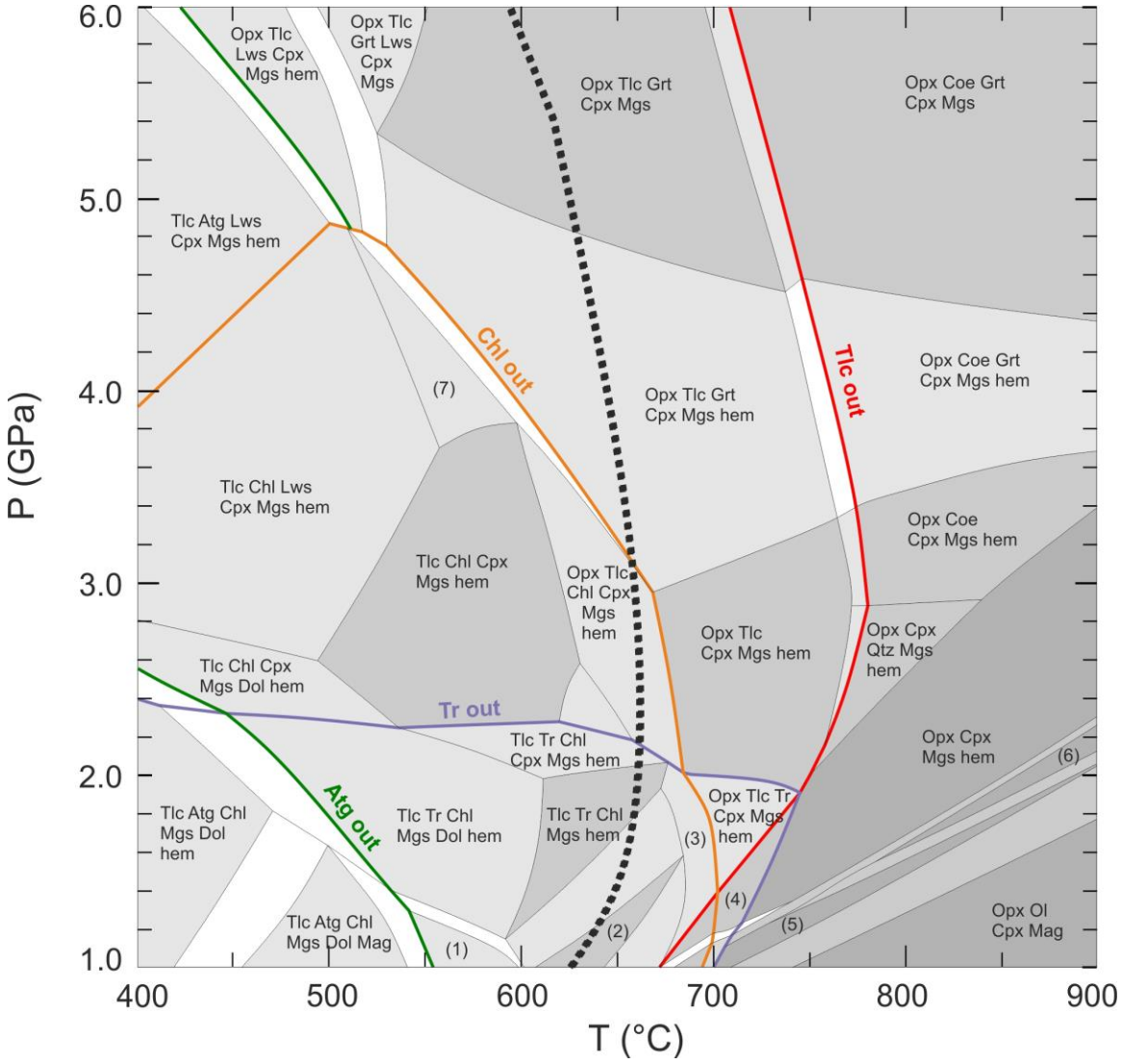

Figure A-6.2. *P–T pseudosection of carbonate-talc rock (Table 6.1). Main devolatilization reactions highlighted in colour; the black dotted line is the antigorite breakdown in pure serpentinite. All fields contain COH-Fluid. Numbered fields are: (1) Tlc Tr Chl Dol Mgs Mag; (2) Tlc Tr Chl Mgs Mag; (3) Opx Tlc Tr Chl Mgs hem; (4) Opx Tr Cpx Mgs hem; (5) Opx Cpx Dol Mag; (6) Opx Cpx Mgs Mag; (7) Tlc Chl Grt Cpx Mgs hem. Phase assemblages in non-labelled fields can be deduced from neighbouring fields with lower variance (darker grey shading).*

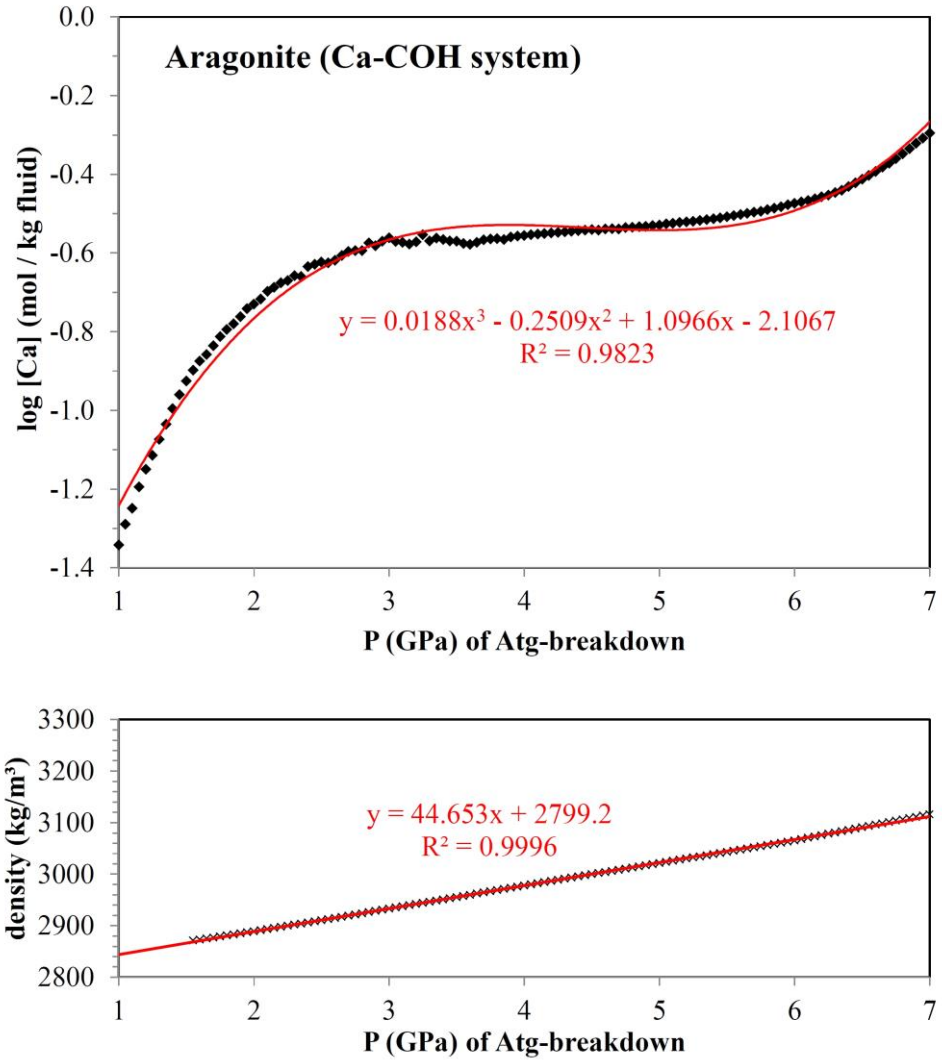

Figure A-6.3. *Predicted total solubility (log Ca, molal) and solid rock density of aragonite in the Ca-COH system (solid black symbols) at the P–T conditions of Atg breakdown in serpentinite (calculation methods see Sec. 6.3), and P-dependent interpolations (solid red) used for mass-balance calculations (Fig. 6.10).*

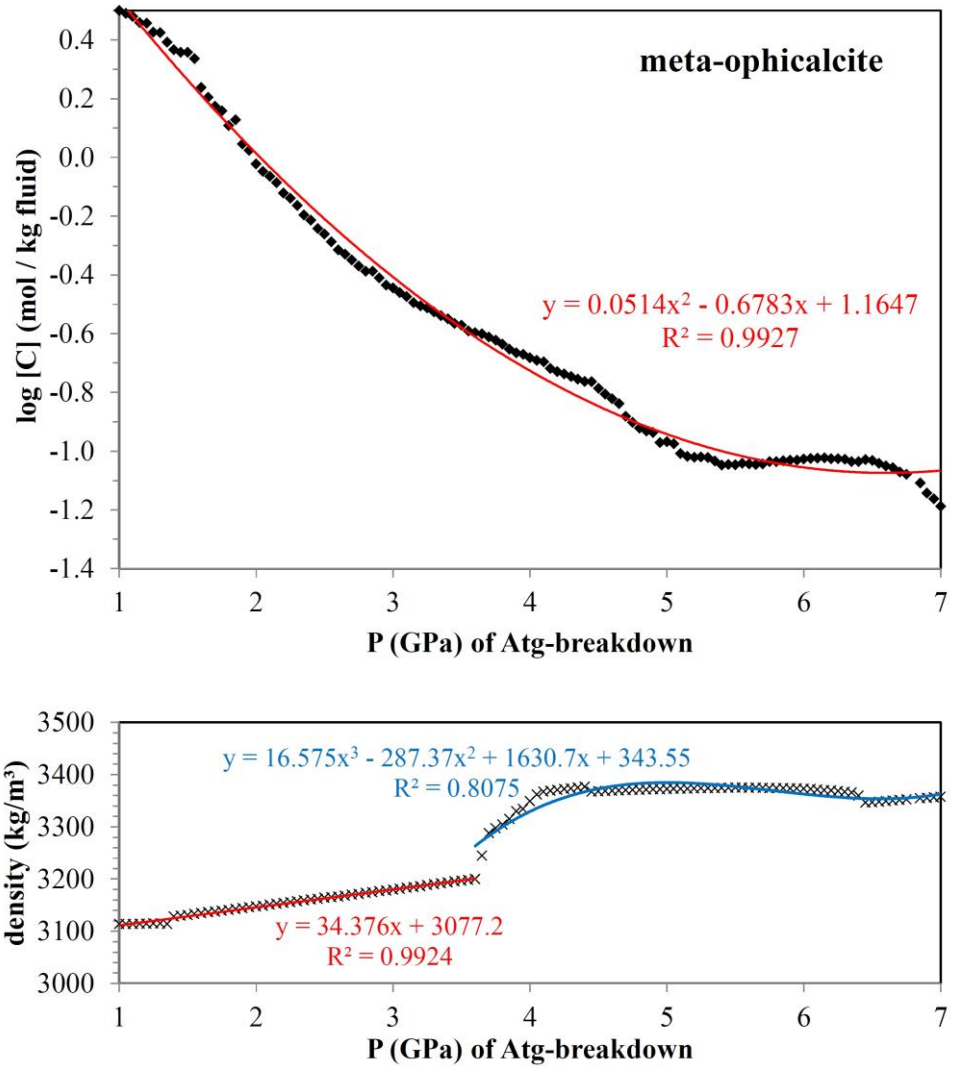

Figure A-6.4. *Predicted total carbon solubility (log C, molal) and solid rock density of meta-ophicalcite (solid black symbols) at the P–T conditions of Atg breakdown in serpentinite (calculation methods see Sec. 6.3), and P-dependent interpolations (red and blue solid curves) used for mass-balance calculations (Fig. 6.10).*

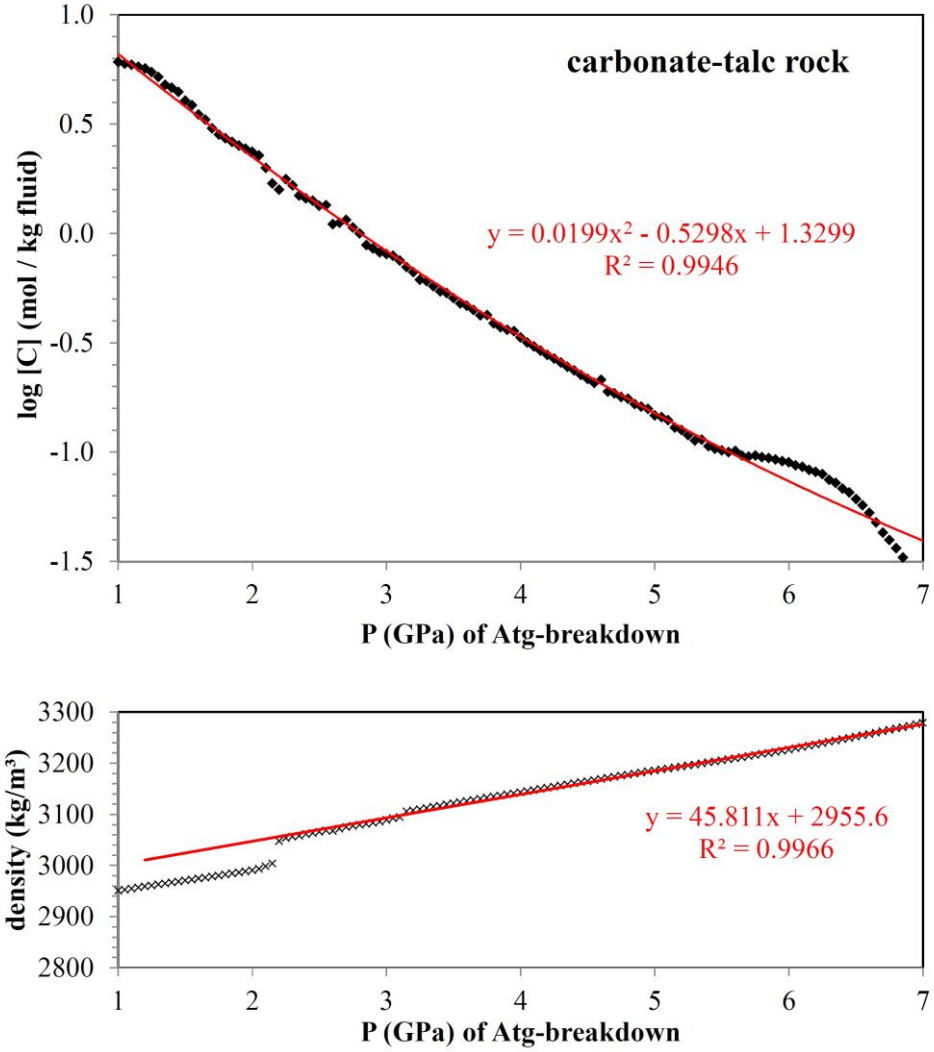

Figure A-6.5. *Predicted total carbon solubility (log C, molal) and solid rock density (solid black symbols) of carbonate-talc rock at the P–T conditions of Atg breakdown in serpentinite (calculation methods see Sec. 6.3), and P-dependent interpolations used for mass-balance calculations (Fig. 6.10).*

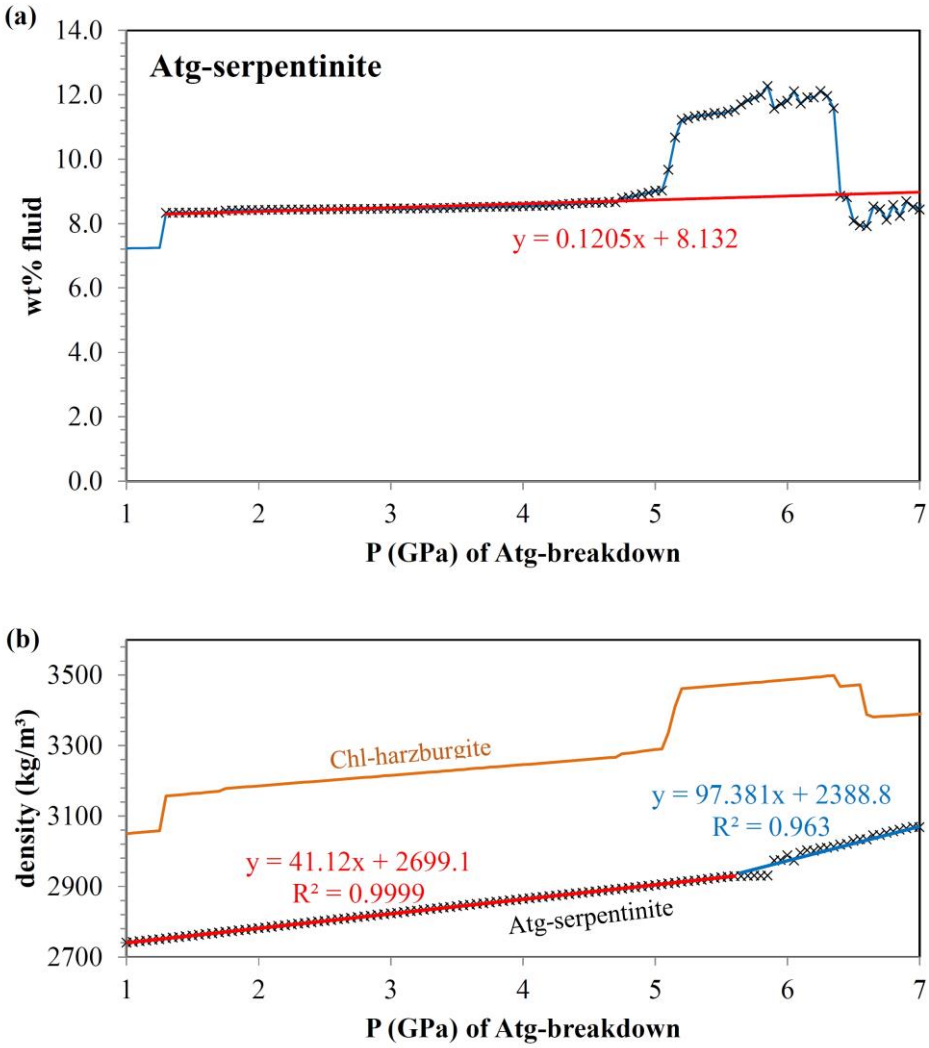

Figure A-6.6. (a) *Fluid release and* ***(b)*** *solid rock density of Atg-serpentinite at variable pressure (black crosses), and P-dependent interpolations used for mass-balance calculations (Fig. 6.10). Higher fluid release at P > 5.2 GPa in (a) is due to lack of chlorite as an intermediate reaction step for the specific bulk composition (cf. Fig. 6.1); this effect was ignored here. (b) Linear regressions of the density at 40 °C lower temperature than the antigorite breakdown are used (blue and red lines and equations); also shown is the solid rock density of the reaction product Chl-harzburgite at 20 °C higher than the antigorite breakdown (orange line).*

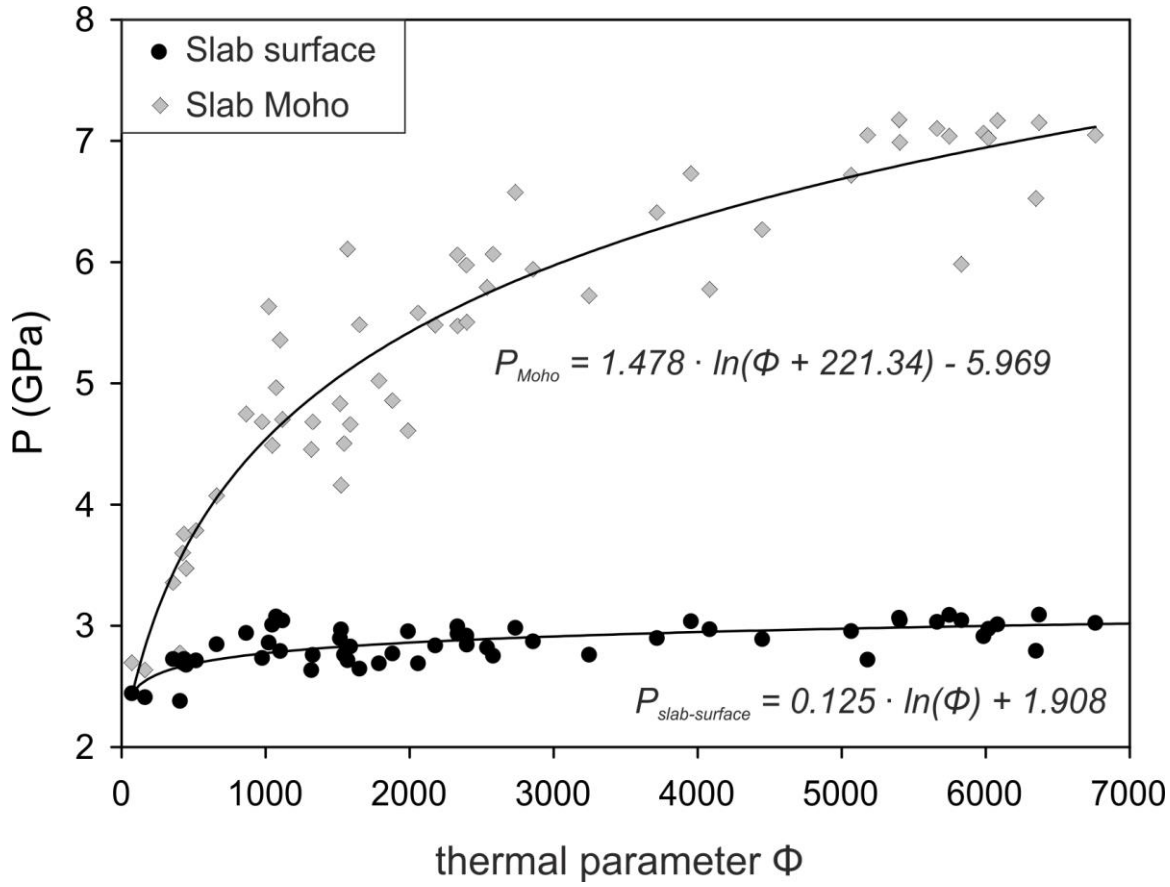

Figure A-6.7. *Pressure of antigorite serpentinite dehydration at the slab surface and Moho of different subduction zones as predicted by the D80 thermal subduction model (Syracuse et al., 2010), plotted against their thermal parameter Φ (cf. Appendix Table A-6.2). Solid lines and equations show logarithmic fits used in mass-balance calculations (cf. Fig. 6.10).*

Part III

CONCLUSIONS AND PERSPECTIVES

7 Conclusions

This thesis provides new insights into the mechanisms and controlling factors of carbonation of peridotites in forearc settings and the fate of serpentinite-hosted carbon during high-pressure metamorphism based on natural examples from ophiolites and metamorphic terranes, and improves our understanding of the role of hydrated peridotites for deep carbon cycling in subduction zones. Through the combination of field, (micro-) structural, petrological and geochemical data with thermodynamic modelling, the present work sheds new light on: (i) the microstructural and petrological imprint of peridotite carbonation by CO_2-rich fluids in forearc settings as recorded in the Advocate mantle Complex (Newfoundland); (ii) the petrology and phase relations of meta-ophicarbonates undergoing subduction metamorphism to conditions before and after the breakdown and dehydration of antigorite (Nevado-Filábride Complex, Spain); and (iii) the effects of electrolytic fluids and infiltration-driven devolatilization on the stability of serpentinite-hosted carbonate rocks during antigorite dehydration in subduction zones, and their implications for deep carbon fluxes.

The lithological sequence, microstructure and mineral composition of carbonate-bearing Atg-serpentinite, talc-magnesite rich rocks and listvenite in the Advocate Complex (Newfoundland, Canada) preserve a remarkable record of natural carbonation of serpentinized harzburgite by CO_2-rich fluids. Microstructures and mineral assemblages indicate that carbonation of serpentinized peridotite occurred coevally to the transformation of lizardite/chrysotile to antigorite at greenschist facies conditions (c. 300 °C and likely 0.2 – 0.3 GPa). The magnesite growth zonation provides a coherent record of the sequence and progress of carbonation reactions, and, in particular, of the reduction of Fe^{3+} in magnetite and serpentine to Fe^{2+} in magnesite and the related change of the local rock-buffered fluid fO_2 toward oxidizing conditions. Stable carbon and oxygen isotope compositions of magnesite suggest that carbonation of serpentinized harzburgite occurred due to infiltration of CO_2-rich, metamorphic fluids derived from carbon-bearing metasediments of underlying, higher-grade crustal units. The present results, along with other listvenite occurrences elsewhere, show that in nature the complete replacement of ultramafic rocks by carbonate-quartz assemblages is favoured in forearc settings and during active thrusting, and that listvenites possibly form a

substantial carbon reservoir in the leading edge of the mantle wedge in cold subduction zones.

Subduction-related, serpentinite-hosted, carbonate-silicate rocks from the Nevado-Filábride Complex (Spain) record a prograde metamorphic evolution to conditions prior and beyond the breakdown of antigorite in a warm subduction setting. Thermodynamic modelling and phase relations indicate peak metamorphic conditions for the carbonate-silicate rocks consistent with those recorded in the host serpentinite (Milagrosa massif; 550 – 600 °C and 1.0 – 1.4 GPa) and Chl-harzburgite (Almirez massif; 1.7 – 1.9 GPa and 680 °C), at low fluid X_{CO2}. Microstructures, mineral chemistry, and phase relations show that the hybridized carbonate-silicate rocks formed before peak metamorphism, likely by seawater related hydrothermal alteration, and were modified by subduction metamorphism and deformation. In the CaO–MgO–SiO_2 ternary, these processes resulted in a compositional variability of the NFC serpentine-hosted carbonate-silicate rocks along the serpentinite-calcite mixing trend, similar to that of other serpentinite-hosted carbonate-rocks in paleo-subducted metamorphic terranes. Thermodynamic modelling shows that during prograde subduction metamorphism the compositional variability along this binary determines the temperature of the main devolatilization reactions, the fluid composition, and the mineral assemblages of reaction products. In comparison to classical X_{CO2} molecular fluid models, thermodynamic models considering electrolytic fluids slightly increase the total carbon solubility in fluids at the conditions of interest of this study, without significant changes in the topology of phase relations. Phase relations in the Milagrosa and Almirez (meta) serpentinite-hosted carbonate-silicate rocks are consistent with fluid and rock equilibrium during peak metamorphism. The predominance of molecular CO_2 in contrast to charged carbon-bearing aqueous species at the conditions of high-P antigorite breakdown indicates that carbon release from serpentinite-hosted carbonate-silicate rocks during subduction is intimately linked to devolatilization reactions involving carbonate and silicate minerals and, therefore, mostly dependent on the bulk rock composition. These results from this study show that carbonates can remain stable in (meta) serpentinite-hosted carbonate-silicate rocks despite the relatively high carbon solubility in a warm subduction setting and the high fluid fluxes produced by dehydration reactions in the host serpentinite. In subduction settings where carbonated peridotite in the slab is common (e.g. in slow spreading ocean crust), substantial amounts of carbonate may, therefore, be preserved beyond the conditions of antigorite breakdown at subarc depths, thus allowing recycling of carbon deeper into the mantle.

Thermodynamic modelling shows that carbon loss during the prograde subsolidus devolatilization of meta-ophicalcite and carbonate-talc rocks to subarc depths of warm and cold subduction zones is negligible even if accounting for electrolytic fluids. Due to carbonate-silicate buffer reactions, the carbon solubility in fluids equilibrated with meta-ophicalcite and carbonate-talc rocks at the P–T condition of serpentinite dehydration is, however, substantially higher than in the pure aragonite system. If they remain isolated in the hydrated mantle of the slab up to subarc depths, these carbonate-rocks become potential sources of carbon when fluxed by fluids derived from the dehydration of their serpentinite host. Models of infiltration-driven devolatilization of meta-ophicalcite and carbonate-talc rocks show that carbon release is accompanied by significant Ca loss, which becomes increasingly relevant at high pressures (P > 3.5 GPa) because of the high activity of $CaHCO_3^+$ in the fluid. These models further indicate that the carbon dissolution from these lithologies into antigorite dehydration fluids decreases with increasing time-integrated fluid/rock ratio due to changes in the bulk composition, mineral assemblages and equilibrium fluids. Therefore, predictions of carbon release based only on initial bulk rock compositions and phase assemblages significantly overestimate the carbonate solubility during fluid-infiltration devolatilization reactions.

Mass balance calculations building on the electrolytic fluid models and parameterization of the P–T conditions of Atg-serpentinite dehydration as a function of the thermal parameter, Φ, indicate that the capacity of serpentinite dehydration fluids to dissolve carbonate of meta-ophicalcites and carbonate-talc rocks strongly depends on the subduction regime and slab depth where carbonate rocks are located. The highest carbonate dissolution takes place at the slab surface of warm subduction zones, and strongly decreases at the Moho depth (7 km) of cold subduction zones. The preservation of serpentinite-hosted carbon strongly depends on the mass of carbonate and the mass of serpentinite-derived infiltrating fluids, which is parametrized in our models as the length of a serpentinized mantle column below a carbonate lens of a given thickness. For typical ophicalcite thicknesses in serpentinized mantle observed in passive margins, these models show that, even in hot subduction zones, meta-ophicalcites can be preserved beyond the antigorite-serpentinite dehydration, thus carrying carbon into the deep mantle as carbonate-bearing garnet-clinopyroxene-olivine rocks. In contrast, fluid infiltration during antigorite dehydration readily dissolves carbonate–talc rocks and transforms them into orthopyroxenite in most subduction thermal regimes. Hence, carbon sequestered in the forearc by melange or wedge serpentinites in the form of carbonate-talc

rocks will be released again at subarc depths if such rocks are eroded and dragged down by the subducting slab.

7.1 Perspectives

The results of the present Ph.D. thesis are a step forward for the understanding of the carbonation and related high-pressure fluid-rock interactions in peridotite, and their implications for chemical mass-fluxes in subduction zones. The thesis results also point out several problems and open questions that deserve further in-depth studies. In particular, the interplay between rock deformation, fluid pathways, and chemical reactions, and the role of redox-sensitive elements and reduced aqueous species for the transfer of oxygen during carbonation reactions and fluid-mediated carbon release in subduction zones remain subjects to future investigations.

The mechanisms that allow carbonation of peridotite to proceed in nature until its complete replacement by listvenite also deserve further study. A better understanding of these mechanisms may help to improve strategies for the artificial permanent carbon sequestration by mineral carbonation. The observations from the Advocate listvenites obtained in this Ph.D. thesis, along with similar observation in occurrences elsewhere, point to a decisive role of deformation and tectonic stresses to sustain high permeability that enables prolonged influx of CO_2-bearing fluids despite the volume increase during the reaction progress of carbonation reactions. Microstructures recorded in the Fe-growth zonation in magnesite and different vein generations make the Advocate listvenites an ideal natural laboratory to continue to investigate the dynamic interplay between deformation, (nano) porosity, permeability, and dissolution-precipitation reactions. Fluid inclusions, radiogenic and unconventional stable isotopes, and trace element geochemistry may provide more insights into the fluid provenance and the role of reduced carbon *versus* inorganic carbonate species in fluids for the evolution of the oxygen fugacity in forearc settings.

Mineral textures and morphologies contain valuable information about the mechanisms and timescales of dehydration reactions and fluid drainage in subduction zones, as shown for the transformation of Atg-serpentinite to Chl-harzburgite (Dilissen et al., 2018). Likewise, mixed-volatile devolatilization reactions in carbonate-silicate rocks —such as the Almirez meta-ophicalcites studied in this thesis— may be related to characteristic textures and microstructures that can shed new light on the mechanisms of mineral dissolution during subduction metamorphism and fluid infiltration at high pressure.

Modelling of aqueous geochemistry of high-pressure fluids can be expected to improve considerably in the near future due to new experiments that allow refinement of equilibrium constants and activity relations in thermodynamic databases and solution models. This refined dataset will improve the modelling capability for minor aqueous components, such as sulphur, fluorine and nitrogen species, which are highly relevant for trace element mass transfer and redox equilibria during fluid–rock interaction. The thermodynamic models presented in this Ph.D. thesis are based on a simplified chemical system that, nevertheless, allow to identify the principal relations and mechanisms during fluid-rock interaction, which subsequently can be used to develop more complex models accounting for other volatiles, dissolved salts, and other minor solute components.

Part IV

REFERENCES

8 References

Abers, G. A., van Keken, P. E., Kneller, E. A., Ferris, A. & Stachnik, J. C. (2006). The thermal structure of subduction zones constrained by seismic imaging: Implications for slab dehydration and wedge flow. *Earth and Planetary Science Letters* **241**, 387-397.

Aftabi, A. & Zarrinkoub, M. H. (2013). Petrogeochemistry of listvenite association in metaophiolites of Sahlabad region, eastern Iran: Implications for possible epigenetic Cu–Au ore exploration in metaophiolites. *Lithos* **156-159**, 186-203.

Ague, J. J. & Nicolescu, S. (2014). Carbon dioxide released from subduction zones by fluid-mediated reactions. *Nature Geoscience* **7**, 355-360.

Aharon, P. (1988). A stable-isotope study of magnesites from the Rum Jungle Uranium Field, Australia: Implications for the origin of strata-bound massive magnesites. *Chemical Geology* **69**, 127-145.

Akbulut, M., Piskin, O. & Karayigit, A. I. (2006). The genesis of the carbonatized and silicified ultramafics known as listvenites: a case study from the Mihaliccik region (Eskisehir), NW Turkey. *Geological Journal* **41**, 557-580.

Al-Aasm, I. S., Taylor, B. E. & South, B. (1990). Stable isotope analysis of multiple carbonate samples using selective acid extraction. *Chemical Geology: Isotope Geoscience section* **80**, 119-125.

Alt, J. C., Crispini, L., Gaggero, L., Levine, D., Lavagnino, G., Shanks, P. & Gulbransen, C. (2018). Normal faulting and evolution of fluid discharge in a Jurassic seafloor ultramafic-hosted hydrothermal system. *Geology* **46**, 523-526.

Alt, J. C., Garrido, C. J., Shanks, W. C., Turchyn, A., Padrón-Navarta, J. A., López Sánchez-Vizcaíno, V., Gómez Pugnaire, M. T. & Marchesi, C. (2012). Recycling of water, carbon, and sulfur during subduction of serpentinites: A stable isotope study of Cerro del Almirez, Spain. *Earth and Planetary Science Letters* **327-328**, 50-60.

Alt, J. C., Schwarzenbach, E. M., Früh-Green, G. L., Shanks Iii, W. C., Bernasconi, S. M., Garrido, C. J., Crispini, L., Gaggero, L., Padrón-Navarta, J. A. & Marchesi, C. (2013). The role of serpentinites in cycling of carbon and sulfur: Seafloor serpentinization and subduction metamorphism. *Lithos* **178**, 40-54.

Alt, J. C., Shanks, W. C., Bach, W., Paulick, H., Garrido, C. J. & Beaudoin, G. (2007). Hydrothermal alteration and microbial sulfate reduction in peridotite and gabbro exposed by detachment faulting at the Mid-Atlantic Ridge, 15°20′N (ODP Leg 209): A sulfur and oxygen isotope study. *Geochemistry, Geophysics, Geosystems* **8**, Q08002.

Alt, J. C. & Teagle, D. A. H. (1999). The uptake of carbon during alteration of ocean crust. *Geochimica et Cosmochimica Acta* **63**, 1527-1535.

Allen, D. E. & Seyfried, W. E. (2003). Compositional controls on vent fluids from ultramafic-hosted hydrothermal systems at mid-ocean ridges: An experimental study at 400°C, 500 bars. *Geochimica et Cosmochimica Acta* **67**, 1531-1542.

Andreani, M., Luquot, L., Gouze, P., Godard, M., Hoisé, E. & Gibert, B. (2009). Experimental study of carbon sequestration reactions controlled by the percolation of CO_2-rich brine through peridotites. *Environmental Science & Technology* **43**, 1226-1231.

Angiboust, S., Pettke, T., De Hoog, J. C. M., Caron, B. & Oncken, O. (2014). Channelized fluid flow and eclogite-facies metasomatism along the subduction shear zone. *Journal of Petrology* **55**, 883-916.

Anovitz, L. M. & Essene, E. J. (1987). Phase equilibria in the system $CaCO_3$–$MgCO_3$–$FeCO_3$. *Journal of Petrology* **28**, 389-415.

Arai, S., Ishimaru, S. & Mizukami, T. (2012). Methane and propane micro-inclusions in olivine in titanoclinohumite-bearing dunites from the Sanbagawa high-P metamorphic belt, Japan: Hydrocarbon activity in a subduction zone and Ti mobility. *Earth and Planetary Science Letters* **353-354**, 1-11.

Ash, C. H. & Arksey, R. L. (1989). The Atlin ultramafic allochthon: ophiolitic basement within the Cache Creek terrane; tectonic and metallogenic significance. *British Columbia Geological Survey Field Report* **104N/12**.

Aydal, D. (1990). Gold-bearing listwaenites in the Araç Massif, Kastamonu, Turkey. *Terra Nova* **2**, 43-52.

Bach, W., Garrido, C. J., Paulick, H., Harvey, J. & Rosner, M. (2004). Seawater-peridotite interactions: First insights from ODP Leg 209, MAR 15°N. *Geochemistry, Geophysics, Geosystems* **5**, Q09F26.

Bach, W., Paulick, H., Garrido, C. J., Ildefonse, B., Meurer, W. P. & Humphris, S. E. (2006). Unraveling the sequence of serpentinization reactions: petrography, mineral chemistry, and petrophysics of serpentinites from MAR 15°N (ODP Leg 209, Site 1274). *Geophysical Research Letters* **33**.

Bach, W., Rosner, M., Jöns, N., Rausch, S., Robinson, L. F., Paulick, H. & Erzinger, J. (2011). Carbonate veins trace seawater circulation during exhumation and uplift of mantle rock: Results from ODP Leg 209. *Earth and Planetary Science Letters* **311**, 242-252.

Bachmann, F., Hielscher, R. & Schaeben, H. (2010). Texture analysis with MTEX-Free and open source software toolbox. *Solid State Phenomena*, 63-68.

Bebout, G. E. (1991). Field-based evidence for devolatilization in subduction zones: Implications for arc magmatism. *Science* **251**, 413.

Bebout, G. E. & Penniston-Dorland, S. C. (2016). Fluid and mass transfer at subduction interfaces — The field metamorphic record. *Lithos* **240-243**, 228-258.

Bédard, J. H. (2000). The Betts Cove ophiolite and its cover rocks, Newfoundland. *Geological Survey of Canada Bulletin 550*.

Bédard, J. H. & Escayola, M. (2010). The Advocate ophiolite mantle, Baie Verte, Newfoundland: regional correlations and evidence for metasomatism. *Canadian Journal of Earth Sciences* **47**, 237-253.

Bédard, J. H., Lauzière, K., Tremblay, A. & Sangster, A. (1998). Evidence for forearc seafloor-spreading from the Betts Cove ophiolite, Newfoundland: oceanic crust of boninitic affinity. *Tectonophysics* **284**, 233-245.

Behn, M. D., Kelemen, P. B., Hirth, G., Hacker, B. R. & Massonne, H.-J. (2011). Diapirs as the source of the sediment signature in arc lavas. *Nature Geoscience* **4**, 641.

Behr, W. M. & Platt, J. P. (2012). Kinematic and thermal evolution during two-stage exhumation of a Mediterranean subduction complex. *Tectonics* **31**, TC4025.

Beinlich, A., Plümper, O., Hövelmann, J., Austrheim, H. & Jamtveit, B. (2012). Massive serpentinite carbonation at Linnajavri, N–Norway. *Terra Nova* **24**, 446-455.

Belogub, E. V., Melekestseva, I. Y., Novoselov, K. A., Zabotina, M. V., Tret'yakov, G. A., Zaykov, V. V. & Yuminov, A. M. (2017). Listvenite-related gold deposits of the South Urals (Russia): A review. *Ore Geology Reviews* **85**, 247-270.

Berman, R. G. (1988). Internally-consistent thermodynamic data for minerals in the system Na_2O–K_2O–CaO–MgO–FeO–Fe_2O_3–Al_2O_3–SiO_2–TiO_2–H_2O–CO_2. *Journal of Petrology* **29**, 445-522.

Berner, R. A. (1999). A new look at the long-term carbon cycle. *GSA Today* **9**, 1-6.

Berner, R. A. & Kothavala, Z. (2001). Geocarb III: A revised model of atmospheric CO_2 over Phanerozoic time. *American Journal of Science* **301**, 182-204.

Bjerga, A., Konopásek, J. & Pedersen, R. B. (2015). Talc–carbonate alteration of ultramafic rocks within the Leka Ophiolite Complex, Central Norway. *Lithos* **227**, 21-36.

Bodinier, J. L. & Godard, M. (2007). Orogenic, Ophiolitic, and Abyssal Peridotites. In: Holland, H. D. & Turekian, K. K. (eds.) *Treatise on Geochemistry*. Oxford: Pergamon, 1-73.

Bonatti, E., Lawrence, J. R., Hamlyn, P. R. & Breger, D. (1980). Aragonite from deep sea ultramafic rocks. *Geochimica et Cosmochimica Acta* **44**, 1207-1214.

Booth-Rea, G., Martínez-Martínez, J. M. & Giaconia, F. (2015). Continental subduction, intracrustal shortening, and coeval upper-crustal extension: P-T evolution of subducted south Iberian paleomargin metapelites (Betics, SE Spain). *Tectonophysics* **663**, 122-139.

Boskabadi, A., Pitcairn, I. K., Broman, C., Boyce, A., Teagle, D. A. H., Cooper, M. J., Azer, M. K., Stern, R. J., Mohamed, F. H. & Majka, J. (2017). Carbonate alteration of ophiolitic rocks in the Arabian–Nubian Shield of Egypt: sources and compositions of the carbonating fluid and implications for the formation of Au deposits. *International Geology Review* **59**, 391-419.

Bouysse, P. (1984). The Lesser Antilles island-arc-structure and geodynamic evolution. *Initial Reports of the Deep Sea Drilling Project, 78A*, 83-103.

Brenker, F. E., Vincze, L., Vekemans, B., Nasdala, L., Stachel, T., Vollmer, C., Kersten, M., Somogyi, A., Adams, F., Joswig, W. & Harris, J. W. (2005). Detection of a Ca-rich lithology in the Earth's deep (>300 km) convecting mantle. *Earth and Planetary Science Letters* **236**, 579-587.

Bretscher, A., Hermann, J. & Pettke, T. (2018). The influence of oceanic oxidation on serpentinite dehydration during subduction. *Earth and Planetary Science Letters* **499**, 173-184.

Bromiley, G. D. & Pawley, A. R. (2003). The stability of antigorite in the systems $MgO–SiO_2–H_2O$ (MSH) and $MgO–Al_2O_3–SiO_2–H_2O$ (MASH): The effects of Al^{3+} substitution on high-pressure stability. *American Mineralogist* **88**, 99-108.

Bucher-Nurminen, K. (1990). Transfer of mantle fluids to the lower continental crust: Constraints from mantle mineralogy and Moho temperature. *Chemical Geology* **83**, 249-261.

Bucher-Nurminen, K. (1991). Mantle fragments in the Scandinavian caledonides. *Tectonophysics* **190**, 173-192.

Bucher, K. & Grapes, R. (2011). *Petrogenesis of Metamorphic Rocks*. Springer Heidelberg Dordrecht London New York: Springer.

Burnham, A. D., Thomson, A. R., Bulanova, G. P., Kohn, S. C., Smith, C. B. & Walter, M. J. (2015). Stable isotope evidence for crustal recycling as recorded by superdeep diamonds. *Earth and Planetary Science Letters* **432**, 374-380.

Burton, M. R., Sawyer, G. M. & Granieri, D. (2013). Deep carbon emissions from volcanoes. *Reviews in Mineralogy and Geochemistry* **75**, 323-354.

Caciagli, N. C. & Manning, C. E. (2003). The solubility of calcite in water at 6–16 kbar and 500–800 °C. *Contributions to Mineralogy and Petrology* **146**, 275-285.

Cannat, M., Fontaine, F. & Escartín, J. (2010). Serpentinization and associated hydrogen and methane fluxes at slow spreading ridges. In: Rona, P. A., Devey, C. W., Dyment, J. & Murton, B. J. (eds.) *Diversity Of Hydrothermal Systems on Slow Spreading Ocean Ridges*: American Geophysical Union, 241-264.

Carter, L. B. & Dasgupta, R. (2016). Effect of melt composition on crustal carbonate assimilation: Implications for the transition from calcite consumption to skarnification and associated CO_2 degassing. *Geochemistry, Geophysics, Geosystems* **17**, 3893-3916.

Castonguay, S., van Staal, C. R., Joyce, N., Skulski, T. & Hibbard, J. P. (2014). Taconic metamorphism preserved in the baie verte peninsula, Newfoundland Appalachians: Geochronological evidence for ophiolite obduction and subduction and exhumation of the leading edge of the Laurentian (Humber) margin during closure of the Taconic seaway. *Geoscience Canada* **41**, 459-482.

Clerc, C., Boulvais, P., Lagabrielle, Y. & de Saint Blanquat, M. (2014). Ophicalcites from the northern Pyrenean belt: A field, petrographic and stable isotope study. *International Journal of Earth Sciences* **103**, 141-163.

Codillo, E. A., Le Roux, V. & Marschall, H. R. (2018). Arc-like magmas generated by mélange-peridotite interaction in the mantle wedge. *Nature Communications* **9**, 2864.

Coltat, R., Boulvais, P., Branquet, Y., Collot, J., Epin, M. E. & Manatschal, G. (2019). Syntectonic carbonation during synmagmatic mantle exhumation at an ocean-continent transition. *Geology* **47**, 183-186.

Collins, N. C., Bebout, G. E., Angiboust, S., Agard, P., Scambelluri, M., Crispini, L. & John, T. (2015). Subduction zone metamorphic pathway for deep carbon cycling: II. Evidence from HP/UHP metabasaltic rocks and ophicarbonates. *Chemical Geology* **412**, 132-150.

Connolly, J. A. D. (2005). Computation of phase equilibria by linear programming: A tool for geodynamic modeling and its application to subduction zone decarbonation. *Earth and Planetary Science Letters* **236**, 524-541.

Connolly, J. A. D. (2009). The geodynamic equation of state: What and how. *Geochemistry, Geophysics, Geosystems* **10**, Q10014.

Connolly, J. A. D. & Cesare, B. (1993). C–O–H–S fluid composition and oxygen fugacity in graphitic metapelites. *Journal of Metamorphic Geology* **11**, 379-388.

Connolly, J. A. D. & Galvez, M. E. (2018). Electrolytic fluid speciation by Gibbs energy minimization and implications for subduction zone mass transfer. *Earth and Planetary Science Letters* **501**, 90-102.

Connolly, J. A. D. & Trommsdorff, V. (1991). Petrogenetic grids for metacarbonate rocks — pressure-temperature phase-diagram projection for mixed-volatile systems. *Contributions to Mineralogy and Petrology* **108**, 93-105.

Cook-Kollars, J., Bebout, G. E., Collins, N. C., Angiboust, S. & Agard, P. (2014). Subduction zone metamorphic pathway for deep carbon cycling: I. Evidence from HP/UHP metasedimentary rocks, Italian Alps. *Chemical Geology* **386**, 31-48.

Chao, F., Farrow, C. M. & Leake, B. E. (1986). Polydymite and chrome-rich fuchsite in virginite from Baie Verte, Newfoundland. *Mineralogical Magazine* **50**, 723-724.

Chi, G. & Lavoie, D. (2000). A combined fluid-inclusion and stable isotope study of Ordovician ophicalcite units from southern Quebec Appalachians, Quebec. *Current Research*. Geological Survey of Canada, Report 2000-D5, 1-9.

Chian, D., Louden, K. E., Minshull, T. A. & Whitmarsh, R. B. (1999). Deep structure of the ocean-continent transition in the southern Iberia Abyssal Plain from seismic refraction profiles: Ocean Drilling Program (Legs 149 and 173) transect. *Journal of Geophysical Research: Solid Earth* **104**, 7443-7462.

Dasgupta, R. (2013). Ingassing, storage, and outgassing of terrestrial carbon through geologic time. *Reviews in Mineralogy and Geochemistry* **75**, 183-229.

Dasgupta, R. & Hirschmann, M. M. (2010). The deep carbon cycle and melting in Earth's interior. *Earth and Planetary Science Letters* **298**, 1-13.

Dasgupta, R., Hirschmann, M. M. & Withers, A. C. (2004). Deep global cycling of carbon constrained by the solidus of anhydrous, carbonated eclogite under upper mantle conditions. *Earth and Planetary Science Letters* **227**, 73-85.

Debret, B., Andreani, M., Munoz, M., Bolfan-Casanova, N., Carlut, J., Nicollet, C., Schwartz, S. & Trcera, N. (2014). Evolution of Fe redox state in serpentine during subduction. *Earth and Planetary Science Letters* **400**, 206-218.

Debret, B., Bolfan-Casanova, N., Padrón-Navarta, J. A., Martin-Hernandez, F., Andreani, M., Garrido, C. J., López Sánchez-Vizcaíno, V., Gómez-Pugnaire, M., Muñoz, M. & Trcera, N. (2015). Redox state of iron during high-pressure serpentinite dehydration. *Contributions to Mineralogy and Petrology* **169**, 1-18.

Debret, B. & Sverjensky, D. A. (2017). Highly oxidising fluids generated during serpentinite breakdown in subduction zones. *Scientific Reports* **7**, 10351.

Deines, P. (2002). The carbon isotope geochemistry of mantle xenoliths. *Earth-Science Reviews* **58**, 247-278.

Delacour, A., Früh-Green, G. L., Bernasconi, S. M., Schaeffer, P. & Kelley, D. S. (2008). Carbon geochemistry of serpentinites in the Lost City Hydrothermal System (30°N, MAR). *Geochimica et Cosmochimica Acta* **72**, 3681-3702.

Deschamps, F., Godard, M., Guillot, S. & Hattori, K. (2013). Geochemistry of subduction zone serpentinites: A review. *Lithos* **178**, 96-127.

Dilissen, N., Hidas, K., Garrido, C. J., Kahl, W.-A., López Sánchez-Vizcaíno, V. & Padrón-Navarta, J. A. (2018). Textural evolution during high-pressure dehydration of serpentinite to peridotite and its relation to stress orientations and kinematics of subducting slabs: Insights from the Almirez ultramafic massif. *Lithos* **320-321**, 470-489.

Dolejš, D. (2013). Thermodynamics of aqueous species at high temperatures and pressures: Equations of state and transport theory. *Reviews in Mineralogy and Geochemistry* **76**, 35-79.

Dreimanis, A. (1962). Quantitative gasometric determination of calcite and dolomite by using Chittick apparatus. *Journal of Sedimentary Research* **32**, 520-529.

Duncan, M. S. & Dasgupta, R. (2017). Rise of Earth's atmospheric oxygen controlled by efficient subduction of organic carbon. *Nature Geoscience* **10**, 387-392.

Dvir, O. & Kessel, R. (2017). The effect of CO_2 on the water-saturated solidus of K-poor peridotite between 4 and 6 GPa. *Geochimica et Cosmochimica Acta* **206**, 184-200.

Eickmann, B., Bach, W. & Peckmann, J. (2009a). Authigenesis of carbonate minerals in modern and Devonian ocean-floor hard rocks. *The Journal of Geology* **117**, 307-323.

Eickmann, B., Bach, W., Rosner, M. & Peckmann, J. (2009b). Geochemical constraints on the modes of carbonate precipitation in peridotites from the Logatchev Hydrothermal Vent Field and Gakkel Ridge. *Chemical Geology* **268**, 97-106.

Emam, A. & Zoheir, B. (2013). Au and Cr mobilization through metasomatism: Microchemical evidence from ore-bearing listvenite, South Eastern Desert of Egypt. *Journal of Geochemical Exploration* **125**, 34-45.

Engi, M. & Lindsley, D. H. (1980). Stability of titanian clinohumite: Experiments and thermodynamic analysis. *Contributions to Mineralogy and Petrology* **72**, 415-424.

Escayola, M., Garuti, G., Zaccarini, F., Proenza, J. A., Bédard, J. H. & Vanstaal, C. (2011). Chromitite and platinum-group-element mineralization at middle arm brook, central advocate ophiolite complex, Baie Verte Peninsula, Newfoundland, Canada. *Canadian Mineralogist* **49**, 1523-1547.

Escayola, M., Proenza, J., van Staal, C., Rogers, N. & Skulski, T. (2009). The Point Rousse listvenites, Baie Verte, Newfoundland: altered ultramafic rocks with potential for gold mineralization. *Current Research*: Newfoundland and Labrador Department of Natural Resources, Geological Survey Report 09-1, 1-12.

Evans, B. W. (2004). The serpentinite multisystem revisited: Chrysotile is metastable. *International Geology Review* **46**, 479-506.

Evans, B. W. (2008). Control of the Products of Serpentinization by the $Fe^{2+}Mg_{-1}$ exchange potential of olivine and orthopyroxene. *Journal of Petrology* **49**, 1873-1887.

Evans, B. W. & Trommsdorff, V. (1983). Fluorine hydroxyl titanian clinohumite in Alpine recrystallized garnet peridotite: compositional controls and petrologic significance. *American Journal of Science* **283 A**, 355-369.

Evans, K. A. (2011). Metamorphic carbon fluxes: how much and how fast? *Geology* **39**, 95-96.

Evans, K. A., Reddy, S. M., Tomkins, A. G., Crossley, R. J. & Frost, B. R. (2017). Effects of geodynamic setting on the redox state of fluids released by subducted mantle lithosphere. *Lithos* **278-281**, 26-42.

Faccenda, M. (2014). Water in the slab: A trilogy. *Tectonophysics* **614**, 1-30.

Facq, S., Daniel, I., Montagnac, G., Cardon, H. & Sverjensky, D. A. (2014). In situ Raman study and thermodynamic model of aqueous carbonate speciation in equilibrium with aragonite under subduction zone conditions. *Geochimica et Cosmochimica Acta* **132**, 375-390.

Facq, S., Daniel, I., Montagnac, G., Cardon, H. & Sverjensky, D. A. (2016). Carbon speciation in saline solutions in equilibrium with aragonite at high pressure. *Chemical Geology* **431**, 44-53.

Falk, E. S. & Kelemen, P. B. (2015). Geochemistry and petrology of listvenite in the Samail ophiolite, Sultanate of Oman: Complete carbonation of peridotite during ophiolite emplacement. *Geochimica et Cosmochimica Acta* **160**, 70-90.

Faul, U. H., Garapić, G. & Lugović, B. (2014). Subcontinental rift initiation and ocean-continent transitional setting of the Dinarides and Vardar zone: Evidence from the Krivaja–Konjuh Massif, Bosnia and Herzegovina. *Lithos* **202-203**, 283-299.

Ferrando, S., Groppo, C., Frezzotti, M. L., Castelli, D. & Proyer, A. (2017). Dissolving dolomite in a stable UHP mineral assemblage: Evidence from Cal-Dol marbles of the Dora-Maira Massif (Italian Western Alps). *American Mineralogist* **102**, 42-60.

Ferry, J. M. (1995). Fluid flow during contact metamorphism of ophicarbonate rocks in the Bergell Aureole, Val Malenco, Italian Alps. *Journal of Petrology* **36**, 1039-1053.

Ferry, J. M. (2001). Calcite inclusions in forsterite. *American Mineralogist* **86**, 773-779.

Forster, B., Braga, R., Aulbach, S., Lo Po, D., Bargossi, G. M. & Mair, V. (2017). A petrographic study of carbonate phases in the Ulten zone ultramafic rocks: Insights into carbonation in the mantle wedge and exhumation-related decarbonation. *Ofioliti* **42**, 105-127.

Franz, G. & Ackermand, D. (1980). Phase relations and metamorphic history of a clinohumite-chlorite-serpentine-marble from the Western Tauern Area (Austria). *Contributions to Mineralogy and Petrology* **75**, 97-110.

Franzolin, E., Schmidt, M. W. & Poli, S. (2011). Ternary Ca–Fe–Mg carbonates: Subsolidus phase relations at 3.5 GPa and a thermodynamic solid solution model including order/disorder. *Contributions to Mineralogy and Petrology* **161**, 213-227.

Frezzotti, M. L. & Ferrando, S. (2015). The chemical behavior of fluids released during deep subduction based on fluid inclusions. *American Mineralogist* **100**, 352-377.

Frezzotti, M. L., Selverstone, J., Sharp, Z. D. & Compagnoni, R. (2011). Carbonate dissolution during subduction revealed by diamond-bearing rocks from the Alps. *Nature Geoscience* **4**, 703-706.

Frost, B. R. (1985). On the stability of sulfides, oxides, and native metals in serpentinite. *Journal of Petrology* **26**, 31-63.

Frost, B. R. & Beard, J. S. (2007). On silica activity and serpentinization. *Journal of Petrology* **48**, 1351-1368.

Fryer, P., Wheat, C. G. & Mottl, M. J. (1999). Mariana blueschist mud volcanism: Implications for conditions within the subduction zone. *Geology* **27**, 103-106.

Galvez, M. E., Beyssac, O., Martinez, I., Benzerara, K., Chaduteau, C., Malvoisin, B. & Malavieille, J. (2013). Graphite formation by carbonate reduction during subduction. *Nature Geoscience* **6**, 473-477.

Galvez, M. E., Connolly, J. A. D. & Manning, C. E. (2016). Implications for metal and volatile cycles from the pH of subduction zone fluids. *Nature* **539**, 420-424.

Galvez, M. E., Manning, C. E., Connolly, J. A. D. & Rumble, D. (2015). The solubility of rocks in metamorphic fluids: A model for rock-dominated conditions to upper mantle pressure and temperature. *Earth and Planetary Science Letters* **430**, 486-498.

García del Real, P., Maher, K., Kluge, T., Bird, D. K., Brown, G. E., Jr. & John, C. M. (2016). Clumped-isotope thermometry of magnesium carbonates in ultramafic rocks. *Geochimica et Cosmochimica Acta* **193**, 222-250.

Garrido, C. J., López Sánchez-Vizcaíno, V., Gómez-Pugnaire, M. T., Trommsdorff, V., Alard, O., Bodinier, J. L. & Godard, M. (2005). Enrichment of HFSE in chlorite-harzburgite produced by high-pressure dehydration of antigorite-serpentinite: Implications for subduction magmatism. *Geochemistry, Geophysics, Geosystems* **6**, Q01J15.

Gieré, R. (1987). Titanian clinohumite and geikielite in marbles from the Bergell contact aureole. *Contributions to Mineralogy and Petrology* **96**, 496-502.

Gil Ibarguchi, J. I., Ábalos, B., Azcarraga, J. & Puelles, P. (1999). Deformation, high-pressure metamorphism and exhumation of ultramafic rocks in a deep subduction/collision setting (Cabo Ortegal, NW Spain). *Journal of Metamorphic Geology* **17**, 747-764.

Gómez-Pugnaire, M. T., Franz, G. & López Sánchez-Vizcaíno, V. (1994). Retrograde formation of NaCl-scapolite in high pressure metaevaporites from the Cordilleras Béticas (Spain). *Contributions to Mineralogy and Petrology* **116**, 448-461.

Gómez-Pugnaire, M. T., Nieto, F., Abad, I., Velilla, N., Garrido, C. J., Acosta-Vigil, A., Barich, A., Hidas, K. & López Sánchez-Vizcaíno, V. (in press). Alpine Metamorphism in the Betic Internal Zones. In: Quesada, C. & Oliveira, J. T. (eds.) *The geology of Iberia: A geodynamic approach. Volume 3: The Alpine Cycle*. New York: Springer, 1-26.

Gómez-Pugnaire, M. T., Rubatto, D., Fernández-Soler, J. M., Jabaloy, A., López Sánchez-Vizcaíno, V., González-Lodeiro, F., Galindo-Zaldívar, J. & Padrón-Navarta, J. A. (2012). Late Variscan magmatism in the Nevado-Filábride Complex: U-Pb geochronologic evidence for the pre-Mesozoic nature of the deepest Betic complex (SE Spain). *Lithos* **146–147**, 93-111.

Gorman, P. J., Kerrick, D. M. & Connolly, J. A. D. (2006). Modeling open system metamorphic decarbonation of subducting slabs. *Geochemistry, Geophysics, Geosystems* **7**, Q04007.

Grosch, E. G., Vidal, O., Abu-Alam, T. & McLoughlin, N. (2012). P-T constraints on the metamorphic evolution of the Paleoarchean Kromberg type-section, Barberton Greenstone Belt, South Africa. *Journal of Petrology* **53**, 513-545.

Grove, T. L., Chatterjee, N., Parman, S. W. & Médard, E. (2006). The influence of H_2O on mantle wedge melting. *Earth and Planetary Science Letters* **249**, 74-89.

Grozeva, N. G., Klein, F., Seewald, J. S. & Sylva, S. P. (2017). Experimental study of carbonate formation in oceanic peridotite. *Geochimica et Cosmochimica Acta* **199**, 264-286.

Grützner, T., Klemme, S., Rohrbach, A., Gervasoni, F. & Berndt, J. (2017). The role of F-clinohumite in volatile recycling processes in subduction zones. *Geology* **45**, 443-446.

Hacker, B. R. (2008). H_2O subduction beyond arcs. *Geochemistry, Geophysics, Geosystems* **9**, Q03001.

Hacker, B. R., Peacock, S. M., Abers, G. A. & Holloway, S. D. (2003). Subduction factory 2. Are intermediate-depth earthquakes in subducting slabs linked to metamorphic dehydration reactions? *Journal of Geophysical Research: Solid Earth* **108**.

Halls, C. & Zhao, R. (1995). Listvenite and related rocks: perspectives on terminology and mineralogy with reference to an occurrence at Cregganbaun, Co. Mayo, Republic of Ireland. *Mineralium Deposita* **30**, 303-313.

Hansen, L. D., Dipple, G. M., Gordon, T. M. & Kellett, D. A. (2005). Carbonated serpentinite (listwanite) at Atlin, British Columbia: A geological analogue to carbon dioxide sequestration. *Canadian Mineralogist* **43**, 225-239.

Harvey, J., Garrido, C. J., Savov, I., Agostini, S., Padrón-Navarta, J. A., Marchesi, C., López Sánchez-Vizcaíno, V. & Gómez-Pugnaire, M. T. (2014). ^{11}B-rich fluids in subduction zones: The role of antigorite dehydration in subducting slabs and boron isotope heterogeneity in the mantle. *Chemical Geology* **376**, 20-30.

Hayes, J. M. & Waldbauer, J. R. (2006). The carbon cycle and associated redox processes through time. *Philosophical Transactions of the Royal Society B: Biological Sciences* **361**, 931-950.

Helgeson, H. C., Delany, J. M., Nesbitt, H. W. & Bird, D. K. (1978). Summary and critique of the thermodynamic properties of rock-forming minerals. *American Journal of Science* **278 -A**.

Helgeson, H. C. & Kirkham, D. H. (1976). Theoretical prediction of the thermodynamic properties of aqueous electrolytes at high pressures and temperatures. III. Equation of state for aqueous species at infinite dilution. *American Journal of Science* **276**, 97-240.

Helgeson, H. C., Kirkham, D. H. & Flowers, G. C. (1981). Theoretical prediction of the thermodynamic behavior of aqueous electrolytes by high pressures and temperatures; IV. Calculation of activity coefficients, osmotic coefficients, and apparent molal and standard and relative partial molal properties to 600 degrees C and 5kb. *American Journal of Science* **281**, 1249-1516.

Hermann, J., Troitzsch, U. & Scott, D. (2016). Experimental subsolidus phase relations in the system $CaCO_3$–$CaMg(CO_3)_2$ up to 6.5 GPa and implications for subducted marbles. *Contributions to Mineralogy and Petrology* **171**, 84.

Herzberg, C. (2016). Petrological evidence from Komatiites for an early Earth carbon and water cycle. *Journal of Petrology* **57**, 2271-2287.

Hinsbergen, D. J. J., Vissers, R. L. M. & Spakman, W. (2014). Origin and consequences of western Mediterranean subduction, rollback, and slab segmentation. *Tectonics* **33**, 393-419.

Hinsken, T., Bröcker, M., Strauss, H. & Bulle, F. (2017). Geochemical, isotopic and geochronological characterization of listvenite from the Upper Unit on Tinos, Cyclades, Greece. *Lithos* **282-283**, 281-297.

Hirschmann, M. M. (2018). Comparative deep Earth volatile cycles: The case for C recycling from exosphere/mantle fractionation of major (H_2O, C, N) volatiles and from H_2O/Ce, CO_2/Ba, and CO_2/Nb exosphere ratios. *Earth and Planetary Science Letters* **502**, 262-273.

Hoefs, J. (2009). *Stable Isotope Geochemistry*. Berlin Heidelberg: Springer.

Hoffman, P. F., Kaufman, A. J., Halverson, G. P. & Schrag, D. P. (1998). A Neoproterozoic Snowball Earth. *Science* **281**, 1342.

Holland, T., Baker, J. & Powell, R. (1998). Mixing properties and activity-composition relationships of chlorites in the system MgO–FeO–Al_2O_3–SiO_2–H_2O. *European Journal of Mineralogy* **10**, 395-406.

Holland, T. & Powell, R. (1991). A Compensated-Redlich-Kwong (CORK) equation for volumes and fugacities of CO_2 and H_2O in the range 1 bar to 50 kbar and 100-1600°C. *Contributions to Mineralogy and Petrology* **109**, 265-273.

Holland, T. & Powell, R. (1996). Thermodynamics of order-disorder in minerals; II, Symmetric formalism applied to solid solutions. *American Mineralogist* **81**, 1425-1437.

Holland, T. & Powell, R. (1998). An internally consistent thermodynamic data set for phases of petrological interest. *Journal of Metamorphic Geology* **16**, 309-343.

Hövelmann, J., Austrheim, H., Beinlich, A. & Anne Munz, I. (2011). Experimental study of the carbonation of partially serpentinized and weathered peridotites. *Geochimica et Cosmochimica Acta* **75**, 6760-6779.

Hövelmann, J., Putnis, C. V., Ruiz-Agudo, E. & Austrheim, H. (2012). Direct nanoscale observations of CO_2 sequestration during brucite [$Mg(OH)_2$] dissolution. *Environmental Science & Technology* **46**, 5253-5260.

Hürlimann, R. (1999). Die Hochdruckmetamorphose der Ultramafika und der angrenzenden Nebengesteine am Cerro del Almirez, Sierra Nevada, Spanien (Teil II). *Unpublished Diploma thesis*: ETH Zürich, 105.

Hyndman, R. D. & Peacock, S. M. (2003). Serpentinization of the forearc mantle. *Earth and Planetary Science Letters* **212**, 417-432.

Ildefonse, B., Blackman, D. K., John, B. E., Ohara, Y., Miller, D. J., MacLeod, C. J. & Integrated Ocean Drilling Program Expeditions 304/305 Science Party. (2007). Oceanic core complexes and crustal accretion at slow-spreading ridges. *Geology* **35**, 623-626.

Irwin, H., Curtis, C. & Coleman, M. (1977). Isotopic evidence for source of diagenetic carbonates formed during burial of organic-rich sediments. *Nature* **269**, 209-213.

Jabaloy-Sánchez, A., Gómez-Pugnaire, M. T., Padrón-Navarta, J. A., López Sánchez-Vizcaíno, V. & Garrido, C. J. (2015). Subduction- and exhumation-related structures preserved in metaserpentinites and associated metasediments from the Nevado–Filábride Complex (Betic Cordillera, SE Spain). *Tectonophysics* **644–645**, 40-57.

Jamieson, R. A. (1990). Metamorphism of an Early Palaeozoic continental margin, western Baie Verte Peninsula, Newfoundland. *Journal of Metamorphic Geology* **8**, 269-288.

Johannes, W. (1967). Zur Bildung und Stabilität von Forsterit, Talk, Serpentin, Quarz und Magnesit im System MgO–SiO_2–H_2O–CO_2. *Contributions to Mineralogy and Petrology* **15**, 233-250.

Johannes, W. (1969). An experimental investigation of the system MgO–SiO_2–H_2O–CO_2. *American Journal of Science* **267**, 1083-1104.

Johnson, J. W., Oelkers, E. H. & Helgeson, H. C. (1992). SUPCRT92: A software package for calculating the standard molal thermodynamic properties of minerals, gases, aqueous species, and reactions from 1 to 5000 bar and 0 to 1000°C. *Computers & Geosciences* **18**, 899-947.

Johnston, F. K. B., Turchyn, A. V. & Edmonds, M. (2011). Decarbonation efficiency in subduction zones: Implications for warm Cretaceous climates. *Earth and Planetary Science Letters* **303**, 143-152.

Kahl, W. A., Jöns, N., Bach, W., Klein, F. & Alt, J. C. (2015). Ultramafic clasts from the South Chamorro serpentine mud volcano reveal a polyphase serpentinization history of the Mariana forearc mantle. *Lithos* **227**, 99-147.

Kampschuur, W. & García Monzón, G. (1975). Vera. *Mapa Geologico de España*: Instituto Geologico y Minero de España.

Kelemen, P., Godard, M., Johnson, K. T. M., Okazaki, K., Manning, C. E., Urai, J. L., Michibayashi, K., Harris, M., Coggon, J. A., Teagle, D. A. H. & and the Oman Drilling Project Phase I Science Party. (2017). Peridotite carbonation at the leading edge of the mantle wedge: OmDP Site BT1. *AGU Fall meeting, abstract V24E-06*.

Kelemen, P. B., Hart, S. R. & Bernstein, S. (1998). Silica enrichment in the continental upper mantle via melt/rock reaction. *Earth and Planetary Science Letters* **164**, 387-406.

Kelemen, P. B. & Manning, C. E. (2015). Reevaluating carbon fluxes in subduction zones, what goes down, mostly comes up. *Proceedings of the National Academy of Sciences* **112**, E3997-4006.

Kelemen, P. B. & Matter, J. (2008). In situ carbonation of peridotite for CO_2 storage. *Proceedings of the National Academy of Sciences* **105**, 17295-17300.

Kelemen, P. B., Matter, J., Streit, E. E., Rudge, J. F., Curry, W. B. & Blusztajn, J. (2011). Rates and mechanisms of mineral carbonation in peridotite: Natural processes and recipes for enhanced, in situ CO_2 capture and storage. In: Jeanloz, R. & Freeman, K. H. (eds.) *Annual Review of Earth and Planetary Sciences, Vol 39*, 545-576.

Kendrick, M. A., Scambelluri, M., Hermann, J. & Padrón-Navarta, J. A. (2018). Halogens and noble gases in serpentinites and secondary peridotites: Implications for seawater subduction and the origin of mantle neon. *Geochimica et Cosmochimica Acta* **235**, 285-304.

Kerrick, D. M. (2001). Present and past nonanthropogenic CO_2 degassing from the solid earth. *Reviews of Geophysics* **39**, 565-585.

Kerrick, D. M. & Connolly, J. A. D. (1998). Subduction of ophicarbonates and recycling of CO_2 and H_2O. *Geology* **26**, 375-378.

Kerrick, D. M. & Connolly, J. A. D. (2001a). Metamorphic devolatilization of subducted marine sediments and the transport of volatiles into the Earth`s mantle. *Nature* **411**, 293.

Kerrick, D. M. & Connolly, J. A. D. (2001b). Metamorphic devolatilization of subducted oceanic metabasalts: implications for seismicity, arc magmatism and volatile recycling. *Earth and Planetary Science Letters* **189**, 19-29.

Kidd, W. (1974). The Evolution of the Baie Verte Lineament, Burlington Peninsula, Newfoundland. Ph.D. Thesis. Darwin College: Cambridge.

Kidd, W. S. F., Dewey, J. F. & Bird, J. M. (1978). The Mings Bight Ophiolite Complex, Newfoundland: Appalachian oceanic crust and mantle. *Canadian Journal of Earth Sciences* **15**, 781-804.

Kirchner, K. L., Behr, W. M., Loewy, S. & Stockli, D. F. (2016). Early Miocene subduction in the western Mediterranean: Constraints from Rb-Sr multimineral isochron geochronology. *Geochemistry, Geophysics, Geosystems* **17**, 1842-1860.

Klein, F., Bach, W., Humphris, S. E., Kahl, W. A., Jöns, N., Moskowitz, B. & Berquó, T. S. (2014). Magnetite in seafloor serpentinite-Some like it hot. *Geology* **42**, 135-138.

Klein, F., Bach, W. & McCollom, T. M. (2013). Compositional controls on hydrogen generation during serpentinization of ultramafic rocks. *Lithos* **178**, 55-69.

Klein, F. & Garrido, C. J. (2011). Thermodynamic constraints on mineral carbonation of serpentinized peridotite. *Lithos* **126**, 147-160.

Klein, F., Humphris, S. E., Guo, W., Schubotz, F., Schwarzenbach, E. M. & Orsi, W. D. (2015). Fluid mixing and the deep biosphere of a fossil Lost City-type hydrothermal system at the Iberia Margin. *Proceedings of the National Academy of Sciences* **112**, 12036-12041.

Klein, F., Marschall, H. R., Bowring, S. A., Humphris, S. E. & Horning, G. (2017). Mid-ocean Ridge serpentinite in the Puerto Rico trench: from seafloor spreading to subduction. *Journal of Petrology* **58**, 1729-1754.

Klein, F. & McCollom, T. M. (2013). From serpentinization to carbonation: New insights from a CO_2 injection experiment. *Earth and Planetary Science Letters* **379**, 137-145.

Kohn, M. J., Castro, A. E., Kerswell, B. C., Ranero, C. R. & Spear, F. S. (2018). Shear heating reconciles thermal models with the metamorphic rock record of subduction. *Proceedings of the National Academy of Sciences* **115**, 11706-11711.

Kokh, M. A., Akinfiev, N. N., Pokrovski, G. S., Salvi, S. & Guillaume, D. (2017). The role of carbon dioxide in the transport and fractionation of metals by geological fluids. *Geochimica et Cosmochimica Acta* **197**, 433-466.

Koziol, A. M. & Newton, R. C. (1998). Experimental determination of the reaction; magnesite + enstatite = forsterite + CO_2 in the ranges 6-25 kbar and 700–1100 ºC. *American Mineralogist* **83**, 213-219.

Kralik, M., Aharon, P., Schroll, E. & Zachmann, D. (1989). Carbon and oxygen isotope systematics of magnesites: a review. In: Moeller, P. (ed.) *Magnesite - Geology, Mineralogy, Geochemistry, Formation of Mg-Carbonates*. Berlin - Stuttgart: Borntraeger, 197-223.

Laborda-López, C., López Sánchez-Vizcaíno, V., Marchesi, C., Gómez-Pugnaire, M. T., Garrido, C. J., Jabaloy-Sánchez, A., Padrón-Navarta, J. A. & Hidas, K. (2018). High-P metamorphism of rodingites during serpentinite dehydration (Cerro del Almirez, Southern Spain): Implications for the redox state in subduction zones. *Journal of Metamorphic Geology* **36**, 1141-1173.

Lafay, R., Baumgartner, P. L., Schwartz, S., Picazo, S., Montes-Hernandez, G. & Vennemann, T. (2017). Petrologic and stable isotopic studies of a fossil hydrothermal system in ultramafic environment (Chenaillet ophicalcites, Western Alps, France): processes of carbonate cementation. *Lithos* **294-295**, 319-338.

Lagabrielle, Y., Vitale Brovarone, A. & Ildefonse, B. (2015). Fossil oceanic core complexes recognized in the blueschist metaophiolites of Western Alps and Corsica. *Earth-Science Reviews* **141**, 1-26.

Lavoie, D. & Cousineau, P. A. (1995). Ordovician ophicalcites of southern Quebec Appalachians: a proposed early seafloor tectonosedimentary and hydrothermal origin. *Journal of Sedimentary Research A: Sedimentary Petrology & Processes*, 2.

Li, B. & Massonne, H. J. (2018). Two Tertiary metamorphic events recognized in high-pressure metapelites of the Nevado-Filábride Complex (Betic Cordillera, S Spain). *Journal of Metamorphic Geology* **36**, 603-630.

Li, J.-L., Klemd, R., Gao, J. & Meyer, M. (2014). Compositional zoning in dolomite from lawsonite-bearing eclogite (SW Tianshan, China): Evidence for prograde metamorphism during subduction of oceanic crust. *American Mineralogist* **99**, 206-217.

López Sánchez-Vizcaíno, V. (1994). Evolucion petrológica y geoquímica de las rocas carbonáticas y litogías asociadas en el área de Macael-Cóbdar (Almería), Complejo Nevado-Filábride, Cordilleras Béticas (SE de España). Ph.D. Thesis, University of Granada.

López Sánchez-Vizcaíno, V., Connolly, J. A. D. & Gomez-Pugnaire, M. T. (1997). Metamorphism and phase relations in carbonate rocks from the Nevado-Filibride Complex (Cordilleras Beticas, Spain): Application of the Ttn+Rt+Cal+Qtz+Gr buffer. *Contributions to Mineralogy and Petrology* **126**, 292-302.

López Sánchez-Vizcaíno, V., Gómez-Pugnaire, M. T., Garrido, C. J., Padrón-Navarta, J. A. & Mellini, M. (2009). Breakdown mechanisms of titanclinohumite in antigorite serpentinite (Cerro del Almirez massif, S. Spain): A petrological and TEM study. *Lithos* **107**, 216-226.

López Sánchez-Vizcaíno, V., Rubatto, D., Gómez-Pugnaire, M. T., Trommsdorff, V. & Müntener, O. (2001). Middle Miocene high-pressure metamorphism and fast exhumation of the Nevado-Filabride Complex, SE Spain. *Terra Nova* **13**, 327-332.

López Sánchez-Vizcaíno, V., Trommsdorff, V., Gómez-Pugnaire, M. T., Garrido, C. J., Müntener, O. & Connolly, J. A. D. (2005). Petrology of titanian clinohumite and olivine at the high-pressure breakdown of antigorite serpentinite to chlorite harzburgite (Almirez Massif, S. Spain). *Contributions to Mineralogy and Petrology* **149**, 627-646.

Ludwig, K. A., Kelley, D. S., Butterfield, D. A., Nelson, B. K. & Früh-Green, G. (2006). Formation and evolution of carbonate chimneys at the Lost City Hydrothermal Field. *Geochimica et Cosmochimica Acta* **70**, 3625-3645.

Macpherson, C. G., Hilton, D. R. & Hammerschmidt, K. (2010). No slab-derived CO_2 in Mariana Trough back-arc basalts: Implications for carbon subduction and for temporary storage of CO_2 beneath slow spreading ridges. *Geochemistry, Geophysics, Geosystems* **11**, Q11007.

Malaspina, N. & Tumiati, S. (2012). The role of C-O-H and oxygen fugacity in subduction-zone garnet peridotites. *European Journal of Mineralogy* **24**, 607-618.

Malvoisin, B. (2015). Mass transfer in the oceanic lithosphere: Serpentinization is not isochemical. *Earth and Planetary Science Letters* **430**, 75-85.

Malvoisin, B., Chopin, C., Baronnet, A., Brunet, F., Bezacier, L. & Guillot, S. (2017). Fe–Ni-rich silicate aggregates formed after sulfides in high-pressure serpentinites. *Journal of Petrology* **58**, 963-978.

Mallik, A., Dasgupta, R., Tsuno, K. & Nelson, J. (2016). Effects of water, depth and temperature on partial melting of mantle-wedge fluxed by hydrous sediment-melt in subduction zones. *Geochimica et Cosmochimica Acta* **195**, 226-243.

Manning, C. E. (2004). The chemistry of subduction-zone fluids. *Earth and Planetary Science Letters* **223**, 1-16.

Manning, C. E., Shock, E. L. & Sverjensky, D. (2013). The chemistry of carbon in aqueous fluids at crustal and upper mantle conditions: experimental and theoretical constraints. *Reviews in Mineralogy & Geochemistry* **75**, 109-148.

Marchesi, C., Garrido, C. J., Padrón-Navarta, J. A., López Sánchez-Vizcaíno, V. & Gomez-Pugnaire, M. T. (2013). Element mobility from seafloor serpentinization to high-pressure dehydration of antigorite in subducted serpentinite: Insights from the Cerro del Almirez ultramafic massif (southern Spain). *Lithos* **178**, 128-142.

Marschall, H. R. & Schumacher, J. C. (2012). Arc magmas sourced from mélange diapirs in subduction zones. *Nature Geoscience* **5**, 862.

Martínez-Martínez, J. M., Torres-Ruiz, J., Pesquera, A. & Gil-Crespo, P. P. (2010). Geological relationships and U-Pb zircon and $^{40}Ar/^{39}Ar$ tourmaline geochronology of gneisses and tourmalinites from the Nevado–Filabride complex (western Sierra Nevada, Spain): Tectonic implications. *Lithos* **119**, 238-250.

Marty, B. & Tolstikhin, I. N. (1998). CO_2 fluxes from mid-ocean ridges, arcs and plumes. *Chemical Geology* **145**, 233-248.

Mason, E., Edmonds, M. & Turchyn, A. V. (2017). Remobilization of crustal carbon may dominate volcanic arc emissions. *Science* **357**, 290.

Mateeva, T., Wolff, G. A., Manatschal, G., Picazo, S., Kusznir, N. J. & Wheeler, J. (2017). Preserved organic matter in a fossil Ocean Continent Transition in the Alps: the example of Totalp, SE Switzerland. *Swiss Journal of Geosciences* **110**, 457-478.

Matter, J. M. & Kelemen, P. B. (2009). Permanent storage of carbon dioxide in geological reservoirs by mineral carbonation. *Nature Geoscience* **2**, 837-841.

Maurice, J., Bolfan-Casanova, N., Padrón-Navarta, J. A., Manthilake, G., Hammouda, T., Hénot, J. M. & Andrault, D. (2018). The stability of hydrous phases beyond antigorite breakdown for a magnetite-bearing natural serpentinite between 6.5 and 11 GPa. *Contributions to Mineralogy and Petrology* **173**, 86.

Mazzoli, S., Martín-Algarra, A., Reddy, S. M., López Sánchez-Vizcaíno, V., Fedele, L. & Noviello, A. (2013). The evolution of the footwall to the Ronda subcontinental mantle peridotites: insights from the Nieves Unit (western Betic Cordillera). *Journal of the Geological Society* **170**, 385-402.

McCollom, T. M. & Bach, W. (2009). Thermodynamic constraints on hydrogen generation during serpentinization of ultramafic rocks. *Geochimica et Cosmochimica Acta* **73**, 856-875.

McCollom, T. M., Klein, F., Robbins, M., Moskowitz, B., Berquó, T. S., Jöns, N., Bach, W. & Templeton, A. (2016). Temperature trends for reaction rates, hydrogen generation, and partitioning of iron during experimental serpentinization of olivine. *Geochimica et Cosmochimica Acta* **181**, 175-200.

Mellini, M., Trommsdorff, V. & Compagnoni, R. (1987). Antigorite polysomatism: behaviour during progressive metamorphism. *Contributions to Mineralogy and Petrology* **97**, 147-155.

Ménez, B., Pasini, V. & Brunelli, D. (2012). Life in the hydrated suboceanic mantle. *Nature Geoscience* **5**, 133.

Ménez, B., Pasini, V., Guyot, F., Benzerara, K., Bernard, S. & Brunelli, D. (2018). Mineralizations and transition metal mobility driven by organic carbon during low-temperature serpentinization. *Lithos* **323**, 262-276.

Menzel, M. D., Garrido, C. J., López Sánchez-Vizcaíno, V., Marchesi, C., Hidas, K., Escayola, M. P. & Delgado Huertas, A. (2018). Carbonation of mantle peridotite by CO_2-rich fluids: the formation of listvenites in the Advocate ophiolite complex (Newfoundland, Canada). *Lithos* **323**, 238-261.

Menzel, M. D., Garrido, C. J., López Sánchez-Vizcaíno, V., Hidas, K. & Marchesi, C. (2019). Subduction metamorphism of serpentinite-hosted carbonates beyond antigorite-serpentinite dehydration (Nevado-Filábride Complex, Spain). *Journal of Metamorphic Geology* **(in press)**.

Merkulova, M. V., Muñoz, M., Brunet, F., Vidal, O., Hattori, K., Vantelon, D., Trcera, N. & Huthwelker, T. (2017). Experimental insight into redox transfer by iron- and sulfur-bearing serpentinite dehydration in subduction zones. *Earth and Planetary Science Letters* **479**, 133-143.

Mikhail, S., Barry, P. H. & Sverjensky, D. A. (2017). The relationship between mantle pH and the deep nitrogen cycle. *Geochimica et Cosmochimica Acta* **209**, 149-160.

Mizuochi, H., Satish-Kumar, M., Motoyoshi, Y. & Michibayashi, K. (2010). Exsolution of dolomite and application of calcite-dolomite solvus geothermometry in high-grade marbles: an example from Skallevikshalsen, East Antarctica. *Journal of Metamorphic Geology* **28**, 509-526.

Molina, J. F. & Poli, S. (2000). Carbonate stability and fluid composition in subducted oceanic crust: an experimental study on H_2O-CO_2-bearing basalts. *Earth and Planetary Science Letters* **176**, 295-310.

Mottl, M. J., Wheat, C. G., Fryer, P., Gharib, J. & Martin, J. B. (2004). Chemistry of springs across the Mariana forearc shows progressive devolatilization of the subducting plate. *Geochimica et Cosmochimica Acta* **68**, 4915-4933.

Müller, R. D. & Dutkiewicz, A. (2018). Oceanic crustal carbon cycle drives 26-million-year atmospheric carbon dioxide periodicities. *Science Advances* **4**.

Müller, R. D., Sdrolias, M., Gaina, C. & Roest, W. R. (2008). Age, spreading rates, and spreading asymmetry of the world's ocean crust. *Geochemistry, Geophysics, Geosystems* **9**, Q04006.

Navarro, R., Pereira, D., Gimeno, A. & Barrio, S. d. (2013). Verde Macael: A serpentinite wrongly referred to as a marble. *Geosciences* **3**, 102-113.

Nestola, F., Korolev, N., Kopylova, M., Rotiroti, N., Pearson, D. G., Pamato, M. G., Alvaro, M., Peruzzo, L., Gurney, J. J., Moore, A. E. & Davidson, J. (2018). $CaSiO_3$ perovskite in diamond indicates the recycling of oceanic crust into the lower mantle. *Nature* **555**, 237.

Newton, R. C. & Manning, C. E. (2002). Experimental determination of calcite solubility in H_2O–NaCl solutions at deep crust/upper mantle pressures and temperatures: Implications for metasomatic processes in shear zones. *American Mineralogist* **87**, 1401-1409.

Nosouhian, N., Torabi, G. & Arai, S. (2016). Amphibole-bearing listwaenites from the Paleozoic Bayazeh ophiolite (Central Iran). *Italian Journal of Geosciences* **135**, 109-119.

Ohnmacht, W. (1974). Petrogenesis of Carbonate-orthopyroxenites (Sagvandites) and related rocks from Troms, Northern Norway. *Journal of Petrology* **15**, 303-324.

Oze, C., Bird, D. K. & Fendorf, S. (2007). Genesis of hexavalent chromium from natural sources in soil and groundwater. *Proceedings of the National Academy of Sciences* **104**, 6544-6549.

Padrón-Navarta, J. A., Hermann, J., Garrido, C. J., López Sánchez-Vizcaíno, V. & Gómez-Pugnaire, M. T. (2010a). An experimental investigation of antigorite dehydration in natural silica-enriched serpentinite. *Contributions to Mineralogy and Petrology* **159**, 25-42.

Padrón-Navarta, J. A., López Sánchez-Vizcaíno, V., Garrido, C. J. & Gomez-Pugnaire, M. T. (2011). Metamorphic record of high-pressure dehydration of antigorite serpentinite to chlorite harzburgite in a subduction setting (Cerro del Almirez, Nevado-Filabride Complex, Southern Spain). *Journal of Petrology* **52**, 2047-2078.

Padrón-Navarta, J. A., López Sánchez-Vizcaíno, V., Garrido, C. J., Gómez-Pugnaire, M. T., Jabaloy, A., Capitani, G. C. & Mellini, M. (2008). Highly ordered antigorite from Cerro del Almirez HP-HT serpentinites, SE Spain. *Contributions to Mineralogy and Petrology* **156**, 679-688.

Padrón-Navarta, J. A., López Sánchez-Vizcaíno, V., Hermann, J., Connolly, J. A. D., Garrido, C. J., Gómez-Pugnaire, M. T. & Marchesi, C. (2013). Tschermak's substitution in antigorite and consequences for phase relations and water liberation in high-grade serpentinites. *Lithos* **178**, 186-196.

Padrón-Navarta, J. A., Tommasi, A., Garrido, C. J. & López Sánchez-Vizcaíno, V. (2012). Plastic deformation and development of antigorite crystal preferred orientation in high-pressure serpentinites. *Earth and Planetary Science Letters* **349-350**, 75-86.

Padrón-Navarta, J. A., Tommasi, A., Garrido, C. J., López Sánchez-Vizcaíno, V., Gómez-Pugnaire, M. T., Jabaloy, A. & Vauchez, A. (2010b). Fluid transfer into the wedge controlled by high-pressure hydrofracturing in the cold top-slab mantle. *Earth and Planetary Science Letters* **297**, 271-286.

Padrón-Navarta, J. A., Tommasi, A., Garrido, C. J. & Mainprice, D. (2015). On topotaxy and compaction during antigorite and chlorite dehydration: an experimental and natural study. *Contributions to Mineralogy and Petrology* **169**, 35.

Padrón-Navarta, J. A. (2010). A Coupled Petrological and Petrophysical Study of high Pressure Dehydration Reactions in Subduction Settings. Insights from the Betic Cordillera and the Kohistan Paleo-arc. Ph.D. thesis, University of Granada.

Penniston-Dorland, S. C., Kohn, M. J. & Manning, C. E. (2015). The global range of subduction zone thermal structures from exhumed blueschists and eclogites: Rocks are hotter than models. *Earth and Planetary Science Letters* **428**, 243-254.

Petriglieri, J. R., Salvioli-Mariani, E., Mantovani, L., Tribaudino, M., Lottici, P. P., Laporte-Magoni, C. & Bersani, D. (2015). Micro-Raman mapping of the polymorphs of serpentine. *Journal of Raman Spectroscopy* **46**, 953-958.

Pfiffner, M. & Trommsdorff, V. (1998). The high-pressure ultramafic-mafic-carbonate suite of Cima Lunga-Adula, central Alps: excursions to Cima di Gagnone and Alpe Arami. *Schweizerische Mineralogische und Petrographische Mitteilungen* **78**, 337-354.

Picazo, S., Lafay, R., Faucheux, V. & Vennemann, T. (2019). New constraints on carbonation associated with brecciation in hyper-extended margins (example of Iberia and Newfoundland margins). *Terra Nova* **(in press)**.

Picazo, S., Manatschal, G., Cannat, M. & Andréani, M. (2013). Deformation associated to exhumation of serpentinized mantle rocks in a fossil Ocean Continent Transition: The Totalp unit in SE Switzerland. *Lithos* **175-176**, 255-271.

Piccoli, F., Vitale Brovarone, A. & Ague, J. J. (2018). Field and petrological study of metasomatism and high-pressure carbonation from lawsonite eclogite-facies terrains, Alpine Corsica. *Lithos* **304-307**, 16-37.

Piccoli, F., Vitale Brovarone, A., Beyssac, O., Martinez, I., Ague, J. J. & Chaduteau, C. (2016). Carbonation by fluid-rock interactions at high-pressure conditions: Implications for carbon cycling in subduction zones. *Earth and Planetary Science Letters* **445**, 146-159.

Plank, T. & Langmuir, C. H. (1998). The chemical composition of subducting sediment and its consequences for the crust and mantle. *Chemical Geology* **145**, 325-394.

Platt, J. P., Anczkiewicz, R., Soto, J.-I., Kelley, S. P. & Thirlwall, M. (2006). Early Miocene continental subduction and rapid exhumation in the western Mediterranean. *Geology* **34**, 981-984.

Platt, J. P., Behr, W. M., Johanesen, K. & Williams, J. R. (2013). The Betic-Rif Arc and its orogenic hinterland: A review. *Annual Review of Earth and Planetary Sciences* **41**, 313-357.

Plümper, O., John, T., Podladchikov, Y. Y., Vrijmoed, J. C. & Scambelluri, M. (2017). Fluid escape from subduction zones controlled by channel-forming reactive porosity. *Nature Geoscience* **10**, 150-156.

Poli, S. (2015). Carbon mobilized at shallow depths in subduction zones by carbonatitic liquids. *Nature Geoscience* **8**, 633-636.

Pozzorini, D. & Früh-Green, G. L. (1996). Stable isotope systematics of the Ventina Ophicarbonate Zone, Bergell contact aureole. *Schweizerische Mineralogische und Petrographische Mitteilungen* **76**, 549-564.

Proyer, A., Mposkos, E., Baziotis, I. & Hoinkes, G. (2008). Tracing high-pressure metamorphism in marbles: Phase relations in high-grade aluminous calcite–dolomite marbles from the Greek Rhodope massif in the system $CaO–MgO–Al_2O_3–SiO_2–CO_2$ and indications of prior aragonite. *Lithos* **104**, 119-130.

Puga, E., Fanning, M., Díaz de Federico, A., Nieto, J. M., Beccaluva, L., Bianchini, G. & Díaz Puga, M. A. (2011). Petrology, geochemistry and U–Pb geochronology of the Betic Ophiolites: Inferences for Pangaea break-up and birth of the westernmost Tethys Ocean. *Lithos* **124**, 255-272.

Qing, H. & Veizer, J. (1994). Oxygen and carbon isotopic composition of Ordovician brachiopods: Implications for coeval seawater. *Geochimica et Cosmochimica Acta* **58**, 4429-4442.

Qiu, T. & Zhu, Y. (2015). Geology and geochemistry of listwaenite-related gold mineralization in the Sayi gold deposit, Xinjiang, NW China. *Ore Geology Reviews* **70**, 61-79.

Quesnel, B., Boulvais, P., Gautier, P., Cathelineau, M., John, C. M., Dierick, M., Agrinier, P. & Drouillet, M. (2016). Paired stable isotopes (O, C) and clumped isotope thermometry of magnesite and silica veins in the New Caledonia Peridotite Nappe. *Geochimica et Cosmochimica Acta* **183**, 234-249.

Ramezani, J., Dunning, G. R. & Wilson, M. R. (2000). Geologic setting, geochemistry of alteration, and U-Pb age of hydrothermal zircon from the silurian stog'er tight gold prospect, Newfoundland Appalachians, Canada. *Exploration and Mining Geology* **9**, 171-188.

Ranero, C. R., Phipps Morgan, J., McIntosh, K. & Reichert, C. (2003). Bending-related faulting and mantle serpentinization at the Middle America trench. *Nature* **425**, 367-373.

Rice, J. M. (1980). Phase equilibria involving humite minerals in impure dolomitic limestones. *Contributions to Mineralogy and Petrology* **71**, 219-235.

Robinson, P. T., Malpas, J., Zhou, M.-F., Ash, C., Yang, J.-S. & Bai, W.-J. (2005). Geochemistry and Origin of Listwanites in the Sartohay and Luobusa Ophiolites, China. *International Geology Review* **47**, 177-202.

Rouméjon, S., Cannat, M., Agrinier, P., Godard, M. & Andreani, M. (2015). Serpentinization and Fluid Pathways in Tectonically Exhumed Peridotites from the Southwest Indian Ridge (62–65°E). *Journal of Petrology* **56**, 703-734.

Rüpke, L. H. & Hasenclever, J. (2017). Global rates of mantle serpentinization and H_2 production at oceanic transform faults in 3-D geodynamic models. *Geophysical Research Letters* **44**, 6726-6734.

Rüpke, L. H., Morgan, J. P., Hort, M. & Connolly, J. A. D. (2004). Serpentine and the subduction zone water cycle. *Earth and Planetary Science Letters* **223**, 17-34.

Russell, M. J., Hall, A. J. & Martin, W. (2010). Serpentinization as a source of energy at the origin of life. *Geobiology* **8**, 355-371.

Sánchez-Valle, C. (2013). Structure and thermodynamics of subduction zone fluids from spectroscopic studies. *Reviews in Mineralogy and Geochemistry* **76**, 265-309.

Sapienza, G. T., Scambelluri, M. & Braga, R. (2009). Dolomite-bearing orogenic garnet peridotites witness fluid-mediated carbon recycling in a mantle wedge (Ulten Zone, Eastern Alps, Italy). *Contributions to Mineralogy and Petrology* **158**, 401-420.

Scambelluri, M., Bebout, G. E., Belmonte, D., Gilio, M., Campomenosi, N., Collins, N. & Crispini, L. (2016). Carbonation of subduction-zone serpentinite (high-pressure ophicarbonate; Ligurian Western Alps) and implications for the deep carbon cycling. *Earth and Planetary Science Letters* **441**, 155-166.

Scambelluri, M., Bottazzi, P., Trommsdorff, V., Vannucci, R., Hermann, J., Gòmez-Pugnaire, M. T. & López Sánchez-Vizcaíno, V. (2001). Incompatible element-rich fluids released by antigorite breakdown in deeply subducted mantle. *Earth and Planetary Science Letters* **192**, 457-470.

Scambelluri, M., Cannaò, E. & Gilio, M. (2019). The water and fluid-mobile element cycles during serpentinite subduction. A review. *European Journal of Mineralogy*.

Scambelluri, M., Müntener, O., Ottolini, L., Pettke, T. T. & Vannucci, R. (2004). The fate of B, Cl and Li in the subducted oceanic mantle and in the antigorite breakdown fluids. *Earth and Planetary Science Letters* **222**, 217-234.

Scambelluri, M., Pettke, T., Rampone, E., Godard, M. & Reusser, E. (2014). Petrology and trace element budgets of high-pressure peridotites indicate subduction dehydration of serpentinized mantle (Cima di Gagnone, Central Alps, Switzerland). *Journal of Petrology* **55**, 459-498.

Schandl, E. S. & Naldrett, A. J. (1992). CO_2 metasomatism of serpentinites, south of Timmins, Ontario. *Canadian Mineralogist* **30**, 93-108.

Scheele, N. & Hoefs, J. (1992). Carbon isotope fractionation between calcite, graphite and CO_2: an experimental study. *Contributions to Mineralogy and Petrology* **112**, 35-45.

Schlaphorst, D., Kendall, J. M., Collier, J. S., Verdon, J. P., Blundy, J., Baptie, B., Latchman, J. L., Massin, F. & Bouin, M. P. (2016). Water, oceanic fracture zones and the lubrication of subducting plate boundaries-insights from seismicity. *Geophysical Journal International* **204**, 1405-1420.

Schmidt, M. W. & Poli, S. (2014). 4.19 Devolatilization during subduction. In: Holland, H. D. & Turekian, K. K. (eds.) *Treatise on Geochemistry: Second Edition*, 669-701.

Schneider, M. E. & Eggler, D. H. (1986). Fluids in equilibrium with peridotite minerals: Implications for mantle metasomatism. *Geochimica et Cosmochimica Acta* **50**, 711-724.

Schönbächler, M. (1999). Die Hochdruckmetamorphose der Ultramafika und der angrenzenden Nebengesteine am Cerro de Almirez, Sierra Nevada, Südspanien. Teil I. *Unpublished Diploma thesis*: ETH Zürich, 113.

Schreyer, W., Ohnmacht, W. & Mannchen, J. (1972). Carbonate-orthopyroxenites (sagvandites) from Troms, northern Norway. *Lithos* **5**, 345-364.

Schroeder, T., Bach, W., Jöns, N., Jöns, S., Monien, P. & Klügel, A. (2015). Fluid circulation and carbonate vein precipitation in the footwall of an oceanic core complex, Ocean Drilling Program Site 175, Mid-Atlantic Ridge. *Geochemistry, Geophysics, Geosystems* **16**, 3716-3732.

Schwartz, S., Guillot, S., Reynard, B., Lafay, R., Debret, B., Nicollet, C., Lanari, P. & Auzende, A. L. (2013). Pressure-temperature estimates of the lizardite/antigorite transition in high pressure serpentinites. *Lithos* **178**, 197-210.

Schwarzenbach, E. M., Caddick, M. J., Petroff, M., Gill, B. C., Cooperdock, E. H. G. & Barnes, J. D. (2018). Sulphur and carbon cycling in the subduction zone mélange. *Scientific Reports* **8**, 15517.

Schwarzenbach, E. M., Früh-Green, G. L., Bernasconi, S. M., Alt, J. C. & Plas, A. (2013). Serpentinization and carbon sequestration: A study of two ancient peridotite-hosted hydrothermal systems. *Chemical Geology* **351**, 115-133.

Schwarzenbach, E. M., Gill, B. C., Gazel, E. & Madrigal, P. (2016). Sulfur and carbon geochemistry of the Santa Elena peridotites: Comparing oceanic and continental processes during peridotite alteration. *Lithos* **252–253**, 92-108.

Sharma, S. D., Patil, D. J. & Gopalan, K. (2002). Temperature dependence of oxygen isotope fractionation of CO_2 from magnesite-phosphoric acid reaction. *Geochimica et Cosmochimica Acta* **66**, 589-593.

Shen, T., Hermann, J., Zhang, L., Lü, Z., Padrón-Navarta, J. A., Xia, B. & Bader, T. (2014). UHP metamorphism documented in Ti-chondrodite- and Ti-clinohumite-bearing serpentinized ultramafic rocks from Chinese southwestern Tianshan. *Journal of Petrology* **56**, 1425-1458.

Shock, E. L. & Helgeson, H. C. (1988). Calculation of the thermodynamic and transport properties of aqueous species at high pressures and temperatures: Correlation algorithms for ionic species and equation of state predictions to 5 kb and 1000°C. *Geochimica et Cosmochimica Acta* **52**, 2009-2036.

Sieber, M. J., Hermann, J. & Yaxley, G. M. (2018). An experimental investigation of C–O–H fluid-driven carbonation of serpentinites under forearc conditions. *Earth and Planetary Science Letters* **496**, 178-188.

Siivola, J. & Schmid, R. (2007). A systematic nomenclature for metamorphic rocks 12. List of mineral abbreviations. *Recommendations by the IUGS Subcommission on the Systematics of Metamorphic Rocks*.

Skulski, T., Castonguay, S., McNicoll, V., van Staal, C., Kidd, W., Rogers, N., Morris, W., Ugalde, H., Slavinski, H. & Spicer, W. (2010). Tectonostratigraphy of the Baie Verte oceanic tract and its ophiolite cover sequence on the Baie Verte Peninsula. *Current Research*: Newfoundland and Labrador Department of Natural Resources, Geological Survey Report 10-1, 315-337.

Skulski, T., Castonguay, S., Staal, C. v., Rogers, N., McNicoll, V., Kerr, A. & Escayola, M. (2009). Baie Verte Peninsula: an evolving geological story. In: Rogers, N. & Kerr, A. (eds.) *Annual Fall Field Trip Report*: Geological Association of Canada Newfoundland and Labrador Section.

Smith, D. (2013). Mantle spread across the sea floor. *Nature Geoscience* **6**, 247.

Smith, E. M., Shirey, S. B., Richardson, S. H., Nestola, F., Bullock, E. S., Wang, J. & Wang, W. (2018). Blue boron-bearing diamonds from Earth's lower mantle. *Nature* **560**, 84-87.

Snow, J. E. & Dick, H. J. B. (1995). Pervasive magnesium loss by marine weathering of peridotite. *Geochimica et Cosmochimica Acta* **59**, 4219-4235.

Sofiya, A., Ishiwatari, A., Hirano, N. & Tsujimori, T. (2017). Relict chromian spinels in Tulu Dimtu serpentinites and listvenite, Western Ethiopia: implications for the timing of listvenite formation. *International Geology Review* **59**, 1621-1631.

Spandler, C., Hartmann, J., Faure, K., Mavrogenes, J. A. & Arculus, R. J. (2008). The importance of talc and chlorite "hybrid" rocks for volatile recycling through subduction zones; evidence from the high-pressure subduction melange of New Caledonia. *Contributions to Mineralogy and Petrology* **155**, 181-198.

Spandler, C. & Pirard, C. (2013). Element recycling from subducting slabs to arc crust: A review. *Lithos* **170-171**, 208-223.

Srikantappa, C., Raith, M. & Ackermand, D. (1985). High-grade regional metamorphism of ultramafic and mafic rocks from the Archaean Sargur terrane, Karnataka, South India. *Precambrian Research* **30**, 189-219.

Stagno, V. (2019). Carbon, carbides, carbonates and carbonatitic melts in the Earth's interior. *Journal of the Geological Society*, jgs2018-2095.

Stern, R. J. (2002). Subduction zones. *Reviews of Geophysics* **40**, 3-1-3-38.

Stewart, E. M. & Ague, J. J. (2018). Infiltration-driven metamorphism, New England, USA: Regional CO_2 fluxes and implications for Devonian climate and extinctions. *Earth and Planetary Science Letters* **489**, 123-134.

Streit, E., Kelemen, P. & Eiler, J. (2012). Coexisting serpentine and quartz from carbonate-bearing serpentinized peridotite in the Samail Ophiolite, Oman. *Contributions to Mineralogy and Petrology* **164**, 821-837.

Stucki, A. (2001). High grade Mesozoic ophiolites of the Southern Steep Belt, Central Alps. Ph.D. Thesis, Swiss Federal Institute of Technology Zürich (ETH).

Sverjensky, D. A. (2019). Thermodynamic modelling of fluids from surficial to mantle conditions. *Journal of the Geological Society* **176**, 348-374.

Sverjensky, D. A., Harrison, B. & Azzolini, D. (2014a). Water in the deep Earth: The dielectric constant and the solubilities of quartz and corundum to 60 kb and 1200 °C. *Geochimica et Cosmochimica Acta* **129**, 125-145.

Sverjensky, D. A., Stagno, V. & Huang, F. (2014b). Important role for organic carbon in subduction-zone fluids in the deep carbon cycle. *Nature Geoscience* **7**, 909-913.

Syracuse, E. M., van Keken, P. E. & Abers, G. A. (2010). The global range of subduction zone thermal models. *Physics of the Earth and Planetary Interiors* **183**, 73-90.

Tao, R., Zhang, L., Tian, M., Zhu, J., Liu, X., Liu, J., Höfer, H. E., Stagno, V. & Fei, Y. (2018). Formation of abiotic hydrocarbon from reduction of carbonate in subduction zones: Constraints from petrological observation and experimental simulation. *Geochimica et Cosmochimica Acta* **239**, 390-408.

Tian, M. & Ague, J. J. (2014). The impact of porosity waves on crustal reaction progress and CO_2 mass transfer. *Earth and Planetary Science Letters* **390**, 80-92.

Timmerman, S., Koornneef, J. M., Chinn, I. L. & Davies, G. R. (2017). Dated eclogitic diamond growth zones reveal variable recycling of crustal carbon through time. *Earth and Planetary Science Letters* **463**, 178-188.

Tiraboschi, C., Tumiati, S., Sverjensky, D., Pettke, T., Ulmer, P. & Poli, S. (2017). Experimental determination of magnesia and silica solubilities in graphite-saturated and redox-buffered high-pressure COH fluids in equilibrium with forsterite + enstatite and magnesite + enstatite. *Contributions to Mineralogy and Petrology* **173**, 2.

Tominaga, M., Beinlich, A., Lima, E. A., Tivey, M. A., Hampton, B. A., Weiss, B. & Harigane, Y. (2017). Multi-scale magnetic mapping of serpentinite carbonation. *Nature Communications* **8**, 1870.

Treves, B. E. & Harper, G. D. (1994). Exposure of serpentinites on the ocean floor: sequence of faulting and hydrofracturing in the northern Apennine ophicalcites. *Ofioliti* **19**, 435-466.

Trommsdorff, V. & Connolly, J. A. D. (1996). The ultramafic contact aureole about the Bregaglia (Bergell) tonalite: Isograds and a thermal model. *Schweizerische Mineralogische und Petrographische Mitteilungen* **76**, 537-547.

Trommsdorff, V. & Evans, B. W. (1972). Progressive metamorphism of antigorite schist in the Bergell tonalite aureole (Italy). *American Journal of Science* **272**, 423-437.

Trommsdorff, V. & Evans, B. W. (1977a). Antigorite-ophicarbonates: Contact metamorphism in Valmalenco, Italy. *Contributions to Mineralogy and Petrology* **62**, 301-312.

Trommsdorff, V. & Evans, B. W. (1977b). Antigorite-ophicarbonates: Phase relations in a portion of the system CaO-MgO-SiO_2-H_2O-CO_2. *Contributions to Mineralogy and Petrology* **60**, 39-56.

Trommsdorff, V., López Sánchez-Vizcaíno, V., Gomez-Pugnaire, M. T. & Müntener, O. (1998). High pressure breakdown of antigorite to spinifex-textured olivine and orthopyroxene, SE Spain. *Contributions to Mineralogy and Petrology* **132**, 139-148.

Tumiati, S., Fumagalli, P., Tiraboschi, C. & Poli, S. (2013). An experimental study on COH-bearing peridotite up to 3·2 GPa and implications for crust–mantle recycling. *Journal of Petrology* **54**, 453-479.

Tumiati, S., Tiraboschi, C., Sverjensky, D. A., Pettke, T., Recchia, S., Ulmer, P., Miozzi, F. & Poli, S. (2017). Silicate dissolution boosts the CO_2 concentrations in subduction fluids. *Nature Communications* **8**, 616.

Ulmer, P. & Trommsdorff, V. (1995). Serpentine stability to mantle depths and subduction-related magmatism. *Science* **268**, 858.

van Keken, P. E., Hacker, B. R., Syracuse, E. M. & Abers, G. A. (2011). Subduction factory: 4. Depth-dependent flux of H_2O from subducting slabs worldwide. *Journal of Geophysical Research* **116**, B01401.

van Noort, R., Spiers, C. J., Drury, M. R. & Kandianis, M. T. (2013). Peridotite dissolution and carbonation rates at fracture surfaces under conditions relevant for in situ mineralization of CO_2. *Geochimica et Cosmochimica Acta* **106**, 1-24.

van Staal, C., Chew, D., Zagorevski, A., McNicoll, V., Hibbard, J., Skulski, T., Escayola, M., Castonguay, S. & Sylvester, P. (2013). Evidence of Late Ediacaran hyperextension of the Laurentian Iapetan Margin in the Birchy Complex, Baie Verte Peninsula, Northwest Newfoundland: Implications for the opening of Iapetus, formation of peri-Laurentian microcontinents and Taconic – Grampian orogenesis. *Geoscience Canada* **40**, 94-117.

Varas-Reus, M. I., Garrido, C. J., Marchesi, C., Bodinier, J.-L., Frets, E., Bosch, D., Tommasi, A., Hidas, K. & Targuisti, K. (2016). Refertilization processes in the subcontinental lithospheric mantle: the record of the Beni Bousera orogenic peridotite (Rif Belt, Northern Morocco). *Journal of Petrology* **57**, 2251-2270.

Vitale Brovarone, A., Beltrando, M., Malavieille, J., Giuntoli, F., Tondella, E., Groppo, C., Beyssac, O. & Compagnoni, R. (2011). Inherited Ocean–Continent Transition zones in deeply subducted terranes: Insights from Alpine Corsica. *Lithos* **124**, 273-290.

Vitale Brovarone, A., Chu, X., Martin, L., Ague, J. J., Monié, P., Groppo, C., Martinez, I. & Chaduteau, C. (2018). Intra-slab COH fluid fluxes evidenced by fluid-mediated decarbonation of lawsonite eclogite-facies altered oceanic metabasalts. *Lithos* **304-307**, 211-229.

Vitale Brovarone, A., Martinez, I., Elmaleh, A., Compagnoni, R., Chaduteau, C., Ferraris, C. & Esteve, I. (2017). Massive production of abiotic methane during subduction evidenced in metamorphosed ophicarbonates from the Italian Alps. *Nature Communications* **8**, 14134.

Wada, I. & Wang, K. (2009). Common depth of slab-mantle decoupling: Reconciling diversity and uniformity of subduction zones. *Geochemistry, Geophysics, Geosystems* **10**, Q10009.

Waldron, J. W. F. & van Staal, C. (2001). Taconian orogeny and the accretion of the Dashwoods block: A peri-Laurentian microcontinent in the Iapetus Ocean. *Geology* **29**, 811-814.

Walowski, K. J., Wallace, P. J., Hauri, E. H., Wada, I. & Clynne, M. A. (2015). Slab melting beneath the Cascade Arc driven by dehydration of altered oceanic peridotite. *Nature Geoscience* **8**, 404-408.

Warren, J. M. (2016). Global variations in abyssal peridotite compositions. *Lithos* **248**, 193-219.

Wassmann, S. & Stöckhert, B. (2013). Rheology of the plate interface — Dissolution precipitation creep in high pressure metamorphic rocks. *Tectonophysics* **608**, 1-29.

Weiss, M. (1997). Clinohumites: a field and experimental study. Ph.D. Thesis, Swiss Federal Institute of Technology Zürich (ETH).

Whalen, J. B., McNicoll, V. J., van Staal, C. R., Lissenberg, C. J., Longstaffe, F. J., Jenner, G. A. & van Breeman, O. (2006). Spatial, temporal and geochemical characteristics of Silurian collision-zone magmatism, Newfoundland Appalachians: An example of a rapidly evolving magmatic system related to slab break-off. *Lithos* **89**, 377-404.

Whitney, D. L. & Evans, B. W. (2010). Abbreviations for names of rock-forming minerals. *American Mineralogist* **95**, 185-187.

Will, T. M., Powell, R. & Holland, T. (1990). A calculated petrogenetic grid for ultramafic rocks in the system CaO–FeO–MgO–Al_2O_3–SiO_2–CO_2–H_2O at low pressures. *Contributions to Mineralogy and Petrology* **105**, 347-358.

Williams-Jones, A. E., Migdisov, A. A. & Samson, I. M. (2012). Hydrothermal mobilisation of the Rare Earth Elements – a tale of "Ceria" and "Yttria". *Elements* **8**, 355-360.

Woodland, A. B., Bulatov, V. K., Brey, G. P., Girnis, A. V., Höfer, H. E. & Gerdes, A. (2018). Subduction factory in an ampoule: Experiments on sediment–peridotite interaction under temperature gradient conditions. *Geochimica et Cosmochimica Acta* **223**, 319-349.

Zahnle, K., Arndt, N., Cockell, C., Halliday, A., Nisbet, E., Selsis, F. & Sleep, Norman H. (2007). Emergence of a habitable planet. In: Fishbaugh, K. E., Lognonné, P., Raulin, F., Des Marais, D. J. & Korablev, O. (eds.) *Geology and Habitability of Terrestrial Planets*. New York, NY: Springer New York, 35-78.

Zhang, L., Yang, J., Robinson, P. T., Xiong, F., Chen, Y., Lai, S. & Chen, M. (2015). Origin of Listwanite in the Luobusa Ophiolite, Tibet, implications for chromite stability in hydrothermal systems. *Acta Geologica Sinica - English Edition* **89**, 402-417.

Zhang, Z. & Duan, Z. (2005). Prediction of the PVT properties of water over wide range of temperatures and pressures from molecular dynamics simulation. *Physics of the Earth and Planetary Interiors* **149**, 335-354.

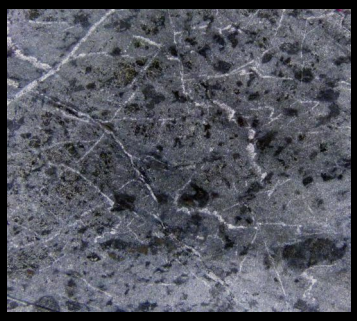

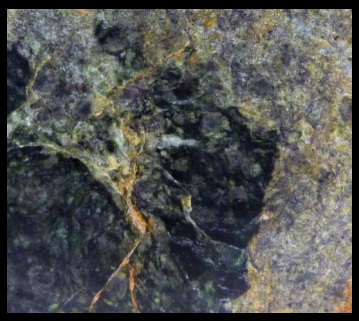


Subduction of oceanic lithosphere is the only active flux of carbon from Earth's atmosphere-hydrosphere-crustal system reservoirs into the deep convecting mantle. Serpentinites in the mantle wedge of the forearc can sequester and store carbon derived from the subducting slab and exert an important control of the carbon mass balance in subduction zones. At subarc depths of subduction zones, devolatilization reactions and fluid-rock interactions mostly regulate the balance between the carbon returned by arc volcanism and that retained and transported by subducting slabs into the deep mantle. Dehydration of antigorite serpentinite at these depths releases large amount of fluids that react with other slab lithologies, playing a decisive role in modulation of the deep carbon fluxes.

The main aim of the present Ph.D. thesis is to improve our understanding of carbonation processes of serpentinized peridotite and the fate of serpentinite-hosted carbon during high-pressure metamorphism, to better constrain their role in the deep carbon cycle of subduction zones. To advance in this overall research goal, this Ph.D. thesis presents the results of two natural case studies of key processes of carbon transfer during fluid-rock interaction in subduction zones: (i) listvenites from the Baie Verte ophiolite (Newfoundland, Canada), a natural analogue for carbon storage in the forearc mantle of subduction zones by carbonation of peridotites; and (ii) meta-ophicarbonates from the Nevado-Filábride Complex (Spain), that provide unprecedented insights into the stability of carbonates during subduction metamorphism and antigorite-serpentinite dehydration. The combination of field, (micro) structural, petrological and geochemical data with thermodynamic modelling sheds new light on the interactions between fluids and the hydrated mantle that regulate carbon mobility at forearc and subarc depths of subduction zones. Using thermodynamic models of prograde and infiltration-driven devolatilization reactions at high pressure in serpentinite-hosted meta-carbonate rocks, this thesis further investigates the effects of electrolytic fluid compositions and open-system flux of serpentinite dehydration fluids on fluid-mediated carbon release in subduction zones.

IACT
INSTITUTO ANDALUZ DE CIENCIAS DE LA TIERRA
Research Group on
Petrology, Geochemistry and Geochronology
Thesis Memoir n°9